

Shanmuganathan Rajasekar Miguel A.F. Sanjuan

Nonlinear Resonances



Springer Complexity

Springer Complexity is an interdisciplinary program publishing the best research and academic-level teaching on both fundamental and applied aspects of complex systems – cutting across all traditional disciplines of the natural and life sciences, engineering, economics, medicine, neuroscience, social and computer science.

Complex Systems are systems that comprise many interacting parts with the ability to generate a new quality of macroscopic collective behavior the manifestations of which are the spontaneous formation of distinctive temporal, spatial or functional structures. Models of such systems can be successfully mapped onto quite diverse "real-life" situations like the climate, the coherent emission of light from lasers, chemical reaction-diffusion systems, biological cellular networks, the dynamics of stock markets and of the internet, earthquake statistics and prediction, freeway traffic, the human brain, or the formation of opinions in social systems, to name just some of the popular applications.

Although their scope and methodologies overlap somewhat, one can distinguish the following main concepts and tools: self-organization, nonlinear dynamics, synergetics, turbulence, dynamical systems, catastrophes, instabilities, stochastic processes, chaos, graphs and networks, cellular automata, adaptive systems, genetic algorithms and computational intelligence.

The three major book publication platforms of the Springer Complexity program are the monograph series "Understanding Complex Systems" focusing on the various applications of complexity, the "Springer Series in Synergetics", which is devoted to the quantitative theoretical and methodological foundations, and the "SpringerBriefs in Complexity" which are concise and topical working reports, case-studies, surveys, essays and lecture notes of relevance to the field. In addition to the books in these two core series, the program also incorporates individual titles ranging from textbooks to major reference works.

Editorial and Programme Advisory Board

Henry Abarbanel, Institute for Nonlinear Science, University of California, San Diego, USA

Dan Braha, New England Complex Systems Institute and University of Massachusetts Dartmouth, USA

Péter Érdi, Center for Complex Systems Studies, Kalamazoo College, USA and Hungarian Academy of Sciences, Budapest, Hungary

Karl Friston, Institute of Cognitive Neuroscience, University College London, London, UK

Hermann Haken, Center of Synergetics, University of Stuttgart, Stuttgart, Germany

Viktor Jirsa, Centre National de la Recherche Scientifique (CNRS), Université de la Méditerranée, Marseille, France

Janusz Kacprzyk, System Research, Polish Academy of Sciences, Warsaw, Poland

Kunihiko Kaneko, Research Center for Complex Systems Biology, The University of Tokyo, Tokyo, Japan

Scott Kelso, Center for Complex Systems and Brain Sciences, Florida Atlantic University, Boca Raton, USA

Markus Kirkilionis, Mathematics Institute and Centre for Complex Systems, University of Warwick, Coventry, UK

Jürgen Kurths, Nonlinear Dynamics Group, University of Potsdam, Potsdam, Germany

Andrzej Nowak, Department of Psychology, Warsaw University, Poland

Hassan Qudrat-Ullah, York University, Toronto, Ontario, Canada

Linda Reichl, Center for Complex Quantum Systems, University of Texas, Austin, USA

Peter Schuster, Theoretical Chemistry and Structural Biology, University of Vienna, Vienna, Austria

Frank Schweitzer, System Design, ETH Zurich, Zurich, Switzerland

Didier Sornette, Entrepreneurial Risk, ETH Zurich, Zurich, Switzerland

Stefan Thurner, Section for Science of Complex Systems, Medical University of Vienna, Vienna, Austria

Springer Series in Synergetics

Founding Editor: H. Haken

The Springer Series in Synergetics was founded by Herman Haken in 1977. Since then, the series has evolved into a substantial reference library for the quantitative, theoretical and methodological foundations of the science of complex systems.

Through many enduring classic texts, such as Haken's *Synergetics and Information and Self-Organization*, Gardiner's *Handbook of Stochastic Methods*, Risken's *The Fokker Planck-Equation* or *Haake*'s *Quantum Signatures of Chaos*, the series has made, and continues to make, important contributions to shaping the foundations of the field.

The series publishes monographs and graduate-level textbooks of broad and general interest, with a pronounced emphasis on the physico-mathematical approach.

More information about this series at http://www.springer.com/series/712

Shanmuganathan Rajasekar • Miguel A.F. Sanjuan

Nonlinear Resonances



Shanmuganathan Rajasekar School of Physics Bharathidasan University Tiruchirappalli, Tamil Nadu India Miguel A.F. Sanjuan Department of Physics Universidad Rey Juan Carlos Móstoles, Madrid, Spain

ISSN 0172-7389 Springer Series in Synergetics ISBN 978-3-319-24884-4 DOI 10.1007/978-3-319-24886-8

ISSN 2198-333X (electronic)

ISBN 978-3-319-24886-8 (eBook)

Library of Congress Control Number: 2015956614

Springer Cham Heidelberg New York Dordrecht London © Springer International Publishing Switzerland 2016

This work is subject to copyright. All rights are reserved by the Publisher, whether the whole or part of the material is concerned, specifically the rights of translation, reprinting, reuse of illustrations, recitation, broadcasting, reproduction on microfilms or in any other physical way, and transmission or information storage and retrieval, electronic adaptation, computer software, or by similar or dissimilar methodology now known or hereafter developed.

The use of general descriptive names, registered names, trademarks, service marks, etc. in this publication does not imply, even in the absence of a specific statement, that such names are exempt from the relevant protective laws and regulations and therefore free for general use.

The publisher, the authors and the editors are safe to assume that the advice and information in this book are believed to be true and accurate at the date of publication. Neither the publisher nor the authors or the editors give a warranty, express or implied, with respect to the material contained herein or for any errors or omissions that may have been made.

Printed on acid-free paper

Springer International Publishing AG Switzerland is part of Springer Science+Business Media (www.springer.com)

To Professor M. Lakshmanan To my parents Isidro and Florentina

Preface

Resonance is one of the fundamental phenomena exhibited by nonlinear systems and is important in physics, engineering and biology. It refers to a realization of a maximum response of a dynamical system. In an oscillating system, the response is primarily due to the ability of the system to store and transfer energy received from an external forcing source into an internal oscillating mode. Resonance can be deterministic or stochastic and can be realized in microscopic and macroscopic systems. Both single and coupled systems can display resonance behaviour. It is beneficial in many applications and also leads to instability and disasters in certain systems.

Resonance can be induced in dynamical systems by means of external forces. Different kinds of external forces give rise to distinct types of resonances. An enhanced maximum response of a system at a frequency due to an external periodic force is termed a forced resonance or simply a resonance. Some of the other fascinating types of resonances are (1) stochastic resonance—induced by a weak noise at the frequency of the applied periodic force, (2) vibrational resonance induced by a high-frequency force at the low-frequency of the external force, (3) coherence resonance—induced by an external noise in the absence of any external periodic force, (4) ghost resonance—induced by a multi-frequency force at a frequency absent in the external force, (5) parametric resonance—induced by a periodic variation of a parameter of the system, (6) autoresonance—induced by an external force with time-dependent frequency and (7) chaotic resonance due to a perturbation of chaotic nature. Among these types, the resonance due to an additive force with a single frequency and parametric resonance occur both in linear and nonlinear systems. Other resonances take place only in nonlinear systems. In addition to the above resonances, in certain systems the amplitude of the response is found to be either zero or minimum at one or more frequencies or at certain values of a control parameter. This phenomenon is termed *antiresonance*. Salient features of the above-mentioned resonances and antiresonance have been investigated in mathematical model equations of physically interesting systems and in real experimental systems. Theoretical procedures and statistical measures are developed to identify and explore the various features of resonances.

viii Preface

In the near future, the features of resonances are expected to lead to advanced technological applications. For example, many macro, micro and nanoscale oscillators and devices working in resonant modes as filters, nonlinear mixers, sensors, atomic scale imaging and amplifiers are found to give rise to higher efficiency and greatly improved performance.

This book presents basic aspects and salient features of the above-mentioned various nonlinear resonances and antiresonance. Particularly, for each resonance, it covers theoretical concepts, illustration, case studies, mechanism, characterization, numerical simulation, experimental realization, quantum analogue, applications and significant progresses made over the years. It is self-contained, mathematical derivations show all the main steps, and the techniques involved in numerical simulation are clearly described so that a reader is able to reproduce the results presented. This is written in a simple language and prototype and paradigmatic model equations are used to illustrate the mechanisms of resonances and describe the theoretical procedures. This is primarily developed as a text at the postgraduate level and also as a reference book for researchers working and/or interested in the dynamics of resonances.

This book is structured into 14 chapters and 3 appendices. The book begins with a detailed introduction to the phenomenon of a forced resonance in Chap. 1. Through a theoretical treatment, the occurrence of resonance in certain physically interesting nonlinear systems driven by a single deterministic periodic external force is discussed. Some notable applications of forced resonances are mentioned. Chapter 2 presents theory, characterization and applications of stochastic resonance, and a quantum analogue of stochastic resonance is pointed out. Chapter 3 is devoted to the theoretical analysis of the biharmonic force induced vibrational resonance in monostable nonlinear systems. Resonance with nonsinusoidal periodic forces, the effect of noise and the role of asymmetry of a potential on resonance are discussed. The features of both stochastic and vibrational resonances in multistable and excitable systems are presented in Chap. 4. Occurrences of both stochastic and vibrational resonances in spatially periodic potential (pendulum) system and in a modified Chua's circuit model equation with periodic characteristic curve of Chua's diode are analysed in Chap. 5. The role of the number of equilibrium points on resonances is explored. Furthermore, the characteristic differences between these two types of resonances are enumerated.

Chapter 6 mainly deals with vibrational resonances in the Duffing oscillator with time-delayed feedback. Notable examples of time-delay in different branches of science are enumerated. The role of constant single time-delay, multiple time-delay, integrative time-delay, distributed time-delay and state-dependent time-delay and the influence of strength of time-delayed feedback are analysed. Next, Chap. 7 reports on the resonance enhanced signal propagation in unidirectionally coupled nonlinear systems. Particularly, the influence of forced, vibrational and stochastic resonances on signal propagation is explored. Chapter 8 covers experimental observation of vibrational resonance in single Chua's circuit, overdamped bistable system, vertical cavity surface emitting laser system, an excitable electronic circuit and unidirectionally coupled Chua's circuits. In the next chapter, ghost-stochastic

Preface

resonance induced by noise and ghost-vibrational resonance due to a high-frequency force are covered. Both single and coupled systems are taken for analysis. The phenomenon of parametric resonance is dealt in Chap. 10. Particularly, its occurrence in certain linear and nonlinear systems, analog circuit simulation results and its certain signatures in quantum systems are presented.

Chapter 11 is devoted to autoresonance. The role of limiting phase trajectories on autoresonance is examined. The features of autoresonance in optical waveguides and four-wave mixing are elucidated. Its quantum analogue is shown to be ladder climbing of energy with time. Coherence resonance and chaotic resonance are treated in Chap. 12. Theory of coherence resonance is presented with reference to a two-state noise driven system. Resonance-like behaviour induced by certain kinds of chaotic perturbations and Gaussian white noise is analysed. The response of linear and nonlinear systems to time-varying frequency of the driving external force and monotonic increase of a parameter with time are discussed in the next chapter. Such perturbations are shown to give rise to a slow passage of trajectories through resonance and resonance tongues. The role of initial conditions on the maximum response is discussed. The final chapter is primarily concerned with the identification and analysis of antiresonance in both single and coupled oscillators. Analog circuit simulation results are also presented. Finally, equilibrium point analysis, analytical expression for the roots of a cubic equation and description of analog circuit construction for an ordinary differential equation are presented in the appendices.

We are indebted to J. Kurths, K. Thamilmaran, V. Chinnathambi, V.M. Gandhimathi, S. Jeyakumari, V. Ravichandran, S. Arathi, C. Jeevarathinam, R. Jothimurugan, J.M. Casado, M. Coccolo, A. Daza, J. Seoane, G. Litak, J. Used, A. Wagemakers, J.H. Yang, S. Zambrano, K. Abirami and S. Rajamani for many years of collaboration without which it would not have been possible to write this book. One of us (S.R) thanks P. Philominathan, T. Arivudainambi, A. Venkatesan and K. Murali for their suggestions and encouragement. All the analog circuit simulation studies presented in this book are prepared in collaboration with K. Thamilmaran and R. Jothimurugan. It is a great pleasure to thank them. Finally, we extend our thanks to our family members for their great support, cooperation and encouragement during the course of preparation of this work.

Tiruchirapalli, Tamil Nadu, India Móstoles, Madrid, Spain July 2015 S. Rajasekar Miguel A.F. Sanjuan

Contents

| Harr | nonic and N | Nonlinear Resonances |
|------|-------------|--|
| 1.1 | Simple E | Examples of Resonance |
| | 1.1.1 | What is the Effect of Resonance? |
| | 1.1.2 | Realization of Periodic Forces |
| 1.2 | Nonlinea | r Resonance in the Duffing Oscillator |
| | 1.2.1 | Theoretical Equation for the Amplitude |
| | | of Oscillation |
| | 1.2.2 | Resonance in a Linear System |
| | 1.2.3 | Hysteresis and Jump Phenomenon |
| | | in the Duffing Oscillator |
| | 1.2.4 | Analog Circuit Simulation |
| | 1.2.5 | Resonance in the Overdamped Duffing Oscillator |
| 1.3 | Pendulur | m System |
| 1.4 | | scillator |
| 1.5 | | nd Nonlinear Jerk Systems |
| 1.6 | Van der I | Pol Oscillator |
| | 1.6.1 | Theoretical Treatment |
| | 1.6.2 | Numerical Verification |
| | | Analog Circuit Simulation |
| 1.7 | Resonance | ce in Micro- and Nano-Electromechanical |
| | | ors |
| | | A Double Clamped 3C-SiC Nanoscale Beam |
| | | A Doubly Clamped Cr-Au Bilayer NEM Resonator |
| 1.8 | | her Examples of Resonance |
| | 1.8.1 | Resonance Magnetoelectric Effect |
| | | Nonlinear Resonance Ultrasonic Spectroscopy |
| | | Crack Breathing and Resonance |
| 1.9 | Quantum | Resonance |
| 1.10 | Applicati | ions of Resonance |

xii Contents

| | 1.11 | Resonance Disaster | 34 |
|---|--------|--|----|
| | 1.12 | Concluding Remarks | 35 |
| | Refere | ences 3 | 36 |
| 2 | Stoch | astic Resonance 3 | 39 |
| | 2.1 | Characterization of Stochastic Resonance | 10 |
| | 2.2 | Stochastic Resonance in Duffing Oscillator | 11 |
| | | 2.2.1 Time-Series Plot 4 | 12 |
| | | 2.2.2 Mean Residence Time | 14 |
| | | 2.2.3 Power Spectrum and SNR 4 | 15 |
| | | | 17 |
| | 2.3 | Theory of Stochastic Resonance | 19 |
| | | 2.3.1 Analytical Expression for Power Spectrum | 50 |
| | | | 53 |
| | 2.4 | Stochastic Resonance in a Coupled Oscillator 5 | 55 |
| | 2.5 | Stochastic Resonance in a Magnetic System 5 | 57 |
| | 2.6 | | 51 |
| | 2.7 | Linear Systems with Additive and Multiplicative Noises 6 | 54 |
| | | | 54 |
| | | | 54 |
| | | | 66 |
| | 2.8 | Stochastic Resonance in Quantum Systems 6 | 59 |
| | | 2.8.1 A Particle in a Double-Well Potential 6 | 59 |
| | | 2.8.2 A Double Quantum Dot System | 70 |
| | 2.9 | | 71 |
| | | | 72 |
| | | | 72 |
| | | | 73 |
| | | | 73 |
| | | 2.9.5 Stochastic Resonance in Sensory and Animal | |
| | | · · · · · · · · · · · · · · · · · · · | 75 |
| | | | 75 |
| | | | 76 |
| | | | 76 |
| | | | 77 |
| | 2.10 | Noise-Induced Stochastic Resonance Versus | |
| | | Noise-Induced Synchronization | 77 |
| | 2.11 | • | 78 |
| | | | 78 |
| 3 | Vibra | ational Resonance in Monostable Systems | 33 |
| | 3.1 | · | 34 |
| | | | 35 |
| | | · | 37 |
| | 3.2 | | 39 |

Contents xiii

| | 3.3 | Quintic | Oscillator | 90 |
|---|--------|-----------------|---|------------|
| | | 3.3.1 | Theoretical Expression for the Response Amplitude | 92 |
| | | 3.3.2 | Single-Well Potential $(\omega_0^2, \beta, \gamma > 0)$ | 93 |
| | | 3.3.3 | Single-Well Potential $(\omega_0^2, \gamma > 0, \beta < 0,$ | |
| | | | $\beta^2 < 4\omega_0^2 \gamma) \dots$ | 96 |
| | | 3.3.4 | Double-Hump Single-Well Potential | |
| | | | $(\omega_0^2 > 0, \beta$ -Arbitrary, $\gamma < 0)$ | 97 |
| | 3.4 | Asymr | netric Duffing Oscillator | 100 |
| | | 3.4.1 | Theoretical Expression for Response Amplitude | 101 |
| | | 3.4.2 | Asymmetry Induced Additional Resonance | 102 |
| | | 3.4.3 | Resonance with Nonsinusoidal Periodic Forces | 103 |
| | | 3.4.4 | Effect of Noise on Resonance | 105 |
| | 3.5 | Overda | amped Asymmetric Duffing Oscillator | 105 |
| | 3.6 | Morse | Oscillator | 106 |
| | 3.7 | Quanti | ım Mechanical Morse Oscillator | 110 |
| | 3.8 | Signifi | cance of Biharmonic Signals | 114 |
| | 3.9 | Conclu | Iding Remarks | 115 |
| | Refere | ences | | 116 |
| 4 | Vihra | tional R | esonance in Multistable and Excitable Systems | 119 |
| • | 4.1 | | damped Double-Well Duffing Oscillator | 120 |
| | | 4.1.1 | Theoretical Approach | 121 |
| | | 4.1.2 | Vibrational Resonance for $\alpha_1 = \alpha_2 = 1$ | 122 |
| | | 4.1.3 | Role of Depth of the Potential Wells | 125 |
| | | 4.1.4 | Role of Location of the Minima of the Potential | 126 |
| | 4.2 | | amped Double-Well Duffing Oscillator | 127 |
| | 4.3 | | ance in a Triple-Well Potential System | 128 |
| | 4.4 | | onal Resonance in an Excitable System | 131 |
| | 4.5 | | stic Resonance in FitzHugh–Nagumo Equation | 134 |
| | 4.6 | | iding Remarks | 136 |
| | | | | 136 |
| _ | | | | |
| 5 | | | nd Stochastic Resonances in Spatially | 120 |
| | | • | ms | 139 |
| | 5.1 | 5.1.1 | onal Resonance in Underdamped Pendulum System | 140 |
| | | 3.1.1 | Analytical Expression for the Response | 140 |
| | | 5.1.0 | Amplitude Q | |
| | | 5.1.2 | Connection Between Resonance and ω_r | |
| | 5.0 | 5.1.3 | * * | |
| | 5.2 | | onal Resonance in Overdamped Pendulum System | 145 |
| | 5.3 | | onal Resonance in a Modified Chua's Circuit Equation | 146 |
| | | 5.3.1 5.3.2 | The Modified Chua's Circuit Model Equation | 146 |
| | | | Role of Number of Breakpoints <i>N</i> on Resonance | 148 |
| | 5.4 | 5.3.3 Stocke | Jump Phenomenon | 150 152 |
| | J.4 | Stocha | Suc Resonance in the Pendulum System | 132 |

xiv Contents

| | 5.5 | | stic Resonance in a Multi-Scroll Chua's | |
|---|--------|----------|--|-----|
| | | | t Equation | 155 |
| | 5.6 | | arison Between Stochastic and Vibrational Resonances | 158 |
| | 5.7 | | iding Remarks | 159 |
| | Refere | ences | | 160 |
| 6 | Nonli | near and | l Vibrational Resonances in Time-Delayed Systems | 161 |
| | 6.1 | Time-I | Delay is Ubiquitous | 162 |
| | 6.2 | Nonlin | ear Resonance in Time-Delayed Duffing Oscillator | 164 |
| | | 6.2.1 | Theoretical Expression for Response Amplitude | 164 |
| | | 6.2.2 | Response Amplitude A Versus the Control | |
| | | | Parameters ω , γ and α | 166 |
| | 6.3 | Resona | ance in a Linear System with Time-Delayed Feedback | 169 |
| | 6.4 | | ional Resonance in an Underdamped | |
| | | and Ti | me-Delayed Duffing Oscillator | 171 |
| | | 6.4.1 | Theoretical Expression for the Response | |
| | | | Amplitude <i>Q</i> | 171 |
| | | 6.4.2 | Resonance Analysis in the Double-Well System | 172 |
| | | 6.4.3 | Resonance Analysis in the Single-Well System | 176 |
| | 6.5 | | ional Resonance in an Overdamped Duffing Oscillator | 177 |
| | 6.6 | | Common Effects of Time-Delayed Feedback | 180 |
| | 6.7 | | of Multi Time-Delayed Feedback | 182 |
| | 6.8 | | ional Resonance with Some Other | |
| | | | Delayed Feedbacks | 185 |
| | | 6.8.1 | Gamma Distributed Time-Delayed Feedback | 185 |
| | | 6.8.2 | Integrative Time-Delayed Feedback | 188 |
| | | 6.8.3 | State-Dependent Time-Delayed Feedback | 190 |
| | | 6.8.4 | Feedback with Random Time-Delay | 195 |
| | 6.9 | Conclu | ading Remarks | 198 |
| | Refere | ences | | 198 |
| 7 | Signa | l Propag | gation in Unidirectionally Coupled Systems | 203 |
| | 7.1 | | cance of Unidirectional Coupling | 204 |
| | 7.2 | Nonlin | near Resonance and Signal Propagation | 206 |
| | | 7.2.1 | Theoretical Treatment | 206 |
| | | 7.2.2 | Analysis of Effect of One-Way Coupling | 208 |
| | | 7.2.3 | Unidirectionally Coupled Linear Systems | 211 |
| | 7.3 | Vibrati | ional Resonance and Signal Propagation | 211 |
| | | 7.3.1 | Theoretical Treatment | 212 |
| | | 7.3.2 | Effect of δ and g on Q_i | 214 |
| | 7.4 | Stocha | stic Resonance and Signal Propagation | 217 |
| | | 7.4.1 | One-Way Coupled Bellows Map | 217 |
| | | 7.4.2 | Numerical Results | 218 |
| | 7.5 | Conclu | ıding Remarks | 222 |
| | Refere | ences | - | 222 |

Contents xv

| 8 | Exper | rimental Observation of Vibrational Resonance | 225 |
|----|--------|---|-----|
| | 8.1 | Single Chua's Circuit | 226 |
| | 8.2 | Analog Simulation of the Overdamped Bistable System | 230 |
| | 8.3 | Vertical Cavity Surface Emitting Laser System | 232 |
| | 8.4 | An Excitable Electronic Circuit | 235 |
| | 8.5 | Unidirectionally Coupled Chua's Circuits | 236 |
| | 8.6 | Concluding Remarks | 239 |
| | Refere | ences | 239 |
| 9 | Ghost | t Resonances | 241 |
| | 9.1 | Ghost-Stochastic Resonance in a Single System | 242 |
| | | 9.1.1 System with Periodic Forces | 242 |
| | | 9.1.2 System with Aperiodic Forces | 245 |
| | 9.2 | Ghost-Stochastic Resonance in a Network System | 247 |
| | 9.3 | Ghost-Vibrational Resonance in a Single System | 249 |
| | | 9.3.1 Theoretical Calculation of $Q(\omega_0)$ | 250 |
| | 9.4 | Effect of k , n and $\Delta\omega_0$ on Resonance | 253 |
| | 9.5 | Ghost-Vibrational Resonance in a Network System | 255 |
| | | 9.5.1 Description of the Network Model | 255 |
| | | 9.5.2 Undamped Signal Propagation | 255 |
| | | 9.5.3 A Network with All the Units Driven | |
| | | by External Forces | 257 |
| | 9.6 | Ghost-Vibrational Resonance in Chua's Circuit | 258 |
| | 9.7 | Concluding Remarks. | 259 |
| | Refere | ences | 260 |
| 10 | Paran | netric Resonance | 261 |
| | 10.1 | Examples of Parametric Resonance | 262 |
| | 10.2 | Parametric Instability in a Linear System | 263 |
| | 10.2 | 10.2.1 Illustration of Parametric Resonance | 264 |
| | | 10.2.2 Theoretical Treatment | 267 |
| | | 10.2.3 Analog Simulation | 268 |
| | 10.3 | Parametrically Driven Pendulum | 270 |
| | 10.0 | 10.3.1 Effective Parametric Resonance | 274 |
| | 10.4 | The Quasiperiodic Mathieu Equation | 276 |
| | 10.5 | Quantum Parametric Resonance in a Two-Coupled Systems | 280 |
| | 10.6 | Applications | 285 |
| | 10.0 | 10.6.1 Parametric Resonance Based Scanning | 203 |
| | | Probe Microscopy | 287 |
| | 10.7 | Concluding Remarks. | 288 |
| | | ences | 289 |
| | | | |
| 11 | | resonance | 293 |
| | 11.1 | Illustration of Autoresonance | 294 |
| | 11.2 | Threshold Analysis | 295 |

xvi Contents

| | 11.3 | Parametric Autoresonance in the Duffing Oscillator | 299 |
|----|--------|---|-----|
| | | 11.3.1 Approximate Solution | 300 |
| | | 11.3.2 Analytical Theory of Parametric Autoresonance | 301 |
| | | 11.3.3 Dynamics in the Neighbourhood of (I^*, ψ^*) | 303 |
| | | 11.3.4 Analytical Solution of Equation (11.33) | 305 |
| | | 11.3.5 Dynamics for Arbitrary Initial Conditions | 306 |
| | | 11.3.6 Effect of Damping | 306 |
| | 11.4 | Autoresonance and Limiting Phase Trajectories | 307 |
| | | 11.4.1 Approximate Solution | 308 |
| | | 11.4.2 Limiting Phase Trajectories | 309 |
| | | 11.4.3 Autoresonance | 313 |
| | 11.5 | Autoresonance in Optical Guided Waves | 314 |
| | 11.6 | Energy Conversion in a Four-Wave Mixing | 316 |
| | 11.7 | Autoresonance in a Nonlinear Wave System | 319 |
| | 11.8 | A Quantum Analogue of Autoresonance | 322 |
| | 11.9 | Applications | 326 |
| | 11.10 | Concluding Remarks | 329 |
| | Refere | nces | 329 |
| 12 | Coher | ence and Chaotic Resonances | 333 |
| | 12.1 | An Illustration of Coherence Resonance | 334 |
| | 12.2 | Mechanism of Coherence Resonance | 336 |
| | 12.3 | Coherence Resonance in a Modified Chua's Circuit | |
| | | Model Equations | 337 |
| | 12.4 | Theory of Coherence Resonance | 340 |
| | | 12.4.1 A Two-State Model | 341 |
| | 12.5 | Chaotic Resonance | 344 |
| | | 12.5.1 Generating Similar Noise and Chaos | 345 |
| | | 12.5.2 Effect of Chaotic Perturbations | 347 |
| | 12.6 | Conclusion | 349 |
| | Refere | nces | 349 |
| 13 | Slow P | Passage Through Resonance and Resonance Tongues | 351 |
| | 13.1 | Passage Through Resonance in Duffing Oscillator | 352 |
| | 13.2 | Mathieu Equation with Parametric Perturbation | 356 |
| | | 13.2.1 Single Parametric Resonance | 356 |
| | | 13.2.2 Theoretical Treatment | 358 |
| | | 13.2.3 Two Parametric Resonance | 360 |
| | | 13.2.4 Three Resonance Tongues | 363 |
| | 13.3 | Nonlinear Systems with Parametric Perturbation | 363 |
| | 13.4 | Concluding Remarks. | 365 |
| | Refere | | 366 |

Contents xvii

| | 14.1 | Multiple Resonance and Antiresonance in Coupled Systems | |
|--------|------------------------------------|--|--|
| | | | 36 |
| | | 14.1.1 Theoretical Treatment for Two-Coupled Oscillators | 36 |
| | | 14.1.2 Resonance and Antiresonance in a Linear System | 37 |
| | | 14.1.3 Two-Coupled Duffing Oscillators | 37 |
| | | 14.1.4 Analog Simulation of Two-Coupled Duffing | |
| | | Oscillators | 37 |
| | | 14.1.5 Response of <i>n</i> -Coupled Oscillators | 37 |
| | 14.2 | Parametric Antiresonance | 37 |
| | | 14.2.1 Parametrically Driven van der Pol Oscillator | 37 |
| | 14.3 | Suppression of Parametric Resonance | 38 |
| | 14.4 | Stochastic Antiresonance | 38 |
| | 14.5 | Coherence Antiresonance | 38 |
| | 14.6 | Concluding Remarks | 38 |
| | Refere | ences | 38 |
| | | | |
| | Closes | fication of Equilibrium Points of Two-Dimensional Systems | 20 |
| A | Classi | incution of Equilibrium Forms of Two Emicusional Systems | 39 |
| | | ence | |
| | Refere | ence | 39 |
| В | Refere Roots | of a Cubic Equation | 39 39 |
| В | Refere Roots | ence | 39 |
| В | Refere Roots Refere | of a Cubic Equation | 39 39 39 |
| B C | Refere Roots Refere | of a Cubic Equation | 39 39 |
| B C | Refere Roots Refere Analo | of a Cubic Equation | 39 39 39 39 |
| B C | Refere Roots Refere Analo | of a Cubic Equation ence g Circuit Simulation of Ordinary Differential Equations Building Blocks of an Analog Circuit C.1.1 Inverting Amplifier | 39 39 39 |
| B C | Refere Roots Refere Analo | of a Cubic Equation | 39 39 39 39 40 |
| B C | Refere Roots Refere Analo | of a Cubic Equation ence g Circuit Simulation of Ordinary Differential Equations Building Blocks of an Analog Circuit C.1.1 Inverting Amplifier C.1.2 An Inverting Summing Amplifier C.1.3 A Subtractor | 39 39 39 39 40 40 |
| B C | Refere Roots Refere Analo | of a Cubic Equation ence g Circuit Simulation of Ordinary Differential Equations Building Blocks of an Analog Circuit C.1.1 Inverting Amplifier C.1.2 An Inverting Summing Amplifier C.1.3 A Subtractor C.1.4 An Integrator | 39 39 39 39 40 40 40 |
| B C | Refere Roots Refere Analo | of a Cubic Equation ence g Circuit Simulation of Ordinary Differential Equations Building Blocks of an Analog Circuit C.1.1 Inverting Amplifier C.1.2 An Inverting Summing Amplifier C.1.3 A Subtractor | 39 39 39 39 40 40 40 40 |

Chapter 1 Harmonic and Nonlinear Resonances

A physical system can be constituted by a single particle or a collection of particles. When a system exhibits a to-and-fro motion it is called an *oscillator*. A familiar example of an oscillator is a wall-clock pendulum. The oscillation of an oscillator can be periodic, quasiperiodic or even chaotic (which is a bounded nonperiodic motion of a deterministic nonlinear system with a high sensitive dependence on the initial conditions [1–3]). Oscillations are called *free* or *natural* when they take place after some initial action on a system in absence of any external forces. In a real physical system the amplitude of the natural oscillations decay due to the energy dissipation, and in the long time limit the system comes to a rest state which is an equilibrium position.

When the oscillations are due to the effect of an applied external periodic force, they are commonly termed as *forced*. Typically, a forced oscillation gets its steady state after a transient motion. The period of the forced periodic oscillation is an integral multiple of the period of the periodic driving force. Suppose that we increase the frequency ω of the external periodic force from a small value. In a typical case, the amplitude of the oscillation increases, reaches a significantly large value at a certain value of the frequency and then decreases with further increase in the value of the frequency ω . This phenomenon where a maximum amplitude appears is called a *resonance* [4–7]. For example, a pendulum can be excited to a high amplitude with a weak periodic driving force by varying the angular frequency ω of the driving force. The frequency at which the amplitude of oscillation becomes maximum is termed as *resonant frequency*. When the system is linear and the damping is weak the resonant frequency is approximately equal to the natural frequency ω_0 of the system. At the resonant frequency, even a small amplitude periodic driving force will be able to produce large amplitude oscillations.

The term resonance (from Latin *resonantia* 'echo,' from *resonare* 'resound') originates from the field of acoustics, particularly realized in musical instruments, e.g., when strings, without direct excitation by the player, started to vibrate and to produce sound. In the year 1739 the Swiss mathematician and physicist Leonhard

1

Euler (1707–1783) solved the ordinary differential equation governing a forced harmonic oscillator and found the resonance phenomenon. Taking an initially cautionary approach to resonance analysis, the Italo-French mathematician Joseph Louis Lagrange (1736–1813) first explored the various concepts of resonance by working with sound and music. Later, Hermann von Helmholtz (1821–1894), a German physicist, also wrote extensively on the phenomenon of resonance, particularly with respect to the physics of music, sound waves and the mechanics of the human ear. Of special importance is his book *On the Sensations of Tone as a Physiological Basis for the Theory of Music* [8] where it first appeared a nonlinear system with a quadratic nonlinearity.

Resonance occurs in linear and nonlinear systems. However, there are some similarities and differences between linear and nonlinear resonances. Resonance occurs in many branches of physics, engineering and biology. We have mechanical resonance (resonant vibrations of mechanical devices like a playground swing and a quartz watch), acoustic resonance (resonant vibrations in musical instruments and human vocal cords), electrical resonance (resonance of tuned circuits in televisions and radios) and optical resonance (creation of coherent light in a laser cavity). Certain objects show resonance due to vibrations inside them (called *resonators*). Examples include vibrating strings, quartz crystals, microwave cavities and laser rods.

The present chapter discusses resonance in deterministic dynamical systems, both linear and nonlinear, induced by a single periodic force and then it points out some of its applications.

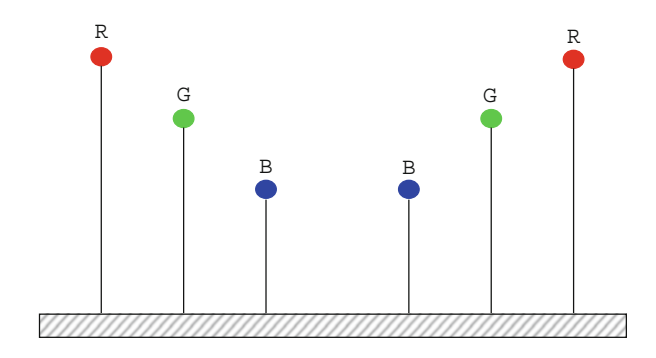
1.1 Simple Examples of Resonance

A classic and simple example of resonance is the oscillatory motion of a swing in a playground. The rest state of the swing is its stable equilibrium position. Suppose a mother is pushing her child on a swing. To start with, the mother pulls the seat of the swing back and releases it. The swing moves toward the equilibrium position then moves up again on the other side. At the equilibrium point its speed is the largest. When the speed becomes zero at the other side, then the swing reverses its direction. If the mother gives no further pushes then due to the friction of the chain of the swing against the support along the bar, the amplitude of the oscillation of the swing decreases and finally it would come to a halt. In order to make the swing to move to-and-fro without a halt, the mother has to push the swing at the right time. The right time is the one at which the swing is at its maximum amplitude. At this moment, the pushing motion of the mother and the motion of the swing are in resonance.

Galileo Galilei (1564–1642) described an instance of resonance that is still used in the ringing of heavy free-swinging tower bells:

"Even as a boy, I observed that one man alone by giving impulses at the right instant was able to ring a bell so large that when four, or even six, men seized the

Fig. 1.1 An experimental setup to realize a large vibration due to resonance



rope and tried to stop it they were lifted from the ground, all of them together being unable to counterbalance the momentum which a single man, by properly timed pulls, had given it."

1.1.1 What is the Effect of Resonance?

The effect of resonance is to produce a large vibration. This can be easily realizable. Consider an apparatus consisting of, say, three set of two identical plastic bobs mounted on an elastic metal pole which are then mounted on a metal bar as shown in Fig. 1.1 (http://www.physicsclassroom.com). The lengths of the metal poles are different so that the natural frequencies of vibrations of the attached bobs are different. To distinguish the bobs they can be coloured. Let the bobs attached with longer and shorter poles to be coloured red and blue, respectively. The bob attached to the intermediate pole is coloured green. The natural frequency of the red colour bob is smaller, while that of the blue colour bob is the highest. Suppose a red bob is disturbed. It does not only vibrate with its natural frequency, but it also forces the attached bar to exhibit a vibration at the same frequency. This in turn drives the other red bob into vibration at the same natural frequency. The mechanism for the vibration of the second red bob is precisely the resonance. The first red bob vibrating at a given natural frequency forces the second red bob with the same frequency. Though the green and blue bobs are also disturbed by the vibration of the first bob, only the second red bob vibrates with a large amplitude.

1.1.2 Realization of Periodic Forces

In the context of the resonance one speaks about systems driven by one or more external periodic forces. Often, a periodic force is treated as a simple external

perturbation to induce oscillatory motion and different nonlinear phenomena in damped nonlinear oscillators. In many physical, engineering and biological systems, as well as in electronic circuits, it is not only easy to introduce a periodic force but it also represents an inherent part of them. For example, a periodic force represents a periodic seasonal variation in ecological systems [9], an injection current in lasers [10], imaging and audio pumping waves in an acoustic field [11], oscillations introduced to mechanical devices by means of a electromagnetic vibration generator [3], an input voltage/current source in electronic circuits [3, 12], membrane current in neuronal axons [13, 14], pacemakers' activity in real life systems [15], an applied illumination in photolithography-assisted techniques in chemical reactions [16, 17] and so on.

1.2 Nonlinear Resonance in the Duffing Oscillator

For certain types of nonlinear systems, particularly oscillators with polynomial type potentials or forces, it is possible to obtain an approximate theoretical expression for the oscillation amplitude and then one can analyse the occurrence of resonance as well as the effect of various parameters on the resonance. This section considers this for the ubiquitous Duffing oscillator.

Consider the Duffing oscillator equation

$$\ddot{x} + d\dot{x} + \omega_0^2 x + \beta x^3 = f \cos \omega t . \tag{1.1}$$

This model was introduced by the German Electrical Engineer Georg Caspar Duffing (1861–1944) in 1918 [18] to describe the hardening spring effect observed in several mechanical problems and is used as a prototype model to investigate various nonlinear phenomena. In Eq. (1.1) ω_0 is the natural frequency, β is the stiffness constant and d is the damping constant. Equation (1.1) can be treated as the equation of motion of a particle of unit mass in the potential well

$$V(x) = \frac{1}{2}\omega_0^2 x^2 + \frac{1}{4}\beta x^4 \tag{1.2}$$

subjected to a viscous drag force of strength d and driven by an external periodic force of frequency ω and amplitude f. In recent years micro- and nano-mechanical oscillators are developed as an alternative to the conventional oscillators (such as quartz oscillators) due to their compatibility with typical semiconductor processing and high sensitivity. The most popular and the simplest resonator utilized in micro- and nano-mechanical resonant sensors is the clamped-clamped (c-c) beam resonator [19]. The dynamics of a c-c beam is modelled by the damped and forced Duffing oscillator equation. Resonance behaviour has been studied in an experimental

system consisting of a short, cylindrical ferrite magnet hanging from a soft steel spring [20]. The mathematical model equation of this system is shown to be the Duffing oscillator equation.

1.2.1 Theoretical Equation for the Amplitude of Oscillation

For small values of β and f it is reasonable to expect a periodic motion of the system with period $2\pi/\omega$. Suppose ω_0^2 and $\beta>0$. Then in absence of the driving force $f\cos\omega t$, the system (1.1) has only one equilibrium point and is $(x,\dot{x})=(0,0)$. The determination of equilibrium points (fixed points) and their stability analysis are presented in the Appendix A. The equilibrium points of (1.1) without $f\cos\omega t$ can be obtained by substituting $\dot{x}=0$ and $\ddot{x}=0$. Obviously the equilibrium point $(x,\dot{x})=(0,0)$ is unstable in the presence of the driving force. Oscillatory motion takes place about this equilibrium point.

Assume the periodic solution of (1.1) as

$$x(t) = a(t)\cos\omega t + b(t)\sin\omega t, \qquad (1.3)$$

where a(t) and b(t) are slowly varying functions of time t. If an oscillatory motion occurs in a system about a point which is not the origin, then in Eq. (1.3) one can add c(t). For example, when $\omega_0^2 < 0$ and $\beta > 0$ the system (1.1) has three equilibrium points and are $(x_0, \dot{x}_0) = (0, 0)$ and $(x_{\pm}, \dot{x}_0) = (\pm \sqrt{|\omega_0^2|/\beta}, 0)$. The origin is unstable while the other two are stable for f = 0. For $|f| \ll 1$ periodic orbits with period $2\pi/\omega$ occurs about the points (x_{\pm}, \dot{x}_0) . In this case, it is necessary to include c(t) in the solution (1.3). Furthermore, if the potential of the system is asymmetric about the origin, then c(t) is necessary in the solution (1.3).

Substitution of the solution (1.3) and

$$x^{3} \approx \frac{3}{4} \left(a^{2} + b^{2} \right) \left(a \cos \omega t + b \sin \omega t \right) \tag{1.4}$$

in Eq. (1.1), neglecting \ddot{a} , \ddot{b} , $d\dot{a}$ and $d\dot{b}$ as they are assumed to be small and then equating the coefficients of $\sin \omega t$ and $\cos \omega t$ separately to zero give

$$\dot{a} = -\frac{b}{2\omega} \left[\omega^2 - \omega_0^2 - \frac{3}{4}\beta \left(a^2 + b^2 \right) \right] - \frac{1}{2}da , \qquad (1.5a)$$

$$\dot{b} = \frac{a}{2\omega} \left[\omega^2 - \omega_0^2 - \frac{3}{4}\beta \left(a^2 + b^2 \right) \right] - \frac{1}{2}db + \frac{f}{2\omega} . \tag{1.5b}$$

Introducing the transformation

$$a(t) = A(t)\cos\phi(t), \quad b(t) = A(t)\sin\phi(t) \tag{1.6}$$

with $A^2 = a^2 + b^2$, Eq. (1.5) become

$$\dot{A} = -\frac{1}{2}dA + \frac{f}{2\omega}\sin\phi,\tag{1.7a}$$

$$A\dot{\phi} = \frac{A}{2\omega} \left[\omega^2 - \omega_0^2 - \frac{3}{4}\beta A^2 \right] + \frac{f}{2\omega} \cos \phi . \tag{1.7b}$$

In the long time limit, after a transient motion, the solution (1.3) becomes periodic with period $2\pi/\omega$ provided a(t) and b(t) become constants as $t \to \infty$. The limiting values of a and b are related to the equilibrium points of Eq. (1.7) and are obtained by setting $\dot{A} = \dot{\phi} = 0$, $A(t) = A^*$, $\phi(t) = \phi^*$ and dropping '*' in A and ϕ for simplicity. The result is

$$dA\omega = f\sin\phi,\tag{1.8a}$$

$$A\left[\omega_0^2 - \omega^2 + \frac{3}{4}\beta A^2\right] = f\cos\phi \ . \tag{1.8b}$$

From Eq. (1.8) it is easy to obtain

$$A^{2} \left[\left(\omega_{0}^{2} - \omega^{2} + \frac{3}{4} \beta A^{2} \right)^{2} + d^{2} \omega^{2} \right] - f^{2} = 0$$
 (1.9)

and

$$\phi = \tan^{-1} \left[\frac{d\omega}{\omega_0^2 - \omega^2 + \frac{3}{4}\beta A^2} \right] . \tag{1.10}$$

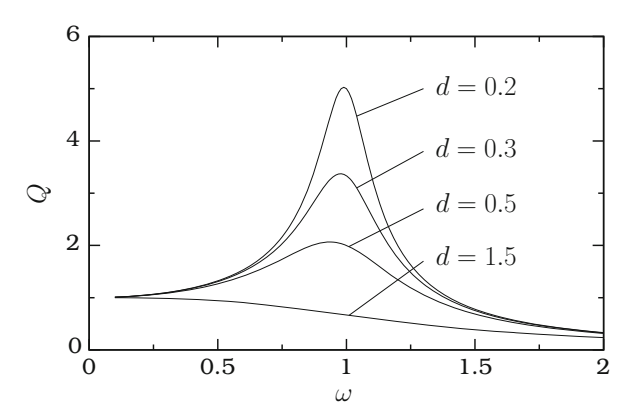
We define the quantity A/f as the response amplitude Q. The oscillation amplitude A or the response amplitude Q of the Duffing oscillator is given through Eq. (1.9) and is called *frequency-response equation* [3, 7]. For fixed values of the parameters, A or Q can be determined by solving Eq. (1.9). The frequency-response analysis is widely utilized by practising engineers to understand the behaviour of a system.

1.2.2 Resonance in a Linear System

Before studying the resonance in the nonlinear system (1.1) using Eq. (1.9) we will consider the linear system ($\beta = 0$) with $\omega_0^2 = 1$ and f = 0.1. The response amplitude of the oscillation of the linear system is given by

$$Q = \frac{A}{f} = \frac{1}{\sqrt{S}}, \quad S = (\omega_0^2 - \omega^2)^2 + d^2\omega^2.$$
 (1.11)

Fig. 1.2 Frequency-response curves of the linear version of Eq. (1.1) ($\beta=0$) for few values of the damping coefficient d with $\omega_0^2=1$ and f=0.1



The condition for Q to be maximum is $dS/d\omega = 0$ and $d^2S/d\omega^2 < 0$. From these conditions the value of ω at which Q becomes maximum is obtained as

$$\omega_{\text{max}} = \sqrt{\omega_0^2 - \frac{d^2}{2}} \,. \tag{1.12}$$

There is no resonance for $d>\sqrt{2\omega_0^2}$. Figure 1.2 shows the influence of the damping coefficient d on the response amplitude Q. For each fixed value of $d<\sqrt{2\omega_0^2}$ as ω increases from a small value, Q increases and reaches a maximum value at $\omega=\omega_{\max}$ given by Eq. (1.12) and then decreases. The value of Q at ω_{\max} decreases for increasing values of d. Furthermore, Q is a single-valued function of ω . Moreover, in Fig. 1.2 notice that the linear system always responds in the same manner as we sweep the angular frequency ω in the forward and reverse directions. However, nonlinear systems display different responses for forward and reverse sweep for certain range of parameter values as shown in the following.

1.2.3 Hysteresis and Jump Phenomenon in the Duffing Oscillator

For the Duffing oscillator system in Eq. (1.9) the powers of A are even and the highest power is 6. Hence, with $A' = A^2$ the frequency-response Eq. (1.9) becomes a cubic equation for the amplitude A'. Since +A and -A represent oscillatory solutions with the same amplitude, Eq. (1.9) can have either three real roots or only one real root. Ready-made formulas are available for the roots of cubic Eq. (1.9) [21]. In this book cubic equations occur at many places in studying the resonance

dynamics. All the real roots of them have to be determined for the analysis of the underlying resonance behaviour. Therefore, in Appendix B the analytical method of determining all the roots of a general cubic equation is presented. For Eq. (1.9) there is another simple way for the calculation of a possible value of A.

From Eq. (1.9) one can write

$$\omega = \frac{1}{2} \left[\left(2\alpha - d^2 \right) \pm \sqrt{\left(2\alpha - d^2 \right)^2 + 4 \left(\frac{f^2}{A^2} - \alpha^2 \right)} \right] , \qquad (1.13a)$$

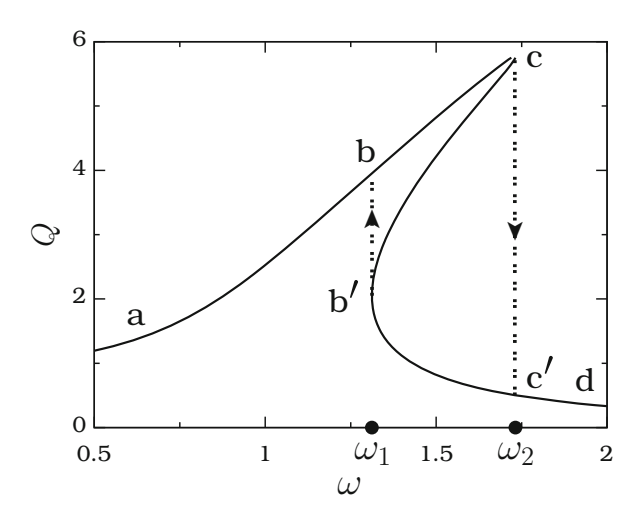
where

$$\alpha = \omega_0^2 + \frac{3}{4}\beta A^2 \,. \tag{1.13b}$$

This equation can be used to draw the frequency-response $(\omega - A)$ or $(\omega - Q)$ curve. Start with a small value of A with increment, say, 0.005. For each value of A calculate the corresponding values of ω and then plot ω versus Q(=A/f).

Figure 1.3 shows the plot of Q versus ω for $\omega_0^2 = 1$, d = 0.1, $\beta = 2$ and f = 0.2. The frequency-response is not symmetric about $\omega = \omega_0$, but it leans to the right (for $\beta > 0$) of $\omega = \omega_0$. For $\omega_1 < \omega < \omega_2$ there are three possible values of Q and only one value for the rest of the intervals of ω . The multi-valuedness of Q leads to *jump* or *hysteresis phenomenon*. When the angular frequency ω of the external periodic force increases from a small value, the response amplitude Q increases steadily and reaches a maximum value ω at $\omega = \omega_2$. Further increase of ω gives rise to a sudden discontinuous jump of Q from ω to ω . When ω is varied in the forward direction from a small value, then ω follows the path abcc'd. In contrast to this, if ω decreases from a large value, then ω follows the path dc'b'ba. That is,

Fig. 1.3 Frequency-response of the Duffing oscillator, Eq. (1.1), with $\omega_0^2 = 1$, d = 0.1, $\beta = 2$ and f = 0.2



there is no jump at $\omega = \omega_2$, however there occurs a jump at $\omega = \omega_1$ from a lower value to a higher value of Q. The response amplitude traces two different paths in the interval $[\omega_1, \omega_2]$ when ω is varied in the forward and reverse directions resulting in the hysteresis phenomenon. The portion b'c of the response curve is unstable and cannot be realized in numerical and experimental simulations. The values of ω_1 and ω_2 obtained in the numerical simulation are 1.31 and 1.74, respectively, while their values calculated from theoretical analysis are 1.31 and 1.73, respectively.

We can numerically integrate Eq. (1.1) with an initial condition $(x(0), \dot{x}(0))$ starting near the origin for the starting value of ω . Leave the solution corresponding to, say, first 500 drive cycles as a transient and then using the solution over the next few drive cycles compute the oscillation amplitude A(Q) is then A/f. For the next value of ω we can use the last value of (x, \dot{x}) of the previous ω as the initial condition. Continuing this process over the chosen range of values of ω , the path abcc'd can be realized. To observe dc'b'ba, we can repeat the above by starting from the large value of ω and decreasing it step by step.

For $\omega < \omega_1$ and $\omega > \omega_2$ the system (1.1) admits only one periodic solution with period $T = 2\pi/\omega$. For $\omega \in [\omega_1, \omega_2]$ there are two stable periodic solutions (corresponding to the branches bc and b'c') and one unstable solution (the branch b'c). Figure 1.4 displays the phase portrait of the orbits for $\omega = 1 < \omega_1$, 1.4 (lying in the interval $[\omega_1, \omega_2]$) and $2 < \omega_2$). For $\omega = 1.4$ there are two stable periodic orbits. One orbit has a small amplitude while the amplitude of the other orbit is relatively large. These two orbits are realized for a different set of initial conditions.

The effect of the parameters d, β and f on the resonance can be studied from Eq. (1.9). Figure 1.5a illustrates the effect of the nonlinear coefficient β . For $\beta < 0$ and > 0 the response amplitude curves lean towards left-side and right-side, respectively. In quasiperiodic photonic crystals based on the so-called Thue-Morse sequence and with the Kerr (or cubic) nonlinearity, an intensity-dependent self-phase modulation is noticed. This effect is found to shift the resonance frequencies. The direction of the shift depends on the sign of the coefficient of the nonlinearity. For a positive nonlinear coefficient the resonances in the transmission spectrum is found to bend towards the bandgap regions [22].

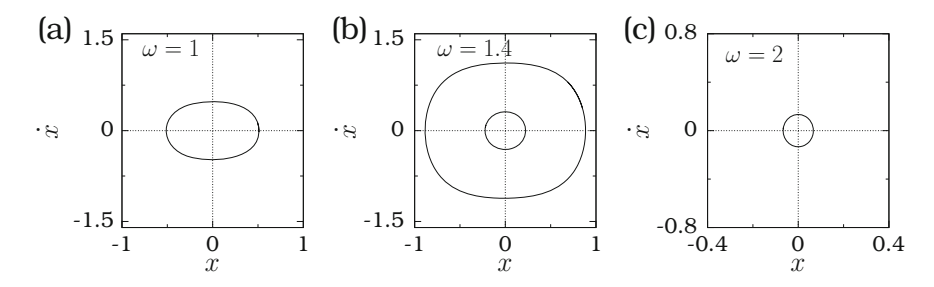


Fig. 1.4 Phase portrait of the orbits of the Duffing oscillator Eq. (1.1) for three values of ω . (a) $\omega = 1$, (b) $\omega = 1.4$ and (c) $\omega = 2$. The values of the other parameters are $\omega_0^2 = 1$, d = 0.1, $\beta = 2$ and f = 0.2

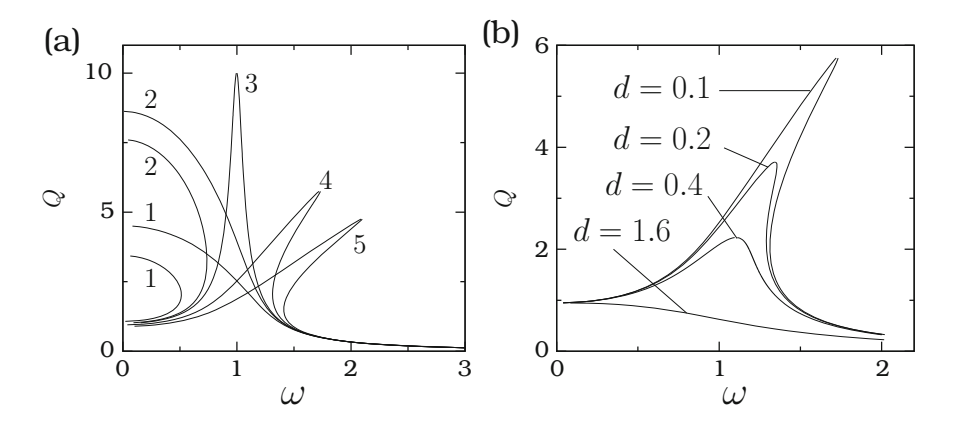


Fig. 1.5 Q versus ω for few values of (**a**) β and (**b**) d for the Duffing oscillator with $\omega_0^2 = 1$ and f = 0.2. In the subplot (**a**) the values of β for the curves 1–5 are -2, -0.5, 0, 2 and 5, respectively and d = 0.1. For the subplot (**b**) the value of β is 2

The role of the damping coefficient d on the resonance is clearly seen in Fig. 1.5b. Both ω_{max} and Q_{max} decrease for increasing values of d. For d values greater than a critical value, there is no resonance. For example, in Fig. 1.5b for d=1.6, Q decreases continuously with ω .

1.2.4 Analog Circuit Simulation

The resonance behaviour found in the Duffing oscillator can be realized in the real experimental systems including the analog circuit simulation of Eq. (1.1). In this book certain resonance phenomena will be demonstrated through an analog circuit simulation of the equation of motion of certain systems. In view of this in Appendix C the construction of analog circuits for the evolution equations described by ordinary differential equations is shown. One can construct an analog circuit for certain types of ordinary differential equations either using real electronic circuit elements or through a circuit simulation software.

The details of the construction of an analog circuit for the Duffing oscillator is presented in Appendix C. Figure C.5 shows an analog circuit for Eq. (1.1). In this circuit instead of the driving force $\cos \omega t$ the force $\sin \omega t$ is used. The circuit is constructed using real circuit elements. In the circuit, we fix the values of the parameters as $R1 = 100 \,\mathrm{k}\Omega$, $R2 = 10 \,\mathrm{k}\Omega$, and $R3 = 10 \,\mathrm{k}\Omega$, $C = 100 \,\mathrm{nf}$ and $F = 0.1 \,\mathrm{V}$. The corresponding values of the parameters in Eq. (C.15) are then computed as d = 0.1, $\omega_0^2 = 1$, $\beta = 1$ and f = 0.1. Figure 1.6a, b present the frequency-response curves obtained in the numerical and analog circuit simulation

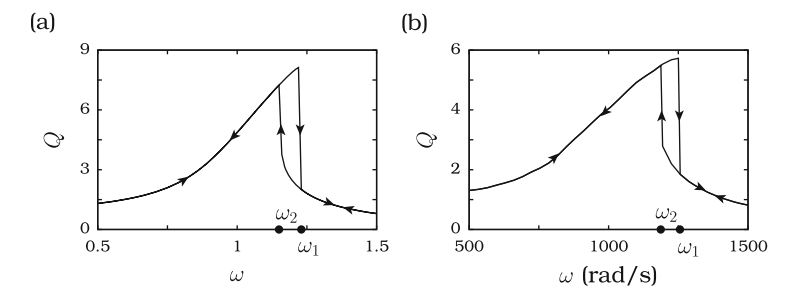


Fig. 1.6 Frequency-response curves of the Duffing oscillator obtained by (a) numerical and (b) analog circuit simulations

of Eq. (C.14). The qualitative features of the curves in the two simulations are the same. In the numerical simulation the values of ω_1 and ω_2 are 1.23 and 1.15, respectively. In the analog circuit simulation ω_1 and ω_2 are 1.26 and 1.19, respectively.

1.2.5 Resonance in the Overdamped Duffing Oscillator

The overdamped version of the system (1.1) is given by

$$\dot{x} + \omega_0^2 x + \beta x^3 = f \cos \omega t . \tag{1.14}$$

Seeking the solution of the form of Eq. (1.3) gives

$$\dot{A} = -\omega_0^2 A - \frac{3}{4}\beta A^3 + f\cos\phi , \qquad (1.15a)$$

$$A\dot{\phi} = A\omega - f\sin\phi \ . \tag{1.15b}$$

From the steady state solution of Eq. (1.15) the equations for A and ϕ are obtained as

$$A^{2} \left[\omega^{2} + \left(\omega_{0}^{2} + \frac{3}{4} \beta A^{2} \right)^{2} \right] = f^{2}$$
 (1.16)

and

$$\phi = \tan^{-1}\left(\frac{\omega}{\omega_0^2 + \frac{3}{4}\beta A^2}\right). \tag{1.17}$$

Fig. 1.7 Frequency-response curve for the overdamped Duffing system with $\omega_0^2=1$, f=0.2 and for the two values of β

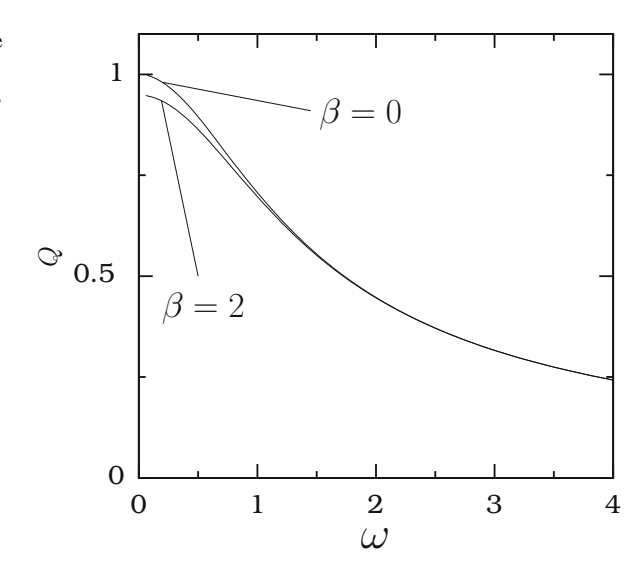


Figure 1.7 shows Q(=A/f) as a function of ω for $\beta=0$ and 2 with $\omega_0^2=1$ and f=0.2. Q decreases rapidly with ω and there is no resonance in both linear and nonlinear systems.

The next few sections are devoted to a brief discussion about the resonant dynamics in certain physically important linear and nonlinear systems.

1.3 Pendulum System

The equation of motion of a pendulum bob in a resistive medium with damping coefficient d and driven by a periodic force is given by

$$\ddot{\theta} + d\dot{\theta} + \sin\theta = f\cos\omega t . \tag{1.18}$$

The above equation is widely studied because it models many physical phenomena. For example, it describes the dynamics of rf-driven Josephson junction and phase-locked voltage-controlled oscillations. A detailed review of the theoretical and experimental investigation of various nonlinear dynamics of Eq. (1.18) was presented in [23–26]. In the absence of damping and external periodic force the potential of the pendulum system is $V(\theta) = -\cos\theta$ and is spatially periodic. A feature of the undamped and periodically driven pendulum is that it exhibits

anomalous and normal diffusions for a range of values of the angular frequency ω [27–29].

Seeking the solution of (1.18) in the form (1.3) and for small values of f, a(t) and b(t), approximating

$$\sin \theta \approx \theta - \frac{1}{6} \theta^{3}$$

$$\approx a \cos \omega t + b \sin \omega t - \frac{1}{8} (a^{2} + b^{2}) (a \cos \omega t + b \sin \omega t) \qquad (1.19)$$

and following the same procedure used for the Duffing oscillator in the previous section lead to (with $A^2 = a^2 + b^2$)

$$A^{2} \left[\left(1 - \omega^{2} - \frac{1}{8} A^{2} \right)^{2} + d^{2} \omega^{2} \right] - f^{2} = 0.$$
 (1.20)

We compare the frequency-response Eq. (1.20) of the pendulum system with that of the Duffing oscillator given by Eq. (1.9). In the approximation (1.19), since the coefficient of the nonlinear term becomes negative the response amplitude lean towards the left-side as shown in Fig. 1.8a, where d=0.04 and f=0.05. When ω is increased from a small value, the response amplitude Q follows the path abcc'd and a sudden jump from a lower value to a higher value takes place at $\omega=0.9385$. As ω decreases from a large value the jump occurs at $\omega=0.856$. The effect of the damping strength d on the response amplitude is shown in Fig. 1.8b. The effect of d is to reduce the oscillation amplitude.

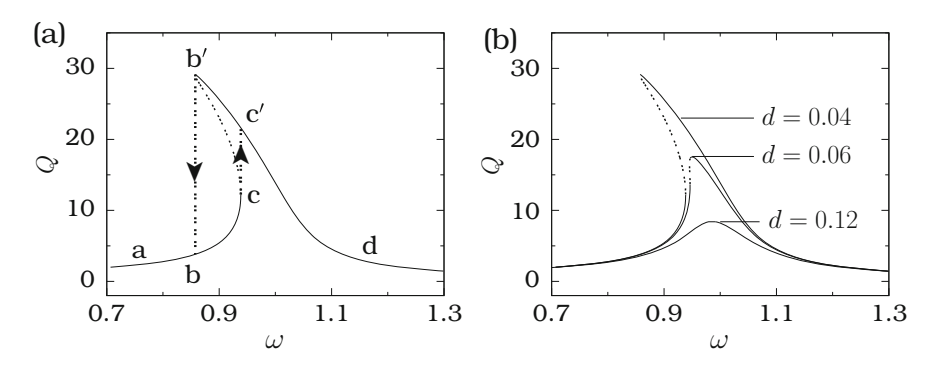


Fig. 1.8 Variation of Q with ω for the pendulum system (1.18) with f=0.05. The value of d for the subplot (a) is 0.04

1.4 Morse Oscillator

Another interesting nonlinear oscillator is the damped and driven Morse oscillator given by

$$\ddot{x} + d\dot{x} + \beta e^{-x} (1 - e^{-x}) = f \cos \omega t.$$
 (1.21)

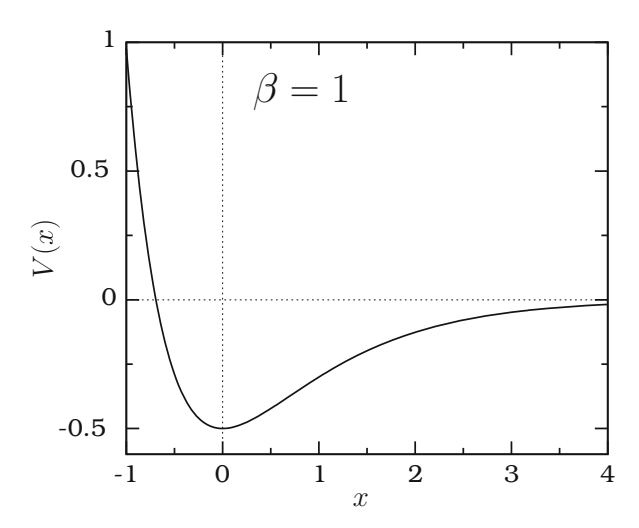
The Morse potential is named after physicist Philip M. Morse. Philip McCord Morse (1903–1985), was an American physicist, administrator and pioneer of operations research in World War II. He is considered to be the father of operations research in the U.S. The Morse potential was introduced as a useful model for the interatomic potential and fitting the vibrational spectra of diatomic molecules. It is also used to describe the photo-dissociation of molecules, multi-photon excitation of the diatomic molecules in dense medium or in gaseous cell under high pressure and pumping of a local model of a polyatomic molecule by an infrared laser [30–33]. The existence and bifurcations of periodic orbits have been studied in detail [34, 35].

In absence of damping and forcing the potential of the system is

$$V(x) = \frac{1}{2}\beta e^{-x} (e^{-x} - 2) . (1.22)$$

Figure 1.9 shows the plot of V(x) for $\beta = 1$. The equilibrium point of the unforced system is $(x, \dot{x}) = (0, 0)$. Oscillatory motion of the periodically driven system (1.21) occurs around the origin. However, from the shape of the potential it is clear that the centre of the forced oscillation need not be always the origin. Therefore, we write

Fig. 1.9 Shape of the potential of the Morse oscillator



1.4 Morse Oscillator 15

the solution of (1.21) for small values of the amplitude of the driving force as

$$x(t) = c(t) + a(t)\cos\omega t + b(t)\sin\omega t$$

= $c(t) + u(t)$. (1.23)

With

$$e^{-x} \approx e^{c} \left[1 - u + \frac{1}{2}u^{2} - \frac{1}{6}u^{3} \right],$$
 (1.24a)

$$e^{-2x} \approx e^{2c} \left[1 - 2u + 2u^2 - \frac{4}{3}u^3 \right],$$
 (1.24b)

$$u^2 \approx \frac{1}{2} \left(a^2 + b^2 \right) \,, \tag{1.24c}$$

$$u^{3} \approx \frac{3}{4} \left(a^{2} + b^{2} \right) \left(a \cos \omega t + b \sin \omega t \right) \tag{1.24d}$$

and $A = a^2 + b^2$ the frequency-response relation is

$$A^{2} \left[\omega^{2} + \beta e^{-c} (1 - 2e^{-c}) + \frac{1}{8} e^{-c} (1 - 8e^{-c}) A^{2} \right]$$

+ $d^{2} \omega^{2} A^{2} = f^{2}$, (1.25a)

$$e^{-c} - \frac{(4+A^2)}{4(1+A^2)} = 0. ag{1.25b}$$

As done for the other systems, one can draw the frequency-response curve by calculating the ω values for fixed values of A in a suitable range. Figure 1.10a shows

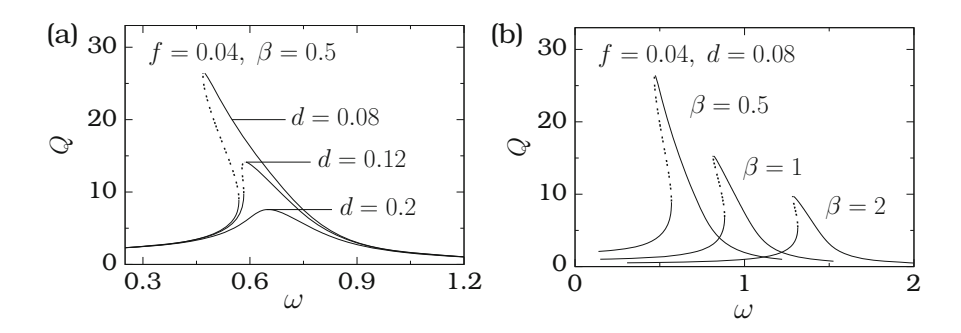
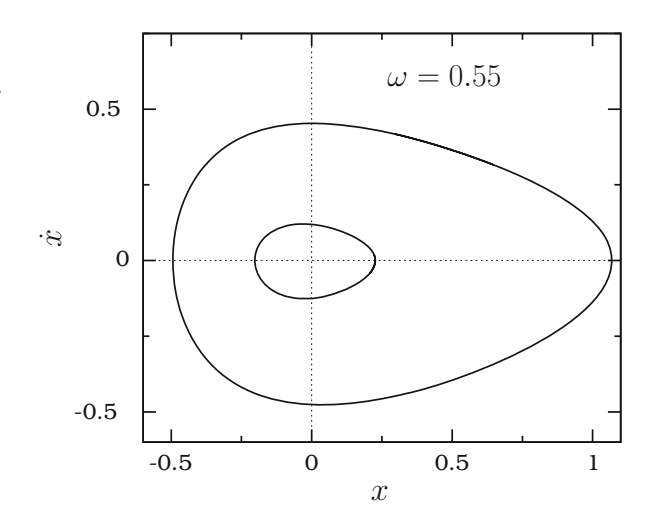


Fig. 1.10 Dependence of Q versus ω of the Morse oscillator on (a) the damping coefficient d and (b) β , coefficient of the nonlinear term. The *continuous* and *dashed curves* represent stable and unstable branches, respectively

Fig. 1.11 Phase portrait of the two coexisting periodic orbits of the Morse oscillator for f=0.04, $\beta=0.5$, d=0.08 and $\omega=0.55$. Note that the centers of the orbits are not the origin



the response amplitude Q versus ω for a few fixed values of d where f=0.04 and $\beta=0.5$.

For d=0.08, the theoretically predicted values of ω at which jumps in the response curve occur are 0.47 and 0.57, while in the numerical simulation jumps occur at 0.5 and 0.58. Figure 1.11 shows the coexistence of small and large amplitude periodic orbits for $\omega=0.55$. The centers of the orbits are not the origin, that is, $c\neq 0$ in Eq. (1.23). The effect of β on the response is depicted in Fig. 1.10b for d=0.08. As β increases the response curve moves in the forward direction and the maximum amplitude decreases with the increase of β .

1.5 Linear and Nonlinear Jerk Systems

Consider the third-order system of the form

$$\ddot{x} + d\ddot{x} + a\dot{x} + F(x) = 0. {(1.26)}$$

An equation of the above form is called a *jerk equation* [36–38]. The third derivative term \ddot{x} is called *jerk*. Such equations model the jerk circuit introduced to generate a family of scroll grid attractors [39–41]. For the linear form of $F(x) = \omega_0^2 x$ and driven by the periodic force $f \cos \omega t$ the general solution of (1.26) is $x(t) = x_h(t) + x_p(t)$. x_p , the solution of the homogeneous part of the jerk equation is given by

$$x_{\rm h} = C_1 e^{m_1 t} + C_2 e^{m_2 t} + C_3 e^{m_3 t} , (1.27)$$

where m_1 , m_2 and m_3 are the roots of the cubic equation

$$m^3 + dm^2 + am + \omega_0^2 = 0 ag{1.28}$$

and C_1 , C_2 and C_3 are integration constants. Assuming the particular solution of the jerk equation as $x_p(t) = A\cos(\omega t + \phi)$, the amplitude A is determined as

$$A = \frac{f}{\left[\omega^2 (\omega^2 - a^2)^2 + (\omega_0^2 - d\omega^2)^2\right]^{1/2}}$$
(1.29)

and

$$\phi = \tan^{-1} \left[\frac{\omega \left(\omega^2 - a \right)}{\omega_0^2 - d\omega^2} \right] . \tag{1.30}$$

For a real and bounded solution, the requirement is that the real part of all the roots of (1.28) should be negative. Even if one of the roots has a positive real part, then the solution will diverge with time t. The Routh–Hurwitz criterion [42] for all the roots of Eq. (1.28) to have negative real part is a, d > 0 and $ad^2 > \omega_0^2$. When this condition is satisfied $x_h(t) \to 0$ in the limit $t \to \infty$ and in the long time limit, the solution of the periodically driven linear jerk equation is given by

$$x(t) = A\cos(\omega t + \phi). \tag{1.31}$$

The response amplitude becomes maximum at

$$\omega = \omega_{\text{max}} = \left[\frac{-u_1 \pm \sqrt{u_1^2 - 4u_2}}{2} \right]^{1/2} , \qquad (1.32a)$$

where

$$u_1 = \frac{2}{3} (d^2 - 2a^2), \quad u_2 = \frac{1}{3} (a^4 - 2d\omega_0^2).$$
 (1.32b)

Figure 1.12a shows Q versus ω for a few values of d, where a=1, $\omega_0^2=1$ and f=0.1. For d<1 the motion of the system is unbounded. As d increases from 1 both ω_{\max} and Q_{\max} decrease. The effect of a on Q is shown in Fig. 1.12b for d=1.1. ω_{\max} increases (while Q_{\max} decreases) with increase in a.

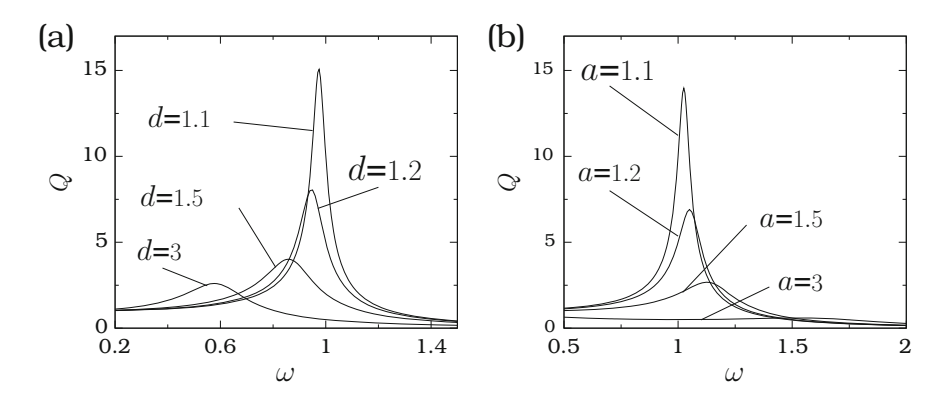


Fig. 1.12 Frequency-response curve for the linear jerk equation for (a) four values of d with a=1 and (b) four values of a with d=1.1. The values of ω_0^2 and f are 1 and 0.1, respectively

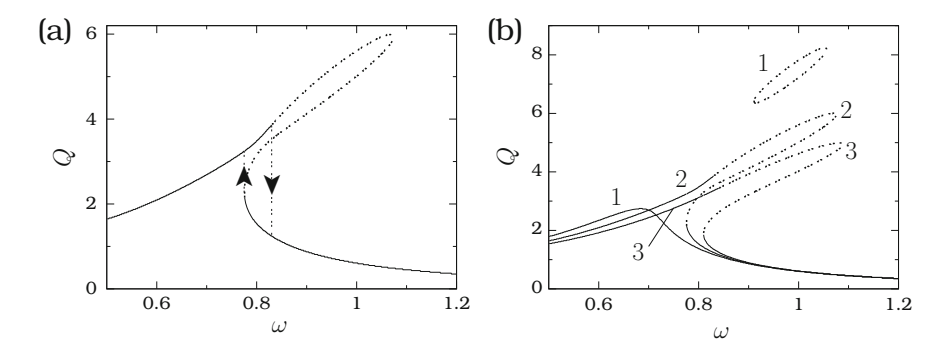


Fig. 1.13 Q versus ω for the nonlinear jerk system for (**a**) d=2.7, a=1, f=0.1, $\omega_0^2=1$ and $\beta=8$. *Continuous* and *dashed curves* represent stable and unstable branches. (**b**) Q versus ω for $\beta=4$ (curve 1), 8 (curve 2) and 12 (curve 3)

Next, we consider the periodically driven jerk equation with the nonlinear function $F(x) = \omega_0^2 x + \beta x^3$. The frequency-response equation is worked out as

$$A^{2} \left[\left(\omega_{0}^{2} - d\omega^{2} + \frac{3}{4}\beta A^{2} \right)^{2} + \omega^{2} \left(a - \omega^{2} \right)^{2} \right] = f^{2} . \tag{1.33}$$

Now, we compare Eq. (1.33) with the frequency-response Eq. (1.9) of the Duffing oscillator. Figure 1.13a presents Q versus ω for d=2.7, a=1, $\omega_0^2=1$ and $\beta=8$. The hysteresis and the jump phenomenon are clearly evident. Jump in the response amplitude occurs at $\omega=0.775$ and 0.83 when ω is varied in the forward and reverse directions, respectively. In Fig. 1.13b the frequency-response curves for

three values of β are plotted. For $\beta=4$ there is no hysteresis and jump in the response amplitude. The stable and unstable branches of the response curve are well separated. For $\beta=8$ and 12, these two branches are smoothly joined and further for a range of values of ω , the response has multi-valuedness leading to hysteresis. The unstable branch of the response curve of a jerk system is quite different from other systems considered earlier in this chapter.

1.6 Van der Pol Oscillator

The damping term in the systems considered so far in this chapter is linear. There are numerous physically and biologically interesting systems with nonlinear damping. One such a famous and prototype nonlinearly damped system is the van der Pol oscillator [3]. Balthasar van der Pol (1889–1959) was a Dutch physicist. The van der Pol oscillator appeared first in the year 1928 in [43] written in collaboration with Jan van der Mark (1893–1961).

The dynamics of the van der Pol oscillator with a periodic driving force is governed by the equation

$$\ddot{x} - \epsilon \left(1 - x^2\right) \dot{x} + \omega_0^2 x = f \cos \omega t . \tag{1.34}$$

In the absence of the external force (f = 0) the damping is positive for |x| < 1 and negative for |x| > 1. The origin is the equilibrium point and is stable for $\epsilon < 0$. For $\epsilon > 0$ the equilibrium point is unstable, however, a stable limit cycle orbit is developed [3].

For $0 < \epsilon \ll 1$ and for $|f| \ll 1$ unlike the case of the systems with linear damping, it is reasonable to expect the presence of periodic components with both the frequencies ω_0 and ω in the long time solution. This is supported by the numerical simulation.

1.6.1 Theoretical Treatment

For resonance analysis we assume that the solution of the system (1.34) in the long time limit as

$$x = a_1 \cos \omega t + b_1 \sin \omega t + a_2 \cos \omega_0 t + b_2 \sin \omega_0 t \tag{1.35}$$

and carrying out the analysis as done for the other systems in this chapter, so that the equations for the amplitudes A_1 and A_2 with $a_i = A_i \cos \theta_i$, $b_i = A_i \sin \theta_i$ can be

obtained. For $\omega \neq \omega_0$ and $\Delta \omega = |\omega - \omega_0|$ is not very small the equations for A_1 and A_2 are

$$A_1^6 - \frac{8}{3}A_1^4 + \frac{16}{9} \left[1 + \frac{\left(\omega_0^2 - \omega^2\right)^2}{\epsilon^2 \omega^2} \right] A_1^2 - \frac{16f^2}{9\epsilon^2 \omega^2} = 0 , \qquad (1.36a)$$

$$A_2 = \sqrt{4 - 2A_1^2} \ . \tag{1.36b}$$

The equations for $A_1(\omega)$ and $A_2(\omega_0)$ are decoupled. With $A_1^2 = A_1'$, Eq. (1.36a) becomes a cubic equation for A_1' . For the case of $\omega = \omega_0$ with $x(t) = a \cos \omega_0 t + b \sin \omega_0 t$ and $a = A \cos \theta$ and $b = A \sin \theta$ the result is

$$A^3 - 4A + \frac{4f}{\epsilon \omega_0} = 0. ag{1.37}$$

On the other hand, for $\omega^2 \gg \omega_0^2$ Eq. (1.36a) can be approximated as

$$A^{2} \left[A_{1}^{4} - \frac{8}{3} A_{1}^{2} + \frac{16}{9} \left(1 + \frac{\omega^{2}}{\epsilon^{2}} \right) \right] \approx 0.$$
 (1.38)

Its roots are

$$A_1^2 = 0, \quad A_1^2 = \frac{4}{3} \left(1 \pm i \frac{\omega}{\epsilon} \right) .$$
 (1.39)

That is, for $\omega^2 \gg \omega_0^2$ the only possible real value of A_1 is zero and therefore, $A_2 = 2$.

1.6.2 Numerical Verification

Fix the values of the parameters as $\epsilon=0.01$, $\omega_0^2=1$, f=0.1 and vary the frequency ω . With $Q(\omega)=A_1(\omega)/f$ and $Q(\omega_0)=A_2(\omega_0)/f$, Fig. 1.14 presents the dependence of $Q(\omega)$ and $Q(\omega_0)$ on ω . Both theoretically and numerically computed values of $Q(\omega)$ and $Q(\omega_0)$ are plotted in this figure. $Q(\omega)$ versus ω displays a typical resonance curve similar to that of a linear system. Both theoretical treatment and numerical simulation support the presence of both the frequencies ω and ω_0 in the response. When ω increases from a small value $Q(\omega)$ [or $A_1(\omega)$] increases from a small value while $Q(\omega_0)$ [or $A_2(\omega_0)$] decreases from 20. That is, $A_2(\omega_0)$ decreases from the value 2. For small values of $A_1(\omega)$, Eq. (1.36b) can be approximated as $A_2(\omega_0) \approx 2$.

1.6 Van der Pol Oscillator 21

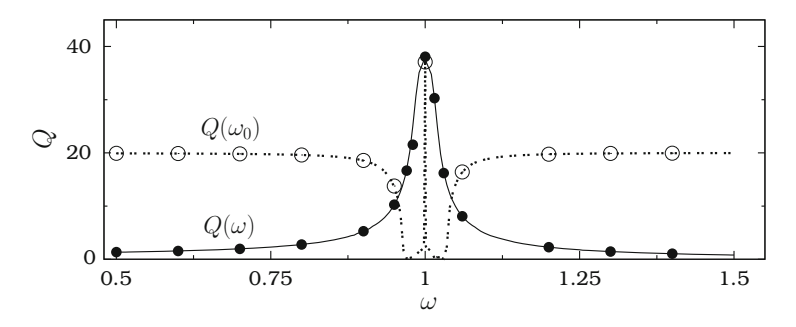


Fig. 1.14 $Q(\omega)$ and $Q(\omega_0)$ versus ω for the van der Pol oscillator with $\epsilon = 0.01$, $\omega_0^2 = 1$ and f = 0.1. The *continuous* and *dashed curves* are numerically computed values of $Q(\omega)$ and $Q(\omega_0)$, respectively. The *symbols* mark the theoretical prediction

When $\omega = \omega_0$ the response amplitude equation is Eq. (1.37). For f = 0.1, $\epsilon = 0.01$ and $\omega_0 = 1$ the cubic Eq. (1.37) has only one real root and is

$$A = \frac{2}{\sqrt{3}} \left(e^{\phi/3} + e^{-\phi/3} \right), \quad \phi = 3.25587. \tag{1.40}$$

That is, A=3.80832 and Q=38.0832. The same result is realized in the numerical computation of Q at $\omega=\omega_0$. Resonance occurs at $\omega=\omega_0$. An interesting observation in Fig. 1.14 is that on either side of $\omega=\omega_0$ the amplitude of the component of the solution with the frequency ω decreases rapidly from the maximum value with the variation of ω . For $\omega\ll\omega_0$ and $\omega\gg\omega_0$ the dominant frequency present in the solution is ω_0 . In the linearly damped oscillators the amplitude of oscillation decays to zero for $\omega\gg\omega_0$ where ω_0 is the natural frequency of oscillation. In contrast to this in the van der Pol oscillator when the damping is nonlinear and the sign of the damping term depends on the value of x(t), the oscillation continues. The readers can investigate the response behaviour in the van der Pol oscillator with the addition of a cubic term βx^3 .

In a linearly damped and periodically driven weak nonlinear oscillator the frequency of the response is the same as the frequency ω of the driving force. The response does not contain the natural frequency of the system because the response of the unforced system is decaying due to the linear damping. In the nonlinearly damped (but weak) and unforced systems (self-excited systems), like the van der Pol oscillator for $\epsilon \ll 1$, this frequency is the natural frequency ω_0 of the system. In forced self-excited systems, it is reasonable to expect the response to contain both the frequencies ω and ω_0 with different response amplitude. When $|\omega-\omega_0|$ is small enough, then as seen in the van der Pol oscillator the dominant frequency is the frequency ω of the driving force. The system is then said to be *frequency-locked* or *phase-locked*. The external force has *entrained* the self-excited oscillator and the oscillation of the unforced self-excited system is said to be *quenched*.

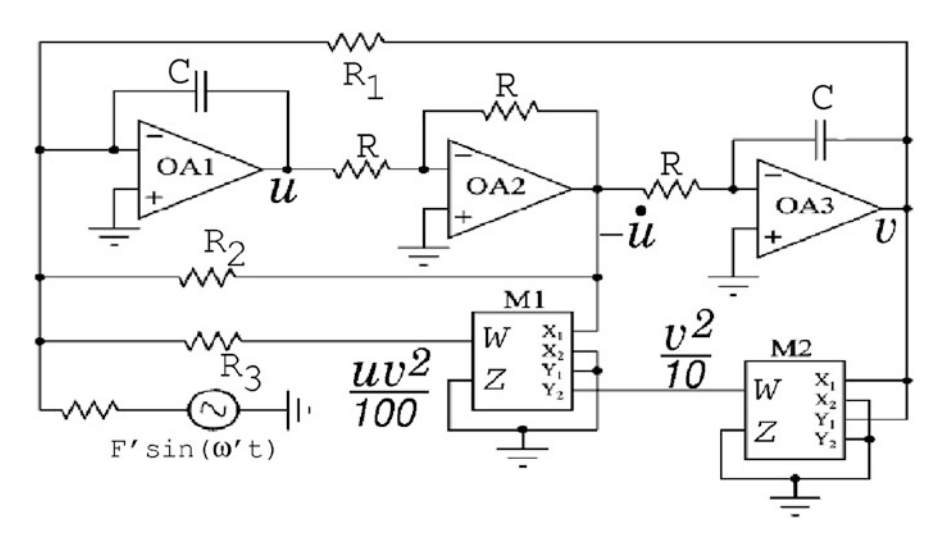


Fig. 1.15 Analog circuit for the van der Pol oscillator equation

1.6.3 Analog Circuit Simulation

The theoretically and numerically predicted results can be also realized in an analog circuit simulation. A PSpice circuit simulation of the van der Pol oscillator equation has been performed. The relevant analog circuit for the van der Pol oscillator equation is given in Fig. 1.15. In terms of the parameters of the circuit elements the equations governing the evolution of the variables u and v representing the output voltages of the operational amplifiers OA1 and OA3, respectively, are given by

$$\dot{u} = -\frac{1}{C} \left[\frac{v}{R_1} - \frac{u}{R_2} + \frac{uv^2}{100R_3} + \frac{F'}{R} \sin \omega' t \right] , \qquad (1.41a)$$

$$\dot{v} = \frac{u}{RC} \,. \tag{1.41b}$$

In term of v the above equation is written as

$$RC^2\ddot{v} - RC\left(\frac{1}{R_2} - \frac{1}{100R_3}v^2\right)\dot{v} + \frac{v}{R_1} = \frac{F'}{R}\sin\omega' t$$
, (1.42)

where in the last term F' is replaced by -F' as it is a sinusoidal term. Introduction of the change of variables

$$t = RC\tau, \quad \omega' = RC\omega, \quad v = x, \quad F' = f$$
 (1.43)

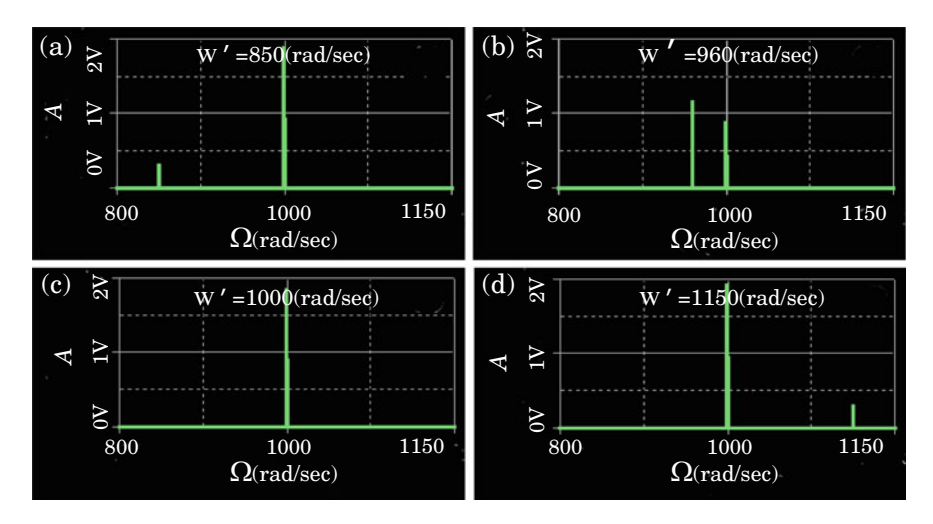


Fig. 1.16 Power spectrum of the state variable v of the van der Pol analog circuit for four values of ω'

transforms Eq. (1.42) into the dimension less form

$$\ddot{x} - \frac{R}{R_2} \left(1 - \frac{R_2}{100R_3} x^2 \right) \dot{x} + \frac{R}{R_1} x = f \sin \omega \tau . \tag{1.44}$$

Defining

$$\epsilon = \frac{R}{R_2}, \ R_3 = 10 \,\mathrm{k}\Omega, \ R_2 = 100 R_3, \ \omega_0^2 = \frac{R}{R_1}$$
 (1.45)

brings Eq. (1.44) into Eq. (1.34). For $\epsilon=0.01$, $\omega_0^2=1$ in the circuit one has to choose $R=10\,\mathrm{k}\Omega$ and $R_1=R=10\,\mathrm{k}\Omega$. The value of C was fixed as 100 nF. For $\epsilon=0.01$, $\omega_0^2=1$ and f=0.1 power spectrum was obtained for four values of ω . In Fig. 1.16a for $\omega'=850$ (rad/s) (in dimensionless form the corresponding value of ω is 0.85) the power spectrum has two peaks one at the frequency $\Omega=\omega'=850$ and another at the natural frequency 1000 ($\omega_0=1$). The dominant frequency present in the output signal is the natural frequency of the system. For $\omega'=960$ (Fig. 1.16b) the dominant frequency is the frequency of the driving periodic force. In Fig. 1.16d for $\omega'=1150$ the amplitude of the periodic component of the output signal with the frequency ω' is much weaker than the amplitude of the component with the natural frequency $\omega_0=1000$. The power spectrum clearly shows the presence of the frequencies ω' and ω_0 . $A(\omega')$ and $A(\omega_0)$ were obtained for a range of values of ω' and are presented in Fig. 1.17. The results in this figure are the same as those obtained through analytical and numerical analysis.

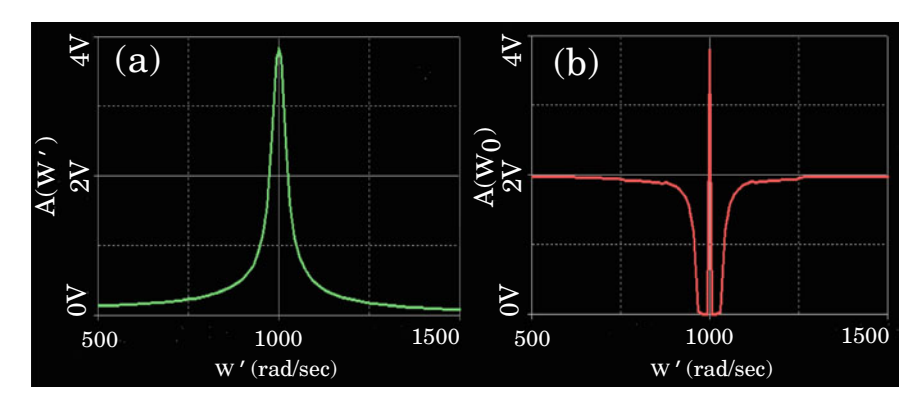


Fig. 1.17 (a) $A(\omega')$ and (b) $A(\omega_0)$ measured as a function of the frequency of the driving periodic force in the analog simulation of van der Pol oscillator equation

1.7 Resonance in Micro- and Nano-Electromechanical Resonators

Nano-electromechanical (NEM) resonators are useful in various mechanical and electrical devices, particularly, for oscillators, filters and sensors [44–46]. The realization of NEM devices is due to the great advances made in the fabrication and detection techniques. For example, NEM resonators based on graphene [47–50], 3C-SiC [51, 52] and Cr-Au [53], micromechanical resonators made of Pd and Au [54] and electrostatically actuated resonators [55] have been fabricated and studied. A variety of useful applications can be implemented by applying external driving forces. Resonance is a simple phenomenon that can be realized by varying the frequency of an external force. As a consequence of it, a deeper understanding of resonance dynamics in NEM resonators is necessary for choosing specific operating conditions. In many applications of NEM resonators the nonlinear resonance region is the highly useful region of operation.

The graphene and nanotube resonators, when actuated electrostatically by employing an oscillating voltage between the resonators and gate electrode, act as a frequency mixer. They yield a mixing current that has a characteristic shape similar to a typical nonlinear resonance curve of the Duffing oscillator [56]. Nonlinear resonance is noticed in a theoretical model equation of response of a carbon nanotube-cantilever with a tip-mass subjected to an electrostatic excitation. Such resonators are useful for detecting tiny masses. The resonance dynamics was found with increasing applied voltage and tip-mass [57]. The resonances were affected by increasing the applied ac and dc voltages. A resonance curve similar to the one shown in Fig. 1.3 including the jump phenomenon has been experimentally realized with a microcantilever system driven by an ac excitation amplitude and at a vacuum pressure. The mathematical model equation of this system is obtained as

$$\ddot{z} + (d_1 + d_2 z^2) \dot{z} + z + \beta z^3 = f \cos \omega t, \tag{1.46}$$

where z is the normalized vertical displacement of the cantilever [58]. Two examples of a NEM resonator experimental setup fabricated and its observed resonance observed has been reported in [51, 53] and are presented in the remaining part of this section.

1.7.1 A Double Clamped 3C-SiC Nanoscale Beam

Single crystal 3C-SiC films were prepared on silicon wafer employing the chemical vapour deposition method [51]. In the preparation a mixture of propane and silane and hydrogen were used at a heteroepitaxial atmospheric pressure. The precursors were propane and silane and the carrier gas was hydrogen. By the e-beam lithography process, doubly clamped nanoscale beams were fabricated making use of the 3C-SiC grown silicon substrate. The pattern was defined by the e-beam lithography. It was developed in a methyl isobutyl ketone. Conductivity for magnetometer transduction was improved by depositing a metallic layer by a thermal evaporator. Additional metallic layer of Al was used in the samples. The SiC-grown wafer was then etched employing the reactive ion etching process with a CF_4/O_2 gas mixture at 300 mTorr and for 3 min.

Figure 1.18 depicts the experimental setup where clamped-clamped nano-beams were suspended for magnetomotive excitation. In this figure the electromagnetic excitation principle is represented by arrows. The dimensions of the resonators were $12\,\mu m$ long $100\,\mu m$ wide and $30\,nm$ thickness. The resonators were kept in a vacuum chamber at room temperature and at 1 Tesla magnetic field. An Agilent E5071C network analyzer was used for radio-frequency excitation and frequency

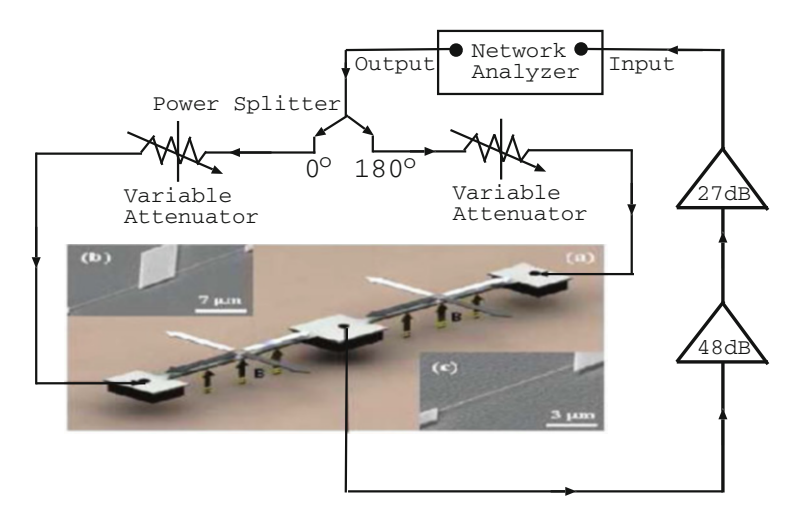


Fig. 1.18 Fabricated clamped-clamped resonators and schematic measurement setup [51]. (Reproduced with permission from Seong Chan Jun et al., New J. Phys. **12**, 043023 (2010). Copyrighted by IOP Publishing & Deutsche Physikalische Gesellschaft. CC BY-NC-SA.)

domain measurement. A few tens of μV ac drive was applied through the beam in a vertical magnetic filed. This has induced lateral vibrations of the beam. The resulting electromotive force voltage was measured.

The evolution equation for the lateral displacement y of the beam is constructed as [51]

$$\ddot{y} + \dot{y}(2\gamma_1 + \gamma_2 \dot{y}^2) + \omega_0^2 y + \beta y^3 = f_0 + f_1 \cos \omega t, \tag{1.47}$$

where the parameters in the above equation are suitably rescaled parameters of the experimental system.

The system was in a linear regime for low level (for example $10 \,\mu\text{V}$) of driving voltage V_{ac} and driven to a nonlinear region by applying a sufficiently large V_{ac} . Response amplitude V_{EMF} was measured by varying the frequency of the ac drive at zero dc power for several fixed values of V_{ac} .

Figure 1.19 reports both experimental and theoretical resonance curves for three fixed values of the amplitude of the driving power. The theoretically computed $V_{\rm EMF}$ values closely match with the $V_{\rm EMF}$ measured in the experiment. For illustrative purposes, the frequency in Fig. 1.19 is stated as the actual frequency minus the resonance frequency in the linear region, that is, the resonance frequency at a small value of driving power. Both shift in the resonance frequency and increase in $V_{\rm EMF}$ at resonance were clearly observed with increase in the driving power.

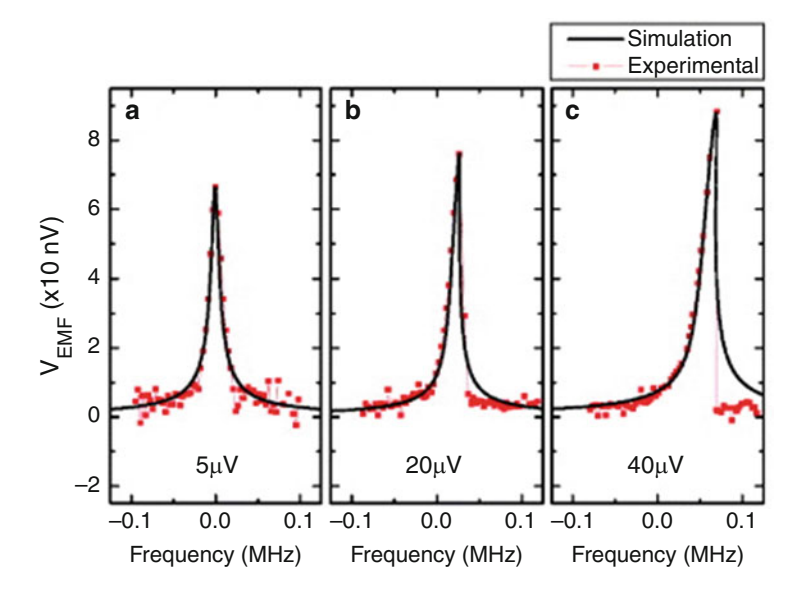


Fig. 1.19 V_{EMF} versus the rescaled driving frequency for three fixed values of the driving power for the NEM resonators system [51]. The *continuous curve* and the *solid circles* are the theoretical and experimental results, respectively. (Reproduced with permission from Seong Chan Jun et al., New J. Phys. **12**, 043023 (2010). Copyrighted by IOP Publishing & Deutsche Physikalische Gesellschaft. CC BY-NC-SA.)

1.7.2 A Doubly Clamped Cr-Au Bilayer NEM Resonator

The experimental setup used for the resonance study with a doubly clamped Cr-Au bilayer NEM resonators is shown in Fig. 1.20a [53]. The dimension of the structure was 500 nm width, $5 \,\mu m$ of length and 110 nm of thickness. To make the device to work near zero dc bias voltage a constant offset voltage $V_{\rm off} = -4V$ was applied.

Figure 1.20b presents the variation of amplitude with the frequency $f_{\rm ac}$ of an applied ac voltage ($V_{\rm ac}$). Measurements were performed by varying $f_{\rm ac}$ in the forward and reverse directions without dc bias-voltage. The response curve shows

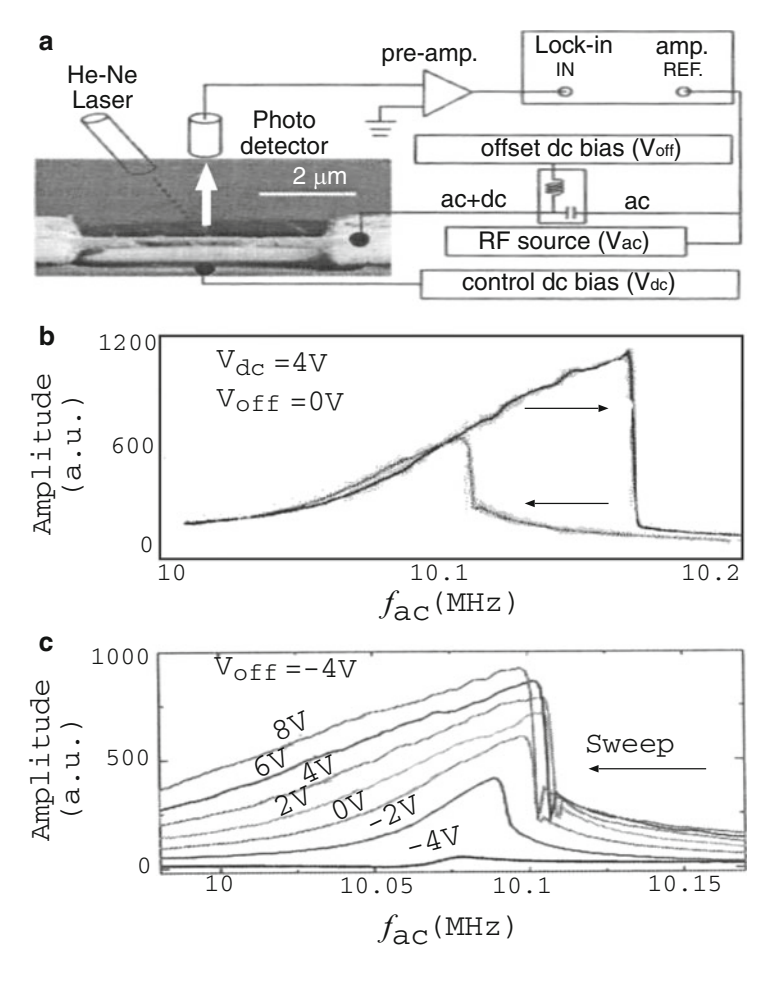


Fig. 1.20 (a) Experimental setup of a Cr-Au resonator. (b) Frequency-response curve with $V_{\rm off} = 0 \, \text{V}$, $V_{\rm dc} = 4 \, \text{V}$ and with the amplitude of V_{ac} as 0.5 V. The *arrow* marks indicate the direction of sweep. (c) Response curve for several fixed values of $V_{\rm dc}$ with $V_{\rm off} = -4 \, \text{V}$ [53]. (Reprinted with permission from H. Noh, S.B. Shim, M. Jung, Z.G. Khim, J. Kim, Appl. Phys. Lett. **97**, 033116 (2010). Copyright [2010], AIP Publishing LL.)

the occurrence of the jump phenomenon and hysteresis similar to the Duffing oscillator. In a certain frequency region there are two accessible states and the response depends strongly on the direction of the sweep. Figure 1.20c reports the dependence of a resonance curve on the dc bias voltage. The measurements were done with decreasing $f_{\rm ac}$ from a large value. Generally, the operating frequency band (OFB) is defined as a frequency region where the resonance peak can be varied monotonically with the dc bias voltage. For the device considered, the resonance peak at the dc bias voltages of 0 V and 4 V were found to be 10.103 MHz and 10.109 MHz, respectively, giving the OFB width as 6 kHz. It has been pointed out that the OFB width is crucial for practical applications and a wide OFB is desirable for an stable memory operation and other similar applications.

1.8 Some Other Examples of Resonance

When a single-mode erbium-doped ring laser is subjected to a cavity-loss modulation, then the output of the laser is found to display linear resonance for low driving amplitude and a nonlinear resonance in the case of higher amplitudes [59]. Resonance curves of an infinitely long cable on a tensionless foundation are shown to display hysteresis and jump phenomenon [60]. This section presents a few other notable examples of resonance.

1.8.1 Resonance Magnetoelectric Effect

In magnetostrictive-piezoelectric composite bilayer structures an alternating electric field is developed when a constant bias and alternating magnetic fields are applied. This phenomenon is known as magnetoelectric (ME) effect. In certain magnetostrictive-piezoelectric composite structures resonance excitation of an alternating electric field is realized in a zero bias field and in a weak bias field. Its magnitude is found to be quadratic with respect to the applied alternating magnetic-field amplitude [61]. The above resonance behaviour is, for example, observed in an experiment with a rectangular bilayer plate of lead zirconate titanate and permendur alloy with a length of L=28.7 mm, a width of 4.6 mm, a piezoelectric layer thickness of 0.16 mm.

1.8.2 Nonlinear Resonance Ultrasonic Spectroscopy

The alkali-silica reaction (ASR) is considered as a form of deterioration reducing the life time of concrete structures. A nonlinear impact resonance acoustic spectroscopy technique is proposed as a reliable measurement technique for quickly quantify

the damages associated with ASR in concrete specimens. This method is based on the measurements of the nonlinear vibration or acoustic responses of concrete specimens. In a concrete microcracks distribution is thought of as forming a network and become the source of strong nonlinear acoustic response of concrete. Here the stress-strain relationship is nonlinear. In a test with a typical concrete the response amplitude of the concrete versus the frequency of impact has shown a resonance like behaviour. The resonance frequency of the specimen is found to show a downward shift with the increase of impact strength. The amount of the downward shift is observed to be proportional to the amount of damage occurring in the specimen specified in terms of the density of microcracks [62].

1.8.3 Crack Breathing and Resonance

One of the important defects in structures is a crack. It may lead to a dangerous effect on the performance of the structures. A crack is able to alter the value of the stiffness and to reduce the frequency of a structure. When a structure is subjected to an external load, it undergoes a vibration and a crack will open and close repeatedly. This phenomenon is termed as *crack breathing*. It occurs in a rotating blade or in a turbine blade. During crack breathings the stiffness in the region of crack may vary leading to the marked change in the response behaviour. This property can be used for detection of cracks. The frequency-response curve is found to show a clear resonance at a frequency and the resonance frequency depends on the crack ratio (crack length/blade width) [63]. The response amplitude is shown to be greatly different for linear and nonlinear cracked blades.

1.9 Quantum Resonance

In this section the effect of an additive periodic force in quantum mechanical systems is reviewed [64, 65]. The Schrödinger equation of a one-dimensional quantum mechanical system is given by

$$i\hbar \frac{\partial \psi}{\partial t} = (H^{(0)} + \lambda H^{(1)}) \psi = H\psi, \quad \lambda \ll 1$$
 (1.48a)

where

$$H^{(0)} = -\frac{\hbar^2}{2m} \frac{\mathrm{d}^2}{\mathrm{d}x^2} + V(x), \quad H^{(1)} = W(x) \mathrm{e}^{-\mathrm{i}\omega t}. \tag{1.48b}$$

In Eq. (1.48) $H^{(0)}$ is the unperturbed part of the Hamiltonian H and the system $H^{(0)}\phi = E\phi$ is assumed to be exactly solvable. $H^{(1)}$ is the applied perturbation. For a system subjected to an additive periodic force W(x) = x.

Let $(E_n, \phi_n(x))$ are the eigenpairs of the time-independent unperturbed system. Then $\phi_n(x, t)$ is given by

$$\phi_n(x,t) = \phi_n(x) e^{-iE_n t/\hbar}$$
 (1.49)

When a quantum mechanical system is subjected to a time-dependent external field the system undergoes transitions between the energy eigenstates. Consequently, the interest lies in knowing the probability of finding the system in a fth state at time t.

Assume that the perturbation $H^{(1)}$ is switched-on at t = 0. The solution of (1.48) is written as

$$\psi(x,t) = \sum_{n} a_n(t)\phi_n(x) e^{-iE_n t/\hbar},$$
 (1.50)

where $a_n(t)$, the probability amplitude of finding the system in the quantum state $\phi_n(x,t)$ at time t, to be determined.

To compute $a_n(t)$ substitute (1.50) in (1.48) which gives

$$i\hbar \sum_{n} \dot{a}_{n} e^{-iE_{n}t/\hbar} \phi_{n} = \lambda \sum_{n} a_{n} H^{(1)} e^{-iE_{n}t/\hbar} \phi_{n}. \qquad (1.51)$$

Multiplication of Eq. (1.51) by ϕ_f^* and integrating overall space leads to

$$i\hbar \dot{a}_f = \lambda \sum_n a_n e^{i(\omega_{fn} - \omega)t} H_{fn} , \qquad (1.52a)$$

where

$$\omega_{fn} = (E_f - E_n)/\hbar, \quad H_{fn} = \int_{-\infty}^{\infty} \phi_f^* W(x) \phi_n \, \mathrm{d}x. \tag{1.52b}$$

Next, we expand $a_f(t)$ in a power series as

$$a_f(t) = a_f^{(0)} + \lambda a_f^{(1)} + \lambda^2 a_f^{(2)} + \cdots$$
 (1.53)

The evolution equations for $a_f^{(0)}$ and $a_f^{(1)}$ are obtained as

$$i\hbar \dot{a}_f^{(0)} = 0,$$
 (1.54)

$$i\hbar \dot{a}_{f}^{(1)} = \sum_{n} a_{n}^{(0)} e^{i(\omega_{fn} - \omega)t} H_{fn}$$
 (1.55)

Equation (1.54) gives $a_f^{(t)} = a_f^{(0)}$. Equation (1.55) is a set of coupled integrodifferential equations. For a system with m discrete eigenstates Eq. (1.55) consists of m equations and in each equation the right-side has m terms. In order to simplify the problem one can modify it in a slightly different manner. For example, assume that the perturbation is switched-on at t = 0 and switched-off at t = T. At t = 0the system is, say, in the eigenstate ϕ_i . Then $a_{ni}^{(0)} = \delta_{ni}$. Once the perturbation is switched-off the system settles down to a stationary state and we denote this final state as f. What is the probability of finding the system in the state f after time T? We denote this probability as $P_{fi} = a_f^* a_f$. Now, Eq. (1.55) takes the form

$$\dot{a}_f^{(1)} = \frac{1}{i\hbar} e^{i(\omega_f - \omega)t} H_{fi}. \tag{1.56}$$

Integration of the above equation from 0 to T gives

$$a_f^{(1)}(T) = \frac{H_{fi}}{i\hbar} \int_0^T e^{i(\omega_{fi} - \omega)t} dt = \frac{H_{fi}}{\hbar(\omega_{fi} - \omega)} \left(1 - e^{i(\omega_{fi} - \omega)T} \right). \tag{1.57}$$

Then

$$P_{fi}(T) = \frac{4|H_{fi}|^2}{\hbar^2(\omega_{fi} - \omega)^2} \sin^2\left[(\omega_{fi} - \omega)T/2\right]. \tag{1.58}$$

For $H^{(1)} = W(x) \cos \omega t$

$$\dot{a}_f^{(1)} = \frac{H_{fi}}{2i\hbar} \left[e^{i(\omega_{fi} - \omega)t} + e^{i(\omega_{fi} + \omega)t} \right]. \tag{1.59}$$

Integration of this equation leads to

$$a_f^{(1)}(T) = \frac{H_{fi}}{2\hbar} \left[\frac{1 - e^{i(\omega_{fi} + \omega)T}}{\omega_{fi} + \omega} + \frac{1 - e^{i(\omega_{fi} - \omega)T}}{\omega_{fi} - \omega} \right]$$
(1.60)

and

$$P_{fi}(T) = \frac{|H_{fi}|^2 |s|^2}{4\hbar^2}, \quad |s|^2 = \left| \frac{1 - e^{i(\omega_{fi} + \omega)T}}{\omega_{fi} + \omega} + \frac{1 - e^{i(\omega_{fi} - \omega)T}}{\omega_{fi} - \omega} \right|^2. \quad (1.61)$$

If $H^{(1)} = W(x) \sin \omega t$ then

$$P_{fi}(T) = \frac{|H_{fi}|^2 |s|^2}{4\hbar^2}, \quad |s|^2 = \left| \frac{1 - e^{i(\omega_{fi} + \omega)T}}{\omega_{fi} + \omega} - \frac{1 - e^{i(\omega_{fi} - \omega)T}}{\omega_{fi} - \omega} \right|^2. \quad (1.62)$$

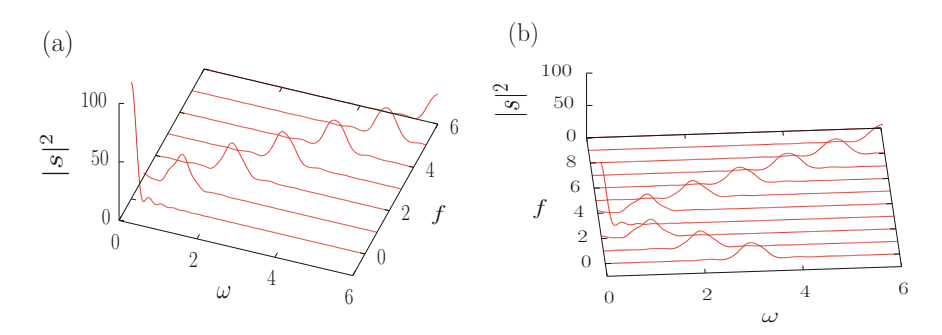


Fig. 1.21 Variation of $|s|^2$ as a function of ω and f for (a) i = 0 and (b) i = 3 with T = 10. The system is quantum linear harmonic oscillator

The term $|s|^2$ in Eqs. (1.61) and (1.62) becomes appreciably large (representing a resonance) only when either $\omega_{fi} + \omega$ or $\omega_{fi} - \omega$ in the denominator is ≈ 0 . That is, $\omega_{fi} = \pm \omega$ or $E_f = E_i \pm \hbar \omega$.

In P_{fi} the quantity $|H_{fi}|^2$ is independent of ω and depends on the perturbation and the eigenfunctions of the system of interest. $|s|^2$ depends on ω and the energy eigenvalues. Consider a quantum linear harmonic oscillator for which $E_n = (n + \frac{1}{2})\hbar\omega_0$ where ω_0 is the classical frequency of a classical linear harmonic oscillator and choose $H^{(1)} = W(x)\cos\omega t$. Figure 1.21 displays $|s|^2$ versus ω and f for i = 0 and 3 for T = 10. Here \hbar and ω_0 are set to unity for simplicity. Then $\omega_{fi} = f - i$. In Fig. 1.21a for the system being initially in the ground state, a dominant resonance peak occurs at $\omega = \omega_{f0} = f$. The case of i = 3 is shown in Fig. 1.21b. Resonance behaviour in the quantum Morse oscillator driven by a single harmonic force and a biharmonic force is discussed in Sect. 3.7.

1.10 Applications of Resonance

Resonance plays a key role in radio, television and swings on playgrounds. It can be used to generate vibrations with a specific frequency or to select specific frequencies from a complex oscillation containing several frequencies. It plays a vital role in the outer ionization and energy absorption in near-infrared laser-driven rare gas and metal clusters [66]. In epidemiology, periodic cycles of measles [67, 68], childhood diseases [69], wild life diseases [70, 71] and invasion properties of species [72] were explained through nonlinear resonance. The following are some of the notable applications of resonance.

 A familiar application of resonance is the radio tuning device. Each radio station broadcasts its own specific frequency. All broadcast waves offer a periodic impressed force to the receiving circuit of a radio. The tuning knob changes the capacitance or inductance. When the frequency of a particular station falls

- within the domain of the resonant frequencies of the circuit, the amplitude of the signal of that particular station may be heard, while all other signals remain below the audible level. In the same way, the receiver used with a radio telescope can be tuned to detect signals in the vicinity of a particular wavelength.
- 2. Quartz crystals (crystalline silica, SiO₂) are indispensable component of modern electronic technology. Nowadays, they are employed to generate frequencies to control various communication systems. They also become the isochronous element in most of the clocks, watches and computers. When a quartz crystal is squeezed or stretched, a voltage is developed across the face of the crystal and this effect is reversible. When the polarity of the applied voltage is altered, the crystal will expand or contract rapidly, thereby producing a vibration that makes quartz especially useful. When a quartz crystal is set to vibrate at its natural frequency, by means of the applied voltage, it is said to be in *resonance*. The notable point is that a crystal in resonance will maintain a constant and unfaltering frequency. In a quartz time-piece, a small ring shaped piece of crystal is made to vibrate at its natural frequency. A microchip measures the number of times the quartz vibrates each second and uses that information to maintain the accurate time.
- Several resonant objects can vibrate at harmonics of the fundamental (strongest)
 resonance frequency. Many clocks keep time by resonance in a pendulum or
 balance wheel.
- 4. Resonant electronic circuits are useful for voltage and current amplification and also play a key role in filters, timers and mixers. For example, a resonant circuit can be used to block a frequency or range of frequencies, thus acting as a sort of frequency filter to strain certain frequencies out of a mix of others. Resonance can be employed to maintain AC circuit oscillations at a constant frequency.
- 5. Resonance is also used in guitars and pianos as well as wood wind instruments.
- 6. The variations of helium dielectric permittivity in superconductors are due to nonlinear resonances [73].
- 7. In a human body, vibration and resonance stimulate the five senses: colour, light, sound, touch and aroma (smell). Vibrational therapy/medicine is essentially based on the fact that all matters vibrate to specific frequency and utilizing a resonant vibration, balance of matters can be restored [74].
- 8. The nonlinear resonant response of biological tissue to the action of an electromagnetic field is used to investigate cases of suspected diseases like cancer [74].
- 9. Resonance is used to shatter gall stones in patients using ultrasound.
- 10. The phenomenon of absorption and re-emission of electromagnetic radiation by nuclei in a magnetic field is called *nuclear magnetic resonance* (NMR). The absorption of energy from the field and the re-emission of energy are at a specific resonance frequency of a particular substance. The resonance frequency depends on the strength of the applied field and the magnetic properties of the isotope of the atoms. This feature is exploited in NMR

- spectroscopy to study crystals, noncrystalline materials and molecular physics and is used in magnetic resonance imaging (MRI).
- 11. Certain nano-electromechanical systems (NEMS) have emerged as devices for successful memory operations. Such devices are broadly classified into static and dynamic devices depending upon the presence or absence of resonance. In NEMS operation in nonlinear regime is unavoidable [75]. In this regime, the resonant frequency is found to have a strong dependence with the amplitude of oscillation. As a consequence of it, fluctuation in frequency results due to the amplitude fluctuation. This is considered as a major drawback of operating NEMS in the nonlinear regime. However, experimentally, stabilization of the frequency of oscillation in NEMS is achieved by coupling two different vibrational modes through an internal resonance. Here the exchange of energy between modes is such that the resonance of one vibration mode essentially absorbs the fluctuation in the frequency and amplitude of the other [76].

1.11 Resonance Disaster

As noted easier, a system at resonance is able to execute a large amplitude vibration. Essentially, at the resonance the system can absorb more energy and occasionally exhibit violent vibrations resulting in disaster of bridges, buildings and airplanes. In view of this, when designing such constructions the engineers must ensure that the resonant frequencies of the components of the objects should not match the driving frequencies. To avoid resonant disasters shock mounts can be installed to absorb resonant frequencies, so that the energy absorbed by the components of the system dissipates. Several accidents recorded [77, 78] in the past history were reported to be due to the occurrence of a resonance behaviour. Some examples of resonance disaster are following.

1. The rule that troops must break step when crossing a bridge may have originated in England after the collapse of the Broughton suspension bridge near Manchester in 1831 [77, 78]. This accident occurred when a regiment had a field-day and were on their way back to their quarters. When they got upon the suspension bridge, the men who were marching found that the structure vibrated with the measured step with which they marched. Resonance was induced by transfer of momentum from the soldiers to the bridge structure. As a greater number of them got upon the bridge, the vibration went on increasing until the head of the column had reached the one side of the river. The bridge fell to the bottom of the river. The immediate cause was the powerful vibration communicated to the bridge by the uniform step of the soldiers. The amplitudes of vibration went on increasing with every step. This caused the weight of the bridge to act with successive jerks on the stay-chains. One of the cross-bolts by which the links of the chains are joined together got broken and the bridge collapsed.

Collapse of Angers bridge over the marine river in Angers, France on April 16, 1850 was also attributed to the marching of few hundreds of French soldiers. Violent resonant vibrations have been occurred in Tacoma Narrows bridge in Puget sound, Washington in 1940 and the millennium bridge, London in 2000.

- 2. The Scottish scientist John Scott Russell (1808–1882) noted with great clarity, that a suspension bridge is vulnerable to resonance because, the structure has a set of characteristic frequencies. A suspension bridge over the Ohio river at Wheeling was completed in 1849. The deck of the bridge was destroyed by a strong wind storm in 1854.
- 3. In 1959 and 1960 several Electra turboprop planes crashed. The investigations indicated that the disintegration of the planes was due to mechanical resonance (http://en.wikipedia.org/wiki/Lockheed-L-188-Electra). In particular, one of the machine packages not fastened securely oscillated at a frequency within the peak of the resonance curve of the wing. These oscillations acted as an impressed force and the wing's vibration increased beyond the elastic limit. After the wing had broken and was torn off, the rest of the plane disintegrated rapidly.
- 4. A nonlinear resonance jump is important in the analysis of a turbine generator positioning system of hydroelectric power plants. It can cause a severe damage to mechanical, hydroelectric and electrical systems [79].

1.12 Concluding Remarks

This chapter discussed the occurrence of resonance in certain linear and nonlinear systems where a marked enhancement of the oscillation amplitude is produced when the frequency of the applied periodic force is varied. In nonlinear systems, resonance is generally observed at a frequency ω different from the natural frequency of the systems.

Undriven systems that are undamped or with certain types of nonlinear damping can exhibit an oscillatory behaviour. What is the nature of the dependence of the frequency of oscillation on the amplitude of oscillation in such systems? In the linear harmonic oscillator the frequency of oscillation is independent of the amplitude of oscillation and is equal to the natural frequency ω_0 . The amplitude of oscillation monotonically increases with energy. In the isochronous oscillators, where the damping term is nonlinear, in the absence of external periodic driving force, different set of initial conditions give different amplitude periodic solutions. However, all the periodic orbits have the same frequency. An example of such a system is the modified Emden equation [80, 81].

Suppose the frequency and the amplitude of the external periodic force is such that the amplitude of the output signal is weak. For example, this is the case when the frequency ω is set at a value far before or far after the resonance. The output signal is weak in the presence of the external periodic force. Now, one can ask: *Is it possible to realize resonance dynamics by some other sources? What are the ways by which a system can be brought to a resonance region? What are the mechanisms*

and features of such approaches? Can these approaches be useful for practical applications? We have very positive answers to these. The response of certain class of nonlinear systems to a weak periodic signal can be enhanced by means of an appropriate noise [82], a high-frequency periodic force [83] or a chaotic signal [84]. The enhancement of the response of a system due to the applied weak noise, a highfrequency periodic force or a chaotic signal are termed as stochastic resonance, vibrational resonance and chaotic resonance, respectively. In certain nonlinear systems a resonance-like phenomenon is induced by a weak noise in the absence of external periodic force and is called *coherence resonance* [85]. There is another kind of resonance, namely, parametric resonance [86] due to the periodic perturbation of parameter of a system. In *autoresonance* [87] the frequency of the driving force is varied appropriately with time which leads to a significant growth of amplitude of oscillation. These resonances have received a great deal of interest over the past decade or so. Theoretical treatments and numerical tools have been developed to investigate them under different environments. Experimental analysis of them has also been made. They also found many applications in various branches of science and engineering. The present book is concerned with the various resonances. In the next chapter we consider the stochastic resonance phenomenon.

References

- 1. E. Ott, Chaos in Dynamical Systems (Cambridge University Press, Cambridge, 1997)
- 2. H.G. Schuster, W. Just, Deterministic Chaos: An Introduction (Wiley-VCH, Weinhein, 2005)
- 3. M. Lakshmanan, S. Rajasekar, *Nonlinear Dynamics: Integrability, Chaos and Patterns* (Springer, Berlin, 2003)
- G. Galileo, Galileo first introduced the notion of resonance (resonanza), in *Dialogues Concerning Two New Sciences*, translated by H. Crew and A. De Salvio (Dover, New York, 1954), pp. 97–99
- 5. N. Minorsky, Nonlinear Oscillations (Van Nostrand, New York, 1962)
- 6. A.H. Nayfeh, D.T. Mook, *Nonlinear Oscillations* (Wiley, New York, 1979)
- D.W. Jordan, P. Smith, Nonlinear Ordinary Differential Equations (Oxford University Press, Oxford, 2007)
- 8. H. von Helmholtz, On the Sensations of Tone as a Physiological Basis for the Theory of Music (Dover Publications, New York, 1954). This is a republication of the second (1885) edition of the A.J. Ellis translation of Die Lehre von den Tonempfindungen, as originally published by Longmans & Co
- 9. F. Borgogno, P. D'odorico, F. Laio, L. Ridolfi, J. Theor. Biol. 293, 65 (2012)
- 10. V.N. Chizhevsky, G. Giacomelli, Phys. Rev. A 71, 011801(R) (2005)
- 11. A. Maksimov, Ultrasonics 35, 79 (1997)
- 12. L. Fortuna, M. Frasca, M.G. Xibilia, Chua's Circuit Implementations-Yesterday, Today and Tomorrow (World Scientific, Singapore, 2009)
- 13. E.M. Izhikevich, *Dynamical Systems in Neuroscience: The Geometry of Excitability and Bursting* (The MIT Press, Cambridge, 2005)
- 14. S. Rajasekar, M. Lakshmanan, J. Theor. Biol. 166, 275 (1994)
- 15. M. Perc, Phys. Rev. E 76, 066203 (2007)
- 16. B.T. Ginn, B. Steinbock, M. Kahveci, O. Steinbock, J. Phys. Chem. A 108, 1325 (2004)
- 17. T. Okano, K. Miyakawa, Phys. Rev. E 82, 027202 (2010)

References 37

18. G. Duffing, Erzwungene Schwingungen bei veränderlicher Eigenfrequenz und ihre technische Bedeutung (Vieweg, Braunschweig, 1918)

- 19. K.L. Ekinci, M.L. Roukes, Rev. Sci. Instrum. 76, 061101 (2005)
- 20. G. Donoso, C.L. Ladera, Eur. J. Phys. 33, 1473 (2012)
- L.A Pipes, L.R Harvill, Applied Mathematics for Engineers and Physicists (McGraw-Hill, New York, 1970)
- 22. V. Grigoriev, F. Biancalana, New J. Phys. 12, 053041 (2010)
- 23. H. Heng, R. Doerner, B. Hubinger, W. Martienssen, Int. J. Bifurcation Chaos 4, 751 (1994)
- 24. H. Heng, R. Doerner, B. Hubinger, W. Martienssen, Int. J. Bifurcation Chaos 4, 761 (1994)
- 25. E.I. Butikov, Eur. J. Phys. 29, 215 (2008)
- 26. J. Aguirre, C.R. Vianna, M.A.F. Sanjuan, Rev. Mod. Phys. 81, 331 (2009)
- 27. J.A. Blackburn, N. Gronbecg-Jensen, Phys. Rev. E 81, 333 (2009)
- 28. M.N. Popeseu, Y. Braiman, F. Family, M.G.E. Hantschel, Phys. Rev. E 58, R4057 (1998)
- 29. S. Harish, S. Rajaseker, K.P.N. Murthy, Phys. Rev. E **65**, 046214 (2002)
- 30. J.R. Ackerhalt, P.O.M. Milonni, Phys. Rev. A 34, 1211 (1986)
- 31. M.E. Goggin, P.W. Milonni, Phys. Rev. A 37, 796 (1988)
- 32. D. Beigie, S. Wiggins, Phys. Rev. A 45, 4803 (1992)
- 33. A. Memboeuf, S. Aubry, Physica D **207**, 1 (2005)
- 34. W. Knob, W. Lauterborn, J. Chem. Phys. 93, 3950 (1990)
- 35. Z. Jing, J. Deng, J. Yang, Chaos, Solitons Fractals 35, 486 (2008)
- 36. J.C. Sprott, Phys. Lett. A 228, 271 (1997)
- 37. S.J. Linz, J.C. Sprott, Phys. Lett. A 259, 240 (1999)
- 38. J.C. Sprott, Phys. Lett. A 266, 19 (2000)
- 39. M.E. Yakin, O. Ozoguz, J.A.K. Suykens, J. Vandewalle, Int. J. Bifurcation Chaos 12, 23 (2002)
- 40. Y. Simin, L. Jin Hu, H. Leung, G. Chen, IEE Trans. Circuits Syst. I 52, 1459 (2005)
- 41. M.E. Yalcin, Chaos, Solitons Fractals 34, 1659 (2005)
- 42. G. Schmidt, A. Tondl, Nonlinear Vibrations (Cambridge University Press, Cambridge, 1986)
- 43. B. van der Pol, J. van der Mark, The heartbeat considered as a relaxation oscillation, and an electrical model of the heart. Phil. Mag. Suppl. 6, 763 (1928)
- 44. X.M.H. Huang, C.A. Zorman, M. Mehregany, M.L. Roukes, Nature 421, 496 (2003)
- 45. H.G. Craighead, Science 290, 1532 (2000)
- S.C. Jun, X.M.H. Huang, M. Manolidis, C.A. Zorman, M. Mehregany, J. Hone, Nanotech. 17, 1506 (2006)
- 47. A. Croy, D. Midtvedt, A. Isacsson, J.M. Kinaret, Phys. Rev. B 86, 235435 (2012)
- J.S. Bunch, A.M. van der Zande, S.S. Verbridge, I.W. Frank, D.M. Tanenbaum, J.M. Parpia, H.G. Craighead, P.L. McEven, Science 315, 490 (2007)
- A. Eriksson, S. Lee, A.A. Sourab, A. Isacsson, R. Kaunisto, J.M. Kinaret, E.E.B. Campbell, Nanolett. 8, 1224 (2008)
- A. Eichler, J. Moser, J. Chaste, M. Zdrojeck, I. Wilson-Rae, A. Bachtold, Nat. Nanotechnol. 6, 339 (2011)
- S.C. Jun, S. Moon, W. Kim, J.H. Cho, J.Y. Kang, Y. Jung, H. Yoon, J. Shin, I. Song, J.Y. Choi, J.H. Choi, M.J. Bae, I.T. Han, S. Lee, J.M. Kim, New J. Phys. 12, 043023 (2010)
- 52. X.M.H. Huang, X.L. Feng, C.A. Zorman, M. Mehregany, M.L. Roukes, New J. Phys. 7, 247 (2005)
- 53. H. Noh, S.B. Shim, M. Jung, Z.G. Khim, J. Kim, Appl. Phys. Lett. 97, 033116 (2010)
- 54. S. Zaitsev, O. Shtempluck, E. Buks, O. Gottlieb, Nonlinear Dyn. 67, 859 (2012)
- 55. F.M. Alsaleem, M.I. Younis, H.M. Ouakad, J. Micromech. Microeng. 19, 045013 (2009)
- 56. A. Eichler, J. Moser, J. Chaste, M. Zdrojek, I.W. Rae, A. Bachtold, Nat. Tech. 6, 339 (2011)
- 57. I.K. Kim, S.I. Lee, J. Appl. Phys. **114**, 104303 (2013)
- B. Jeong, H. Cho, M.F. Yu, A.F. Vakakis, D.M. McFarland, L.A. Bergman, ACS Nano 7, 8547 (2013)
- 59. A. Ghosh, R. Vijaya, Pramana J. Phys. **83**, 147 (2014)

- L. Demeio, S. Lenci, in *Proceedings of the 8th International Conference on Structural Dynamics, EURODYN2011* (2011), Leuven, ed. by G. De Roeck, G. Degrande, G. Lombaert, G. Muller
- 61. V.M. Laltin, D.A. Filippov, T.O. Firsova, Tech. Phys. Lett. 40, 237 (2014)
- P. Viramani, F. Faridazar, Accelerated determination of ASR susceptibility during concrete prism testing through nonlinear resonance ultrasonic spectroscopy (Federal Highway Administration Report, Georgetown, 2013)
- 63. S.O. Waheed, N.H. Mostafa, D.H. Jawad, World J. Mech. 1, 21 (2011)
- S. Rajasekar, R. Velusamy, Quantum Mechanics 1: The Fundamentals (CRC Press, Boca Raton, 2015)
- 65. L.I. Schiff, *Quantum Mechanics* (McGraw-Hill, Singapore, 1968)
- E. Campos-Canton, J.G. Barajas-Ramirez, G. Solis-Perales, R. Fermat, Chaos 20, 013116 (2010)
- 67. K. Dietz, Overall population patterns in the transmission cycle of infectious disease agents, in *Population Biology of Infectious Diseases*, ed. by R.M. Anderson, R.M. May (Springer, New York, 1982), pp. 87–102
- 68. B.T. Grenfell, B. Bolker, A. Kleczkowski, Seasonality, demography and the dynamics of measles in developed countries, in *Epidemic Models: Their Structure and Relation to Data*, ed. by D.Mollison (Cambridge University Press, Cambridge, 1995), pp. 248–268
- 69. D.J.D. Earn, P. Rohani, B.M. Bolker, B.T. Grenfell, Science 287, 667 (2000)
- 70. J.M. Ireland, R.A. Norman, J.V. Greenman, J. Theor. Biol. 231, 229 (2004)
- 71. M.G. Roberts, R.R. Kao, Math. Biosci. 149, 23 (1998)
- 72. J.V. Greenman, R.A. Norman, J. Theor. Biol. 247, 492 (2007)
- 73. M. Kundu, D. Bauer, Phys. Rev. Lett. 99, 123401 (2005)
- 74. R. Gerber, Vibrational Medicine (Bear and Company, Santa Fe, 1988)
- 75. H.W.Ch. Postma, I. Kozinsky, A. Husain, M.L. Roukes, Appl. Phys. Lett. 86, 223105 (2005)
- 76. D. Antonio, D. Zanette, D. Lopez, Nat. Commun. 3, 806 (2012)
- J.C. Vedruccio, E. Mascia, V. Martines, Int. Rev. Armed Forces Medical Services 78, 120 (2005)
- 78. T.F. Peters, Transitions in Engineering: Guillaume Henri Dufour and the Early 19th Century Cable Suspension Bridge (Birkhauser, Basel, 1987)
- 79. K. Horvat, M. Miskovic, O. Kuljaca, Ind. Technol. 2, 881 (2006)
- 80. F.M. Mahomed, P.G.L. Leach, Quest. Math. 8, 241 (1985)
- V.K. Chandrasekar, M. Senthilvelan, M. Lakshmanan, Proc. R. Soc. A Math. Phys. Eng. Sci. 461, 2451 (2005)
- 82. L. Gammaitonic, P. Hänggi, P. Jung, F. Marchesoni, Rev. Mod. Phys. 70, 223 (1998)
- 83. P.S. Landa, P.V.E. McClintock, J. Phys. A 33, L433 (2000)
- 84. S. Zambrano, J.M. Casado, M.A.F. Sanjuan, Phys. Lett. A 366, 428 (2007)
- 85. A.S. Pikovsky, J. Kurths, Phys. Rev. Lett. 78, 775 (1997)
- 86. T.I. Fossen, H. Nijmeijer (eds.), *Parametric Resonance in Dynamical Systems* (Springer, Berlin, 2011)
- 87. J. Fajans, L. Friedland, Am. J. Phys. 69, 1096 (2001)

Chapter 2 Stochastic Resonance

Noise is often thought of as interfering with signal detection and information transmission. Static on a radio-station, ancillary conversations in a crowded room and flashing neon light along a busy thoroughfare all tend to obscure or distract from the desired information. Now, it has been realized that certain noise-induced phenomena are of great use in various contexts. One such noise-induced phenomenon which has a wide range of applications in various branches of science and engineering is stochastic resonance. Consider a double-well potential system (bistable system) driven by a weak periodic force of frequency ω . The amplitude of the external driving force is so small that there is no cross-well motion. When noise is added to the system, then at an appropriate noise intensity, a periodic switching between the two wells takes place. At this optimum value of noise intensity the signal-to-noise ratio measured at the frequency ω becomes a maximum. This noise-induced phenomenon is called *stochastic resonance* [1, 2].

The stochastic resonance phenomenon was first introduced by the Italian physicists Benzi et al. [1] to explain the periodicity of earth's ice ages. The eccentricity of the orbit of the earth varies with a periodicity of about 10⁵ years, but according to current theories the variation is not strong enough to cause a dramatic climate change. Suppose the ice-covered and water-covered earth correspond to the two local minima. The variation of eccentricity with the period 10⁵ years is too weak to induce the transition from ice-covered to water-covered earth and vice-versa. By introducing a bistable potential Benzi et al. [1] suggested that a cooperative phenomenon between the weak periodic variation in the eccentricity (the signal) and the other random fluctuations might account for the strong periodicity observed. Motivated by their work, the effect of noise has been investigated in nonlinear systems. Many fascinating phenomena like stochastic resonance [3, 4], noise-enhanced stability [5, 6], noise-delayed extinction [7], noise-induced intermittency [8, 9], synchronization [10-12], phase transition [13], pattern formation [14], linearization [15, 16], stochastic transport in ratchets [17], mixed mode oscillations [18, 19] and collective firing in excitable media [20, 21] have been reported. A phenomenon

similar to stochastic resonance was found in an experiment with acoustically excited turbulent, submerged jets [22] where the role of noise is played by turbulence. Being noisy, nature takes advantages of such noise-induced processes to employ random fluctuations as an agent of self-organization and improved performance. This is the prime reason why living systems work so reliably in spite of the presence of various sources of noise.

Stochastic resonance was found in numerous systems ranging from astronomic macrocosm to quantum micro-cosmology. For example, it was found in a ring laser [23], Schmidt trigger [24, 25], tunnel diode [26], electron-paramagnetic-resonance systems [27], monostable systems [28], nanomechanical oscillators [29], carbon nanotube transistors [30, 31], small world networks [32], delayed-feedback systems [33–35], chemical systems [36], financial models [37] and social systems [38]. Stochastic resonance has been investigated in threshold crossing (TC) systems also called *excitable systems* because their output signal consist of pulses which can be emitted when the noisy input crosses some threshold [39, 40].

The present chapter, briefly summarizes first the characterization of stochastic resonance in terms of signal-to-noise ratio, mean residence time and probability distribution of residence times. This is followed by a numerical illustration of stochastic resonance in a double-well Duffing oscillator. Next, a theory of stochastic resonance for a overdamped bistable system is given. The occurrence of stochastic resonance in an optomechanically coupled oscillator, a magnetic system and in a monostable system is also discussed. Realization of stochastic resonance in quantum systems is brought out. Finally, some of its applications are enumerated.

2.1 Characterization of Stochastic Resonance

Consider a bistable system driven by a weak periodic force and an additive noise exhibiting stochastic resonance. Quantities such as signal-to-noise ratio (*SNR*), input-output gains, cross-correlation, mutual information, channel capacity, detection probability and propagation distance are useful to analyze the performance of the system in the presence of noise.

What are the signatures of stochastic resonance? The most common measure used to characterize stochastic resonance is SNR. Suppose the input signal is the sine-wave $S(t) = f \sin \omega t$. The power spectrum of the noisy signal is a superposition of a background power spectral density and delta-spikes centered at $\Omega = (2n+1)\omega$ with $n = 0, \pm 1, \dots, SNR$ is the ratio of the Fourier coefficient and the value of the noise at the frequency ω . That is, it measures how much the system output, say x(t), contains the input signal frequency ω . Often it is defined as

$$SNR = 10 \log_{10} \left(\frac{S(\omega)}{N(\omega)} \right) dB . \qquad (2.1)$$

The signal power $S = |X(\omega)|^2$ is the magnitude of the output power spectrum $X(\Omega)$ at the frequency ω . S can be used as a measure of the response of the system to the external driving force. The background noise spectrum $N(\omega)$ at the input frequency ω is some average of $|X(\Omega)|^2$ at nearby frequencies. In a typical stochastic resonance phenomenon, SNR increases with the noise intensity D, peaks at an optimum value of D and then decreases smoothly for higher values of D.

Other statistical tools useful for the characterization of stochastic resonance are the mean residence time ($T_{\rm MR}$) and probability distribution of residence time ($P(T_{\rm R})$). A residence time in a well is defined as a time duration spent by the system in it before switching to another well. Mean residence time is the average over a large number of residence times. In the absence of noise, the motion of the system is confined to a well or an equilibrium state. That is, before the noise-induced dynamics, the residence time of the system in each well is infinite. When the noise intensity is increased at a certain value of the noise intensity, say $D_{\rm c}$, the system begins to visit the other well also. For D values, just above $D_{\rm c}$, $T_{\rm MR}$ of the system in a well is very large, say, $T_{\rm MR} \gg T/2$ where $T=2\pi/\omega$ is the period of the input periodic signal. In a symmetric bistable system $T_{\rm MR}$ in the two wells are equal and moreover at resonance (at which SNR is maximum) $T_{\rm MR}=T/2$. In asymmetric systems at resonance periodic switching between the wells occur but with different switching rates for the left- and right-wells. For large values of the noise intensity, erratic switching between the wells occur.

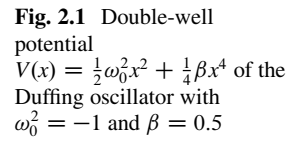
The $P(T_R)$ demonstrates coherence of the stochastic response with the modulation. This quantity shows a sequence of strong Gaussian-like peaks centered at odd integer multiples of the modulation half period T/2 and exponentially decaying maximum amplitudes.

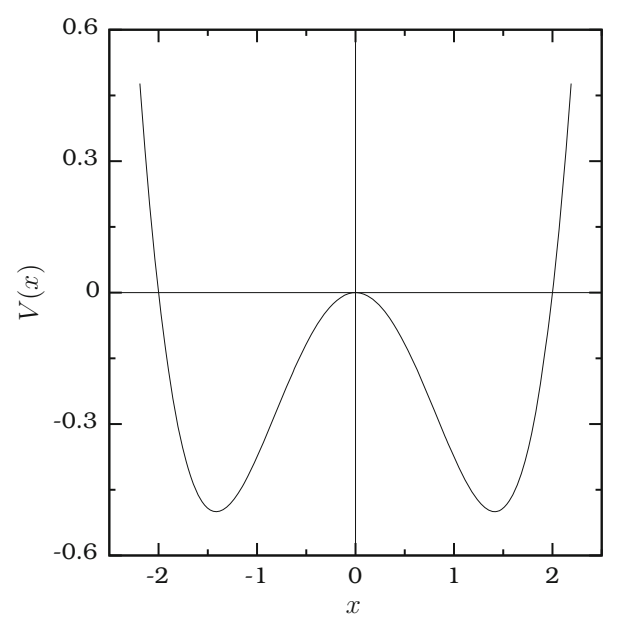
2.2 Stochastic Resonance in Duffing Oscillator

Let us illustrate the stochastic resonance phenomenon in the Duffing oscillator

$$\ddot{x} + d\dot{x} + \omega_0^2 x + \beta x^3 = f \sin \omega t + \xi(t) . \tag{2.2}$$

The term $f \sin \omega t$ is normally interpreted as representing the signal which is to be amplified. The noise term is often an additive Gaussian white noise with the moments $\langle \xi(t) \rangle = 0$, $\langle \xi(t) \xi(s) \rangle = D\delta(t-s)$ and D is the noise intensity (variance). Fix the parameters as $\omega_0^2 = -1$, $\beta = 0.5$, d = 0.5, $\omega = 0.05$. In the absence of the noise term $\xi(t)$, for small values of the amplitude f of the driving signal, two period-f (= f (f) orbits coexist. Each of the two wells of the potential (Fig. 2.1) has one periodic orbit. As the value of f increases, the interval of the state variable f covered by the periodic orbits increase. For f (f) are a critical value of f, the trajectory makes a periodic transition from one well to another well forming a cross-well periodic orbit. The critical value of f, f, at which cross-well orbit first occurs is 0.56.





Now, fix f at 0.38, a value $< f_c$, so that the additional force is weak. Here, the term weak means that in the absence of noise the periodic force alone is unable to move a particle from one well to the other one. Let us investigate the effect of added noise by varying the noise intensity D. In the numerical simulation Eq. (2.2) is integrated with the time step $\Delta t = (2\pi/\omega)/2000$ from t to $t+\Delta t$ without the noise term. Then, the noise is added to the state variable x as $x(t+\Delta t) \to x(t+\Delta t) + \sqrt{D\Delta t} \, \xi(t)$ where $\xi(t)$ represents Gaussian random numbers with zero mean and variance D. This procedure is repeated.

2.2.1 Time-Series Plot

Figure 2.2 shows a time series plot for few values of D. For small values of D the motion is confined to one well alone as in Fig. 2.2a. The system exhibits the behaviour similar to that of the noise free case but slightly perturbed by the noise. This type of behaviour occurs for $D < D_c = 0.011$. At this critical value of D crosswell behaviour occurs. The trajectory jumps randomly from one well to another. In Fig. 2.2b for D = 0.05 just above D_c , the state variable x switches irregularly and rarely between positive and negative values, that is, between the two wells. In the presence of forcing, the system initially in the well, say, V_+ (x > 0) is forced by the noise to leave the well. Then, the system enters the well V_- (x < 0) and wanders irregularly there for some time and jumps back to the well V_+ and so on. The switching is not periodic. As the value of D increases further, the switching

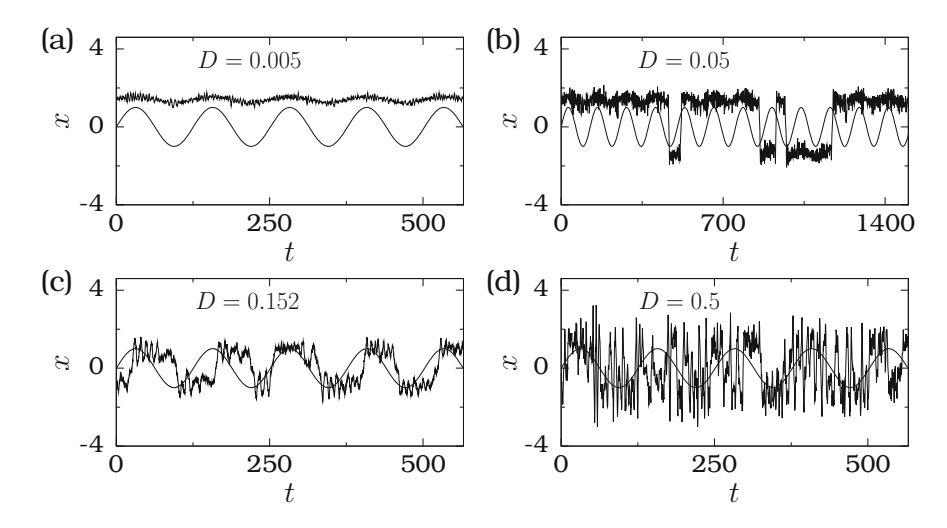


Fig. 2.2 Time series plot of Eq. (2.2) in the presence of periodic external force for four values of noise intensity D. The parameters of the system are $\omega_0^2 = -1$, $\beta = 0.5$, d = 0.5, f = 0.38 and $\omega = 0.05$. The external force $f \sin \omega t$ is also shown

between the wells increases. At D=0.152 (Fig. 2.2c) almost periodic switching is observed. The periodicity of the noise-induced oscillation in the time behaviour of x is the same of the driving periodic force. This is the signature of the stochastic resonance. Further increase of the noise intensity produces a loss of coherence. For sufficiently large values of D, the motion is strongly dominated by the noise. In this case intermittent dynamics disappears and the trajectory jumps erratically between the wells. This is shown in Fig. 2.2d for D=0.5. From the above, it is clear that the phenomenon of stochastic resonance is simply an event of potential barrier crossing, where the transition from one local equilibrium situation to the other happens in the presence of noise. An indication of stochastic resonance is that the flow of information through a system is maximized when the input noise intensity is set to a certain value.

Let us point out the mechanism of stochastic resonance. When a weak periodic signal is applied to a bistable system, it serves to periodically modulate the potential by raising and lowering the wells as shown in Fig. 2.3. Essentially, the additive forcing changes alternately the relative depth of the potential wells, increasing the probability of jumps between wells twice per modulation period. At a critical value of the noise intensity, the particle in a well arrives at the neighbourhood of the local maximum (barrier), almost when the barrier height seen by it is minimum so that the noise is able to push it to the other well. Thus, there is a synchronization between the periodic force and the output signal resulting in a periodic switching of the particle from one well to another well. The essential ingredients for stochastic resonance consists of a nonlinear system, a weak signal and a source of noise. In bistable systems, the underlying mechanism of stochastic resonance is easily appreciated,

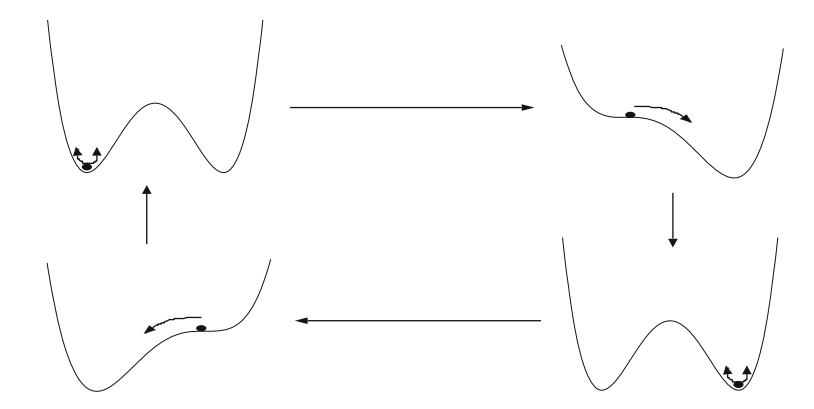


Fig. 2.3 Periodic modulation of the potential wells by the driving periodic force and the switching motion of the particle from one well to another induced by the additive noise

and in fact has been known since 1929 with the work of Peter Debye (1884–1966), a Dutch-American physicist and physical chemist, and Nobel laureate in Chemistry, on reorienting polar molecules [41].

2.2.2 Mean Residence Time

In order to get a deep understanding of the observed dynamics and the influence of noise one can compute the mean residence time, switching rate and SNR. For a fixed noise intensity D, residence times $T_{\rm R}$ on each well are computed for a set of 10^5 transitions. Then mean residence time $T_{\rm MR}$ is calculated. One can define the switching rate T' as the number of times the particle jumped from one well to another per driving period of the external periodic force. Figure 2.4 shows the numerically computed $T_{\rm MR}$ and T' as a function of the noise intensity D. For $D < D_{\rm c}$, there is no switching and so $T_{\rm MR}$ is infinity and T' is zero. $T_{\rm MR}$ decreases with increase in D. For values of D just above $D_{\rm c}$, the mean residence time is much larger than the period of the driving force indicating that the chance for the system to switch from one potential well to another is very small.

For $D=0.152~T_{\rm MR}\approx\pi/\omega\approx62.83185\cdots$. In this case nearly periodic switching between the two wells V_+ and V_- occur. This is clearly evident in Fig. 2.4. At this critical value of D the switching rate is 2. Later, it will be shown that the SNR is maximum at this critical value of D. Denote the value of D at which $T_{\rm MR}\approx\pi/\omega$ and T'=2 as $D_{\rm MAX}$. When T'=2 there is a co-operation between the periodic driving force and the noise. The trajectory switches between the positive and negative values with the period approximately half of the period of the applied external periodic force. Nearly at the end of one half of a drive cycle the trajectory in one well is likely to jump to the other well and after the next half cycle it is likely

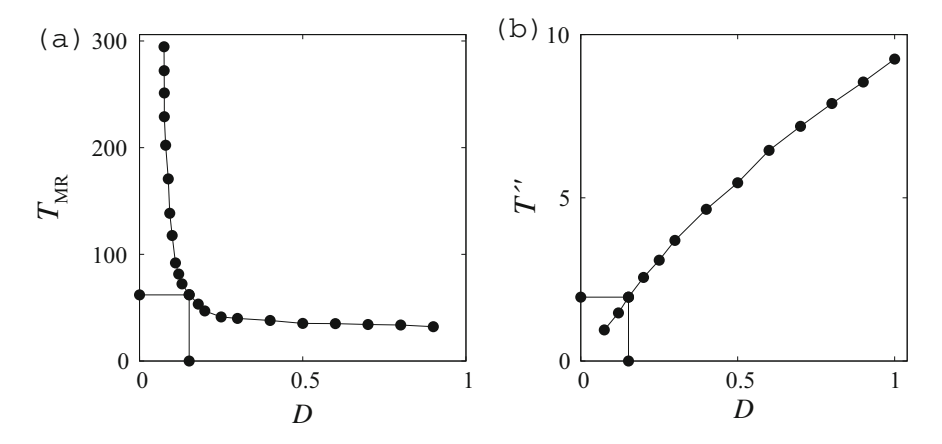


Fig. 2.4 Mean residence time $T_{\rm MR}$ and switching rate T' as a function of noise intensity D for the Duffing oscillator. The *solid circle* on the D-axis denotes the value of D at which resonance occurs and the corresponding *solid circles* on the y-axis in the subplots (a) and (b) denote the corresponding values of $T_{\rm MR}(=T/2)$ and T'(=2), respectively

to return back. This is the signature of stochastic resonance. Note that at $D=D_{\rm MAX}$ not only $T_{\rm MR}\approx\pi/\omega$ but residence times $T_{\rm R}$ are all $\approx\pi/\omega$. For other values of D with $D>D_{\rm c}$, $T_{\rm R}$ are randomly distributed over a range. Thus the relevant condition for resonance to occur is to tune the noise intensity to an optimum value so that synchronization between the drive and the output signal occurs. In symmetric bistable systems this corresponds to setting $T_{\rm MR}$ as T/2. In asymmetric bistable systems $T_{\rm MR}$ at resonance is different [42]. For $D>D_{\rm MAX}$ loss of coherence is produced and the mean residence time of the system is much smaller than the value T/2. This means that the system will not wait for the relevant potential barrier to assume a minimum value.

2.2.3 Power Spectrum and SNR

Now, characterize stochastic resonance by using SNR, which can be calculated from the power spectrum. To obtain the power spectrum of the variable x, a set of 2^{10} data collected at a time interval of $(2\pi/\omega)/10$ is used. The output of the fast Fourier transform (FFT) routine is the spectral density of the output signal. More accurate spectral densities are obtained by averaging over 25 different realizations of Gaussian random numbers. To calculate SNR, the peak height of the signal and the broad-band noise level at the signal frequency ω are measured. The peak height is directly read from the FFT data. To calculate the background of the power spectrum about ω , consider the power spectrum in the interval $[\omega - \Delta\omega, \omega + \Delta\omega]$ after

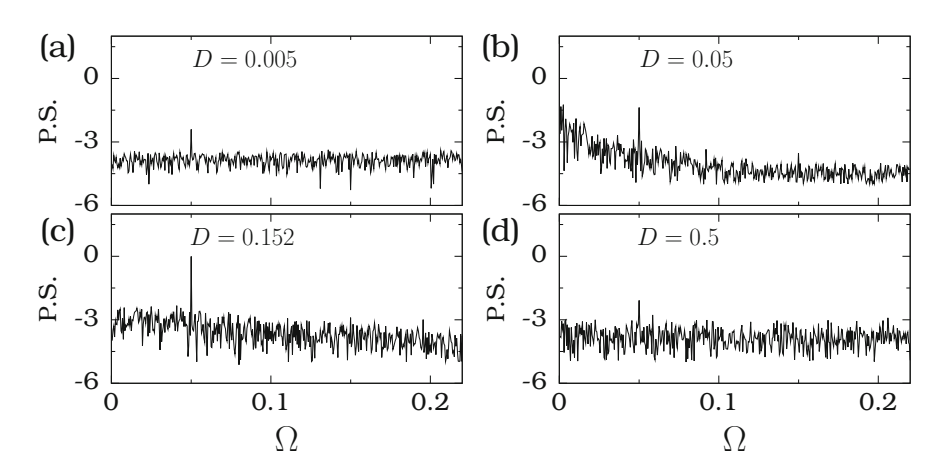


Fig. 2.5 Power spectral density of x-component of the state variable of the Duffing oscillator for different values of noise intensity D. The main peak in the spectrum is at the frequency ($\omega = 0.05$) of the periodic driving force

subtracting the spike at the frequency ω . The average value of the power spectrum in the above interval is taken as the background noise level at ω .

Figure 2.5 depicts the power spectra for four different values of D. In all the subplots, the power spectrum has a peak at the frequency $\omega=0.05$ of the system riding on a broad noise background. The interplay between noise and periodic driving force results in a sharp increase of the signal power spectrum about the forcing frequency ω . When the noise intensity D is increased from D_c , the height of the peak increases for a while and then decreases. This is a signature of stochastic resonance. The amplitude of the noise background is obtained by averaging the spectral density for Ω in the interval 0.04–0.06 after eliminating the peak at the periodic driving frequency $\omega=0.05$. Equation (2.1) gives the value of *SNR* in units of decibel. It is calculated for a range of noise intensity above $D_c=0.011$.

Signal and noise power densities used to calculate SNR are plotted against D in Fig. 2.6a. Figure 2.6b shows the plot of SNR as a function of D. In Fig. 2.6a as D increases, the noise and signal levels increase. The noise level attains a maximum at D=0.09. When D is increased further, the noise level is almost flat. On the other hand, the signal level increases for D values above D_c and attains a maximum level at D=0.152 and then begins to decrease. Though for D in the interval [0,4] both the signal and noise levels increase, the former increases relatively at a higher rate. As a result the SNR increases with noise intensity D and peaks at $D_{MAX}=0.152$. For $D>D_{MAX}$ the noise level is almost constant whereas the signal level decreases. Consequently, the SNR decreases with D for $D>D_{MAX}$. For D values just above D_c , the time series plot shows rare switching between the wells. That is, for low intensity the combination of noise and external periodic force occasionally gives the system a kick sufficiently large to cross the barrier between the two wells. As D increases, at 0.152 a transition between the two wells is induced for almost over every half

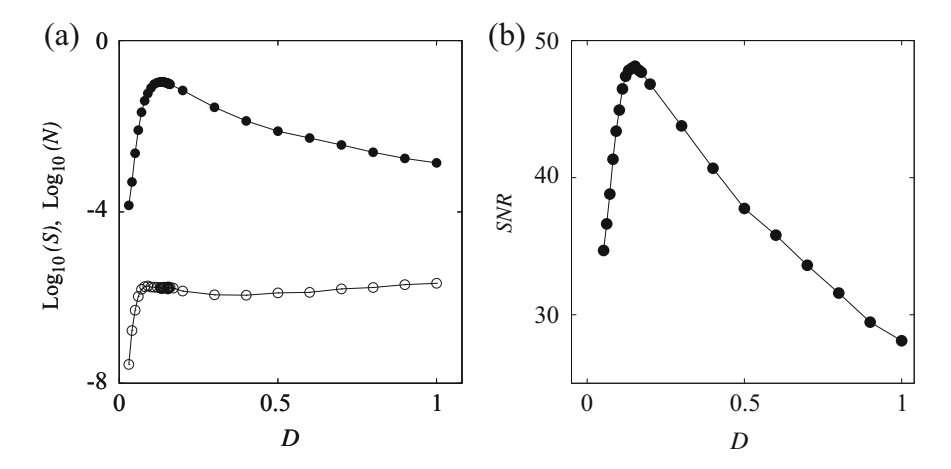


Fig. 2.6 (a) Output signal density (marked by *filled circle*) and noise power density (marked by *open circle*) as a function of input noise intensity D for the Duffing oscillator. (b) Signal-to-noise ratio (*SNR*) as a function of input noise intensity for $\omega_0^2 = -1$, $\beta = 0.5$, d = 0.5, f = 0.38 and $\omega = 0.05$

period of the driving force which resulted in the maximum of *SNR*. As D is further increased, switching become frequent and irregular so that the power in the Fourier spectra is distributed widely over a wide range of frequencies thereby leading to a decrease in *SNR*. Stochastic resonance indicates that the flow of information through the system is maximized when the input noise intensity is set to an optimum value (D_{MAX}) . Note that *SNR* vanishes for both $D \to 0$ and $D \to \infty$ and it peaks at a critical value. The point is that the performance of the system with an optimum noise is better than its performance without noise.

2.2.4 Probability Distribution of Residence Times

Although the power spectrum is the most widely used coherence measure, it is not the only possibility. An alternative quantity, which also clearly demonstrates the stochastic resonance phenomenon is the probability distribution of normalized residence times. This is obtained as follows. For a fixed noise intensity D, 10^5 residence times T_R on a well are computed. Then, normalized residence times are obtained by dividing T_R by T, where $T = 2\pi/\omega$ is the period of the weak periodic force $f \sin \omega t$. The distribution of normalized residence times is shown in Fig. 2.7 for four different values of the noise intensity D with $\omega = 0.05$. The distribution shows a sequence of strong Gaussian-like peaks centered near the discrete set $T_R/T = n + \frac{1}{2}$, $n = 0, 1, 2, \ldots$ That is, $P(T_R)$ has peaks at odd integral multiples of half of the forcing period, T/2. The height of the peaks decrease with their order n. These peaks correspond to the appropriate times for the system to make transitions

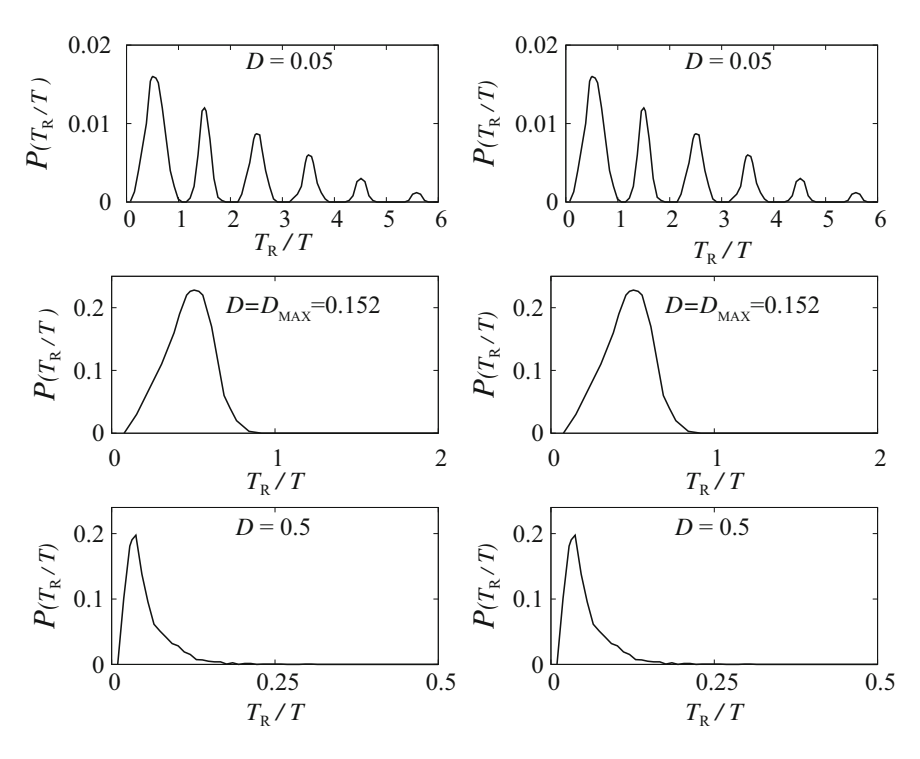
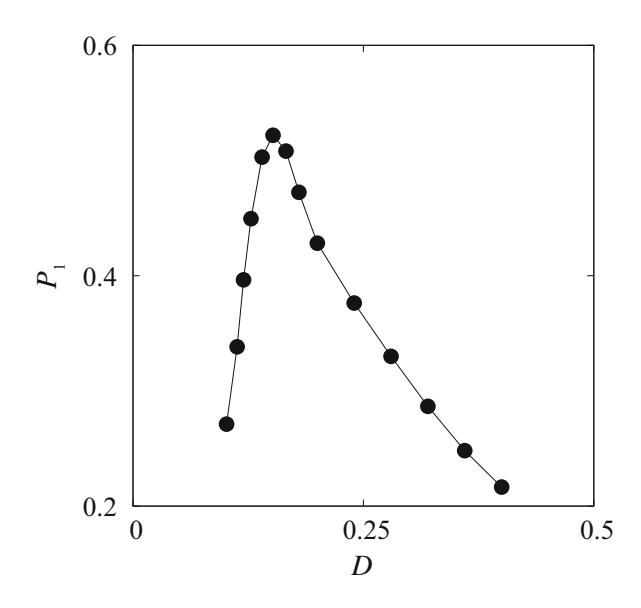


Fig. 2.7 Normalized residence time distribution for different values of noise intensity D. Left-column and right-column subplots are for the left-well and the right-well, respectively

between the potential wells. At these times the relevant potential barrier becomes a minimum. This happens when the potential $V(x,t) = V(x) - fx \sin \omega t$ is tilted most extremely to the left or right. If the system moves at this time into the other well, then it will reside in that well for almost T/2 time duration until the new relevant barrier height becomes a minimum. Thus, T/2 is a more suitable residence time interval. If the system is unable to switch to the other well in a T/2 time interval, then it has to wait another one complete period of the drive until the relevant potential barrier takes a minimum value. In this case, the residence time becomes 3T/2 and is the location of the second peak in Fig. 2.7.

Let us denote the maximum of peaks in the successive Gaussian type distribution as P_n . A meaningful criterion of stochastic resonance based on normalized residence times distribution is the variation of the height of the peak (P_1) at the half driving period [4]. Figure 2.8 shows the numerically computed P_1 as a function of D. For values of D nearly above D_c , T_R/T is distributed relatively over a wide interval of time. As D increases, the range of T_R decreases and hence $P(T_R)$ of smaller T_R increases. This happens up to $D = D_{\text{MAX}} = 0.152$. Consequently, P_1 increases from a small value and reaches a maximum at $D = D_{\text{MAX}}$. As D is further increased P_1 decreases.

Fig. 2.8 Numerically computed P_1 as a function of D for the Duffing oscillator



Stochastic resonance in the electronic circuit simulation of the Duffing oscillator, Eq. (2.2), has been reported in [43]. Badzey and Mohanty [44] fabricated two double-clamped damped nanomechanical beams from single-crystal of silicon making use of an e-beam lithography and dry etching and observed stochastic resonance.

2.3 Theory of Stochastic Resonance

The overdamped bistable system

$$\dot{x} = -\frac{dV}{dx} + \xi(t) , \quad V(x,t) = -\frac{1}{2}\omega_0^2 x^2 + \frac{1}{4}\beta x^4 - fx\cos\omega t$$
 (2.3)

with ω_0^2 and $\beta > 0$ is used as a prototype model equation for developing theoretical approaches and investigating various features of stochastic resonance. In the above equation ξ is a Gaussian white noise with variance D. In the absence of the periodic driving the double-well potential has two minima $x_{\pm} = \pm c = \pm \sqrt{\omega_0^2/\beta}$ and a maximum x' (the location of the maximum of the potential separating the two wells) at the origin. The barrier heights of the two wells are equal and are $h_{\pm} = \omega_0^4/(4\beta)$. It is possible to obtain expressions for signal and noise output from bistable systems which agree with numerical and experimental analysis thereby providing much insight into the physical source of the stochastic resonance phenomenon. McNamara

and Wiesenfeld [45] developed a theory for stochastic resonance based on a rate equation approach. In the following, their theory is briefly presented.

2.3.1 Analytical Expression for Power Spectrum

Let us treat the dynamical variable as discrete. It can be either x_+ or x_- with probabilities $n_{\pm} = P(x = x_{\pm})$. For a continuous variable, as with the double-well system, write

$$n_{-} = 1 - n_{+} = \int_{-\infty}^{x'} P(x) \, \mathrm{d}x \,,$$
 (2.4)

where the probability density is

$$P(x,t) = n_{+}(t)\delta(x - x_{+}) + n_{-}(t)\delta(x - x_{-}).$$
 (2.5)

The values of x_{\pm} are chosen suitably so that the error in the variance of x is minimum. For simplicity, assume that the system is symmetrical about x=0 and hence $x_{\pm}=\pm c$. The variance of an unmodulated two-state system in its steady state $(n_{\pm}=1/2)$ is

$$\langle x^2 \rangle = \int_{-\infty}^{\infty} x^2 P(x) \, \mathrm{d}x = x_+^2 n_+ + x_-^2 n_- = c^2 \,.$$
 (2.6)

The master equation [46] governing the evolution of n_+ is

$$\frac{\mathrm{d}n_{+}}{\mathrm{d}t} = -\frac{\mathrm{d}n_{-}}{\mathrm{d}t} = W_{-}(t)n_{-} - W_{+}(t)n_{+}$$

$$= W_{-} - [W_{-} + W_{+}]n_{+}, \qquad (2.7)$$

where $W_{\pm}(t)$ is the transition rate out of the state x_{\pm} . The solution of Eq. (2.7) is

$$n_{+}(t) = \frac{1}{g(t)} \left[n_{+}(t_0)g(t_0) + \int_{t_0}^{t} W_{-}(t')g(t') dt' \right], \qquad (2.8a)$$

where

$$g(t) = e^{\int_{0}^{t} W_{+}(t') + W_{-}(t') dt'}.$$
 (2.8b)

If the system is subjected to a periodic signal $f_0 \cos \omega t$ then

$$W_{\pm}(t) = F(\mu \pm f_0 \cos \omega t) . \tag{2.9}$$

The time dependence of $W_{\pm}(t)$ is due to the external driving force. W_{\pm} can be expanded in the small parameter $\eta = f_0 \cos \omega t$ as

$$W_{\pm} = \frac{1}{2} \left(\alpha_0 \mp \alpha_1 f_0 \cos \omega t + \alpha_2 f_0^2 \cos^2 \omega t + \cdots \right) , \qquad (2.10a)$$

$$W_{+} + W_{-} = \alpha_0 + \alpha_2 f_0^2 \cos^2 \omega t + \cdots, \qquad (2.10b)$$

where $\alpha_0 = 2F(\mu)$ and $\alpha_n = 2(-1)^n d^n F/d\eta^n$. Now, integration of Eq. (2.7) gives, to first-order in η ,

$$n_{+}(t|x_{0},t_{0}) = \frac{1}{2} \left\{ e^{-\alpha_{0}(t-t_{0})} \left[2\delta_{x_{0}c} - 1 - \frac{\alpha_{1}f_{0}\cos(\omega t_{0} - \phi)}{(\alpha_{0}^{2} + \omega^{2})^{1/2}} \right] + 1 + \frac{\alpha_{1}f_{0}\cos(\omega t - \phi)}{(\alpha_{0}^{2} + \omega^{2})^{1/2}} \right\},$$

$$(2.11)$$

where $\phi = \tan^{-1}(\omega/\alpha_0)$. In Eq. (2.11) the Kronecker delta function is 1 if the system is initially in the '+' state and 0 if it is in the '-' state. $n_+(t|x_0, t_0)$ is the conditional probability that x(t) was in the + state at time t given that the state at time t_0 was x_0 .

Equation (2.11) provides a useful statistical information. For example, the auto-correlation function is given by McNamara and Wiesenfeld [45]

$$\langle x(t)x(t+\tau)|x_{0},t_{0}\rangle = c^{2}n_{+}(t+\tau|+c,t)n_{+}(t|x_{0},t_{0})$$

$$-c^{2}n_{+}(t+\tau|-c,t)n_{-}(t|x_{0},t_{0})$$

$$-c^{2}n_{-}(t+\tau|+c,t)n_{+}(t|x_{0},t_{0})$$

$$+c^{2}n_{-}(t+\tau|-c,t)n_{-}(t|x_{0},t_{0})$$

$$= c^{2}\left\{ \left[2n_{+}(t+\tau|+c,t)-1+2n_{+}(t+\tau|-c,t)-1\right] \right\}$$

$$\times n_{+}(t|x_{0},t_{0}) - \left[2n_{+}(t+\tau|-c,t)-1\right] \right\}. (2.12)$$

In the limit $t_0 \to -\infty$

$$\langle x(t)x(t+\tau)\rangle = c^{2} e^{-\alpha_{0}|\tau|} \left[1 - \frac{\alpha_{1}^{2} f_{0}^{2} \cos^{2}(\omega t - \phi)}{\alpha_{0}^{2} + \omega^{2}} \right] + \frac{c^{2} \alpha_{1}^{2} f_{0}^{2} \left\{ \cos \omega \tau + \cos \left[\omega (2t + \tau) + 2\phi \right] \right\}}{2 \left(\alpha_{0}^{2} + \omega^{2} \right)} . \quad (2.13)$$

The power spectrum, which is the Fourier transform of the auto-correlation function, is a function of t and Ω . In an experiment, typically, one may take an

ensemble of many time series t_1, t_2, \dots , compute the power spectrum for each one and then take the average of them. The result is

$$\langle S(\Omega) \rangle_{t} = \frac{\omega}{2\pi} \int_{0}^{2\pi/\omega} S(\Omega, t) dt$$

$$= \frac{\omega}{2\pi} \int_{-\infty}^{\infty} \int_{0}^{2\pi/\omega} \langle x(t)x(t+\tau) \rangle e^{-i\Omega\tau} d\tau dt$$

$$= \int_{-\infty}^{\infty} \left\{ c^{2} e^{-\alpha_{0}|\tau|} \left(1 - \frac{\alpha_{1}^{2} f_{0}^{2}}{2(\alpha_{0}^{2} + \omega^{2})} \right) + \frac{c^{2} \alpha_{1}^{2} f_{0}^{2} \cos \omega \tau}{2(\alpha_{0}^{2} + \omega^{2})} \right\} e^{-i\Omega\tau} d\tau$$

$$= \frac{2c^{2} \alpha_{0}}{\alpha_{0}^{2} + \Omega^{2}} \left(1 - \frac{\alpha_{1}^{2} f_{0}^{2}}{2(\alpha_{0}^{2} + \omega^{2})} \right)$$

$$+ \frac{\pi c^{2} \alpha_{1}^{2} f_{0}^{2}}{2(\alpha_{0}^{2} + \omega^{2})} \left[\delta(\Omega - \omega) + \delta(\Omega + \omega) \right]. \tag{2.14}$$

Then

$$\langle S(\Omega) \rangle_t = \langle S(\Omega) \rangle_t + \langle S(-\Omega) \rangle_t$$

$$= \frac{4c^2 \alpha_0}{\alpha_0^2 + \Omega^2} \left(1 - \frac{\alpha_1^2 f_0^2}{2(\alpha_0^2 + \omega^2)} \right) + \frac{\pi c^2 \alpha_1^2 f_0^2}{\alpha_0^2 + \omega^2} \delta(\Omega - \omega) . \quad (2.15)$$

The power spectrum given by Eq. (2.15) consists of two parts:

- The signal output (the second term in the equation): It is a delta-function at the input signal frequency ω .
- The broad-band noise output: It is a Lorentzian hump centered at $\Omega = 0$. The noise spectrum is the product of the Lorentzian obtained with f = 0 and a correction factor representing the effect of the signal on the noise. For sufficiently small signal amplitude, this factor is nearly the unity.

The effect of the correction factor is the reduction of the noise power. This reduction is most pronounced for low-frequency ($\omega \ll \alpha_0$) and large amplitude of the input signal. The signal has the effect of transferring power from the broad-band into the delta-function spike. Assume that the total output power (signal+noise) is independent of the parameter f_0 and ω . This is a consequence of Parseval's relation, namely, the time integral of the square of the signal is equal to the integral of the power spectrum over all frequencies and moreover the system takes on discrete values $\pm c$ at all times.

2.3.2 Determination of Signal-to-Noise Ratio

The above two-state theory is valid when the drive frequency and the inter-well transition rates are much slower than the intra-well relaxation rate. The correctness of Eq. (2.15) has been verified by numerically integrating Eq. (2.3) and from the obtained power spectrum [45]. The potential V(x,t) given in Eq. (2.3) can be rewritten as $V(x,t) = h_{+}[-2(x/c)^{2} + (x/c)^{4}] - V_{1}(x/c)\cos\omega t$ with $V_{1} = fc$. When f = 0, in the system (2.3), the mean first-passage time is given by the Kramers time (the average time taken by a particle to cross the region x < 0 (x > 0) for a set of initial conditions taken around $x = x_{-}(x_{+})$

$$\tau_{\text{MFP}} = \frac{1}{W} = \frac{2\pi e^{2h_+/D}}{(|V''(0)|V''(c))^{1/2}} = \frac{\sqrt{2}\pi e^{2h_+/D}}{\omega_0^2} \ . \tag{2.16}$$

The Kramers rate formula is derived under the assumption that the probability density within a well is roughly at equilibrium and is a Gaussian distribution centered about the minimum. For $f \neq 0$ there is an interaction between the drive and the noise resulting in a resonance in the *SNR*. Assume that

$$W_{\pm}(t) = \frac{\omega_0^2}{\sqrt{2}\pi} e^{-2(h_{+} \pm V_1 \cos \omega t)/D} . \tag{2.17}$$

In Eq. (2.17) ω must be much smaller than the characteristic rate for probability to equilibrate within a well. Since the rate is $V''(\pm c)$ the value of ω must be $\ll V''(\pm c) = 2\omega_0^2$.

A comparison of Eqs. (2.9) and (2.17) gives $\mu = h_+/D$, $f_0 = V_1/D = fc/D$ and

$$F(\mu + f_0 \cos \omega t) = \frac{\omega_0^2}{\sqrt{2}\pi} e^{-2(\mu + f_0 \cos \omega t)}, \qquad (2.18a)$$

$$\alpha_0 = 2F(\eta = 0) = \frac{\sqrt{2}\,\omega_0^2}{\pi}\,\mathrm{e}^{-2h_+/D}\,,$$
 (2.18b)

$$\alpha_1 = -2 \frac{\mathrm{d}F}{\mathrm{d}\eta}\Big|_{\eta=0} = \frac{2\sqrt{2}\,\omega_0^2}{\pi}\,\mathrm{e}^{-2h_+/D} = 2\alpha_0 \ .$$
 (2.18c)

A substitution of the above in the expression for S gives $S = S_s(\omega)\delta(\Omega - \omega) + S_n(\Omega, \omega)$ where

$$S_{\rm s} = \left[\frac{\frac{8\omega_0^4 f^2 c^4}{\pi D^2} e^{-4h_+/D}}{\frac{2\omega_0^4}{\pi^2} e^{-4h_+/D} + \omega^2} \right] , \qquad (2.19)$$

$$S_{n} = \left[1 - \frac{\frac{4\omega_{0}^{4}f^{2}c^{2}}{\pi^{2}D^{2}}e^{-4h_{+}/D}}{\frac{2\omega_{0}^{4}}{\pi^{2}}e^{-4h_{+}/D} + \omega^{2}}\right] \left[\frac{\frac{4\sqrt{2}\omega_{0}^{2}c^{2}}{\pi}e^{-2h_{+}/D}}{\frac{2\omega_{0}^{4}}{\pi^{2}}e^{-4h_{+}/D} + \Omega^{2}}\right].$$
(2.20)

Then SNR is worked out as

$$SNR = \frac{S_{s}(\omega)}{S_{n}(\Omega = \omega, \omega)}$$

$$= \frac{\sqrt{2} \,\omega_{0}^{2} f^{2} c^{2}}{D^{2}} e^{-2h_{+}/D} \left[1 - \frac{\frac{4\omega_{0}^{4} f^{2} c^{2}}{\pi^{2} D^{2}} e^{-4h_{+}/D}}{\frac{2\omega_{0}^{4}}{\pi^{2}} e^{-4h_{+}/D} + \omega^{2}} \right]^{-1}$$

$$\approx \frac{\sqrt{2} \,\omega_{0}^{2} f^{2} c^{2}}{D^{2}} e^{-2h_{+}/D} . \tag{2.21}$$

Notice that for $D \ll h_+$ the exponential term decays to 0 very rapidly than the term D^2 and so $SNR \to 0$. On the other hand, for very large values of D, $e^{-2h_+/D} \approx 1$ while D^2 diverges leading to $SNR \to 0$. At a moderate noise level, SNR will become a maximum and the corresponding noise intensity, denoted as D_{MAX} , becomes $\approx h_+$. From the expression of SNR, one can observe that the signal output increases with increase in the input signal amplitude and the output noise decreases very slightly. Figure 2.9 shows SNR versus D for two values of ω_0^2 .

The above two-state theory was extended to an asymmetric double-well potential system [47]. Landa et al. [48] proposed a theory of stochastic resonance for weakly damped bistable systems. In their approach, the response to a harmonic signal of a nonlinear stochastic system was represented by the response to the same signal of

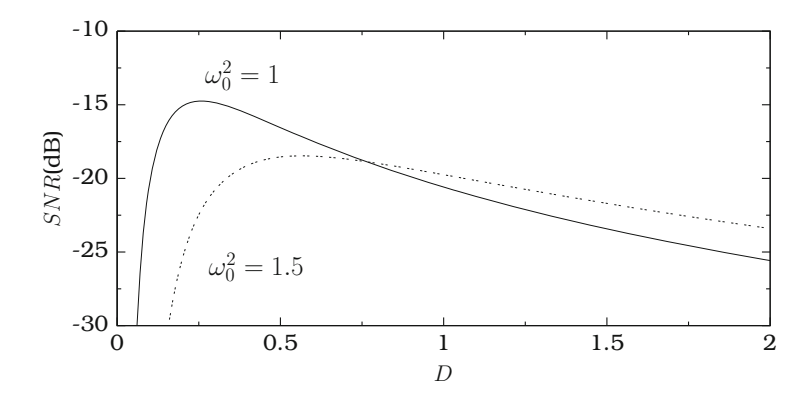


Fig. 2.9 SNR versus D with $f=0.1,~\beta=1.0,~\omega=0.1$ and for two values of ω_0^2 for the overdamped bistable system

an effective linear noise free system. The latter is defined by an effective stiffness and an effective damping which depend on the nonlinearity of the system, the parameters of the signal and the intensity of the noise. An analytical two-state theory for stochastic resonance for a bistable system driven by noise and a rectangular periodic signal was also developed [49]. Stochastic resonance in multistable systems was investigated in [50, 51].

2.4 Stochastic Resonance in a Coupled Oscillator

Mueller et al. [52] reported their observation of stochastic resonance in a macroscopic torsion oscillator. Figure 2.10 depicts the experimental system [52]. The torsion balance oscillator shown in Fig. 2.10a is a precision force measurement device, sensitive down to the femto-Newton range. The oscillator is made of a gold coated glass plate of size $50 \text{ mm} \times 10 \text{ mm} \times 0.15 \text{ mm}$ and doubly suspended on a 15 cm long, $25 \,\mu\text{m}$ diameter tungsten wire. The mass and moment of inertia (*I*) of the oscillator body are $\sim 0.2 \, \text{g}$ and $4.6 \times 10^{-8} \, \text{Kgm}^2$, respectively. The natural frequency of the oscillator is $\omega_0 = 0.36 \, \text{Hz}$ and the quality factor is ~ 2600 .

In the experiment, a laser beam was reflected from the centre of the oscillator and detected by a quadrant diode detector followed by a lock-in-amplifier (LIA). The angular position voltage was sampled at a rate of 5 kHz. The digitized signal was fed to a computerized digital control loop and was then converted to an analog output signal applied to two electronic electrodes. To generate optomechanical coupling, the gold coated glass plate was served as the moving flat mirror of a

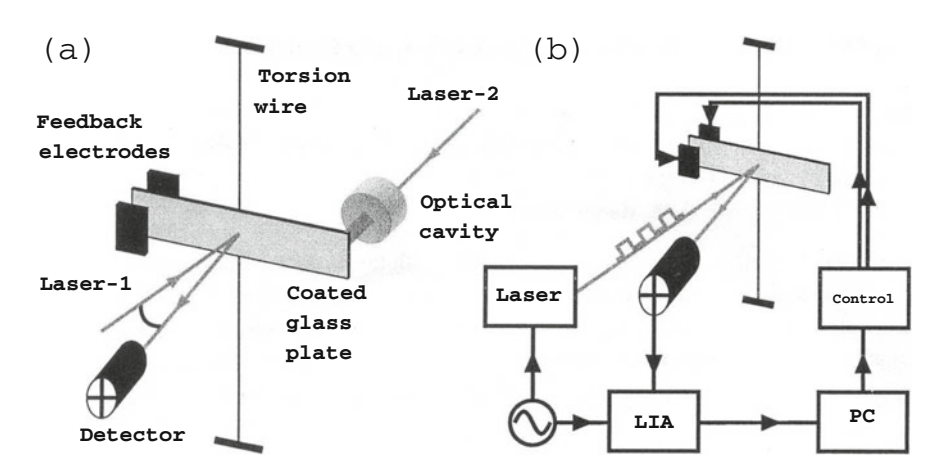


Fig. 2.10 Experimental arrangement of the optomechanically coupled oscillator [52]. (a) The torsion balance oscillator. (b) Block diagram of the set up. (Reprinted with permission from F. Mueller, S. Heugel, L.J. Wang, Phys. Rev. A **79**, 031804(R) (2009). Copyright (2009) by the American Physical Society.)

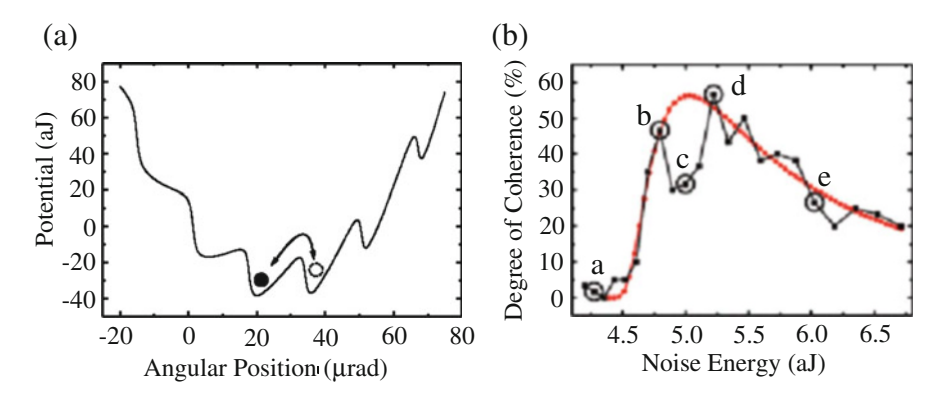


Fig. 2.11 (a) The multistable optomechanical potential generated with an optical cavity input power of 32mW [52]. (b) Degree of coherence versus noise energy. *Dots* are the experimental result and *continuous smooth curve* is the theoretical result given by Eq. (2.21) [52]. (Reprinted with permission from F. Mueller, S. Heugel, L.J. Wang, Phys. Rev. A **79**, 031804(R) (2009). Copyright (2009) by the American Physical Society.)

hemispherical optical cavity. Another spherical mirror with a curvature radius of 25 mm was mounted opposite to the glass plate at a distance of 12.5 mm. A second laser with a wavelength of \sim 660 nm was coupled in. This cavity formed Laguerre–Gaussian TEM₀₀ and TEM₂₀ modes. The finesse of the optical cavity was F=11 and the mean mirror reflectivity was R=0.87. The measurement sensitivity of the oscillator was $100 \, \mathrm{fN}$ (15 $\mu \mathrm{W}$ of optical power) for the detection of radiation pressure in total reflection. The entire set up was kept in a high vacuum ($10^{-7} \, \mathrm{mbar}$) and was mounted on top of an active vibration isolation system.

The multistable potential of the system is shown in Fig. 2.11a. The minima of the potential were formed by TEM₀₀ cavity modes with an angular spacing of \sim 16 μ rad. In the experiment, the mechanical torsion constant of the free system was set to $\tau =$ 9.6×10^{-8} Nm/rad, for which the period of the oscillation was $T_0 = 4.3$ s. Using a cavity optical input power $P_{\rm in} = 32 \,\mathrm{mW}$ the torsion balance was optomechanically coupled. An electronic square-wave signal was applied to the feedback electrodes with $\omega = 200 \, \pi \, \text{mHz}$ and $f = 0.79 \, \text{pNm}$. Noise energy is varied from 4.4 to 6 aJ. The two centered TEM₀₀ mode potential with minima at \sim 20 μ rad and \sim 36 μ rad with an average potential depth of ~ 20 aJ were considered for signal analysis. The period of the excitation signal, $T = 10 \,\mathrm{s}$, was divided into number of intervals of width 0.15 s. Mueller, Heugel and Wang determined the number of residence times in each bin from the time series. Figure 2.11b shows the plot of degree of coherence, ratio of number of occurrences of residence times in the range $T/2 \pm 0.5$ s and total number of residence times in the range 0 to T, versus the noise energy. The degree of coherence was found to be maximum at the noise energy 5.2 aJ. In the Fig. 2.11b the noise energies corresponding to the data points marked as a, b, c, d and e are 4.4aJ, 4.8aJ, 5aJ, 5.2aJ and 6aJ, respectively.

2.5 Stochastic Resonance in a Magnetic System

An example of bistable magnetic elements is the single-domain magnetic particles with anisotropy in the direction of easy magnetization. Here, two stable states have opposite orientations of the magnetic moment vector along the direction of easy magnetization. Isavnin [53] theoretically studied the occurrence of stochastic resonance dynamics of the magnetic moment vector of a superparamagnetic particle with the additional external constant magnetic field applied along one of the directions of easy magnetization. Temperature (T) is considered in place of the noise intensity D.

Let us consider the uniaxial single-domain ferromagnetic particle and denote the angle between the magnetization vector M and the direction of the easy magnetization as θ , the volume of the particle as V, and K as the anisotropy constant. The energy due to the interaction of the magnetic moment of the superparamagnetic particle with the anisotropy field is $-KV\cos^2\theta$. The interaction with the external constant magnetic field is $-\mu_0 MH_1 V\cos\theta$. Then the magnetic energy of the particle is

$$E(\theta) = -KV\cos^2\theta - \mu_0 MH_1 V\cos\theta. \qquad (2.22)$$

In the presence of the external field $H\cos\omega t$ applied along the direction of easy magnetization $E(\theta,t)$ is

$$E(\theta, t) = E(\theta) - \mu_0 MHV \cos \theta \cos \omega t. \qquad (2.23)$$

For the two wells of $E(\theta, t = 0)$ the two local minima are at $\theta_1 = 0$ and $\theta_2 = \pi$ and a local maximum is at $\theta_3 = \cos^{-1}(-\mu_0 M H_1/(2K))$. The potential is shown in Fig. 2.12. The barrier heights of the left-well and the right-well are

$$h_{-} = E(\theta_3) - E(\theta_1) = \frac{(\mu_0 M H_1)^2}{4K} + KV + \mu_0 M H_1 V$$
, (2.24a)

$$h_{+} = E(\theta_{3}) - E(\theta_{2}) = \frac{(\mu_{0}MH_{1})^{2}}{4K} + KV - \mu_{0}MH_{1}V$$
. (2.24b)

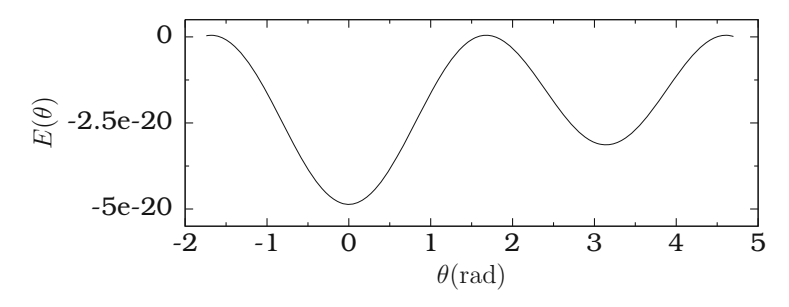


Fig. 2.12 $E(\theta)$ versus θ of a single-domain ferromagnetic particle system. The values of the parameters are $K=4\times10^4\,\mathrm{J/m^3}$, $V=10^{-24}\,\mathrm{m^3}$, $M=1.72\times10^6\,\mathrm{A/m}$, $H_1=4\times10^3\,\mathrm{A/m}$ and $\mu_0=4\pi\times10^{-7}\,\mathrm{H/m}$

The field is assumed to be sufficiently weak so that the orientation of the magnetic moment vector of the particle is unchanged. This is the case for $\mu_0 MHV < h_{\pm}$.

To apply the theory discussed in Sect. 2.3, assume that the magnetic moment vector takes only two states corresponding to the minima of the double-well potential. By introducing $x = M\cos\theta$, one can specify the projection of the magnetization vector on to the direction of easy magnetization having two values $\pm M$ at $\theta = \theta_2 = \pi$ and $\theta = \theta_1 = 0$. Denote $n_{\pm}(t)$ as the probabilities for x to be $x_{\pm} = \pm M$ and $W_{\pm}(t)$ as the rates of particle escape from x_{\pm} states. Then the evolution equations for n_{+} and n_{-} are given by Eq. (2.7). $W_{\pm}(t)$ are given by Isavnin [53]

$$W_{\pm}(t) = \alpha_0 e^{-\frac{h_{\pm}}{k_{\rm B}T} \pm f \cos \omega t}$$
, $f = \frac{\mu_0 MHV}{k_{\rm B}T}$, (2.25)

where $k_{\rm B}$ is the Boltzmann constant, T is the temperature and α_0 is of the order of the frequency of ferromagnetic resonance which is $10^9 - 10^{10} \, {\rm s}^{-1}$ for single-domain iron particles. One can note that $W_+(t) \neq W_-(t)$. With the probability density function $P(x,t) = n_+ \delta(x-x_+) + n_- \delta(x-x_-)$

$$\langle x^2 \rangle = \int_{-\infty}^{\infty} x^2 P(x) \, \mathrm{d}x = x_+^2 n_+ + x_-^2 n_- = M^2 \,.$$
 (2.26)

The solution $n_+(t)$ is given by Eq. (2.8).

Expanding $W_{\pm}(t)$ in a series in the small parameter $\eta = f \cos \omega t$ one obtains the lowest-order

$$W = W_{-}(t) + W_{+}(t) = \alpha_0 e^{-h_{-}/(k_B T)} + \alpha_0 e^{-h_{+}/(k_B T)}. \qquad (2.27)$$

Then

$$n_{+}(t|t_{0}) = e^{-W(t-t_{0})} \left[n_{+}(t_{0}) - \frac{F}{W} - \frac{fF\cos(\omega t_{0} - \phi)}{\sqrt{W^{2} + \omega^{2}}} \right] + \frac{F}{W} + \frac{fFW\cos(\omega t - \phi)}{\sqrt{W^{2} + \omega^{2}}} , \qquad (2.28a)$$

where

$$F = \alpha_0 e^{-h_-/(k_B T)}$$
, $\phi = \tan^{-1}(\omega/W)$. (2.28b)

F is the Kramers rate of escape of the system from the left-well of the asymmetric potential. In the limit of $t_0 \to -\infty$

$$n_{+}(t) = \frac{F}{W} + \frac{fF\cos(\omega t - \phi)}{\sqrt{W^{2} + \omega^{2}}}$$
 (2.29)

Next,

$$\langle x(t) \rangle = \int_{-\infty}^{\infty} x P(x) dx$$

$$= M(2n_{+}(t) - 1)$$

$$= M \left[\frac{2F}{W} + \frac{2Ff \cos(\omega t - \phi)}{\sqrt{W^{2} + \omega^{2}}} - 1 \right]. \tag{2.30}$$

The component of $\langle x(t) \rangle$ which changes with the external driving frequency is

$$\langle x_{\omega}(t) \rangle = \frac{2MFf \cos(\omega t - \phi)}{\sqrt{W^2 + \omega^2}}$$
$$= \frac{2MFf(W \cos \omega t + \omega \sin \omega t)}{W^2 + \omega^2} . \tag{2.31}$$

Writing the modulating signal as $H(t) = He^{i\omega t}$ the magnetization M(t) can be expressed as

$$M(t) = H(\text{Re}\gamma \cos \omega t + \text{Im}\gamma \sin \omega t), \qquad (2.32)$$

where χ is the complex susceptibility. The above two equations give

$$\operatorname{Re}\chi = \frac{2MfFW}{H(W^2 + \omega^2)} = \frac{2\mu_0 V M^2 F W}{k_{\rm B} T(W^2 + \omega^2)},$$
 (2.33a)

$$Im\chi = \frac{2MfF\omega}{H(W^2 + \omega^2)} = \frac{2\mu_0 V M^2 F \omega}{k_B T(W^2 + \omega^2)},$$
 (2.33b)

$$|\chi| = \frac{2\mu_0 V M^2 F}{k_{\rm B} T \sqrt{W^2 + \omega^2}}$$
 (2.33c)

 χ exhibits resonance dynamics when the temperature parameter is varied. For the analysis fix the values of the parameters as $K=4\times 10^4\,\mathrm{J/m^3}$, $V=10^{-24}\,\mathrm{m^3}$, $M=1.72\times 10^6\,\mathrm{A/m}$, $H=10^3\,\mathrm{A/m}$ and $\mu_0=4\pi\times 10^{-7}\,\mathrm{H/m}$. Figure 2.13 shows Re χ , Im χ and $|\chi|$ as a function of temperature T for three values of H_1 . The maximum value of susceptibility decreases with increase in H_1 . In Fig. 2.14 $|\chi|$ is plotted for three values of the anisotropy parameter K. The effect of K can be clearly seen in this figure.

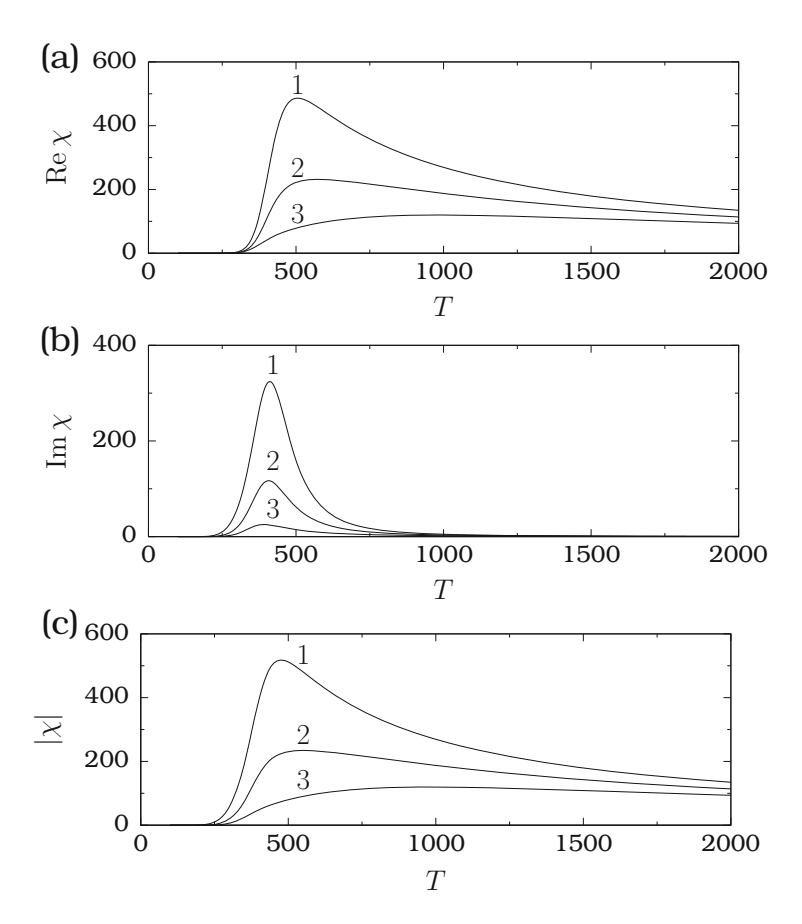


Fig. 2.13 Variation of (a) Re χ , (b) Im χ and (c) $|\chi|$ as a function of temperature T (in kelvin). The curves 1, 2 and 3 are for $H_1=0$ A/m, 5×10^3 A/m and 10^4 A/m, respectively

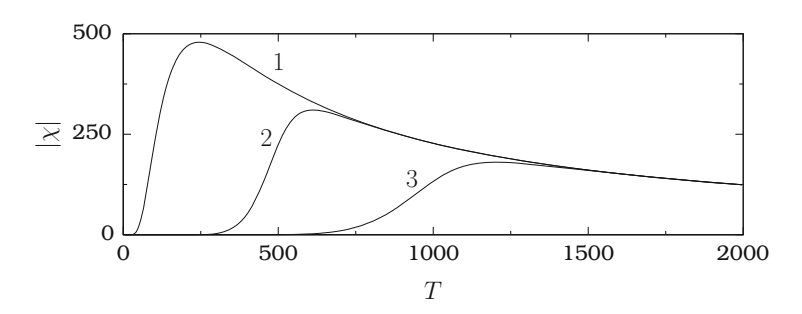


Fig. 2.14 $|\chi|$ versus T (in kelvin). The curves 1, 2 and 3 are for $K=10^4$ J/m³, 5×10^4 J/m³ and 10^5 J/m³, respectively, with $H_1=10^3$ A/m

2.6 Stochastic Resonance in a Monostable System

In a monostable system with additive noise nonmonotonic increase in the signal amplitude and continuous decrease in the noise amplitude take place [54]. However, stochastic resonance does not occur. Consider the overdamped nonlinear system

$$\dot{x} + \beta x^3 - \gamma - x\xi(t) = f\cos\omega t + \eta(t) , \qquad (2.34)$$

where $\beta > 0$, γ is the bias term and $\xi(t)$ and $\eta(t)$ are uncorrelated white noise with zero mean and the variance given by $\langle \xi(t)\xi(s)\rangle = 2D_{\rm m}\delta(t-s)$ and $\langle \eta(t)\eta(s)\rangle = 2D_{\rm a}\delta(t-s)$, respectively. The intensities of the additive and multiplicative noises are denoted as $D_{\rm a}$ and $D_{\rm m}$, respectively. In the absence of noise and periodic force the system has only one stable state. Guo et al. [55] have obtained an analytic expression for *SNR* for the system (2.34).

The Fokker–Planck equation for the probability density P(x, t) is

$$\frac{\partial P(x,t)}{\partial t} = -\frac{\partial}{\partial x} F(x,t) P(x,t) + \frac{\partial^2}{\partial x^2} \left[G(x) P(x,t) \right] , \qquad (2.35a)$$

where

$$F(x,t) = -\beta x^2 + \gamma + D_{\rm m}x + f\cos\omega t$$
, $G(x) = D_{\rm m}x^2 + D_{\rm a}$. (2.35b)

In the adiabatic limit, that is, a small enough value of ω so that the time for the system to reach a local equilibrium is smaller than the period $1/\omega$,

$$P_{\rm st}(x) = \frac{C_{\rm st}}{\sqrt{G(x)}} e^{-V_{\rm eff}(x)/D_{\rm m}},$$
 (2.36)

where $C_{\rm st}$ is the normalization constant and

$$V_{\text{eff}}(x) = \int_{-\infty}^{x} \frac{D_{\text{m}}}{G(x)} \left(-V'(x) + \gamma + f \cos \omega t \right) dx, \qquad (2.37a)$$

$$V(x) = -\frac{1}{2}D_{\rm m}x^2 + \frac{1}{4}\beta x^4 \ . \tag{2.37b}$$

In the presence of multiplicative noise the effective potential $V_{\rm eff}(x)$ of the monostable system becomes a bistable form with the stable equilibrium points at $x_{\pm} = \pm \sqrt{D_{\rm m}/\beta}$ and the unstable point at $x_0 = 0$.

The transition rates for the system to move out of x_{\pm} are obtained as

$$W_{\pm}(t) = \frac{1}{2\pi} \sqrt{|V''(x_0)V''(x_{\pm})|} e^{[V_{\text{eff}}(x_{\pm}) - V_{\text{eff}}(x_0)]/D_{\text{m}}}$$
$$= W_{\pm 0} e^{\mp kf \cos \omega t} , \qquad (2.38a)$$

where

$$W_{\pm 0} = \frac{D_{\rm m}}{\sqrt{2}\pi} e^{\mp k\gamma - \Delta\phi/(2D_{\rm m})}$$
 (2.38b)

with

$$k = \frac{1}{\sqrt{D_{\rm m}D_{\rm a}}} \tan^{-1} \left(\frac{D_{\rm m}}{\sqrt{\beta D_{\rm a}}}\right) , \qquad (2.38c)$$

$$\Delta \phi = D_{\rm m} \left[\left(1 + \frac{\beta}{D_{\rm a}} \right) \ln \left(\frac{D_{\rm m}^2 + \beta D_{\rm a}}{\beta D_{\rm a}} \right) - 1 \right] \,. \tag{2.38d}$$

The master equations governing the probabilities $n_{\pm} = P(x = x_{+}^{s})$ are given by

$$\frac{\mathrm{d}n_{\pm}}{\mathrm{d}t} = \mp W_{+}(t)n_{+} \pm W_{-}(t)n_{-} \,. \tag{2.39}$$

Then, following the procedure described in Sect. 2.3 for bistable systems it is easy to obtain [55]

$$S = S_s(\Omega)\delta(\Omega - \omega) + S_n(\Omega, \omega) , \qquad (2.40a)$$

where

$$S_{\rm s}(\Omega) = \frac{4\pi D_{\rm m} v^2}{\beta(u^2 + \omega^2)} ,$$
 (2.40b)

$$S_{\rm n}(\Omega,\omega) = \frac{4D_{\rm m}u}{\beta(u^2 + \Omega^2)} \left(\frac{1}{\cosh^2(k\gamma)} - \frac{2v^2}{u^2 + \Omega^2} \right) , \qquad (2.40c)$$

$$u = \frac{\sqrt{2} D_{\text{m}} \cosh(k\gamma)}{\pi} e^{-\Delta\phi/(2D_{\text{m}})}, \qquad (2.40d)$$

$$v = \frac{D_{\rm m}fk}{\sqrt{2\pi}\cosh(k\gamma)} e^{-\Delta\phi/(2D_{\rm m})}.$$
 (2.40e)

Then

$$SNR = \frac{D_{\rm m} f^2 k^2 (u^2 + \omega^2) e^{-\Delta \phi / (2D_{\rm m})}}{2\sqrt{2} \left[u^2 + \omega^2 - 2v^2 \cosh^2(k\gamma) \right] \cosh(k\gamma)} . \tag{2.41}$$

Figure 2.15 depicts the variation of SNR with $D_{\rm m}$ for $D_{\rm a}=0.1$, $\gamma=0.7$, $\omega=0.01$ and f=0.01 and for three values of the coefficient β of the nonlinear term in Eq. (2.34). As β increases, the critical value of $D_{\rm m}$ at which SNR becomes maximum also increases. The $SNR_{\rm MAX}$ decreases with increase in β . In Fig. 2.16 the dependence of SNR on the bias term γ for three values of the amplitude of the

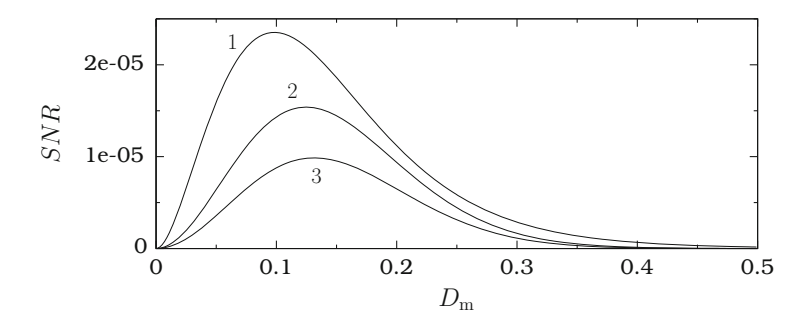


Fig. 2.15 SNR versus $D_{\rm m}$ for $D_{\rm a}=0.1,\,\gamma=0.7,\,\omega=0.01,f=0.01.$ The curves 1, 2 and 3 are for $\beta=1,\,5$ and 10, respectively

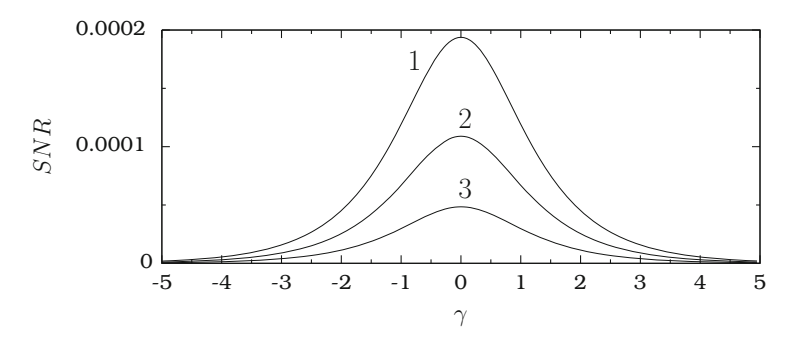


Fig. 2.16 SNR versus the bias term γ for $\beta=2$, $D_{\rm a}=0.5$, $D_{\rm m}=0.8$ and $\omega=0.01$. The curves 1, 2 and 3 are for f=0.01, 0.015 and 0.02, respectively

driving force is plotted. For a fixed value of f the SNR decreases with increase in γ due to the increase in the barrier height of $V_{\rm eff}$. Further, SNR is maximum always at $\gamma=0$. The reason for this is the following. The barrier heights of the two wells are identical for $\gamma=0$ where as for $\gamma\neq0$ the barrier height of one well is higher than the other and also higher than that of the case $\gamma=0$. Consequently, when γ is varied from a negative value, stochastic resonance occurs at $\gamma=0$.

Experimentally, the occurrence of stochastic resonance in NbN superconducting strip-line resonators in a monostable zone with one stable state and one unstable state has been reported [56]. The system was driven by an amplitude modulated signal and noise. Maximum signal amplification was observed at an optimum value of mean injected pump power. At the resonance, during one half of the modulation period, nearly regular spikes in reflected power were noticed, while during the second half only few noise-induced spikes occurred. This dynamics was found to give rise a very strong gain. Stochastic resonance has been studied in an asymmetrical monostable system with two periodic forces and multiplicative and additive noise [57].

2.7 Linear Systems with Additive and Multiplicative Noises

Three ingredients namely nonlinearity, a periodic signal and a random force were thought of as the necessary conditions for the occurrence of stochastic resonance. Let us first identify the effect of additive Gaussian noise in a linear system.

2.7.1 Effect of Additive Noise Only

Consider the motion of a particle in a single-well potential $V(x,t) = \frac{1}{2}\omega_0^2 x^2 - fx \cos \omega t$. The equation of motion of the overdamped version of the system is

$$\dot{x} = -\omega_0^2 x + f \cos \omega t + \xi(t) . \tag{2.42}$$

The autocorrelation function, one-sided power spectrum and *SNR* are obtained as [45]

$$\langle x(t)x(t+\tau)\rangle = \frac{D}{2\omega_0^2} e^{-\omega_0^2|\tau|} + \frac{f^2}{2(\omega_0^4 + \omega^2)} \cos \omega \tau ,$$
 (2.43)

$$S(\Omega) = \frac{2D}{\omega_0^4 + \Omega^2} + \frac{\pi f^2}{\omega_0^4 + \omega^2} \delta(\Omega - \omega) , \qquad (2.44)$$

$$SNR = \frac{\pi f^2}{2D} \ . \tag{2.45}$$

The *SNR* of the linear system is independent of the parameters ω_0^2 and ω and is simply the input *SNR*. *SNR* continuously decreases with increase in noise implying degrading of the performance of the system.

The influence of noises other than Gaussian white noise in additive and multiplicative forms has been investigated by few groups on linear systems. For example, stochastic resonance was observed in linear systems for Gaussian coloured noise [58–60], Poissonian noise [61], composite noise [62], signal modulated coloured noise [63], correlated noise [64, 65], multiplicative asymmetric dichotomous noise [55, 66] and multiplicative noise modulated by a bias periodic external force [67].

2.7.2 Effect of Multiplicative Noise Only

The effect of additive noise in a nonlinear system is changing of the internal thermal motion of the system by switching it between the coexisting equilibrium states. In a linear system there is only one potential well or one equilibrium state. Note that the internal structure of the system, for example, the shape of the potential

or the number of equilibrium states cannot be altered by the additive noise. Thus, stochastic resonance cannot be observed in a linear system driven by additive noise only. In Sect. 2.6 a creation of bistability in the monostable nonlinear system by a multiplicative noise is observed. The point is that a multiplicative noise can be able to induce a bistability in a linear system also. Li and Han [66] have shown the occurrence of stochastic resonance in an overdamped linear system with multiplicative asymmetric dichotomous noise where the noise takes two asymmetric values -E and kE, with E, k > 0. They obtained an analytical expression for SNR [66]. Berdichevsky and Gitterman [68] considered the following linear system:

$$\dot{x} = -\omega_0^2 x - a_1 x \xi(t) + f \sin \omega t . \tag{2.46}$$

When the noise term $\xi(t)$ is chosen as a Gaussian white noise, the quantity $\langle x(t) \rangle$ is found to be remain bounded and is a monotonic function of the noise intensity D. There is no stochastic resonance in this case. For the exponentially correlated noise with the auto-correlation time τ , that is,

$$\langle \xi(t)\xi(t')\rangle = e^{-|t-t'|/\tau} , \qquad (2.47)$$

they obtained $\langle x(t) \rangle$. In this case, also a monotonic variation of $\langle x(t) \rangle$ is noticed.

In the case of dichotomous noise with $a_1\tau < 1$, $a_1^2 < \omega_0^4 + \omega_0^2/\tau$, the amplitude of the stationary solution depends on the parameters ω_0^2 , f, ω , a_1 and τ . $\langle x(t) \rangle$ is found to be maximum at

$$(a_1)_{\text{max}} = \sqrt{\omega_0^4 + \frac{\omega_0^2}{\tau} - \omega^2}$$
 (2.48)

In the presence of dichotomous noise, the system moves along the parabola $U_1 = (\omega_0^2 + a_1)x^2/2$, then jumps to the parabola $U_2 = (\omega_0^2 - a_1)x^2/2$ at the rate $1/\tau$ and so on. For $a_1 > \omega_0^2$ but $a_1 < \sqrt{\omega_0^4 + \frac{\omega_0^2}{\tau}}$ the parabolas U_1 and U_2 have curvatures with opposite sign and act in opposite direction tending to increase (decrease) the x of a particle. Accordingly, the amplitude of the stationary signal has a maximum as a function of the noise intensity.

An overdamped linear system with quadratic multiplicative coloured noise and driven by a periodic signal has been considered in [69]. Applying functional integral techniques, an analytical expression for the mean value of the state variable x, $\langle x \rangle_{st}$, was obtained. The amplitude of $\langle x \rangle_{st}$ was found to show a stochastic resonance-like profile with the inverse of the correlation time of the coloured noise.

2.7.3 Effect of Multiplicative and Additive Noises

Consider the system

$$\dot{x} = -(\omega_0^2 + \xi(t))x + f\cos\omega t + \eta(t) , \qquad (2.49)$$

where ξ and η are a Gaussian noise with zero mean and correlation functions given by

$$\langle \xi(t)\xi(s)\rangle = \sigma_1 e^{-\lambda|t-s|}, \qquad (2.50a)$$

$$\langle \eta(t)\eta(s)\rangle = \sigma_2 e^{-\lambda|t-s|},$$
 (2.50b)

$$\langle \xi(t)\eta(s)\rangle = \langle \eta(t)\xi(s)\rangle = 0$$
. (2.50c)

Choosing the noise as asymmetric dichotomous, Ning and Xu [70] derived an analytical expression for *SNR* and have shown the occurrence of stochastic resonance in the above linear system.

Let us assume that $\xi(t)$ assumes the values A_1 and $-B_1$ and $\eta(t)$ takes the values A_2 and $-B_2$ with A_1 , A_2 , B_1 and $B_2 > 0$. The rate for the transition from A_1 to $-B_1$ is say α_1 while from $-B_1$ to A_1 is α_2 . β_1 and β_2 are the rates for the transitions A_2 to $-B_2$ and $-B_2$ to A_2 , respectively. Writing

$$\sigma_1 = A_1 B_1, \quad \lambda = \alpha_1 + \alpha_2, \quad \Lambda_1 = A_1 - B_1,$$
 (2.51a)

$$\sigma_2 = A_2 B_2, \quad \lambda = \beta_1 + \beta_2, \quad \Lambda_2 = A_2 - B_2$$
 (2.51b)

one can obtain

$$\frac{\mathrm{d}\langle x\rangle}{\mathrm{d}t} = -\omega_0^2 \langle x\rangle - \langle \xi(t)x\rangle + f\cos\omega t , \qquad (2.52a)$$

$$\frac{\mathrm{d}\langle x^2 \rangle}{\mathrm{d}t} = -2\omega_0^2 \langle x^2 \rangle - 2\langle \xi(t)x^2 \rangle + 2f\langle x \rangle \cos \omega t + 2\langle \eta(t)x \rangle . \tag{2.52b}$$

Multiplying Eq. (2.49) by $\xi(t)$, averaging and using

$$\frac{\mathrm{d}}{\mathrm{d}t}\langle \xi(t)x\rangle = \left\langle \xi(t)\frac{\mathrm{d}x}{\mathrm{d}t}\right\rangle - \lambda\langle \xi(t)x\rangle \tag{2.53}$$

one gets

$$\frac{\mathrm{d}}{\mathrm{d}t}\langle \xi(t)x\rangle = -(\omega_0^2 + \lambda)\langle \xi(t)x\rangle - \langle \xi^2(t)x\rangle
= -(\omega_0^2 + \lambda)\langle \xi(t)x\rangle - A_1B_1\langle x\rangle - (A_1 - B_1)\langle \xi(t)x\rangle
= -(\omega_0^2 + \lambda)\langle \xi(t)x\rangle - \sigma_1\langle x\rangle - A_1\langle \xi(t)x\rangle .$$
(2.54)

Equation (2.54) together with Eq. (2.52a) form a system of equations for the two unknowns $\langle x \rangle$ and $\langle \xi(t)x \rangle$. In the limit $t \to \infty$

$$\langle x \rangle = \frac{f}{f_3} \left(f_1 \cos \omega t + f_2 \sin \omega t \right) ,$$
 (2.55a)

where

$$f_1 = \omega_0^2 \omega^2 + (\omega_0^2 + \Lambda_1 + \lambda) b_1 b_2$$
, (2.55b)

$$f_2 = \omega \left[\omega^2 + \left(\omega_0^2 + \Lambda_1 + \lambda \right)^2 + \sigma_1 \right], \qquad (2.55c)$$

$$f_3 = (\omega^2 + b_1^2)(\omega^2 + b_2^2)$$
, (2.55d)

$$b_{1,2} = \omega_0^2 + \epsilon_{1,2} = \omega_0^2 + \frac{\lambda + \Lambda_1}{2} \pm \sqrt{\frac{(\lambda + \Lambda_1)^2}{4} + \sigma_1}$$
 (2.55e)

In a similar manner one can obtain the stationary second moment as

$$\langle x^{2} \rangle_{\text{st}} = \left\{ \frac{\sigma_{2} \left[2(\omega_{0}^{2} + \Lambda_{1} + \lambda)^{2} + (\omega_{0}^{2} + \Lambda_{1})\lambda + 2\sigma_{1} \right]}{(\omega_{0}^{2} + \lambda)(\omega_{0}^{2} + \Lambda_{1} + 2\lambda) - \sigma_{1}} + \frac{f^{2}}{2f_{3}} \left[f_{1}(2\omega_{0}^{2} + 2\Lambda_{1} + \lambda) - 2(\omega^{2} - b_{1}b_{2})\sigma_{1} \right] \right\} \times \left[\omega_{0}^{2}(2\omega_{0}^{2} + 2\Lambda_{1} + \lambda) - 2\sigma_{1} \right]^{-1}.$$
(2.56)

Integration of Eq. (2.49) gives

$$x(t+\tau) = x(t)g(\tau)e^{-\omega_0^2\tau} + f \int_0^{\tau} e^{-\omega_0^2v}g(v)\cos\left[\omega(t+\tau-v)\right] dv + \int_0^{\tau} e^{-\omega_0^2v}h(v) dv , \qquad (2.57a)$$

where

$$g(v) = \left\langle e^{-\int_0^v \xi(u) \, du} \right\rangle, \quad h(t - v) = \left\langle \eta(v) e^{-\int_v^t \xi(u) \, du} \right\rangle. \tag{2.57b}$$

Expanding the exponentials in Eq. (2.57b) in series and evaluating the integrals results in

$$g(v) = \frac{1}{\epsilon_1 - \epsilon_2} \left(\epsilon_1 e^{-\epsilon_2 v} - \epsilon_2 e^{-\epsilon_1 v} \right) , \quad h(t - v) = 0 . \tag{2.58a}$$

Now, multiplication of Eq. (2.57a) by x(t) and averaging gives

$$\langle x(t+\tau)x(t)\rangle = \langle x^2\rangle_{\rm st}g(\tau)e^{-\omega_0^2\tau} + \frac{f\langle x\rangle}{\epsilon_1 - \epsilon_2} \left[f_4\sin\omega t + f_5\cos\omega t\right],$$
(2.59a)

where

$$f_4 = \frac{\epsilon_2 b_1 \sin \omega \tau - \epsilon_2 \omega f_6}{b_1^2 + \omega^2} + \frac{\epsilon_1 \omega f_7 - \epsilon_1 b_2 \sin \omega \tau}{b_2^2 + \omega^2} , \qquad (2.59b)$$

$$f_5 = -\frac{\epsilon_2 \omega \sin \omega \tau + \epsilon_2 b_1 f_6}{b_1^2 + \omega^2} + \frac{\epsilon_1 b_2 f_7 + \epsilon_1 \omega \sin \omega \tau}{b_2^2 + \omega^2} , \qquad (2.59c)$$

$$f_{6,7} = \cos \omega \tau - e^{-b_{1,2}\tau} . {(2.59d)}$$

Averaging of $\langle x(t+\tau)x(t)\rangle$ over the period $2\pi/\omega$ of the external force $f\cos\omega t$ gives

$$\langle x(t+\tau)x(t)\rangle_{\rm st} = \langle x^2\rangle_{\rm st}g(\tau)e^{-\omega_0^2\tau} + \frac{f^2(f_1f_5 + f_2f_4)}{2f_3(\epsilon_1 - \epsilon_2)}$$
 (2.60)

Then the power spectrum is $S(\Omega) = S_s(\Omega)\delta(\Omega - \omega) + S_n(\Omega, \omega)$ where

$$S_{\rm s} = \frac{\pi f^2(u_2 l_1 - u_1 l_2)}{2f_3(\epsilon_1 - \epsilon_2)} , \qquad (2.61a)$$

$$S_{n} = \frac{2\langle x^{2}\rangle_{st}(b_{2}l_{1} - b_{1}l_{2})}{(\epsilon_{1} - \epsilon_{2})} + \frac{f^{2}}{f_{3}(\epsilon_{1} - \epsilon_{2})} \left[\frac{b_{1}l_{2}u_{1}}{b_{1}^{2} + \Omega^{2}} - \frac{b_{2}l_{1}u_{2}}{b_{2}^{2} + \Omega^{2}} \right]$$
(2.61b)

with

$$l_{1,2} = \frac{b_{1,2} - \omega_0^2}{b_{2,1}^2 + \Omega^2} , \quad u_{1,2} = f_2 \Omega + f_1 b_{1,2} . \tag{2.61c}$$

Then $SNR = S_s(\Omega = \omega)/S_n(\Omega = \omega)$.

Figure 2.17a shows SNR versus ω for three values of f for fixed values of other parameters. For $f=0.5,\,0.6$ and 0.7 SNR becomes maximum at $\omega=1.14,\,1.32$ and 1.48, respectively. For each fixed value of ω the value of SNR increases with f. In Fig. 2.17b SNR profile is shown for three values of Λ_1 . For $\Lambda_1=0.001,\,0.01$ and 0.02 resonance is found at 0.36, 0.366 and 0.38, respectively. As Λ_1 increases the SNR value also increases.

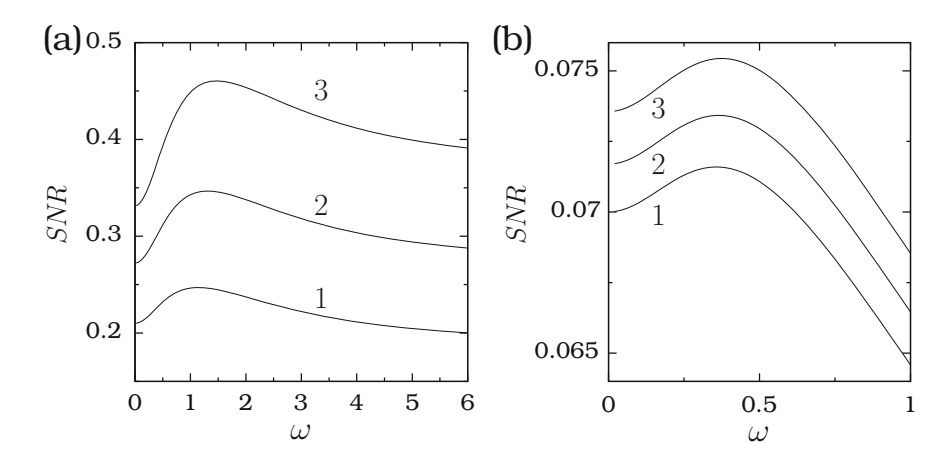


Fig. 2.17 Variation of *SNR* versus ω in the linear system with $\omega_0^2=1$, $\lambda=\sigma_1=\sigma_2=1$ and $\Lambda_1=\Lambda_2=1$. The curves 1, 2 and 3 in the subplot (**a**) are for f=0.5, 0.6 and 0.7, respectively. The curves 1, 2 and 3 in the subplot (**b**) are for $\Lambda_1=0.001, 0.01$ and 0.02, respectively, with f=0.5 and $\Lambda_2=1$

2.8 Stochastic Resonance in Quantum Systems

Stochastic resonance has been studied in certain quantum systems [44, 71–74]. Two-state theory and Feynman path integral approach were used to obtain *SNR*. This section considers two quantum systems and theoretically point outs the occurrence of stochastic resonance.

2.8.1 A Particle in a Double-Well Potential

Let us consider a quantum mechanical particle in a double-well potential and assume that the depth of the left-well and right-well are unequal, $h_- = h_+ + \epsilon$ [71]. The system is subjected to a periodic forcing with frequency ω and a random noise characterized by a temperature T.

Expanding $W_{\pm}(t)$ in Eq. (2.9) as $W_{\pm}(t) = W_{\pm 0} + w_{\pm} \cos \omega t + \cdots$ the rate equation can be solved and the correlation function to the order $(w_{\pm})^2$ can be determined. For the case of transition rates obeying the detailed balance

$$W_{+}/W_{-} = e^{(\epsilon_0 + \delta\epsilon\cos\omega t)/(k_B T)}, \qquad (2.62)$$

where $k_{\rm B}$ is the Boltzmann constant, SNR is obtained as [71]

$$SNR = \frac{\pi W_{+0}}{4 \left(1 + e^{\epsilon_0 / (k_{\rm B} T_0)} \right)} \left[\delta \left(\frac{\epsilon}{k_{\rm B} T} \right) \right]^2 . \tag{2.63}$$

For a sinusoidally modulated asymmetry energy, the quantity $\epsilon = \epsilon_0 + \delta_\epsilon \cos \omega t$ is $\delta(\epsilon/k_{\rm B}T) = \delta_\epsilon/k_{\rm B}T_0$. Then the *SNR* given by Eq. (2.63) becomes

$$SNR = \frac{\alpha T'^2}{1 + e^{T'}}, \quad \alpha = \frac{\pi W_{\pm 0} \delta_{\epsilon}^2}{4\epsilon_0^2}, \quad T' = \frac{\epsilon_0}{k_{\rm B} T_0}.$$
 (2.64)

Lofstedt and Coppersmith pointed out the difference between the classical and quantum stochastic resonances. Quantum stochastic resonance does not occur in a system with symmetric potential. This is because in the symmetric well, $\epsilon/k_{\rm B}T\ll 1$ the transition rates W_{\pm} have power-law dependence on T. In the asymmetric case when $\epsilon_0/k_{\rm B}T_0\gg 1$, due to the detailed balance factor the transition rate W_{-} is exponentially small and the particle is confined to the lower well. The signal is thus suppressed. For $k_{\rm B}T_0\sim\epsilon_0$ the relative occupation in the upper well is sensitive to the temperature. On the other hand, for $k_{\rm B}T_0\gg\epsilon_0$, the relative occupations in the two wells are almost equal and the signal decreases.

2.8.2 A Double Quantum Dot System

Joshi [74] considered a system of a double quantum dot with only two nondegenerate and weakly coupled energy levels with energies E_1 and E_2 . The level 1 is occupied while the level 2 is empty in the absence of any external perturbation. There is no tunnelling of the particles between the two quantum dots since they are weakly coupled. Such a system can represent two energy states in two different wells. The Hamiltonian of the system is

$$H(t) = H_0(t) + H_{\text{int}}(t)$$
, (2.65a)

where

$$H_0 = \frac{1}{2}E(t)(|2\rangle\langle 2| - |1\rangle\langle 1|), \quad H_{\text{int}} = \zeta(|2\rangle\langle 1| + |1\rangle\langle 2|), \quad (2.65b)$$

$$E(t) = E_0 + \alpha \mathcal{E}(t)$$
, $\mathcal{E}(t) = \mathcal{E}_0 \cos \omega t$, (2.65c)

where α is a constant, ζ is the coupling strength between the two dots and $\mathcal{E}(t)$ is the external field (which can be applied to the dots via gate electrodes). The applied field leads to an oscillation of the two energy levels. Note that in the usual stochastic

resonance phenomenon the wells of the potential are tilted periodically by means of external periodic force.

The master equation for the statistical operator ρ is given by

$$\frac{\partial \rho}{\partial t} = -\frac{i}{\hbar} [H(t), \rho] + \mathcal{L}_r \rho + \mathcal{L}_w \rho , \qquad (2.66)$$

where $\mathcal{L}_r\rho$ is the Liouville operator for reservoir tunnelling and $\mathcal{L}_w\rho$ governs inter dot particle relaxation. At low bias voltage the tunnelling of electrons through the double dot is suppressed by Coulomb blockade. Such conditions are appropriate to investigate stochastic resonance in the system. Using the master Eq. (2.66) evolution equation for density matrix elements ρ_{11} , ρ_{12} , ρ_{21} and ρ_{22} of the density matrix can be obtained. Here ρ_{11} and ρ_{22} are the probabilities for the electron to be in the left-dot and right-dot, respectively. ρ_{12} and ρ_{21} are the off-diagonal matrix elements. Assume that the potential of the double dot has local minima at $\pm x_m$ and the height of the potential barrier measured from the lower state $|1\rangle$ is ΔV and D is the intensity of the Gaussian white noise with zero mean. The applied periodic signal changes the relative separation of the states. When the noise intensity is varied, then at an optimum value the random switching frequency becomes close to the signal frequency leading to a higher probability for transition between the states.

Following the two-state theory described in Sect. 2.3 and under the assumption that the interaction between the dots is small and hence its contribution to *SNR* is negligible, Joshi finally obtained the *SNR* as [74]

$$SNR = \frac{\pi r_{\rm K} f_{\rm s}^2}{2(D/\Delta V)^2} \left(1 - \frac{2r_{\rm K}^2 f_{\rm s}^2}{(D/\Delta V)^2 (\omega^2 + 4r_{\rm K}^2)} \right)^{-1} , \qquad (2.67a)$$

where

$$r_{\rm K} = \frac{1}{\sqrt{2}\pi} \,\mathrm{e}^{-\Delta V/D} \;, \quad f_{\rm s} = \frac{\mathcal{E}_0 x_{\rm m}}{\Delta V} \;.$$
 (2.67b)

For very small D the exponential term falls to zero rapidly so SNR is almost zero. For very large D, the exponential term reaches 1 but the term D^2 in the denominator makes SNR again to zero. For moderate values of D, there is the maximum near $D \sim \Delta V$.

2.9 Applications of Stochastic Resonance

The features of stochastic resonance have been studied experimentally in psychophysics, electrophysiology, human vision, hearing and tactile, animal behaviour and single and multiunit activity recording. Role of stochastic resonance in brain function including detection of weak signals, synchronization and coherence among

neuronal assemblies, phase resetting, carrier signals, animal avoidance and feeding behaviours were also investigated. A weak signal refers to a signal with amplitude much lower than the amplitude of background noise. Stochastic resonance is quite interesting for biological systems particularly in neurobiological systems, since it may provide a mechanism for such systems to detect and process weak signals. In neural systems, stochastic resonance has been shown in peripheral sensory neuron [75], neurotransmitter quantum or spike processing neuron [76], neural parallel array and network [77–83]. Collins group [84] has shown experimentally that the postural sway of both young and elderly individuals during quiet standing could be significantly reduced by applying subsensory mechanical noise to the feet. An excellent review on application of stochastic resonance in sensory information process was presented by Moss and his coworkers in [85]. This section points out some of the promising applications of stochastic resonance.

2.9.1 Vibration Energy Harvesting

Gammaitoni et al. [86] proposed a way of converting vibrational energy to electrical energy making use of stochastic dynamics. They considered a piezoelectric oscillator represented by the equations

$$\ddot{x} = \omega_0^2 x - \beta x^3 - d\dot{x} + K_v V + D\xi(t) , \qquad (2.68a)$$

$$\dot{V} = K_c \dot{x} - \frac{1}{\tau_p} V , \qquad (2.68b)$$

where V is the voltage drop and x is the relevant observable of the oscillator dynamics, d is the damping coefficient, K_v is the coupling coefficient relating the oscillations to the voltage and K_c is the coupling constant of the piezoelectric sample. τ_p is related to the coupling capacitance C and to the resistive load R ($\tau_p = RC$). $\xi(t)$ is a random force, a stochastic process with Gaussian distribution, zero mean and unit variance. $V_{\rm rms}$ versus ω_0^2 exhibits a nonmonotonic variation. $V_{\rm rms}$ is found to be maximum at an optimum value of ω_0^2 for fixed values of the other parameters.

2.9.2 Stochastic Encoding [87]

Stochastic encoding or transmission has been found in many systems ranging from molecular level to the nervous activity [88–91]. At molecular level molecules undergo continuous changes and in thermal equilibrium with the medium. It is possible to achieve communication between a cell and its external world making use

of a channel that open and close in a different situation (monostable ion channel). There are two consequences with this:

- The modulation of ion current by external stimuli would be difficult and less flexible.
- Economy of the cell.

In voltage-gated channels the membrane potential modulates the chances of opening and closing. Consequently, if the dependence of the rate constants on the potential is steep, the number of channels (N(t)) which are open can vary enormously in a stimulus cycle. There is no current when a channel is closed and the current is V/R, where R being the resistance of the channel when it is opened. The jump between 0 and V/R is much higher than the peak-to-peak amplitude of the time-varying component of V/R. Consequently, when the rate constants for the 0 - V/R transitions depend very steeply on the potential, the current through the membrane can be substantially modulated than in the case of channels opened at a regular rate. In the first case the current is N(t)V/R while in the second case it is $N(t) \pm (V/R)$. Now, the peak-to-peak amplitude is greater. In this way, the stochastic mechanism acts as an amplifier enhancing the amplitude of the current passing through the membrane. That is, stochastically switching ion channels amplify the signal. Proteins have a lot of energetically nearly equivalent states and they switch thermally between these states so stochastic transmission is readily at hand for cell communication. Stochastic switching is present in neural activity also and it can serve as a tool to transmit information about high frequencies using nerve fibers. Further, stochastic encoding could be simpler to decode at the cortical level than the patterns transmitted particularly when deterministic phase-locking takes place.

2.9.3 Weak Signal Detection

The measurement of very weak forces is of great important. A gravitational wave detector is a typical example for a measurement system with very high precision. The combined optomechanical system exhibiting different characteristics and physical phenomena such as the optical spring effect and multistability become important. Here stochastic resonance can occur when noise is added and one may realize the enhancement of *SNR* in precision measurement. Signal detection employing stochastic resonance has been studied in [92, 93].

2.9.4 Detection of Weak Visual and Brain Signals

In human information processing, noise-enhanced performance is well established. In active sensory systems, however, an additional source of noise is self-generated [94, 95]. For example, consider the human visual system. When one looks at

stationary scenes, the oculomotor system moves an object of interest into the foveal part of the retina. However, one can notice a rapid adaptation of the visual system to a constant input. This adaptation leads to perceptual fading when the retinal image is experimentally stabilized in the laboratory paradigm of retinal stabilization. As a consequence, a built-in mechanism exists in the visual system. One has to fixate an object for the visual analysis of bleaching. It is to be noted that our eyes are never at a fixed state and undergo continuous motion. Such involuntarily and unconsciously miniature eye movements are produced when one fixate a stationary target. These fixational eye movements represent self-generated noise which serves significant perceptual functions. The fixational eye movements are traditionally interpreted as oculomotor noise [96].

Starzynski and Engbert [97] investigated fixational eye movements of 19 participants (with mean age 23.3 years) under the influence of external noise. In the experiment, the target stimulus performed a random walk with varying noise intensity. The random motion of the stimulus was implemented on a computer with a constant distribution of spatial increments but with rates of position change which is characterized by the diffusion constant. Noise-enhanced target discrimination was observed. Particularly, response times versus the diffusion constant exhibited U shape curve. That is, response time is minimum for an optimum value of diffusion constant. Starzynski and Engbert have pointed out that the noise artificially applied in their laboratory study was very likely to occur in natural settings where postural fluctuations [98] act as a noise source which is external with respect to the oculomotor system.

Human threshold for detection of luminance variations across space has been studied in the presence of noise. Ward and his co-workers [99] performed an experiment where observers were requested to recognize striped and nonstriped visual stimuli. Contrast was changed according to an adaptive technique and depending on the correct and incorrect answer of an observer. Noise (random amounts from Gaussian distribution) was implemented in the form of randomly changing the grey level of each pixel in the stimulus. The presence of noise was found to decrease the contrast threshold of detection of weak spatial modulations in luminance.

Stochastic resonance in more complex systems, such as human tactile sensing neural networks of mammalian brains and the blood pressure control system in the human brain system have been well established [100–104]. In the human, there is a large variety of chaotic firing of neuron networks and columns that function as complex oscillators, as well as spontaneous electrochemical noises. Such noisy signals provide internal noise sources to trigger stochastic resonance in brain. Stochastic resonance has been observed in the human brain's visual processing area [105].

The hippocampus is a brain tissue essential for learning and short-term memory. A hippocampal network model consists of two layers CA1 and CA3. Pyramidal cells in CA3 are connected to pyramidal cells in CA1. The CA3 network causes spontaneous irregular activity while the CA1 network does not. The activity of CA3 causes membrane potential fluctuations in CA1 pyramid cells. The CA1 network

also receives a subthreshold signal through the perforant path. The subthreshold perforant path signals can fire CA1 pyramid cells in cooperation with the membrane potential fluctuations that work as a noise. The firing of the CA1 network shows typical features of stochastic resonance [106]. It has also been shown that the stochastic resonance improves subthreshold detection in a single hippocampal CA1 cell [107].

2.9.5 Stochastic Resonance in Sensory and Animal Behaviour

Experiments on the feeding behaviour of the juvenile paddle fish have shown the enhancement of perception of sensory information and also affecting animal behaviour. Animal can perceive the enhancement of information available in the peripheral sensory system with external noise and they can make use of this noise-improved information for feeding or predator avoidance. For example, in an experiment the tail-fan of crayfish was covered with hydrodynamically sensitive hairs, each one innervated by sensory neurons that converge on inter-neurons in the sixth ganglion [108, 109]. Extra-cellular recordings were made from the sensory neurons in the root. *SNR* was measured from the power spectra of the recorded spike trains. It became maximum at an optimal noise intensity. This behaviour was also observed in an analog simulation of a model neuron [110].

Another experiment was done with paddle fish. An electrosensitive paddle fish has a long anterior rostrum, which is covered with few thousands of electrosensitive organs and are capable of detecting and tracking the weak electric fields generated by the swimming and feeding motions of its favourite prey zooplankton Daphnia. The generated electric field around the Daphnia is dipole-shaped. Consequently, when an individual plankton is farther from the rostrum, the weaker the electrical signal at the rostral surface. The result is dropping beneath the perceptive ability of the animal at certain limiting distance. When an external noise was added in the form of a random electric field applied parallel to the fish long axis, the perceptive ability was improved. The fish was able to extend the capture distance range in the presence of optimal noise [111–113].

2.9.6 Human Psychophysics Experiments

In psychophysics, noise usually interferes with detection and identification of a signal—a process called *masking*. Research on masking in vision, touch and audition indicated that at very low levels of signal and mask intensity, it is easier to detect the signal in the presence of the mask than alone when the two are added inphase with each other [114]. Detection of weak signal is found to be more difficult for higher intensities of the mask. This phenomenon is explained by the energy addition of the signal and masking which makes the signal+mask discriminable

from the mask alone when signal+mask is near threshold but not when the mask is very intense or very weak. Threshold for human visual perception, effects of noise and stochastic resonance in the perception of gratings, ambiguous figures and in three-dimensional perception of autostereograms were studied through many psychophysics experiments [115–121].

2.9.7 Noise in Human Muscle Spindles and Hearing

It has been shown that the sensitivity of muscle-spindle receptors to a weak movement signal would be enhanced by adding noise through the tendon of the parent muscle. Cordo et al. [122] recorded firing activity of individual muscle-spindle afferents from the radial nerve in healthy human subjects. When an afferent is isolated, the subject's right-wrist is passively rotated by a manipulandum, with a small amplitude sinusoidal wave form. They applied a noise input by a tendon stimulator to stretch the appropriate muscle. In most of the examined afferents the calculated *SNR* rapidly increased to a peak and then slowly decreased. That is, the presence of a particular nonzero level of noise enhanced the sensitivity of the muscle-spindle receptor to the weak input signal.

In a hearing system, noise-enhanced peripheral sensory response has been demonstrated experimentally and theoretically [123–125]. The enhanced effect of noise on hearing sensitivity indicates that hearing performance is involved in a nonlinear mechanism in which fluctuation and noise are important and even beneficial. The source of the nonlinearity is the sensory hair cell. It has been shown that inner hair cells response in temporal pattern to sinusoidal signal was enhanced by optimal noise. Experiments [123–125] have shown that by adding noise of certain level, human can detect near threshold pure tone better than without noise.

A conceptual model has shown that stochastic resonance can optimize the bone remodelling process where the mechanical noisy stimulus is related to the stochastic nature of the activation of osteoblasts and osteoclasts through the connection between bone remodelling and external mechanical stimuli [126].

2.9.8 Electrophysiological Signals

The spontaneous background signals in an EEG are usually considered as noise with respect to stimulus or event related electrophysiological events. Information about neuronal interaction and changes in brain functional states are contained in the spontaneous brain signals. The analysis of these signals is important in sensory information processing. The occurrence of stochastic resonance in central neural system can be explored with the help of electrophysiological techniques. The added noise signal was found to improve the cortical somatosensory response to mechanical tactile simulation. Response amplitude versus noise intensity appeared

as an inverted U shape indicating enhancement of response at certain noise level [127]. Stochastic resonance was observed in the spinal and cortical stages of the sensory encoding. This was demonstrated in anesthetized cats with the coherence between spinal and cortical responses to tactile stimulation. Increase in the response amplitude and power of the first even harmonics of the cortical response to steady state contrast stimulation have been observed. This effect might be from activation of complex cells in striate visual cortex based on the nonlinear properties that these cells and steady-state contrast stimulation share [128].

2.9.9 Stochastic Resonance in Raman and X-Ray Spectra

Sometimes due to weak signal the intensity of Raman spectrum and X-ray diffraction of certain solutions corresponding to certain frequencies may not be clearly visible. They can be amplified by adding impurities as noise. An example is found in the case of alcohol solutions of CCl₄. Increase in the intensity at a particular wave number has been realized when the concentration of CCl₄ is varied.

2.10 Noise-Induced Stochastic Resonance Versus Noise-Induced Synchronization

When the time variation of state variables \mathbf{X}_1 of one system follows with the state variables \mathbf{X}_2 of another identical system (coupled or uncoupled) then the two systems are said to be *synchronized*. There are different types of synchronization [129–132]. When $\mathbf{X}_1 = \mathbf{X}_2$ then the synchronization is termed as *general* or *complete*. Synchronization of two or more identical systems (with different initial conditions) exhibiting chaotic dynamics can be achieved by different kinds of deterministic coupling of the systems. Interestingly, noise can be used to synchronize two identical uncoupled systems started with different initial conditions [10, 133]. That is, two identical chaotic systems driven by the same noise forget their initial states and evolve to an identical state after transient.

It is to be noted that noise-induced resonance refers to a phenomenon wherein a maximum response of a system (not necessarily coupled systems) at an optimal value of noise intensity is realised and can be detected by measuring the statistical measure SNR. Noise-induced synchronization can be identified by direct comparison of the state variables \mathbf{X}_1 and \mathbf{X}_2 of two chaotic systems. To realize noise-induced resonance the system under consideration must have certain kind of bistability and it can occur in a single degree of freedom nonlinear system. Synchronization occurs in coupled systems or uncoupled more than one systems.

Synchronization is found to play an important role in information transmission and processing [134, 135]. It can be related to cognition and movement control

in brain function. It has been pointed out that in the human perception process synchronization of gamma wave in space and time occurs [136]. On the other hand, occurrence of synchronization may results in epilepsy [137] and Parkinson diseases [138]. Chaos synchronization is investigated with applications to secure communication and neural activity [132].

2.11 Concluding Remarks

In this chapter, the occurrence of stochastic resonance in systems like excitable, spatially periodic, maps and networks have not been considered. Such systems will be taken up in later chapters. Certain variant forms of stochastic resonance have been reported in the literature. For example, when the input signal is an aperiodic, like a frequency modulated one, the noise-induced resonance is called aperiodic stochastic resonance. Such a resonance was demonstrated by Collins et al. [139] on rat slowly adapting a type of afferents. In the experiment, each neuron was subjected to a perithreshold aperiodic stimulus and a noise. When the noise intensity was varied, a typical stochastic resonance profile was observed which indicates that external noise into sensory neurons could improve their abilities to detect weak signals. Aperiodic resonance was found in the theoretical FitzHugh-Nagumo model equations [140] and overdamped bistable systems [141]. In the double stochastic resonance [142] an extended system is subjected to both a multiplicative noise and an additive noise. Bimodality of the mean field of the network is induced by the multiplicative noise while the change in the response is governed by the additive noise. Splitting of the stochastic resonance peak thereby resulting in double stochastic resonance is observed in an optomechanical read-out device [52] and in an asymmetric barrier system [143]. Other extension of the concept of stochastic resonance such as stochastic giant resonance [144], stochastic multi-resonance [145, 146], autonomous stochastic resonance [147], geometric stochastic resonance [148] and control of stochastic resonance [149] were reported. Signal detection using residence time statistics was analysed in [150, 151].

References

- 1. R. Benzi, A. Sutera, A. Vulpiani, J. Phys. A 14, L453 (1981)
- 2. C. Nicolis, Sol. Phys. 74, 473 (1981)
- 3. P. Jung, Phys. Rep. **234**, 175 (1993)
- 4. L. Gammaitonic, P. Hänggi, P. Jung, F. Marchesoni, Rev. Mod. Phys. 70, 223 (1998)
- 5. A. Agudov, B. Spagnolo, Phys. Rev. E **64**, 035102(R) (2001)
- 6. R.N. Mantegna, B. Spagnolo, Phys. Rev. Lett. 76, 563 (1996)
- 7. D. Valenti, A. Fiasconaro, B. Spagnolo, Phys. A **331**, 477 (2004)
- 8. E.G. Gwinn, R.M. Westervelt, Phys. Rev. A 33, 4143 (1986)
- 9. S. Rajasekar, M.C. Valsakumar, S. Paul Raj, Phys. A 261, 417 (1998)

References 79

- 10. D. He, P. Shi, L. Stone, Phys. Rev. E 67, 027201 (2003)
- 11. A. Neiman, Phys. Rev. E 49, 3484 (1994)
- 12. R. Kouhi Esfahani, F. Shabazi, K. Aghababaei Bamani, Phys. Rev. E 86, 036204 (2012)
- 13. B. Lindner, J.G. Ojalvo, A. Neiman, L.S. Geier, Phys. Rep. 392, 321 (2004)
- 14. J.M.R. Parrondo, C. Van der Broeck, J. Buceta, F.J. de la Rubia, Phys. A **224**, 153 (1996)
- 15. X. Yu, E.R. Lewis, IEEE Trans. Biomed. Eng. **30**, 36 (1989)
- M.I. Dykman, D.G. Luchinsky, R. Mannella, P.V.E. McClintock, H.E. Short, N.D. Stein, N.G. Stocks, Phys. Lett. A 193, 61 (1994)
- 17. F. Marchesoni, Phys. Lett. A 237, 126 (1998)
- 18. C.B. Muratov, E.V. Eijnden, Chaos 18, 015111 (2008)
- 19. N. Yu, R. Kuske, Y.X. Li, Chaos 18, 015112 (2008)
- 20. S. Kadar, J. Wang, K. Showalter, Nature **391**, 770 (1998)
- 21. C.J. Tessone, A. Scire, R. Toral, P. Colet, Phys. Rev. E 75, 016203 (2007)
- 22. P.S. Landa, V.G. Ushakov, Pis'ma Zh. Eksp. Teor. Fiz. 86, 356 (2007)
- 23. B. McNamara, K. Wiesenfeld, R. Roy, Phys. Rev. Lett. 60, 2626 (1988)
- 24. S. Fauve, F. Heslot, Phys. Lett. A 97, 5 (1983)
- 25. F. Moss, Ber. Bunsenges. Phys. Chem. 95, 303 (1991)
- 26. R.N. Mantigna, B. Spargnola, Phys. Rev. E 49, R1792 (1994)
- 27. L. Gammaitoni, M. Martinelli, L. Pardi, S. Santucci, Phys. Rev. Lett. 67, 1799 (1991)
- 28. N. Stocks, N. Stei, P.V.E. McClintock, J. Phys. A 26, 385 (1993)
- 29. R.L. Badzey, P. Mohanty, Nature **437**, 995 (2005)
- 30. I.Y. Lee, X.I. Liu, B. Kosko, C.W. Zhou, Nano Lett. 3, 1683 (2003)
- 31. I. Lee, X. Liu, C. Zhou, B. Kosko, IEEE Trans. Nanotechnol. 5, 613 (2006)
- 32. M. Perc, Phys. Rev. E 76, 066203 (2007)
- 33. C. Masoller, Phys. Rev. Lett. 88, 034102 (2002)
- 34. X. Gu, S. Zhu, D. Wu, Eur. Phys. J. D 42, 461 (2007)
- 35. Y. Jin, H. Hu, Phys. A 382, 423 (2007)
- 36. Y. Gong, B. Xu, H. Han, X. Ma, Phys. A 387, 407 (2008)
- 37. X.M. Mao, K. Sun, Q. Ouyang, Chin. Phys. **11**, 1106 (2002)
- 38. R. Wallace, D. Wallace, H. Andrews, Environ. Plan. A **29**, 525 (1997)
- K. Wiesenfeld, D. Pierson, E. Pantazelou, Ch. Dames, F. Moss, Phys. Rev. Lett. 72, 2125 (1994)
- L. Gammaitoni, M. Locher, A.R. Bulsara, P. Hanggi, J. Neff, K. Wiesenfeld, W.L. Ditto, M.E. Inchiso, Phys. Rev. Lett. 82, 4574 (1999)
- 41. P. Debye, *Polar Molecules* (Dover, New York, 1929)
- 42. S. Arathi, S. Rajasekar, J. Kurths, Int. J. Bifurcation Chaos 21, 2729 (2011)
- W. Fu-Zhong, C. Wei-Shi, Q. Guang-Rong, G. De-Yong, L. Jun-Ling, Chin. Phys. Lett. 20, 28 (2003)
- 44. R.L. Badzey, P. Mohanty, Nature 437, 995 (2005)
- 45. B. McNamara, K. Wiesenfeld, Phys. Rev. A 39, 4854 (1989)
- 46. C.W. Garuner, Handbook of Stochastic Methods (Springer, Berlin, 1985)
- 47. H.S. Wio, S. Bowzal, Braz. J. Phys. 29, 136 (1999)
- 48. P.S. Landa, I.A. Khovano, P.V.E. McClintock, Phys. Rev. E 77, 011111 (2008)
- J. Casado-Pascual, J. Gomez-Ordonoz, M. Morillo, P. Hanggi, Phys. Rev. Lett. 91, 210601 (2003)
- 50. C. Nicolis, Phys. Rev. E **82**, 011139 (2010)
- 51. S. Saikia, A.M. Jayannavar, M.C. Mahato, Phys. Rev. E 83, 061121 (2011)
- 52. F. Mueller, S. Heugel, L.J. Wang, Phys. Rev. A 79, 031804(R) (2009)
- 53. A.G. Isavnin, Russ. Phys. J. 48, 694 (2005)
- 54. N.V. Agudov, A.V. Krichigin, Int. J. Bifurcation Chaos 18, 2833 (2008)
- 55. G. Guo, Y.R. Zhou, S.Q. Jiang, T.X. Gu, J. Phys. A Math. Gen. 39, 1386 (2006)
- 56. E. Segev, B. Abdo, O. Shtempluck, E. Buks, Phys. Rev. B 77, 012501 (2008)
- 57. L.X. Dong, G. Feng, Z. Yu-Rong, Commun. Theor. Phys. **51**, 283 (2009)
- 58. A.V. Barzykin, K. Seki, Europhys. Lett. 40, 117 (1997)

- 59. Z. Liang-Ying, C. Li, W. Da Jin, W. Jun, Chin. Phys. Lett. 20, 25 (2003)
- 60. K. Marujama, F. Shibata, Phys. A 149, 447 (1988)
- 61. V. Bezak, Czech. J. Phys. 48, 529 (1998)
- 62. A.V. Barzykin, K. Seki, F. Shibata, Phys. Rev. E 57, 6555 (1998)
- 63. L. Cao, D.J. Wu, Europhys. Lett. 61, 593 (2003)
- 64. V. Berdichevsky, M. Gitterman, Phys. Rev. E 60, 1464 (1999)
- 65. L. Cao, D.J. Wu, Phys. Scr. 76, 539 (2007)
- 66. J. Li, Y.X. Han, Phys. Rev. E 74, 051115 (2006)
- 67. S. Jiang, F. Guo, Y. Zhou, T. Gu, Phys. A 375, 483 (2007)
- 68. V. Berdichevsky, M. Gitterman, Europhys. Lett. 36, 161 (1996)
- 69. H. Calisto, F. Mora, E. Tirapegui, Phys. Rev. E 74, 022102 (2006)
- 70. L. Ning, W. Xu, Phys. A **382**, 415 (2007)
- 71. R. Lofstedt, S.N. Coppersmith, Phys. Rev. Lett. 72, 1947 (1994)
- 72. V.J. Menon, N. Chanana, Y. Singh, Phys. A 275, 505 (2000)
- 73. A. Joshi, M. Xiao, Phys. Rev. A 74, 013817 (2006)
- 74. A. Joshi, Phys. Rev. E 77, 020104(R) (2008)
- 75. N. Daichi, M.J. Douglas, P. Grigg, J.J. Collins, Phys. Rev. Lett. 82, 2402 (1999)
- 76. Z. Long, Y. Qin, Phys. Rev. Lett. 91, 208103 (2003)
- 77. N.G. Stocks, Phys. Rev. Lett. **84**, 2310 (2000)
- 78. Z. Liu, Y. Lai, A. Nachman, Phys. Lett. A 297, 75 (2002)
- 79. G. Mato, Phys. Rev. E **59**, 3339 (1999)
- 80. T. Yang, Phys. Lett. A 245, 79 (1998)
- 81. T. Kanamaru, T. Horita, Y. Okabe, Phys. Lett. A 255, 23 (1999)
- 82. O. Kwon, H.T. Moon, Y. Okabe, Phys. Lett. A 298, 319 (2002)
- 83. F. Duan, F.C. Blondeau, D. Abbott, Phys. Lett. A 372, 2159 (2008)
- A. Priplata, J. Niemi, M. Salen, J. Harry, L.A. Lipsitz, J.J. Collins, Phys. Rev. Lett. 89, 238101 (2002)
- 85. F. Moss, L.M. Ward, W.G. Sannita, Clin. Neurophysiol. 115, 267 (2004)
- 86. L. Gammaitoni, I. Neri, H. Vocca, Appl. Phys. Lett. **94**, 164102 (2009)
- 87. D. Petracchi, Chaos Solitons Fractals 11, 1827 (2000)
- 88. H.A. Braun, H. Wissing, K. Schaefer, M. Hirsch, Nature **367**, 270 (1994)
- P. Cordo, J.T. Inglis, S. Verschueren, J.J. Collins, D.M. Merfeld, S. Rosenblum, S. Buckley, F. Moss, Nature 383, 769 (1996)
- 90. M.I. Dykman, P.V.E. McClintock, Nature 388, 344 (1997)
- 91. S.M. Bezrukov, I. Vodyanoy, Nature **388**, 633 (1997)
- 92. F. Duan, D. Abbott, Phys. A 376, 173 (2007)
- 93. F. Capeau-Blondeau, F. Duan, D. Abbott, Phys. A 387, 2394 (2008)
- 94. S. Martinez-Conde, S.L. Macknik, D.H. Hubel, Nat. Rev. Neurosci. 5, 229 (2004)
- 95. D. Kleinfeld, E. Ahissar, M.E. Diamond, Curr. Opin. Neurobiol. 16, 435 (2006)
- 96. K. Ciuffreda, B. Tannen, Eye Movement Basics for the Clinician (Mosby, St. Louis, 1995)
- 97. C. Starzynski, R. Engbert, Chaos 19, 015112 (2009)
- 98. R. Engbert, Neuron 49, 168 (2006)
- L.M. Ward, S. Desai, D. Rootman, M.S. Tata, F. Moss, Bull. Am. Phys. Soc. 46, N23.002 (2001)
- 100. J.J. Collins, T.T. Imhoff, P. Grigg, Phys. Rev. E 56, 923 (1997)
- 101. E. Simonotto, M. Riani, C. Seife, M. Roberts, J. Twitty, F. Moss, Phys. Rev. Lett. 78, 1186 (1997)
- 102. K.A. Richardson, T.T. Imhoff, P. Grigg, J.J. Collins, Chaos 8, 599 (1998)
- 103. I. Hidaka, D. Nozaki, Y. Yamamoto, Phys. Rev. Lett. 85, 3740 (2000)
- 104. W.C. Stacey, D.M. Durand, J. Neurophysiol. 83, 1394 (2000)
- 105. T. Mori, S. Kai, Phys. Rev. Lett. 88, 218101 (2002)
- 106. M. Yoshida, H. Hayashi, K. Tateno, S. Ishizuka, Neural Netw. 15, 117 (2002)
- 107. W.C. Stacey, D.M. Durand, J. Neurophysiol. 83, 1394 (2000)
- 108. J.K. Douglass, L.A. Wilkens, J. Comp. Physiol. A 183, 23 (1998)

References 81

- 109. J.K. Douglass, L.A. Wilkens, E. Pantazelou, F. Moss, Nature 365, 337 (1993)
- F. Moss, J.K. Douglass, L.A. Wilkens, D. Pierson, E. Pantazelou, Ann. N. Y. Acad. Sci. 706, 76 (1993)
- 111. D. Russell, L.A. Wilkens, F. Moss, Nature 402, 219 (1999)
- 112. D. Russell, A. Tucker, B. Wettring, B. Neiman, A. Wilkens, F. Moss, Fluctuation Noise Lett. 2, L71 (2001)
- 113. J. Freund, L. Schimansky-Geier, B. Beisner, A. Neiman, D. Russell, T. Yakusheva, F. Moss, J. Theor. Biol. 214, 71 (2002)
- 114. D. Laming, Sensory Analysis (Academic, New York, 1986)
- 115. K.H. Norwich, Information, Sensation and Perception (Academic, San Diego, 1993)
- 116. M. Riani, E. Simonoto, Phys. Rev. Lett. 72, 3120 (1994)
- 117. F. Speranza, G. Moraglia, B.A. Schneider, Percept. Mot. Skills 84, 829 (1997)
- 118. E. Simonotto, F. Spano, M. Riani, A. Ferrari, F. Levrero, A. Pilot, P. Renzetti, R.C. Parodi, F. Sardanelli, P. Vitali, J. Twittya, F. Chiou-Tanf, F. Moss, Neurocomputing 26–27, 511 (1999)
- 119. T. Ditzinger, M. Stadler, D. Struber, J. Kelso, Phys. Rev. E 62, 2566 (2000)
- 120. M. Piana, M. Canfora, M. Riani, Phys. Rev. E 62, 1104 (2000)
- 121. L.M. Ward, A. Neiman, F. Moss, Biol. Cybern. 87, 91 (2002)
- P. Cordo, J.T. Inglis, S. Verschusen, J.J. Collins, D.M. Merfeld, S. Rosenblum, S. Buckley, F. Moss, Nature 383, 769 (1996)
- 123. Z.C. Long, F. Shao, Y.P. Zhang, Y.G. Qin, Phys. Lett. A 323, 434 (2004)
- 124. I.C. Gebeshuber, Chaos Solitons Fractals 11, 1855 (2000)
- 125. F. Jamarillo, K. Wiesenfeld, Chaos Solitons Fractals 11, 1869 (2000)
- 126. M. Rusconi, A. Zaikin, N. Marwan, J. Kurths, Phys. Rev. Lett. 100, 128101 (2008)
- 127. E. Manjarrez, O.D. Martinez, I. Mendez, A. Flores, Neurosci. Lett. 324, 213 (2002)
- 128. R. Srebo, P. Malladi, Phys. Rev. E 59, 2566 (1999)
- 129. L.M. Pecora, T.L. Carroll, Phys. Rev. Lett. 64, 821 (1990)
- 130. L.M. Pecora, T.L. Carroll, Phys. Rev. A 44, 2374 (1991)
- 131. M. Lakshmanan, S. Rajasekar, *Nonlinear Dynamics: Integrability, Chaos and Patterns* (Springer, Berlin, 2003)
- 132. A. Pikovsky, M. Rosenblum, J. Kurths, *Synchronization: A Universal Concept in Nonlinear Sciences* (Cambridge University Press, Cambridge, 2003)
- 133. S. Golbin, A. Pikovsky, Phys. Rev. E **71**, 045201 (2005)
- 134. T. Pereira, M.S. Baptista, J. Kurths, Eur. Phys. J. 146, 155 (2007)
- 135. T. Nowotny, R. Huerta, M.I. Rabinovich, Chaos 18, 037119 (2008)
- 136. E. Rodriguez, N. George, J.P. Lachaux, J. Martinerie, F.J. Varela, Nature 397, 430 (1999)
- 137. F. Mormann, T. Kreuz, R.G. Andrzejak, P. David, K. Lehnertz, C.E. Elger, Epilepsy Res. 53, 173 (2003)
- 138. P. Tass, M.G. Rosenblum, J. Weule, J. Kurths, A. Pikovsky, J. Volkmann, A. Schnitzler, H.J. Freund, Phys. Rev. Lett. 81, 3291 (1998)
- 139. J.J. Collins, T.T. Imhoff, P. Grigg, J. Neurophysiol. **76**, 642 (1996)
- C. Heneghan, C.C. Chow, J.J. Collins, T.T. Imhoff, S.R. Lowen, M.C. Teich, Phys. Rev. E 54, R2228 (1996)
- 141. J.J. Collins, C.C. Chow, A.C. Capela, T.T. Imhoff, Phys. Rev. E 54, 5575 (1996)
- 142. A.A. Zaikin, J. Kurths, L. Schimansky-Geier, Phys. Rev. Lett. 85, 227 (2000)
- 143. M. Borromeo, F. Marchesoni, Phys. Rev. E 81, 012102 (2010)
- 144. J. Li, Phys. Rev. E **76**, 021113 (2007)
- 145. R. Rosenfeld, J.A. Freund, A. Neiman, L. Schimansky-Geier, Phys. Rev. E 64, 051107 (2001)
- 146. Q. Wang, M. Perc, Z. Duan, G. Chen, Chaos 19, 023112 (2009)
- 147. G.S. Jeon, M.Y. Choi, Phys. Rev. B 66, 064514 (2002)
- 148. P.K. Ghosh, R. Glavey, F. Marchesoni, S.E. Savel'ev, F. Nori, Phys. Rev. E 84, 011109 (2011)
- 149. J.F. Lindner, J. Mason, J. Neff, B.J. Breen, W.L. Ditto, A.R. Bulsara, Phys. Rev. E 63, 041107 (2001)
- 150. A.R. Bulsara, C. Seberino, L. Gammaitonic, Phys. Rev.E 67, 016120 (2003)
- 151. A. Nikitin, N.G. Stocks, A.R. Bulsara, Phys. Rev. E 68, 036133 (2003)

Chapter 3 Vibrational Resonance in Monostable Systems

The previous chapter is concerned with the occurrence of stochastic resonance in certain nonlinear systems and some of its applications. The stochastic resonance phenomenon can be realized when a bistable or a multistable system is driven by a weak periodic force and additive noise of appropriate intensity. Injection of noise to a nonlinear system, through a cooperative interaction, brings assistance to the weak signal in eliciting a more efficient response by overcoming a potential barrier or a threshold. The Russian physicist Polina Landa and the British physicist Peter McClintock [1] investigated the dynamics of a bistable system driven by a biharmonical external periodic force with two different frequencies, say, ω and Ω with $\Omega \gg \omega$. That is, they replaced the noise term applied to observe stochastic resonance by a relatively high-frequency force. When the amplitude or frequency of the high-frequency force is varied they found a nonmonotonic variation of the amplitude of the output signal at the low-frequency ω of the input signal. Specifically, the amplitude of the output signal increased from a small value, reached a maximum at one or two critical values of the control parameter and then decayed. Since this phenomenon is induced by a relatively high-frequency force at the lowfrequency ω of the input signal, it is termed as *vibrational resonance*.

Gitterman [2] and Blekhman and Landa [3] proposed analytical treatments for analysing vibrational resonance. Since then, this resonance phenomenon has been studied theoretically, numerically and experimentally in many oscillators, excitable systems, networks and maps. For example, its occurrence has been examined in a noise-induced structure [4], FitzHugh–Nagumo equation [5–7], quintic oscillator [8, 9], two-coupled overdamped oscillator [10, 11], overdamped bistable systems [12–14], coupled oscillators [15, 16], asymmetric potential system [17] and synthetic gene network [18]. Experimental evidence of the vibrational resonance has been demonstrated in analog simulations of the overdamped Duffing oscillator [12], in an excitable electronic circuit with Chua's diode [5] and in a bistable optical cavity laser [19–21]. Theoretical approaches for vibrational resonance in the presence of

additive white noise [22] and applicable for overdamped bistable systems [14, 23] have been proposed. The case of $\Omega = n\omega$ where n is an integer is also analysed [24].

The present and the next few chapters are primarily devoted for vibrational resonance in different kinds of nonlinear systems. This chapter considers a monostable state Duffing oscillator, a quintic oscillator and a Morse oscillator driven by two periodic forces of frequency ω and Ω . For $\Omega \gg \omega$ the solution of these systems can be assumed to consist of a slow motion X(t) with frequency ω and a fast motion $\psi(t,\Omega t)$ with frequency Ω . Using a theoretical approach, an approximate analytical expression for the amplitude of the slow motion can be obtained. By making use of this theoretical expression for the amplitude of oscillation, it is possible to analyze the occurrence of vibrational resonance. It is also possible to determine the values of ω , Ω and the amplitude of the high-frequency force at which the resonance. Furthermore, comparison of the theoretical predictions with the numerical calculation, and also the analysis of how the asymmetry of the potential well of the Duffing oscillator affects the vibrational resonance are presented.

3.1 Duffing Oscillator

The equation of motion of the Duffing oscillator driven by two periodic forces is given by

$$\ddot{x} + d\dot{x} + \omega_0^2 x + \beta x^3 = f \cos \omega t + g \cos \Omega t, \quad \Omega \gg \omega. \tag{3.1}$$

The potential of the system in the absence of periodic force and damping is

$$V(x) = \frac{1}{2}\omega_0^2 x^2 + \frac{1}{4}\beta x^4 . {(3.2)}$$

Depending upon the sign of ω_0^2 and β the potential can be of the following four forms that are depicted in Fig. 3.1:

- $\omega_0^2 > 0$, $\beta > 0$: V(x) is a single-well potential with the minimum at x = 0 (see Fig. 3.1a).
- $\omega_0^2 < 0$, $\beta > 0$: The potential is of a double-well form with two minima at $x = \pm \sqrt{|\omega_0^2|/\beta}$ and a local maximum at x = 0 (see Fig. 3.1b).
- $\omega_0^2 > 0$, $\beta < 0$: V(x) has a single-well form with a double-hump (see Fig. 3.1c). It has a local minimum at x = 0 and two maxima at $x = \pm \sqrt{\omega_0^2/|\beta|}$.
- $\omega_0^2 < 0$, $\beta < 0$: The potential is an inverted single-well with the maximum at x = 0 (see Fig. 3.1d). This potential is not of physical relevance.

The first three cases of V(x) have become a classical central model to describe nonlinear phenomena. In Chap. 1, the occurrence of nonlinear resonance and jump phenomenon in the system (3.1) with the single-well case has been shown, while

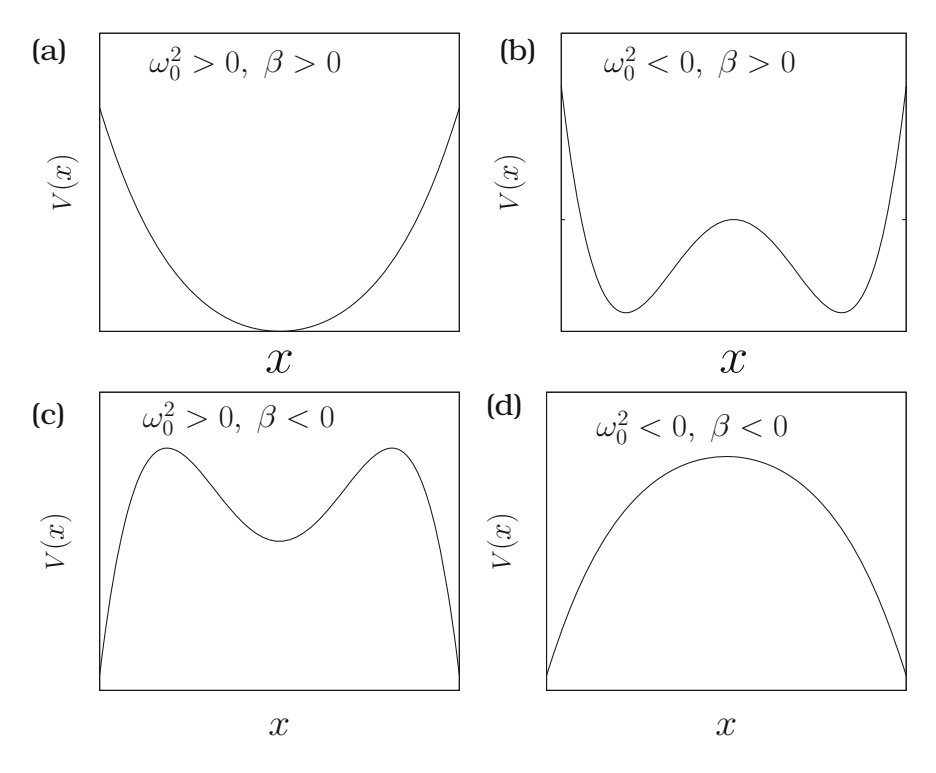


Fig. 3.1 Four forms of the potential function V(x) given by Eq. (3.2)

the occurrence of stochastic resonance in the double-well case has been discussed in Chap. 2. In the present section, vibrational resonance in the single-well case of the Duffing oscillator is considered. The double-well system will be treated in the next chapter.

3.1.1 Theoretical Description of Vibrational Resonance

For $\Omega \gg \omega$, due to the difference in time scales of the low-frequency force $f \cos \omega t$ and the high-frequency force $g \cos \Omega t$, it is reasonable to assume that the solution of the system (3.1) consists of a slow motion X(t) with frequency ω and period $T=2\pi/\omega$ and a fast motion $\psi(t,\Omega t)$ with frequency Ω and period $2\pi/\Omega$. Let us write $x=X+\psi$ and assume that the mean value of ψ , $\langle \psi \rangle$, with respect to time $\tau=\Omega t$ is

$$\langle \psi \rangle = \frac{1}{2\pi} \int_0^{2\pi} \psi \, d\tau = 0 . \tag{3.3}$$

(3.5)

Substitution of $x = X + \psi$ and use of Eq. (3.3) give the following equation of motion for X and ψ :

$$\ddot{X} + d\dot{X} + \left(\omega_0^2 + 3\beta\langle\psi^2\rangle\right)X + \beta X^3 + \beta\langle\psi^3\rangle = f\cos\omega t, \qquad (3.4)$$

$$\ddot{\psi} + d\dot{\psi} + \omega_0^2 \psi + 3\beta X^2(\psi - \langle\psi\rangle) + 3\beta X\left(\psi^2 - \langle\psi^2\rangle\right)$$

$$+\beta\left(\psi^3 - \langle\psi^3\rangle\right) = g\cos\Omega t. \qquad (3.5)$$

where

$$\langle \psi^m \rangle = \frac{1}{2\pi} \int_0^{2\pi} \psi^m \, \mathrm{d}\tau \ . \tag{3.6}$$

Since ψ is rapidly varying, it is reasonable to assume that $\ddot{\psi} \gg \dot{\psi}$, ψ , ψ^2 and ψ^3 and neglect all the terms in the left-side of Eq. (3.5) except the term $\ddot{\psi}$. This approximation, called *inertial approximation* [25], leads to the equation $\ddot{\psi} = g \cos \Omega t$, the solution of which is given by

$$\psi = -\frac{g}{\Omega^2} \cos \Omega t \,. \tag{3.7}$$

The approximation can be improved by including the damping and the linear terms in ψ . With the ψ given by Eq. (3.7) one finds

$$\langle \psi^2 \rangle = \frac{g^2}{2\Omega^4}, \quad \langle \psi^3 \rangle = 0.$$
 (3.8)

Then the equation for the slow motion becomes

$$\ddot{X} + d\dot{X} + C_1 X + \beta X^3 = f \cos \omega t \,, \quad C_1 = \omega_0^2 + \frac{3\beta g^2}{2\Omega^4} \,. \tag{3.9}$$

Equation (3.9) can be viewed as the equation of motion of a system with the effective potential

$$V_{\text{eff}}(X) = \frac{1}{2}C_1X^2 + \frac{1}{4}\beta X^4 . \qquad (3.10)$$

The shape, the number of local maxima and minima and their location of the potential V(x) depend on the parameters ω_0^2 and β . For the effective potential (V_{eff}) , those depend also on the parameters g and Ω . Consequently, by varying g or Ω new equilibrium states can be created or the number of equilibrium states can be reduced. However, for the single-well case of V(x), both ω_0^2 and β are positive parameters which makes $C_1 > 0$ and hence V_{eff} is always of a single-well form. That is, the

shape of $V_{\rm eff}$ remains as a single-well when the parameter g or Ω is varied. Slow oscillations take place about the equilibrium point $X^* = 0$.

When $X^* \neq 0$, one can introduce the change of variable $Y = X - X^*$ in Eq. (3.9) and obtain the equation of motion for the deviation of the slow variable X from the equilibrium point X^* . Because $X^* = 0$ for the system (3.1) with a single-well the equation for Y is the same as that of X. For $f \ll 1$ and in the limit $t \to \infty$, assume that $|X| \ll 1$ and neglect the nonlinear terms in Eq. (3.9). Then, the solution of the linear version of Eq. (3.9) in the limit $t \to \infty$ is $A_L \cos(\omega t + \phi)$ where

$$A_{\rm L} = \frac{f}{\sqrt{\left(\omega_{\rm r}^2 - \omega^2\right)^2 + d^2 \omega^2}} , \quad \phi = \tan^{-1} \left(\frac{d\omega}{\omega^2 - \omega_{\rm r}^2}\right) , \tag{3.11}$$

where $\omega_r^2 = C_1$. ω_r is the *resonant frequency* of the linear version of the equation of motion of the slow variable X(t). To characterize the vibrational resonance, we define the response amplitude Q as

$$Q = \frac{A_{\rm L}}{f} = \frac{1}{\sqrt{(\omega_{\rm r}^2 - \omega^2)^2 + d^2 \omega^2}} \,. \tag{3.12}$$

Now we analyze the vibrational resonance using Eq. (3.12) and we verify numerically the theoretical results.

3.1.2 Analysis of Vibrational Resonance

One can study the resonance dynamics by varying the parameter ω or g or Ω . From Eq. (3.12) it is clear that at resonance the function $S=(\omega_r^2-\omega^2)^2+d^2\omega^2$ becomes a minimum. Thus, a local minimum of S represents a resonance. When a parameter, say, g is varied then resonance occurs at a value of $g=g_{\rm VR}$, which is a root of the equation $S_g={\rm d}S/{\rm d}g=4(\omega_r^2-\omega^2)\omega_r\omega_{\rm rg}=0$ and $S_{gg}|_{g=g_{\rm VR}}=8\omega\omega_{\rm rg}^2>0$ where $\omega_{\rm rg}={\rm d}\omega_{\rm r}/{\rm d}g$. The resonance condition is $\omega_{\rm r}^2=\omega^2$. Q becomes maximum whenever the resonant frequency $\omega_{\rm r}$ matches with the angular frequency ω of the input periodic signal. The condition $\omega_r^2=\omega^2$ gives

$$g_{\rm VR} = \sqrt{2\Omega^4(\omega^2 - \omega_0^2)/3\beta} \ .$$
 (3.13)

Resonance cannot occur for $\omega^2 < \omega_0^2$. There will be only one resonance for $\omega^2 > \omega_0^2$. g_{VR} is independent of the parameters d and f, however, Q depends on them.

In order to compare the theoretically calculated Q and $g_{\rm VR}$ one can compute the response amplitude from the numerical solution of Eq. (3.1). Numerical Q is given by

$$Q = \frac{\sqrt{Q_{\rm S}^2 + Q_{\rm C}^2}}{f} \,, \tag{3.14a}$$

where

$$Q_{\rm C} = \frac{2}{nT} \int_0^{nT} x(t) \cos \omega t \, dt, \quad Q_{\rm S} = \frac{2}{nT} \int_0^{nT} x(t) \sin \omega t \, dt.$$
 (3.14b)

In the above equations $T = 2\pi/\omega$ and n can be taken as, say, 200.

We fix the parameters as $\omega_0^2=1$, $\beta=1$, d=0.5, f=0.1, $\omega=1.5$ and $\Omega=15$. Figure 3.2a, b show Q versus g and ω_r^2 versus g, respectively. In Fig. 3.2a continuous and dashed curves represent theoretical and numerical results. Numerically computed Q is in well agreement with the theoretical approximation. As g increases from zero, the value of Q increases monotonically, then reaches a maximum at $g=g_{\rm VR}$ and finally decreases. The theoretical and numerical values of $g_{\rm VR}$ are 205.40 and 202.85, respectively. In Fig. 3.2b the resonant frequency starts from the value $\sqrt{\omega_0^2}=1$ and increases monotonically with g. At $g=g_{\rm VR}$, $\omega_{\rm r}$ matches with the frequency ω and ω becomes a maximum. The above resonance phenomenon is termed as *vibrational resonance* [1, 3] as it is induced by the high-frequency force. From Eq. (3.12), at resonance $Q=Q_{\rm max}=1/(d\omega)$. Note that $g_{\rm VR}$ is independent of d while $Q_{\rm max}$ depends on d and ω only. For any fixed values of the parameters the response amplitude at resonance is always $1/(d\omega)$.

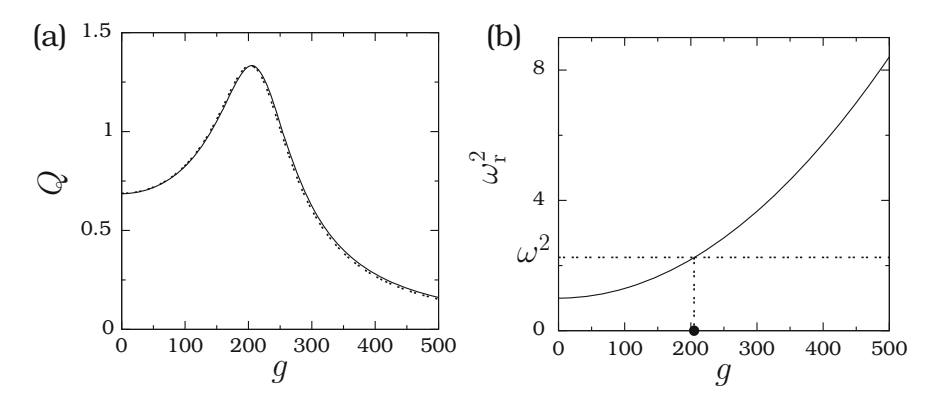


Fig. 3.2 (a) Variation of Q with g for the Duffing oscillator with $\omega_0^2=1$, $\beta=1$, d=0.5, f=0.1, $\omega=1.5$ and $\Omega=15$. The *continuous* and *dashed lines* represent theoretically and numerically computed, respectively, values of Q. (b) Plot of theoretical ω_r^2 versus g. The *horizontal dashed line* represents $\omega_r^2=\omega^2$ and the *solid circle* on the g-axis marks the value of $g=g_{VR}$

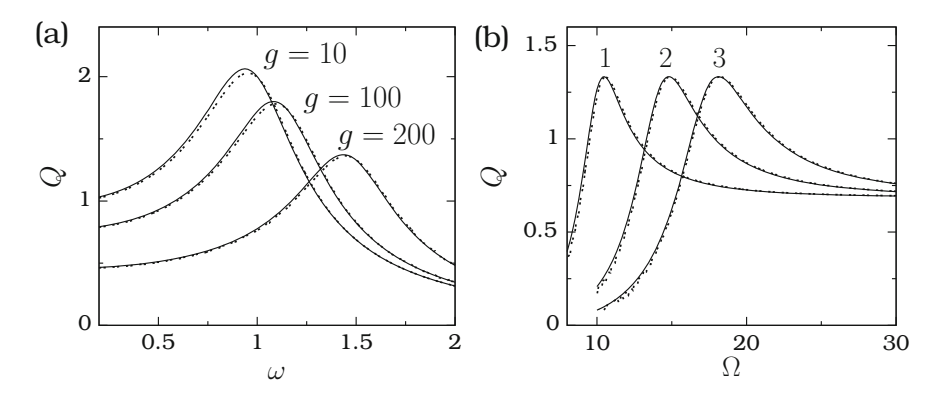


Fig. 3.3 (a) Dependence of Q with the frequency ω for the Duffing oscillator with $\omega_0^2=1$, $\beta=1$, d=0.5, f=0.1, $\Omega=15$ and for three values of g. (b) Q versus the frequency Ω of the high-frequency force. The values of g for the curves 1, 2 and 3 are g=100, 200 and 300, respectively, and $\omega=1.5$. In both the subplots the *continuous* and *dashed lines* represent theoretically and numerically computed, respectively, values of Q

Vibrational resonance can be realized by varying the parameters ω and Ω also. From $\omega_{\rm r}^2=\omega^2$ we obtain

$$\Omega_{\rm VR} = \left[\frac{3\beta g^2}{2(\omega^2 - \omega_0^2)} \right]^{1/4}, \quad \omega^2 > \omega_0^2.$$
 (3.15)

The condition $dS/d\omega = 0$ gives

$$\omega_{\rm VR} = \sqrt{\omega_{\rm r}^2 - \frac{d^2}{2}} , \quad \omega_{\rm r}^2 > d^2/2 .$$
 (3.16)

Figure 3.3a, b show the plots of Q versus ω and Q versus Ω for three fixed values of g. $\omega_{\rm VR}$ and $\Omega_{\rm VR}$ vary with g. When ω is varied the resonant frequency remains constant because it is independent of ω and the mechanism of resonance is the minimization of the function S. $g_{\rm VR}$ and $\Omega_{\rm VR}$ are independent of d while $\omega_{\rm VR}$ depends on d. When g or Ω is varied, resonance occurs only if $\omega^2 > \omega_0^2$ while if ω is varied then the condition for resonance is $\omega_{\rm r}^2 > d^2/2$.

3.2 Effect of High-Frequency Force in a Linear System

Having studied vibrational resonance in the nonlinear Duffing oscillator one can ask: What is the effect of the high-frequency force in a linear system? Can one observe vibrational resonance in a linear system? To answer these questions we consider Eq. (3.1) without the nonlinear term ($\beta = 0$). The linear equation can be easily

integrated and the exact analytical solution is given by

$$x(t) = A_1 e^{m+t} + A_2 e^{m-t} + A_{\omega} \cos(\omega t + \phi_1) + A_{\Omega} \cos(\Omega t + \phi_2)$$
, (3.17a)

where

$$m_{\pm} = \frac{1}{2} \left(-d \pm \sqrt{d^2 - 4\omega_0^2} \right),$$
 (3.17b)

$$A_{\omega} = \frac{f}{\sqrt{(\omega_0^2 - \omega^2)^2 + d^2 \omega^2}}, \quad A_{\Omega} = \frac{g}{\sqrt{(\omega_0^2 - \Omega^2)^2 + d^2 \Omega^2}}, \quad (3.17c)$$

$$\phi_1 = \tan^{-1} \left(\frac{d\omega}{\omega^2 - \omega_0^2} \right), \quad \phi_2 = \tan^{-1} \left(\frac{d\Omega}{\Omega^2 - \omega_0^2} \right)$$
 (3.17d)

and A_1 and A_2 are integration constants to be determined by the initial conditions. For $\omega_0^2>0$ and d>0, in the limit $t\to\infty$ the first two terms in the solution x(t) decay to zero and are termed as *transients*. In the long time limit the solution is given by the last two periodic terms. The solution essentially consists of two frequencies ω and Ω . The amplitudes of the solution at the frequencies ω and Ω are A_{ω} and A_{Ω} , respectively. From (3.17c) note that A_{ω} is independent of the amplitude g and the frequency Ω . That is, the amplitude A_{ω} is unaffected by the presence of the high-frequency force in a linear system. Therefore, one cannot speak about vibrational resonance in a linear system driven by two periodic forces.

3.3 Quintic Oscillator

The equation of motion of the quintic oscillator driven by two periodic forces is given by

$$\ddot{x} + d\dot{x} + \omega_0^2 x + \beta x^3 + \gamma x^5 = f \cos \omega t + g \cos \Omega t, \quad \Omega \gg \omega. \tag{3.18}$$

The potential of the system in the absence of damping and external force is

$$V(x) = \frac{1}{2}\omega_0^2 x^2 + \frac{1}{4}\beta x^4 + \frac{1}{6}\gamma x^6.$$
 (3.19)

The shape of the potential V(x) (Fig. 3.4) depends on the sign of the three parameters ω_0^2 , β and γ . It can be a single-well, double-well, triple-well, single-well with double-hump, double-well with double-hump and an inverted single-well. The potential V(x) is used to model optical bistability in a dispersive medium where the refractive index is dependent on the optical intensity [26]. A triple-well case of the above potential is found to improve image sharpening in the presence of noise [27]

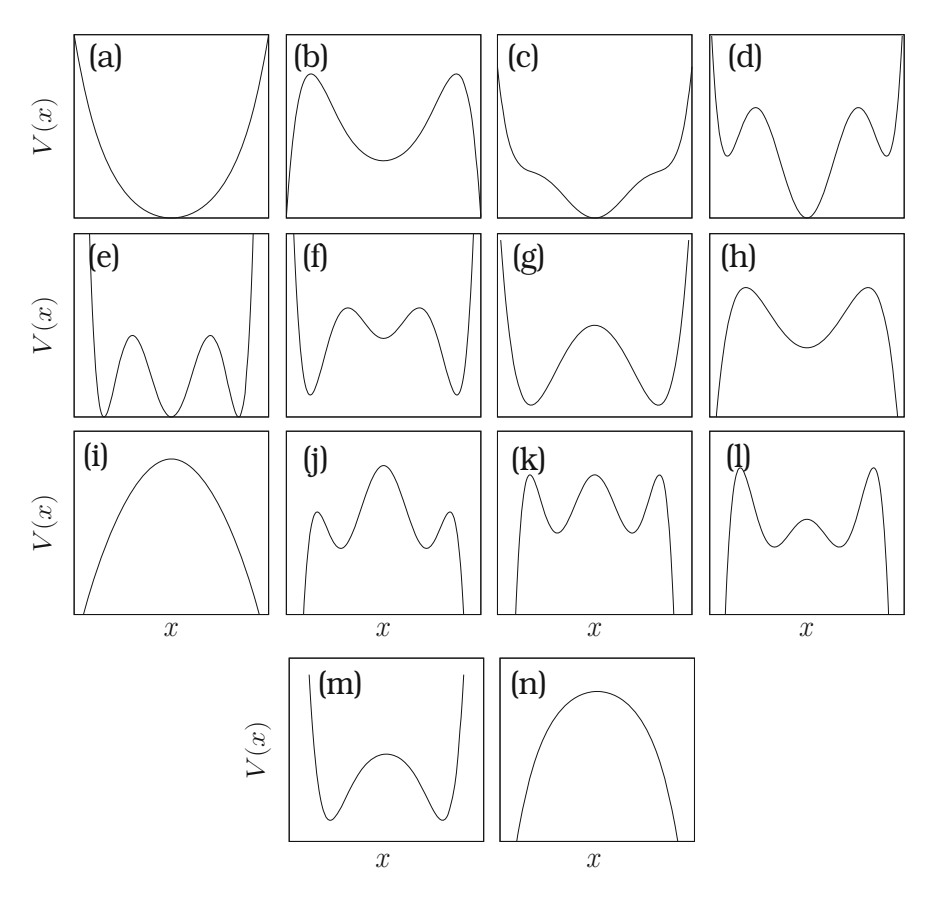


Fig. 3.4 Dependence of shape of the potential of the quintic oscillator. (a) $ω_0^2$, β, γ > 0. (b) $ω_0^2$, β > 0, γ < 0. (c) $ω_0^2$, γ > 0, β < 0 and $β^2 < 4ω_0^2γ$. (d) $ω_0^2$, γ > 0, β < 0 and $4ω_0^2γ < β^2 < 16ω_0^2γ/3$. (e) $ω_0^2$, γ > 0, β < 0 and $β^2 = 16ω_0^2γ/3$. (f) $ω_0^2$, γ > 0, β < 0 and $β^2 > 16ω_0^2γ/3$. (g) $ω_0^2 < 0$, β, γ > 0. (h) $ω_0^2 > 0$, β, γ < 0. (i) $ω_0^2$, γ < 0, β > 0 and $β^2 < 4ω_0^2γ$. (j) $ω_0^2$, γ < 0, β > 0 and $4ω_0^2γ < β^2 < 16ω_0^2γ/3$. (k) $ω_0^2$, γ < 0, β > 0 and $β^2 = 16ω_0^2γ/3$. (l) $ω_0^2$, γ < 0, β > 0 and $β^2 > 16ω_0^2γ/3$. (m) $ω_0^2$, β < 0, γ > 0. (n) $ω_0^2$, β, γ < 0

and is also used to represent partially folded intermediates in proteins [28]. Such intermediates can accelerate the protein folding. Equation (3.18) in the absence of external periodic forces models a magneto-elastic beam in the nonuniform field of permanent magnets [29]. Various nonlinear phenomena have been studied in the quintic oscillator [30–39]. The effect of asymmetry in the depths of the three wells on the characteristics of stochastic resonance has been reported [40].

Theoretical Expression for the Response Amplitude

We analyse now the occurrence of vibrational resonance in the system (3.18) with specific emphasis with single-well forms of the potential V(x). Consider the following parametric choices:

- 1. ω_0^2 , β , $\gamma > 0$ (single-well) (Fig. 3.4a), 2. ω_0^2 , $\gamma > 0$, $\beta < 0$, $\beta^2 < 4\omega_0^2\gamma$ (single-well) (Fig. 3.4c) and 3. $\omega_0^2 > 0$, β -arbitrary, $\gamma < 0$ (double-hump single-well) (Fig. 3.4b, h).

The possibility of multiple vibrational resonance in the single-well cases of the system (3.18) is shown in the following.

Seeking the solution of (3.18) in the form $x(t) = X(t) + \psi(t, \Omega t)$ gives equations similar to Eqs. (3.4) and (3.5) with additional terms due to the fifthorder nonlinearity in (3.18). The approximation $\ddot{\psi} = g \cos \Omega t$ with the solution $\psi = -(g/\Omega^2)\cos\Omega t$ gives

$$\langle \psi \rangle = \langle \psi^3 \rangle = \langle \psi^5 \rangle = 0 , \quad \langle \psi^2 \rangle = \frac{g^2}{2\Omega^4} , \quad \langle \psi^4 \rangle = \frac{3g^4}{8\Omega^4} .$$
 (3.20)

Then the equation of motion for the slow variable becomes

$$\ddot{X} + d\dot{X} + C_1 X + C_2 X^3 + \gamma X^5 = f \cos \omega t , \qquad (3.21a)$$

where

$$C_1 = \omega_0^2 + \frac{3\beta g^2}{2\Omega^4} + \frac{15\gamma g^4}{8\Omega^8}, \quad C_2 = \beta + \frac{5\gamma g^2}{\Omega^4}$$
 (3.21b)

and the effective potential for the slow motion is

$$V_{\text{eff}}(X) = \frac{1}{2}C_1X^2 + \frac{1}{4}C_2X^4 + \frac{1}{6}\gamma X^6.$$
 (3.22)

The equilibrium points about which slow oscillations occur are given by

$$X_{1}^{*} = 0, \quad X_{2,3}^{*} = \pm \left[\frac{-C_{2} + \sqrt{C_{2}^{2} - 4C_{1}\gamma}}{2\gamma} \right]^{1/2} ,$$

$$X_{4,5}^{*} = \pm \left[\frac{-C_{2} - \sqrt{C_{2}^{2} - 4C_{1}\gamma}}{2\gamma} \right]^{1/2} . \tag{3.23}$$

Suppose $\gamma > 0$. Then the following cases arise:

Case (i): $C_1, C_2 > 0$ or $C_1 > 0, C_2 < 0$ with $C_2^2 < 4C_1\gamma$ $X_1^* = 0$ is the only equilibrium point.

Case (ii): $C_1 < 0$, C_2 -arbitrary

There are three equilibrium points and are X_1^* , $X_{2,3}^*$.

Case (iii): $C_1 > 0$, $C_2 < 0$ with $C_2^2 > 4C_1\gamma$

There are five equilibrium points given by Eq. (3.23).

The change of variable $Y = X - X^*$ in Eq. (3.21) gives

$$\ddot{Y} + d\dot{Y} + \omega_{\rm r}^2 Y + \alpha_1 Y^2 + \alpha_2 Y^3 + \alpha_3 Y^4 + \gamma Y^5 = f \cos \omega t \,, \qquad (3.24a)$$

where

$$\omega_{\rm r}^2 = C_1 + 3C_2X^{*2} + 5\gamma X^{*4}, \quad \alpha_1 = 3C_2X^* + 10\gamma X^{*3},$$
 (3.24b)

$$\alpha_2 = C_2 + 10\gamma X^{*2}, \quad \alpha_3 = 5\gamma X^*.$$
 (3.24c)

The solution of the linear version of Eq. (3.24) in the limit $t \to \infty$ is $A_L \cos(\omega t + \phi)$ where A_L is given by Eq. (3.11). Equation (3.12) gives the response amplitude Q.

3.3.2 Single-Well Potential (ω_0^2 , β , $\gamma > 0$)

For ω_0^2 , β , $\gamma > 0$, V(x) is a single-well potential (Fig. 3.4a) with a local minimum at x = 0. The quantities C_1 and C_2 given by Eq. (3.21b) are now positive. Therefore, the effective potential is always a single-well potential when g or Ω is varied. The slow motion is around the equilibrium point $X_1^* = 0$ and $\omega_r^2 = C_1$.

The condition $S_g = 0$ gives

$$g_{\rm VR} = \Omega^2 \left[\frac{-b + \sqrt{b^2 - 4ac}}{2a} \right]^{1/2}$$
, (3.25a)

where

$$a = \frac{15}{8} \gamma$$
, $b = \frac{3}{2} \beta$, $c = \omega_0^2 - \omega^2$, $\omega^2 > \omega_0^2$. (3.25b)

Equation (3.25b) implies that for $\omega < \omega_0^2$ there is no resonance and for each value of $\omega > \omega_0^2$ resonance occur at only one value of $g = g_{\rm VR}$. Now we fix the values of the parameters as $\omega_0^2 = \beta = \gamma = 1, f = 0.05, d = 0.3$ and $\Omega = 10$. In Fig. 3.5a for $\omega = 0.5$ as g increases, Q decreases and there is no resonance. For $\omega = 1.25$ and $\omega = 2$ resonance occurs at g = 52.75 and 96.25, respectively. Figure 3.5b shows the plot of $g_{\rm VR}$ versus ω . $g_{\rm VR}$ increases with increase in $\omega > \omega_0^2 = 1$.

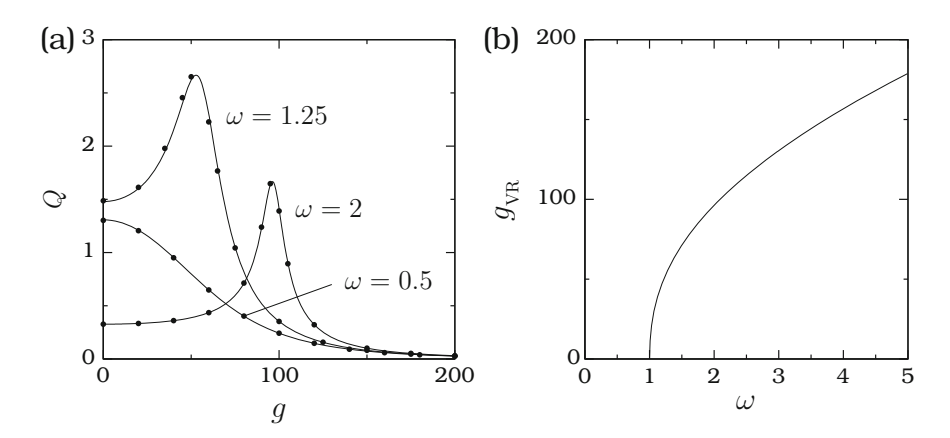


Fig. 3.5 (a) Response amplitude Q versus g for three values of ω for the system (3.18) with the case ω_0^2 , β and $\gamma > 0$. Continuous curve represents theoretically calculated Q while solid circles represent numerically computed Q. The values of the other parameters are $\omega_0^2 = \beta = \gamma = 1$, f = 0.05, d = 0.3 and $\Omega = 10$. (b) Plot of theoretical $g_{\rm VR}$ versus ω

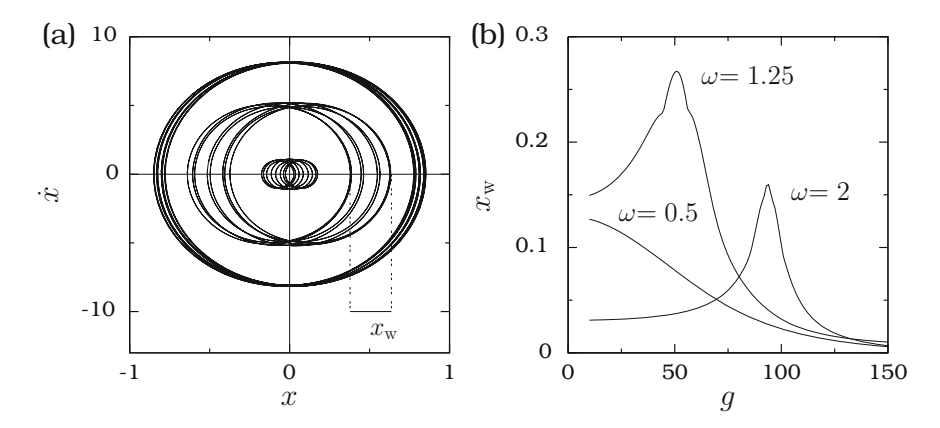


Fig. 3.6 (a) Phase portrait of the solution of Eq. (3.18) for three values of g where $\omega = 1.25$. The corresponding values of g for the inner orbit to the outer orbit are 10, 52.75 and 80, respectively. $x_{\rm w}$ denotes the width of the orbit for g = 52.75. (b) Variation of width of the orbit, $x_{\rm w}$, as a function of g for three values of ω corresponding to Fig. 3.5a

The influence of resonance in X can be seen in the width of the orbit of the system (3.18). Figure 3.6a shows the phase portrait of the system (3.18) for three values of g where $\omega = 1.25$. The width of the orbit denoted as x_w is marked in this figure for the orbit corresponding to g = 52.75. In Fig. 3.6b x_w against g is plotted for three values of ω . Compare this figure with Fig. 3.5b. The variation of x_w is similar to the variation of Q. x_w is maximum at resonance.

Since the system (3.18) can exhibit a variety of bifurcations of periodic orbits leading to chaotic motion and bifurcations of chaotic attractor, it is important to

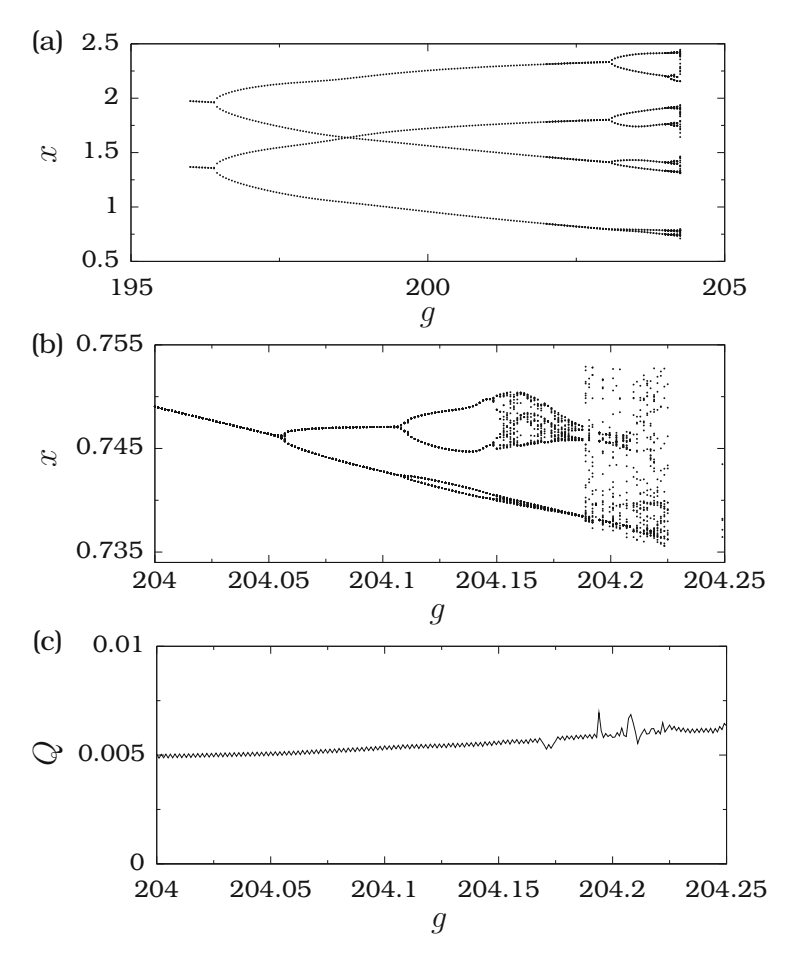


Fig. 3.7 (a) Bifurcation diagram showing a period-doubling phenomenon and chaotic dynamics. (b) Magnification of a small part of the bifurcation sequence. (c) Numerically computed response amplitude corresponding to the subplot (b)

examine the occurrence of them using bifurcation diagrams and phase portraits. For certain cases of the parametric choices considered above, chaotic motion occurs for sufficiently large values of the control parameter g, particularly, far after or far before resonance. An example is presented in Fig. 3.7a for $\omega=2$. For 0 < g < 177.2 a period-T solution occurs. When g is varied further period doubling phenomenon leading to chaotic motion, intermittency dynamics occur and are clearly seen in Fig. 3.7b, which is a magnification of a small part of the bifurcation diagram shown in Fig. 3.7a. The onset of the chaotic motion and a sudden widening of a chaotic attractor occur at g=204.153 and 204.19, respectively. For g values just above 204.2745 a period-T solution occurs. In Fig. 3.7c, the numerically calculated Q is plotted corresponding to Fig. 3.7b. In the period-doubling and

chaotic regime $Q \ll 1$, that is, there is no enhancement of the amplitude of the signal at the low-frequency.

3.3.3 Single-Well Potential $(\omega_0^2, \gamma > 0, \beta < 0, \beta^2 < 4\omega_0^2\gamma)$

Next, we consider the system (3.18) with the single-well potential of the form shown in Fig. 3.4c where ω_0^2 , $\gamma > 0$, $\beta < 0$, $\beta^2 < 4\omega_0^2\gamma$. In this case, the sign of both C_1 and C_2 can be changed by varying either g or Ω . The effective potential can change into other forms. Figure 3.8 depicts $V_{\rm eff}$ for three values of g where $\omega_0^2 = 1$, $\beta = -1.9$, $\gamma = 1$ and $\Omega = 10$. $V_{\rm eff}$ is a single-well potential for g = 70 and 100, while it becomes a double-well potential for g = 90.

The value of $g_{\rm VR}$ when the effective potential is a single-well is given by Eq. (3.25) for $\omega^2 > \omega_0^2$ whereas for $\omega_0^2 - \frac{3\beta^2}{10\nu} < \omega^2 < \omega_0^2$

$$g_{\rm VR} = \Omega^2 \left[\frac{-b \pm \sqrt{b^2 - 4ac}}{2a} \right]^{1/2} .$$
 (3.26)

When $V_{\rm eff}$ becomes a double-well, an analytical expression for $g_{\rm VR}$ is difficult to find. In this case $g_{\rm VR}$ can be calculated numerically. Since $S_g = 4(\omega_{\rm r}^2 - \omega^2)\omega_{\rm r}\omega_{\rm rg} = 0$ at resonance $g_{\rm VR}$ can be computed numerically by analysing the cases $\omega_{\rm r}^2 - \omega^2 = 0$ and $\omega_{\rm rg} = 0$. Figure 3.9a shows $g_{\rm VR}$ against ω . $g_{\rm VR} = 87.05$ for $\omega > 0.412$ arises from $\omega_{\rm rg} = 0$. For $\omega < 0.412$ resonance occurs at four values of g. Three resonances occur for $0.412 < \omega < 1$. For $\omega > 1$ two resonances occur. $V_{\rm eff}$ is a single-well for 0 < g < 74.14 (region-I), double-well for 74.14 < g < 98.5 (region-II) and again become a single-well for g > 98.5 (region-III). In the region-I a resonance takes

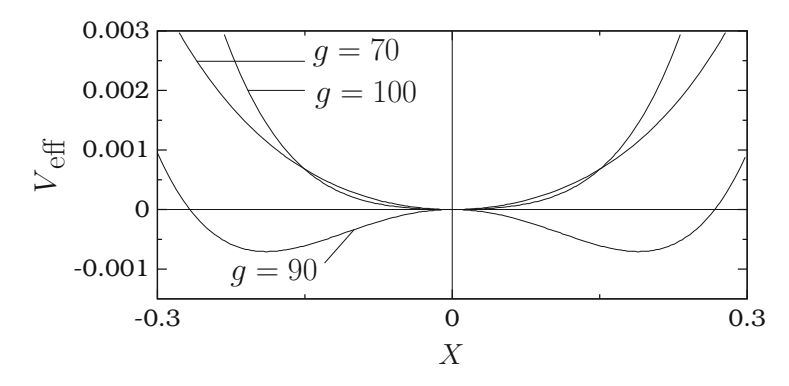


Fig. 3.8 Shape of the effective potential $V_{\rm eff}$, Eq. (3.22), for $\omega_0^2=1, \beta=-1.9, \gamma=1, \Omega=10$ and for three values of g

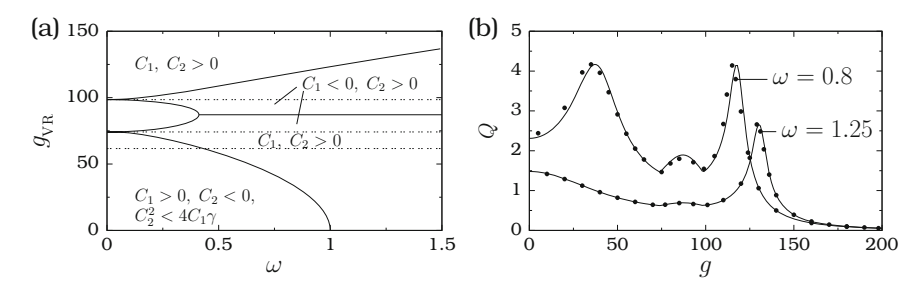


Fig. 3.9 (a) g_{VR} versus ω with $\omega_0^2 = 1$, $\beta = -1.9$, $\gamma = 1$ and $\Omega = 10$. The effective potential is a single-well for 0 < g < 61.65 where $C_1 > 0$, $C_2 < 0$, $C_2^2 < 4C_1\gamma$ and 61.65 < g < 74.14 where C_1 , $C_2 > 0$; double-well for 74.14 < g < 98.5 where $C_1 < 0$, $C_2 > 0$ and again a single-well for g > 98.5 where C_1 , $C_2 > 0$. (b) Q versus g for two values of ω where $\Omega = 10$, d = 0.3 and f = 0.05. The *continuous curves* represent the theoretical results, while the *solid circles* are numerically computed values of Q

place only if $\omega^2 < \omega_0^2 (= 1)$; in the region-II resonance occurs at two values of g for $\omega < 0.412$ while one resonance takes place at $g_{\rm VR} = 87.05$ for $\omega > 0.412$; in the region-III single resonance occurs. The resonance curves in the regions I and III for $\omega^2 < \omega_0^2$ are given by Eq. (3.26) while the curve in the region-III for $\omega^2 > \omega_0^2$ is given by Eq. (3.25). The resonance curve in the region-II corresponds to doublewell case of $V_{\rm eff}$. In Fig. 3.9b the resonance at three values of g for $\omega = 0.8$ can be clearly seen. The value of g at $g_{\rm VR} = 87.05$ is much smaller than the values of other $g_{\rm VR}$. The value of g decreases when ω increases.

In the single-well system (3.18) with $\omega_0^2 = 1$, $\beta = -1.9$, $\gamma = 1$, when g is varied from 0 the effective potential undergoes transitions from a single-well to a double-well and then to a single-well and multiple resonance takes place. Next, an example of multiple resonance where the form of the effective potential remains as a double-hump single-well is presented.

3.3.4 Double-Hump Single-Well Potential ($\omega_0^2 > 0$, β -Arbitrary, $\gamma < 0$)

V(x) is a single-well double-hump potential (Fig. 3.4b or h) for $\omega_0^2 > 0$, β -arbitrary, $\gamma < 0$ with a local minimum at x = 0 and two local maxima at $x = \pm \left[-\beta - \sqrt{\beta^2 - 4\omega_0^2 \gamma} \right] / (2\gamma)$. Assume that $\beta > 0$ and fix $\omega_0^2 = 1$, $\beta = 3$, $\gamma = -1$, $\Omega = 10$. For 0 < g < 78.55 $V_{\rm eff}$ is a single-well double-hump potential with C_1 , $C_2 > 0$; for $78.55 < g < g_c = 161.3925$ it is again of same form but with $C_1 > 0$, $C_2 < 0$ and for $g > g_c$ it is an inverted potential. That is, the shape of $V_{\rm eff}$ does not change into a double-well or a triple-well as g varies from zero. However,

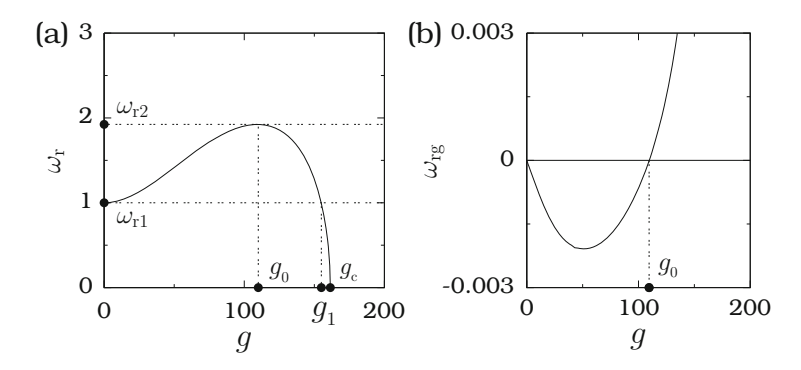


Fig. 3.10 (a) ω_r versus g and (b) ω_{rg} versus g for $\omega_0^2 = 1$, $\beta = 3$, $\gamma = -1$ and $\Omega = 10$

multiple resonance occurs when g varies. For $g < g_c$ the resonant frequency is $\sqrt{C_1}$ and for $g > g_c$ the motion of the system becomes unbound.

Figure 3.10 shows a plot of ω_r versus g and ω_{rg} versus g. In Fig. 3.10a as g increases from 0 the value of ω_r increases from $\omega_{r1} = 1$, reaches a maximum value $\omega_{r2} = 1.924$ at $g = g_0 = 109.54$, then decreases and reaches again the value ω_{r1} at $g = g_1 = 155$. This is because C_1 , the square-root of which is ω_r , is a nonmonotonically varying function of g.

Figure 3.10 implies the following:

- For $0 < \omega < \omega_{\rm r1}$ the quantity $\omega_{\rm r}^2 \omega^2$ is zero for a value of g in the interval $[g_1 = 155, g_{\rm c} = 161.3925]$ and thus a resonance.
- For each value of ω in the interval $[\omega_{r1}, \omega_{r2}]$, $\omega_r^2 \omega^2 = 0$ for two values of g in the interval $[0, g_1]$ and hence two resonances—one for $g < g_0$ and another for $g_0 < g < g_1$.
- $\omega_{rg} = 0$ at $g = g_0$ with $S_{gg} = -36(\omega_{r2}^2 \omega^2)/\omega_{r2}^2$. There is only one resonance for $\omega > \omega_{r2}$ and is at $g = g_0$.

Interestingly, analytical expressions for $g_{\rm VR}$ due to $\omega_{\rm rg}=0$ and $\omega_{\rm r}^2-\omega^2=0$ can be obtained. $\omega_{\rm rg}=0$ gives

$$g_{\rm VR} = g_0 = \Omega^2 \sqrt{\frac{2\beta}{5|\gamma|}}, \quad \omega > \omega_{\rm r}(g_0) = \omega_{\rm r2}.$$
 (3.27)

On the other hand, $\omega_r^2 - \omega^2 = 0$ gives

$$g_{\rm VR} = \Omega^2 \left[\frac{b + \sqrt{b^2 + 4|a|(\omega_0^2 - \omega^2)}}{2|a|} \right]^{\frac{1}{2}}, \quad \omega^2 < \omega_0^2$$
 (3.28)

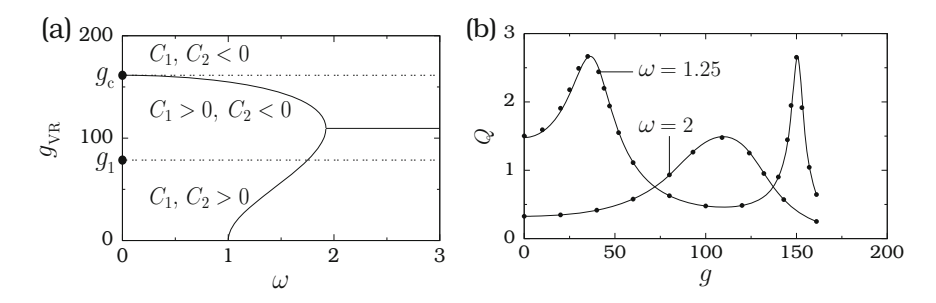


Fig. 3.11 (a) ω versus g_{VR} for the system (3.18) with $\omega_0^2=1$, $\beta=3$, $\gamma=-1$ and $\Omega=10$. $V_{\rm eff}$ is a single-well double-hump form for $0< g< g_c=161.3925$ where $C_1>0$ and C_2 -arbitrary and becomes an inverted single-well for $g>g_c$. (b) Q as a function g for two values of ω where f=0.05 and d=0.3. The *continuous curves* represent the theoretical result while the *solid circles* are the numerically computed Q.

and

$$g_{\rm VR} = \Omega^2 \left[\frac{b \pm \sqrt{b^2 - 4|a(\omega_0^2 - \omega^2)|}}{2|a|} \right]^{\frac{1}{2}}, \quad \omega_0^2 < \omega^2 < \omega_{\rm r}^2(g_0) = \omega_0^2 + \frac{3\beta^2}{10|\gamma|}, \tag{3.29}$$

where a and b are given by Eq. (3.25b).

Figure 3.11a depicts ω versus $g_{\rm VR}$. Figure 3.11b shows the variation of Q versus g for two fixed values of ω with d=0.3 and f=0.05. In Fig. 3.11b Q at $g=g_0$ is a minimum for $\omega=1.25$ and it becomes a maximum for $\omega=2$. For $\omega=1.25$ two resonances occur—one at g=36.5 and another at 150.6. For $\omega=2$ there is only one resonance and it takes place at $g=g_0$. In the double-hump single-well system multiple resonance occurs because the resonant frequency ω_r of the slow motion is a nonmonotonically varying function of g. Even though the effective potential does not change into a double-well or a triple-well form, as g increases from 0 the resonant frequency increases for a while and then decreases. Consequently, for a range of fixed values of ω , ($\omega_r^2-\omega^2$) in the expression for Q becomes minimum (= 0) at two values of g. Therefore, two resonances take place as g varies for a certain range of fixed values of ω .

In the case of the Duffing oscillator, the occurrence of a multiple resonance is not possible when the potential is a single-well or a double-hump single-well form. This is because for the single-well case the resonant frequency $\omega_{\rm r}=\sqrt{C_1}$ increases monotonically from $\sqrt{\omega_0^2}$ as g increases from 0 (see Fig. 3.2b) and only one resonance occurs for $\omega^2>\omega_0^2$ at $g=g_{\rm VR}$ given by Eq. (3.13). For the single-well

double-hump potential as g increases from 0, $\omega_{\rm r}$ decreases monotonically from $\sqrt{\omega_0^2}$ and $\omega_{\rm r}=\omega$ at

$$g_{\rm VR} = \sqrt{\frac{2\Omega^4 \left(\omega_0^2 - \omega^2\right)}{3|\beta|}} , \quad \omega^2 < \omega_0^2$$
 (3.30)

and a resonance. As g increases further at

$$g = g_1 = \sqrt{\frac{2\Omega^4 \omega_0^2}{3|\beta|}} \tag{3.31}$$

the resonant frequency become 0 and for $g>g_1$ the effective potential becomes an inverted single-well and the motion of the system is unbounded since the applied high-frequency force makes the system to overcome the barriers at the two maxima of the potential. Thus, at most one resonance occur in the Duffing oscillator with the single-well double-hump potential. Whereas in the expression for C_1 in $V_{\rm eff}$ of the quintic oscillator there are two terms depending on g and the sign of these two terms are different. The result is that $\omega_r^2=C_1$ oscillates over a certain range of g (or Ω) leading to a multiple resonance.

3.4 Asymmetric Duffing Oscillator

The equation of motion of the asymmetric Duffing oscillator driven by a biharmonic force is

$$\ddot{x} + d\dot{x} + \frac{dV}{dx} = f\cos\omega t + g\cos\Omega t, \qquad (3.32)$$

where $\Omega\gg\omega$ and the asymmetric potential of the system in the absence of damping and external force is

$$V(x) = \frac{1}{2}\omega_0^2 x^2 + \frac{1}{3}\alpha x^3 + \frac{1}{4}\beta x^4.$$
 (3.33)

The potential is symmetric when $\alpha=0$. V(x) is asymmetric due to the term $\frac{1}{3}\alpha x^3$. For ω_0^2 , α , $\beta>0$ the potential V(x) has a single-well form (Fig. 3.12a) for $\alpha^2<4\omega_0^2\beta$ and double-well form for $\alpha^2>4\omega_0^2\beta$. When $\omega_0^2<0$, $\beta>0$, α -arbitrary V(x) becomes a double-well potential (Fig. 3.12b). In this section we analyse [17] the occurrence of vibrational resonance in the system (3.32) with the single-well potential shown in Fig. 3.12a.

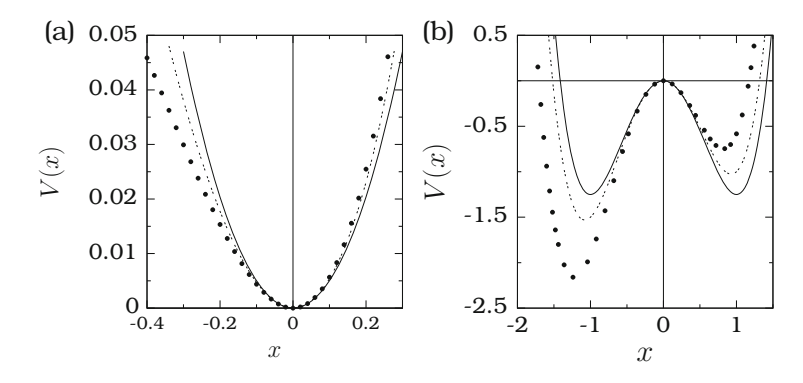


Fig. 3.12 Shape of the asymmetric potential V(x) given by Eq. (3.33) for (**a**) $\omega_0^2 = \beta = 1$ and $\alpha = 0$ (continuous line), 0.75 (dashed line), 1.9 (solid circles) and (**b**) $\omega_0^2 = -5$, $\beta = 5$ and $\alpha = 0$ (continuous line), 0.75 (dashed line), 2 (solid circles)

3.4.1 Theoretical Expression for Response Amplitude

For the system (3.32) the equation for the slow variable X in $x(t) = X(t) + \psi(t, \Omega t)$ is

$$\ddot{X} + d\dot{X} + C_2X + \alpha X^2 + \beta X^3 + C_1 = f \cos \omega t , \qquad (3.34a)$$

where

$$C_1 = \frac{\alpha g^2}{2\Omega^4}, \quad C_2 = \omega_0^2 + \frac{3\beta g^2}{2\Omega^4}.$$
 (3.34b)

Slow oscillations take place about the equilibrium points X^* which are the roots of the cubic equation

$$\beta X^{*3} + \alpha X^{*2} + C_2 X^* + C_1 = 0. {(3.35)}$$

If Eq. (3.35) has three real roots, then we designate them as $X_{\rm L}^*$, $X_{\rm M}^*$ and $X_{\rm R}^*$ with $X_{\rm L}^* < X_{\rm M}^* < X_{\rm R}^*$. When $V_{\rm eff}$ becomes a double-well potential, then $X_{\rm L}^*$ and $X_{\rm R}^*$ are the local minimum of left- and right-wells, respectively, while $X_{\rm M}^*$ is the local maximum of it.

Substitution of $X = Y + X^*$, where Y is the deviation of the slow motion from X^* , in Eq. (3.34a), gives

$$\ddot{Y} + d\dot{Y} + \omega_{\rm r}^2 Y + \alpha' Y^2 + \beta Y^3 = f \cos \omega t , \qquad (3.36a)$$

where

$$\omega_{\rm r}^2 = C_2 + 2\alpha X^* + 3\beta X^{*2}, \quad \alpha' = \alpha + 3\beta X^*.$$
 (3.36b)

The amplitude of oscillation of the linear version of Eq. (3.36) in the limit $t \to \infty$ and $f \ll 1$ and the response amplitude Q are given by Eqs. (3.11) and (3.12), respectively.

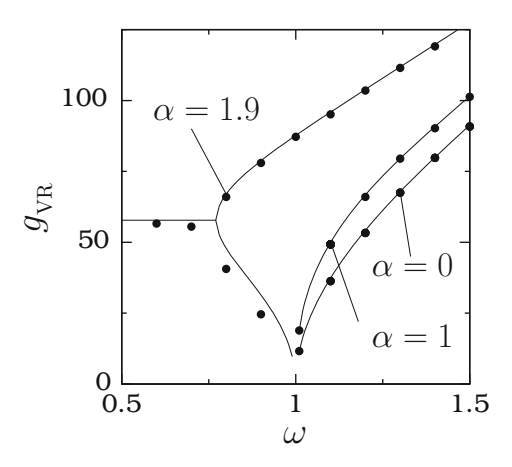
3.4.2 Asymmetry Induced Additional Resonance

In the asymmetric system $X^* \neq 0$ and ω_r is a complicated function of the parameters. Analytical expression for g_{VR} is difficult to find. However, g_{VR} can be determined from $S_g = 0$.

We choose the values of the parameters as $\omega_0^2=1$, $\beta=1$, d=0.3, f=0.05, $\Omega=10$. V(x) is a single-well potential for $0<\alpha<2$ and a double-well potential for $\alpha>2$. Now, we consider the case $0<\alpha<2$. Figure 3.13 shows both theoretically and numerically computed $g_{\rm VR}$ as a function of ω for $\alpha=0$, 1 and 1.9. Notice the absence of resonance for $\omega<1$ in Fig. 3.13, for $\alpha=0$. That is, in the symmetric system if $\omega<1$ (= ω_0^2) an enhancement of the amplitude of the signal at the low-frequency ω is not possible when the amplitude g of the high-frequency force is varied. This is the case for $0<\alpha<1$.23. In this interval of α , ω_r increases monotonically with g from the value 1 and hence no resonance appears for $\omega<1$. An interesting result is the observation of double resonance for $\alpha\in[1.23,2]$. As shown in Fig. 3.13 for $\alpha=1.9$, a double resonance occurs when g is varied from zero for each fixed value of $\omega\in[0.7721,1]$.

Figure 3.14 shows the variation of ω_r , ω_{rg} and Q with the control parameter g. The following results are obtained from Fig. 3.13.

Fig. 3.13 Variation of $g_{\rm VR}$ with ω for three values of α for the asymmetric Duffing oscillator. The *continuous line* is the theoretical prediction of vibrational resonance while the *solid circle* represents the value of $g_{\rm VR}$ calculated from the numerical solution of the system



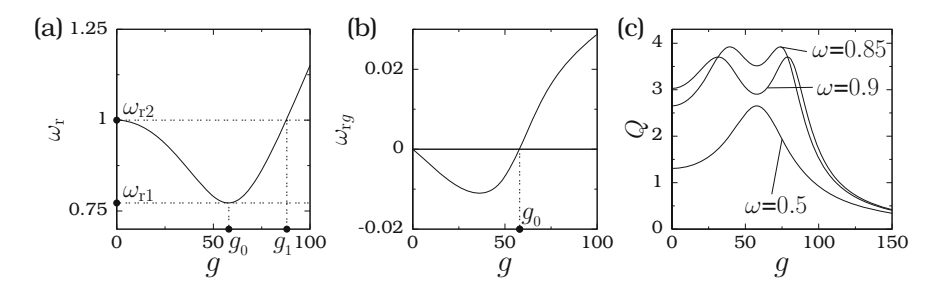


Fig. 3.14 (a) Variation of ω_r with g for $\alpha=1.9$ for the asymmetric Duffing oscillator. (b) ω_{rg} (= $d\omega_r/dg$) versus g for $\alpha=1.9$. ω_r and ω_{rg} are calculated from Eq. (3.36b). (c) Numerically computed Q versus g with single-well potential for three values of ω

- $\omega_{rg} = 0$ at $g_0 = 57.8$ and because $S_g = 4(\omega_r^2 \omega^2)\omega_r\omega_{rg}$ the function S becomes a minimum at this value of g. Hence, a resonance at $g = g_0$ for $0 < \omega < \omega_{r1}$. In Fig. 3.14c, for $\omega = 0.5$ there is only one resonance. For $0 < \omega < \omega_{r1}$, g_{VR} remains a constant (see Fig. 3.13) because ω_r is independent of ω and $\omega_r^2 \omega^2 \neq 0$.
- Corresponding to each value of g in the interval $[0, g_0]$, there is another value of g in the interval $[g_0, g_1 = 88]$ both having the same value of ω_r . Consequently, for each fixed value of $\omega \in [\omega_{r1}, \omega_{r2} = 1]$, the quantity $\omega_r^2 \omega^2$ is 0 for two values of g. Hence, there are two resonances. This is shown in Fig. 3.14c for $\omega = 0.85$ and $\omega = 0.9$. In the symmetric single-well system only one resonance is possible and the corresponding g_{vR} is given by Eq. (3.13). The additional resonance is due to the asymmetry introduced in the system. Such an additional resonance due to the asymmetry occurs in the quintic oscillator also [17].
- When $\omega > \omega_{\rm r2}$ then $\omega_{\rm r}^2 \omega^2 = 0$ for a value of $g > g_1$ and hence a resonance.

For $\omega > \omega_{r1}$ the resonance is due to the matching of the resonant frequency ω_{r} with the frequency ω of the input signal while for $0 < \omega < \omega_{r1}$ though $\omega_{r} \neq \omega$ a resonance occurs due to the minimization of the function S.

3.4.3 Resonance with Nonsinusoidal Periodic Forces

Now we explore the effect of α on the vibrational resonance by using nonsinusoidal and arbitrary binary shape periodic input signals. Consider the following periodic signals in place of $f \cos \omega t$:

$$h_1(t) = f \begin{cases} \cos \omega t, & 0 \le t < \pi/\omega \\ (2\omega/\pi)t - 3, & \pi/\omega \le t < 2\pi/\omega, \end{cases}$$
(3.37)

$$h_2(t) = f \begin{cases} (\omega/\pi)t - 1/2, & 0 \le t < \pi/\omega \\ -(\omega/\pi)t + 3/2, & \pi/\omega \le t < 2\pi/\omega, \end{cases}$$
(3.38)

$$h_{3}(t) = f \begin{cases} 1, & 0 \le t < \pi/(4\omega) \\ -0.5, & \pi/(4\omega) \le t < 3\pi/(4\omega) \\ 0.5, & 3\pi/(4\omega) \le t < \pi/\omega \\ -0.75, & \pi/\omega \le t < 5\pi/(4\omega) \\ 1, & 5\pi/(4\omega) \le t < 7\pi/(4\omega) \\ -0.25, & 7\pi/(4\omega) \le t < 2\pi/\omega. \end{cases}$$
(3.39)

In all the above three signals $t = \text{mod}(2\pi/\omega)$. Figure 3.15a shows the numerically calculated Q versus g for $\alpha = 1.9$ with the different input signals with the same frequency $\omega = 0.85$ and amplitude f = 0.05. The high-frequency force is again $g \cos \Omega t$. In all the cases a double resonance occurs. g_{VR} values for the signals $f \cos \omega t$, $h_1(t)$, $h_2(t)$ and $h_3(t)$ are (34,72), (38,80), (95,177) and (42,71), respectively. The effect of asymmetry is similar for all the forms of the periodic input signals considered. The above result indicates that the form of the high-frequency force need not be same as the input signal. For any arbitrary periodic signal of frequency ω amplification of the amplitude of the output signal at the frequency ω can be achieved by using the force $g \cos \Omega t$.

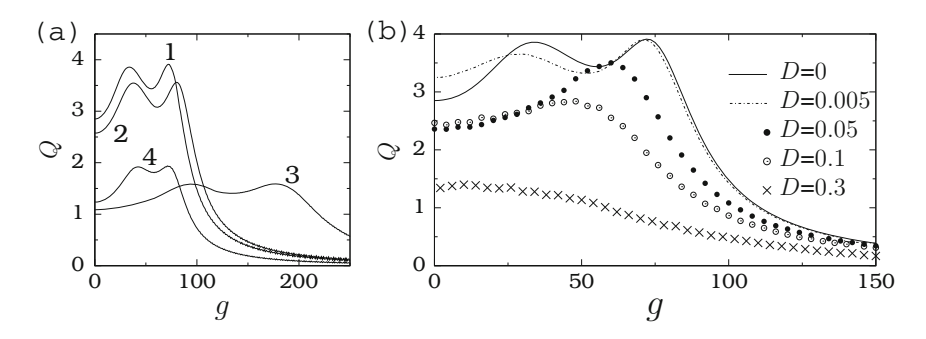


Fig. 3.15 (a) Q versus g for (3.34). For the curves 1–4 the low-frequency signal being $f \cos \omega t$, $h_1(t)$, $h_2(t)$ and $h_3(t)$, respectively. The high-frequency force is $g \cos \Omega t$. Here $\omega_0^2 = 1$, $\beta = 1$, d = 0.3, f = 0.05, $\omega = 0.85$, $\alpha = 1.9$ and $\Omega = 10$. (b) Q versus the amplitude g in the absence of external noise and for four fixed values of D with $\alpha = 1.9$. The low-frequency input signal is $f \cos \omega t$ with f = 0.05 and $\omega = 0.85$

3.4.4 Effect of Noise on Resonance

Next, we illustrate the effect of additive Gaussian white noise $\eta(t)$, with zero mean and the correlation function $\langle \eta(t)\eta(t+\tau)\rangle = D\delta(t-\tau)$ where D is the variance or intensity of the noise, in the system (3.34) with a double resonance. In the numerical calculation of Q, 2×10^3 trajectories, $x^{(i)}(t)$, are generated by numerically integrating the equation of motion for every realization of the noise $\eta(t)$. The same initial conditions are used for all the trajectories. The first 500 drive cycles of low-frequency force is left as transient. After every integration step the average of all $x^{(i)}(t)$ denoted as $\langle x(t)\rangle$ is calculated. This average quantity is used for the calculation of Q. In Fig. 3.15b numerically calculated Q versus Q is plotted for four values of the noise intensity along with the noise free resonance curve. A double resonance with slight shift in the values of Q0. In Fig. 3.15b one can notice the following:

- An increase in the noise intensity first suppress the resonance occurring at a lower value of the amplitude of the high-frequency force and then the other resonance.
- The value of g_{VR} moves towards the origin with D. The Gaussian white noise contains all the frequencies. As pointed out in [12, 22], the portion of the noise corresponding to the high-frequency interval is the source for the decrease in the value of g_{VR} .
- Q, specifically Q_{max} , decreases when D increases. The part of noise with frequencies other than the high-frequency region degrade the performance of the system by decreasing the value of Q.

Casado-Pascual and Baltanas [41] presented a theoretical treatment for the analytical calculation of the response amplitude Q for the overdamped bistable system driven by a biharmonic force and an additive Gaussian white noise. The obtained analytical expression for Q predicts that

- the location of the maximum characterizing the resonance shifts to the left as the noise strength increases,
- the increase in the noise intensity lowers the maximum value of the resonance curve and
- the resonance disappears for large enough values of the noise intensity.

These theoretical predictions are in a very good agreement with the numerical result presented in Fig. 3.15b.

3.5 Overdamped Asymmetric Duffing Oscillator

The equation of motion of the overdamped version of the asymmetric Duffing oscillator is

$$\dot{x} = -\omega_0^2 x - \alpha x^2 - \beta x^3 + f \cos \omega t + g \cos \Omega t. \tag{3.40}$$

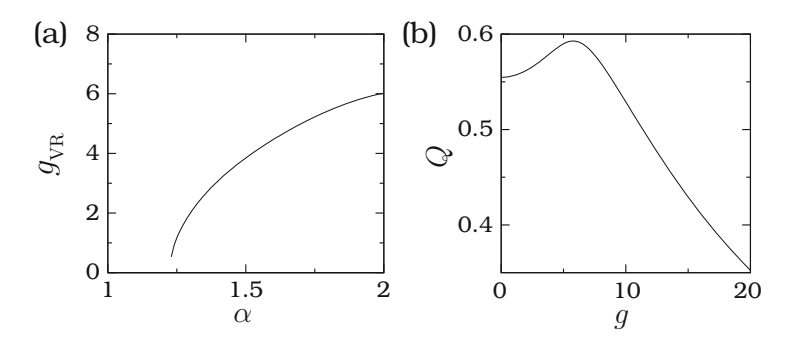


Fig. 3.16 (a) α versus g_{VR} for a single-well case of the overdamped system (3.40) with $\omega_0^2 = 1$, $\beta = 1$ and $\Omega = 10$. (b) Q versus g for the single-well case with $\alpha = 1.9, f = 0.05$ and $\omega = 0.85$

The amplitude $A_{\rm L}$ of the low-frequency oscillation of the system (3.40) is obtained as

$$A_{\rm L} = \frac{f}{\sqrt{\omega_{\rm r}^2 + \omega^2}} \,, \tag{3.41}$$

where ω_r^2 is given by Eq. (3.36b) and C_1 and C_2 in Eq. (3.34b) become now

$$C_1 = \frac{\alpha g^2}{2\Omega^2}, \quad C_2 = \omega_0^2 + \frac{3\beta g^2}{2\Omega^2}.$$
 (3.42)

For the system (3.40) with a symmetric single-well (ω_0^2 , $\beta > 0$, $\alpha = 0$) as g increases ω_r^2 increases from ω_0^2 monotonically and hence there is no resonance. Resonance occurs in the asymmetric system for a range of values of α . For example, Fig. 3.16a shows $g_{\rm VR}$ versus α for $\omega_0^2 = 1$, $\beta = 1$ and $\Omega = 10$. As shown in Fig. 3.16b, for $\omega = 0.85$, f = 0.05 and $\alpha = 1.9$ resonance takes place at g = 5.78. The vibrational resonance in the system (3.40) is due to the presence of asymmetry in the potential function and it can be observed in other overdamped nonlinear asymmetric systems as well.

3.6 Morse Oscillator

In the earlier sections oscillators with a single-well potential V(x) where $V(x) \to \infty$ as $|x| \to \infty$ are considered. The present section is devoted for the single-well Morse oscillator [42] for which $V(x) \to \infty$ as $x \to -\infty$ and $V(x) \to 0$ as $x \to \infty$.

The equation of motion of the Morse oscillator is

$$\ddot{x} + d\dot{x} + \beta \left(e^{-x} - e^{-2x} \right) = f \cos \omega t + g \cos \Omega t , \quad \beta > 0.$$
 (3.43)

3.6 Morse Oscillator 107

The occurrence of a nonlinear resonance in the above system in absence of the high-frequency force is discussed in Sect. 1.4. The potential of the system is given by Eq. (1.22). Figure 1.9 depicts the form of the Morse potential for $\beta=1$. The Morse potential is also a monostable potential. One can compare V(x) of Morse oscillator with those of Duffing (Fig. 3.1a, c) and quintic (Fig. 3.4a–c, h) oscillators.

Seeking the solution of Eq. (3.43) of the form $x(t) = X(t) + \psi(t, \Omega t)$ gives

$$\ddot{X} + d\dot{X} + \beta e^{-X} \langle e^{-\psi} \rangle - \beta e^{-2X} \langle e^{-2\psi} \rangle = f \cos \omega t , \qquad (3.44)$$

and

$$\ddot{\psi} + d\dot{\psi} + \beta e^{-X} \left(e^{-\psi} - \langle e^{-\psi} \rangle \right) - \beta e^{-2X} \left(e^{-2\psi} - \langle e^{-2\psi} \rangle \right) = g \cos \Omega t. \quad (3.45)$$

Approximating Eq. (3.45) as $\ddot{\psi} = f \cos \Omega t$ gives

$$\psi = \mu \cos \Omega t, \quad \mu = \frac{g}{\Omega^2} \,. \tag{3.46}$$

For the solution Eq. (3.46)

$$\langle e^{-\psi} \rangle = \frac{1}{T} \int_0^T e^{-\psi} dt = \frac{1}{2\pi} \int_0^{2\pi} e^{-\mu \cos \tau} d\tau = I_0(\mu) ,$$
 (3.47a)

$$\langle e^{-2\psi} \rangle = I_0(2\mu) , \qquad (3.47b)$$

where $I_0(y)$ is the zeroth-order modified Bessel function. Then, the equation for X is

$$\ddot{X} + d\dot{X} + \beta I_0(\mu) e^{-X} - \beta I_0(2\mu) e^{-2X} = f \cos \omega t.$$
 (3.48)

Equation (3.48) can be viewed as the equation of motion of a system with the effective potential

$$V_{\text{eff}}(X) = \frac{1}{2}\beta e^{-X} \left(I_0(2\mu)e^{-X} - 2I_0(\mu) \right) . \tag{3.49}$$

In order to illustrate the effect of g on $V_{\rm eff}$ the variation of $I_0(\mu)$ and $I_0(2\mu)$ versus g and $V_{\rm eff}$ versus X are shown in Fig. 3.17a, b, respectively. I_0 increases monotonically with g. The local minimum of $V_{\rm eff}(X)$ about which oscillation occurs is (the fixed point of (3.48) in the absence of the driving force $f \cos \omega t$)

$$X^* = -\ln\left(\frac{I_0(\mu)}{I_0(2\mu)}\right). \tag{3.50}$$

 $I_0(2\mu)$ increases more rapidly than $I_0(\mu)$ with g. Consequently, as g increases X^* moves away from origin and $V_{\rm eff}$ becomes more and more flat for $X > X^*$ as shown in Fig. 3.17b.

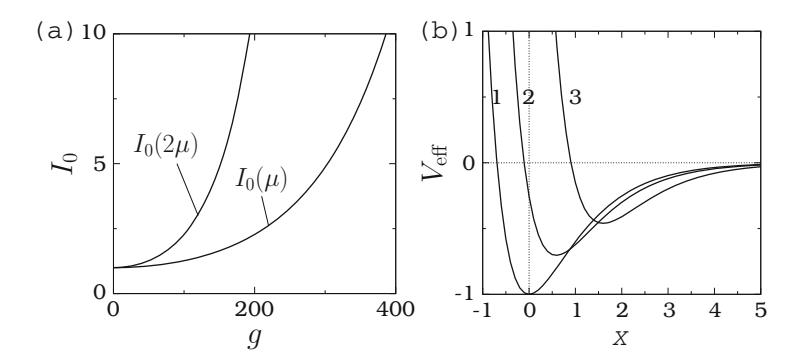


Fig. 3.17 (a) Variation of zeroth-order modified Bessel functions $I_0(\mu)$ and $I_0(2\mu)$ with g. The value of Ω is 10. (b) Influence of g on the shape of the effective potential of the variable X of the Morse oscillator. Here $\beta=2$ and $\Omega=10$. The values of g for the curves 1, 2 and 3 are 0, 100 and 200, respectively

Substituting $X = Y + X^*$, where Y is the deviation of X from X^* , in Eq. (3.48), and approximating $e^{-Y} \approx 1 - Y$, $e^{-2Y} \approx 1 - 2Y$, one obtains the linear equation

$$\ddot{Y} + d\dot{Y} + \omega_r^2 Y = f \cos \omega t , \qquad (3.51)$$

where the square of the resonant frequency is given by

$$\omega_{\rm r}^2 = \frac{\beta I_0^2(\mu)}{I_0(2\mu)} \,. \tag{3.52}$$

The solution of (3.51) in the limit $t \to \infty$ and $f \ll 1$ is $A_L \cos(\omega t + \phi)$ where A_L and ϕ are given by Eq. (3.11) and the response amplitude is given by Eq. (3.12).

The values of the control parameter at which resonance occurs (Q becomes maximum) correspond to the minimum of S. The following are the key results from the theoretical and numerical calculations of Q [42]:

- 1. For a fixed value of g when ω is varied, the resonance occurs when $\omega = \omega_{VR}$ given by Eq. (3.16).
- 2. An analytical expression for g_{VR} is difficult to obtain because ω_r^2 is a complicated function of g. Figure 3.18a, b present the variation of Q and ω_r^2 with the control parameter g for three fixed values of β . Resonance occurs when the resonant frequency matches with the angular frequency ω of the external low-frequency force
- 3. At g = 0, $I_0(\mu) = I_0(2\mu) = 1$ and $\omega_r^2(g = 0) = \beta$. As g increases as shown in Fig. 3.17a $I_0(\mu)$ and $I_0(2\mu)$ increases rapidly with $I_0(2\mu)$ growing faster than $I_0(\mu)$ and, consequently, ω_r^2 decreases rapidly from the value of β for a while

3.6 Morse Oscillator 109

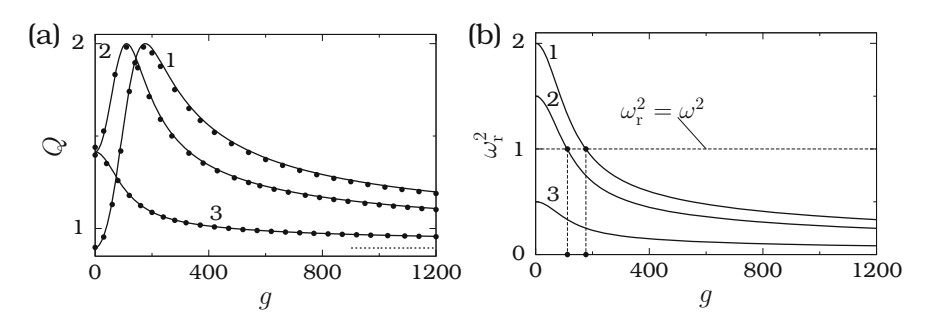


Fig. 3.18 (a) Q versus g and (b) ω_r^2 versus g for the Morse oscillator with d=0.5, f=0.1, $\omega=1$ and $\Omega=10$. The values of β for the curves 1, 2 and 3 are 2, 1.5 and 0.5, respectively. In the subplot (a) the *solid circles* are numerical Q while the *continuous line* is the theoretical Q. The horizontal dotted line represents the limiting value of Q. In the subplot (b) the two solid circles on the g axis mark the values of g at which resonance occurs for g = 2 and 1.5

and then decays to zero slowly. The maximum value of ω_r^2 is β and this happens at g=0. ω_r^2 is always less than ω^2 for $\beta<\omega^2$, that is, $\omega_r^2-\omega^2\neq 0$ for g>0 implying no resonance. This is shown in Fig. 3.18a for $\beta=0.5$ and $\omega=1$ for which Q decreases continuously with g.

- 4. For $\beta > \omega^2$, as g increases from zero, ω_r^2 decreases and becomes ω^2 at only one value. Hence, there is only one resonance. This is shown in Fig. 3.18 for $\beta = 1.5$ and 2 with $\omega = 1$.
- 5. g_{VR} depends on Ω , ω and β and is independent of d and f. Q decreases with increase in the value of d.
- 6. For very large values of $g,\,\omega_{\rm r}^2\to 0$ and Q approaches the limiting value $Q_{\rm L}$ given by

$$Q_{\rm L}(g \to \infty) = \frac{1}{\omega \sqrt{\omega^2 + d^2}} \,. \tag{3.53}$$

That is, Q does not decay to zero but approaches the above limiting value for fixed values of the system parameters. This limiting value depends only on the parameters ω and d. The point is that when $\omega_r^2 \to 0$, Eq. (3.51) becomes the damped free particle driven by the periodic force whose solution is

$$Y(t) = fQ_{L}\cos(\omega t + \Phi), \quad \Phi = \tan^{-1}(d/\omega) . \tag{3.54}$$

For the Duffing and quintic oscillators considered earlier in this chapter, V(x) (as well as the effective potential) $\to \infty$ as $x \to \pm \infty$. In this case the resonant frequency diverges and thus Q decays to zero for large values of g.

3.7 Quantum Mechanical Morse Oscillator

The focus of this section is to consider a quantum mechanical system subjected to the biharmonic external field and identify the effect of variation of the control parameters g and Ω . The reference system is chosen as the quantum mechanical Morse oscillator. Applying a perturbation theory employed in Sect. 1.9 obtain an analytical expression for the first-order transition probability P_f for a transition from an ith eigenstate to an fth state in Time T caused by the applied field. Thereby, one can analyse the influence of high-frequency field on P_f [42].

For the unperturbed Morse oscillator

$$H^{(0)} = \frac{1}{2m}p_x^2 + V(x), \quad V(x) = \frac{1}{2}\beta e^{-x} (e^{-x} - 2)$$
 (3.55)

the stationary state energy eigenfunctions and the energy eigenvalues obtained by solving the time-independent Schrödinger equation are [43–45]

$$\phi_n = N_n z^{\lambda - n - 1/2} e^{-z/2} L_n^k(z),$$
 (3.56a)

where

$$z = 2\lambda e^{-x}, \quad \lambda^2 = \frac{m\beta}{\hbar^2}, \quad N_n = \left(\frac{k \, n!}{(2\lambda - n - 1)!}\right)^{1/2},$$
 (3.56b)

$$k = 2\lambda - 2n - 1$$
, $L_n^k(z) = \frac{z^{-k}e^z}{n!} \frac{d^n}{dz^n} e^{-z} z^{n+k}$ (3.56c)

and

$$E_n = -\frac{\hbar^2}{2m} \left(\lambda - n - \frac{1}{2} \right)^2, \quad n = 0, 1, \dots \text{ and } n < \lambda - \frac{1}{2}.$$
 (3.57)

In Eq. (3.56c) $L_n^k(z)$ are the generalized Laguerre polynomials. The Morse oscillator admits a finite number of bound states. The number of bound states can be changed by varying the parameter β . Set the values of \hbar and m as unity for convenience. Then for $\beta = 9$

$$E_0 = -3.125, E_1 = -1.125, E_2 = -0.125.$$
 (3.58)

There are only three bound states.

With the perturbation $H^{(1)} = xW(t)$, $W(t) = F\cos\omega t + g\cos\Omega t$, the perturbation theory leads to

$$a_f^{(1)}(T) = \frac{s H_{fi}}{2h},$$
 (3.59a)

where

$$s = (r_{1+} + r_{1-})F + (r_{2+} + r_{2-})g, (3.59b)$$

$$r_{1\pm} = \frac{1 - e^{i(\omega_{fi} \pm \omega)T}}{\omega_{fi} \pm \omega}, \quad r_{2\pm} = \frac{1 - e^{i(\omega_{fi} \pm \Omega)T}}{\omega_{fi} \pm \Omega},$$
 (3.59c)

$$\omega_{fi} = (E_f - E_i)/\hbar, \quad H_{fi} = \int_{-\infty}^{\infty} \phi_f^* x \phi_i \, \mathrm{d}x.$$
 (3.59d)

The transition probability for *i*th state to *f*th state is given by $P_f(T) = \left| a_f^{(1)}(T) \right|^2$. In $a_f^{(1)}(T)$ the term *s* alone depends on the parameters F, ω , g and Ω of the external field and T. Therefore, study the variation of the quantity $|s|^2$ with the parameters of the external field.

Fix $\beta=9$, F=0.05, $T=\pi$ and suppose the system is initially in the ground state (i=0). Figure 3.19 shows $\log |s|^2$ versus ω for g=0. The first-order correction to transition probability displays a sequence of resonance peaks with decreasing amplitude. The following results are notable from Eqs. (3.59b, c) and Fig. 3.19. s consists of only r_{1+} and r_{1-} and $\omega_{00}=0$, $\omega_{10}=2$ and $\omega_{20}=3$. Then for the states f=0, 1 and 2 the quantity r_{1+} can be neglected when $\omega\approx0$, 2 and 3, respectively, because the denominator in r_{1-} is ≈ 0 . Thus, the first-order transition probability for the states f=0, 1 and 2 becomes maximum at $\omega=0$, 2 and 3, respectively. For $\omega\approx0$ the values of $|s|^2$ for f=0, 1 and 2 are $\approx4F^2\pi^2$, 0 and $16F^2/9$, respectively. The transition probability for the state f=1 is ≈ 0 . For the f=0 state $|s|^2=0$ when $\omega=1,2,\cdots$ and it becomes maximum when $\omega=n+\frac{1}{2}, n=1,2,\cdots$. In the case of f=1 at $\omega=4$, f=1, f

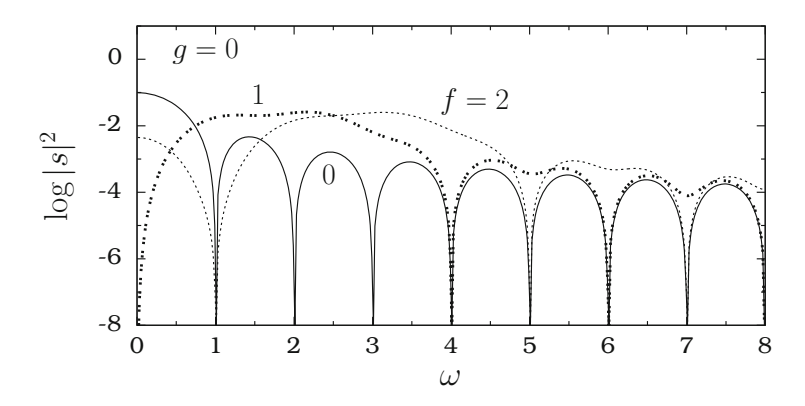


Fig. 3.19 $\log |s|^2$ versus ω for the states f=0,1 and 2 for $\beta=9,F=0.05,g=0,T=\pi$ and i=0

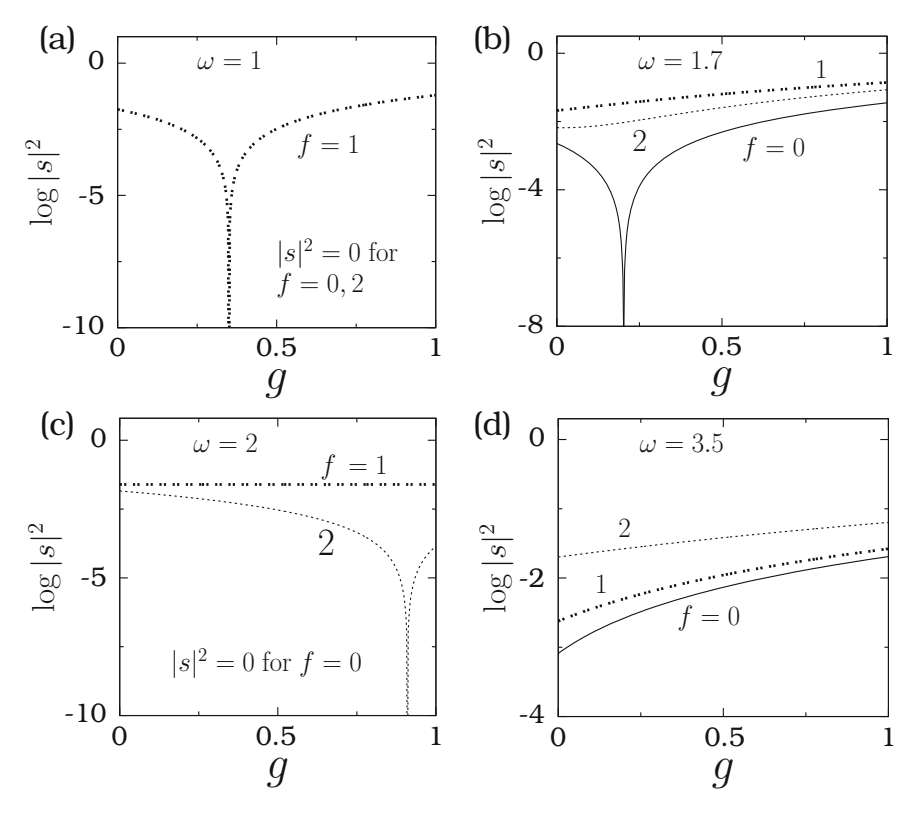


Fig. 3.20 Variation of $|s|^2$ (in log scale) with the amplitude g of the high-frequency external field for four fixed values of the frequency ω of the low-frequency external field. The value of Ω is fixed as 5ω

Next, include the high-frequency field and vary its amplitude g and the frequency Ω . Figure 3.20 presents the results for a few fixed values of ω with $\Omega=5\omega$. When $\omega=1$, in Eq. (3.59b), $r_{1+}+r_{1-}=0$ and $r_{2+}+r_{2-}=0$ for f=0 and 2 and hence the increase of g has no effect on $|s|^2$. For the f=1 state s=(8/3)F-(8/21)g. As g increases the quantity $|s|^2$ decreases from (8/3)F, becomes 0 at g=7F(=0.35). Then it increases with further increase in the value of g as shown in Fig. 3.20a. The first-order transition probability of the state f=1 shows anti-resonance at g=0.35. Anti-resonance can be observable for other states also for certain choices of ω . For example, in Fig. 3.20b, c corresponding to $\omega=1.7$ and 2, respectively, anti-resonance occurs for f=0 state and f=2 state. In Fig. 3.20d where $\omega=3.5$ $|s|^2$ increases monotonically with the control parameter g for all the three states.

Because r_{2+} and r_{2-} [given by Eq. (3.59c)] contain terms which are sinusoidal functions of Ω the first-order transition probability can exhibit a sequence of resonance peaks when Ω is varied. This is shown in Fig. 3.21 for four sets of values of ω and g. In all the cases Ω is varied from 5ω . In Fig. 3.21a–c $|s|^2$ becomes 0 at

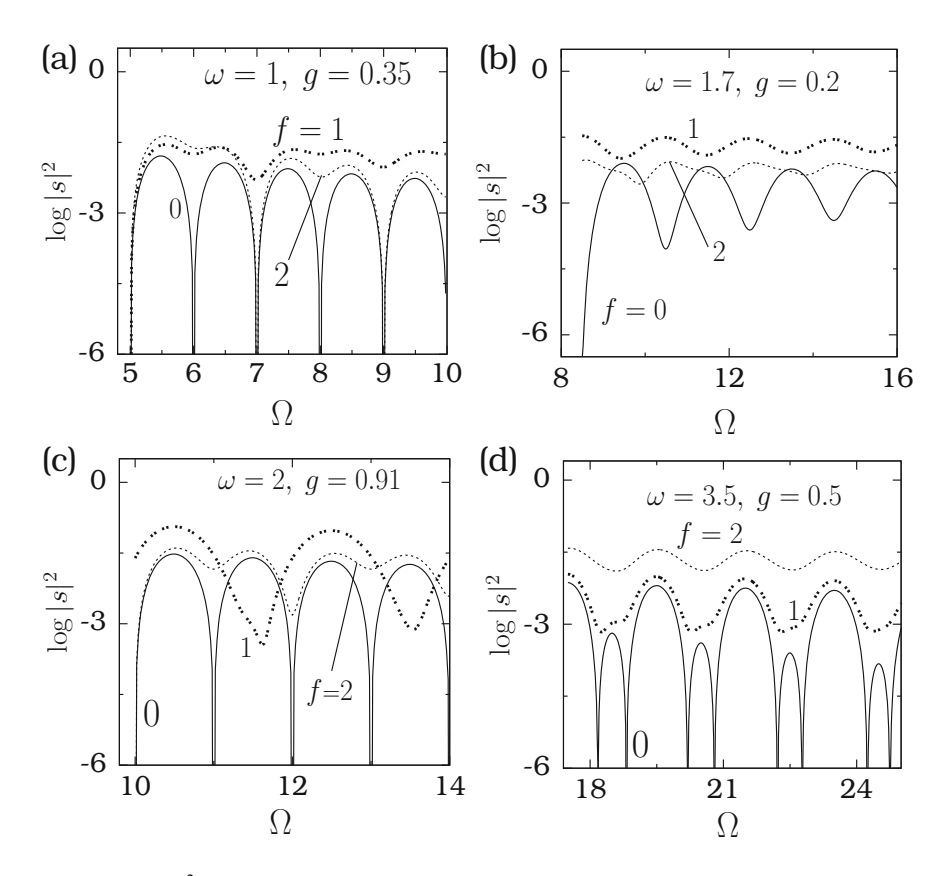


Fig. 3.21 $\log |s|^2$ versus Ω (the frequency of the high-frequency external field) for four sets of values of ω and g

the starting value of Ω for the f=0 state. $|s|^2 \neq 0$ for wide ranges of values of Ω . Transition probability of all the states show a sequence of resonance peaks. In Fig. 3.21d $|s|^2$ of f=0 state is close to its values of the other two states. However, as Ω increases $|s|^2$ of the f=1 and f=2 states oscillate but $\neq 0$. In contrast to this, $|s|^2$ of the f=0 state becomes 0 at certain values of Ω .

It is noteworthy to compare the effect of high-frequency external force in the classical and quantum mechanical Morse oscillators. A classical nonlinear system can exhibit a variety of dynamics when a control parameter is varied. However, in the Morse oscillator for the choice $|f| \ll 1$ and $\Omega \gg \omega$ when the amplitude g of the high-frequency force is varied the system is found to show only periodic motion with period $T=2\pi/\omega$. The response amplitude of the motion displays a single resonance when g or ω or Ω is varied. Resonance occurs when the resonant frequency ω_r matches with the frequency ω . In the case of the quantum mechanical Morse oscillator the simple case of switching-on the external field at t=0 and switching-off it at t=T is considered. In the absence of the high-frequency field the

first-order transition probability P_{fi} shows a sequence of resonances with decreasing amplitude when the parameter ω is increased. The dominant resonance occurs at $\omega = \omega_{fi}$. Resonance is not observed when the amplitude g of the high-frequency field is varied. However, anti-resonance of P_{fi} takes place for certain values of ω . Multiple resonance of P_{fi} occurs when the frequency Ω of the high-frequency field is varied.

3.8 Significance of Biharmonic Signals

The study of the action of two-frequency signal is of great importance in physics, engineering and biology. Particularly, the biharmonic signal in the context of vibrational resonance has been explored. Gerhardt [46] reported the significance of two-frequency bands in long-distance vocal communication in the green treefrog. Two-frequency signals are of interest in laser physics [47], acoustics [48], neuroscience [49] and physics of the ionosphere [50]. The beneficial role of a high-frequency driving has already been exploited as increased drug uptake by brain cells [51], acceleration of bone and muscle repairing [52], resonantly enhanced biogradation of micro-organisms [53] and stimulation treatments in Parkinson's disease [54]. Ultrasonic irradiation of two widely different frequencies has been found to increase cavitation yield [55].

A two-frequency laser unit with a laser, a half-wave plate and an electro-optic modulator was found to give high stability and efficiency [47]. Biharmonic signal transmission is a standard technique in the positioning and navigation in the global positioning system [56]. Occurrence of the Faraday waves in a pattern formation with two-frequency excitation (one is the signal frequency ω and the other is the subharmonic frequency $\omega/2$) [57] and neurobiological reaction controlling by electrical stimulation of different frequencies [58] have been studied. It has been pointed out that though high-frequency electromagnetic radiation is likely to be harmless at the small length scales of sensitive biomolecules, like the DNA helix [59], still it can affect physiological processes at the cell level. It is to be noted that high-frequency electromagnetic waves not only heat up the biological tissues with epidemiological consequences, but such fields from electrical devices such as power-lines, television transmitters, industrial machinery etc, can interfere with the much lower-frequency for example, electrochemical control signals that regulate the ion transport across the cell membranes or the information transformation and processing through neuron networks and sensory nerves [60]. Biharmonic forces have been used to create soliton ratchets [61]. Multi-frequency signal is used in multichannel optical communication systems such as based on wavelength-division multiplexing [62], the analysis of the size and abundance of plankton [63] and the diagnosis conditions of the Antarctic ice sheet [64].

High-frequency oscillation of beach water table due to wave runup and rundown has been observed and analysed [65, 66]. Interestingly, similar high-frequency oscillation of underground water table (in addition to the low-frequency periodic

oscillation of water table due to seasonal variation) can occur due to evaporation, inflow and outflow of water and temperature fluctuation. It can also be artificially realized through irrigation or pumping from the aquifer. Furthermore, a water table rise and drop can be induced by vegetation removal and planting, respectively. Thus, planting additionally short-lived species interacting weakly with species *A* can also lead to a high-frequency variation of the water depth. Therefore, it is realistic to include a biharmonic force in the water table with two well-separated frequencies [67].

In brain dynamics, bursting neurons may exhibit two different times scales [68]. In telecommunication, information carriers are often high-frequency waves modulated by a low-frequency signal that encodes the data [69]. Interaction of fast and slow variables like hares and tortoises is common in ecosystems [70]. Plankton dynamics show slow and fast cycles [71]. Many ecological systems display a slow-fast dynamics. It has been pointed out that the dynamics of vegetation have a time scale greater than one season and much greater than man-induced periodic disturbances [72].

High-frequency alternating currents applied to the nerve is shown to give rise to reversible conduction block [73–75] which has clinical applications. To treat movement disorders such as Parkinson's disease and dystonia high-frequency electrical simulation has been applied clinically through deep-brain simulation electrodes implanted in certain brain regions [76]. High-frequency stimulation is found to enhance and suppress pulse propagation in a discrete FitzHugh–Nagumo model [77]. In the central nervous system a considerable increase in the rate of replenishment of pool of synaptic vesicles by a high-frequency stimulation of presynaptic terminals. This can be used for identifying the mechanism of shortand long-term changes of synapses [78].

3.9 Concluding Remarks

In all the monostable systems considered in this chapter, from the approximate theoretical expression of response amplitude Q of the slow motion, we are able to determine the number of resonances and the values of the control parameters, say, g or Ω or ω at which resonance occurs. In all the cases, as ω varies either no resonance or only one resonance occurs depending on the values of the other parameters. As g is varied, in the Duffing and Morse oscillators, at most one resonance is possible and resonance occurs when $\omega_r = \omega$. In the quintic oscillator with the single-well potential of the form shown in Fig. 3.4b, c, h ω_r oscillates and multiple resonance occurs when $\omega_r = \omega$ and also at $\omega_{rg} = 0$. The occurrence of additional resonance is shown to be due to the presence of the asymmetry in the single-well potential of the Duffing oscillator. In the Duffing and quintic oscillators after the last resonance Q decays to zero with the increase in the parameter g or Ω or ω . In contrast to this in the Morse oscillator Q does not decay to zero but approaches to a constant value with the control parameter, say, g.

The theoretical analysis indicates that to observe resonance bistability and transition of $V_{\rm eff}$ from one form to another form are not necessary. A monostable system can be able to exhibit a multiple vibrational resonance if the resonant frequency $\omega_{\rm r}$ oscillates. Further, not only the case $\omega_{\rm r}^2 - \omega^2 = 0$, but also the case $\omega_{\rm rg} = 0$ with $S_{\rm gg} > 0$ corresponds to a resonance.

References

- 1. P.S. Landa, P.V.E. McClintock, J. Phys. A Math. Gen. 33, L433 (2000)
- 2. M. Gittermann, J. Phys. A Math. Gen. 34, L355 (2001)
- 3. I.I. Blekhman, P.S. Landa, Int. J. Nonlinear Mech. 39, 421 (2004)
- A.A. Zaikin, L. Lopez, J.P. Baltanas, J. Kurths, M.A.F. Sanjuan, Phys. Rev. E 66, 011106 (2002)
- 5. E. Ullner, A. Zaikin, J. Garcia-Ojalvo, R. Bascones, J. Kurths, Phys. Lett. A 312, 348 (2003)
- 6. B. Deng, J. Wang, X. Wei, Chaos 19, 013117 (2009)
- 7. C. Stan, C.P. Cristescu, D. Alexandroaei, M. Agop, Chaos Solitons Fractals 41, 727 (2009)
- S. Jeyakumari, V. Chinnathambi, S. Rajasekar, M.A.F. Sanjuan, Phys. Rev. E 80, 046608 (2009)
- 9. S. Jeyakumari, V. Chinnathambi, S. Rajasekar, M.A.F. Sanjuan, Chaos 19, 043128 (2009)
- 10. V.M. Gandhimathi, S. Rajasekar, J. Kurths, Phys. Lett. A 360, 279 (2006)
- 11. V.M. Gandhimathi, S. Rajasekar, Phys. Scr. **76**, 693 (2007)
- J.P. Baltanas, L. Lopez, I.I. Blechman, P.S. Landa, A. Zaikin, J. Kurths, M.A.F. Sanjuan, Phys. Rev. E 67, 066119 (2003)
- 13. V.N. Chizhevsky, G. Giacomelli, Phys. Rev. E 70, 062101 (2004)
- 14. V.N. Chizhevsky, Int. J. Bifurcation Chaos 18, 1767 (2008)
- 15. B. Deng, J. Wang, X. Wei, Chaos 19, 013117 (2009)
- 16. C. Yao, M. Zhan, Phys. Rev. E **81**, 061129 (2010)
- S. Jeyakumari, V. Chinnathambi, S. Rajasekar, M.A.F. Sanjuan, Int. J. Bifurcation Chaos 21, 275 (2011)
- 18. J. Shi, C. Huang, T. Dong, X. Zhang, Phys. Biol. 7, 036006 (2010)
- 19. V.N. Chizhevsky, E. Smeu, G. Giacomelli, Phys. Rev. Lett. 91, 220602 (2003)
- 20. V.N. Chizhevsky, G. Giacomelli, Phys. Rev. E 73, 022103 (2006)
- 21. V.N. Chizhevsky, G. Giacomelli, Phys. Rev. A 71, 011801(R) (2005)
- 22. J. Casado-Pascual, J.P. Baltanas, Phys. Rev. E 69, 046108 (2004)
- 23. A. Ichiki, Y. Tadokoro, M. Takanashi, J. Phys. A Math. Gen. 45, 385101 (2012)
- 24. C. Yao, Y. Liu, M. Zhan, Phys. Rev. E 83, 061122 (2011)
- 25. I.I. Blekhman, Vibrational Mechanics (World Scientific, Singapore, 2000)
- 26. Y.H. Kao, C.S. Wang, Phys. Rev. E 48, 2514 (1993)
- 27. G. Gilboa, N. Sochen, Y.Y. Zeevi, J. Math. Imaging Vision 20, 121 (2004)
- 28. C. Wagner, T. Kiefhaber, Proc. Natl. Acad. Sci. U. S. A. 96, 6716 (1999)
- 29. G.Z. Li, F.C. Moon, J. Sound Vib. 136, 17 (1990)
- 30. J. Yu, R. Zhang, W. Pan, L. Schimansky-Geier, Phys. Scr. 78, 025003 (2008)
- 31. R. Tchooukuegno, B.R. Nana Nbendjo, P. Woafo, Phys. A 304, 362 (2002)
- 32. R. Tchooukuegno, P. Woafo, Physica D 167, 86 (2002)
- A. Yu Kuzetsova, A.P. Kuznetsov, C. Knudsen, E. Mosekilde, Int. J. Bifurcation Chaos 14, 1241 (2004)
- 34. Z. Jing, Z. Yang, T. Jiang, Chaos Solitons Fractals 27, 722 (2006)
- 35. M. Siewe Siewe, F.M. Moukam Kakmeni, C. Tchawoua, P. Woafo, Phys. A 357, 383 (2005)
- 36. B.R. Nana Nbendjo, P. Woafo, Int. J. Non Linear Mech. 38, 531 (2003)
- 37. F. So, K. Liu, Phys. A 303, 79 (2002)

References 117

- 38. P.K. Ghosh, B.C. Bag, D.S. Ray, Phys. Rev. E 75, 032101 (2007)
- 39. M. Siewe Siewe, C. Tchawoua, S. Rajasekar, Int. J. Bifurcation Chaos 21, 1583 (2011)
- 40. S. Arathi, S. Rajasekar, Phys. Scr. **84**, 065011 (2011)
- 41. J. Casado-Pascual, J.P. Baltanas, Phys. Rev. E 69, 046108 (2004)
- 42. K. Abirami, S. Rajasekar, M.A.F. Sanjuan, Pramana J. Phys. 81, 127 (2013)
- 43. A. Frank, R. Lemus, M. Carvajal, C. Jung, E. Ziemniak, Chem. Phys. Lett. 308, 91 (1999)
- 44. R. Lemus, A. Frank, Chem. Phys. Lett. **349**, 471 (2001)
- 45. R. Lemus, J. Mol. Spectrosc. 225, 73 (2004)
- 46. H.C. Gerhardt, Nature **261**, 692 (1976)
- 47. D. Su, M. Chiu, C. Chen, Precis. Eng. 18, 161 (1996)
- 48. A. Maksimov, Ultrasonics **35**, 79 (1997)
- 49. J. Victor, M. Conte, Vis. Neurosci. 17, 959 (2000)
- 50. V. Gherm, N. Zernov, B. Lundborg, A. Vastberg, J. Atmos. Sol. Terr. Phys. 59, 1831 (1997)
- C.W. Cho, Y. Liu, W.N. Cobb, T.K. Henthorn, K. Liebhei, V. Christians, K.Y. Ng, Pharm. Res. 19, 1123 (2002)
- 52. J.L. Karnes, H.W. Burton, Arch. Phys. Med. Rehabil. **83**, 1 (2002)
- 53. O. Schlafter, T. Onyeche, H. Bormann, C. Schroder, M. Sievers, Ultrasonics 40, 25 (2002)
- 54. K.P. Harikrishnan, G. Ambika, Europhys. J. B 61, 343 (2008)
- 55. R. Feng, Y. Zhao, C. Zhu, T.J. Mason, Ultrason. Sonochem. 9, 231 (2002)
- 56. E.D. Kaplan, Understanding GPS: Principles and Applications (Artech House, London, 1996)
- 57. M. Silber, A.C. Skeldon, Phys. Rev. E 59, 5446 (1999)
- 58. J.S. Han, Trends Neurosci. 26, 17 (2003)
- 59. R.S. Malyapa, Radiat. Res. **149**, 637 (1998)
- 60. M. Borromeo, F. Marchesoni, Europhys. Lett. 72, 362 (2005)
- 61. M. Salerno, Y. Zolotaryuk, Phys. Rev. E 65, 056603 (2002)
- 62. G.P. Agrawal, Fiber-Optic Communication Systems (Wiley, New York, 1992)
- 63. R.B. Mitson, Y. Simard, C. Cross, ICES J. Marine Sci. **53**, 209 (1996)
- S. Fujita, H. Malno, S. Uratsuka, T. Furukawa, S. Mae, Y. Fujii, O. Watanabe, J. Geophys. Res. 104, 13013 (1999)
- 65. E. Waddell, SEPM Spec. Publ. 24, 115 (1996)
- 66. L. Li, D.A. Barry, J.Y. Parlange, C.B. Pattiaratchi, Water Resour. Res. 33, 935 (1997)
- 67. C. Jeevarathinam, S. Rajasekar, M.A.F. Sanjuan, Ecol. Complex. 15, 33 (2013)
- 68. G.M. Shepherd, *The Synaptic Organization of the Brain* (Oxford University Press, Oxford, 1990)
- 69. V. Mironov, V. Sokolov, Radiotekh. Elektron. 41, 1501 (1996)
- 70. S.R. Carpenter, M.G. Turner, Ecosystems **3**, 495 (2000)
- I. Fernandez, J.M. Lopez, J.M. Pascheco, C. Rodriquez, Rev. Acad. Canar. Cienc. 14, 121 (2002)
- 72. L. Ridolfi, P. D'Odorico, F. Laio, J. Theor. Biol. 248, 301 (2007)
- 73. C. Tai, W.C. de Groat, J.R. Roppolo, IEEE Trans. Neural Syst. Rehabil. Eng. 13, 415 (2005)
- D.M. Ackermann, N. Bhadra, E.L. Foldes, K.L. Kilgore, Med. Biol. Eng. Comput. 49, 241 (2011)
- 75. N. Bhadra, E.A. Lahowetz, S.T. Foldes, K.L. Kilgore, J. Comput. Neurosci. 22, 313 (2007)
- 76. M.L. Kringelbach, N. Jenkinson, S.L.F. Owen, T.Z. Aziz, Nat. Rev. Neurosci. 8, 623 (2007)
- 77. I. Ratas, K. Pyragas, Phys. Rev. E 86, 046211 (2012)
- 78. L.Y. Wang, L.K. Kaczmarek, Nature **394**, 384 (1998)

Chapter 4 Vibrational Resonance in Multistable and Excitable Systems

As shown in Chap. 2 bistability is necessary for stochastic resonance. However, for vibrational resonance, bistability is not a necessary requirement. Even a monostable nonlinear system can exhibit double resonance. Thus, one wish to know the features of high-frequency induced resonance in double-well and triple-well systems. For this purpose, consider a multistable system (that is a system with more than one stable equilibrium point) driven by a single periodic force. In a multistable system, for sufficiently small values of f each of the coexisting orbits enclose only one equilibrium point. For higher values of f, a transition between the coexisting equilibrium states takes place. It is important to analyze the influence of such a transition on vibrational resonance. There is another class of systems called excitable systems. They have only one stable fixed point, but perturbations above a certain threshold induce large excursions in phase space, which take the form of spikes or pulses. That is, a rest condition can be transformed into a firing condition near the excitable threshold. Excitability is an essential characteristic of excitable media. Interestingly, many biological, physical and electronic circuit systems are excitable systems. How does vibrational resonance arise in excitable systems?

The goal of the present chapter is to analyse vibrational resonance in double-well and triple-well systems and also in an excitable system. The reference model systems are the double-well Duffing oscillator, the triple-well quintic oscillator and the excitable FitzHugh–Nagumo model equation. The theoretical approach employed in the previous chapter is applicable for the first two systems mentioned above. For the Duffing oscillator, the prime objective is to examine the role of depth of the potential wells and the distance between the location of the minimum and the local maximum of the symmetric double-well potential in both underdamped and overdamped cases. In the underdamped system, at least one resonance and at most two resonances occur and the number of resonances can be altered by varying the depth and location of the minima of the potential wells. In the overdamped system there is always *one and only one resonance* and the value of the amplitude of the high-frequency force at which resonance occurs is independent of the depth

of the wells, but varies linearly with the locations of the minima of the wells. For the triple-well quintic oscillator system the theoretical treatment predicts the occurrence of even four resonances and is supported by numerical simulation. For excitable systems the theoretical approach is not applicable and therefore the occurrence of vibrational resonance in the FitzHugh–Nagumo equation is investigated through numerical simulation. Finally, the stochastic resonance in the excitable FitzHugh–Nagumo equation which we have not dealt in Chap. 2 is pointed out.

4.1 Underdamped Double-Well Duffing Oscillator

Consider the underdamped Duffing oscillator equation

$$\ddot{x} + d\dot{x} + \frac{dV}{dx} = f\cos\omega t + g\cos\Omega t, \qquad (4.1)$$

where the potential V is given by

$$V(x) = -\frac{1}{2}A\omega_0^2 x^2 + \frac{1}{4}B\beta x^4 . {(4.2)}$$

For ω_0^2 , β , A and B>0 the potential V is a symmetric double-well form. When $A=B=\alpha_1$ the potential has a local maximum at $x_0^*=0$ and two minima at $x_\pm^*=\pm\sqrt{\omega_0^2/\beta}$. The depths of the left- and right-wells denoted by $D_{\rm L}$ and $D_{\rm R}$, respectively are same and equal to $\alpha_1\omega_0^4/(4\beta)$. By varying the parameter α_1 the depths of the two wells can be varied keeping the values of x_\pm^* unaltered. Let us call the underdamped system with $A=B=\alpha_1$ as US1. Call Eq. (4.1) with $A=1/\alpha_2^2$ and $B=1/\alpha_2^4$ as US2 in which case $x_0^*=0$ whereas $x_\pm^*=\pm\alpha_2\sqrt{\omega_0^2/\beta}$ and $D_{\rm L}=D_{\rm R}=\omega_0^4/(4\beta)$ is independent of α_2 . Thus, by varying α_2 the depth of the wells of V can be kept constant while the distance between the local maximum and the minima can be changed. Figure 4.1a, b illustrate the effect of α_1 and α_2 .

Changing the depths of the potential wells alone and changing the distance of the local minima of the potential wells from the local maximum can be realized experimentally. For example, in the mechanical model of the Duffing oscillator described in [1], one can introduce the above changes by varying the position of the left-side magnet and its strength. In submicron Bi-wires, modeled by a double-well potential, the applied magnetic field is varied to change the depth of one well [2]. A double-well system with different depths is realized as an appropriate model of auditory nerve fibre response [3].

For the system (4.1) first obtain a theoretical expression for the response amplitude Q[4, 5].

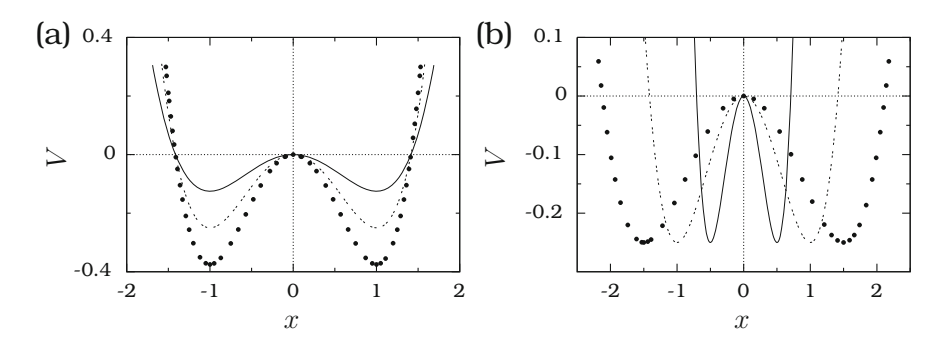


Fig. 4.1 Shape of the potential V given by Eq. (4.2) for $\omega_0^2 = \beta = 1$ and (a) $A = B = \alpha_1$ and (b) $A = 1/\alpha_2^2$, $B = 1/\alpha_2^4$. In the subplots (a) and (b) the values of α_1 and α_2 , respectively, for the *continuous line*, the *dashed line* and the *solid circles* are 0.5, 1 and 1.5, respectively

4.1.1 Theoretical Approach

Following the theoretical treatment used in the previous chapter, the equation of motion for the slow variable X in $x = X + \psi$ is

$$\ddot{X} + d\dot{X} - (A\omega_0^2 - 3B\beta\langle\psi^2\rangle)X + B\beta X^3 + B\beta\langle\psi^3\rangle = f\cos\omega t. \tag{4.3}$$

Approximating $\ddot{\psi} = g \cos \Omega t$ gives $\psi = -(g/\Omega^2) \cos \Omega t$. One obtains $\langle \psi \rangle = \langle \psi^3 \rangle = 0$ and $\langle \psi^2 \rangle = g^2/(2\Omega^4)$. Then, Eq. (4.3) takes the form

$$\ddot{X} + d\dot{X} - C_1 X + C_2 X^3 = f \cos \omega t , \qquad (4.4a)$$

where

$$C_1 = A\omega_0^2 - \frac{3B\beta g^2}{2\Omega^4}, \quad C_2 = B\beta.$$
 (4.4b)

The effective potential of (4.4) in the absence of the low-frequency force is

$$V_{\text{eff}}(X) = -\frac{1}{2}C_1X^2 + \frac{1}{4}C_2X^4.$$
 (4.5)

Substitution of $X = Y + X^*$, where Y is the deviation of slow-motion from X^* , in Eq. (4.4) gives

$$\ddot{Y} + d\dot{Y} + \omega_{\rm r}^2 Y + \beta Y^3 + 3\beta X^* Y^2 = f \cos \omega t , \qquad (4.6a)$$

where the resonant frequency $\omega_{\rm r}$ is given by

$$\omega_{\rm r}^2 = -A\omega_0^2 + \frac{3B\beta g^2}{2\Omega^4} + 3B\beta X^{*2} \,. \tag{4.6b}$$

In the linear approximation for $f \ll 1$ and in the long time limit, $Y(t) = A_L \cos(\omega t + \phi)$ where

$$A_{\rm L} = \frac{f}{\sqrt{(\omega_{\rm r}^2 - \omega^2)^2 + d^2 \omega^2}} = \frac{f}{\sqrt{S}} , \quad \phi = \tan^{-1}(\omega/C_1) . \tag{4.7}$$

The response amplitude is $Q = A_L/f$.

4.1.2 Vibrational Resonance for $\alpha_1 = \alpha_2 = 1$

When $\alpha_1 = \alpha_2 = 1$ the equilibrium points of (4.4) in the absence of the driving force are $(X_0^*, \dot{X}_0^*) = (0, 0), (X_{\pm}^*, \dot{X}_{\pm}^*) = (\pm \sqrt{C_1/\beta}, 0)$. As g increases C_1 decreases from ω_0^2 and becomes < 0 for

$$g > g_{\rm c} = \frac{2\Omega^4 \omega_0^2}{3\beta} = \Omega^2 \sqrt{\frac{2\omega_0^2}{3\beta}}$$
 (4.8)

For $g < g_c$, $(X_{\pm}^*, \dot{X}_{\pm}^*)$ are stable and (X_0^*, \dot{X}_0^*) is unstable while for $g > g_c$ there is only one equilibrium point (X_0^*, \dot{X}_0^*) and is stable. That is, $V_{\rm eff}$ is of the double-well form for $g < g_c$ and becomes a single-well potential for $g > g_c$. One can observe two coexisting slow motions about $(X_{\pm}^*, \dot{X}_{\pm}^*)$ for $g < g_c$ and only one about (X_0^*, \dot{X}_0^*) for $g > g_c$. Furthermore, at $g = g_c$, $\omega_r^2 = 0$ while for other values of g, from Eq. (4.6b),

$$\omega_{\rm r}^2 = \begin{cases} 2\omega_0^2 - \frac{3\beta g^2}{\Omega^4} & \text{for } g < g_{\rm c} \\ -\omega_0^2 + \frac{3\beta g^2}{2\Omega^4} & \text{for } g > g_{\rm c}. \end{cases}$$
(4.9)

When g is treated as a control parameter, vibrational resonance occurs at $g=g_{\rm VR}$ where $g_{\rm VR}$ is a root of the equation $S_g=4(\omega_{\rm r}^2-\omega^2)\omega_{\rm r}\omega_{\rm rg}=0$ with $S_{gg}>0$.

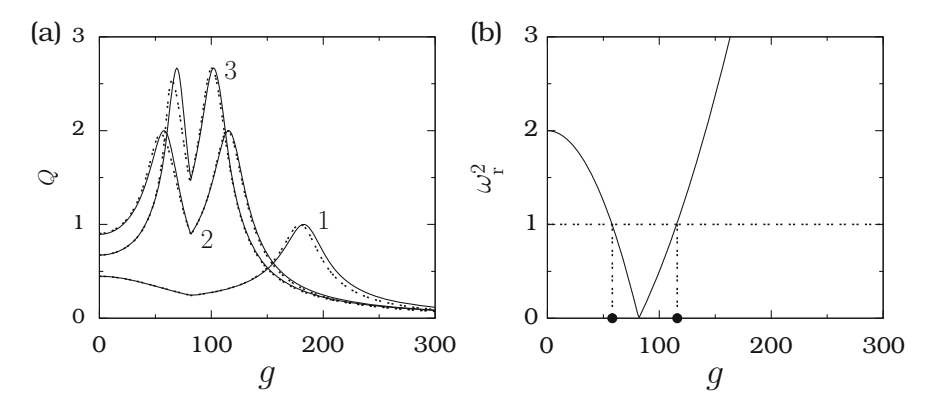


Fig. 4.2 (a) Q versus g for the system (4.1) with $\alpha_1 = \alpha_2 = 1$, $\omega_0^2 = 1$, $\beta = 1$, d = 0.5, f = 0.1, $\Omega = 10$ and for three values of ω . The *continuous* and *dashed curves* represent the theoretical Q and numerically computed Q. The values of ω for the curves 1, 2 and 3 are 2, 1 and 0.75, respectively. (b) ω_r^2 versus g for $\omega = 1$. The two *solid circles* on the g-axis mark the values of g at which resonance occurs. The *horizontal dashed line* corresponds to $\omega_r^2 = \omega^2 = 1$

 $\omega_{\rm r}^2 - \omega^2 = 0$ gives

$$g_{\rm VR}^{(1)} = \Omega^2 \sqrt{\frac{2\omega_0^2 - \omega^2}{3\beta}}, \quad 2\omega_0^2 > \omega^2$$
 (4.10)

$$g_{\rm VR}^{(2)} = \Omega^2 \sqrt{\frac{2(\omega_0^2 + \omega^2)}{3\beta}} \ . \tag{4.11}$$

(What do you infer from $\omega_r = 0$ and $\omega_{rg} = 0$ in $S_g = 0$?).

Resonance occurs at two values of g one for $g < g_c$ and another for $g > g_c$ for $2\omega_0^2 > \omega^2$. For $2\omega_0^2 < \omega^2$ only one resonance is possible at $g = g_{\rm VR}^{(2)} > g_c$. Figure 4.2a shows the variation of Q with g for $\omega_0^2 = 1$, $\beta = 1$, d = 0.5, f = 0.1, $\Omega = 10$ and for three values of ω . As predicted from the theoretical treatment there are two resonances for $\omega = 0.75$ and $1 (2\omega_0^2 > \omega^2)$ and only one resonance for $\omega = 2 (2\omega_0^2 < \omega^2)$. For $\omega = 1$ the theoretically (numerically) predicted values of $g_{\rm VR}$ are 57.73 (54.78) and 115.47 (114.50). Q is locally minimum at $g = g_c$ at which the effective potential $V_{\rm eff}$ changes from double-well form to single-well (see Fig. 4.3). In Fig. 4.2b $\omega_{\rm r}^2 = \omega^2$ at two values of g and these two values are the $g_{\rm VR}$. At $g = g_c$, $\omega_{\rm r}^2 = 0$ and Q is locally minimum.

Further, at $g = g_c Q = 1/\sqrt{\omega^4 + d^2\omega^2}$. At both the resonances $\omega_r^2 - \omega^2 = 0$ and hence $Q_{\text{max}} = 1/(d\omega)$.

Figure 4.4 shows the phase portrait of slow and actual orbits for three values of g. For $g < g_c$ there are two coexisting orbits about each of the two stable equilibrium points (see Fig. 4.4a, d). As $g \to g_c$, X_+^* move towards the origin. This is shown in

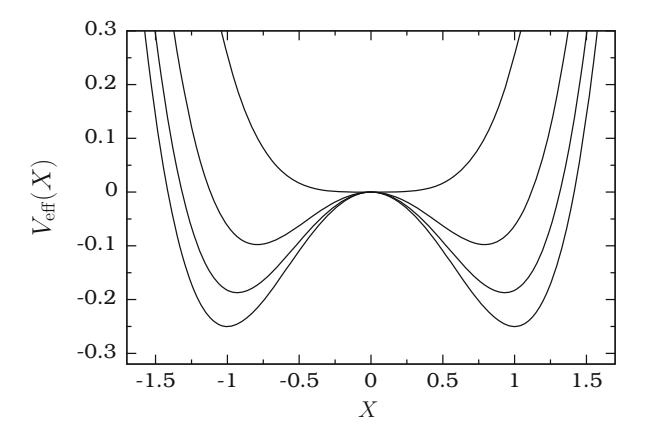


Fig. 4.3 Change in the shape of the effective potential given by Eq. (4.5) as a function of the control parameter g. The values of g for the curves from *bottom* to *top* are 0, 30, 50 and 82. $g_c = 81.64966$. The values of the other parameters are $\omega_0^2 = 1$, $\beta = 1$ and $\Omega = 10$

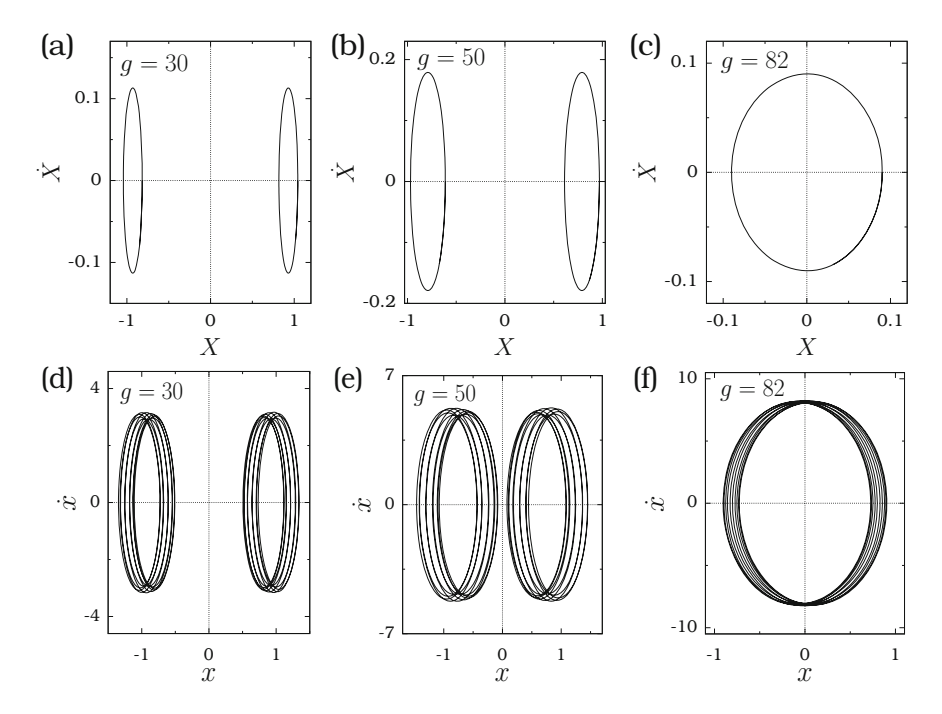


Fig. 4.4 Phase portrait of (a-c) slow oscillation and (d-f) the actual orbit of the Duffing oscillator for three values of g for $\omega=1$

Fig. 4.4b, e for g = 50. For $g > g_c$ the center of the slow orbit is the origin as shown in Fig. 4.4c and f for $g = 82 > g_c$.

4.1.3 Role of Depth of the Potential Wells

When $A = B = \alpha_1$ in the potential V(x) given by Eq. (4.2) then the depth of the two wells can be varied by varying α . In this case $S_g = 0$ gives [5]

$$g_{\rm VR}^{(1)} = \Omega^2 \left[\frac{2\omega_0^2}{3\beta} - \frac{\omega^2}{3\alpha_1\beta} \right]^{1/2}, \quad \alpha_1 > \alpha_{\rm 1c} = \frac{\omega^2}{2\omega_0^2}$$
 (4.12)

$$g_{\rm VR}^{(2)} = \Omega^2 \left[\frac{2\omega_0^2}{3\beta} + \frac{2\omega^2}{3\alpha_1 \beta} \right]^{1/2}, \quad \alpha_1 - \text{arbitrary}.$$
 (4.13)

Equation (4.13) implies that there is always one resonance for any value of $\alpha_1>0$ at $g=g_{\rm VR}^{(2)}$. Another resonance occurs only for $\alpha_1>\alpha_{\rm 1c}$ at $g=g_{\rm VR}^{(1)}$ and $g_{\rm VR}^{(1)}< g_{\rm VR}^{(2)}$. In terms of the depth $D_{\rm L}~(=D_{\rm R})$ of the potential wells the condition for double resonance is $D_{\rm L}>\omega_0^2\omega^2/(8\beta)$. The number of resonances and the value of $g_{\rm VR}$ can be controlled by varying the parameter α_1 , that is, the depth of the two wells of the potential. Further, as ω increases $g_{\rm VR}^{(1)}$ decreases while $g_{\rm VR}^{(2)}$ increases. The separation between the two resonances increases with increase in ω . As α_1 increases from $\alpha_{\rm 1c}, g_{\rm VR}^{(1)}$ increases while $g_{\rm VR}^{(2)}$ decreases. The separation between the two resonances decreases with increase in α_1 . That is, ω and α_1 have opposite effects. In the limit $\alpha_1\to\infty, g_{\rm VR}^{(1)}$ and $g_{\rm VR}^{(2)}\to\Omega^2\sqrt{2\omega_0^2/(3\beta)}$.

To verify the above theoretical predictions, we choose the values of the parameters as $\omega_0^2=1$, $\beta=1$, d=0.5, $\omega=1$, $\Omega=10$ and f=0.05. Figure 4.5a presents theoretical and numerical $g_{\rm VR}$ versus α_1 . Theoretical $g_{\rm VR}$ is in very good agreement with the numerical $g_{\rm VR}$.

To understand the mechanism of single and double resonances, in Fig. 4.5b the resonant frequency ω_r is plotted as a function of g for four values of α_1 . For each fixed value of α_1 as g increases from 0 the resonant frequency ω_r decreases from the value $\sqrt{2\alpha_1\omega_0^2}$ and $\rightarrow 0$ as $g \rightarrow g_c = \Omega^2\sqrt{2\omega_0^2/(3\beta)} = 81.65$. The value of $g(=g_c)$ at which $V_{\rm eff}$ undergoes a bifurcation from a double-well to a single-well is independent of α_1 . For $g > g_c$, $V_{\rm eff}$ becomes a single-well potential and ω_r increases with increase in g. Resonance will take place whenever $\omega_r = \omega$. In Fig. 4.5b for $\alpha_1 = 0.25 < \alpha_{1c} = 0.5$ the ω_r curve intersects the $\omega = 1$ dashed line at only one value of $g > g_0$. In Fig. 4.5c we notice only one resonance for $\alpha = 0.25$. For $\alpha_1 > \alpha_{1c}$ the ω_r curve intersects the $\omega = 1$ line at two values of g: one below g_c and another at above g_c . This is shown in Fig. 4.5b, c for few values of α_1 .

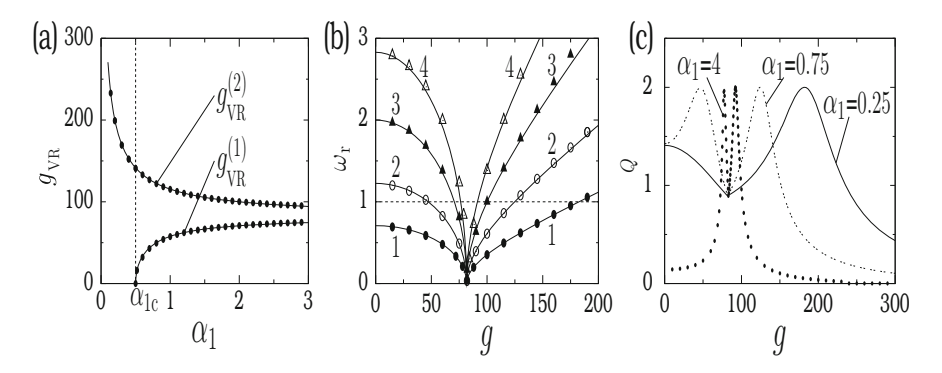


Fig. 4.5 (a) Plot of g_{VR} as a function of the parameter α_1 in US1. *Continuous lines* are theoretical g_{VR} while the *solid circles* are numerically computed g_{VR} . (b) Variation of theoretical (represented by *continuous lines*) and numerically computed (represented by *symbols*) resonant frequencies with g. Numerical resonant frequency is calculated using the numerical solution of Eq. (4.1). The labels 1–4 correspond to $\alpha_1 = 0.25$, 0.75, 2 and 4, respectively. The theoretical and numerical values of ω_r are represented by *curves* and *symbols*, respectively. The *horizontal dashed line* represents $\omega_r = \omega = 1$. (c) Theoretical response amplitude Q versus g for three values of α_1

4.1.4 Role of Location of the Minima of the Potential

For US2 with $A = 1/\alpha_2^2$ and $B = 1/\alpha_2^4$ as α_2 increases the location of the two minima of V(x) move away from the origin in opposite direction, that is, the distance between a minimum and the local maximum $x_0^* = 0$ of the potential increases with increase in α_2 . Now, $S_g = 0$ gives [5]

$$g_{\text{VR}}^{(1)} = \Omega^2 \alpha_2 \left[\frac{2\omega_0^2}{3\beta} - \frac{\alpha_2^2 \omega^2}{3\beta} \right]^{1/2}, \quad \alpha_2 < \alpha_{2c} = \sqrt{\frac{2\omega_0^2}{\omega^2}}$$
 (4.14)

$$g_{\text{VR}}^{(2)} = \Omega^2 \alpha_2 \left[\frac{2\omega_0^2}{3\beta} + \frac{\alpha_2^2 \omega^2}{3\beta} \right]^{1/2}, \ \alpha_2 - \text{arbitrary}.$$
 (4.15)

Figure 4.6a depicts both theoretical and numerical $g_{\rm VR}$ versus α_2 . The difference in the effect of the distance of x_\pm^* from the origin over the depth of the potential wells can be seen by comparing Fig. 4.6a with Fig. 4.5a. In US1 (depth varying potential-well system) two resonances occur above certain critical depth ($\alpha_{\rm 1c}$) of the wells. In contrast to this in US2 two resonances occur only for $\alpha_2 < \alpha_{\rm 2c}$. For $\omega_0^2 = \beta = \omega = 1$, the values chosen in the numerical study, $\alpha_{\rm 2c} = \sqrt{2}$. Equation (4.14) implies that as α_2 increases from a small value (that is, as x_\pm^* moves away from origin) $g_{\rm VR}^{(1)}$ increases and reaches a maximum value $\frac{\Omega^2 \omega_0^2}{\sqrt{3\beta\omega}}$ at $\alpha_2 = \sqrt{\omega_0^2/\omega^2}$.

Then with further increase in α_2 , it decreases and $\rightarrow 0$ as $\alpha_2 \rightarrow \alpha_{2c}$. Note that $g_{VR}^{(2)}$ of US1 decreases with increase in α_1 while $g_{VR}^{(2)}$ of US2 increases with increase in

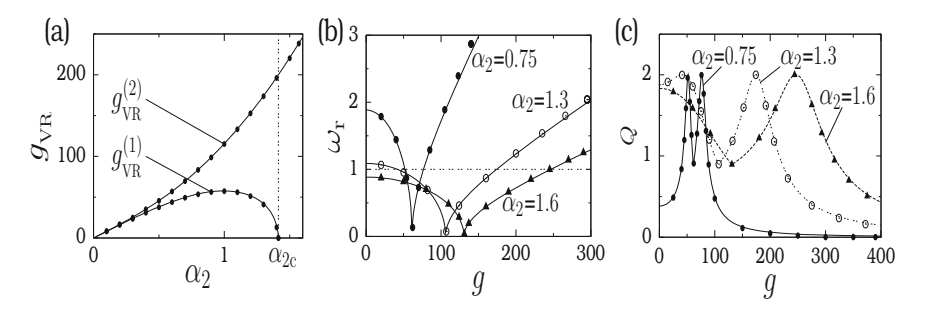


Fig. 4.6 (a) g_{VR} versus α_2 in US2. Continuous lines are theoretical g_{VR} while the solid circles are numerically computed g_{VR} . (b) Theoretical resonant frequency ω_r (marked by continuous lines) and numerically computed ω_r (marked by symbols) versus g for three values of α_2 . The theoretical and numerical values of ω_r are represented by curves and symbols, respectively. (c) Q versus g for three values of α_2

 α_2 . Figure 4.6b shows the variation of ω_r with g for three values of α_2 . Theoretical $\omega_r=0$ at $g=g_0=\Omega^2\alpha_2\sqrt{2\omega_0^2/(3\beta)}$. The bifurcation point g_0 increases linearly with α_2 . Sample response curves for three fixed values of α_2 are shown in Fig. 4.6c. In the double resonance case the separation between the two resonances increases with increase in α_2 . The converse effect is noticed in US1.

4.2 Overdamped Double-Well Duffing Oscillator

Consider the overdamped double-well Duffing oscillator with the equation of motion

$$\dot{x} + \frac{\mathrm{d}V}{\mathrm{d}x} = f\cos\omega t + g\cos\Omega t \ . \tag{4.16}$$

Let us call the system (4.16) with $A = B = \alpha_1$ as OS1 and with $A = 1/\alpha_2^2$ and $B = 1/\alpha_2^4$ as OS2. The response amplitude Q is obtained as [5]

$$Q = \frac{1}{\sqrt{\omega_r^2 + \omega^2}}, \quad \omega_r^2 = -A\omega_0^2 + \frac{3B\beta g^2}{2\Omega^2} + 3B\beta X^{*2}.$$
 (4.17)

Q is maximum when $\omega_r = 0$. It is easy to obtain the following result:

OS1:
$$g_{VR} = \Omega \sqrt{\frac{2\omega_0^2}{3\beta}}$$
. OS2: $g_{VR} = \Omega \alpha_2 \sqrt{\frac{2\omega_0^2}{3\beta}}$. (4.18)

There are several interesting results:

- The most significant result is that g_{VR} of OS1 is independent of the depth of the wells of the symmetric double-well potential.
- g_{VR} of OS1 is $(1/\Omega)$ times the limiting value [in the limit of $\alpha_1 \to \infty$ in Eqs. (4.12) and (4.13)] of US1.
- g_{VR} of OS2 is α_2 times the g_{VR} of OS1. Because g_{VR} of OS2 with $\alpha_2 < 1$ is lower than g_{VR} of OS1 the former is advantageous compared to the latter.
- In OS1 and OS2 there is always one and only one vibrational resonance.
- g_{VR} of OS1 and OS2 corresponds to the value of g at which the effective potential $V_{eff}(X)$ undergoes a bifurcation from double-well to a single-well. In US1 and US2 the resonance does not occur at the bifurcation point $g = g_0$.

4.3 Resonance in a Triple-Well Potential System

In Sect. 3.3 occurrence of vibrational resonance in the system Eq. (3.18) with three forms of monostable potential is analysed. The potential given by Eq. (3.19) becomes of a triple-well form for ω_0^2 , $\gamma > 0$, $\beta < 0$ and $\beta^2 > 4\omega_0^2 \gamma/3$. In the present section the focus is on the quintic oscillator with a triple-well potential [6].

Equations (3.21)–(3.24) are useful for resonance analysis for the triple-well system also. We fix $\omega_0^2 = 3$, $\gamma = 1$, $\beta = -4$ and $\Omega = 10$. In this case the sign of both C_1 and C_2 in Eq. (3.21b) can be changed by varying the parameters g or Ω . Consequently, the shape of the effective potential changes from a triple-well to a double-well and a single-well as indicated in Table 4.1.

For $g > g_0 = 160.60$ (see Table 4.1) the analytical expression for g_{VR} is given by

$$g_{\rm VR} = \Omega^2 \left[\frac{-\beta + \sqrt{\beta^2 + (10\gamma |\omega_0^2 + \omega^2|/3)}}{5\gamma/2} \right]^{1/2} . \tag{4.19}$$

For $g < g_0$ the resonance frequency $\omega_r = \sqrt{\alpha_1}$ (consider the orbits around $X_{4,5}^*$ in the case of a triple-well form of $V_{\rm eff}$) is a complicated function of g and hence one

Table 4.1 Nature of the effective potential $V_{\rm eff}$ of the quintic oscillator, Eq. (3.22), and the sign of C_1 and C_2 for various ranges of g/Ω^2 for $\omega_0^2 = 3$, $\beta = -4$ and $\gamma = 1$

| S. No. | Range of g/Ω^2 | Sign of C_1 and C_2 | Type of $V_{\rm eff}$ |
|--------|--------------------------------|--|-----------------------|
| 1 | $0 < g/\Omega^2 < 0.7876$ | $C_1 > 0, C_2 < 0, C_2^2 > 4C_1\gamma$ | Triple-well |
| 2 | $0.7876 < g/\Omega^2 < 0.8945$ | $C_1, C_2 < 0$ | Double-well |
| 3 | $0.8945 < g/\Omega^2 < 1.6061$ | $C_1 < 0, C_2 > 0$ | Double-well |
| 4 | $g/\Omega^2 > 1.6061$ | $C_1, C_2 > 0$ | Single-well |

can determine g_{VR} numerically from $S = (\omega_r^2 - \omega^2)^2 + d^2\omega^2$. Figure 4.7 depicts g_{VR} versus ω . The curves (a)–(e) are obtained from the following cases:

- Curve a: $C_1 < 0$, $C_2 > 0$. g_{VR} is given by Eq. (4.19).
- Curve b: $C_1 < 0$, $C_2 > 0$ and $\omega_r^2 \omega^2 = 0$.
- Curve c: C₁ < 0, C₂ > 0 and ω_{rg} = 0.
 Curve d: C₁ < 0, C₂ < 0 and ω_r² ω² = 0.
- Curve e: $C_1 > 0$, $C_2 < 0$, $C_2^2 > 4C_1\gamma$ and $\omega_r^2 \omega^2 = 0$.
- Curve f: $C_1 > 0$, $C_2 < 0$ and $\omega_{rg} = 0$.

It is noteworthy to point out that a resonance with $\omega_{rg} = 0$ is not possible in the double-well Duffing oscillator Eq. (4.1). The various curves in Fig. 4.7 can be understood from the plots of $\omega_{\rm r}$ and $\omega_{\rm rg}$ versus g (Fig. 4.8). From Fig. 4.8 one can infer the following:

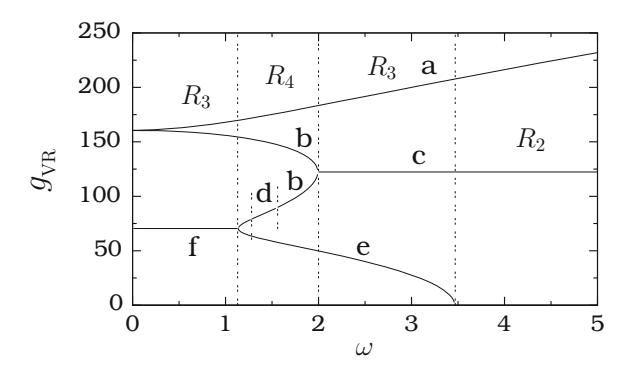


Fig. 4.7 Plot of g_{VR} versus ω for the quintic oscillator with the triple-well potential with $\omega_0^2 = 3$, $\beta = -4$, $\gamma = 1$, $\Omega = 10$. g_{VR} is independent of d. Two, three and four resonances occur in the intervals of ω marked as R_2 , R_3 and R_4 , respectively

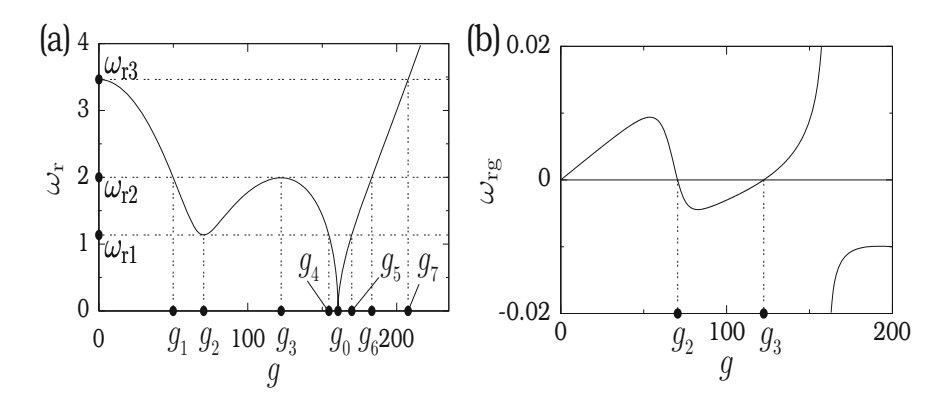


Fig. 4.8 Variation of (a) the resonant frequency ω_r and (b) ω_{rg} with the control parameter g for the quintic oscillator with the triple-well potential. $\omega_{rg} = 0$ at g = 70.4 and 122.4

- 1. As g increases beyond g_0 the value of ω_r continuously increases from 0 and thus there must be one (and only one) resonance at a value of g greater than g_0 . The resulting g_{VR} is the curve a in Fig. 4.7.
- 2. The plot of ω_r has a local minimum at $g=g_2=70.4$ and a local maximum at $g=g_3=122.4$. $\omega_{rg}=0$ at these two values of g. The calculation of S_{gg} indicates that Q is maximum at g_2 for $\omega<\omega_{r1}=1.137$ and at g_3 for $\omega>\omega_{r2}=2.02$. Curves f and c represent these two values of g.
- 3. For $0 < \omega < \omega_{\rm r1} = 1.137$ there are three resonances. The first resonance occurs at $g = g_2$ due to $\omega_{\rm rg} = 0$. The second and third resonances occur in the intervals $[g_4, g_0]$ and $[g_0, g_5]$, respectively due to $\omega_{\rm r}^2 \omega^2 = 0$. In Fig. 4.9a for $\omega = 1$ as g is varied, resonances occur at g = 70.4, 156 and 168.
- 4. For $\omega_{r1} < \omega < \omega_{r2} = 2$, $\omega_r = \omega$ at four values of g, one in each of the intervals $[g_1, g_2]$, $[g_2, g_3]$, $[g_3, g_4]$ and $[g_5, g_6]$. An example of four resonances is shown in Fig. 4.9a for $\omega = 1.25$.
- 5. For $\omega_{r2} < \omega < \omega_{r3} = 3.464$ in addition to the resonance at $g_3 = 122.4$ two more resonances occur—one in the interval $[0, g_1]$ and another one in the interval $[g_6, g_7]$. An example is shown in Fig. 4.9b with $\omega = 2$.
- 6. For $\omega > \omega_{r3}$ two resonances occur—one at $g = g_3$ and another at a value of $g > g_7$. In Fig. 4.9b for $\omega = 5$ the resonance at $g_3 = 122.4$ is too weak and not visible in the scale used.

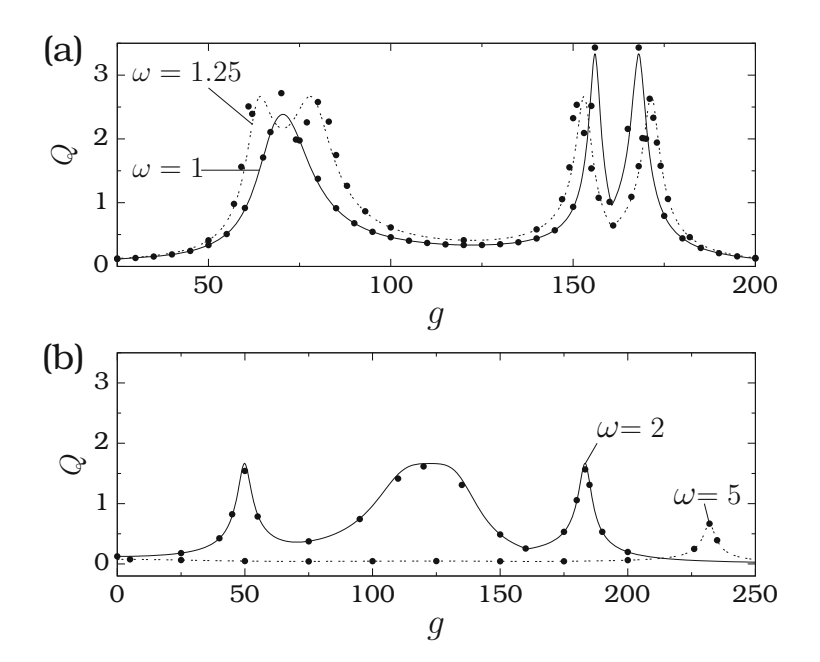


Fig. 4.9 $\,Q$ versus $\,g$ for the triple-well case of the quintic oscillator for four values of $\,\omega$ with $\,d=0.3,\,\Omega=10$ and $\,f=0.05.\,$ Continuous curves are theoretical $\,Q$ while the solid circles are the numerically calculated values of $\,Q$

4.4 Vibrational Resonance in an Excitable System

Neural and cardiac cells are two most prominent examples of excitable systems [7]. Neurons are inherently information processing units. This feature demands them to have specialized mechanisms for reliably detecting extremely weak signals at complex situations. Thus, it is important to explore the possibility of a vibrational resonance and its corresponding mechanisms in excitable systems. Motivated by the above, Ullner and his coworkers [8] considered an electronic circuit based on a Chua's diode and the FitzHugh–Nagumo (FHN) model equation displaying excitable dynamics and shown that for an optimal amplitude of the high-frequency forcing signal amplitude at the low-frequency is enhanced. The vibrational resonance in networks of FHN equation has also been studied [9]. This section presents features of the vibrational resonance in the excitable FHN equation.

The FHN model, named after the American biophysicist Richard FitzHugh (1922–2007) who suggested the system in 1961 [10] and the Japanese Jinichi Nagumo (1926–1999) who created the equivalent circuit the following year in collaboration with, Arimoto and Yoshizawa [11], describes the firing activities of sensory neurons. The FHN model equation is given by Keener and Snyder [12] and Mikhailov [13]

$$\epsilon \dot{x} = x - \frac{1}{3}x^3 - y$$
, (4.20a)

$$\dot{y} = x + a + F(t)$$
, (4.20b)

where x(t) is the activator variable (fast variable representing the membrane potential in the neural case), y(t) is the inhibitor (slow variable related to the superconductivity of the potassium channels existing in the neuron membrane), a is the membrane radius and F(t) is the external signal received by the neuron. The FHN model is a simplified version of the Hodgkin–Huxley model which models in a detailed manner activation and deactivation dynamics of a spiking neuron. In the original papers of FitzHugh, this model was called Bonhoeffer–van der Pol oscillator (named after Karl Friedrich Bonhoeffer and Balthasar van der Pol) because it contains the van der Pol oscillator as a special case.

When the values of the parameters in Eq. (4.20) are sufficient to stimulate spikes, they are said to be *subthreshold*. In the absence of F(t) Eq. (4.20) has only one equilibrium point $(x^*, y^*) = (-a, a(a^2 - 3)/3)$. The stability determining eigenvalues are given by

$$\lambda_{\pm} = \frac{1}{2\epsilon} \left[(1 - a^2) \pm \sqrt{(1 - a^2)^2 - 4\epsilon} \right].$$
 (4.21)

For a>1, $\lambda_{\pm}<0$ and the equilibrium point is a stable node. At a=1, $\lambda_{\pm}=\pm i/\sqrt{\epsilon}$ and a Hopf bifurcation occurs. For 0< a<1 the real part of λ_{\pm} is >0 and

the equilibrium point is an unstable node or focus depending upon the values of a and ϵ . A limit cycle motion occurs for 0 < a < 1.

Suppose $F(t) = f \cos \omega t$. For a > 1 and for sufficiently small values of f oscillatory motion about the equilibrium point occurs. Above a critical value of f the system generates a sequence of spikes. Such spikes do not appear for 0 < a < 1. That is, the system is excitable for values of a > 1. When $\epsilon = 0.01$, a = 1.05 and $\omega = 0.1$, 0.2, 0.3 spikes start appearing for f = 0.096. Now we fix the value of f as 0.01, a value below the excitation threshold value and drive the system by the high-frequency force also, that is, $F(t) = f \cos \omega t + g \cos \Omega t$, $\Omega = 5$ and analyse the occurrence of vibrational resonance. We use a step size $\Delta t = (2\pi/\omega)/10,000$ in the numerical integration of Eq. (4.20) by the fourth-order Runge–Kutta method.

Figure 4.10 shows numerically computed response amplitude as a function of g for three fixed values of ω and Ω . The dependence of the neuron's response on g displays a resonant form with a maximum at an optimum value of g. In Fig. 4.10a when $\omega = 0.2$, $Q \approx 1$ for $g \leq 0.05$, that is, the amplitude of the output oscillation at the frequency ω is the same as the amplitude of the lowfrequency input signal. This interval of g is below the excitation threshold and the output signal is oscillatory and moreover spikes are not developed. This is shown in Fig. 4.11a for g = 0.05. The variable x(t) is periodic with period $T = 2\pi/\omega$ and the oscillation occurs about $x^* = -a = -1.05$. The spikes started appearing from g = 0.051. In Fig. 4.11b spikes appear at regular interval of time and there is one spike per period of the low-frequency input signal. The system begins to process the information encoded in the low-frequency signal. The information process can be improved by further increasing the number of spikes per half period of the lowfrequency signal, since in this way the energy contained at the frequency is also enhanced [8]. As a result Q increases sharply, reaches a maximum at g = 0.057and then decreases sharply. This is the mechanism of vibrational resonance in an

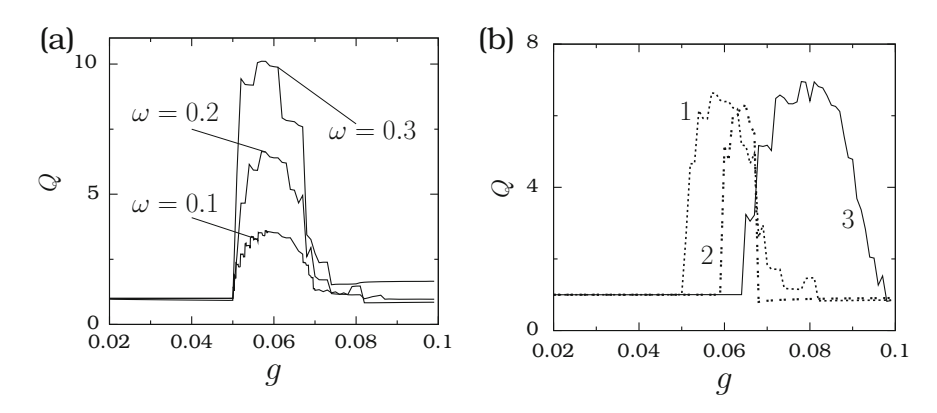


Fig. 4.10 Response amplitude Q of the neuron versus g (a) for three fixed values of ω with $\Omega=5$ and (b) for three fixed values of Ω with $\omega=0.2$. In (b) the values of Ω for the curves 1, 2 and 3 are 5, 3 and 2, respectively. The values of other parameters in Eq. (4.20) are $\epsilon=0.01$, a=1.05 and f=0.01

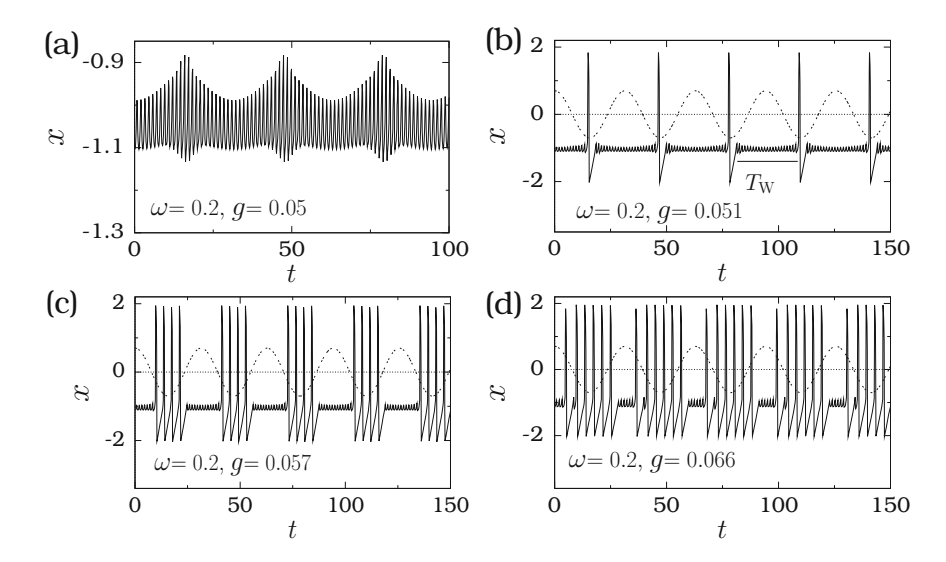


Fig. 4.11 x(t) versus t of the FHN model equation for four values of g. The *continuous* and *dashed* curves are x(t) and the input signal $f \cos \omega t$, respectively. For clarity, the signal $f \cos \omega t$ is rescaled by a factor. In the subplot (b) T_W is the waiting time between two consecutive firings. Vibrational resonance occurs at g = 0.057

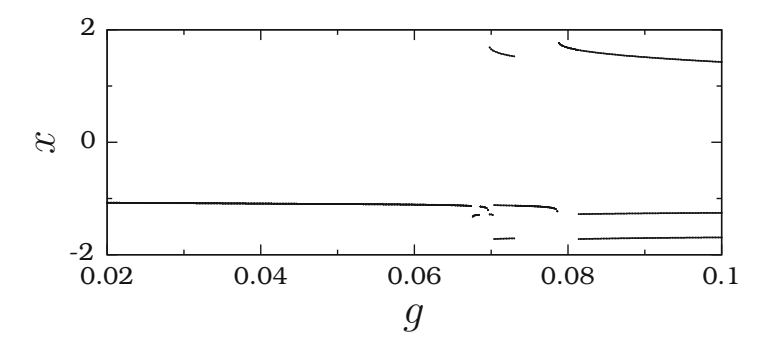


Fig. 4.12 Bifurcation diagram of the FHN model equation

excitable system where an intermediate amplitude of a high-frequency force leads to a resonant response at the low-frequency of the input signal. Q is considerably enhanced for $g \in [0.052, 0.067]$.

The staircase form of dependence of Q on g is caused by the abrupt discrete occurrence of new spikes in the spike train as the forcing amplitude g varies. When g is increased further from the value 0.067 the system fires immediately after reaching the equilibrium point. In this case the dominant frequency of the output is the own frequency of the system and the low-frequency component is weak resulting in degrading the signal processing. Figure 4.12 shows the bifurcation diagram. The motion of the system is periodic with period either T or 3T.

Compare the firing times in Fig. 4.11b, c. Firing takes place only when the low-frequency force is negative. Interestingly, for g=0.057, at which Q is maximum, during lower-half cycle of the input signal the system fires whenever it reaches the equilibrium point while during other half drive cycle there is no spike. In order to characterize vibrational resonance in excitable systems let us define the waiting time $T_{\rm W}$ (also called interspike interval) as the time the system waits in the neighbourhood of the equilibrium point before firing. This time interval is indicated in Fig. 4.11b. As g increases from the value 0.051, $T_{\rm W}$ decreases from a value well above T/2 with increase in g. Resonance occurs when $T_{\rm W} \approx T/2$. Far after resonance $T_{\rm W} \approx 0$.

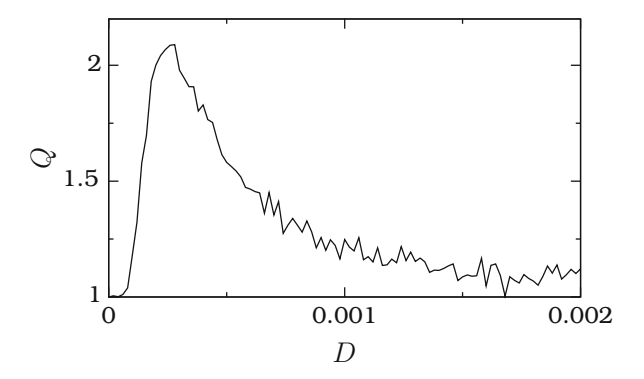
4.5 Stochastic Resonance in FitzHugh–Nagumo Equation

Section 2.2 described the mechanism of stochastic resonance in a bistable system with reference to the Duffing oscillator. In this section we briefly discuss the occurrence of stochastic resonance in the excitable FHN model Eq. (4.20) with $F(t) = f \cos \omega t + \eta(t)$ where $\eta(t)$ is a Gaussian white noise with intensity D.

For the numerical study, we choose a=1.05, $\epsilon=0.01$, f=0.01 and $\omega=0.2$. The response amplitude Q is calculated over 100 drive cycles of the input periodic signal and then averaging is performed for 50 realizations of the noise term. Figure 4.13 shows the numerically computed Q as a function of the noise intensity D. Stochastic resonance occurs at D=0.00028.

For values of D less than the critical value D = 0.00008, noisy oscillatory motion around the equilibrium point without spikes takes place. An example for this type of behaviour is shown in Fig. 4.14a for D = 0.00005. Above the critical value of D spikes start appearing and they occur randomly. The number of spikes over a time interval increases with increasing values of D. This is shown in Fig. 4.14b, c. In this region of D the response amplitude increases with increase in D. At D = 0.00028

Fig. 4.13 *Q* versus the noise intensity *D* of the FHN equation driven by $F(t) = f \cos \omega t + \eta(t)$ where $\eta(t)$ is the Gaussian white noise



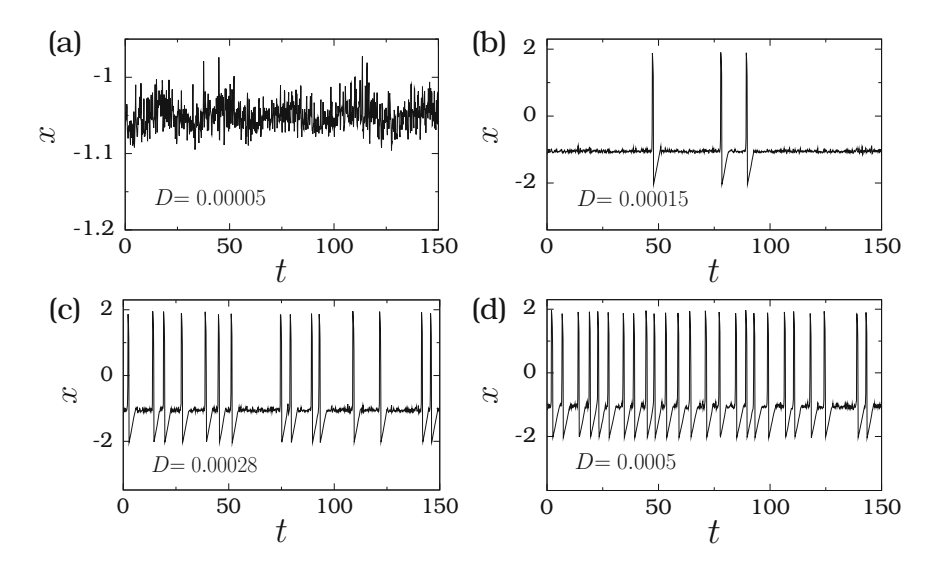


Fig. 4.14 x(t) versus t for a few fixed values of noise intensity D for the FHN equation. Q is maximum for D=0.00028

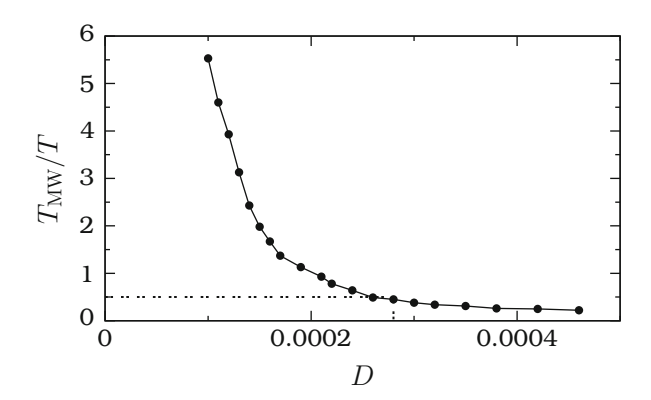


Fig. 4.15 Variation of $T_{\rm MW}/T$ with the noise intensity D for the FHN equation. The dashed line indicates the value of D at which $T_{\rm MW} \approx T/2$

Q becomes a maximum. When D increases further, the number of spikes per drive cycle increases and Q decreases.

In a symmetric bistable system the mean residence time $T_{\rm MR}$ of the system around the two stable states decreases from a large value with increase in D and resonance occurs when $T_{\rm MR}=T/2$, where T is the period of the driving force. For excitable systems, the mean residence time is replaced by the mean waiting time $T_{\rm MW}$ between two consecutive spikes introduced in the previous section (see Fig. 4.11b). 10^4 waiting times are computed and then $T_{\rm MW}/T$ is calculated. This is repeated for a range of values of D. The result is presented in Fig. 4.15. Initially $T_{\rm MW}$

decreases rapidly with D and becomes $\approx T/2$ at D=0.00028 at which Q becomes a maximum. Beyond the resonance $T_{\rm MW}$ decreases slowly with D. The point is that the resonance occurs when $T_{\rm MW} \approx T/2$. In Fig. 4.14b for D=0.00028 though the spikes are not equally spaced with waiting times T/2, the mean waiting time $T_{\rm MW}$ is $\approx T/2$.

Stochastic resonance has been analysed in coupled FHN systems [14], in FHN equation driven by an amplitude modulated, frequency modulated and chaotic signals [15] and also introducing noise in the phase of the input periodic signal [16]. Both vibrational and stochastic resonances are studied in the FHN model equation with multiplicative and additive noises [17].

4.6 Concluding Remarks

Vibrational resonance has been studied in the overdamped bistable system with the asymmetric potential $V(x) = -\frac{1}{2}\alpha x^2 + \frac{1}{4}\beta x^4 - \gamma x$, α , β , $\gamma > 0$ [18] and with $V(x) = 4(x-x^3) + \Delta$ [19], where Δ is a constant parameter describing the level of asymmetry. Single resonance is reported when the amplitude of the high-frequency force or Δ is varied. The occurrence of vibrational resonance has been explained in overdamped systems through a linear response theory [20]. It is possible to realize experimentally in double-well Duffing oscillators where (1) the depth of the right-well remains the same while the depth of the left-well can be altered and (2) the location of the right-well local minimum remains the same, while the local minimum of left-well can be altered. In the vibrational resonance analysis, it has been assumed that $\Omega \gg \omega$. When the ratio $\Omega/\omega = n$ where n is an integer, then for small values of n the resonance is found to be stronger and this is called frequency-resonance-enhanced vibrational resonance [21].

References

- 1. F.C. Moon, P.J. Holmes, J. Sound Vib. 65, 275 (1979)
- 2. N.M. Zimmerman, B. Golding, W.H. Haemmerle, Phys. Rev. Lett. 67, 1322 (1991)
- 3. E. Simiu, Chaotic Transitions in Deterministic and Stochastic Dynamical Systems (Princeton University Press, New Jersey, 2002)
- 4. I.I. Blekhman, P.S. Landa, Int. J. Nonlinear Mech. 39, 421 (2004)
- S. Rajasekar, S. Jeyakumari, V. Chinnathambi, M.A.F. Sanjuan, J. Phys. A Math. Theor. 43, 465101 (2010)
- 6. S. Jeyakumari, V. Chinnathambi, S. Rajasekar, M.A.F. Sanjuan, Chaos 19, 043128 (2009)
- 7. B. Lindner, J. Garcia-Ojalvo, A. Neiman, L. Schimansky-Geier, Phys. Rep. 392, 321 (2004)
- 8. E. Ullner, A. Zaikin, J. Garcia-Ojalvo, R. Bascones, J. Kurths, Phys. Lett. A 312, 348 (2003)
- 9. B. Deng, J. Wang, X. Wei, K.M. Tsang, W.L. Chan, Chaos 20, 013113 (2010)
- 10. R. FitzHugh, Biophys. J. **1**, 445 (1961)
- 11. J. Nagumo, S. Arimoto, S. Yoshizawa, Proc. IRE 50, 2061 (1962)

References 137

- 12. J. Keener, J. Snyder, *Mathematical Physiology* (Springer, New York, 1998)
- 13. A.S. Mikhailov, Foundations of Synergetics (Springer, Berlin, 1994)
- 14. K. Park, Y.C. Lai, Z. Liu, A. Nachman, Phys. Lett. A 326, 391 (2004)
- 15. Y.C. Lai, Z. Liu, A. Nachman, L. Zhu, Int. J. Bifurcation Chaos 14, 3519 (2004)
- 16. X. Liang, L. Zhao, Z. Liu, Phys. Rev. E 84, 031916 (2011)
- 17. H. Zheng-You, Z. Yu-Rong, Chin. Phys. Lett. 28, 110505 (2011)
- 18. V.N. Chizhevsky, G. Giacomelli, Phys. Rev. E 73, 022103 (2006)
- 19. V.N. Chizhevsky, G. Giacomelli, Phys. Rev. E 77, 051126 (2008)
- 20. A. Ichiki, Y. Tadokoro, M. Takanashi, J. Phys. A Math. Theor. 45, 385101 (2012)
- 21. C. Yao, Y. Liu, M. Zhan, Phys. Rev. E 83, 061122 (2011)

Chapter 5 Vibrational and Stochastic Resonances in Spatially Periodic Systems

So far the analysis of stochastic and vibrational resonances has been focused in monostable and bistable systems. It is important to investigate also the resonance dynamics in multistable systems, particularly, in spatially periodic potential systems. This is because there are many nonlinear systems with multistable states and moreover such studies might help us to know how does multistable states affect resonance dynamics and explore the role of them on the characteristics of a resonance. It has been shown that [1] the noise-induced resonant behaviour exhibited in a pendulum (its potential is spatially periodic) is not the stochastic resonance associated with the hopping between the wells. However, the observed resonance is a noise enhanced resonance due to the intra-well motion. In the case of large damping and weak periodic force, the distribution of escape time displayed a series of stochastic resonance-like peaks with noise intensity [2]. Such a character is not observed with a diffusion coefficient. Nicolis [3] investigated the stochastic resonance in a potential with an arbitrary number of minima and maxima. Employing a linear response theory, an optimal number of minima and maxima giving a maximum response is obtained. Saika et al. [4] have shown the occurrence of stochastic resonance in the pendulum system with the driving frequency close to the natural frequency and have used an input energy and a hysteresis loop area as its characteristic measures.

The occurrence of vibrational resonance has been analysed in the pendulum system with periodic potential [5]. In a damped and biharmonically driven pendulum system, when the amplitude of the high-frequency force is varied, the amplitude of oscillation at the low-frequency of the force exhibits a series of resonances approaching a nonzero limiting value. Vibrational ratchet motion is studied in certain systems with spatially periodic potentials driven by a two-frequency force and a noise [6]. In the pendulum system driven by a high-frequency periodic force and a noise, applying the vibrational mechanics scheme, it has been shown that the mobility and the diffusion coefficient are highly sensitive to the mass, even for

large damping values [7]. An experimental realization of vibrational resonance in a periodic potential using cold atoms in an optical lattice has been reported in [8].

The present chapter is devoted for the analysis of vibrational resonance and stochastic resonance in the pendulum system and the modified Chua's circuit equation. The pendulum system has a spatially periodic potential. Using theoretical approaches, the occurrence of vibrational and stochastic resonances will be analysed. Unlike the pendulum system, in the modified Chua's circuit equation the number of equilibrium points (N) and the breakpoints in the nonlinear function can be varied. The numerical investigation on the role of number of equilibrium points on the characteristic features of both the resonances will be made.

5.1 Vibrational Resonance in Underdamped Pendulum System

The equations of motion of the underdamped pendulum system is

$$\ddot{\theta} + d\dot{\theta} + \sin\theta = f\cos\omega t + g\cos\Omega t, \quad \Omega \gg \omega. \tag{5.1}$$

Seeking the solution of (5.1) in the form $\theta = X + \psi$, where X and ψ are the slow and fast motions, respectively, leads to the equation

$$\ddot{X} + \ddot{\psi} + d(\dot{X} + \dot{\psi}) + \cos\psi\sin X + \sin\psi\cos X = f\cos\omega t + g\cos\Omega t.$$
 (5.2)

Due to the presence of the mixed terms $\cos \psi \sin X$ and $\sin \psi \cos X$, add and subtract the terms $\langle \cos \psi \rangle \sin X$ and $\langle \sin \psi \rangle \cos X$, where

$$\langle \cos \psi \rangle = \frac{1}{2\pi} \int_0^{2\pi} \cos \psi(\tau) d\tau, \quad \langle \sin \psi \rangle = \frac{1}{2\pi} \int_0^{2\pi} \sin \psi(\tau) d\tau$$
 (5.3)

and obtain the following set of equations:

$$\ddot{X} + d\dot{X} + \langle \cos \psi \rangle \sin X + \langle \sin \psi \rangle \cos X = f \cos \omega t , \qquad (5.4)$$

$$\ddot{\psi} + d\dot{\psi} + [\cos\psi - \langle\cos\psi\rangle] \sin X + [\sin\psi - \langle\sin\psi\rangle] \cos X$$

$$= g\cos\Omega t. \tag{5.5}$$

5.1.1 Analytical Expression for the Response Amplitude Q

Equation (5.5) can be approximated as $\ddot{\psi} = g \cos \Omega t$ whose solution is $\psi = -(g/\Omega^2) \cos \Omega t$. This solution gives $\langle \cos \psi \rangle = J_0(g/\Omega^2)$ and $\langle \sin \psi \rangle = 0$ where

 J_0 is the zeroth-order Bessel function. Now, Eq. (5.4) becomes

$$\ddot{X} + d\dot{X} + J_0(g/\Omega^2)\sin X = f\cos\omega t. \tag{5.6}$$

Equation (5.6) can be treated as a forced motion of a particle in the effective potential

$$V_{\text{eff}}(X) = -J_0(g/\Omega^2)\cos X. \tag{5.7}$$

Figure 5.1 shows $J_0(g/\Omega^2)$ versus g for $\Omega=10$. J_0 oscillates around the value 0 with decreasing amplitude and $J_0 \to 0$ as $g \to \infty$. Whenever $J_0 > 0$ the minima of $V_{\rm eff}$ are $X_{\rm min}^* = \pm 2n\pi$, $n=0,1,2,\cdots$ and the maxima are $X_{\rm max}^* = \pm (2n+1)\pi$, $n=0,1,2,\cdots$. The locations of the minima and the maxima of $V_{\rm eff}$ are interchanged when the sign of J_0 changes. A consequence of this is that for the values of g for which $J_0 > 0$ slow oscillations occur around the equilibrium points $(X^*, \dot{X}^*) = (X_{\rm min}^*, 0)$, while for $J_0 < 0$ they take place around $(X^*, \dot{X}^*) = (X_{\rm max}^*, 0)$.

The equation of motion for the deviation variable $Y = X - X^*$ is given by

$$\ddot{Y} + d\dot{Y} + (J_0 \cos X^*) \sin Y = f \cos \omega t. \tag{5.8}$$

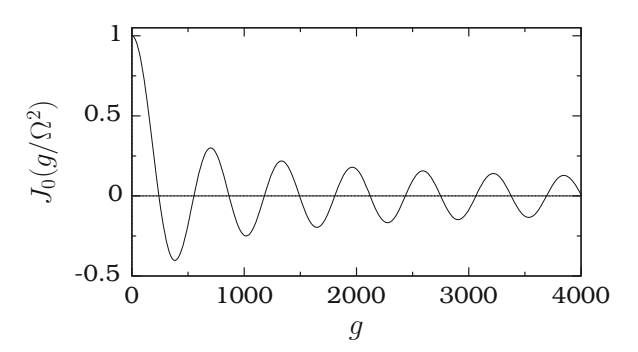
If $J_0 > 0$ (< 0) then $X^* = X^*_{\min}(X^*_{\max})$. Therefore, $J_0 \cos X^* = |J_0|$. For $|f| \ll 1$ we assume that $|Y| \ll 1$ and approximate $\sin Y$ as Y. Then Eq. (5.8) becomes

$$\ddot{Y} + d\dot{Y} + \omega_{\rm r}^2 Y = f \cos \omega t, \quad \omega_{\rm r}^2 = |J_0| \tag{5.9}$$

which is a damped and periodically driven linear equation. The solution of Eq. (5.9) in the long time limit is $Y(t) = A_L \cos(\omega t + \phi)$ where $A_L = f/\sqrt{S}$ and

$$S = (\omega_r^2 - \omega^2)^2 + d^2\omega^2$$
, $\phi = \tan^{-1}[-d\omega/(\omega_r^2 - \omega^2)]$. (5.10)

Fig. 5.1 Variation of the zeroth-order Bessel function with the control parameter g for $\Omega = 10$. Note that J_0 exhibits a damped oscillation. Moreover, the values of g at which $J_0 = 0$ are not equally spaced



5.1.2 Connection Between Resonance and ω_r

Figure 5.2 shows both theoretical and numerical values of Q versus g for four set of values of ω and Ω with f=0.1 and d=1. There are several interesting results on the pendulum system [5] compared to the vibrational resonance in the other systems with nonperiodic potentials.

First, note that the values of g, $g_{\rm VR}$, at which Q becomes maximum (that is, S becomes minimum) are the roots of the equation $S_g={\rm d}S/{\rm d}g=J_{0g}(|J_0|-\omega^2)=0$ with $J_{0g}={\rm d}J_0/{\rm d}g$. Therefore, resonance occurs if $|J_0|=\omega^2$ or $J_{0g}=0$. Recall that $J_0(0)=1$, $|J_0(g/\Omega^2)|<1$ and it oscillates around the value 0 with a decreasing amplitude. Suppose g_c is the value of g above which $|J_0|$ is always $<\omega^2$. Then for $g< g_c$ the values of g at which resonance occurs are the roots of $|J_0|-\omega^2=0$. For $g>g_c$ the resonance values of g are the roots of the equation $J_{0g}=0$. These are clearly seen in Fig. 5.3 which shows the connection between the resonances and ω_r^2 for $\omega=0.5$ and $\Omega=10$. The value of g_c is 761, however the values of $g_{\rm VR}$ are not equally spaced.

Since $|J_0| < 1$, for $\omega \ge 1$ one finds from $Q = 1/\sqrt{S}$ that Q(g) < Q(g = 0). That is, there is no gain in the response amplitude at the frequency $\omega \ge 1$ due to the addition of a high-frequency force. However, due to the damped oscillatory variation of J_0 , the response amplitude Q will show an oscillatory variation and it becomes maximum whenever $|J_0|$ is maximum (that is, $J_{0g} = 0$). The above results are clearly evident in Fig. 5.2 for $\omega = 1$ and 1.25.

For $\omega < 1$, a key result is Q(g) > Q(g = 0). At the resonances occurring for $g < g_c$, $Q_{\text{max}} = 1/(d\omega)$. At other resonances $(g_{\text{VR}} > g_c)$, which are due to the local maxima of ω_r^2 (see Figs. 5.2 and 5.3), the value of Q_{max} slowly decreases from the value $1/(d\omega)$ and approaches the limiting value Q_{L} (indicated by dashed lines in Fig. 5.2) in the limit of $g \to \infty$. These results are clearly seen in Figs. 5.2 and 5.3.

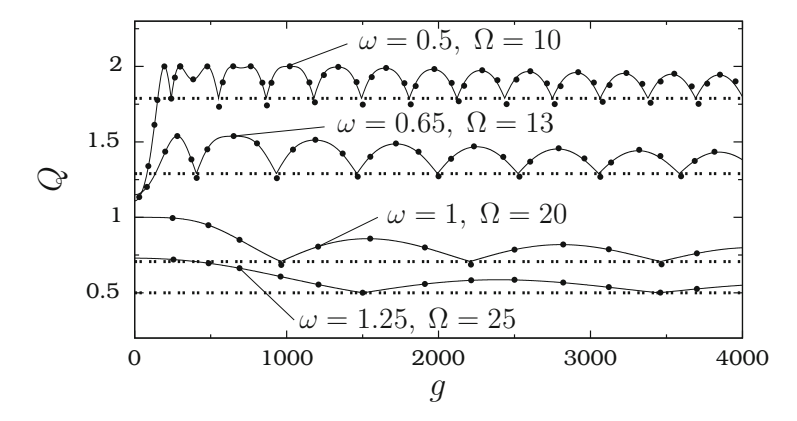
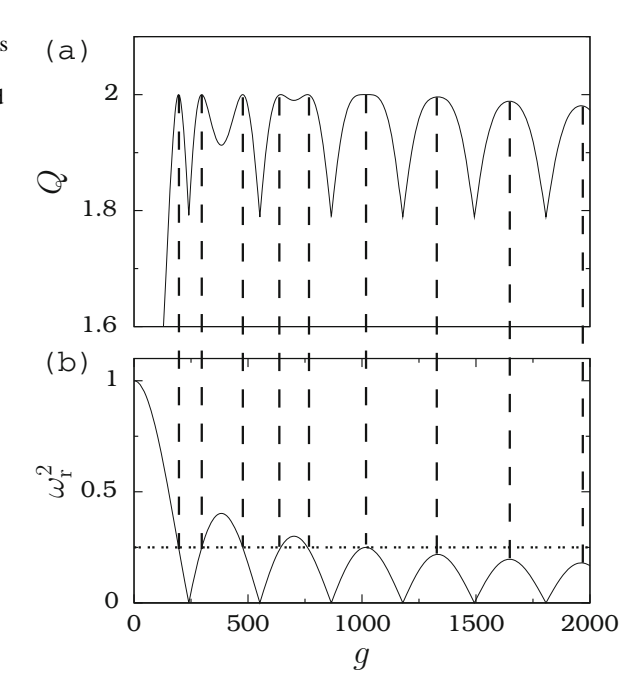


Fig. 5.2 Q versus g for the system (5.1) for a few set of values of ω and Ω . The values of d and f are 1 and 0.1, respectively. The *continuous curve* and the *solid circles* represent the theoretical Q and the numerically computed Q, respectively. The *dashed horizontal lines* indicate the limiting values of Q

Fig. 5.3 Plots of (a) Q versus g and (b) $\omega_r^2 (= |J_0(g/\Omega^2)|)$ versus g for the underdamped pendulum system with $\omega = 0.5$, $\Omega = 10$, f = 0.1 and d = 1. In (b) the horizontal dashed line denotes $\omega_r^2 = \omega^2 = 0.25$. The vertical dashed lines indicate the values of ω_r^2 and g at which Q becomes maximum



An interesting result, for both $\omega > 1$ and $\omega < 1$, is that Q does not decay to 0 whereas in the systems with a finite number of potential wells $Q \to 0$ for sufficiently large values of g because of the monotonic increase of the resonant frequency for large values of g as shown in Chaps. 3 and 4.

5.1.3 Role of Stability of the Equilibrium Points

Let us bring out the connection between vibrational resonance and the stability of the equilibrium points around which slow oscillations take place. The equilibrium points of the system Eq. (5.6) for f=0 are $(X_{\min}^*, \dot{X}^*)=(\pm 2n\pi, 0), n=0,1,2,\cdots$ and $(X_{\max}^*, \dot{X}^*)=(\pm (2n+1)\pi, 0), n=0,1,2,\cdots$. The stability determining eigenvalues are

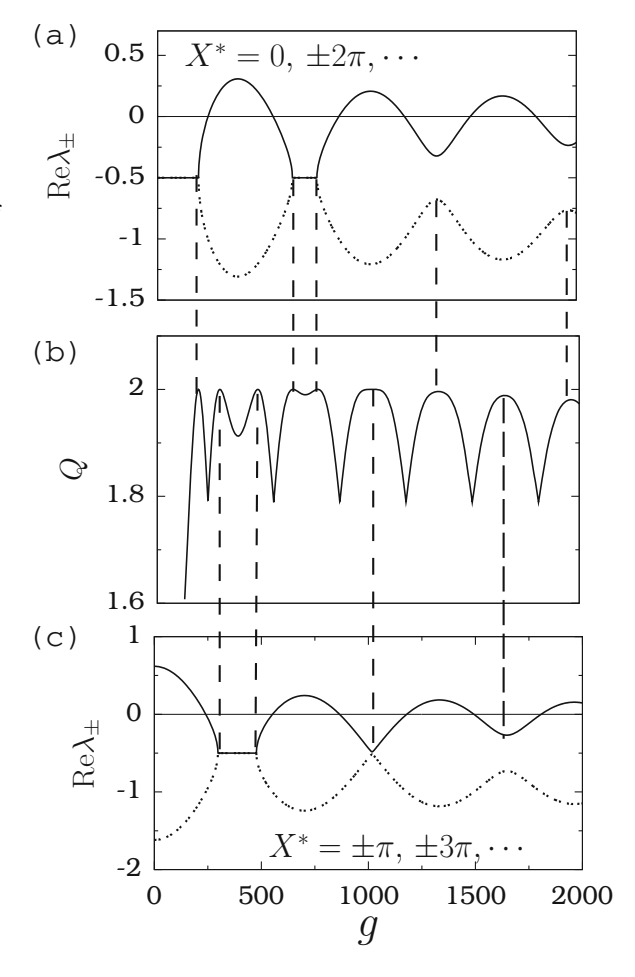
$$\lambda_{\pm} = \frac{1}{2} \left[-d \pm \sqrt{d^2 - 4J_0 \cos X^*} \right] . \tag{5.11}$$

If $J_0 > 0$ then for $(X^*_{\min}, 0)$ Re $\lambda_{\pm} < 0$ and are stable while for $(X^*_{\max}, 0)$ λ_{\pm} are real with $\lambda_{+} > 0$ while $\lambda_{-} < 0$ and are unstable (saddles). The stability is exchanged for $J_0 < 0$. That is, the stability of the equilibrium points is changed when g is varied and the associated bifurcation is the transcritical bifurcation. A consequence of this is that for the values of g for which $J_0 > 0$ slow oscillations occur around the

equilibrium points $(X_{\min}^*, 0)$ while for other values they take place around $(X_{\max}^*, 0)$. Around each of the stable equilibrium points there exists a slow orbit. The coexisting slow orbits and the coexisting actual orbits can be obtained by choosing different initial conditions in the numerical simulation.

Figure 5.4a, c show the variation of $\operatorname{Re}\lambda_\pm$ of $(X^*_{\min},0)$ and $(X^*_{\max},0)$, respectively. As g increases from zero, the eigenvalues of $(X^*_{\min},0)$ are complex conjugate with a negative real part while $\lambda_- < 0 < \lambda_+$ for $(X^*_{\max},0)$. The imaginary part of λ 's of $(X^*_{\min},0)$ decreases in magnitude and at a value of g they are pure real negative. Then at another value of g, one of the eigenvalues of $(X^*_{\min},0)$ becomes positive (while those of $(X^*_{\max},0)$ become complex conjugate with negative real part). At this value of g the stability of $(X^*_{\min},0)$ and $(X^*_{\max},0)$ are exchanged and the associated bifurcation is transcritical. This bifurcation repeats as g increases. Q attains the limiting value Q_L at the bifurcation points. Resonances occur when $(X^*_{\min},0)$ or $(X^*_{\max},0)$ are maximally stable, that is, the real part of the largest eigenvalue is minimum. These can be clearly seen in Fig. 5.4.

Fig. 5.4 Re λ_{\pm} versus the control parameter g of (a) the equilibrium points $(X_{\min}^*, 0)$ and (c) the equilibrium points $(X_{\max}^*, 0)$. Continuous and dashed curves represent $Re\lambda_{+}$ and $Re\lambda_{-}$, respectively. (b) Q versus g of the underdamped pendulum system for d = 1, f = 0.1, $\omega = 0.5$ and $\Omega = 10$. The vertical dashed lines indicate the connection between the resonance and the nature of the eigenvalues of the stable equilibrium points



5.2 Vibrational Resonance in Overdamped Pendulum System

In this section, consider the overdamped pendulum system

$$\dot{\theta} + \sin \theta = f \cos \omega t + g \cos \Omega t. \tag{5.12}$$

Multiresonance occurs in the overdamped pendulum system, however, there are some differences in the mechanism of resonance [5].

For the system Eq. (5.12) one obtains

$$\dot{X} + J_0(g/\Omega)\sin X = f\cos\omega t \tag{5.13}$$

and the response amplitude Q is given by

$$Q = \frac{1}{\sqrt{\omega_{\rm r}^2 + \omega^2}}, \quad \omega_{\rm r} = |J_0|. \tag{5.14}$$

The stability determining the quantity λ of the equilibrium points of Eq. (5.13) with f = 0 are given by

$$\lambda = \begin{cases} \lambda_{\min} = -J_0, & \text{for } X_{\min}^* = 0, \pm 2\pi, \dots \\ \lambda_{\max} = J_0, & \text{for } X_{\max}^* = \pm \pi, \pm 3\pi, \dots \end{cases}$$
 (5.15)

Figure 5.5 presents Q, ω_r and the variation of stability determining eigenvalue λ_{\min} and λ_{\max} of the equilibrium points X_{\min}^* and X_{\max}^* , respectively, versus g. Note that Q displays a series of resonance peaks. In contrast to the underdamped system,

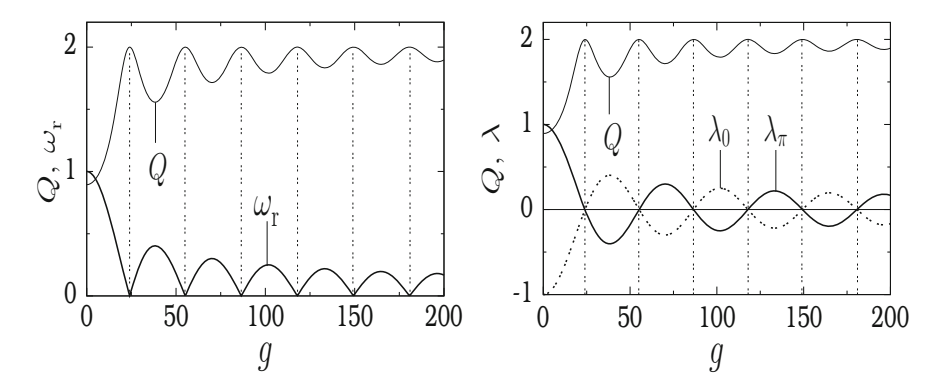


Fig. 5.5 Variation of theoretical Q, resonant frequency ω_r and the eigenvalue λ of the equilibrium points X_{\min}^* and X_{\max}^* (for f=0) of the overdamped pendulum system as a function of g for $\omega=0.5$, $\Omega=10$ and f=0.1

in the overdamped system resonances occur when $\omega_{\rm r}=0$ at which the stability of the equilibrium points $X^*_{\rm min}$ and $X^*_{\rm max}$ are exchanged. Moreover, Q is locally minimum when $\omega_{\rm r}$ becomes a maximum and λ of the stable equilibrium points is minimum (maximally stable). At all the resonance values of g the value of Q is $1/\omega$. Furthermore, for both $\omega<1$ and $\omega>1$ the response amplitude Q(g)>Q(0) and $Q_{\rm L}=1/\omega$.

5.3 Vibrational Resonance in a Modified Chua's Circuit Equation

Chua's circuit is the most widely investigated nonlinear circuit. The voltage-current characteristic of the operational amplifier based Chua's diode (the nonlinear element in the Chua's circuit) is piecewise linear. The Chua's circuit is found to display a rich variety of nonlinear dynamics [9–11]. An interesting attractor of the Chua's circuit is the double-scroll orbit. The original Chua's circuit is modified to generate multi-scroll orbits by replacing the three-segment piecewise linear function with sawtooth functions having multiple breakpoints [12]. A systematic methodology for designing circuits to generate n-scroll orbits has been developed [13–16]. In the modified Chua's circuit equation controlling of unstable equilibrium points and periodic orbits [17], diffusion dynamics and characteristic features of first passage times to nth scroll attractor and residence times on a scroll attractor [18] and the influence of number of equilibrium points on the characteristics of stochastic and coherence resonances [19] have been investigated. The goal of the present section is to report the features of vibrational resonance in the modified Chua's circuit model equation with specific emphasis on the role of the number of breakpoints of piecewise linear function representing the characteristic curve of Chua's diode on the resonance.

5.3.1 The Modified Chua's Circuit Model Equation

The model equation of the modified Chua's circuit [12] driven by the biharmonic force is

$$\dot{x} = \alpha y - \alpha F(x) + f \cos \omega t + g \cos \Omega t, \tag{5.16a}$$

$$\dot{y} = x - y + z,\tag{5.16b}$$

$$\dot{z} = -\beta y,\tag{5.16c}$$

where

$$F(x) = F_1(x)$$

$$= \xi x + \xi A \operatorname{sgn}(x) - \xi A \sum_{j=0}^{n-1} [\operatorname{sgn}(x+2jA) + \operatorname{sgn}(x-2jA)] \quad (5.16d)$$

or

$$F(x) = F_2(x)$$

$$= \xi x - \xi A \sum_{j=0}^{n-1} [\operatorname{sgn}(x + (2j+1)A) + \operatorname{sgn}(x - (2j+1)A)] \quad (5.16e)$$

with

$$\operatorname{sgn}(x) = \begin{cases} 1, & \text{if } x > 0 \\ 0, & \text{if } x = 0 \\ -1, & \text{if } x < 0 \end{cases}$$
 (5.16f)

and α , β , ξ , A > 0, $n \ge 1$. F(x) given by Eq. (5.16d) or (5.16e) is a sawtooth function with amplitude $2A\xi$ and period 2A. Figure 5.6a, b depict the forms of $F_1(x)$ and $F_2(x)$, respectively, for n = 1, $\xi = 0.25$ and A = 0.5. The stable equilibrium points about which scroll orbits occur are given by

$$X^* = (x^*, y^*, z^*)$$

$$= \begin{cases} [\pm (2m-1)A, \ 0, \ \mp (2m-1)A], & \text{for } F_1(x) \\ [0, 0, 0], \ [\pm 2mA, \ 0, \ \mp 2mA], & \text{for } F_2(x) \end{cases}$$
(5.17)

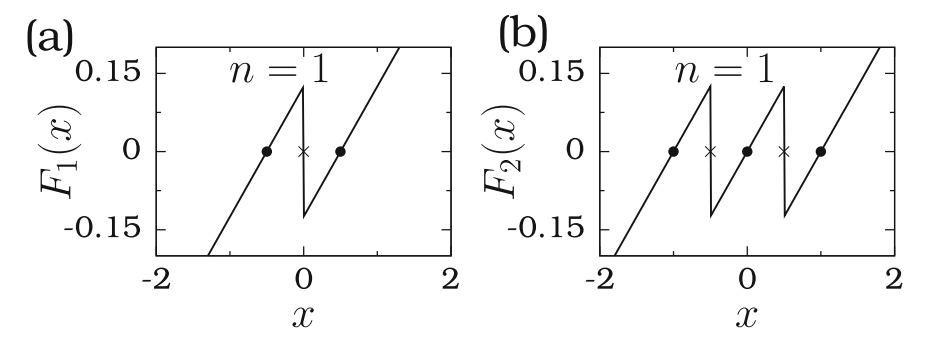


Fig. 5.6 $F_1(x)$ and $F_2(x)$ given by Eqs. (5.16d) and (5.16e), respectively, with n = 1, $\xi = 0.25$ and A = 0.5. The *solid circles* and the *cross* symbol mark the equilibrium points and the breakpoints, respectively

where $m = 1, 2, \dots, n$. The system (5.16) with $F_1(x)$ and in the absence of external forces possesses 2n (even) number of stable equilibrium points and N = 2n - 1 (odd) number of breakpoints. In the case of $F_2(x)$ it admits 2n + 1 (odd) number of stable equilibrium points and N = 2n (even) number of breakpoints. Between two consecutive stable equilibrium points the sawtooth function F(x) has a breakpoint. The number of breakpoints depends on the value of n in Eqs. (5.16d) and (5.16e). The breakpoints are given by

$$x_{\text{bp}}^* = \begin{cases} \pm 2mA, & \text{for } F_1(x) \\ \\ \pm (2m+1)A, & \text{for } F_2(x) \end{cases}$$
 (5.18)

where m = 0, 1, 2, ..., n - 1. Let us analyze the role of the number of breakpoints, N, on vibrational resonance.

5.3.2 Role of Number of Breakpoints N on Resonance

Since the determination of an approximate theoretical expression for the response amplitude is very difficult for Eq. (5.6), we proceed to perform a numerical simulation. From the numerical solution of x(t) the response amplitude Q is computed. We fix the values of the parameters in Eq. (5.16) as $\alpha = 6$, $\beta = 16$, A = 0.5, $\xi = 0.25$, f = 0.1, $\omega = 1$ and $\Omega = 10\omega$.

Figure 5.7 presents the numerically computed Q versus g for several fixed values of N. Vibrational resonance occurs when the control parameter g is varied. In obtaining Fig. 5.7, for each fixed value of N, g is varied from 0 to 75 in step of 0.01. The system (5.16) is numerically integrated using the fourth-order Runge–Kutta method with step size $(2\pi/\omega)/1000$. First 10^3 drive cycles are left as transient and the values of x(t) corresponding to the next 500 drive cycles are used to compute the response amplitude. For g=0 the initial condition is chosen in the neighbourhood of the origin. For other values of g the initial condition is taken as the last value

Fig. 5.7 Variation of the response amplitude Q as a function of g for various fixed values of number of breakpoints N of the system (5.16). F(x) in Eq. (5.16a) is F_1 for odd values of N and F_2 for even values of N. For each fixed value of N, g is varied from 0 to 75

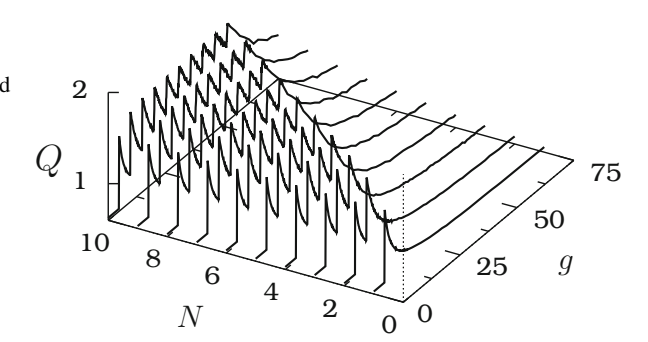
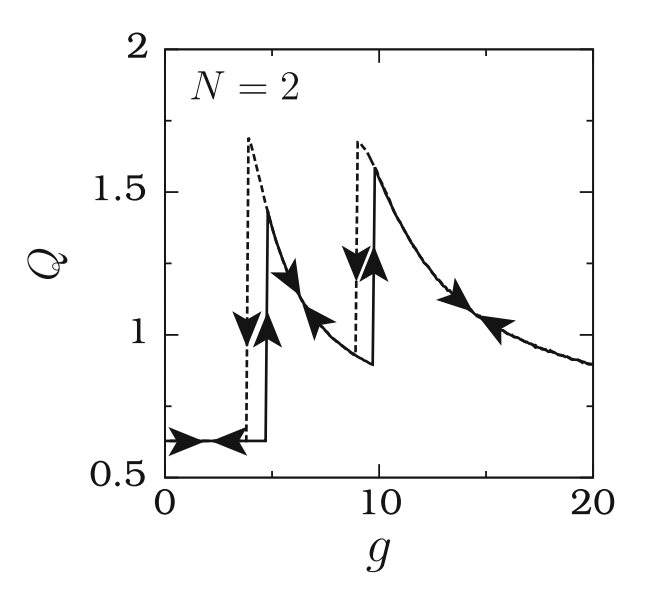


Fig. 5.8 Resonance curves obtained by varying g from 0 to 20 (continuous curve) and from 20 to 0 (dashed curve) for N = 2 with F(x) in Eq. (5.16a) as $F_2(x)$ given by Eq. (5.16e). The arrows indicate the path followed by Q when g is varied in the forward and reverse directions



of (x, y, z) of previous value of g. When g is decreased from a large value, say 75, Q is found to follow a different path near each resonance. An example is shown in Fig. 5.8 for N = 2. In this figure solid and dashed curves represent the resonance curve obtained when g is varied in the forward and reverse directions, respectively.

Before explaining the resonance curves in Fig. 5.8, we point out the influence of the number of breakpoints *N* on resonance.

- For each fixed value of *N* there are *N* resonances.
- In both cases of varying g in the forward direction from 0 and in the reverse direction from a large value, for convenience, we number the resonance peaks from left-side to right-side as $1, 2, \dots, N$. In the former case we denote the values of g at which ith resonance occurs as $g_{\text{VR},F}^{(i)}$ and the corresponding value of the response amplitude as $Q_{\text{max},F}^{(i)}$ while in the latter case these two values are denoted as $g_{\text{VR},R}^{(i)}$ and $Q_{\text{max},R}^{(i)}$, respectively. The values of $g_{\text{VR}}^{(i)}$ and $Q_{\text{max}}^{(i)}$ are independent of N. This is because the shapes of F(x) between various set of successive equilibrium points are the same.
- The values of $g_{VR}^{(i)}$, $i = 1, 2, \dots, N$ are equally spaced for each fixed value of N. Furthermore, $g_{VR}^{(i)}$ varies linearly with i as shown in Fig. 5.9a following the relation $g_{VRR} = 5.304i 0.615$ and $g_{VRR} = 5.334i 1.686$.
- relation $g_{\text{VR,F}} = 5.304i 0.615$ and $g_{\text{VR,R}} = 5.334i 1.686$.

 For each value of N, $Q_{\text{max,F}}^{(i)}$, $i = 1, 2, \cdots, N$ increases with i while $Q_{\text{max,R}}^{(i)}$ decreases with i, however, both of them approach almost the same constant value. This is shown in Fig. 5.9b for N = 15.
- In monostable and bistable systems after the last resonance, the response amplitude decays to zero with the control parameter g. In contrast to this, Q approaches a nonzero limiting value in the system (5.16). We denote Q_L as the value of Q

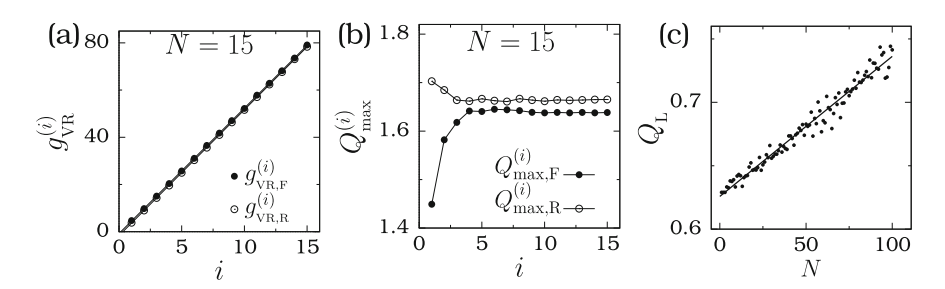


Fig. 5.9 Plots of (a) $g_{\text{NR}}^{(i)}$, the value of g at which Q becomes maximum, versus i (the number of resonance) and (b) $Q_{\text{max}}^{(i)}$, the value of Q at $g = g_{\text{NR}}^{(i)}$, versus i for N = 15. (c) Variation of the limiting value of Q (the value of Q at g = 2000) with the number of breakpoints N. In the subplots (a) and (c) the *continuous lines* are the best straight-line fit to the numerical data

computed at a sufficiently large value of g, say, 2000. Figure 5.9c shows the variation of Q_L with N. Q_L varies linearly with N as $Q_L = 0.62581 + 0.001N$.

5.3.3 Jump Phenomenon

We explain now the resonance curves (solid and dashed curves) in Fig. 5.8 corresponding to N=2. In this case, the function F(x) in Eq. (5.16) is $F_2(x)$ given by Eq. (5.16e). In absence of the biharmonic force, the system has three stable equilibrium points ($x^*=0,\pm 1$) and two breakpoints $x^*_{bp}=\pm 0.5$. When the amplitude of the high-frequency force is varied in Fig. 5.8, one can clearly notice the occurrence of the hysteresis and jumps in the value of the response amplitude. In order to get more insight on the resonance curve, we look at the phase portrait of orbits in the x-y plane along with $F_2(x)$ for six values of g in Fig. 5.10.

For 0 < g < 3.74, there are three coexisting periodic orbits of period- $T(=2\pi/\omega)$, one about each of the stable equilibrium points $x^*=0,\pm 1$ as shown in Fig. 5.10a for g=3. These orbits do not cross the barriers at the breakpoints. The Q of these orbits are all the same and $\ll 1$. There are no stable orbits about the breakpoints $x^*_{\rm bp}=\pm 0.5$. At g=3.74 in addition to the three orbits centered about x^* , two more stable periodic orbits of period-T centered about the two breakpoints $x^*_{\rm bp}$ are born. The five coexisting orbits are displayed in Fig. 5.10b. All these orbits coexist for $3.74 \le g < 4.74$. The Q of the newly born two orbits (marked as L in Fig. 5.10b) are the same and much higher than that of the other three orbits. For example, at g=3.74 the Q of the orbits centered about the equilibrium points (marked as S in Fig. 5.10b) and the breakpoints (marked as L in Fig. 5.10b) are 0.628 and 1.693, respectively. At g=4.74 the S orbits centered about x^* disappear and only the two orbits centered about $x^*_{\rm bp}$ coexist (see Fig. 5.10c). Consequently, when g is varied in the forward direction the response amplitude jumps from a lower value to a higher value at g=4.74.

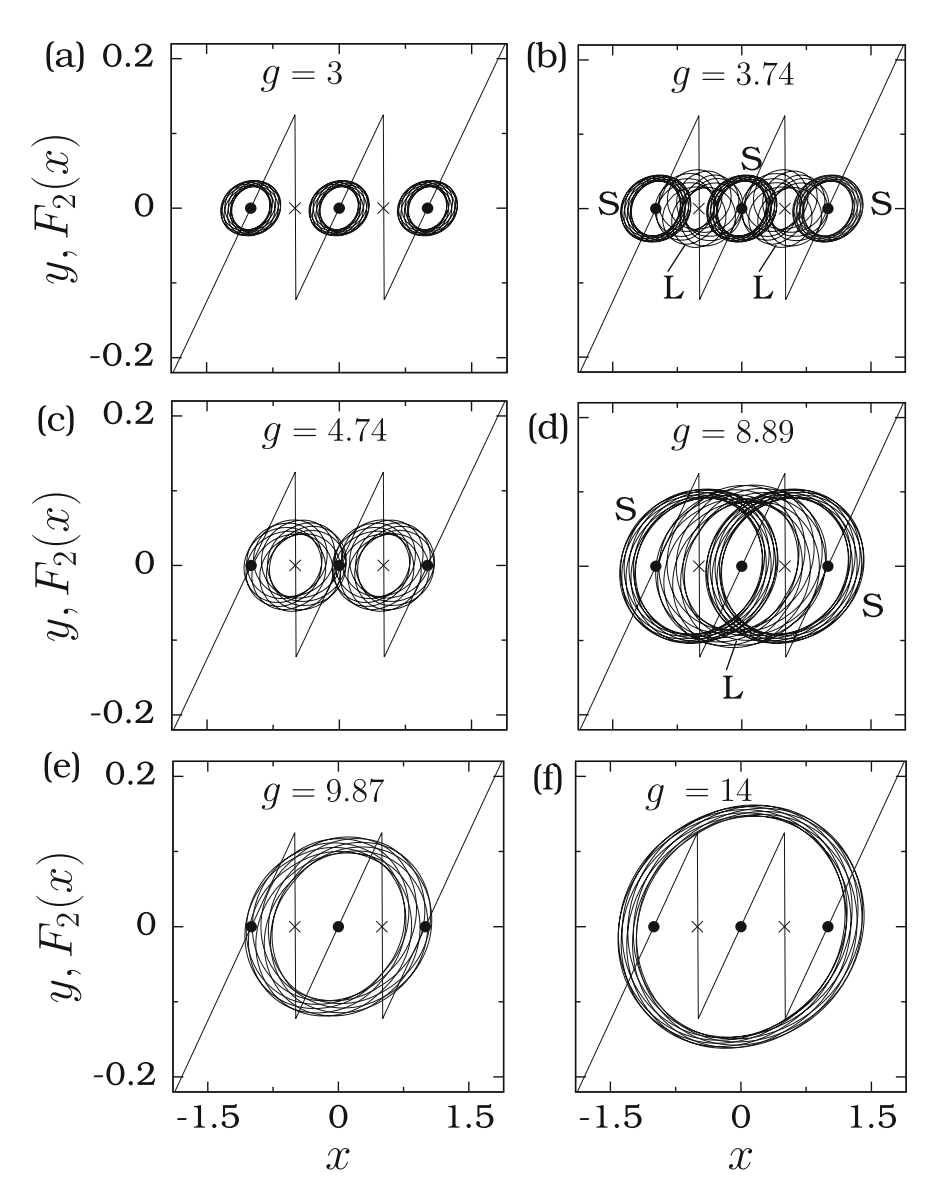


Fig. 5.10 Phase portraits of the coexisting orbits of the system (5.16) with N=2 for various values of g. In the subplots (\mathbf{b}) and (\mathbf{d}) the value of Q for the orbits S is smaller than that of the orbits labelled as L

As g increases further from the value 4.74, the orbits expand and Q at the frequency ω decreases. For 4.74 $\leq g < 8.89$, the two orbits centered about $x_{\rm bp}^*$ alone coexist and moreover they enclose two equilibrium points, one to the left-side and the other to the right-side of the breakpoint. At g = 8.89 the high-frequency

force gives birth to a periodic orbit centered about the equilibrium point $x^* = 0$ and enclosing all the breakpoints. Note that at g = 3.74 the newly born two orbits are centered about the breakpoints. At g = 8.89 the response amplitude of the newly created orbit is 1.67, while that of the other two coexisting orbits is 0.92. The three orbits coexist for $8.89 \le g < 9.87$. When g is varied in the forward direction, then in the above interval the orbits centered about the breakpoints alone realized and hence the resonance curve traces the lower branch (continuous curve) in Fig. 5.8. The upper branch curve (dashed curve) is obtained when g is varied in the reverse direction from the value, say, 20. The small amplitude orbits centered about the breakpoints become unstable at g = 9.87, consequently, in Fig. 5.8 there is a jump in Q from a lower value to a higher value. The value of Q decreases with further increase in g and there is no more periodic orbits are born as shown in Fig. 5.10e, f.

From the above, we generalize the effect of the high-frequency force in the system with l breakpoints and l + 1 equilibrium points. The resonance curve would display l jumps. Denote the value of g at which jumps in Q occur when g is varied in the forward direction as $g_{i1} < g_{i2} < \cdots < g_{il}$. Further, we denote g_{bi} as the value of g at which birth to new orbits occurs ith instant and $g_{bi} < g_{ii}$. For $g < g_{b1}$ there are l+1 orbits centered about the equilibrium points. At $g=g_{bi}$, i=odd (even) l+1-i orbits born with each centered about the l+1-i breakpoints (equilibrium points) with the value of Q higher than those of the l + 2 - i coexisting orbits centered about the equilibrium points (breakpoints). These two set of orbits coexist for $g_{bi} < g < g_{ii}$, i = odd (even). At g_{ii} , i = odd (even) the orbits centered about the equilibrium points (breakpoints) become unstable. For $g_{ii} \le g < g_{b(i+1)}$, i = odd(even), in the numerical simulation one can realize only the orbits centered about the breakpoints (equilibrium points). When g is varied in the forward direction from a small value jumps in the response amplitude Q occur at g_{ii} from a lower value to a higher value. If g is decreased from a value of $g \gg g_{il}$ then jumps in Q occur at g_{bi} from a higher value to a lower value.

5.4 Stochastic Resonance in the Pendulum System

Nicolis [3] investigated theoretically the role of stable and unstable equilibrium points on stochastic resonance for the overdamped pendulum system. The occurrence of stochastic resonance has been shown by using a theoretical approach. The noise intensity at which resonance occurs is found to increase with the frequency of the input periodic signal for various fixed numbers of equilibrium points. This section is a brief review of the analysis presented in [3].

Consider the overdamped version of the pendulum system given by

$$\dot{\theta} = -\frac{\partial U}{\partial \theta} + \eta(t),\tag{5.19}$$

where $\eta(t)$ is a Gaussian white noise with variance σ^2 and $U(\theta, t) = U_0(\theta) + f\theta \sin \omega t$. $U_0(\theta)$ is the potential of the form $U_0(\theta) = -\cos \theta$, $0 \le \theta \le 2\pi n$ with stable (θ_s^*) and unstable (θ_u^*) equilibrium points given by

$$\theta_s^* = (2n+1)\pi, \quad n = 0, 1, \dots, \quad \theta_n^* = 2n\pi, \quad n = 1, 2, \dots.$$
 (5.20)

The Fokker-Planck equation for the probability density $\rho(\theta)$ for the system (5.19) is

$$\frac{\partial \rho}{\partial t} = -\frac{\partial}{\partial \theta} \left[\left(-\frac{\partial U_0}{\partial \theta} + f \sin \omega t \right) \rho \right] + \frac{1}{2} \sigma^2 \frac{\partial^2 \rho}{\partial \theta^2} . \tag{5.21}$$

The solution of (5.21) consists of small-scale diffusion and large-scale transitions. The diffusive motion takes place around each of the stable equilibrium points while the transitions are between neighbouring stable equilibrium points through the intermediate unstable equilibrium points and its rate depends on the potential barrier given by

$$\Delta U = \Delta U_0 - f \Delta \theta \sin \omega t = U_{0,u} - U_{0,s} - f(\theta_u^* - \theta_s^*) \sin \omega t, \tag{5.22}$$

where $\Delta\theta$ is the distance between the adjacent θ_u^* and θ_s^* . The rate is given by the Kramers' formula

$$k(t) = \frac{1}{2\pi} \sqrt{|U_{\rm u}''U_{\rm s}''|} e^{-2\Delta U/\sigma^2},$$
 (5.23)

where prime denotes differentiation with respect to θ .

Let us denote p_i as the transition probability of *i*th state and write $\mathbf{p}(t) = \mathbf{p}_0 + f \delta \mathbf{p}(t)$ where \mathbf{p}_0 is the probability when f = 0 and \mathbf{p}_0 and $\delta \mathbf{p}$ are normalized to unity and zero, respectively. Then write

$$\frac{\mathrm{d}\delta\mathbf{p}}{\mathrm{d}t} = M_0 \delta\mathbf{p} + f \sin \omega t \,\Delta\mathbf{p}_0. \tag{5.24}$$

The solution of (5.24) in the limit of $t \to \infty$ is

$$\delta \mathbf{p}(t) = f(\mathbf{A}\cos\omega t + \mathbf{B}\sin\omega t), \tag{5.25a}$$

where

$$\delta p_i(t) = R_i \sin(\omega t + \phi_i) \tag{5.25b}$$

$$R_i = f\sqrt{A_i^2 + B_i^2}, \quad Q_i = \tan^{-1}\left(\frac{A_i}{B_i}\right).$$
 (5.25c)

Use of (5.25) in (5.24) gives

$$\mathbf{A} = -\left(M_0^2 + \omega^2 I\right)^{-1} \omega(\Delta \mathbf{p}_0), \quad \mathbf{B} = -M_0 \left[\left(M_0^2 + \omega^2 I\right)^{-1} \Delta \mathbf{p}_0 \right]. \tag{5.26}$$

Next, define λ_k and u_k be the eigenspectra of M_0 : $M_0 \mathbf{u}_k = \lambda \mathbf{u}_k$. Expansion of $\Delta \mathbf{p}_0$ in the basis of \mathbf{u}_k is $\Delta \mathbf{p}_0 = \sum_{k=1}^n \gamma_k \mathbf{u}_k$. This results in

$$\mathbf{A} = -\sum_{k=1}^{n} \frac{\omega}{\lambda_k^2 + \omega^2} \gamma_k \mathbf{u}_k, \quad \mathbf{B} = -\sum_{k=1}^{n} \frac{\lambda_k}{\lambda_k^2 + \omega^2} \gamma_k \mathbf{u}_k.$$
 (5.27)

 λ_k and \mathbf{u}_k are calculated as

$$\lambda_{k} = 2k_{0} - 2k_{0} \cos\left[\frac{(k-1)\pi}{n}\right], \quad k = 1, 2, \dots, n,$$

$$u_{1}^{i} = 1, \quad u_{k}^{i} = \cos\left[\frac{(k-1)(2i-1)\pi}{2n}\right],$$

$$i = 1, 2, \dots, n, \quad k = 2, 3, \dots, n.$$
(5.28b)

For k = 1 the norm of \mathbf{u}_k is $N = 1/\sqrt{n}$ while for other values of k the norm is $\sqrt{n/2}$. Then \mathbf{p}_0 and γ_k are obtained as

$$\gamma_k = \begin{cases}
-\frac{8\pi k_0}{Nn\sigma^2} \cos\left[\frac{(k-1)\pi}{2n}\right], & \text{for } k \text{ even} \\
0, & \text{otherwise.}
\end{cases}$$
(5.29a)

Finally, one obtains [3]

$$A_{i} = \frac{8\pi k_{0}}{N^{2}n\sigma^{2}} \sum_{k \text{ even}} \frac{\omega}{\lambda_{k}^{2} + \omega^{2}} \cos\left[\frac{(k-1)\pi}{2n}\right] \cos\left[\frac{(2i-1)(k-1)\pi}{2n}\right],$$

$$(5.30a)$$

$$B_{i} = \frac{8\pi k_{0}}{N^{2}n\sigma^{2}} \sum_{k \text{ even}} \frac{\lambda_{k}}{\lambda_{k}^{2} + \omega^{2}} \cos\left[\frac{(k-1)\pi}{2n}\right] \cos\left[\frac{(2i-1)(k-1)\pi}{2n}\right].$$

$$(5.30b)$$

Figure 5.11a shows the variation of R_i with i (the number of equilibrium states) for three values of ω/k_0 where the values of n and σ^2 are kept constant. R_i is maximum for the two end states i = 1 and n = 30 and it decreases as i moves towards the

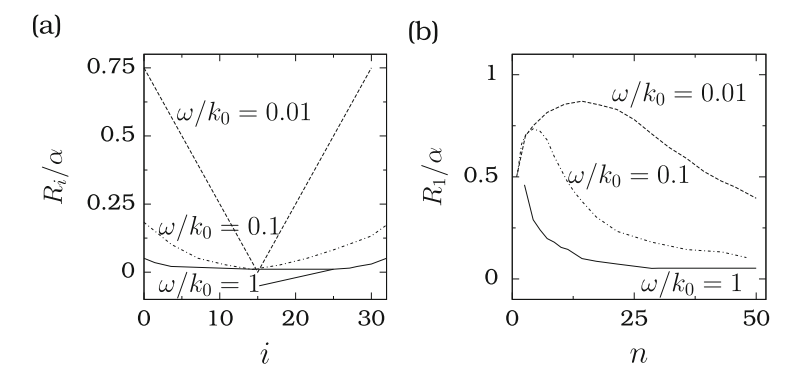


Fig. 5.11 (a) R_i versus i for three fixed values of ω/k_0 . (b) Dependence of R_1 with n for three fixed values of ω/k_0 [3]. (Figure 5.11 adapted with permission from Ref. [3]. Copyrighted by the American Physical Society.)

middle state. Figure 5.11b presents R_1 as a function of n. R_1 is maximum at some specific value of n, that is, there exists an optimal number of equilibrium states for which the response is maximum.

5.5 Stochastic Resonance in a Multi-Scroll Chua's Circuit Equation

The modified Chua's circuit equation driven by a periodic force and noise is given by

$$\dot{x} = \alpha y - \alpha F(x),\tag{5.31a}$$

$$\dot{\mathbf{y}} = \mathbf{x} - \mathbf{y} + \mathbf{z},\tag{5.31b}$$

$$\dot{z} = -\beta y + f \sin \omega t + \eta(t), \tag{5.31c}$$

where F(x) is given by Eq. (5.16d–f). $\eta(t)$ is the Gaussian white noise with mean 0 and intensity D. In this section we analyse the occurrence of stochastic resonance in the system (5.31) with specific emphasize on the role of the parameter N (number of equilibrium points) in Eq. (5.16). The system (5.31) in the absence of external forces with $F_1(x)$ possesses N=2n equilibrium points, while with $F_2(x)$, the system admits N=2n+1 equilibrium points. To realize the system (5.31) with an even, respectively, odd number of equilibrium points, use the functions $F_1(x)$ and $F_2(x)$, respectively, as F(x).

We fix the values of the parameters as $\alpha = 6$, $\beta = 14$, $A_1 = 0.5$, $\xi = 0.25$, $\omega = 0.05$ and f = 0.07, so that the noise free system possesses N coexisting period- $T(= 2\pi/\omega)$ orbits. About each equilibrium point, there exists one periodic orbit. Between two consecutive equilibrium points, there is a finite height barrier located

at the breakpoint. There is no cross-barrier motion for the above parametric choice. Barrier crossing can be induced by the additive noise term. Figure 5.12 presents the SNR profile for $N \in [2, 20]$. In this figure for each fixed value of N, as the noise intensity D increases from a small value the value of SNR increases, reaches a maximum value at a optimum noise intensity denoted as D_{MAX} and then decreases. This is a typical signature of the stochastic resonance phenomenon.

Figure 5.13 shows time series plots for a few values of D with $F(x) = F_1(x)$ and n = 1 (N = 2). For small values of D the motion is confined about each of the two stable equilibrium states as in Fig. 5.13a. In Fig. 5.13b for d = 0.04 the state variable

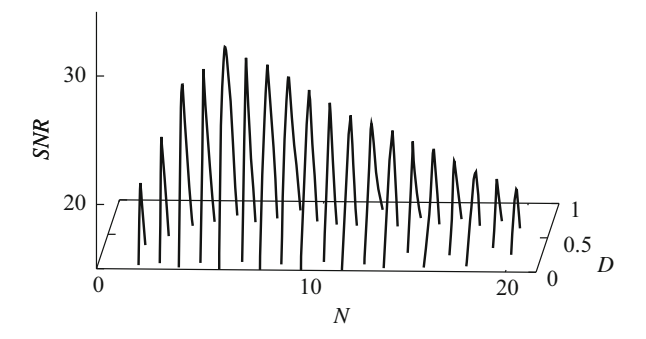


Fig. 5.12 Variation of signal-to-noise ratio (*SNR*) as a function of noise intensity D for $N = 2, 3, \dots, 20$. For even values of N the function F(x) is $F_1(x)$ while for odd values of N the function F(x) is $F_2(x)$

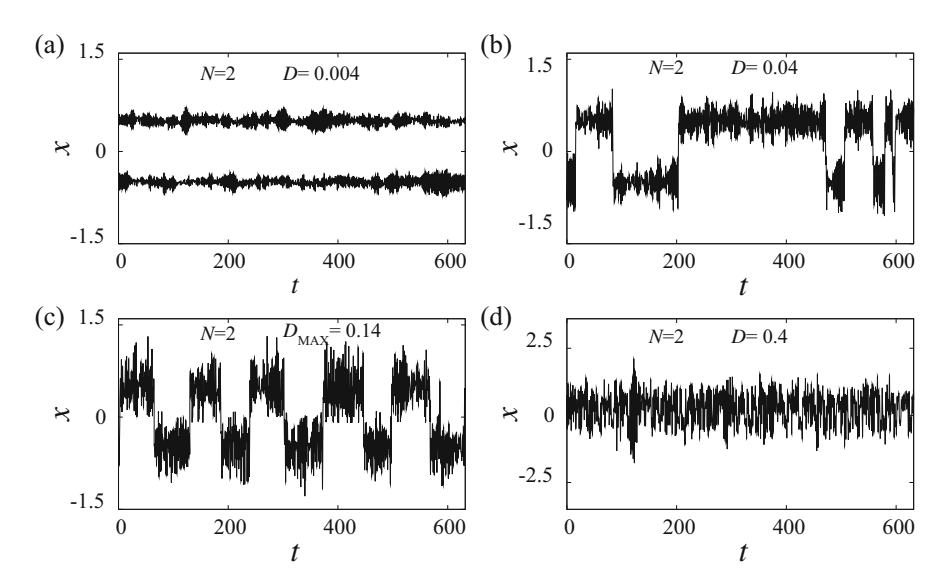


Fig. 5.13 x versus t for four values of noise intensity D of Eq. (5.31) with two equilibrium points (N = 2). For bistability F(x) is chosen as $F_1(x)$ with n = 1 so that N = 2n = 2

switches irregularly but occasionally between the positive and negative values, that is, between the two sides of the barrier. In a bistable oscillator with double-well potential this type of motion corresponds to cross-well motion and the depth of the well and the local maximum of the potential correspond to a barrier height and a breakpoint in the function F(x). One can regard F(x) of Eq. (5.31) as a potential type function. At D=0.14 (see Fig. 5.13c) almost periodic switching is seen. *SNR* is maximum at this value of D. For sufficiently large values of D the trajectory jumps erratically between the two sides of the barrier. This is shown in Fig. 5.13d for D=0.4.

Figure 5.14a, b depict the effect of N on $D_{\rm MAX}$ and $SNR_{\rm MAX}$, respectively. $D_{\rm MAX}$ monotonically increases with N and the variation is not a linear function of N. Though the barrier height remains the same at all the breakpoints and same for all values of $N \geq 2$ the value of $D_{\rm MAX}$ depends on N. Even though $D_{\rm MAX}$ increases with N the N the

Figure 5.15 presents the periodic switching between the coexisting states at $D = D_{\text{MAX}}$ for N = 2, 4 and 6. In this figure corresponding to the two coexisting states (N = 2) the trajectory switches almost periodically between the states. For the case of four and six coexisting states as shown in Fig. 5.15b, c, respectively, the trajectory visits the states one by one from say, left most state to right most state, reverses the direction of visit and so on. One can clearly notice that the time spent about an

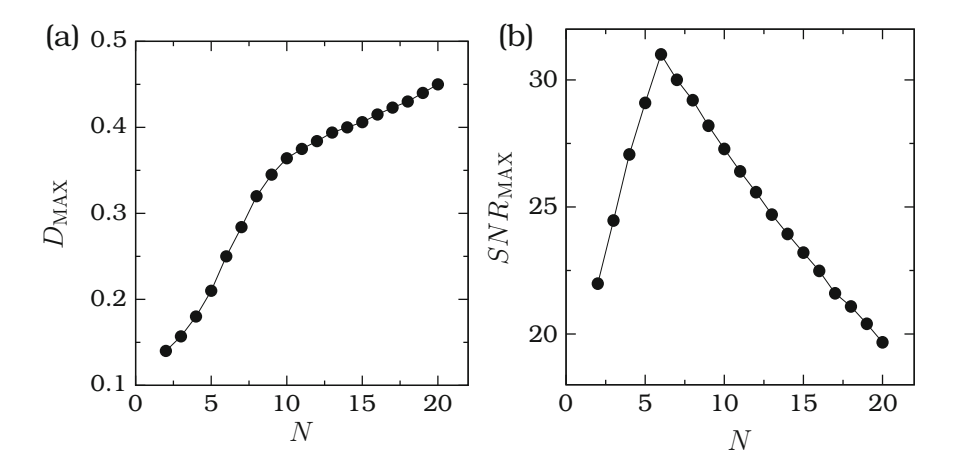


Fig. 5.14 Variation of (a) D_{MAX} and (b) SNR_{MAX} with the number of equilibrium points N

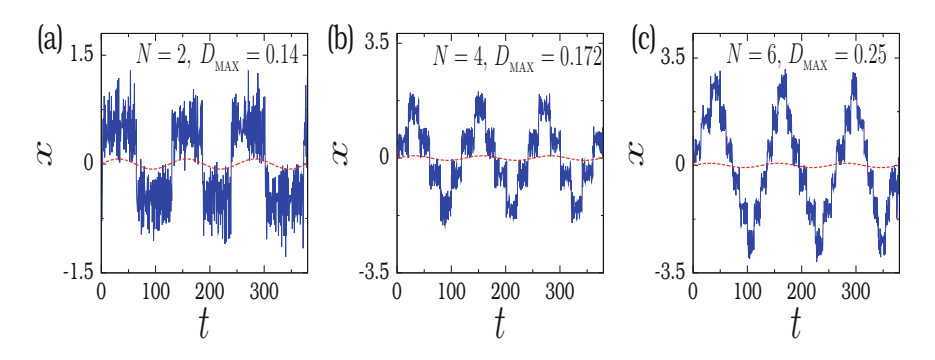


Fig. 5.15 x(t) versus t for three even integer values of N at $D = D_{\text{MAX}}$ at which SNR is maximum. Similar periodic switching to coexisting states occurs for odd integer values of N

equilibrium point varies with N. When the system has N equilibrium points then there are (N-1) breakpoints in the function F(x). Suppose we denote the left most breakpoint as $x_{\rm bp}^{(1)}$, next one as $x_{\rm bp}^{(2)}$ and so on. We call the region $x < x_{\rm bp}^{(1)}$ as R_1 , $x_{\rm bp}^{(1)} < x < x_{\rm bp}^{(2)}$ as R_2 and finally $x > x_{\rm bp}^{(N-1)}$ as R_N . For N > 2 during one drive cycle a trajectory after transient motion enters and leaves the regions R_1 and R_N once while twice the other regions. Denoting $T_{\rm MR}^{(i)}$ as the mean residence time in the ith region then at $D = D_{\rm MAX}$

$$T_{\text{MR}}^{(1)} + 2\sum_{i=2}^{N-1} T_{\text{MR}}^{(i)} + T_{\text{MR}}^{(N)} = T.$$
 (5.32)

For each fixed value of N the mean residence times in each of the N regions are all the same and $T_{MR} = T/[2(N-1)]$. It is possible to realize mean residence time based signal detection. For details see [20–22].

5.6 Comparison Between Stochastic and Vibrational Resonances

Although the stochastic and vibrational resonances profiles are similar, there are characteristic differences between them. Some of them are listed below.

- 1. The noise effect in stochastic resonance of a system is described by a stochastic differential equation, whereas the high-frequency induced vibrational resonance is described by a deterministic equation of motion.
- 2. Some kind of bistability is necessary to realize stochastic resonance. In contrast to this, vibrational resonance can occur even in a monostable nonlinear systems. Both resonances cannot occur in a linear system.

- 3. Noise driven bistable and multistable systems are generally found to show only a single resonance. Multiple vibrational resonance can occur even in certain monostable systems.
- 4. In stochastic resonance the noise changes both the effective stiffness and the damping factor of the system, whereas in the vibrational resonance the high-frequency force changes only the effective stiffness.
- 5. The mechanism of stochastic resonance is the same in both overdamped and underdamped systems. The mechanism of vibrational resonance is different in overdamped and underdamped systems. In the overdamped systems, vibrational resonance always occur at the bifurcation of the equilibrium point about which slow oscillations occur. In the underdamped systems, the response amplitude is minimum at the bifurcation point and resonance occurs when the resonant frequency of the slow oscillation matches with the low-frequency of the input signal or it is locally minimum.
- 6. In the stochastic resonance, at the resonance there is a periodic switching between the bistable states or the potential wells. Cross-well motion is not a precursor for vibrational resonance.
- 7. In a periodic potential system, stochastic resonance is found only for the input signal frequency, much higher than the natural frequency of the system at the bottom of the well. In a periodic potential system, the response amplitude Q(g) (where g is the amplitude of the high-frequency input signal) in the presence of a biharmonic signal shows number of resonance peaks and is always greater than Q(g=0) if the resonant frequency (ω_r) is less than the natural frequency of the system at the bottom of the well. When ω_r is greater than the natural frequency, then there are numerous resonance peaks but Q(g) is always lower than Q(g=0). In both cases, Q never decays to zero and approach a limiting nonzero value, even in the limit of $g \to \infty$.
- 8. In the case of noise-induced resonance, the motion of the system can be chaotic. In the vibrational resonance, at the resonance the motion of the system is nonchaotic and it is periodic for rational values of ω/Ω and quasiperiodic for irrational values of ω/Ω .
- 9. In an excitable system at both stochastic and vibrational resonances, the mean waiting time of the system in the neighbourhood of the equilibrium point between two consecutive firings is T/2, where T is the period of the input periodic signal.
- 10. Both resonances are possible with aperiodic input signals.

5.7 Concluding Remarks

There are few rich features of vibrational resonance and stochastic resonance in the pendulum system and the modified Chua's circuit model equation. In the case of vibrational resonance the stability of the equilibrium points around which slow oscillations occur is altered when the control parameter g is varied. In the conventional vibrational resonance, Q(g) decays to zero for large values of g. Different from this, in the above two systems Q profile displays multiple resonance peaks and Q(g) approaches a limiting nonzero value for large values of g. All the features of vibrational resonance in the pendulum system are explained by the theoretical approach. It has been shown that the number of resonance is equal to the number of breakpoints. An interesting feature of the Chua's circuit is that the number of breakpoints in the characteristic function can be easily varied. Thus, the number of resonances can be easily varied by varying the number of breakpoints.

Regarding the noise-induced resonance, for the modified Chua's circuit system with a number of equilibrium points N ranging from 2 to 20, for each fixed value of N, the quantity SNR is found to be maximum at an optimum noise intensity (D_{MAX}) . D_{MAX} increases with N, while the maximum value of SNR at D_{MAX} (denoted as SNR_{MAX}) increases with N, becomes a maximum at N=6 and then decreases. For each fixed value of N (2 to 20) at resonance almost periodic switching between scroll orbits occur. The mean residence time T_{MR} on a scroll orbit at resonance $(D=D_{\text{MAX}})$ decreases with N. Further, $T_{\text{MR}}(D_{\text{MAX}}) = T/[2(N-1)]$ where $T=2\pi/\omega$ and ω is the frequency of the input periodic signal. Because the nonlinearity in the circuit is a symmetric saw-tooth function, T_{MR} on each scroll is the same.

References

- 1. Y.W. Kim, W. Sung, Phys. Rev. E 57, R6237 (1998)
- 2. J. Kallunki, M. Dube, T. Ala-Nissila, J. Phys. Condens. Matter 11, 9841 (1999)
- 3. C. Nicolis, Phys. Rev. E 82, 011139 (2010)
- 4. S. Saika, A.M. Jayannavar, M.C. Mahato, Phys. Rev. E 83, 061121 (2011)
- 5. S. Rajasekar, K. Abirami, M.A.F. Sanjuan, Chaos 21, 033106 (2011)
- 6. M. Borromeo, F. Marchesoni, Phys. Rev. E 73, 016142 (2006)
- 7. M. Borromeo, F. Marchesoni, Phys. Rev. Lett. 99, 150605 (2007)
- A. Wickenbrock, P.C. Holz, N.A. Abdul Wahab, P. Poonthong, D. Cubero, F. Renzoni, Phys. Rev. Lett. 108, 020603 (2012)
- 9. R.N. Madan, Chua's Circuit: A Paradigm for Chaos (World Scientific, Singapore, 1993)
- L. Fortuna, M. Frasca, M.G. Xibilia, Chua's Circuit Implementations: Yesterday, Today and Tomorrow (World Scientific, Singapore, 2009)
- 11. R. Kilic, A Practical Guide For Studying Chua's Circuits (World Scientific, Singapore, 2010)
- 12. S. Yu, W.K.S. Tang, G. Chen, Int. J. Bifurcation Chaos 17, 3951 (2007)
- 13. G.Q. Zhong, K.F. Man, G. Chen, Int. J. Bifurcation Chaos 12, 2907 (2002)
- S. Yu, J. Lu, H. Leung, G. Chen, IEEE Trans. Circuits Syst. I Fundam. Theory Appl. 52, 1459 (2005)
- 15. J. Lu, G. Chen, Int. J. Bifurcation Chaos 16, 775 (2006)
- 16. E. Campos-Canton, J.G. Barajas-Ramirez, G. Solis-Perales, R. Femat, Chaos 20, 1 (2010)
- 17. A. Boukabou, B. Sayoud, H. Boumaiza, N. Mansouri, Int. J. Bifur. Chaos 19, 3813 (2009)
- G. Sakthivel, S. Rajasekar, K.T. Thamilmaran, S.K. Dana, Int. J. Bifurcation Chaos 22, 1250004 (2012)
- 19. S. Arathi, S. Rajasekar, J. Kurths, Int. J. Bifurcation Chaos 23, 1350132 (2013)
- 20. L. Gammaitoni, A.R. Bulsara, Phys. Rev. Lett. 88, 230601 (2002)
- A.R. Bulsara, C. Seberino, L. Gammaitoni, M.F. Karlson, B. Lundqvist, J.W.C. Robinson, Phys. Rev. E 67, 016120 (2003)
- 22. A. Dari, L. Bosi, L. Gammaitoni, Phys. Rev. E 81, 011115 (2010)

Chapter 6 Nonlinear and Vibrational Resonances in Time-Delayed Systems

When the state of a system at time t depends on its state at a shifted earlier time, say, $t-\alpha$, then a time-delayed feedback term is introduced in the equation of motion of the system. The feedback can be linear or nonlinear. Time-delayed phenomena are ubiquitous in many nonlinear systems due to a finite propagation time in biological networks, finite reaction times, memory effects, etc. [1–4]. On the other hand, in a variety of physical, engineering and biological systems the time-delayed coupling is inevitable because of finite propagation time of transport of information and energy [5–13].

A first-order delay differential equation is of the form

$$\dot{x} = F(t, x(t), x(t - \alpha_i)), \tag{6.1}$$

where $\alpha_i > 0$, $i = 1, 2, \cdots$ are delay times. The time-delays α_i can be of different types depending upon the nature of the sources of the time-delay. In the nonlinear dynamics literature the effect of the following types of time-delay is investigated in a variety of nonlinear systems [4]:

- 1. A single constant delay: $\alpha_i = \alpha = a$ constant, i = 1.
- 2. Multiple time-delay: $\alpha_i = i\alpha$, $\alpha = \text{a constant}$, $i = 1, 2, \dots, m$. An example is $F(x(t \alpha_i)) = \frac{1}{m} \sum_{i=1}^{m} x(t i\alpha)$.
- 3. Integrative time-delay: A delay term of this kind is represented as $\langle x \rangle_{\alpha} = \frac{1}{\alpha} \int_{-\alpha}^{\alpha} x(t') dt'$.
- 4. Distributive time-delay: An example is $\int_0^\infty G(\alpha)x(t-\alpha) \, d\alpha$ where G in the case of gamma distributed delay is $\alpha^{p-1}a^p\mathrm{e}^{-a\alpha}/\Gamma(p)$ with p and a>0.
- 5. Time-dependent delay: $\alpha(t) = a + bt$ or $a + b\sqrt{t}$ with $\alpha < t$.

- 6. State-dependent delay: $\alpha = F(x(t))$. An example is $\alpha(x(t)) = |x(t)|$.
- 7. Random delay: $\alpha = |\xi(t)|$ where $\xi(t)$ is, for example, Gaussian random numbers with mean 0 and variance σ^2 .

Study of various nonlinear phenomena in time-delayed systems has received a great interest. Time-delayed nonlinear systems are found to show interesting dynamical phenomena such as novel bifurcations [14, 15], amplitude death [16], strange nonchaotic attractors [17], hyperchaos [18], stochastic dynamics [19–21], excitation regeneration [22], re-entrance phenomena [23, 24], patterns [25], improvement of synchronization [26], destabilization of synchronous states [27], intermittent transition to synchronization [28, 29], travelling waves [30] and generation of chaotic radiation in a travelling wave tube amplifier [31]. Stochastic resonance has been studied in certain nonlinear systems with time-delay [32–38]. Coherence resonance, a resonance dynamics in the absence of an external periodic force [39] has also been analysed in a time-delayed system. The effect of time-delay has been studied experimentally in the Belousov–Zhabotinsky reaction [40, 41]. Numerical evidence for multiple vibrational resonance induced by time-delayed feedback in overdamped uncoupled and coupled bistable systems [42, 43] has been also reported.

The main goal of the present chapter is to explore the effect of constant and multiple time-delays on vibrational resonance. Before that, it is noteworthy to point out that time-delay is ubiquitous in dynamical systems. We choose the Duffing oscillator as a reference model for all our analysis in this chapter. In certain physical and biological systems, local information is also used in signal amplification. Thus, it is important to analyse the possibility of improving the response of a single system by means of time-delayed feedback signals. Therefore, before investigating the occurrence of vibrational resonance in a time-delayed dynamical system, the enhancement of response of a system in the presence of single periodic force and a time-delayed feedback will be explored. Next, absence of vibrational resonance in a linear system with time-delayed feedback will be shown. Then, the effect of single and multiple time-delay on vibrational resonance in Duffing oscillator will be analysed. Finally, the occurrence of vibrational resonance in the presence of certain other types of time-delayed feedback will be presented.

6.1 Time-Delay is Ubiquitous

Let us enumerate some of the notable examples of time-delay in different branches of science.

1. Propagation delays are common in networks [5], laser arrays [6–8], electronic circuits [9], neural systems [10–12], high-speed milling and optical and optoelectronic circuits.

- 2. In ecological systems, time-delay arises when the gestation or incubation times depend on the variations of the external environment and living conditions due to climate and weather changes [13, 44–46]. In a population growth delay may arise due to age structure, for example, in view of time spent in a larval stage before growing into an adult.
- 3. Typical examples of systems with delays are given by maturation times [46], hydrodynamic problems [47], chemical surface reactions [48] and feedback regulated voltage-controlled oscillators [49, 50].
- 4. It is noteworthy to mention that delayed self-communication is of great significance because of its regulatory mechanism in nature and technology [51, 52]. Examples include excitable gene regulatory systems [53] where time-delay is inevitable due to the slow processing of transcription, translation and translocation, eye movements [54], human balance [55] and optically communicating semiconductor lasers [56].
- 5. In neural networks, communicating between the various areas may take place in delays ranging from few milliseconds to hundreds of milliseconds due to the finite speed of the transfer of data in the axons and dendrites and because of the processing latency in the synapses [57]. In neural systems, the source for a precise firing of basket cells in the hippocampus during Theta and Gamma rhythm is delayed feedback.
- 6. In epidemic model systems delays are introduced to take into account the time spent in various stages of the disease. This is because one does not recover from a disease instantaneously but only after some time.
- 7. Time-delay enters in the immune response models, if the outbreak of a disease caused by an infection is due to biological and environmental processes [58].
- 8. In a chemostat (a device used for the continuous culture of microorganisms) model, time-delay is introduced to account for the time required for conversion of nutrient consumed into viable cells [59].
- 9. Generally, diseases have the incubation period. In the case of malaria, the malaria parasites would undergo certain developments in the host before becoming infections. The period of this development, referred as the incubation period, normally varies from 10 to 21 days in mosquitoes. In rabies the incubation period ranges from 2 weeks to several months. In models of diseases, time-delay is included to account for the incubation period [60, 61].
- 10. In certain medical application, drugs are delivered via bubble transport. Microbubbles filled with a drug are utilized as a transporting agent for delivery and are sent towards a target by means of ultrasound forcing [62–64]. In order to study the behaviour of interacting microbubbles, it is necessary to take into account the speed of sound in the liquid. This will lead to a time-delay in induced pressure waves between bubbles.
- 11. In biochemical reactions, a source of time-delay can be the response time of the last step.
- 12. In coupled systems, coupling transmit one or more variables to the neighbours. Often the transmission time is larger than the internal time scales of the systems. In this case, coupling terms consisting of time-delayed variables are realistic.

Message decoding in chaos based communication systems would require chaos synchronization between multiple time-delayed transmitter and receiver systems. In high speed chaos-based communication systems [65] external cavity semiconductor lasers form an integral part. In practical applications such lasers may be subject to more than one optical reflection. This would lead to multiple time-delays. It has been pointed out that inclusion of several external cavities could provide higher security for such communication systems [66].

In nonlinear optics, periodic and chaotic outputs are realized by a delayed feedback [67]. Such delay induced dynamics is used to design practical systems including high-frequency and broadband optical chaotic oscillators for secure chaos communication [68] or high-speed random number generation [69] or to develop alternative imaging techniques [67]. Experimental evidences are reported for delayed recurrent excitations induced regulation of the structure of the interspike intervals in the presence of noise [70]. Delayed self-coupling in the study of the pacemaker cells of crayfish [71] is found to give rise bursting and high-frequency discharges with relatively long quiescent intervals [72].

6.2 Nonlinear Resonance in Time-Delayed Duffing Oscillator

The equation of motion of the Duffing oscillator with a time-delayed linear feedback term is given by

$$\ddot{x} + d\dot{x} + \omega_0^2 x + \beta x^3 + \gamma x(t - \alpha) = f \cos \omega t. \tag{6.2}$$

Applying a perturbation theory to Eq. (6.2), we obtain a nonlinear equation for the amplitude A of a period- $T(=2\pi/\omega)$ solution and analyze the effect of the time-delayed feedback on the amplitude A [73].

6.2.1 Theoretical Expression for Response Amplitude

Assume the solution of (6.1) as given by Eq. (1.3). Substitution of the solution (1.3) and the approximation of x^3 given by Eq. (1.4) in Eq. (6.2), neglecting \ddot{a} , \ddot{b} , $d\dot{a}$ and $d\dot{b}$ as they are assumed to be small and then equating the coefficients of $\sin \omega t$ and $\cos \omega t$ separately to zero lead to the equations [73]

$$\dot{a} = -\frac{b}{2\omega} \left[\omega^2 - \omega_0^2 - \frac{3}{4}\beta(a^2 + b^2) \right] - \frac{da}{2}$$

$$+ \frac{\gamma}{2\omega} \left[a(t - \alpha)\sin\omega\alpha + b(t - \alpha)\cos\omega\alpha \right], \tag{6.3a}$$

$$\dot{b} = \frac{a}{2\omega} \left[\omega^2 - \omega_0^2 - \frac{3}{4}\beta(a^2 + b^2) \right] - \frac{db}{2} + \frac{f}{2\omega}$$
$$-\frac{\gamma}{2\omega} \left[a(t - \alpha)\cos\omega\alpha - b(t - \alpha)\sin\omega\alpha \right]. \tag{6.3b}$$

Introducing the transformation

$$a(t) = A(t)\cos\theta(t), \quad b(t) = A(t)\sin\theta(t) \tag{6.4}$$

with $A^2 = a^2 + b^2$, Eq. (6.3) become

$$\dot{A} = -\frac{dA}{2} + \frac{f}{2\omega} \sin \theta + \frac{\gamma A(t - \alpha)}{2\omega} \left[\sin \omega \alpha \cos(\theta - \theta(t - \alpha)) - \cos \omega \alpha \sin(\theta - \theta(t - \alpha)) \right], \tag{6.5a}$$

$$A\dot{\theta} = \frac{A}{2\omega} \left[\omega^2 - \omega_0^2 - \frac{3}{4}\beta A^2 \right] + \frac{f}{2\omega} \cos \theta$$

$$-\frac{\gamma A(t - \alpha)}{2\omega} \left[\sin \omega \alpha \sin(\theta - \theta(t - \alpha)) + \cos \omega \alpha \cos(\theta - \theta(t - \alpha)) \right]. \tag{6.5b}$$

In the long time limit, after transient motion, the solution (1.3) is periodic with period- $2\pi/\omega$ provided a(t) and b(t) become constants as $t \to \infty$. The limiting values of a and b are related to the equilibrium points of Eq. (6.5). To determine the equilibrium points of (6.5), we set $\dot{A} = \dot{\theta} = 0$, $A(t - \alpha) = A(t) = A^*$, $\theta(t - \alpha) = \theta(t) = \theta^*$ and drop '*' in A and θ for simplicity. This gives

$$dA\omega - \gamma A \sin \omega \alpha = f \sin \theta \tag{6.6a}$$

and

$$A\left[\omega_0^2 - \omega^2 + \frac{3}{4}\beta A^2\right] + \gamma A\cos\omega\alpha = f\cos\theta. \tag{6.6b}$$

Elimination of $\sin \theta$ and $\cos \theta$ in Eq. (6.6) gives

$$A^{2} \left[\left(\omega_{0}^{2} - \omega^{2} + \frac{3}{4}\beta A^{2} + \gamma \cos \omega \alpha \right)^{2} + (d\omega - \gamma \sin \omega \alpha)^{2} \right] - f^{2} = 0.$$
 (6.7)

An interesting result is that in Eq. (6.7) the time-delay parameter α appears as the argument of sinusoidal functions. If $A(\alpha_0)$ with $0 < \alpha_0 < 2\pi/\omega$ is a solution of Eq. (6.7), then it is also the solution for $\alpha_n = \alpha_0 + n2\pi/\omega$, $n = 1, 2, \cdots$. That is, the response amplitude profile is periodic on α with period $2\pi/\omega$. There is no periodic term in (6.7) for $\gamma = 0$.

6.2.2 Response Amplitude A Versus the Control Parameters ω , γ and α

Now we analyse the variation of the response amplitude [73] with the parameters ω , γ and α . We fix the values of the parameters as $d=0.1, f=0.05, \omega_0^2=1$ and $\beta=2$. Figure 6.1 shows the theoretical response amplitude curve [calculated from Eq. (6.7)] for a range of fixed values of α for $\gamma=0.05$ and -0.05. The effect of positive and negative feedbacks can be clearly seen. The frequency-response curve varies periodically with respect to the control parameter α . In order to compare the theoretical response amplitude A with the numerical value A, we integrate (6.2) using the Euler method with integration step size 0.001. A very good agreement is observed between the theoretical prediction and the numerical simulation.

One of the interesting results, as shown in Fig. 6.1, is the amplification of the amplitude A for both positive and negative values of the feedback strength γ . This feature has practical applications in many systems including nonlinear circuits, lasers and population growth. When the implementation of a particular type of feedback is not advantageous, then one can choose the other form of the feedback. For instance, in nonlinear circuits, particularly in amplifiers, the positive (regenerative) feedback gives large gain factors but with less stable and largely distorted output. In contrast to this, in the case of negative (degenerate) feedback, the gain factor will be relatively lower. However, the output will become relatively more stable with less distortion. When it is desired to have a highly stable and less distorted output signal, one may prefer a negative feedback.

In Fig. 6.1, one can clearly observe hysteresis for a certain range of values of α and ω . In the hysteresis region, the system (6.2) with time-delayed feedback admits two stable period-T solutions and one unstable solution for a range of values of ω . For $\alpha=1.5$, the theory predicts this interval of ω as [1.15, 1.26], while in the numerical simulation this interval of ω is [1.15, 1.25]. For a certain range of values of α , the hysteresis phenomenon is suppressed. Figure 6.2 shows the two coexisting

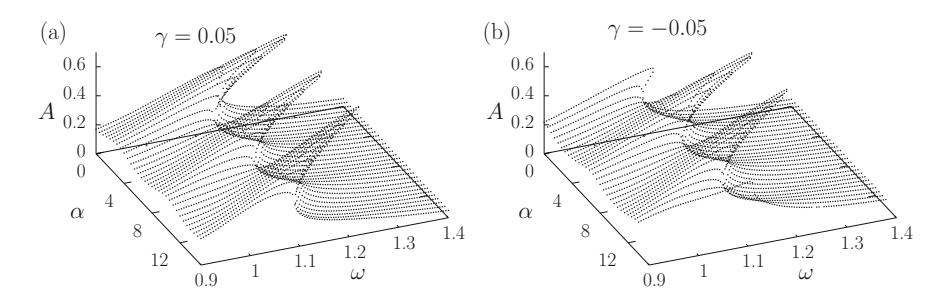
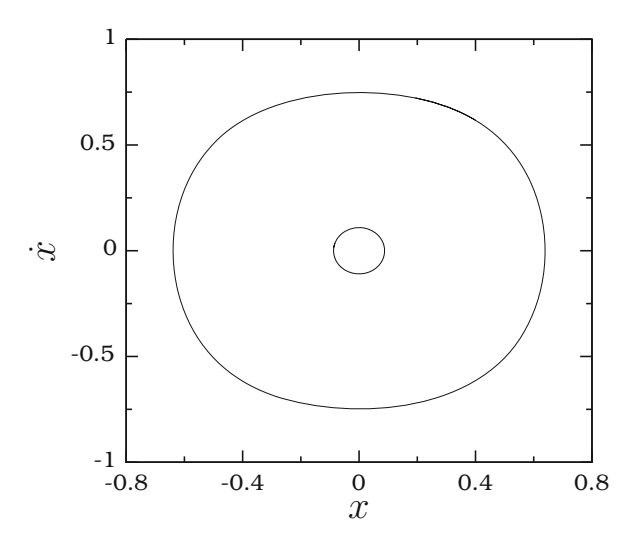


Fig. 6.1 Plot of the amplitude A of the period-T solution of the system (6.2) with a fixed time-delayed feedback $(x(t-\alpha))$ as a function of ω for several fixed values of α in the interval [0, 12] for (a) $\gamma = 0.05$ and (b) $\gamma = -0.05$. The values of the other parameters are d = 0.1, f = 0.05, $\omega_0^2 = 1$ and $\beta = 2$

Fig. 6.2 Phase portrait of the two coexisting periodic orbits of the system (6.2) with time-delayed feedback with $\gamma = 0.05$, $\alpha = 1.5$ and $\omega = 1.25$



period-T orbits of the system (6.2) for $\gamma = 0.05$, $\alpha = 1.5$ and $\omega = 1.25$. Time-delayed feedback is able to create an additional periodic orbit which otherwise would not exist. For example, when f = 0.03, $\gamma = 0.05$ and $\alpha = 1.5$ both large amplitude and small amplitude orbits coexist for $\omega \in [1.092, 1, 1465]$. In the absence of time-delayed feedback, only a small amplitude orbit is present in this interval of ω .

For a range of fixed values of α , we calculate the value of ω (denoted as ω_{max}) at which the response amplitude A of outer and inner orbits become maximum and the corresponding value of A (A_{max}) from the theoretical expression, Eq. (6.7), and also from the numerical solution of the system (6.2). The result is presented in Fig. 6.3 for $\gamma=0.05$ and -0.05. Both ω_{max} and A_{max} vary in a sinusoidal manner with the delay parameter α . The difference in the effect of $\gamma<0$ and $\gamma>0$ can be clearly seen in Fig. 6.3. In this figure one can observe that for a range of values of α the inner orbit is not present.

Next, we vary the delay parameter α for fixed values of ω . An interesting observation from the theoretical equation for A given by Eq. (6.7) is that it has a periodic dependence on α with period-T which is the period of the assumed periodic solution. For both $\gamma=0.05$ and -0.05 and for $\omega<1.092$ and $\omega>1.275$, the amplitude A is single-valued when α is varied. A multiple branch of A is found for $\omega\in[1.092,1.275]$. Figure 6.4a shows multiple branches of A and the path followed in the numerical simulation when α is varied in the forward and reverse directions for $\omega=1.13$ and $\gamma=0.05$.

For $\omega = 1.13$ the multiple branches of A occurs for $\alpha \in [1.53 + 2n\pi/\omega, 2.74 + 2n\pi/\omega]$, $n = 0, 1, \cdots$. When α is increased from a small value, a jump from a higher value of A to a lower value of A suddenly occurs at $\alpha = 2.74 + 2n\pi/\omega$. On the other hand, a jump occurs at $\alpha = 1.53 + 2n\pi/\omega$ from a lower value of A to a higher value of A when α is decreased from a higher value. We take the initial

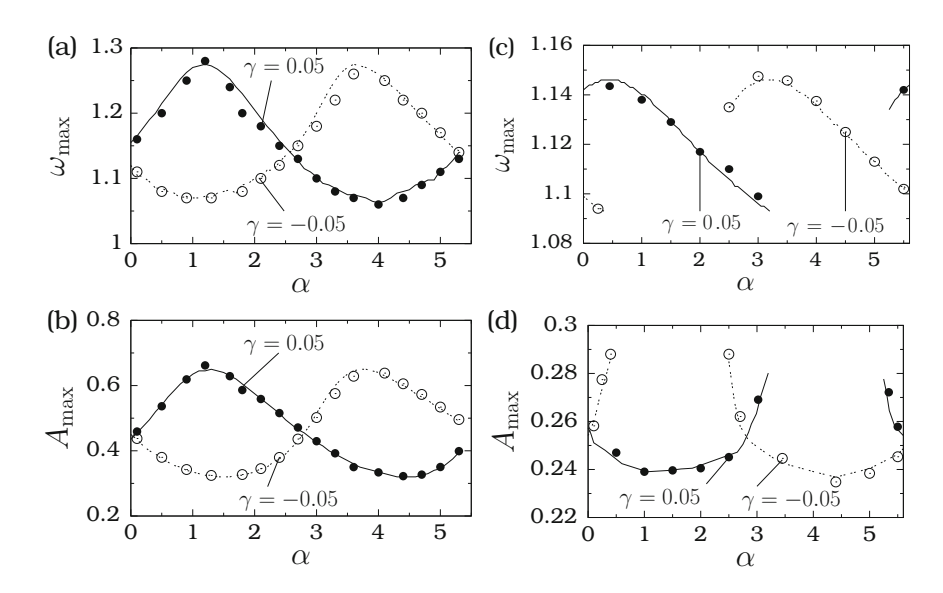


Fig. 6.3 Variation of (a) $\omega_{\rm max}$, at which the response amplitude A of a large orbit (outer orbit shown in Fig. 6.2) becomes maximum and (b) $A_{\rm max}$ of a large orbit with the time-delay parameter α for two fixed values of the strength γ of the fixed time-delayed feedback. The subplots (c) and (d) are for the small amplitude orbit (inner orbit shown in Fig. 6.2). Theoretically and numerically calculated values of $\omega_{\rm max}$ and $A_{\rm max}$ are represented by *lines* and *symbols*, respectively

condition x(t) = 0.5 and $\dot{x}(t) = 0$ for t = 0 to α , in the numerical simulation for the starting value of α . For all other values of α the solution $(x(t), \dot{x}(t))$ corresponding to the previous value of α is chosen as the initial condition. The two coexisting stable branches of A are smoothly connected by the unstable branch. None of these branches exist for the entire range of values of α .

Next, Fig. 6.4c where $\omega=1.22$, gives an example for a different situation where a stable branch (lower branch) exists over the entire range of values of α , while another stable branch occurs for a certain range of α . A consequence of this is that hysteresis cannot occur when α is either increased or decreased from a value. In the numerical simulation, we observe the solution corresponding to the lower branch when the initial condition for the present value of α is chosen as the solution of the previous α . However, if the initial condition is the same for all values of α , then a jump phenomenon can occur for certain set of initial conditions. For example, suppose the initial condition is chosen as $(x(t), \dot{x}(t)) = (0.6, 0)$ for $0 \le t \le \alpha$, then the upper branch of A in Fig. 6.4c is realized for the values of α for which it exists. When α is increased or decreased, a sudden jumping between the upper and lower branches occurs at $\alpha = 0.57 + 2n\pi/\omega$ and $1.89 + 2n\pi/\omega$, $n = 0, 1, \cdots$ as depicted in Fig. 6.4c. This type of behaviour is not found in the Duffing oscillator in absence of time-delay. That is, hysteresis can be suppressed by an appropriate time-delayed feedback. The influence of time-delayed feedback with $\gamma = -0.05$ is shown in

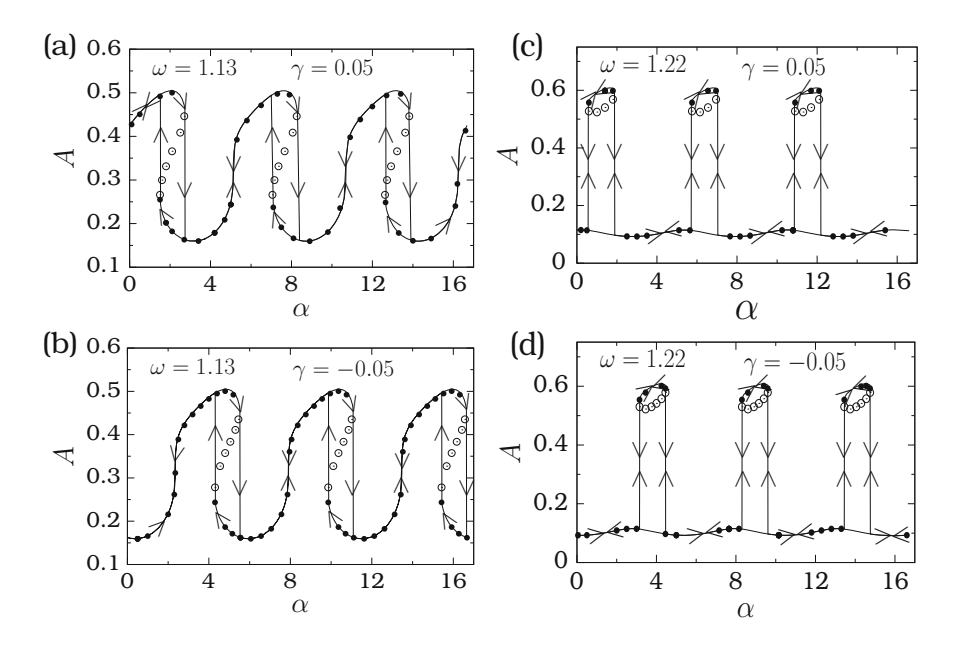


Fig. 6.4 Response amplitude versus the delay parameter α for two set of values of ω and γ . In the subplots (a) and (b) where $\omega=1.13$ different paths are followed when α is increased from 0 and decreased from a large value. In the subplots (c) and (d) where $\omega=1.22$ A follows the same path when α is varied in the forward and backward directions. *Continuous lines* denote the numerical simulation. *Solid* and *open circles* represent the theoretical A in the stable and unstable branches, respectively, of the response curve. A is periodic with period $2\pi/\omega$

Figs. 6.4b, d. These figures can be compared with Figs. 6.4a, c corresponding to the case $\gamma = 0.05$.

6.3 Resonance in a Linear System with Time-Delayed Feedback

This section considers both an underdamped and an overdamped linear system with linear time-delayed feedback and driven by two periodic forces. The equation of motion of the underdamped linear system with a linear time-delayed feedback is given by

$$\ddot{x} + d\dot{x} + \omega_0^2 x + \gamma x(t - \alpha) = f \cos \omega t + g \cos \Omega t, \qquad (6.8)$$

where $\Omega \gg \omega$, $\omega_0^2 > 0$ and d > 0. $\alpha > 0$ is the time-delayed parameter and γ is the strength of the feedback term. The general solution of Eq. (6.8) for f = g = 0 is not known. Equation (6.8) with $f = g = \gamma = 0$ is a damped linear system. Its

equilibrium point $(x^*, \dot{x}^*) = (0, 0)$ is stable. When f = g = 0 and $\gamma \neq 0$, Eq. (6.8) exhibits damped or periodic or growing oscillations depending upon the values of γ and α [4]. In the limit $t \to \infty$ we seek the solution of Eq. (6.8) in the form

$$x(t) = A_{\omega} \cos(\omega t + \phi_{\omega}) + A_{\Omega} \cos(\Omega t + \phi_{\Omega}). \tag{6.9a}$$

The unknowns A_{ω} and ϕ_{ω} are determined as

$$A_{\omega} = \frac{f}{\sqrt{S_{\omega}}}, \ S_{\omega} = \left[\left(\omega_0^2 - \omega^2 \right)^2 + \gamma \cos \omega \alpha \right]^2 + \left[-d\omega + \gamma \sin \omega \alpha \right]^2,$$
(6.9b)

$$\phi_{\omega} = \tan^{-1} \left[\frac{-d\omega + \gamma \sin \omega \alpha}{\omega_0^2 - \omega^2 + \gamma \cos \omega \alpha} \right]. \tag{6.9c}$$

Replacement of ω and f by Ω and g, respectively, in Eqs. (6.9b) and (6.9c) gives A_{Ω} , S_{Ω} and ϕ_{Ω} . In the linear system, the frequencies of the output are the same as those at the input driving force. Changes take place only in the magnitudes and phase factors of the frequency components.

As f(g) increases $A_{\omega}(A_{\Omega})$ also increases. Resonance does not occur at the frequencies ω or Ω when f or g is varied from a small value. Thus, there is no vibrational resonance in the linear system with time-delayed feedback. However, when α is varied, a resonance occurs at the frequency ω . The condition for resonance $\frac{dS}{d\alpha} = 0$ gives the value of α at which resonance occurs:

$$\alpha_{\rm R}(\omega) = \frac{1}{\omega} \tan^{-1} \left(\frac{d\omega}{\omega^2 - \omega_0^2} \right) \,.$$
 (6.10)

 A_{ω} becomes maximum at $\alpha = \alpha_{\rm R}$.

For the overdamped linear system

$$\dot{x} + \omega_0^2 x + \gamma x(t - \alpha) = f \cos \omega t + g \cos \Omega t \tag{6.11}$$

the solution in the limit of $t \to \infty$ is given by Eq. (6.9a) with

$$A_{\omega} = \frac{f}{\sqrt{S_{\omega}}}, \quad S_{\omega} = (\omega_0^2 + \gamma \cos \omega \alpha)^2 + (-\omega + \gamma \sin \omega \alpha)^2, \quad (6.12a)$$

$$\phi_{\omega} = \tan^{-1} \left(\frac{-\omega + \gamma \sin \omega \alpha}{\omega_0^2 + \gamma \cos \omega \alpha} \right) . \tag{6.12b}$$

 A_{Ω} and ϕ_{Ω} are obtained from Eq. (6.12) by replacing f and ω by g and Ω , respectively. Does vibrational resonance occur in the overdamped system?

6.4 Vibrational Resonance in an Underdamped and Time-Delayed Duffing Oscillator

Consider the time-delayed underdamped Duffing oscillator driven by the biharmonic force given by

$$\ddot{x} + d\dot{x} + \omega_0^2 x + \beta x^3 + \gamma x(t - \alpha) = f \cos \omega t + g \cos \Omega t. \tag{6.13}$$

In this section first a theoretical expression for the response amplitude Q in the presence of time-delay feedback in the underdamped Duffing oscillator will be obtained. Using this expression, the occurrence of vibrational resonance in both the double-well and the single-well cases [74] will be analysed.

6.4.1 Theoretical Expression for the Response Amplitude Q

Seeking the solution of Eq. (6.13) for $\Omega \gg \omega$ as $x = X(t) + \psi(t, \tau = \Omega t)$ gives

$$\ddot{X} + d\dot{X} + (\omega_0^2 + 3\beta \langle \psi^2 \rangle)X + \beta(X^3 + \langle \psi^3 \rangle) + \gamma X(t - \alpha)$$

$$+3\beta X^2 \langle \psi \rangle = f \cos \omega t,$$
(6.14)

$$\ddot{\psi} + d\dot{\psi} + \omega_0^2 \psi + 3\beta X^2 (\psi - \langle \psi \rangle) + 3\beta X (\psi^2 - \langle \psi^2 \rangle)$$

+ \beta(\psi^3 - \langle \psi^3 \rangle) + \gamma \psi (\tau - \Omega \alpha) = g \cos \Omega t, (6.15)

where $\langle \psi^n \rangle = (1/2\pi) \int_0^{2\pi} \psi^n d\tau$. Neglecting the nonlinear terms in Eq. (6.15), the solution of the linear version in the limit $t \to \infty$ is $\psi = (g/\mu) \cos(\tau + \phi)$ where

$$\mu^2 = \left(\omega_0^2 - \Omega^2 + \gamma \cos \Omega \alpha\right)^2 + \left(-d\Omega + \gamma \sin \Omega \alpha\right)^2 \tag{6.16a}$$

and

$$\phi = \tan^{-1} \left(\frac{-d\Omega + \gamma \sin \Omega \alpha}{\omega_0^2 - \Omega^2 + \gamma \cos \Omega \alpha} \right). \tag{6.16b}$$

For a fixed value of γ , the quantity μ varies periodically with α with period $2\pi/\Omega$. In absence of time-delay $\mu \approx \Omega^2$. The obtained solution for ψ gives $\langle \psi \rangle = 0$, $\langle \psi^2 \rangle = g^2/(2\mu^2)$ and $\langle \psi^3 \rangle = 0$. Now, Eq. (6.14) becomes [42]

$$\ddot{X} + d\dot{X} + C_1 X + \beta X^3 + \gamma X(t - \alpha) = f \cos \omega t, \tag{6.17a}$$

where

$$C_1 = \omega_0^2 + \frac{3\beta g^2}{2\mu^2}. (6.17b)$$

When f = 0, the equilibrium points of Eq. (6.17) are

$$X_0^* = 0, \quad X_{\pm}^* = \pm \sqrt{-\frac{C_1 + \gamma}{\beta}}$$
 (6.18)

Slow oscillations occur around these equilibrium points.

Next, consider the deviation Y of X from X^* and obtain

$$\ddot{Y} + d\dot{Y} + \omega_{\rm r}^2 Y + 3\beta X^* Y^2 + \beta Y^3 + \gamma Y(t - \alpha) = f \cos \omega t, \qquad (6.19a)$$

where

$$\omega_{\rm r}^2 = C_1 + 3\beta X^{*2}. (6.19b)$$

For the choice $f \ll 1$, $|Y| \ll 1$ and hence the nonlinear terms in Eq. (6.19a) can be neglected. Then its solution in the limit $t \to \infty$ is $A_L \cos(\omega t + \Phi)$ where $A_L = f/\sqrt{S}$,

$$S = \left[\omega_{\rm r}^2 - (\omega^2 - \gamma \cos \omega \alpha)\right]^2 + \left[-d\omega + \gamma \sin \omega \alpha\right]^2 \tag{6.20}$$

and

$$\Phi = \tan^{-1} \left[\frac{-d\omega + \gamma \sin \omega \alpha}{\omega_{\rm r}^2 - (\omega^2 - \gamma \cos \omega \alpha)} \right]. \tag{6.21}$$

An important observation from the theoretical expression of Q is that it has a periodic dependence on α with two periods $2\pi/\omega$ and $2\pi/\Omega$. In the expression for Q the quantity $\omega_{\rm r}^2$ has a periodic dependence on α with period $2\pi/\Omega$. In Q, there are two other terms containing α and are oscillating around γ with period $2\pi/\omega$. There is no periodic term in Q for $\gamma=0$. In the following, we proceed to analyse the occurrence of vibrational resonance separately for the double-well and the single-well cases.

6.4.2 Resonance Analysis in the Double-Well System

The potential of the unforced and undamped version of the system (6.13) for $\omega_0^2 < 0$, $\beta > 0$ and $\gamma = 0$ is of a double-well form. For simplicity, we choose the signs

of γ and ω_0^2 same. In the presence of damping, feedback and biharmonic force the equilibrium points around which slow oscillations take place are given by Eq. (6.18). There are three equilibrium points for $g < g_c$ where

$$g_{\rm c} = \left[\frac{2\mu^2}{3\beta} \left(|\omega_0^2| + |\gamma| \right) \right]^{1/2}$$
 (6.22)

while for $g > g_c$, X_0^* is the only real equilibrium point. The following results are obtained from dS/dg = 0 which is the condition for the response amplitude Q to be maximum at a value of g [74]:

Case 1: $|\gamma| < |\gamma_c| = \omega^2/(1 - \cos \omega \alpha)$

$$g_{\text{VR}}^{(1)} = \left[\frac{\mu^2}{3\beta} \left(2|\omega_0^2| + 3|\gamma| - \omega^2 - |\gamma| \cos \omega \alpha \right) \right]^{1/2} < g_c, \qquad (6.23a)$$

$$g_{\text{VR}}^{(2)} = \left[\frac{2\mu^2}{3\beta} \left(|\omega_0^2| + \omega^2 + |\gamma| \cos \omega \alpha \right) \right]^{1/2} > g_c.$$
 (6.23b)

Case 2: $|\gamma| > |\gamma_c| = \omega^2/(1 - \cos \omega \alpha)$

$$g_{\rm VR}^{(1)} = g_{\rm c}. \tag{6.24}$$

For the case 1 a resonance occurs at two values of g, one at a value of $g < g_c$ and another at a value of $g > g_c$. The response amplitude is the same at these two values of g. For the case 2 only one resonance is possible and it occurs at the bifurcation point g_c . Throughout the analysis, we fix the values of the parameters as d = 0.5, f = 0.1, $\omega = 1$ and $\Omega = 10$. For the double-well case we choose $\omega_0^2 = -1$ and $\beta = 0.1$. For the numerical calculation of Q, Eq. (6.13) is integrated numerically using the Euler method with time step 0.01. The time-delay parameter α takes always multiple values of 0.01.

In absence of time-delayed feedback ($\gamma=0$), the double-well system (6.13) exhibits two resonances for $2|\omega_0^2|>\omega^2$ and one for $2|\omega_0^2|<\omega^2$. For $\gamma\neq0$ the resonance condition is independent of ω_0^2 and depends on the parameters ω , γ and α . Even for $2|\omega_0^2|<\omega^2$ for a range of values of γ and α the system can be induced to show a double resonance. Figure 6.5a presents both theoretical and numerical g_{VR} as a function of γ for $\alpha=1$ and 3. A very good agreement is seen between the theory and the numerical simulation. For $\alpha=1$ and 3 the values of γ are -2.17534 and -0.50251, respectively. There are two resonances for $|\gamma|<|\gamma_c|$ and only one for $|\gamma|>|\gamma_c|$. For $|\gamma|<|\gamma_c|$, as γ increases from 0 two stable slow oscillations take place around γ and γ and γ are γ decreases from γ and γ and reaches the minimum value γ at γ and γ are γ and γ are γ and γ are γ and γ and γ and γ and γ are γ and γ and γ and γ and γ are γ and γ and γ and γ are γ and γ and γ and γ are γ and γ and γ and γ and γ and γ are γ are γ and γ and γ and γ and γ and γ are γ and γ and γ and γ are γ and γ and γ and γ and γ are γ and γ are γ and γ are γ and γ and

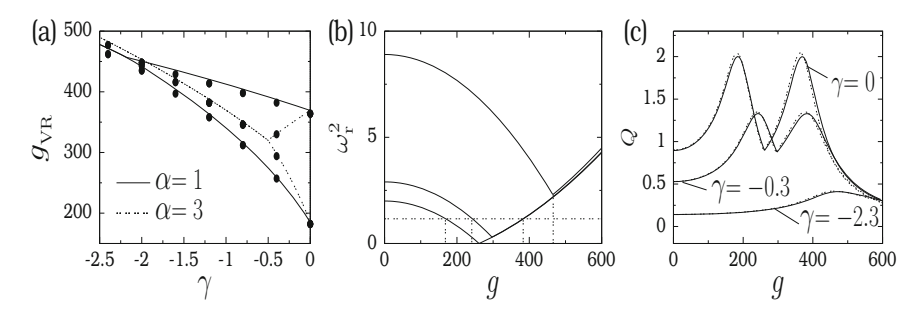


Fig. 6.5 (a) $g_{\rm VR}$ versus the parameter γ for the underdamped system (6.13) with the double-well potential case. The *solid circles* are the numerically computed $g_{\rm VR}$. The *lines* are theoretical $g_{\rm VR}$. The values of the parameters are d=0.5, $\omega_0^2=-1$, $\beta=0.1$, f=0.1, $\omega=1$ and $\Omega=10$. (b) Theoretical ω_r^2 versus the parameter g. From *bottom* to *top curves* the values of γ are 0, -0.3 and -2.3, respectively. The *horizontal dashed* line represents the value of $(\omega^2-\gamma\cos\omega\alpha)$. The *vertical dashed lines* mark the values of $g_{\rm VR}$. (c) Plot of the response amplitude Q as a function of Q for Q and Q and Q while the *dashed lines* are numerically calculated Q

at two values of g, namely at $g_{\rm VR}^{(1)}$ and $g_{\rm VR}^{(2)}$, $\omega_{\rm r}^2 = \omega^2 - \gamma \cos \omega \alpha$ (indicated by the horizontal dashed line in Fig. 6.5b) and hence Q becomes maximum with $Q_{\rm max} = 1/|-d\omega + \gamma \sin \omega \alpha|$. In Fig. 6.5c we notice the appearance of two resonances. In the absence of time-delayed feedback Q becomes maximum when $\omega_{\rm r} = \omega$ and the maximum value of Q is $1/(d\omega)$. For $\gamma = -0.3$ the theoretical values of $g_{\rm VR}^{(1)}$ and $g_{\rm VR}^{(2)}$ are 242.75 and 382.95 while the numerically computed values are 240.34 and 377.43, respectively.

For $|\gamma| > |\gamma_c|$ the value of ω_r^2 is always $> (\omega^2 - \gamma \cos \omega \alpha)$. However, it has a local minimum at $g = g_c$ and thus there occurs a resonance. These are shown in Fig. 6.5b, c for $\gamma = -2.3$. The noteworthy observation is that for $|\gamma| < |\gamma_c|$ the double resonance is due to matching of ω_r^2 with $\omega^2 - \gamma \cos \omega \alpha$, while the single resonance for $|\gamma| > |\gamma_c|$ is due to the local minimization of ω_r^2 . The single resonance always occurs at $g = g_c$ at which the effective potential of the slow variable undergoes a transition from the double-well to a single-well. Note that Q is minimum at $g = g_c$ for $|\gamma| < |\gamma_c|$.

In Fig. 6.5c for $\alpha=1$ the maximum value of the response amplitude is always lower than the case $\gamma=0$. $Q_{\max}(\gamma,g)=Q(\gamma,g_{\mathrm{VR}})>Q(\gamma=0,g_{\mathrm{VR}})$ can be realized for a range of values of α and γ , particularly for $|\gamma|<|\gamma_{\mathrm{c}}|$ and $\alpha\in[(2n-1)\pi/\omega,2n\pi/\omega],$ $n=1,2,\cdots$. Figure 6.6a shows the variation of $Q(g_{\mathrm{VR}})$ in (γ,α) parameter space for $\alpha\in[0,2\pi]$ with $\omega=1$. One can clearly see that $Q(\gamma,g_{\mathrm{VR}})>Q(\gamma=0,g_{\mathrm{VR}})$ for $\alpha\in[\pi,2\pi]$. Figure 6.6b is the three-dimensional plot of Q as a function of γ and q for q=3.5. For q=3.5 the value of q=3.5 the value of q=3.5 and q=3.5 for q=3.5 only one resonance occurs for $|\gamma|>0.51641$.

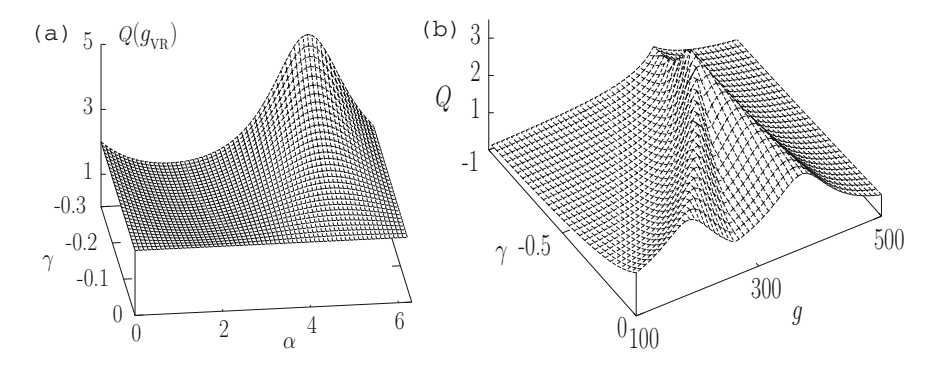


Fig. 6.6 (a) Variation of the maximum value of Q, $Q(g = g_{VR})$, as a function of γ and α for the double-well underdamped system. (b) Three-dimensional plot of Q versus the parameters γ and g for $\alpha = 3.5$

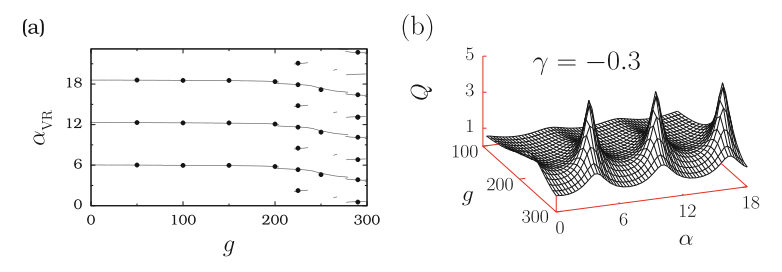


Fig. 6.7 (a) $\alpha_{\rm VR}$ versus the amplitude g of the high-frequency force for $\gamma=-0.3$. The system is the underdamped double-well system. *Continuous lines* and *solid circles* represent theoretically and numerically computed values of $\alpha_{\rm VR}$, respectively. (b) Periodic variation of Q with α for various values of g in the interval [100, 300] for $\gamma=-0.3$

The condition for a resonance to occur when the time-delay parameter α is varied is given by (from $dS/d\alpha = 0$)

$$(\omega_{\rm r}^2 - \omega^2) \,\omega_{\rm r\alpha}^2 + (\omega_{\rm r\alpha}^2 - d\omega^2) \,\gamma \cos \omega \alpha - \gamma \omega \,(\omega_{\rm r}^2 - \omega^2) \sin \omega \alpha = 0, \qquad (6.25)$$

where $\omega_{\rm r\alpha}^2={\rm d}\omega_{\rm r}^2/{\rm d}\alpha$. Analytical expressions for the roots of the above equation are difficult to obtain. However, the roots denoted as $\alpha_{\rm VR}$ can be determined numerically from Eq. (6.25). In Fig. 6.7a $\alpha_{\rm VR}<3\times2\pi/\omega$ are alone plotted. ($\alpha_{\rm VR}$ are periodic with period $2\pi/\omega$). For $\omega=1$ and $\Omega=10$ the ratio $\Omega/\omega=10$ is a rational number. The response amplitude Q is thus periodic in α with period $2\pi/\omega$. This is because the solution of the system (6.13) is periodic with respect to α with period $2\pi/\omega$. Suppose there are m values of $\alpha_{\rm VR}$ in the interval $[0,2\pi/\omega]$. Then, the other values of $\alpha_{\rm VR}>2\pi/\omega$ are given by

$$\alpha_{\text{VR}}^{(i+jm)} = \alpha_{\text{VR}}^{(i)} + j\frac{2\pi}{\omega}, \quad i = 1, 2, \dots, m; \quad j = 1, 2, \dots.$$
 (6.26)

Figure 6.7b presents numerical Q as a function of α and g. The periodicity of Q with respect to the time-delay parameter α can be clearly seen in this figure. Note that when g is varied, since in the expression for A_L or S only ω_r^2 depends on g, the variation of S is due to the variation of ω_r^2 and as pointed out earlier the resonance is due to either the matching of ω_r^2 with $\omega^2 - \gamma \cos \omega \alpha$ or local minimization of ω_r^2 . In contrast to this, when the delay parameter α is varied not only ω_r^2 varies but two other terms in S also vary with α . Consequently, the resonance is due to the local minimization of the quantity S.

6.4.3 Resonance Analysis in the Single-Well System

For ω_0^2 , $\beta > 0$ the potential V(x) of the Duffing oscillator has a single-well shape with a local minimum at x=0. Unlike the double-well system, the effective potential of the slow variable X remains as a single-well when the parameter g is varied. The equilibrium point around which slow oscillation occurs remains as $X_0^*=0$.

The resonance value of g, g_{VR} , is given by Jeevarathinam et al. [74]

$$g_{\rm VR} = \left[\frac{2\mu^2}{3\beta} \left(\omega^2 - \gamma \cos \omega \alpha - \omega_0^2\right)\right]^{1/2}$$
 (6.27a)

provided

$$\omega^2 - \gamma \cos \omega \alpha > \omega_0^2. \tag{6.27b}$$

In the double-well system a resonance is possible for all set of values of γ and α when g is varied. In contrast to this, in the single-well case a resonance is possible only for a set of values of γ and α for which the condition (6.27b) is satisfied. Further, in the double-well system two resonances are possible while in the single-well system at most one resonance is possible. The theoretical approach considered in the present work helps us to choose appropriate values of the parameters to realize vibrational resonance.

Figure 6.8a shows both theoretical and numerical $\alpha_{\rm VR}$ versus g for $\gamma=0.15$. $\alpha_{\rm VR}$ is periodic with period $2\pi/\omega$. For $\alpha\in[0,2\pi/\omega]$ resonance occurs at only one value of α for fixed values of g. In Fig. 6.7a, corresponding to the double-well system, a double resonance is found for a certain range of fixed values of g. The presence of only one resonance in Fig. 6.8a for $\alpha\in[0,2\pi/\omega]$ implies that the variation of μ^2 due to the terms $\gamma\sin\Omega\alpha$ and $\gamma\cos\Omega\alpha$ [see Eq. (6.16a)] is negligible and μ^2 can be approximated as $\mu^2\approx(\omega_0^2-\Omega^2)^2+d^2\Omega^2$. Then from Eq. (6.20) the expression for $\alpha_{\rm VR}$ is obtained as

$$\alpha_{\rm VR} = \frac{1}{\omega} \tan^{-1} \left(\frac{d\omega}{\omega^2 - \omega_{\rm r}^2} \right), \quad \omega_{\rm r}^2 = C_1$$
 (6.28)

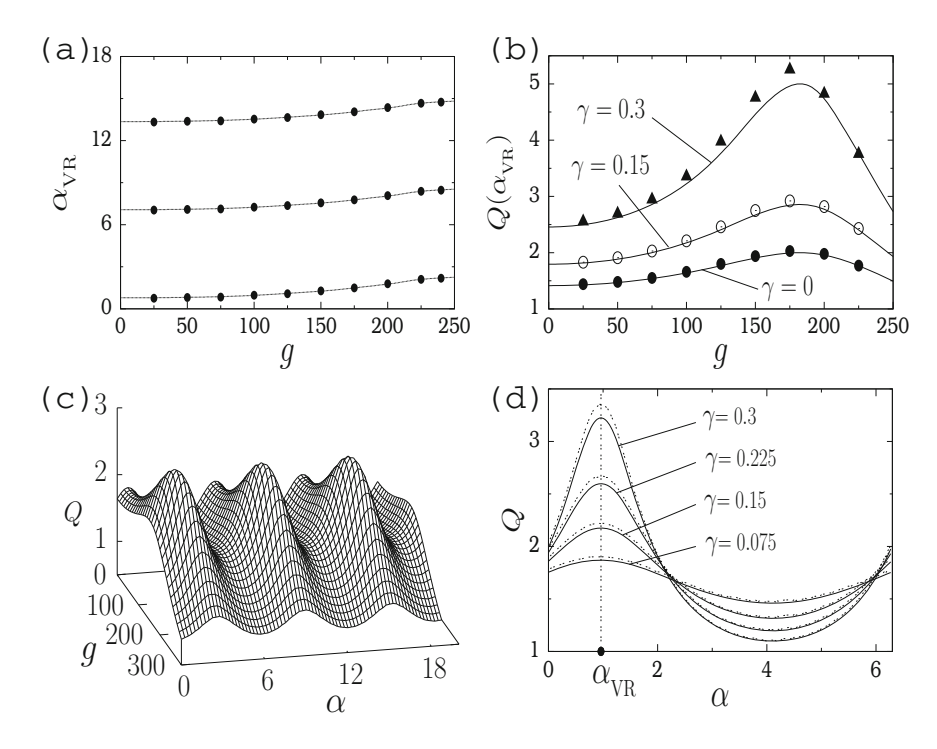


Fig. 6.8 (a) $\alpha_{\rm VR}$ versus g for the single-well underdamped system with $\gamma=0.15,\,d=0.5,\,\omega_0^2=0.5,\,\beta=0.1,\,\gamma=0.15,\,f=0.1,\,\omega=1$ and $\Omega=10$. Continuous lines and solid circles represent theoretically and numerically calculated values of $\alpha_{\rm VR}$, respectively. (b) Variation of $Q(\alpha_{\rm VR})$ with g for three values of γ . The continuous lines and symbols represent theoretically and numerically predicted values of Q, respectively. (c) Periodic variation of Q with Q for various values of Q for Q or Q or Q or Q or Q and Q and Q and Q and Q and Q or Q or Q and Q

and is independent of γ . This is confirmed by numerical simulation. Q versus α is plotted in Fig. 6.8d for g=100 and for few fixed values of γ . Q is maximum at the same value of α , however, its maximum value at resonance varies with γ .

6.5 Vibrational Resonance in an Overdamped Duffing Oscillator

In this section we analyze the occurrence of vibrational resonance in the overdamped system

$$\dot{x} + \omega_0^2 x + \beta x^3 + \gamma x(t - \alpha) = f \cos \omega t + g \cos \Omega t.$$
 (6.29)

The theoretical expression for the response amplitude Q is obtained as [74]

$$Q = \frac{1}{\sqrt{S}}, \quad S = (\omega_{\rm r}^2 + \gamma \cos \omega \alpha)^2 + (-\omega + \gamma \sin \omega \alpha)^2, \quad (6.30a)$$

where

$$\omega_{\rm r}^2 = C_1 + 3\beta X^{*2} \,, \quad C_1 = \omega_0^2 + \frac{3\beta g^2}{2\mu^2} \,,$$
 (6.30b)

$$\mu^2 = (\omega_0^2 + \gamma \cos \Omega \alpha)^2 + (-\Omega + \gamma \sin \Omega \alpha)^2. \tag{6.30c}$$

For $\omega_0^2 < 0$, $\gamma < 0$, $\beta > 0$ (double-well case) the critical value of g, g_c , below which three equilibrium points X_0^* , X_\pm^* exist and above which only one equilibrium point X_0^* exists is again given by Eq. (6.22) with μ^2 given by Eq. (6.30c). Suppose we vary g from zero. From the theoretical expression of Q (or S), the condition for Q to be maximum is $\omega_1^2 - |\gamma| \cos \omega \alpha = 0$. In absence of time-delay ($\gamma = 0$) resonance occurs when $\omega_1^2 = 0$. For $\gamma \neq 0$ and $\gamma = 0$, the slow motion is about $\gamma = 0$.

$$\omega_{\rm r}^2 = |\gamma| + \frac{3\beta}{\mu^2} (g_{\rm c}^2 - g^2), \quad g < g_{\rm c}$$
 (6.31)

while for $g > g_c$ it is about $X_0^* = 0$ and

$$\omega_{\rm r}^2 = |\gamma| + \frac{3\beta}{2\mu^2} (g^2 - g_{\rm c}^2), \quad g > g_{\rm c}.$$
 (6.32)

As g increases from zero, the value of $\omega_{\rm r}^2$ decreases from $2|\omega_0^2|+3|\gamma|$, becomes $|\gamma|$ at $g=g_{\rm c}$ and increases from $|\gamma|$ with further increase in g. $\omega_{\rm r}^2$ is always $\geq |\gamma|$. That is, $\omega_{\rm r}^2-|\gamma|\cos\omega\alpha$ never becomes zero except when $\alpha=2n\pi/\omega$, $n=0,1,2,\cdots$ and $g=g_{\rm c}$. For all other values of α even though $\omega_{\rm r}^2-|\gamma|\cos\omega\alpha$ does not vanish, this quantity becomes a minimum at $g=g_{\rm c}$ and hence a resonance at $g_{\rm VR}=g_{\rm c}$.

For the double-well case, we fix d=0.5, $\omega_0^2=-1$, $\beta=1$, $\gamma=-1$, f=0.1, $\omega=1$ and $\Omega=10$. Figure 6.9 shows $\alpha_{\rm VR}$ versus g for $\gamma=-1$. For small values of g there is only one value of $\alpha_{\rm VR}$. An example is given in Fig. 6.10a for g=1. The number of values of $\alpha_{\rm VR}$ increases with increase in g. In Fig. 6.10b, corresponding to g=8, multiple resonances is clearly seen. Resonance occurs at 10 values of $\alpha_{\rm VR}$ (in the interval $[0,2\pi/\omega]$). (However, $Q(\alpha_{\rm VR})>Q(\gamma=0)$ is found only at few values of $\alpha_{\rm VR}$). The response amplitude profile repeats in every $2\pi/\omega$ intervals of α . For g=12 (Fig. 6.10c) the number of resonances is doubled. At certain values of $\alpha_{\rm VR}$, the value of Q is considerably larger than $Q(\gamma=0)$. The enhancement of Q is reduced for higher values of g as shown in Fig. 6.10d for g=20. Above certain fixed values of g the resonance curve is modulated by the high frequency signal. The modulation period is not strictly $2\pi/\Omega$. For irrational values of the ratio Ω/ω , the response amplitude exhibits a quasiperiodic pattern.

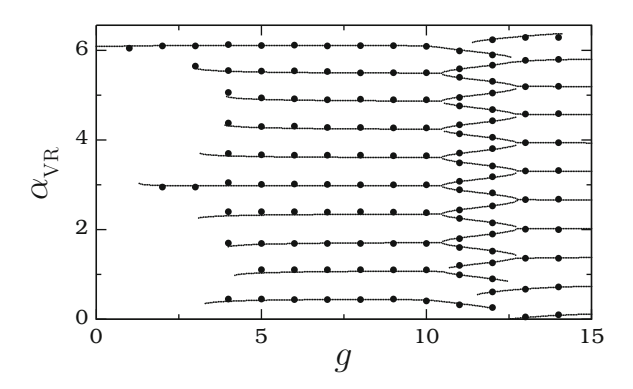


Fig. 6.9 $\alpha_{\rm VR}$ versus g for the overdamped double-well system with $\gamma=-1$. *Continuous lines* and *solid circles* represent theoretical and numerical values of $\alpha_{\rm VR}$, respectively

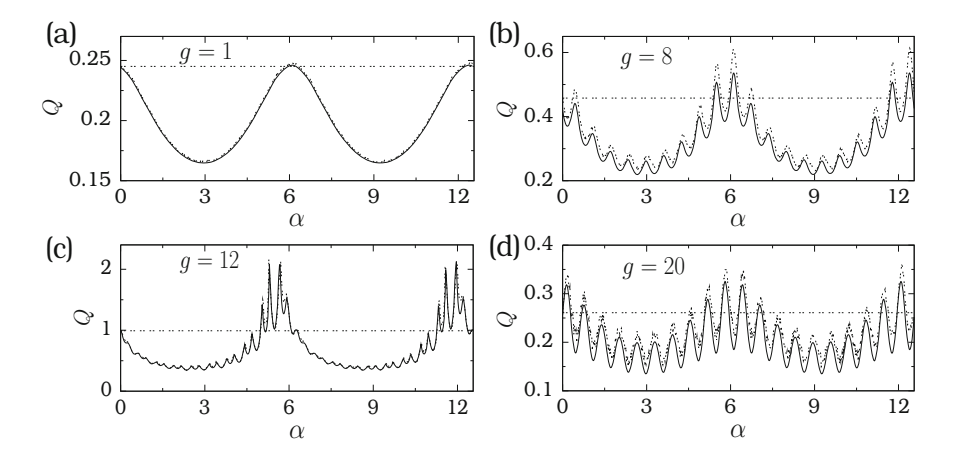


Fig. 6.10 Theoretical (represented by *continuous lines*) and numerical (represented by *dashed lines*) Q as a function of the delay parameter α for four fixed values of the parameter g. The system is the double-well overdamped system with $\gamma = -1$. The *horizontal dashed line* denotes the value of Q in absence of time-delayed feedback

Next, we consider the overdamped single-well system. Since $X_0^*=0$ is the only equilibrium point around which a slow motion occurs, $\omega_{\rm r}^2=C_1$ and it increases monotonically from ω_0^2 when g increases. $g_{\rm VR}$ is given by

$$g_{\rm VR} = \left[\frac{2\mu^2}{3\beta} \left(-\omega_0^2 + \gamma |\cos \omega \alpha|\right)\right]^{1/2},\tag{6.33a}$$

where

$$\alpha \in \left[\left(2n + \frac{1}{2} \right) \frac{\pi}{\omega}, \quad \left(2n + \frac{3}{2} \right) \frac{\pi}{\omega}, \right], \quad n = 0, 1, \dots$$
 (6.33b)

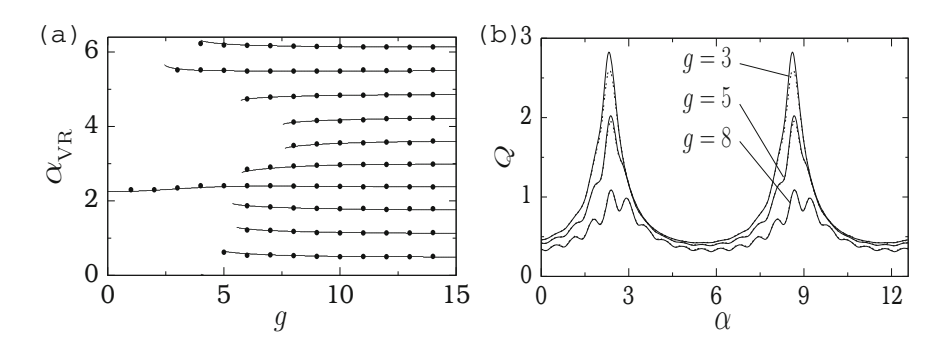


Fig. 6.11 (a) Plot of theoretical α_{VR} (represented by *continuous lines*) and numerical α_{VR} (*solid circles*) versus g for $\gamma = 1$. The system is the single-well overdamped system. (b) Q versus α . Theoretical and numerical values of Q are represented by *continuous* and *dashed lines*, respectively

and

$$\gamma > \gamma_{\rm c} = \frac{\omega_0^2}{|\cos \omega \alpha|}.\tag{6.33c}$$

In the double-well system there is no restriction on the values of ω_0^2 , ω , α and γ for resonance when g is varied. In the single-well system a resonance at a value of g given by (6.33a) occurs only for the parametric restrictions given by Eqs. (6.33b) and (6.33c). An important observation from Eq. (6.33a) is that in absence of time-delay the single-well system cannot exhibit a resonance when g (or Ω) is varied and Q decreases continuously with increase in g. But resonance can be induced by an appropriate time-delayed feedback.

Figure 6.11a presents both theoretically predicted and numerically computed values of $\alpha_{\rm VR} \in [0, 2\pi/\omega]$ for a range of values of g with $\gamma=1$. In Fig. 6.11b Q versus α is shown. In this system also $Q(\alpha)$ is periodic in α with period $2\pi/\omega$ for rational values of Ω/ω and quasiperiodic for irrational values of Ω/ω . In the interval $\alpha \in [0, 2\pi/\omega]$, a single resonance occurs for small values of g (as shown in Fig. 6.11b for g=3). A multiple resonance occur for higher values of g. This is shown in Fig. 6.11b for g=5 and g=5 an

6.6 Some Common Effects of Time-Delayed Feedback

The following common results are realized in the four systems, namely, the underdamped double-well and single-well systems and the overdamped double-well and single-well systems, when the time-delay parameter α is varied:

- There is no parametric restriction for resonance to occur.
- The resonance profile is periodic (quasiperiodic) for rational (irrational) ratio of Ω/ω.
- The number of resonances in the interval $0<\alpha<2\pi/\omega$ is a complicated function of the parameters of the systems.
- Resonance is due to the local minimization of the quantity S.
- Obtaining analytical expressions for α_{VR} and $Q_{max}(\alpha_{VR})$ are very difficult.

When the control parameter g is varied, the key results are the following:

1. Underdamped double-well system (6.13) ($\omega_0^2 < 0, \beta > 0$)

- At least one resonance and at most two resonances are possible. The number of resonances is independent of the parameters ω_0^2 and β .
- For $|\gamma| < |\gamma_c| = \omega^2/(1 \cos \omega \alpha)$ two resonances occur at the values of g given by Eq. (6.23) due to the matching of ω_r^2 with $\omega^2 \gamma \cos \omega \alpha$. $Q_{\text{max}} = 1/|-d\omega + \gamma \sin \omega \alpha|$ and is independent of the parameters ω_0^2 and β .
- For $|\gamma| > |\gamma_c|$ only one resonance is possible and it always occurs at $g = g_c$ given by Eq. (6.24) due to the local minimization of ω_r^2 and $Q_{\text{max}} = 1/\sqrt{S}$ where S is given by Eq. (6.20).

2. Underdamped single-well system (6.13) ($\omega_0^2 > 0, \beta > 0$)

• Only one resonance is possible and it occurs at the value of g given by Eq. (6.27a) provided $\omega^2 - \gamma \cos \omega \alpha > \omega_0^2$. The resonance is due to the matching of ω_r^2 with $\omega^2 - \gamma \cos \omega \alpha$ and $Q_{\text{max}} = 1/|-d\omega + \gamma \sin \omega \alpha|$.

3. Overdamped double-well system (6.29) ($\omega_0^2 < 0$, $\beta > 0$)

• One resonance is always possible and it occurs at $g = g_c$ [given by Eq. (6.24)] where the effective potential of the slow variable X changes from the doublewell to the single-well form. There is no restriction on the parameters ω_0^2 and β . For $\alpha = 2n\pi/\omega$, $n = 0, 1, \cdots$ the resonance is due to the matching of ω_r^2 with $|\gamma| \cos \omega \alpha$ and $Q_{\text{max}} = 1/\omega$. For $\alpha \neq 2n\pi/\omega$, $n = 0, 1, \cdots$ the resonance is due to the local minimization of ω_r^2 and

$$Q_{\text{max}} = \frac{1}{\sqrt{2\gamma^2(1-\cos\omega\alpha) + \omega^2 - 2\omega\gamma\sin\omega\alpha}}.$$
 (6.34)

4. Overdamped single-well system (6.29) ($\omega_0^2 > 0$, $\beta > 0$)

• Only one resonance is possible with $g_{\rm VR}$ given by Eq. (6.33a) for the parametric restrictions given by Eqs. (6.33b) and (6.33c). The resonance is due to the matching of $\omega_{\rm r}^2$ with $-\gamma\cos\omega\alpha$ and $Q_{\rm max}=1/|-\omega+\gamma\sin\omega\alpha|$.

6.7 Effect of Multi Time-Delayed Feedback

It is important to analyse the effect of multiple time-delays as it is a generalization of a single time-delay. There are some notable reports on multi time-delay systems. For example, the presence of two or three time-delayed feedback or coupling terms leads to stabilization of unstable fixed points and bifurcations [75–78], synchronization [79–81], pattern formation [82] and Hopf bifurcation and chaos [13]. Furthermore, dynamics of detritus-based ecosystem [83], seasonal growth in a prey-predator model [84, 85] and experimental study of properties of chaos synchronization in coupled optoelectronic oscillators [86] with more than one time-delay have been reported. Martinenghi et al. [87] proposed a photonic implementation of reservoir computing in which the wavelength of a tunable laser is treated as a dynamical variable with a multiple-delayed feedback topology.

In this section, we consider the Duffing oscillator with multi time-delayed feedback described by

$$\ddot{x} + d\dot{x} + \omega_0^2 x + \beta x^3 + \frac{\gamma}{L} \sum_{l=1}^{L} x(t - l\alpha) = f \cos \omega t + g \cos \Omega t , \qquad (6.35)$$

where L is the number of time-delayed feedback term and we explore the effect of multi time-delay on vibrational resonance [88].

The response amplitude Q is worked out to be $Q = 1/\sqrt{S}$ where

$$S = \left[\omega_{\rm r}^2 - \omega^2 + \frac{\gamma}{L} \sum_{l} \cos l\alpha \omega\right]^2 + \left[d\omega - \frac{\gamma}{L} \sum_{l} \sin l\alpha \omega\right]^2, \quad (6.36)$$

with $\omega_{\rm r}^2$ given by Eq. (6.19b) and μ^2 in Eq. (6.17b) is given by

$$\mu^{2} = \left[\omega_{0}^{2} - \Omega^{2} + \frac{\gamma}{L} \sum_{l} \cos l\alpha \Omega\right]^{2} + \left[d\Omega - \frac{\gamma}{L} \sum_{l} \sin l\alpha \Omega\right]^{2}. \quad (6.37)$$

Now we fix the values of the parameters as d=0.5, $\omega_0^2=-1$, $\beta=0.1$, f=0.1, $\omega=1$ and $\Omega=10$. Figure 6.12 shows both the theoretically and numerically computed response amplitude Q versus the control parameter g for L=1,2,3 and 5 for $\gamma=0.1$ and for two values of α . The result for $\gamma=0$ is also shown in this figure for demonstrating the influence of multi time-delayed feedback. In this figure for each value of L two values of α are chosen in such a way that for one value of it $Q_{\max}(\gamma)>Q_{\max}(\gamma=0)$ (the value of Q at resonance) while for the other value of it $Q_{\max}(\gamma)<Q_{\max}(\gamma=0)$.

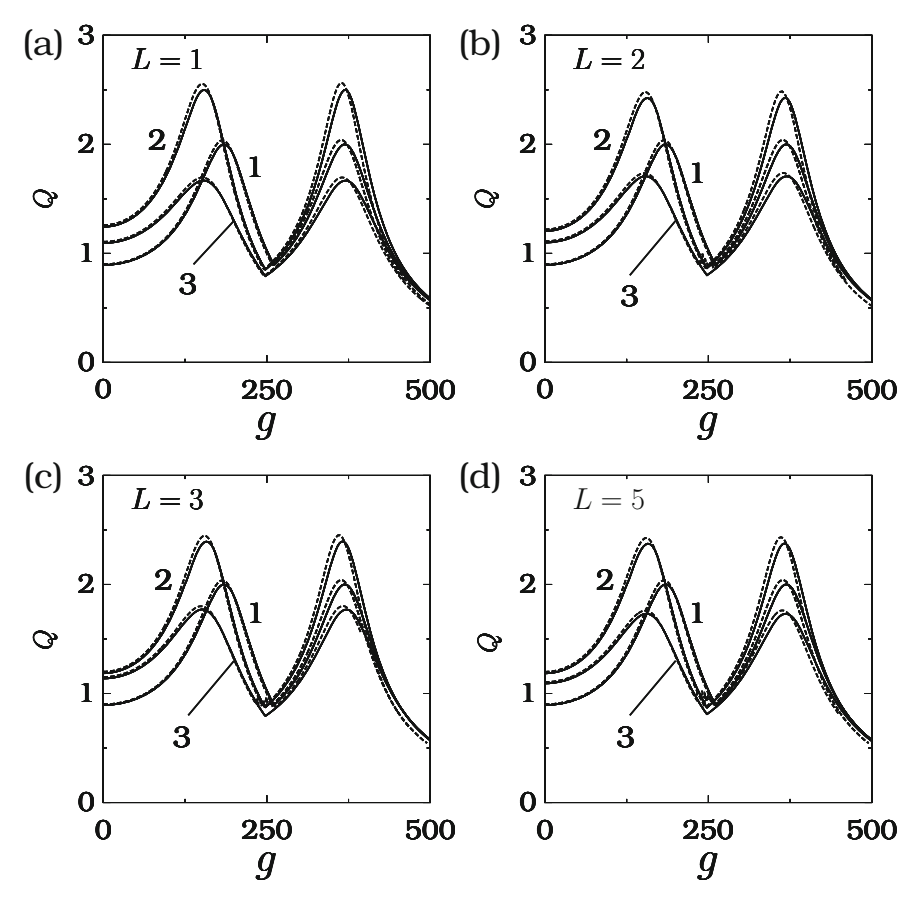


Fig. 6.12 Variation of Q with g for a fixed number of time-delayed feedback term with d=0.5, $\omega_0^2=-1$, $\beta=0.1$, f=0.1, $\omega=1$ and $\Omega=10$. In all the subplots, the curve 1 corresponds to $\gamma=0$. For the curves 2 and 3 the value of γ is 0.1. The *continuous* and *dashed lines* are the theoretically and numerically calculated values of Q, respectively. The values of α are: (a) curve $2(3)-\alpha=1.6(4.6)$. (b) curve $2(3)-\alpha=0.9(5.2)$. (c) curve $2(3)-\alpha=0.6(5.3)$. (d) curve $2(3)-\alpha=0.4(5.8)$

For $\gamma=0.1$ and $\alpha=2.6~Q_{\rm max}$ is >2 for odd values of L, while it is <2 for even values of L and the opposite result occurs for $\alpha=3.4$. In view of this, using the theoretical expression of Q, in $\gamma-\alpha$ parameter space let us identify the regions where $Q_{\rm max}(\gamma)>Q_{\rm max}(\gamma=0)$ for a few fixed values of L. Suppose we choose $\gamma\in[-0.5,0.5]$ and $\alpha\in[0,2\pi/\omega]$ with $\omega=1$. The result is shown in Figs. 6.13a-d. For both $\gamma<0$ and $\gamma>0$ Fig. 6.13 contains L filled bands where $Q_{\rm max}(\gamma)>Q_{\rm max}(\gamma=0)$. The width of the bands are unequal. The filled bands of $\gamma<0$ become the unfilled bands of $\gamma>0$. From the theoretical expression of Q the condition for enhanced response at resonance is $\gamma\sum_l\sin l\alpha\omega>0$. This condition

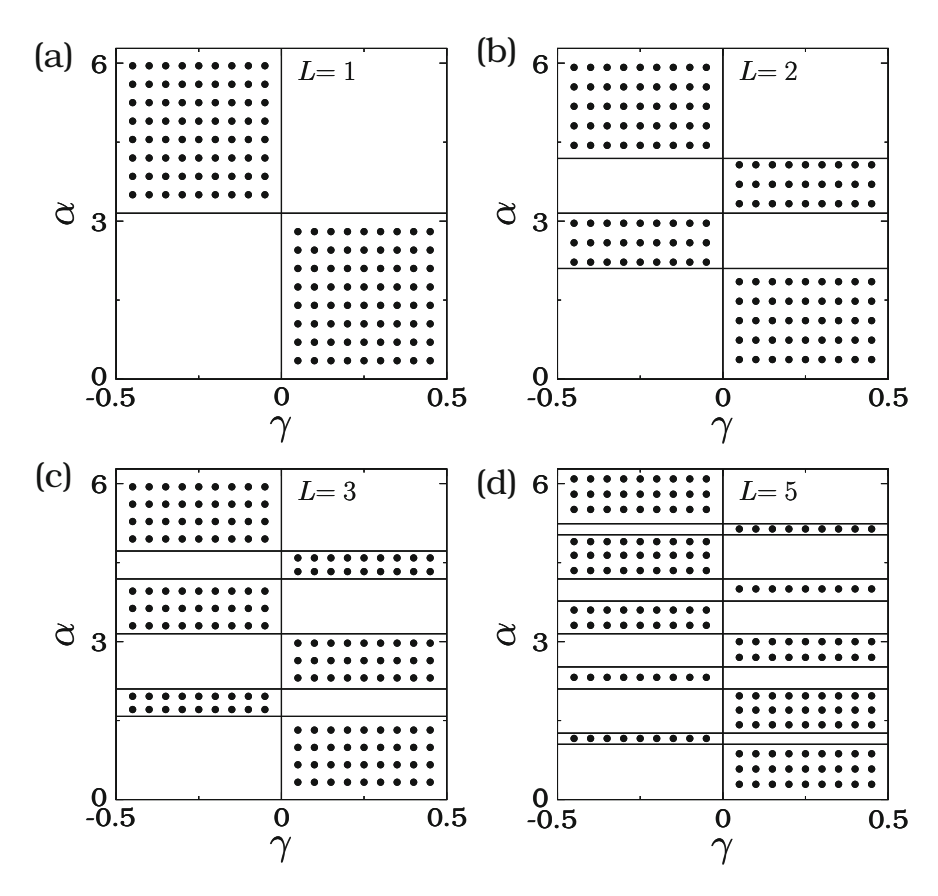


Fig. 6.13 Plot of regions (marked by *solid circles*) in the $\gamma - \alpha$ parameter space where $Q_{\max}(\gamma) > Q_{\max}(\gamma = 0)$ for $\omega = 1$ and (a) L = 1, (b) L = 2, (c) L = 3 and (d) L = 5

is realized in the regions filled with solid circles in Fig. 6.13. For each value of L the total length of α intervals is $\approx \pi$.

For further analysis, we define the gain factor G as $Q_{\max}(\gamma)/Q_{\max}(\gamma=0)$. Figure 6.14 presents the variation of G as a function of the parameters γ and α for few values of L. In this figure, data with G>1 alone are displayed in order to compare it with Fig. 6.13. For wide ranges of α and γ , the gain factor is >2, that is, the delay is able to increase the value of Q at resonance more than two times the value of Q in its absence. The addition of more and more delay terms decreases the maximum value of G. Moreover, it produces new regions with G>1 in the $\gamma-\alpha$ parameter space and decreases the value of G to less than 1 in certain regions where G>1 earlier. The analytical expressions for $g_{\rm VR}^{(1)}$ and $g_{\rm VR}^{(2)}$ for the system (6.35) are given by Eq. (6.23) with the replacement of $\cos\alpha\omega$ by $(1/L)\sum_l\cos l\alpha\omega$.

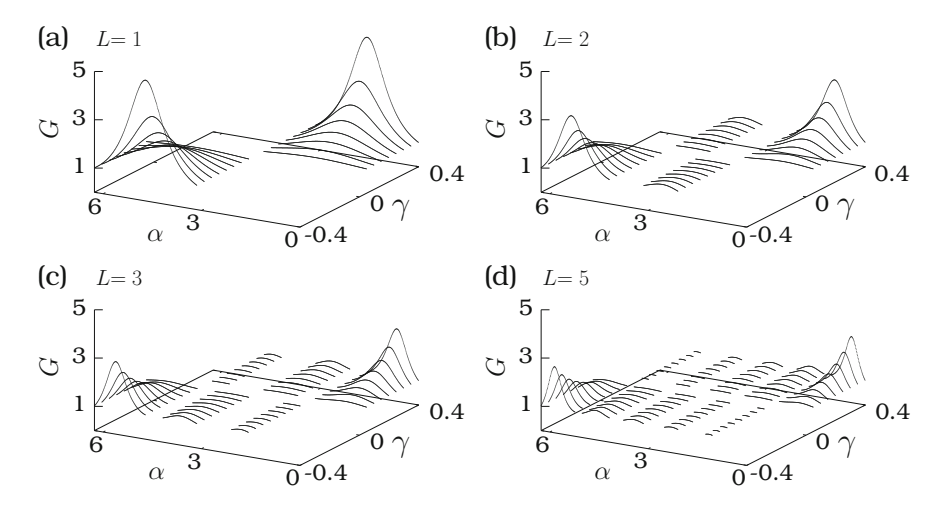


Fig. 6.14 Three-dimensional plot of $G=Q_{\max}(\gamma)/Q_{\max}(\gamma=0)$ versus γ and α for (a) L=1, (b) L=2, (c) L=3 and (d) L=5

6.8 Vibrational Resonance with Some Other Time-Delayed Feedbacks

This section presents briefly the effect of gamma distributed time-delayed, integrative time-delayed, state-dependent and random time-delayed feedbacks in the Duffing oscillator.

6.8.1 Gamma Distributed Time-Delayed Feedback

The dynamics of the Duffing oscillator subjected to a biharmonic force and a gamma distributed time-delayed feedback term is governed by the equation of motion [89]

$$\ddot{x} + d\dot{x} + \omega_0^2 x + \beta x^3 + F(\tau, x(t - \tau)) = f \cos \omega t + g \cos \Omega t, \tag{6.38}$$

where $\Omega \gg \omega$ and F is the gamma distributed time-delayed feedback term given by

$$F(\tau, x(t-\tau)) = \gamma \int_0^\infty G_g(\tau) x(t-\tau) d\tau, \quad G_g(\tau) = \frac{\tau^{p-1} \alpha^p e^{-\alpha \tau}}{\Gamma(p)}.$$
 (6.39)

For simplicity, we fix $\alpha = 1$.

(6.40b)

Applying the theoretical method applied previously the following results are arrived [89]:

$$\psi = A_{\rm H} \cos(\Omega t + \phi) , \qquad (6.40a)$$

$$F(\tau, \psi(\Omega t - \Omega \tau)) = \gamma A_{\rm H} \Omega^{-p} \cos(\Omega t + \theta + \phi), \quad \theta = \frac{p}{\Omega} - \frac{p\pi}{2} ,$$

$$A_{\rm H} = \frac{g}{\mu}, \quad \mu = \left[\left(\Omega^2 - \gamma \Omega^{-p} \cos \theta \right)^2 + \left(\gamma \Omega^{-p} \sin \theta \right)^2 \right]^{1/2}, \tag{6.40c}$$

$$\phi = \tan^{-1} \left(\frac{\gamma \Omega^{-p} \sin \theta}{\Omega^2 - \gamma \Omega^{-p} \cos \theta} \right), \tag{6.40d}$$

$$\langle \psi \rangle = 0, \ \langle \psi^2 \rangle = (1/2\pi) \int_0^{2\pi} \psi^2 \, d\tau = A_H^2 / 2, \ \langle \psi^3 \rangle = 0,$$
 (6.40e)

Then with $Y = X - X^*, X_0^* = 0$ and $X_{\pm}^* = \pm \sqrt{-(C_1 + \gamma)/\beta}$ and $Y = A_L \cos(\omega t + \Phi)$ one obtains

$$F(\tau, x(\Omega t - \Omega \tau)) = \operatorname{Re} \left[\frac{\gamma A_{L} e^{i(\omega t + \Phi)}}{(1 + i\omega)^{p}} \right]$$

$$= \gamma A_{L} \left[a \cos(\omega t + \Phi) - b \sin(\omega t + \Phi) \right], \qquad (6.41a)$$

$$a + ib = 1/(1 + i\omega)^{p}, \qquad (6.41b)$$

$$A_{L} = f/\sqrt{S}, \quad S = (\omega_{r}^{2} - \omega^{2} + \gamma a)^{2} + (d\omega + \gamma b)^{2}, \qquad (6.41c)$$

where $\omega_{\rm r}^2 = \omega_0^2 + 3\beta g^2/(2\mu^2) + 3\beta X^{*2}$. For the case of the double-well potential system, fix the values of the parameters as d = 0.5, $\omega_0^2 = -1$, $\beta = 1$, f = 0.1, $\omega = 1$, $\Omega = 10$ and $\rho = 0.5$. For $g < g_{\rm c}$, where

$$g_{\rm c} = \left[\frac{2\mu^2}{3\beta} \left(|\omega_0^2| - \gamma \right) \right]^{1/2}, \quad \gamma < |\omega_0^2|,$$
 (6.42)

there are three equilibrium points $X_0^*=0$ and X_\pm^* . Slow oscillations take place about X_\pm^* . For $g>g_c$ there is only one equilibrium point X_0^* and a slow motion occurs about it. In the calculation of ω_r^2 , use $X^*=X_\pm^*$ for $g< g_c$ and $X^*=0$ for $g>g_c$.

(i) Resonance occurs at

$$g_{\text{VR}}^{(1)} = \left[\frac{\mu^2}{3\beta} \left(2|\omega_0^2| - \omega^2 + \gamma(a-3)\right)\right]^{1/2} < g_c, \tag{6.43a}$$

$$g_{\rm VR}^{(2)} = \left[\frac{2\mu^2}{3\beta} \left(|\omega_0^2| + \omega^2 - \gamma a \right) \right]^{1/2} > g_{\rm c} \tag{6.43b}$$

provided

$$\gamma_{c1} = \frac{\omega^2}{a-1} < \gamma < \gamma_{c2} = \frac{2|\omega_0^2| - \omega^2}{3-a}.$$
(6.44)

- (ii) For $\gamma > \gamma_{c2}$ there is only one resonance at $g = g_{VR}^{(1)} = g_c$.
- (iii) For $\gamma < \gamma_{c1}$ only one resonance is possible and it takes place at $g_{vr}^{(2)}$.

Figure 6.15 presents the influence of the parameters γ and g on Q for four fixed values of the parameter p appearing in the gamma distributed delays. For p=0.5, the conditions (6.44) are satisfied for $\gamma \in [-4.49843, 0.42857]$. That is, two resonances can occur when g is varied from a small value for values of γ in the above interval. Figure 6.15a confirms this. For p=3.5 two resonance peaks

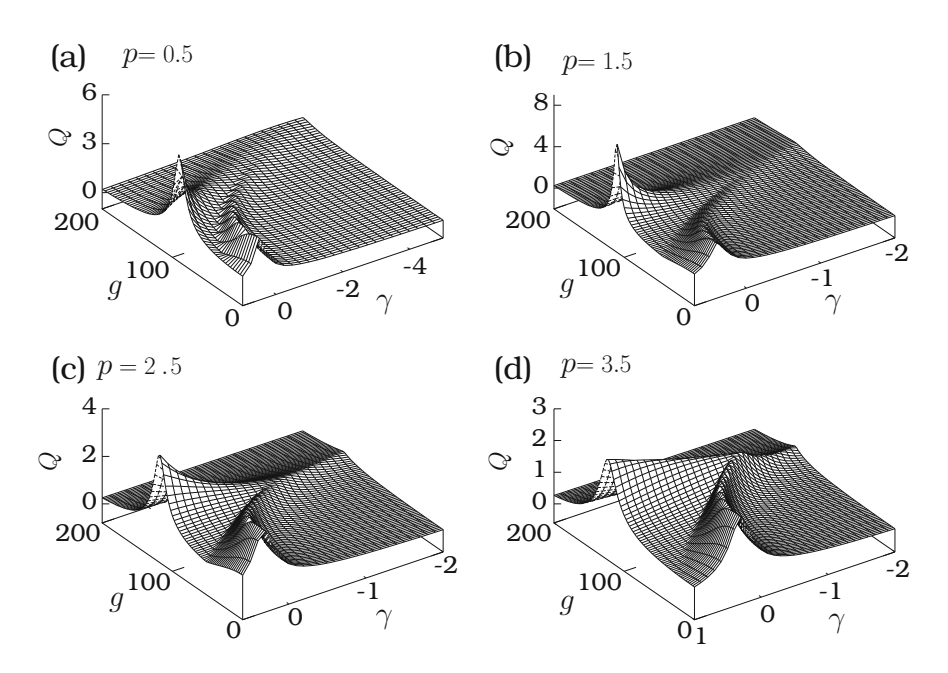


Fig. 6.15 Variation of Q as a function of γ and g for four fixed values of p. The values of the other parameters are d=0.5, $\omega_0^2=-1$, $\beta=1, f=0.1$, $\omega=1$, and $\Omega=10$

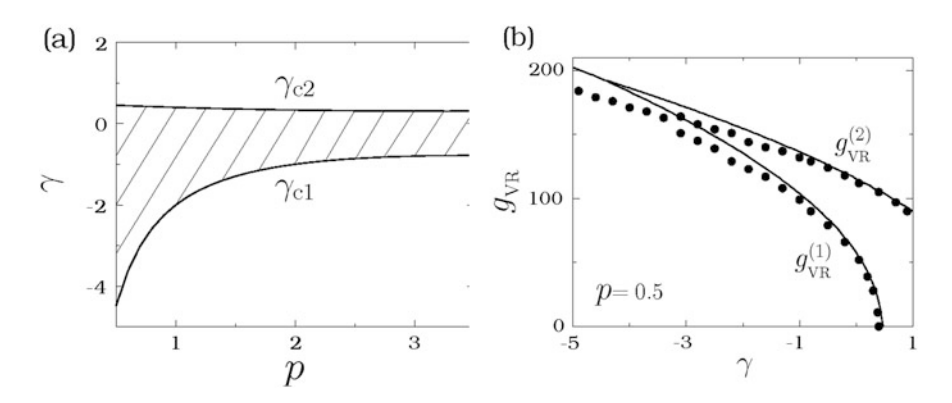


Fig. 6.16 (a) γ_{c1} and γ_{c2} versus p for the double-well potential Duffing oscillator. Two resonances take place in the stripped region while only one resonance occurs in the remaining regions. (b) g_{VR} versus γ for p = 0.5. The *continuous curve* and the *solid circles* are theoretically and numerically computed values of g_{VR} , respectively

can take place for $\gamma \in [-0.78, 0.31]$. In Fig. 6.15, for all values of p the values of q at resonance decrease with a decrease in the value of γ from the value 1. As γ increases from γ_{c1} , both $g_{VR}^{(1)}$ and $g_{VR}^{(2)}$ move away from g_c .

In Fig. 6.16a the variation of γ_{c1} and γ_{c2} with p is plotted. In the stripped regions

In Fig. 6.16a the variation of γ_{c1} and γ_{c2} with p is plotted. In the stripped regions two resonances occur. For the values of γ and p above the curve γ_{c2} , there is only one resonance at $g = g_{VR}^{(2)} > g_c$ given by Eq. (6.43b) while for below the curve γ_{c1} a single resonance occurs at $g = g_c$. Figures 6.15 and 6.16a clearly demonstrate the strong influence of the parameters of the delay feedback term. In Fig. 6.16b theoretical and numerically computed g_{VR} are shown for a range of values of γ with p = 0.5. The theoretical g_{VR} matches closely with the numerical g_{VR} for $|\gamma| < 1$. For $|\gamma| > 1$ the deviation between the theoretical g_{VR} and the numerical g_{VR} increases with an increase in $|\gamma|$.

6.8.2 Integrative Time-Delayed Feedback

The integrative time-delayed feedback term is given by $F(\tau, x(t - \tau)) = (\gamma/\alpha) \int_0^\alpha x(t - \tau) d\tau$. With $x(t) = X(t) + \psi(t, \Omega t)$ the following results are arrived [89]:

$$Y(t) = A_{\rm L}\cos(\omega t + \Phi), \quad A_{\rm L} = \frac{f}{\sqrt{S}}, \quad Q = \frac{1}{\sqrt{S}},$$

$$S = \left[\omega_{\rm r}^2 - \left(\omega^2 - \frac{\gamma}{\omega\alpha}\sin\omega\alpha\right)\right]^2 + \left[d\omega - \frac{\gamma}{\omega\alpha}\left(1 - \cos\omega\alpha\right)\right]^2,$$
(6.45b)

$$\omega_{\rm r}^2 = \omega_0^2 + \frac{3\beta g^2}{2\mu^2} + 3\beta X^{*2},\tag{6.45c}$$

$$\mu^{2} = \left[\omega_{0}^{2} - \Omega^{2} + \frac{\gamma}{\Omega\alpha}\sin\Omega\alpha\right]^{2} + \left[d\Omega - \frac{\gamma}{\Omega\alpha}(1 - \cos\Omega\alpha)\right]^{2}.$$
(6.45d)

Notice the difference between the S's given by Eqs. (6.41c) and (6.45b). Since the solution Y(t) is assumed to be periodic with period $2\pi/\omega$, choose $0 < \alpha < 2\pi/\omega$.

For $\omega_0^2 < 0$, $\beta > 0$ and $\gamma < |\omega_0^2|$ (double-well potential case) the values of g at which resonance occurs are given by

$$g_{\rm VR}^{(1)} = \left[\frac{\mu^2}{3\beta} \left(2|\omega_0^2| - 3\gamma - \omega^2 + \frac{\gamma}{\omega\alpha} \sin \omega\alpha \right) \right]^{1/2} < g_c,$$
 (6.46)

$$g_{\text{VR}}^{(2)} = \left[\frac{2\mu^2}{3\beta} \left(|\omega_0^2| + \omega^2 - \frac{\gamma}{\omega\alpha} \sin\omega\alpha \right) \right]^{1/2} > g_c. \tag{6.47}$$

where g_c is given by Eq. (6.42). For two resonances to occur the condition on γ is $\gamma_{c1} < \gamma < \gamma_{c2}$ where

$$\gamma_{c1} = -\frac{\omega^2}{1 - \frac{1}{\rho \alpha} \sin \omega \alpha}, \quad \gamma_{c2} = \frac{2|\omega_0^2| - \omega^2}{3 - \frac{1}{\rho \alpha} \sin \omega \alpha}.$$
(6.48)

When $\gamma > \gamma_{c2}$, only one resonance is possible with the corresponding g_{vR} given by $g_{vR}^{(2)}$. For $\gamma < \gamma_{c1}$ there will be only one resonance at $g = g_c$.

Figure 6.17a depicts the threshold curves γ_{c1} and γ_{c2} for $\omega_0^2 = -1$, $\beta = 1$, d = 0.5, f = 0.1, $\omega = 1$ and $\Omega = 10$. In the stripped region, two resonances occur while

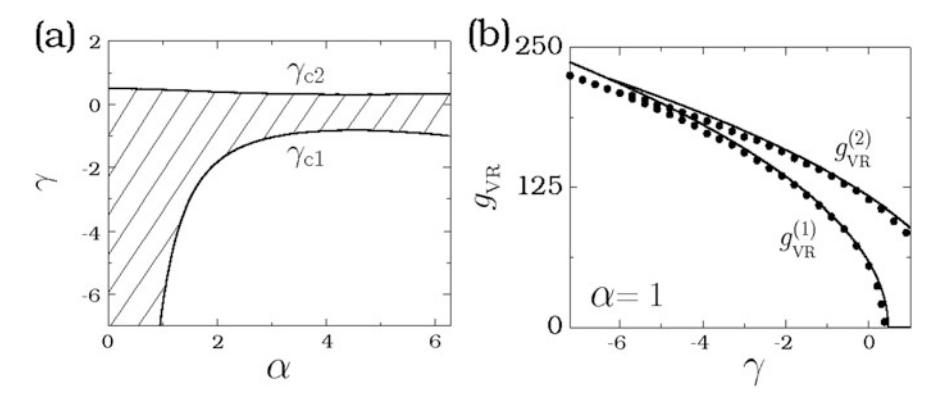


Fig. 6.17 (a) Dependence of γ_{c1} and γ_{c2} with the time-delay α for the Duffing oscillator with an integrative time-delayed feedback term. Two resonances occur in the stripped region. Below and above the stripped region only one resonance is possible. (b) Theoretically predicted (*continuous curve*) and numerically computed (*solid circles*) values of $g_{VR}^{(1)}$ and $g_{VR}^{(2)}$ for $\alpha = 1$ as a function of γ

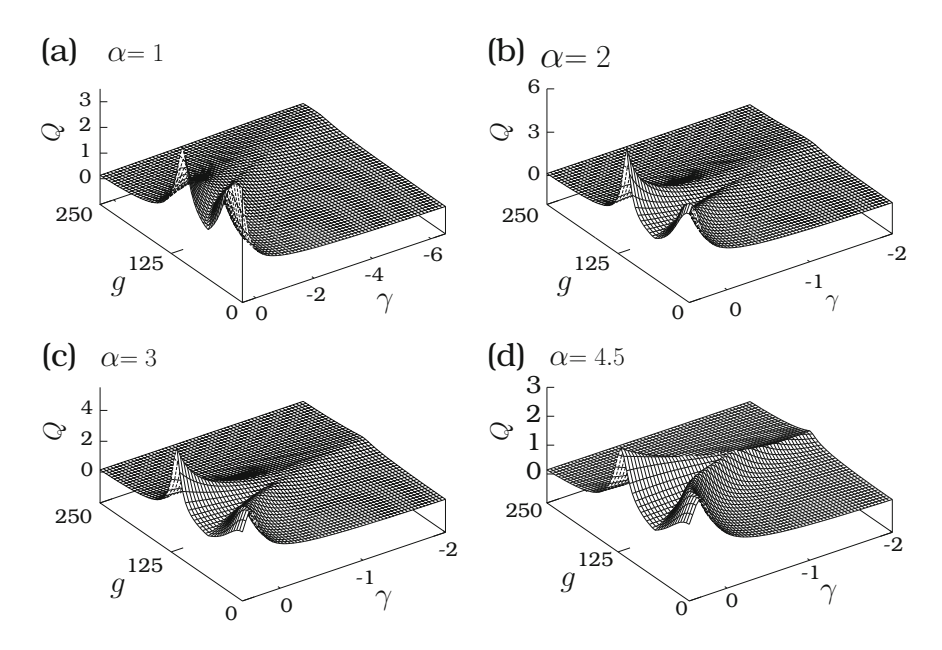


Fig. 6.18 *Q* versus *g* and γ for (a) $\alpha = 1$, (b) $\alpha = 2$, (c) $\alpha = 3$ and (d) $\alpha = 4.5$ for the double-well Duffing oscillator with an integrative time-delayed feedback term

only one resonance occurs in the remaining region. In Fig. 6.17b, both theoretically predicted and numerically computed $g_{VR}^{(1)}$ and $g_{VR}^{(2)}$ are plotted as a function of γ for $\alpha=1$. Here again, the theoretical result closely matches with the numerical simulation.

The influence of the parameters g and γ on Q is depicted in Fig. 6.18 for four fixed values of time-delay α . In this figure, we clearly notice that for γ values below a critical value (γ_{c1}) only one resonance takes place. Comparing Fig. 6.15 of the gamma distributive time-delayed feedback case and Fig. 6.18 of the integrative time-delayed feedback case, the effect of α is found to be similar to that of p.

6.8.3 State-Dependent Time-Delayed Feedback

The goal of the present section is to report the effect of certain forms of state-dependent time-delays (SDTDs) on vibrational resonance. Such time-delays were appeared in the modeling of transmission channels of communication networks [90], in supply networks as a consequence of transportation of materials [91–93], in population dynamics [94] and engine cooling systems [95]. Speed-dependent delays are to be taken into account in the milling processes because of the deformation of the cutting tool [96], automatic landing systems [97], irrigation channels [98] and drill-string vibration model [99]. Queuing delays in internet congestion control

algorithm are shown to be SDTDs. Position-dependent axonal conduction time-delays ranging from 0.1 ms to 44 ms are experimentally noticed in the mammalian neocertex [100].

(A) Sigmoid State-Dependent Time-Delay

Let us consider the Duffing oscillator Eq. (6.13) with the time-delay

$$\alpha = \tau(x(t)) = \frac{\tau_0}{1 + e^{px}},$$
(6.49)

where τ_0 is a positive constant and p is a constant. $\tau(x)$ is sigmoid function. In the numerical simulation choose $\tau(x)$ in multiples of 0.001, that is,

$$\tau(x(t)) = \frac{1}{1000} \text{Int} \left[\frac{1000\tau_0}{1 + e^{px}} \right] , \qquad (6.50)$$

where $\operatorname{Int}(y)$ means integer part of y. Fix the values of the parameters in Eq. (6.13) as $\omega_0^2=-1, \beta=1, d=0.5, f=0.1, \omega=1, \Omega=10$ and $\tau_0=1$. When g is varied for $\gamma=0$ there are two resonances with same response amplitude Q. The resonances occur at g=54 and 115. Figure 6.19 illustrates the variation of Q with γ and g for four different values of p. The effect of γ and p on the resonance and on the value of Q can be clearly seen. For a fixed value of p the values of p at which resonances occur shift towards origin, that is, g_{VR} is decreased. $g_{VR}^{(1)}$ decreases much faster than $g_{VR}^{(2)}$ with increase in the value of γ . However, p at p at p decreases with p whereas its value at p decreases with increase in p. Figure 6.20 depicts the nontrivial variation of p with the parameter p for p and p and p and for two fixed values of p. For p and p and p are p and p are the response amplitude p is strictly not symmetric about p and p are p and p and p and p and p are p and p and p are p and p are p and p are p and p and p and p are p and p are p and p are p and p and p are p and p and p are p and p are p and p and p and p are p and p and p are p are p and p are p are p and p are p and p a

For a range of fixed values of τ_0 the control parameter g is varied from zero and its critical values $g_{\rm VR}$ at which resonance occur and the corresponding value of Q are numerically computed. When there are two resonance one at $g_{\rm VR}^{(1)}$ and another at $g_{\rm VR}^{(2)}$ with $g_{\rm VR}^{(1)} \neq g_{\rm VR}^{(2)}$ we choose the critical value as the one for which Q is large. $g_{\rm VR}$ oscillates with τ_0 . $Q_{\rm max}$ (the value of Q at $g=g_{\rm VR}$) increases with τ_0 reaches a maximum at a value of τ_0 and then decreases. That is, $g_{\rm VR}$ and the value of Q can be controlled by the parameter τ_0 .

(B) Parabolic State-Dependent Time-Delay

Suppose the time-delay is of the form

$$\alpha = \tau(x(t)) = \tau_0(1 + px^2)$$
, (6.51)

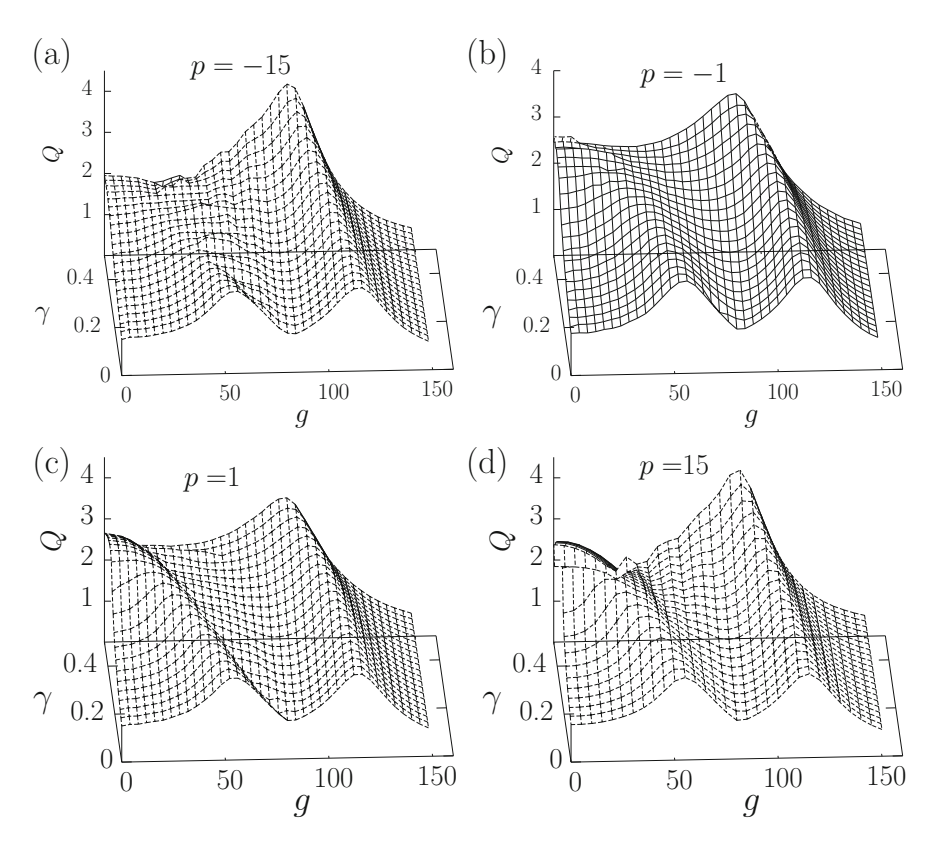


Fig. 6.19 Dependence of Q on the parameters γ and g with sigmoid function type time-delay $\alpha = \tau(x(t))$ given by Eq. (6.49) with (a) p = -15, (b) p = -1, (c) p = 1 and (d) p = 15. The values of other parameters are $\omega_0^2 = -1$, $\beta = 1$, d = 0.5, f = 0.1, $\omega = 1$, $\Omega = 10$ and $\tau_0 = 1$

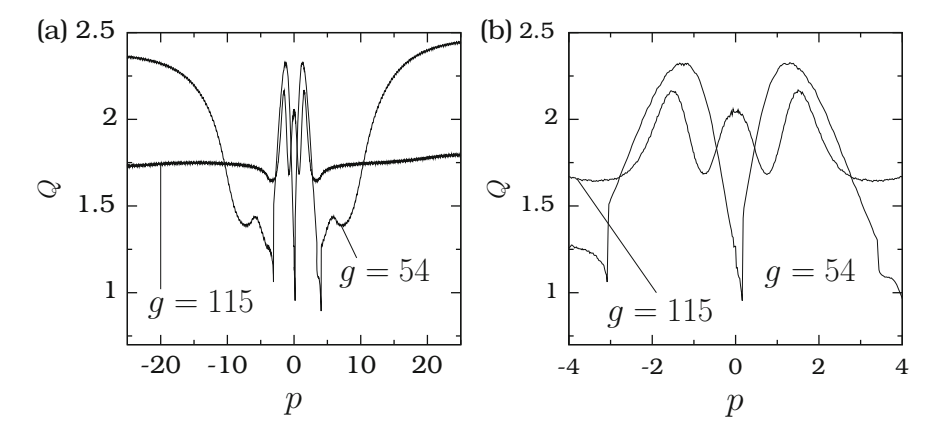


Fig. 6.20 (a) Q versus p for g=54 and 115 at which resonance occurs when $\gamma=0$. Here $\gamma=0.4$ and $\tau_0=1$. (b) Magnification of the subplot (a) in the interval $p\in[-4,4]$

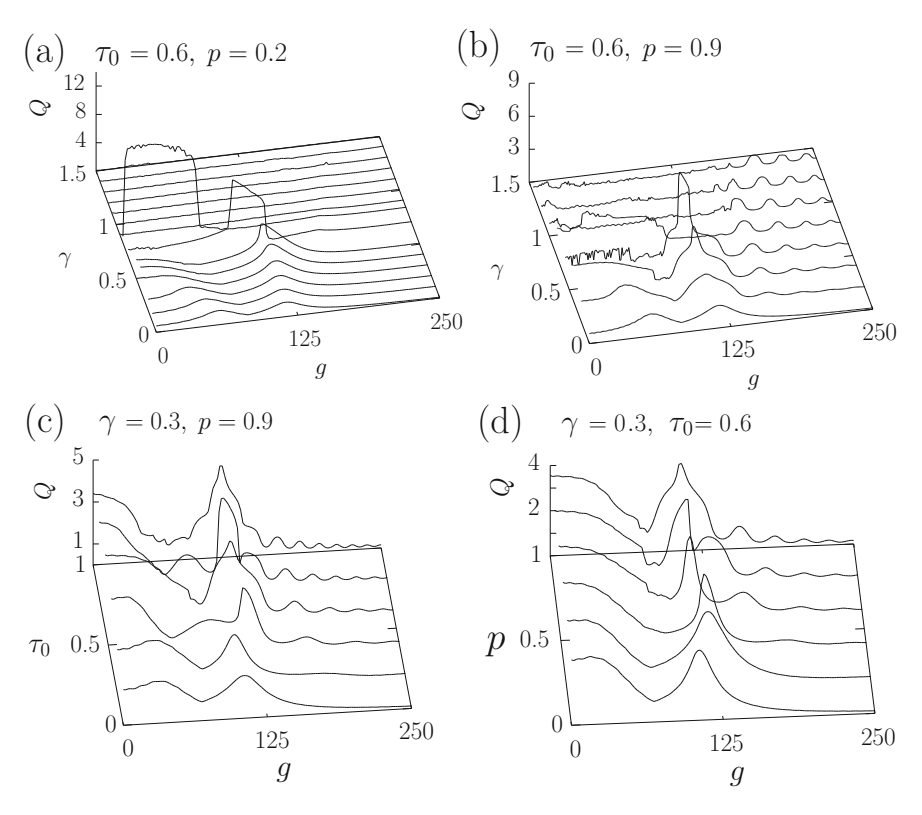


Fig. 6.21 The results for the system (6.13) with the time-delay given by Eq. (6.51). (**a-b**) γ versus g versus Q for p = 0.2 (**a**) and p = 0.9 (**b**) with $\tau_0 = 0.6$. (**c**) τ_0 versus g versus Q for $\gamma = 0.3$ and p = 0.9. (**d**) p versus q versus q for q versus q for q versus q for q versus q for q versus q versus q for q versus q for q versus q versus q for q versus q versus q versus q for q versus q ve

where $\tau(x(t))$ is quadratic in x. In order to make $\tau \ge 0$ we choose p > 0 and $t_0 > 0$. Figure 6.21a, b shows the responsible amplitude profile, Q versus g, for a range of values of γ for $\tau_0 = 0.6$ and for p = 0.2 and 0.9. These two figures can be compared with Fig. 6.19 where time-delay is sigmoid function type. For a range of fixed values of γ and p two resonances occur when the parameter g is varied. $g_{VR}^{(1)}$ and $g_{VR}^{(2)}$ both move towards origin. In Fig. 6.21a (p = 0.2) for $\gamma < 0.5$ there are two resonances, only one resonance for $0.5 < \gamma < 0.95$ while for $\gamma > 0.95$ there is no resonance and $Q(g) \approx 0$ when g is varied. Similar results are found for other values of p. However, in Fig. 6.21b corresponding to p = 0.9, there are number of resonance peaks for each fixed value of γ . The second resonance peak is the dominant resonance for a range of values of g. The amplitude of the resonance peaks decays with increase in g. Figure 6.21c, d depict the effect of τ_0 and p, respectively, on the resonance curve for fixed values of other parameters. Here again a sequence of resonance peaks occur when g is varied. The number of resonance peaks increases with increase in the values of τ_0 and p. The variation of g_{VR} and Q_{max} with τ_0 is similar to the case of the sigmoid function time-delay.

(C) Gaussian State-Dependent Time-Delay

Consider a form of state-dependent delay with $\tau \to 0$ as |x| increases from a small value. An example is the Gaussian form of τ given by

$$\alpha = \tau(x(t)) = \tau_0 e^{-px^2}$$
 (6.52)

The maximum value of τ is τ_0 and is independent of p. The width of the Gaussian curve at half of its maximum ($\tau_0/2$) varies with the parameter p. The width decreases with increase in the value of p. Figure 6.22 presents the effect of the parameters γ , p and g on the response amplitude for $\tau_0 = 1$. For small values of p the system exhibits double resonance when g is varied for a range of fixed values of γ . For γ greater than a critical value only one resonance occurs. This is shown in Fig. 6.22a. Three resonances occur for a range of fixed values of p and q. Three resonances are clearly noticeable in Figs. 6.22b, c. In Fig. 6.22d for p = 5, a

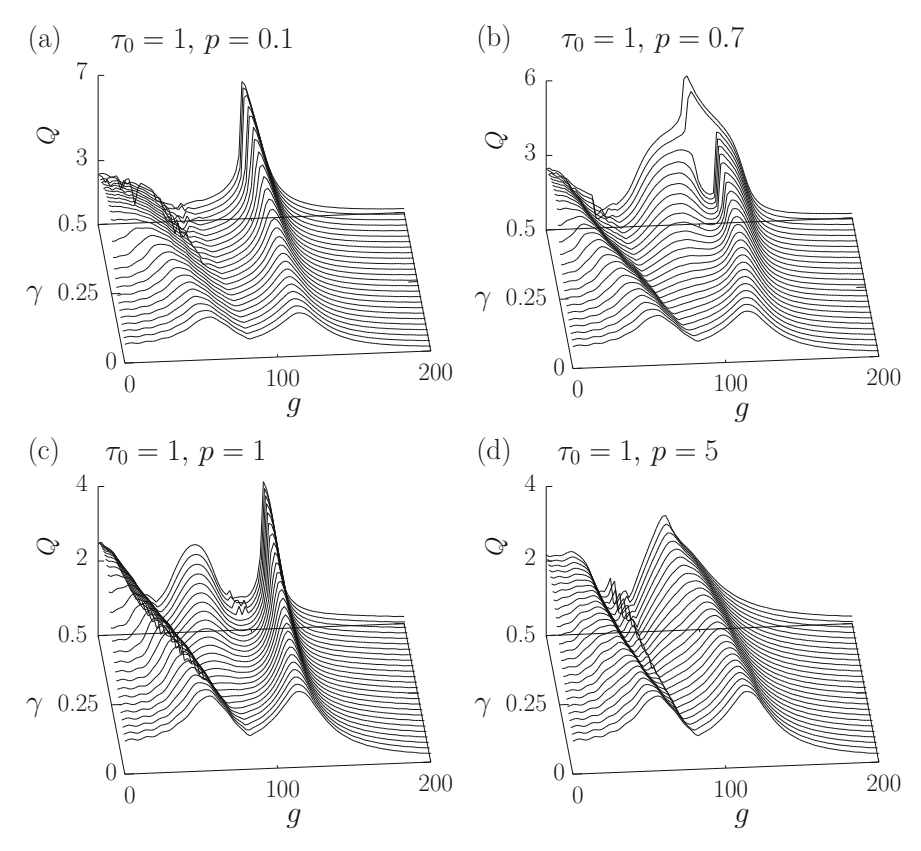


Fig. 6.22 *Q* versus γ versus g for the system (6.13) with the time-delay $\tau(x(t)) = \tau_0 e^{-px^2}$, $\tau_0 = 1$ and for four fixed values of p

large value of p, the middle resonance is weak. Here also the values of g at which resonances occur move towards origin as the value of γ increases. The rate of change of the values of g at which second and third resonances occur is much slower than the first resonance. The values of Q at the resonances increase with increase in the value of γ .

6.8.4 Feedback with Random Time-Delay

So far the focus in this chapter is the influence of different types of time-delayed feedback on the resonance induced at the low-frequency ω by a high-frequency force. In certain systems time-delay can be random. For example, in biochemical reactions, a source of time-delay is the response time of the last step that can be random because of the molecular thermal motion. On the other hand, in population dynamics when the time-delay due to the gestation or incubation times depends on the variations of the external environment and living conditions as a result of climate and weather changes then it has to be treated as a random one [101, 102]. Random delay enters in the immune response models if the outbreak of a disease caused by an infection is due to complicated biological and environmental processes [103]. Random delay is found to give rise to stabilization of steady state and periodic orbits [104–108], synchronization [109, 110], existence of a stationary random solution [111], controlling of systems [112] and bifurcations [113] have been studied in certain systems with random delays. Random delay induced resonance with and without an external periodic force is realized in the Langevin equation [114, 115]. Solutions of certain linear differential equations with random delay have been analyzed in [116].

The goal of this section is to report the resonance in the Duffing oscillator driven by a single frequency force with random time-delayed feedback with out the high-frequency periodic force [117].

Consider the Duffing oscillator equation

$$\ddot{x} + d\dot{x} + \omega_0^2 x + \beta x^3 + \gamma x (t - |\tau|) = f \cos \omega t , \qquad (6.53)$$

where the time-delay τ is a Gaussian white noise with standard deviation σ and zero mean and γ is the strength of the feedback term. Figure 6.23 presents the dependence of the response amplitude Q on γ and σ . When $\omega=0.1$, for a range of fixed values of σ single resonance occurs when γ is varied (Fig. 6.23a). The value of Q at resonance decreases with increase in the value of σ . As shown in Fig. 6.23b a different behaviour takes place for $\omega=1$. For each fixed value of σ there are two resonances when γ is varied from, say -1. The second resonance is the dominant resonance.

The mechanism of the observed resonance can be understood using trajectory plot. Figure 6.24 shows the evolution of x(t) for four fixed values of γ and for $\sigma = 0.1$ and $\omega = 0.1$. For this value of ω the resonance occurs at $\gamma = 0.6$.

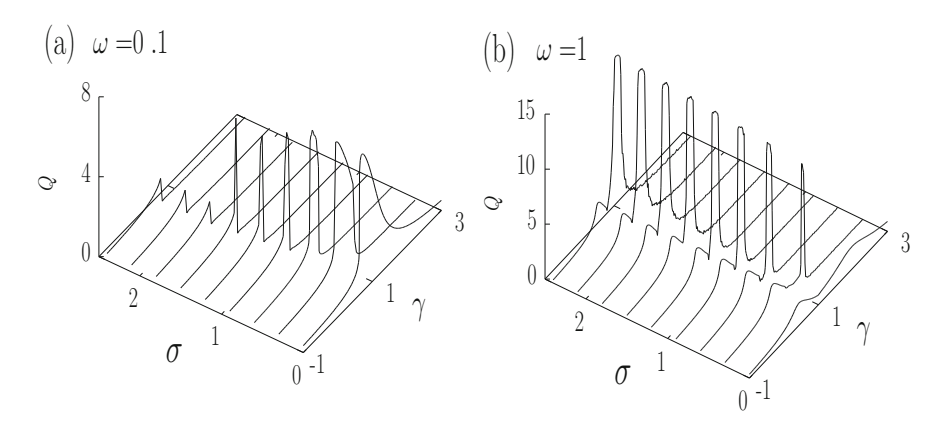


Fig. 6.23 Q versus σ and γ for two values of ω of the system (6.53) with $d=0.5, \omega_0^2=-1, \beta=1$ and f=0.1

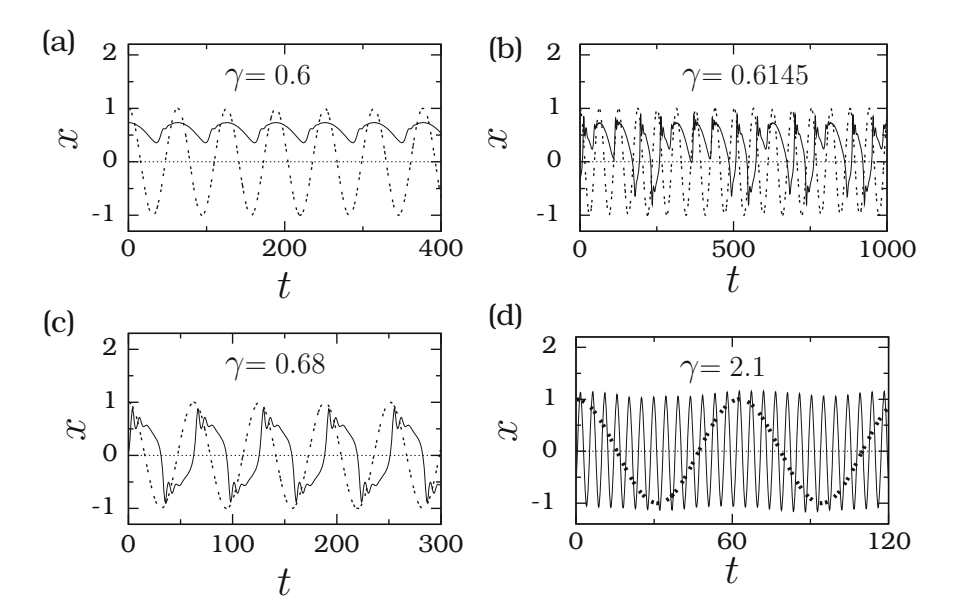


Fig. 6.24 x(t) versus t of the system (6.53) for four values of γ and for $\sigma = 0.1$ and $\omega = 0.1$. The *dotted curve* is the rescaled $f \cos \omega t$ and *continuous curve* is the numerically computed x(t)

In all the subplots of Fig. 6.24 the dotted line is the rescaled input periodic signal $f \cos \omega t$. In Fig. 6.24a ($\gamma = 0.6$) far before resonance x(t) is bounded in the region x > 0 and is almost periodic with the period of the input periodic force. For $\gamma = 0.6145$ (Fig. 6.24b), x(t) switches between the positive and negative values, that is, jumps between the two wells of the double-well potential. The motion is nonperiodic at the time intervals between consecutive jumpings are random. In

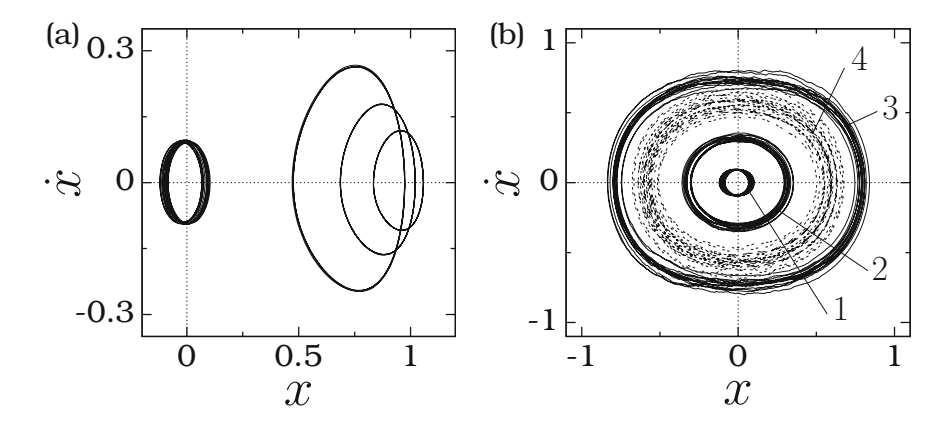


Fig. 6.25 x(t) versus t of the system (6.53) with $\omega = 1$ and $\sigma = 0.1$ and for four values of γ around (**a**) first resonance and (**b**) second resonance. In (**a**) the values of γ for the orbits from right to left are 0.1, 0.25, 0.41 (resonance case) and 1 (at which Q is maximum). In (**b**) the values of γ for the orbits 1 to 4 are 1, 1.7, 1.72 (resonance case) and 2, respectively

Fig. 6.24c corresponding to the resonance case ($\gamma = 0.68$) the solution x(t) appears almost periodic with cross-well motion. The erratic switching between the wells realized in additive noise driven systems far after resonance is not observed for $\gamma \gg 0.68$ in the random delay. The number of switching between the wells per drive period increases with increase in γ (mean residence time in a well decreases with γ).

For $\omega=1$ as shown in Fig. 6.23b there are two resonances when γ is varied. The two resonances occur at $\gamma=0.41$ and 1.72. Now, account these two resonances. Figure 6.25a displays phase portrait of the system for four values of γ for $\sigma=0.1$ and $\omega=1$. As γ increases from zero the center of the orbit moves towards the origin as the amplitude of the orbit increases. For $\sigma=0.41$ the amplitude is maximum, however, the orbit is confined to a single-well alone. As the value of σ is increased further from 0.41 the amplitude of the orbit decreases and the center of the orbit further moves toward the origin. At $\gamma=1$ the response amplitude Q becomes maximum and the center of the orbit becomes the origin. For $\gamma>1$ the center of the orbit remains the same while the amplitude Q shows a nonmonotonic variation.

At $\gamma=1.72~Q$ becomes maximum. This is the second resonance. For $\gamma>1.72$ the response amplitude decreases. The above scenario around the second resonance is presented in Fig. 6.25b. Figures 6.25a and b clearly bring out the differences between the mechanisms of random delay induced two resonances. For sufficiently small ω , for example $\omega=0.1$ (Fig. 6.24), the observed random time-delayed feedback induced resonance is similar to the typical stochastic resonance induced by an additive Gaussian white noise. Here the resonance is due to the almost periodic switching of the trajectories between the two wells. For large ω , for example $\omega=1$ (Fig. 6.25), the induced double resonance is like the vibrational double-resonance observed in underdamped monostable and bistable oscillators induced by

a biharmonic force. There is no periodic switching between the potential wells at resonance. Resonance is found when the parameter σ is varied.

6.9 Concluding Remarks

The effects of the amplitude g of the high-frequency periodic force and the delay-time feedback parameters γ and α on vibrational resonance are explained through a theoretical approach. The presence of time-delayed feedback in the systems considered in this chapter is found to enrich the vibrational resonance phenomenon. Particularly, the time-delay parameter α gives rise to a periodic or quasiperiodic pattern of vibrational resonance profile. This feature of vibrational resonance allows us to select different values (small or large) for the delay-time α to enhance the quality of the weak signal and it can be highly useful in optimizing the operation of multistable systems for the detection and regeneration of signals in a variety of experimental systems. In the overdamped single-well system, resonances cannot occur when g is varied. However, the inclusion of an appropriate time-delayed feedback is found to induce a resonance.

Discussion has been made on the effect of time-delay on vibrational resonance in the underdamped and overdamped Duffing oscillators with double-well and single-well cases of the potential. For $\omega_0^2>0$ and $\beta<0$ the potential of the Duffing oscillator becomes the single-well with double-hump shown in Fig. 3.1. One can also study vibrational resonance with this potential. Unlike the other two potential types, both systems (6.13) and (6.29) with double-hump potential will show bounded motion for $g< g_c=\sqrt{2\mu^2\omega_0^2/(3|\beta|)}$. For $g>g_c$ the effective potential of the slow variable X becomes of an inverted single-well form. In the underdamped double-hump system $g_{\rm VR}$ is given by Eq. (6.23a) provided $0<\omega^2-\gamma\cos\omega\alpha<\omega_0^2$ (compare this condition with Eq. (6.27b) corresponding to the single-well case). For the overdamped double-hump system $g_{\rm VR}$ is given by Eq. (6.33a) provided α lies in the interval given by Eq. (6.33b) and further $\gamma<\gamma_c=\omega_0^2/|\cos\omega\alpha|$ (compare this condition with Eq. (6.33c) to be satisfied for the single-well system).

References

- 1. J. Chiasson, J.J. Loiseau, Applications of Time-Delay Systems (Springer, Berlin, 2007)
- 2. J.J. Loiseau, W. Michiels, S.I. Niculescu and R. Sipahi (eds.), *Topics in Time-Delay Systems: Analysis, Algorithms, and Control* (Springer, Berlin, 2009)
- 3. F.M. Atay, Complex Time-Delay Systems: Theory and Applications (Springer, Berlin, 2010)
- 4. M. Lakshmanan, D.V. Senthilkumar, *Dynamics of Nonlinear Time-Delay Systems* (Springer, Berlin, 2010)
- 5. C.U. Choe, T. Dahms, P. Hovel, E. Scholl, Phys. Rev. E 81, 025205(R) (2010)
- I. Fischer, R. Vicente, J.M. Buldu, M. Peil, C.R. Mirasso, M.C. Torrent, J. Garcia-Ojalvo, Phys. Rev. Lett. 97, 123902 (2006)

References 199

 R. Vincente, L.L. Gollo, C.R. Mirasso, I. Fischer, G. Pipa, Proc. Natl. Acad. Sci. USA 105, 17157 (2008)

- 8. V. Flunkert, O. D'Huys, J. Danckaert, I. Fischer, E. Scholl, Phys. Rev. E 79, 065201(R) (2009)
- 9. D.V. Ramana Reddy, A. Sen, G.L. Johnston, Phys. Rev. Lett. 85, 3381 (2000)
- 10. M. Gassel, E. Glatt, F. Kaiser, Fluct. Noise Lett. 7, L225 (2007)
- 11. M. Bonnin, F. Corinto, M. Gilli, Int. J. Bifurcation Chaos Appl. Sci. Eng. 17, 4033 (2007)
- 12. M.A. Dahlem, Phil. Trans. R. Soc. A **367**, 1079 (2009)
- 13. S. Gakkhar, A. Singh, Commun. Nonlinear Sci. Numer. Simul. 17, 914 (2011)
- 14. K. Pyragas, Phys. Lett. A **170**, 421 (1992)
- 15. A. Prasad, J. Kurths, S.K. Dana, R. Ramaswamy, Phys. Rev. E 74, 035204(R) (2006)
- 16. D.V. Ramana Reddy, A. Sen, G.L. Johnston, Phys. Rev. Lett. 80, 5109 (1998)
- 17. J.T. Sun, Y. Zhang, Y.H. Wang, Chinese Phys. Lett. 25, 2389 (2008)
- 18. D.V. Senthilkumar, M. Lakshmanan, Int. J. Bifurcation Chaos Appl. Sci. Eng. 15, 2895 (2005)
- 19. X. Gu, S. Zhu, D. Wu, Eur. Phys. J. D 42, 461 (2007)
- 20. Y. Jin, H. Hu, Phys. A 382, 423 (2007)
- 21. D. Wu, S.Q. Zhu, Phys. Lett. A 363, 202 (2007)
- 22. B. Kelleher, C. Bonatto, P. Skoda, S.P. Hegarty, G. Huyet, Phys. Rev. E 81, 036204 (2010)
- 23. F. Castro, A.D. Sanchez, H.S. Wio, Phys. Rev. Lett. **75**, 1691 (1995)
- 24. Z.L. Jia, Int. J. Theor. Phys. 48, 226 (2009)
- 25. G. Orosz, J. Moehlis, F. Bullo, Phys. Rev. E 81, 025204(R) (2010)
- 26. M. Dhamala, V.K. Jirsa, M.Z. Ding, Phys. Rev. Lett. **92**, 074104 (2004)
- 27. T.W. Kao, G.B. Ermentrout, Phys. Rev. E **76**, 056206 (2007)
- 28. Q.Y. Wang, G.R. Chen, Chaos 21, 013123 (2011)
- 29. Q.Y. Wang, M. Perc, Z.S. Duan, G.R. Chen, Phys. Rev. E 80, 026206 (2009)
- O. Valles-Codina, R. Mobius, S. Rudiger, L. Schimansky-Geier, Phys. Rev. E 83, 036209 (2011)
- C. Marchewka, P. Larsen, S. Bhattacharjee, J. Booske, S. Sengele, N. Ryskin, V. Titov, Physics Plasmas 13, 013104 (2006)
- 32. I.S. Tsimring, A. Pikovsky, Phys. Rev. Lett. 87, 250602 (2001)
- 33. D. Wu, S.Q. Zhu, Phys. Lett. A 363, 202 (2007)
- 34. M. Borromeo, F. Marchesoni, Phys. Rev. E 75, 041106 (2007)
- 35. L.C. Du, D.C. Mei, J. Stat. Mech. 11, 11020 (2008)
- 36. D. Wu, S.Q. Zhu, X.Q. Luo, Eur. Phys. Lett. **86**, 50002 (2009)
- 37. D.C. Mei, L.C. Du, C.J. Wang, J. Stat. Phys. 137, 625 (2009)
- 38. L.C. Du and D.C. Mei, Phys. A **390**, 3262 (2011)
- 39. N. Buric, K. Todovovic, N. Vasovic, Phys. Rev. E 82, 037201 (2010)
- 40. T. Okano, M. Miyakawa, Phys. Rev. E 82, 027202 (2010)
- J. Houlihan, D. Goulding, Th. Busch, C. Masoller, G. Huyer, Phys. Rev. Lett. 92, 050601 (2004)
- 42. J.H. Yang, X.B. Liu, J. Phys. A: Math. Theor. 43, 122001 (2010)
- 43. J.H. Yang, X.B. Liu, Chaos **20**, 033124 (2010)
- 44. J.P. Finerty, *The Population Ecology of Cycles in Small Mammals* (Yale University Press, New Haven, 1980)
- J.R. Flowerdew, Mammals: Their Reproductive Biology and Population Ecology (Edward Arnold, London, 1987)
- 46. J.M. Cushing, Integro-Differential Equations and Delay Models in Population Dynamics (Springer, Berlin, 1977)
- D. Maza, H. Mancini, S. Boccaletti, R. Genesio, F.T. Arecchi, Int. J. Bifurcation Chaos 8, 1843 (1998)
- 48. N. Khrustova, G. Veser, A. Mikhailov, R. Imbihl, Phys. Rev. Lett. 75, 3564 (1995)
- 49. M. Schanz, A. Pelster, Phys. Rev. E. 67, 056205 (2003)
- 50. L. Larger, J.Goldgebuer, T. Erheux, Phys. Rev. E. **69**, 036210 (2004)
- N. MacDonald, Biological Delay Systems: Linear Stability Theory (Cambridge University Press, Cambridge, 1989)

- 52. M. Hashemi, A. Valizadeh, Y. Azizi, Phys. Rev. E. 85, 021917 (2012)
- 53. G.M. Suel, J. Garcia-Ojalvo, L.M. Liberman, M.B. Elowitz, Nature 440, 545 (2006)
- 54. K. Mergenthaler, R. Engbert, Phys. Rev. Lett. 98, 138104 (2007)
- 55. J.L. Cabrera, J.G. Milton, Phys. Rev. Lett. 89, 158702 (2002)
- S. Bauer, O. Brox, J. Kreissl, B. Sartorius, M. Radziunas, J. Sieber, H.J. Wunsche, F. Henneberger, Phys. Rev. E 69, 016206 (2004)
- 57. W. Gerstner, J.L. van Hemmen, Phys. Rev. Lett. **71**, 312 (1993)
- 58. K.I. Cooke, Y. Kuang, B. Li, Can. Appl. Maths. Q 6, 321 (1998)
- 59. G.S.K. Woekowicz, H. Xia, S. Ruan, SIAM J. Appl. Math. 57, 1281 (1997)
- 60. W. Zhao, T. Zhang, Z. Chang, X. Meng, Y. Liu, J. Appl. Math. ID 154387 1, 1–15 (2013)
- S.M.A.S. Elsheikh, K.C. Patidar, R. Ovifki, IMA J. Appl. Math. 79, 1139 (2014)
 DOI:10.1093/imamat/hxt009
- 62. A.A. Doinikov, R. Manasseh, A. Ooi, J. Acoust. Soc. Am. 117, 47 (2005)
- 63. K. Ferrara, R. Pollard, M. Borden, Annu. Rev. Biomed. Eng. 9, 415 (2007)
- C.R. Heckman, S.M. Sah, R.H. Rand, Commun. Nonlinear Sci. Numer. Simul. 15, 2735 (2010)
- 65. D.M. Kane, K.A. Shore, Unlocking Dynamical Diversity: Optical Feedback Effects on Semiconductor Lasers (Wiley, New York, 2005)
- 66. E.M. Shahverdiev, K.A. Shore, Phys. Rev. E 77, 057201 (2008)
- 67. T. Erneux, P. Glorieux, Laser Dynamics (Cambridge University Press, Cambridge, 2010)
- A. Argyris, D. Syvridis, L. Larger, V. Annovazzi-Lodi, P. Colet, I. Fischer, J. Garcia-Ojalvo, C.R. Mirasso, L. Pesquera, K.A. Shore, Nature 438, 343 (2005)
- A. Uchida, K. Amano, M. Inoue, K. Hirano, S. Naito, H. Someya, I. Oowada, T. Kurashige, M. Shiki, S. Yoshimori, K. Yoshimura, P. Davis, Nat. Photonics 2, 728 (2008)
- 70. A. Bacci, J.R. Huguenard, D.A. Prince, J. Neurosci. 23, 859 (2003); Neuron 49, 119 (2006)
- 71. O. Diez-Martinez, J.P. Segundo, Biol. Cybern. 47, 33 (1983)
- 72. K. Pakdaman, J.F. Vibert, E. Boussard, N. Azmy, Neural Netw. 9, 797 (1996)
- 73. V. Ravichandran, V. Chinnathambi, S. Rajasekar, Pramana J. Phys. 78, 347 (2012)
- 74. C. Jeevarathinam, S. Rajasekar, M.A.F. Sanjuan, Phys. Rev. E 83, 066205 (2011)
- 75. J. Wei, S. Ruan, Phys. D 130, 255 (1995)
- 76. Y. Song, M. Han, Y. Peng, Chaos, Solitons Fractals 22, 1139 (2004)
- 77. A. Ahlborn, U. Parlitz, Phys. Rev. E **72**, 016206 (2005)
- 78. Q. Wei, Z. Yan, W.Y. Hai, Chin. Phys. **16**, 2259 (2007)
- 79. J.E.S. Socolar, D.J. Gauthier, Phys. Rev. E 57, 6589 (1998)
- 80. E.M. Shahverdiev, K.A. Shore, Phys. Rev. E 77, 057201 (2008)
- 81. A. Englert, S. Heiligenthal, W. Kinzel, I. Kanter, Phys. Rev. E 83, 046222 (2011)
- 82. W.S. Lee, J.G. Restrepo, E. Ott, T.M. Antonsen, Chaos 21, 023122 (2011)
- 83. N.H. Gazi, M. Bandyapadhyay, Int. J. Math. Math. Sci. Article ID 25619, 1–28 (2006)
- 84. S. Gakkhar, S.K. Sahani, K. Negi, Chaos, Solitons Fractals 39, 230 (2009)
- 85. S. Gakkhar, K. Negi, S.K. Sahani, Commun. Nonlinear Sci. Numer. Simul. 14, 8507 (2009)
- 86. L. Illing, C.D. Panda, L. Shareshian, Phys. Rev. E 84, 016213 (2011)
- R. Martinenghi, S. Rybalko, M. Jacquot, Y.K. Chembo, L. Larger, Phys. Rev. Lett. 108, 244101 (2012)
- 88. C. Jeevarathinam, S. Rajasekar, M.A.F. Sanjuan, Chaos 23, 013136 (2013)
- C. Jeevarathinam, S. Rajasekar, M.A.F. Sanjuan, J. Appl. Nonlinear Dynamics (in press, 2015)
- 90. E. Witrant, C.C. de-Wit, D. Georges, M. Alamir, IEEE Trans. Autom. Control 52, 1480 (2007)
- R. Sipahi, S. Lammer, D. Helbing, S.I. Niculescu, J. Dyn. Syst. Meas. Contr. 131, 021005 (2009)
- 92. R. Sipahi, F.M. Atay, S.I. Niculescu, SIAM J. Appl. Math. 68, 738 (2007)
- 93. J.D. Sterman, Business Dynamics: Systems Thinking and Modeling for a Complex World (McGraw-Hill, New York, 2000)
- 94. J.M. Mahaffy, J. Belair, M.C. MacKey, J. Theor. Biol. 190, 135 (1998)
- 95. M. Hansen, J. Stoustrup, J.D. Bendtsen, in 18th IFAC World Congress (2011)

References 201

- 96. Y. Altntas, S. Engin, E. Budak, J. Manuf. Sci. Eng. 121, 173 (1999)
- 97. D. Helbing, Rev. Mod. Phys. **73**, 1067 (2001)
- 98. X. Litrico, V. Fromion, Appl. Math. Model. 28, 677 (2004)
- 99. K. Nandakumar, M. Wiercigroch, J. Sound Vib. 332, 2575 (2013)
- 100. H.A. Swadlow, J. Neurophysiol. **68**, 505 (1992)
- J.P. Finertz, The Population Ecology and Cycles in Small Mammals (Yale University Press, New Heaven, 1980)
- J.R. Flowerden, Mammals: Their Reproductive Biology and Population Ecology (Edward Arnold, London, 1987)
- 103. K.I. Cooke, Y. Kuang, B. Li Can. Appl. Math. Q. 6, 321 (1998)
- 104. A.C. Marti, M. Ponce, C. Masoller, Phys. Rev. E 72, 066217 (2005)
- 105. X. Liu, S. Zhang, F. Zhang, Chaos, Solitons Fractals 24, 1299 (2005)
- 106. D. Yue, Y.J. Zhang, E.G. Tian, C. Perg, IEEE Trans. Neural Netw. 19, 1299 (2008)
- 107. X. Lon, Q. Ye, B. Cui, Neuro Comput. 73, 759 (2010)
- 108. S. Blythe, X. Mao, X. Liao, J. Frankl. Inst. 338, 481 (2001)
- 109. C. Massoller, A.C. Marti, Phys. Rev. Lett. 94, 134102 (2005)
- 110. G. Wen, G.G. Wang, C. Lin, X. Han, G. Li, Chaos, Solitons Fractals 29, 1142 (2006)
- 111. T. Caraballo, P.E. Kloeden, J. Real, J. Dyn. Diff. Equat. 18, 863 (2006)
- 112. J. Nilsson, B. Bernhardsson, S. Wittenmark, Automatica 34, 57 (1998)
- 113. L.M.T. Romero, B. Lindley, I.B. Schwartz, Phys. Rev. E 86, 056202 (2012)
- 114. Z. Sun, X. Yang, W. Xu, Phys. Rev. E 85, 061125 (2012)
- 115. S.L. Gao, K. Wei, S.C. Zhong, H. Ma, Phys. Rev E 86, 025002 (2012)
- 116. P.L. Krapivsky, J.M. Luck, K. Mallick, J. Stat. Mech: Theory Exp. 10, P10008 (2011)
- L. Ravisankar, V. Ravichandran, V. Chinnathambi, S. Rajasekar, Int. J. Theor. Appl. Phys. 4, 1 (2014)

Chapter 7 Signal Propagation in Unidirectionally Coupled Systems

A *network* is defined as a collection of points (called *nodes* or *vertices*) joined together in pairs by lines called *edges*. Many systems in physics, engineering, biology and social sciences can be thought of as networks. An array of coupled systems can be considered as a network where the nodes represent the elements or units of the system and the edges represent the interactions or couplings between them. Networks of coupled systems are used to model biological oscillator networks [1–5], excitable media [6], neural networks [7–10] and genetic networks [11–13]. A network composed of a number of interacting systems (identical or nonidentical) often forms a complex dynamical system with new fascinating properties that are not realizable in the individual systems. The fascinating properties include synchronous oscillations, induced oscillations, fast system response, computational power and so on.

Internet is a simple example of a network in which the nodes are computers while the optical fiber cables or telephone lines connecting the computers are edges. Genetic networks are the networks of connections between proteins either directly or indirectly interact with one another in living cells. Such interactions make up a dynamic genetic regulatory network which acts as a complex dynamic system for controlling cellular functions. In an ecological network, the nodes are the species in an ecosystem while the predator-prey relationships form the edges.

In molecular biology, networks are used to represent the patterns of chemical reactions of chemicals in the cell. Patterns of connections between brain cells are represented by networks. Cells and micro-organisms respond to their environments through an interconnected network of receptors, messengers and other signalling molecules [14, 15]. Networks of flux gate magnetometers are shown to be useful to enhance the utility and sensitivity of a large class of nonlinear sensors such as the magnetometers, ferroelectric detectors for electric fields [16, 17].

Study of networks with different types of couplings and connectivity topology is important because they carry information from one unit to another and act as a source of amplification of information. This would help us to learn and understand the role of connectivity topology in networks. There are different kinds of networks [5]. In general networks are classified into weighted networks, directed networks, bipartite networks, unidirectional networks, cyclic and acyclic directed networks, bidirectional networks, random networks and small-world networks. Study of features of various nonlinear phenomena in different types of networks is of great significance. In this chapter we restrict ourselves to the study of nonlinear resonance, stochastic resonance and vibrational resonance in unidirectionally coupled nonlinear systems. In a network of unidirectionally coupled systems, information flow is produced along one direction, for example, from ith system to jth system (i > i) and no information flows from jth system to jth system. In unidirectionally coupled systems, we investigate the role of coupling on the enhancement of the response amplitude. In all the three types of resonances the network system displays undamped signal propagation (that is, the response amplitude of the last unit is greater than that of the first unit) for certain range of values of the coupling parameter. We employ a theoretical approach for nonlinear resonance and vibrational resonance. We identify the conditions for undamped signal propagation. When the number of units increases, the response amplitude approaches a limiting value. We point out the determination of this limiting value.

7.1 Significance of Unidirectional Coupling

It is of great significance to introduce external perturbations, like weak input periodic signal and weak noise, to only one unit of a network and also consider a simple connectivity, for example, unidirectional linear coupling and investigate the signal propagation through the units. In a unidirectionally coupled network of systems the information flow is along one direction. The output of *i*th unit is fed to (i+1)th unit only through a coupling term. The time evolution of one or more state variables of *i*th unit depends on one or more state variables of the (i-1)th unit. The dynamics of the (i-1)th unit does not depend on the state variables of the *i*th unit. The dynamics of the first unit is independent of other units. The output of the last unit is not fed to any other unit. Figure 7.1a shows the pictorial representation of 10 units coupled unidirectionally. Here, the *i*th unit is coupled to the (i+1)th unit only, that is, the number of coupling is one. Coupling of the *i*th unit with, for example, i+1, i+2, \cdots , i+m, units give rise a unidirectionally coupled systems with m coupling. Figure 7.1b depicts an example with two couplings.

A set up of a network of the above type has applications in digital sonar arrays, networks of sensory neurons, analog to digital converters, where arrays are useful for the transmission of an input signal. For chaos synchronization and communication in coupled lasers often in the transmitter receiver set up the transmitter laser is unidirectionally coupled to a receiver laser [18].

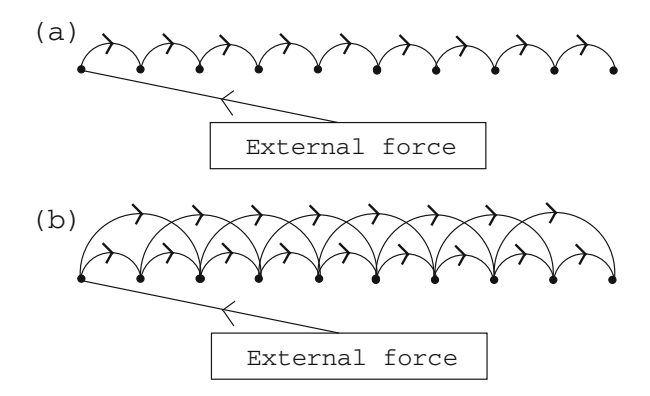


Fig. 7.1 Examples of one-way coupled networks with 10 units. The dynamics of the first unit is independent of the other units and this is alone driven by external forces. (a) *i*th unit $(i \neq 1)$ is linearly coupled to (i - 1)th unit. The *arrow mark* indicates that the output of *i*th unit is fed to (i + 1)th unit only through the linear coupling term. (b) *i*th unit (i > 2) is linearly coupled to both (i - 1)th and (i - 2)th sites while the second site (i = 2) is coupled to the first site only

There are few interesting dynamics realized as a result of unidirectional coupling. One-way coupling was introduced by In and his collaborators [16, 19] to induce oscillations in undriven, overdamped and bistable systems. The mechanism for the generation of oscillations is described for a three-coupled network of overdamped Duffing oscillators [20]. The response of three-(one-way) coupled core magnetometer systems to a periodic magnetic-flux signal applied to all the three units is explored. The response is found to be either synchronized to the signal frequency or to one-third of it [21]. In one-way coupled systems propagation of waves of dislocations in equilibria are found [22]. One-way coupling is utilized in electronic sensors and microelectronic circuits [17] and is found to assist the propagation of localized nonlinear waves [23, 24]. Experimental evidences of propagation and annihilation of solitons in a mechanical array of unidirectionally coupled oscillators [25] and an electronic circuit in two-dimensions [26] are reported. Improved transmission of low-frequency signal by the combined action of high-frequency input signal and one-way coupling has been found in coupled nonlinear systems [27-29].

In biology also unidirectionally coupled structures constitute one of the simplest topologies of practical interest. We cite now an example from the field of gene regulatory network. A network of transcriptional regulators of considerable interest is the repressilator model. It is a network consisting of n genes with the protein product of ith gene represses the expression of (i + 1)th gene with periodic boundary conditions. Oscillatory dynamics is found in an experimentally constructed repressilator with three cells [30]. Occurrence of monostable, spiral and limit cycle dynamics are analysed in a mathematical model of repressilator with

three genes [31, 32]. A repressilator system with even number of genes is found to exhibit multistability while with odd number of genes display a stable limit cycle [33]. Existence of quasi-stable travelling wave periodic solutions is analysed both theoretically and numerically in unidirectionally coupled repressilators [34, 35].

7.2 Nonlinear Resonance and Signal Propagation

We consider *n* Duffing oscillators coupled unidirectionally. The equation of motion of the coupled systems is given by

$$\ddot{x}_1 + d\dot{x}_1 + \omega_0^2 x_1 + \beta x_1^3 = f \cos \omega t, \tag{7.1a}$$

$$\ddot{x}_i + d\dot{x}_i + \omega_0^2 x_i + \beta x_i^3 = \delta x_{i-1}, \quad i = 2, 3, \dots, n.$$
 (7.1b)

Assume that the values of all parameters in Eq. (7.1) are > 0. In the system (7.1) the first oscillator alone driven by the periodic signal $f \cos \omega t$. The other oscillators are coupled unidirectionally. The system (7.1) is capable of displaying a variety of nonlinear phenomena. Here the interest is on the resonance behaviour and enhancement of amplitude of periodic response of the system due to unidirectional coupling. Therefore, choose $f \ll 1$ so that in Eq. (7.1a) periodic oscillation takes place about the equilibrium point.

By applying a perturbation theory to the system (7.1), it is possible to obtain a set of coupled nonlinear equations for the amplitudes of the period- $T = 2\pi/\omega$ solutions of the oscillators. Then, one can analyse the influence of one-way coupling on response amplitudes and resonance [36].

7.2.1 Theoretical Treatment

Assume the periodic solution of (7.1) as

$$x_i(t) = a_i(t)\cos\omega t + b_i(t)\sin\omega t, \tag{7.2}$$

where $a_i(t)$ and $b_i(t)$ are slowly varying functions of time t. Write

$$x_i^3 \approx \frac{3}{4} \left(a_i^2 + b_i^2 \right) \left(a_i \cos \omega t + b_i \sin \omega t \right), \tag{7.3a}$$

$$\dot{x}_i(t) = \dot{a}_i \cos \omega t + \dot{b}_i \sin \omega t - a_i \omega \sin \omega t + b_i \omega \cos \omega t \tag{7.3b}$$

$$\ddot{x}_i(t) = -2\dot{a}_i\omega\sin\omega t + 2\dot{b}_i\omega\cos\omega t - a_i\omega^2\cos\omega t - b_i\omega^2\sin\omega t, \quad (7.3c)$$

where in Eq. (7.3c) \ddot{a}_i and \ddot{b}_i are neglected because of their smallness. Substitution of (7.2)–(7.3) in (7.1), dropping $d\dot{a}_i$ and $d\dot{b}_i$ as they are assumed to be small and then equating the coefficients of $\sin \omega t$ and $\cos \omega t$ separately to zero lead to

$$\dot{a}_i = -\frac{b_i}{2\omega} \left[\omega^2 - \omega_0^2 - \frac{3}{4}\beta \left(a_i^2 + b_i^2 \right) \right] - \frac{1}{2}da_i + S_a, \tag{7.4a}$$

$$\dot{b}_i = \frac{a_i}{2\omega} \left[\omega^2 - \omega_0^2 - \frac{3}{4}\beta \left(a_i^2 + b_i^2 \right) \right] - \frac{1}{2}db_i + S_b, \tag{7.4b}$$

where

for
$$i = 1$$
: $S_a = 0$, $S_b = \frac{f}{2\omega}$, (7.5a)

for
$$i > 1$$
: $S_a = -\frac{\delta b_{i-1}}{2\omega}$, $S_b = \frac{\delta a_{i-1}}{2\omega}$. (7.5b)

Next, we introduce the transformation

$$a_i(t) = A_i(t)\cos\theta_i(t), \quad b_i(t) = A_i(t)\sin\theta_i(t)$$
 (7.6)

with $A_i^2 = a_i^2 + b_i^2$. Then Eq. (7.4) become

$$\dot{A}_i = -\frac{1}{2}dA_i + S_A, \quad A_i\dot{\theta}_i = \frac{A_i}{2\omega} \left[\omega^2 - \omega_0^2 - \frac{3}{4}\beta A_i^2\right] + S_\theta,$$
 (7.7a)

where for i = 1

$$S_A = \frac{f}{2\omega} \sin \theta_1, \quad S_\theta = \frac{f}{2\omega} \cos \theta_1$$
 (7.8a)

and for i > 1

$$S_A = \frac{\delta}{2\omega} A_{i-1} \sin(\theta_i - \theta_{i-1}), \quad S_\theta = \frac{\delta}{2\omega} A_{i-1} \cos(\theta_i - \theta_{i-1}). \tag{7.8b}$$

The response of the system (7.1) in the long time limit is periodic with period-T (= $2\pi/\omega$) provided $A_i(t)$ and $\theta_i(t)$ become constants as $t \to \infty$ and are the equilibrium points of Eq. (7.7). To find the equilibrium points of (7.7) set $\dot{A}_i = \dot{\theta}_i = 0, A_i(t) = A_i^*, \theta_i(t) = \theta_i^*$ and drop * in A_i and θ_i . The result is [36]

$$A_i^2 \left[\omega_0^2 - \omega^2 + \frac{3}{4} \beta A_i^2 \right]^2 + d^2 \omega^2 A_i^2 = \begin{cases} f^2, & \text{for } i = 1\\ \delta^2 A_{i-1}^2, & \text{for } i > 1 \end{cases}$$
 (7.9)

and

$$\theta_i = \theta_{i-1} + \tan^{-1} \left[\frac{d\omega}{\omega_0^2 - \omega^2 + \frac{3}{4}\beta A_i^2} \right], \quad \theta_0 = 0.$$
 (7.10)

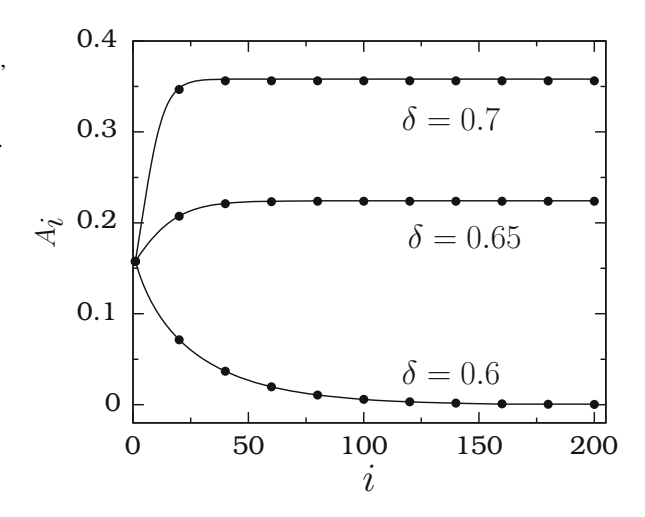
When i=1 Eq. (7.9) is the frequency-response equation of the first oscillator. For i>1 Eq. (7.9) is independent of f and depends on the coupling constant δ and the response amplitude A_{i-1} of the (i-1)th oscillator. Equation (7.9) (for i>1) is the coupling strength-response (amplitude) equation of the ith oscillator. The amplitude and phase of the ith oscillator with i>1 depend on the amplitude and phase, respectively, of the (i-1)th oscillator. A_i 's and θ_i 's can be determined by solving Eqs. (7.9) and (7.10) successively.

7.2.2 Analysis of Effect of One-Way Coupling

Now, analyse the influences of the coupling strength on the response amplitudes A_i and resonance. We fix the values of the parameters as d = 0.5, $\omega_0^2 = 1$, $\beta = 1$ and f = 0.1 and n = 200. Equation (7.9) contains even powers of A_i . It can be viewed as a cubic equation in terms of A_i^2 . Explicit analytical expressions for the roots of a cubic equation is given in [37]. Equation (7.9) can admit either one real root or three real roots. First, we determine the values of A_1 and then successively calculate A_2 , A_3 , \cdots .

Figure 7.2 shows both theoretically and numerically computed A_i versus i for a few fixed values of δ with $\omega = 0.7$. The theoretical A_i 's very closely match with numerically calculated A_i 's. For $\delta = 0.6$ as i increases the amplitudes A_i of oscillation of the consecutive oscillators decrease and the distant oscillators do

Fig. 7.2 Variation of the response amplitudes A_i with i, the number of oscillators, for three values of the coupling strength δ of the system (7.1). The *continuous lines* and *solid circles* represent theoretical and numerical values of A_i . The values of the parameters are d = 0.5, $\omega_0^2 = 1$, $\beta = 1$, f = 0.1 and $\omega = 0.7$



not oscillate but settle to the equilibrium state which is the origin. The coupled oscillators exhibit damped signal propagation $(A_i \to 0 \text{ as } i \to \infty)$. When $\delta = 0.65$ and 0.7 in Fig. 7.2 A_i increases with i and then reaches a saturation. Though the first oscillator alone is driven by the periodic force, the one-way coupling gives rise enhanced signal propagation $(A_i > A_1 \text{ for } i \gg 1)$ over the coupled oscillators. This is a quintessence feature of one-way coupling. The point is that for the parametric values corresponding to the undamped signal propagation, there exists a critical number of oscillators to realize a maximum value of the response amplitude of the last oscillator. This critical number of oscillators and the maximum amplitude depend on the control parameters ω and δ .

Interestingly, the value of the saturated amplitude denoted as $A_{\rm L}$ (limiting value of A in the limit of very large i) and the condition on δ for undamped signal propagation can be determined from Eq. (7.9). $A_{\rm L}=0$ and $A_{\rm L}>A_{\rm l}$ for damped and undamped signal propagation, respectively. Equation (7.9) for i>1 can be treated as a map between A_{i-1} and A_i . The stable equilibrium states of Eq. (7.9) are the values of $A_{\rm L}$. For i>1, to obtain the equilibrium states set $A_i=A_{i-1}=A_{\rm L}$. This gives $A_{\rm L}=0$ and

$$A_{\rm L\pm} = \left[\frac{4}{3\beta} \left(\omega^2 - \omega_0^2 \pm \sqrt{\delta^2 - d^2 \omega^2} \right) \right]^{1/2}.$$
 (7.11)

Now, there are two cases:

Case 1: $\omega^2 < \omega_0^2$

When $\omega^2 < \omega_0^2$, $A_L = 0$ is the only equilibrium state for $\delta < \delta_c$ with

$$\delta_{\rm c} = \sqrt{\left(\omega^2 - \omega_0^2\right)^2 + d^2 \omega^2} = \frac{f}{A_{\rm linear}},$$
 (7.12)

where A_{linear} is the response amplitude of the linear part of Eq. (7.1a) ($\beta = 0$). $A_{\text{L}} = 0$ and $A_{\text{L}\pm}$ are the equilibrium states for $\delta > \delta_{\text{c}}$.

Case 2: $\omega^2 > \omega_0^2$

 $A_{\rm L}=0$ is the only equilibrium state for $\delta < d\omega$. For $d\omega < \delta < \delta_{\rm c}$ the equilibrium states are $A_{\rm L}=0$ and $A_{\rm L\pm}$. When $\delta > \delta_{\rm c}$ the equilibrium states are $A_{\rm L}=0$ and $A_{\rm L\pm}$.

Next, find the condition on δ for enhanced and undamped signal propagation. The difference between the equations for A_1 and A_i , i > 1 is only in the last term in Eq. (7.9). For A_1 the last term is f^2 while for A_i it is $\delta^2 A_{i-1}^2$. In order to have $A_2 > A_1$ the condition is $\delta^2 A_1^2 > f^2$, that is, $\delta > \delta_{\rm u} = f/A_1$. The value of A_1 for $\omega = 0.7$ and f = 0.1 is 0.1577 and $\delta_{\rm u} = 0.634$. That is, undamped signal propagation occurs for $\delta > 0.634$ and is confirmed in the numerical simulation. $A_{\rm L\pm}$ given by Eq. (7.11) depend on all the parameters of the system except f. Further, $A_{\rm L+}(A_{\rm L-})$ increases (decreases) with increase in the value of δ .

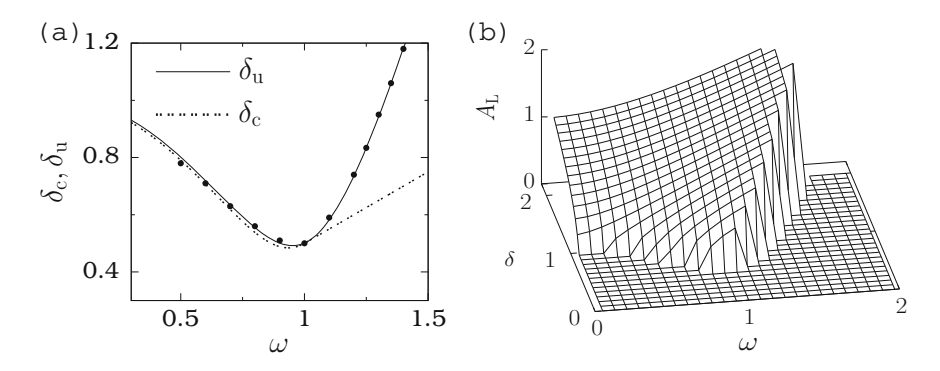


Fig. 7.3 (a) Theoretical δ_c (dotted curve) and δ_u (continuous curve) versus ω for the system (7.1). The solid circles are the numerically computed values of δ_u . (b) Variation of A_L with the parameters δ and ω . Zero and nonzero values of A_L represent damped and undamped signal propagations, respectively

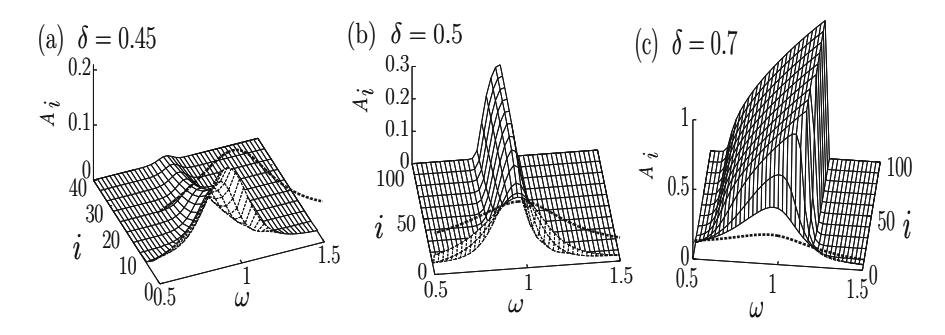


Fig. 7.4 A_i versus i and ω for the system (7.1). A_i is shown only for some selected values of i. The *thick curve* represents A_1

In Fig. 7.3a shows the dependence of δ_c and δ_u with ω . For the values of ω and δ below the lower curve $A_L=0$ is the only equilibrium state and is stable. In the regions between the upper and lower curves in addition to $A_L=0$, a nontrivial A_L also exists with $A_L(\neq 0) < A_1$. The nontrivial state is unstable while the state $A_L=0$ is stable. In the regions above, the upper curve $A_L=0$ is unstable while the nontrivial $A_L>A_1$ is stable leading to an enhanced undamped signal propagation. Undamped signal propagation with $A_L(\neq 0) < A_1$ is not observed. Figure 7.3b presents A_L versus δ and ω . For each fixed value of ω , A_L increases monotonically with δ for $\delta>\delta_u$.

Figure 7.4 presents the frequency-response amplitude profile of various oscillators for a few fixed values of δ . For $\delta = 0.45$, in Fig. 7.3b $A_L = 0$ for all values of ω . In Fig. 7.4a for all values of ω , A_i decays to zero as i increases. The output signal damps out as it propagates through the oscillators. When $\delta = 0.5$ in Fig. 7.3b note that $A_L \neq 0$ for a small range of values of ω implying undamped signal propagation

and is evident in Fig. 7.4b. The range of ω values for which undamped signal propagation takes place increases with increase in δ . This is clearly seen in Fig. 7.4a–c. In Fig. 7.4c where $\delta = 0.7$ for first certain number of oscillators the response amplitude A_i increases with ω , reaches a maximum and then decreases smoothly. For distant oscillators after reaching a maximum value A_i suddenly jumps to a lower value.

7.2.3 Unidirectionally Coupled Linear Systems

For the unidirectionally coupled linear systems $[\beta = 0)$ in Eq. (7.1)] we obtain

$$A_{1} = \frac{f}{\sqrt{(\omega_{0}^{2} - \omega^{2})^{2} + d^{2}\omega^{2}}}, \quad A_{i} = \frac{\delta A_{i-1}}{\sqrt{(\omega_{0}^{2} - \omega^{2})^{2} + d^{2}\omega^{2}}}, \quad i = 2, 3, \dots, n.$$

$$(7.13)$$

Replacing i by i + 1 and expressing A_{i+1} in terms of A_1 give

$$A_{i+1} = \left(\frac{\delta}{\sqrt{(\omega_0^2 - \omega^2)^2 + d^2 \omega^2}}\right)^i A_1, \quad i = 1, 2, \dots, n-1.$$
 (7.14)

For fixed values of the parameters if $\delta/\sqrt{(\omega_0^2-\omega^2)^2+d^2\omega^2}<1$ then A_i decreases with increase in i. For $\delta/\sqrt{(\omega_0^2-\omega^2)^2+d^2\omega^2}>1$ as i increases monotonically. That is, either A_i decays to zero or diverges with i. There is no nontrivial variation of A_i with i depending upon the values of the parameters.

7.3 Vibrational Resonance and Signal Propagation

In the previous section, we have shown the undamped signal propagation induced by unidirectional coupling in the n-coupled Duffing oscillators in which only the first oscillator is driven by a single periodic force. In the present section, we focus our interest on the effect of unidirectional coupling on vibrational resonance in n coupled Duffing oscillators. The equation of motion of the network system is

$$\ddot{x}_1 + d\dot{x}_1 + \omega_0^2 x_1 + \beta x_1^3 = f \cos \omega t + g \cos \Omega t, \tag{7.15a}$$

$$\ddot{x}_i + d\dot{x}_i + \omega_0^2 x_i + \beta x_i^3 = \delta x_{i-1}, \quad i = 2, 3, \dots, n.$$
 (7.15b)

We first apply the theoretical treatment employed in Sect. 3.1 for a single Duffing oscillator to the n-coupled oscillators system (7.15) [27].

7.3.1 Theoretical Treatment

Writing $x_i = X_i + \psi_i$, where X_i 's and ψ_i 's are slow and fast variables, respectively, and following the procedure described in Sect. 3.1 one can finally arrive at the following results:

$$\psi_i = \mu_i \cos(\Omega t + \Phi), \quad \Phi = \tan^{-1}\left(\frac{d\Omega}{\Omega^2 - \omega_0^2}\right),$$
 (7.16a)

$$\mu_1 = \frac{g}{\sqrt{(\Omega^2 - \omega_0^2)^2 + d^2 \Omega^2}},$$
(7.16b)

$$\mu_i = \frac{\delta \mu_{i-1}}{\sqrt{(\Omega^2 - \omega_0^2)^2 + d^2 \Omega^2}}, \quad i = 2, 3, \dots, n$$
 (7.16c)

$$Y_i(t) = Q_i f \cos(\omega t + \phi_i), \tag{7.17a}$$

where

$$Q_1 = \frac{1}{\sqrt{(\omega_{\rm rl}^2 - \omega^2)^2 + d^2 \omega^2}}, \quad Q_i = P_i Q_{i-1}$$
 (7.17b)

$$P_i = \frac{\delta}{\sqrt{(\omega_{\rm ri}^2 - \omega^2)^2 + d^2 \omega^2}}, \quad i = 2, 3, \dots, n$$
 (7.17c)

$$\omega_{ri}^2 = C_i + 3\beta X_i^{*2}, \quad C_i = \omega_0^2 + \frac{3}{2}\beta\mu_i^2, \quad i = 1, 2, \dots n$$
 (7.17d)

$$X_1^* \left(X_1^{*2} + \frac{C_1}{\beta} \right) = 0, (7.17e)$$

$$X_i^{*3} + \frac{C_i}{\beta} X_i^* - \frac{\delta}{\beta} X_{i-1}^* = 0, \quad i = 2, 3, \dots, n.$$
 (7.17f)

Note that, in obtaining the theoretically calculated Q_i , the nonlinear terms in the equations of motion of the fast variables ψ_i and the slow variables $Y_i (= X_i - X_i^*)$. In the system of n-coupled oscillators, the error in the theoretical Q_i 's due to the above approximation grows with the oscillator number i when $Q_i > 1$ for $i \gg 1$. Figure 7.5 shows the variation of theoretical and numerical Q_i with i for d = 0.5, $\omega_0^2 = 1$, $\beta = 1$, f = 0.1, $\omega = 1.5$, $\Omega = 15$, $\delta = 1.6$ and for few values of g. The numerically computed Q_i approaches a constant value for $i \gg 1$, while the

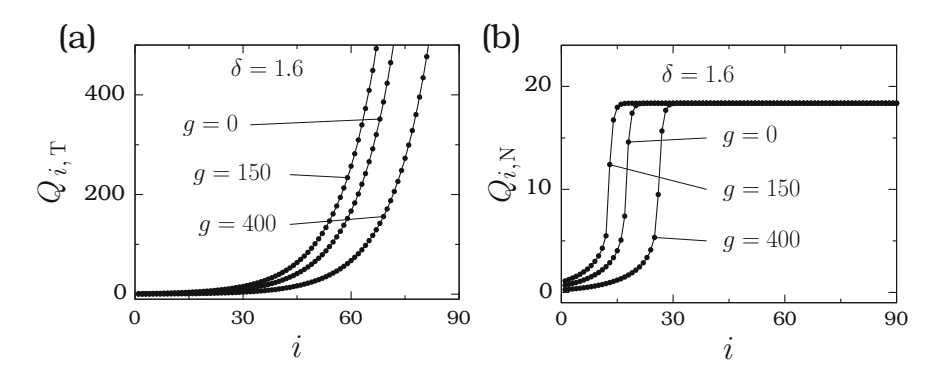


Fig. 7.5 (a) $Q_{i,\text{T}}$, theoretically calculated Q_i , versus i and (b) $Q_{i,\text{N}}$, numerically computed Q_i , versus i for the system (7.15) with d=0.5, $\omega_0^2=1$, $\beta=1,f=0.1$, $\omega=1.5$, $\Omega=15$, $\delta=1.6$ and for three values of g

theoretically computed Q_i diverges with i for all the fixed values of g including the case g = 0.

In obtaining μ_i given by Eqs. (7.16b) and (7.16c), it has been assumed that $\ddot{\psi}_i \gg \psi_i^2$ and ψ_i^3 . This can be valid in the case of i=1, where the first oscillator is driven by the high-frequency force $g\cos\Omega t$. Because the other oscillators are not driven explicitly by the force $g\cos\Omega t$, the assumption $\ddot{\psi}_i \gg \psi_i^2$ and ψ_i^3 is not valid. Moreover, in the analytical calculation of Q_i also the nonlinear terms in the equations of Y_i are neglected. There are errors due to the neglect of the nonlinear terms in the equations of ψ_i and Y_i and further the errors in ψ_i and Y_i propagate to the (i+1)th oscillator through the coupling term. As a result, $\Delta Q_i = Q_{i,N} - Q_{i,T}$ is negligible for the first few oscillators and becomes large for $i \gg 1$.

In order to minimize the error in the theoretical Q_i and also to minimize the propagation of this error through the consecutive oscillators, we keep the nonlinear terms in the calculation of the amplitudes of oscillation of the fast and slow variables [27]. Now assume

$$\psi_i = \mu_i \cos(\Omega t + \phi_i), \quad X_i = A_i \cos(\omega t + \theta_i). \tag{7.18}$$

Substitution of the above solutions in the equations

$$\ddot{\psi}_1 + d\dot{\psi}_1 + \omega_0^2 \psi_1 + \beta \psi_1^3 = g \cos \Omega t, \tag{7.19a}$$

$$\ddot{\psi}_i + d\dot{\psi}_i + \omega_0^2 \psi_i + \beta \psi_i^3 = \delta \psi_{i-1}, \tag{7.19b}$$

$$\ddot{X}_1 + d\dot{X}_1 + \omega_{01}^2 X_1 + \beta X_1^3 = f \cos \omega t, \tag{7.19c}$$

$$\ddot{X}_i + d\dot{X}_i + \omega_{0i}^2 X_i + \beta X_i^3 = \delta X_{i-1}, \tag{7.19d}$$

where $i = 2, 3, \dots, n$ and $\omega_{0j}^2 = \omega_0^2 + (3/2)\beta\mu_j^2, j = 1, 2, \dots, n$ gives

$$\mu_i^6 + a_\mu \mu_i^4 + b_\mu \mu_i^2 - R_{i\mu} = 0, \tag{7.20}$$

$$A_i^6 + a_{iA}A_i^4 + b_{iA}A_i^2 - R_{iA} = 0, \quad i = 1, 2, \dots, n$$
 (7.21)

with

$$a_{\mu} = \frac{8}{3\beta} \left(\omega_0^2 - \Omega^2 \right), \quad b_{\mu} = \frac{16}{9\beta^2} \left[\left(\omega_0^2 - \Omega^2 \right)^2 + d^2 \Omega^2 \right], \quad (7.22a)$$

$$R_{1\mu} = \frac{16g^2}{9\beta^2}, \quad R_{1A} = \frac{16f^2}{9\beta^2}, \quad a_{iA} = \frac{8}{3\beta} \left(\omega_{0i}^2 - \omega^2\right),$$
 (7.22b)

$$b_{iA} = \frac{16}{9\beta^2} \left[\left(\omega_{0i}^2 - \omega^2 \right)^2 + d^2 \omega^2 \right], \quad i = 1, 2, \dots, n$$
 (7.22c)

$$R_{i\mu} = \frac{16\delta^2 \mu_{i-1}^2}{9\beta^2}, \quad R_{iA} = \frac{16\delta^2 A_{i-1}^2}{9\beta^2}. \quad i = 2, 3, \dots, n.$$
 (7.22d)

Equations (7.20) and (7.21) can be viewed as cubic equations for the variables μ_i^2 and A_i^2 , respectively. We determine μ_i , A_i and then $Q_i = A_i/f$ by solving Eqs. (7.20) and (7.21).

7.3.2 Effect of δ and g on Q_i

First, check the validity of the theoretical approach. In Fig. 7.6a both the theoretically calculated Q_i and the numerically computed Q_i as a function of i is plotted for three values of g with $\delta=1.6$. The theoretical expression Q_i closely matches with the numerical value Q_i . For each fixed value of g as i increases, Q_i increases rapidly to a higher value and finally it attains a saturation value. The plot of Q_i versus i displays a kink-like dependence. This indicates that there is a critical number of oscillators for realizing the maximum response and this number depends on the control parameters. An important result in Fig. 7.6a is that $Q_i > Q_1$ for i > 1, even in absence of the high-frequency force. That is, a coupling alone is able to give rise to an enhanced undamped signal propagation in the coupled oscillators. Figure 7.6b illustrates the effect of the coupling strength on Q_i . For $\delta=1.2$ damped signal propagation occurs while for $\delta=1.6$ and 2 an undamped signal propagation takes place.

In Fig. 7.6 for $i \gg 1$, Q_i becomes a constant. We call this limiting value of Q_i as Q_L . Interestingly, is easy to determine μ_L , A_L and hence $Q_L = A_L/f$ from

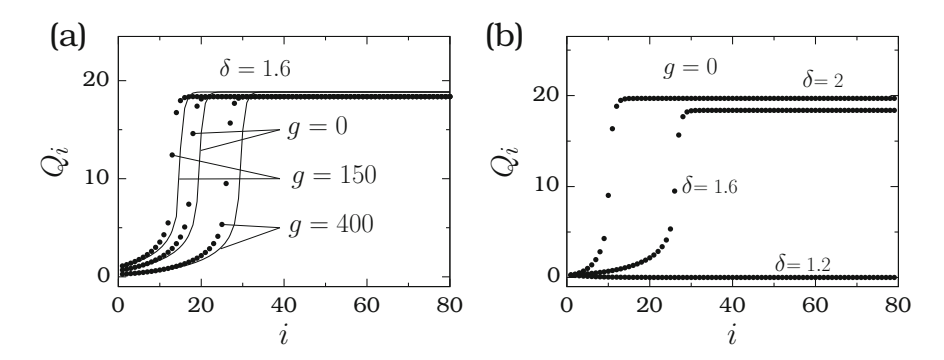


Fig. 7.6 Variation of theoretical Q_i (continuous curve) and numerical Q_i (solid circles) with i for (a) three values of g with $\delta = 1.6$. The system is (7.15). (b) Plot of theoretical Q_i as a function of i for g = 0 and for three values of δ

Eqs. (7.20) and (7.21), respectively. For large i, substitution of $\mu_i = \mu_{i-1} = \mu_L$ and $A_i = A_{i-1} = A_L$ in Eqs. (7.20) and (7.21) gives

$$\mu_{\rm L} = 0, \quad \left\{ \frac{4}{3\beta} \left[\Omega^2 - \omega_0^2 \pm \sqrt{\delta^2 - d^2 \Omega^2} \right] \right\}^{1/2}$$
 (7.23)

and

$$A_{\rm L} = 0, \quad \left\{ \frac{4}{3\beta} \left[\omega^2 - \omega_{\rm 0L}^2 \pm \sqrt{\delta^2 - d^2 \omega^2} \right] \right\}^{1/2},$$
 (7.24)

where $\omega_{0L}^2 = \omega_0^2 + (3/2)\beta\mu_L^2$. $A_L = 0$ and $\neq 0$ correspond to a damped and an undamped signal propagations, respectively. One can determine the condition on the parameter δ for undamped signal propagation. In Fig. 7.6 in all the examples of undamped signal propagation, we can observe that $Q_2 > Q_1$. Therefore, assume that if $Q_2 > Q_1$ then

$$Q_i \ge Q_{i-1} \ge \dots > Q_3 > Q_2 > Q_1.$$
 (7.25)

For Q_1 and Q_2 very good satisfactory analytical expressions are given by Eq. (7.17b) with i = 2. The condition for $Q_2 > Q_1$ is $P_2 > 1$ where

$$P_2 = \frac{\delta}{\sqrt{(\omega_{\rm r2}^2 - \omega^2)^2 + d^2 \omega^2}}, \quad \omega_{\rm r2}^2 = \omega_0^2 + \frac{3\beta g^2 \delta^2}{2\Omega^8}.$$
 (7.26)

Because of the term Ω^8 the second term in $\omega_{\rm r2}^2$ can be neglected. Then $P_2>1$ becomes

$$\delta > \delta_{\rm u} = \sqrt{(\omega_0^2 - \omega^2)^2 + d^2 \omega^2}.$$
 (7.27)

Undamped signal propagation can be realizable for $\delta > \delta_{\rm u}$. For d=0.5, $\omega_0^2=1$, $\omega=1.5$, the value of $\delta_{\rm u}$ is 1.4577. That is, undamped signal propagation takes place for $\delta > \delta_{\rm u}=1.4577$.

In the *n*-coupled systems (7.15) Q_L and δ_u are independent of the control parameter g. That is, signal transduction at the low-frequency of the input signal is induced in the coupled oscillators by the coupling term and not by the highfrequency force applied to the first oscillator. However, Q_i depends on g for values of i not very large. To illustrate this in Fig. 7.7, Q_i versus i and g is plotted for $\delta = 1.2$ and 1.6. For $\delta = 1.2 < \delta_{\rm u} = 1.4577$ as i increases the response amplitude profile decays to zero. For $\delta = 1.6 > \delta_u$, for each fixed value of g the response amplitude $Q_i > Q_1$ for i > 1. For the first few number of oscillators the response amplitude profile clearly displays vibrational resonance at a value of g. For each fixed value of g, Q_i increases and attains the limiting value Q_L . It is noteworthy to point out that $Q_L \neq 0$ for g = 0. Signal transduction takes place even in the absence of a high-frequency force. The significance of this result is that a weak signal detection and amplification can be achieved either by driving a single nonlinear system by a high-frequency periodic signal or by means of sufficient number of one-way coupled oscillators without driving the oscillators by a high-frequency signal. The theoretical treatment used in the present study clearly brings out the role of the high-frequency periodic force and the unidirectional coupling on the response amplitude and signal transduction in the network system.

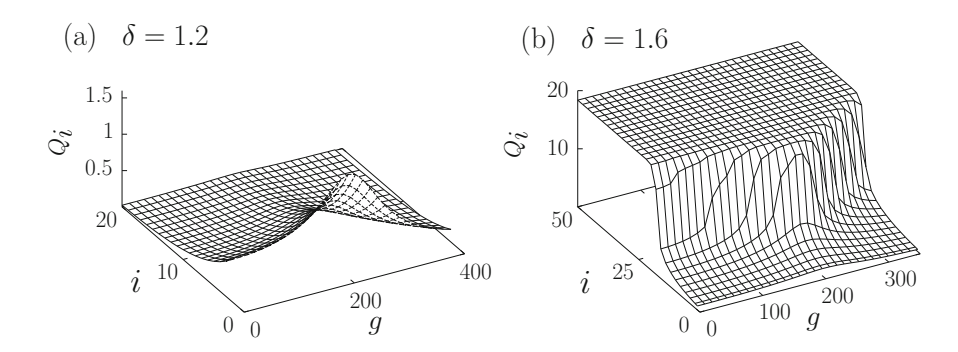


Fig. 7.7 Q_i versus i and g for (a) $\delta = 1.2$ and (b) $\delta = 1.6$ of the system (7.15)

7.4 Stochastic Resonance and Signal Propagation

Investigation of features of stochastic resonance in networks of nonlinear systems is of a great significance primarily because of its constructive role in enhancement of weak signal detection and transmission. In networks, it has been shown that the spatiality may broaden the scope of stochastic resonance [38–41]. In a network system stochastic resonance can be enhanced by a coupling term and this phenomenon is termed as enhanced stochastic resonance [38]. In Hodgkin-Huxley neuronal networks increase in the network randomness (that is increase in the number of nodes with random connectivity) is found to increase the temporal coherence and spatial synchronization [42]. Resonance-like effect depending on the number of systems, whereby an optimal number systems leading to the maximum overall coherence has been reported [43, 44]. Resonance is found in certain networks where all the systems are driven by noise, while only one system is subjected to a weak periodic signal [45, 46]. Doubly stochastic resonance consisting of a noise-induced phase transition has been observed in a conventional nonlinear lattice of coupled overdamped oscillators [47]. Double resonance peaks were found to occur in the Ising model network driven by an oscillating magnetic field [48]. Improvement of signal-to-noise ratio is possible in an uncoupled parallel array of bistable system subjected to a common noise [49]. Stochastic resonance has been studied in coupled threshold elements [50], Ising model [51], Barabasi-Albert network [52, 53], arrays of comparators [54] and in a Bär model [55].

This section explores the noise assisted enhanced signal propagation in unidirectionally coupled systems with the first system alone driven by a weak input periodic signal and Gaussian white noise. We choose each unit in the network as the bistable discrete Bellows map [56–58]. This map possesses the basic ingredients to display noise-induced resonance. The discrete equation is chosen instead of a continuous time dynamical system, mainly because the former requires relatively very less computational time and resources. Often discrete maps served as convenient models for discovering new phenomena and identifying their features. The other resonances considered in this book can also be realizable in discrete systems.

7.4.1 One-Way Coupled Bellows Map

The unidirectionally coupled N Bellows maps is given by

$$x_{n+1}^{(1)} = \frac{rx_n^{(1)}}{1 + \left(x_n^{(1)}\right)^b} + f\cos\omega n + \sqrt{D}\,\xi(n),\tag{7.28a}$$

$$x_{n+1}^{(i)} = \frac{rx_n^{(i)}}{1 + \left(x_n^{(i)}\right)^b} + \delta x_n^{(i-1)}, \quad i = 2, 3, \dots, N.$$
 (7.28b)

 $\xi(n)$ is a Gaussian white noise with the statistical properties $\langle \xi(n) \rangle = 0$, $\langle \xi(n)\xi(n') \rangle = \delta(n-n')$, D is noise intensity. We choose the value of b in the Bellows map as 2. The map $x_{n+1} = rx_n/(1+x_n^2)$ admits only one fixed point $x^* = 0$ for $0 < r \le 1$. For r > 1, it has three fixed points: $x^* = 0$ (unstable) and $x_{\pm}^* = \pm \sqrt{r-1}$ (stable). That is, the map has bistable state for r > 1. In order to realize stochastic resonance in the bistable case drive the map by a weak periodic signal $f \cos \omega n$ and the Gaussian white noise. We fix the values of the parameters in the network as r = 2, b = 2, f = 0.3, $\omega = 0.1$, N = 400 and vary the noise intensity and the coupling strength δ . The values of f is below the subthreshold, that is, in the absence of noise the periodic force alone is unable to induce transition between the two stable fixed points.

7.4.2 Numerical Results

To characterize the noise-induced resonance numerically compute the response amplitude Q_i at the input signal frequency ω . Q_i is given by

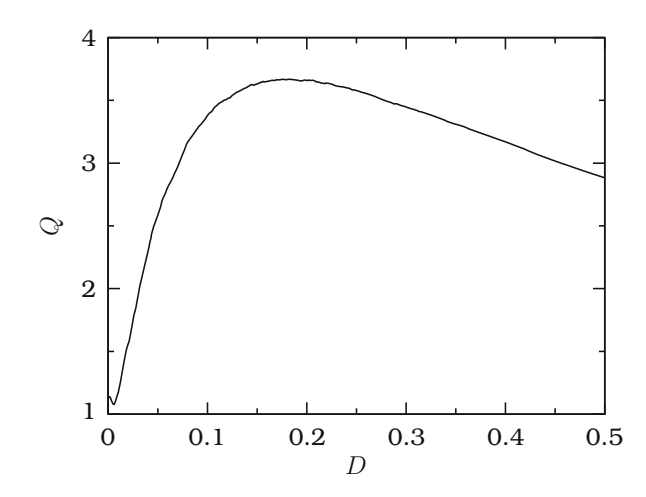
$$Q_i = \frac{\sqrt{Q_{i,C}^2 + Q_{i,S}^2}}{f},\tag{7.29a}$$

$$Q_{i,C} = \frac{2}{T_t} \sum_{n=1}^{T_t} x_n^{(i)} \cos \omega n, \quad Q_{i,S} = \frac{2}{T_t} \sum_{n=1}^{T_t} x_n^{(i)} \sin \omega n, \quad (7.29b)$$

where $t = 2\pi/\omega$ is the period of the input signal $f \cos \omega n$ and T is chosen as 1000. Q_i is often used as a measure for stochastic resonance [45, 46, 59, 60].

Now, we point out the occurrence of stochastic resonance in the first unit of the network the dynamics of which is independent of the other units. In Fig. 7.8

Fig. 7.8 Numerically computed Q as a function of the intensity of noise for the Bellows map (7.28a)



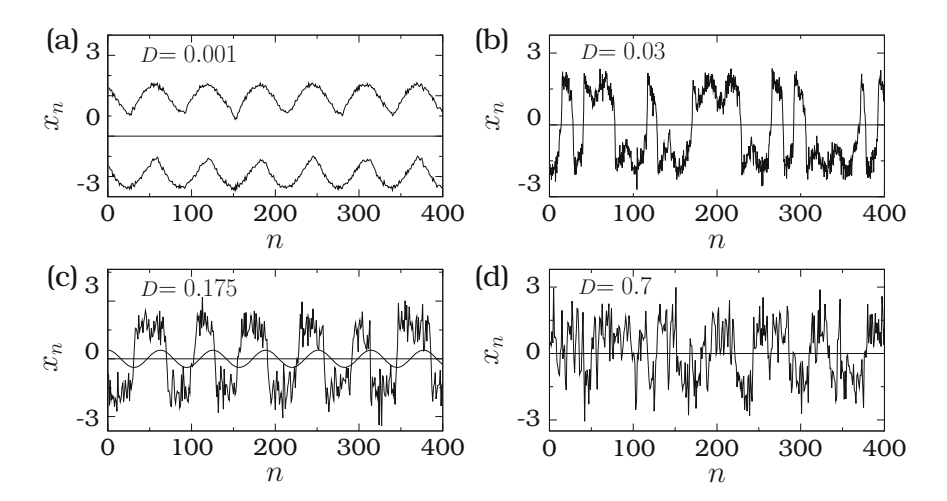


Fig. 7.9 Time series plot of the Bellows map (7.28a) for few fixed values of noise intensity. (a) D = 0.001, (b) D = 0.03, (c) D = 0.175 and (d) D = 0.7. For D = 0.001 there are two coexisting orbits

as D increases from a small value the response amplitude Q_1 increases, reaches a maximum value at $d=D_{\max}=0.175$ and decreases with further increase in D. Figure 7.9 shows x_n versus n for four values of D. For $D\ll D_{\max}$ the iterated values rarely switches between the two stable fixed points. At D=0.175 the iteration plot, $x_n^{(1)}$ versus n, shows almost periodic switching between the regions x>0 and x<0. Numerically computed mean residence times in the regions x<0 and x>0 are x=00. For x=01 and x=02. For x=02 are x=03 an erratic switching between these two regions takes place.

Now, we report the results of an extensive numerical simulation on the network system (7.28), varying the parameters δ and D. We restrict ourselves to $\delta \in [0, 1]$ and $D \in [0, 1]$. Figure 7.10 presents the effect of the coupling strength δ and D on the response amplitude of the various units. For small values of δ when D is varied typical noise-induced resonance takes place only in the first few units and in the other units $Q_i = 0$ for the entire range of D. This is seen in Fig. 7.10a. In this case for the units far from the first unit $x_n^{(i)}$ becomes a constant. When $\delta > 0.237$ all the units display stochastic resonance and moreover resonance occurs at the same value of D in all the units. For $0.237 < \delta < 0.4$ the response amplitude of the last unit is less than Q_1 . In Fig. 7.10b for $\delta = 0.27$ Q_i decreases with the unit number i. That is, an undamped signal propagation occurs, however, there is no enhancement of the output signal (at the frequency ω) of the last unit because Q of the last unit is < 1. For δ > 0.4 Q_{max} increases and becomes a constant with the unit number *i*. Further, Q_{max} of ith unit $(i \neq 1)$ is greater than that of the first unit. An example for this is shown in Fig. 7.10c where $\delta = 0.75$. For clarity in Fig. 7.11a Q_i versus i is displayed for a few fixed values of D. For each value of D, Q_i exhibits sigmoidal type variation with i. In Fig. 7.11a for D = 0.002 and 0.005, we observe that $Q_i < Q_1$ while $Q_i > Q_1$ for other values of D.

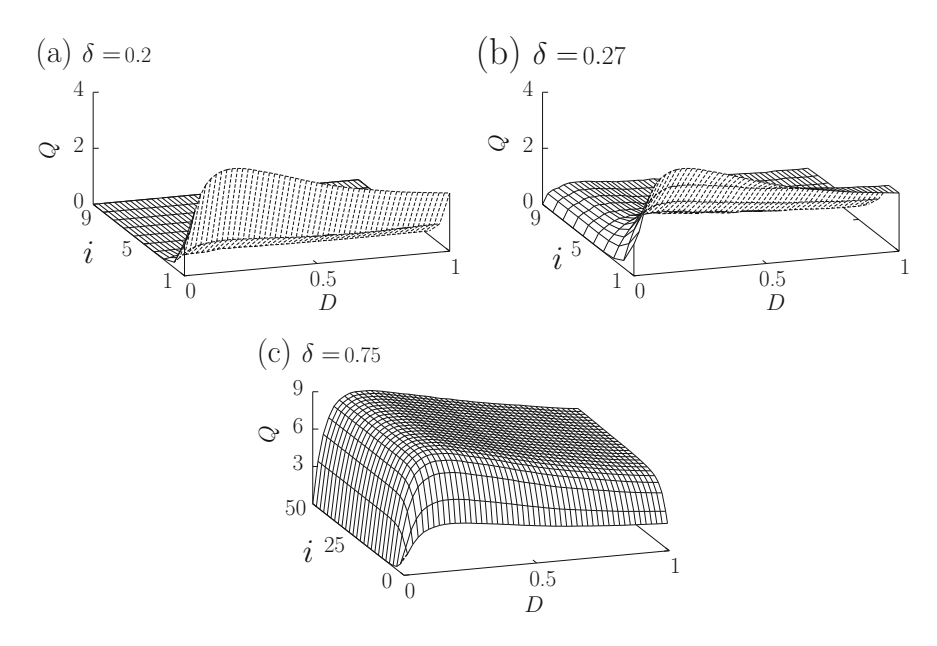


Fig. 7.10 Three-dimensional plots of variation of the response amplitude Q as a function of unit number i and noise intensity D for three values of δ for the network system given by Eq. (7.28). The values of the parameters are r=2, b=2, f=0.3, $\omega=0.1$ and N=400

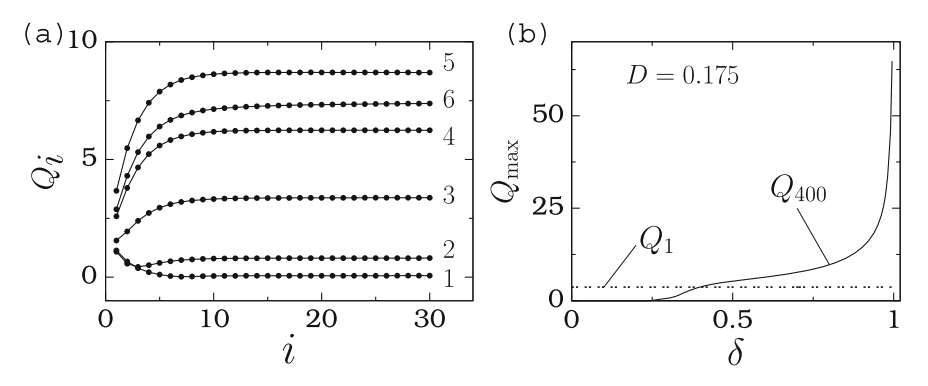


Fig. 7.11 (a) Variation of the response amplitude with the unit number i for six fixed values of D with $\delta = 0.75$. The values of D for the curves 1–6 are 0.002, 0.005, 0.02, 0.05, 0.175 and 0.5, respectively. (b) Q_{max} of the last unit with the parameter δ . The *dashed line* represents the value of Q_1 which is independent of δ

In the numerical simulation for $\delta > 0.4$ an enhanced undamped signal propagation (that is, $Q_{400} > Q_1$) occurs except for very small values of D. Though the weak periodic signal and noise is applied to the first unit alone, the linear coupling linking it to the second unit is able to stimulate it to exhibit stochastic resonance. And this phenomenon propagates to the successive units through simple

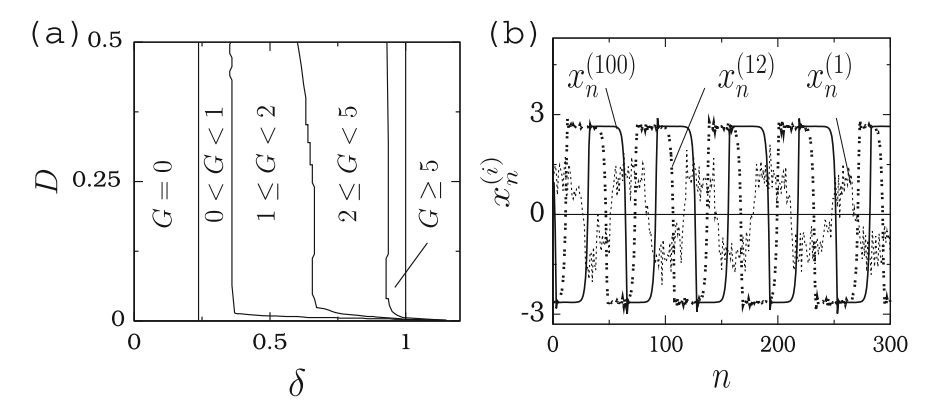


Fig. 7.12 (a) Regions of various ranges of gain factor G in the (δ, D) parameter space of the network system given by Eq. (7.28). The motion is unbounded for $\delta > 1$. (b) $x_n^{(i)}$ versus n for the units i = 1, 12 and 100 of the network (7.28) with $\delta = 0.75$ and D = 0.175 at which the response amplitude becomes a maximum. $x_n^{(i)}$ exhibits periodic switching between the regions x > 0 and x < 0

unidirectional coupling. Figure 7.11b displays the variation of Q_{\max} of the last unit with the coupling strength δ . It varies rapidly for values of δ near 1. The observed enhancement in Q is due to the unidirectional coupling. For $\delta > 1$ the iterations $x_n^{(1)}$ diverge.

Now, we define the gain factor $G = Q_N/Q_1$ with N = 400. And we compute it numerically for values of D and δ in the interval [0,1]. Regions in (δ,D) parameter space with 5 ranges of G, namely, =0, <1, [1,2], [2,5] and >5 are depicted in Fig. 7.12a. The coupling strength has a strong influence on G. The gain factor G is 0 for small values of δ for the entire range of noise intensity considered. On the other hand, it increases with increase in δ for fixed values of D.

Figure 7.12b presents an interesting result. For $\delta > 0.237$ for each fixed value of D the number of oscillations of $x_n^{(i)}$ in the regions x < 0 (x > 0) before switching to x > 0 (x < 0) decreases with increase in the unit number i. This is clearly evident in Fig. 7.12b where $x_n^{(i)}$ versus n is plotted for i = 1, 12 and 100 for $\delta = 0.75$ and D = 0.175. For large i the coupling term weakens the oscillation in the regions x < 0 and x > 0 and the output signal appears as a rectangular pulse. That is, the one-way coupling with appropriate strength gives rise undamped propagation of signal in the form of rectangular pulse. The Fourier series of such a signal will contain frequencies $l\omega$ where $l = 1, 2, \cdots$ with decaying amplitudes. Figure 7.12b corresponds to the case at which stochastic resonance occurs. $x_n^{(i)}$ exhibits almost periodic switching between the two regions x < 0 and x > 0. Note that $x_n^{(i)}$'s are not synchronized in the sense that switching of the various units from one region to another region does not occur at almost the same value of n. At resonance mean residence times of all the units are found to be T/2 where $T = 2\pi/\omega$.

7.5 Concluding Remarks

In all the three resonances in the unidirectionally coupled systems, for a range of values of coupling strength, the response amplitude increases with increase in the number of oscillators and reaches a saturation. That is, there exists a critical number of oscillators to have a maximum response and a further increase in the number of oscillators is ineffective in enhancing a response amplitude. In both cases of the first system driven by a single force and a biharmonic force the applied perturbation method enables us to predict (1) the response amplitude of each oscillator, (2) the saturation value of the response amplitude and (3) the critical value of the coupling strength above which undamped signal propagation occurs. The results reported in this chapter, in general, can be realized in networks of other bistable systems as well as in excitable systems with the same connectivity topology.

References

- 1. A.T. Winfree, *The Geometry of Biological Time* (Springer, New York, 1980)
- 2. Y. Kuramoto, Chemical Oscillations, Waves and Turbulence (Springer, Berlin, 1984)
- 3. S.H. Strogatz, I. Stewart, Sci. Am. 269, 102 (1993)
- 4. P.C. Bressloff, S. Coombes, B. De Souza, Phys. Rev. Lett. 79, 2791 (1997)
- 5. M.E.J. Newman, Networks: An Introduction (Oxford University Press, Oxford, 2010)
- 6. M. Gerhardt, H. Schuster, J.J. Tysor, Science **247**, 1563 (1990)
- 7. G. Joya, M.A. Atencia, F. Sandovai, Neuro Comput. 43, 219 (2002)
- 8. Z. Wang, Y. Wang, Y. Liu, IEEE Trans. Neural Netw. 21, 11 (2010)
- 9. J.J. Collins, C.C. Chow, T.T. Imhoff, Nature **376**, 236 (1995)
- 10. L.E. Abbott, C. van Vreeswijk, Phys. Rev. E **48**, 1483 (1993)
- 11. H. Bolouri, E.H. Davidson, BioEssays 24, 1118 (2002)
- 12. H. De Jong, J. Comput. Biol. 9, 67 (2002)
- 13. F. Ren, J. Cao, Neurocomputing 71, 834 (2008)
- 14. D. Bray, J. Theor. Biol. **143**, 215 (1990)
- 15. D. Alon, Science **301**, 1866 (2003)
- 16. V. In, A.R. Bulsara, A. Palacios, P. Longhini, A. Kho, Phys. Rev. E 72, 045104 (2005)
- 17. B. Razavi, Fundamentals of Microelectronics (Wiley, New York, 2008)
- 18. A. Locquet, C. Masoller, C.R. Mirasso, Phys. Rev. E 65, 56205 (2002)
- V. In, A. Kho, J.D. Neff, A. Palacios, P. Longhini, B.K. Meadows, Phys. Rev. Lett. 91, 244101 (2003)
- A.R. Bulsara, V. In, A. Kho, P. Longhini, A. Palacios, W. Rappel, J. Acerbron, S. Baglio, B. Ando, Phys. Rev. E 70, 036103 (2004)
- 21. V. In, A.R. Bulsara, A. Palacios, P. Longhini, A. Kho, Phys. Rev. E 72, 045104 (2005)
- 22. J.F. Linder, A.R. Bulsara, Phys. Rev. E **74**, 020105 (2006)
- 23. T. Dauxois, M. Payrard, *Physics of Solitons* (Cambridge University Press, Cambridge, 2006)
- J.M. Carcione, Wave Fields in Inelastic, Porous and Electromagnetic Media (Elsevier, Amsterdam, 2007)
- J.F. Lindner, K.M. Patton, P.M. Odenthal, J.C. Gallagher, B.J. Breen, Phys. Rev. E 78, 066604 (2008)
- B.J. Breen, A.B. Doud, J.R. Grimm, A.H. Tanasse, S.J. Tanasse, J.E. Lindner, K.J. Maxted, Phys. Rev. E 83, 037601 (2011)
- 27. C. Yao, M. Zhan, Phys. Rev. E 81, 061129 (2010)

References 223

- 28. C. Jeevarathinam, S.Rajasekar, M.A.F. Sanjuan, Chaos 23, 013136 (2013)
- S. Rajasekar, J. Used, A. Wagemakers, M.A.F. Sanjuan, Commun. Nonlinear Sci. Numer. Simul. 17, 3435 (2012)
- 30. M.B. Elowitz, S. Leibler, Nature 403, 335 (2000)
- 31. K.Y. Kim, D. Lepzelter, J. Wang, J. Chem. Phys. 126, 034702 (2007)
- 32. O. Buse, R. Perez, Phys. Rev. E 81, 066206 (2010)
- S. Muller, J. Hofbauer, L. Endler, C. Flamm, S. Widder, P. Schuster, J. Math. Biol. 53, 905 (2006)
- 34. N. Strelkowa, M. Barahona, J. R. Soc. Interface 7, 1071 (2010)
- 35. N. Strelkowa, M. Barahona, Chaos 21, 023104 (2011)
- 36. S. Rajamani, S. Rajasekar, Phys. Scr. 88, 015010 (2013)
- L.A. Pipes, L.R. Harvill, Applied Mathematics for Engineers and Physics (McGraw-Hill, New York, 1970)
- 38. J.F. Lindner, B.K. Meadows, W.L. Ditto, M.E. Inchisoa, A.R. Bulsara, Phys. Rev. Lett. 75, 3 (1995)
- 39. M. Locher, G.A. Johnson, E.R. Hunt, Phys. Rev. Lett. 77, 4698 (1996)
- J.F. Lindner, B.K. Meadows, W.L. Ditto, M.E. Inchiosa, A.R. Bulsara, Phys. Rev. E 53, 2081 (1996)
- 41. N. Sungar, J.P. Sharpe, S. Weber, Phys. Rev. E 62, 1413 (2000)
- 42. O. Kwon, H.T. Moon, Phys. Lett. A 298, 319 (2002)
- 43. A. Pikovsky, A. Zaikin, M.A. de la Casa, Phys. Rev. Lett. 88, 050601 (2001)
- 44. M. Ozer, M. Uzuntarla, T. Kayikcioglu, L.J. Graham, Phys. Lett. A 372, 6498 (2008)
- 45. M. Perc, Phys. Rev. E 78, 036105 (2008)
- 46. M. Ozer, M. Perc, M. Uzuntarla, Phys. Lett. A 375, 965 (2009)
- 47. A. Zaikin, J. Kurths, L. Schimansky-Geier, Phys. Rev. Lett. 85, 227 (2000)
- 48. H. Hong, B.J. Kim, M.Y. Choi, Phys. Rev. E 66, 011107 (2002)
- 49. F.D. Duan, F. Chapeau-Blondeau, D. Abbott, Phys. Lett. A 372, 2159 (2008)
- 50. A. Krawiecki, Physica A 333, 505 (2004)
- 51. A. Krawiecki, Int. J. Mod. Phys. B 18, 1759 (2004)
- 52. A.L. Barabasi, R. Albert, Science 286, 509 (1999)
- 53. J.A. Acebron, S. Lozano, A. Arenas, Phys. Rev. Lett. 99, 128701 (2007)
- 54. D. Rousseau, F. Chapeau-Blondeau, Phys. Lett. A **321**, 280 (2004)
- 55. P. McGraw, M. Menzinger, Phys. Rev. E 83, 037102 (2011)
- 56. T.S. Bellows, J. Anim. Ecol. **50**, 139 (1981)
- 57. K. Masutani, Bull. Math. Biol. 55, 1 (1993)
- 58. S. Sinha, P.K. Das, Pramana J. Phys. 48, 87 (1997)
- 59. M. Perc, Phys. Rev. E 76, 066203 (2007)
- 60. M. Gosak, D. Korosak, M. Marhl, New J. Phys. 13, 013012 (2011)

Chapter 8 Experimental Observation of Vibrational Resonance

This chapter focuses on the experimental observation of vibrational resonance. One of the first examples where vibrational resonance was experimentally observed was in Baltanas et al. [1]. The authors considered an analog simulation of the overdamped Duffing oscillator with two stable equilibrium states and one unstable equilibrium state. The system is driven by a biharmonic force. A resonant-like behaviour was realized when the amplitude or the frequency of the high-frequency component was varied. The experimental result was confirmed by the numerical simulation. Later, Ullner et al. [2] reported the occurrence of vibrational resonance in an excitable electronic circuit. Also Chizhevsky and his collaborators [3, 4] presented an experimental observation of vibrational resonance in a vertical cavity surface emitting laser. This device is capable of displaying a bistability of polarization states of the emitted field that can be monitored by the applied injection current. It has been shown that observed resonance can be used for the detection of low-level noisy signals. Occurrence of stochastic resonance in this system was also reported [5, 6]. In nonlinear circuit analysis, the bistable Chua's circuit is commonly used as a prototype circuit to investigate a variety of dynamics. Experimental evidences for vibrational resonance in a single Chua's circuit and enhanced signal transmission in a system of unidirectionally coupled n Chua's circuits driven by a biharmonic signal were reported [7].

The present chapter demonstrates the occurrence of vibrational resonance in a bistable single Chua's circuit, in the analog simulation of the overdamped bistable Duffing oscillator, in a vertical cavity surface emitting laser and in an excitable electronic circuit with Chua's diode. The presence of undamped signal propagation of a low-frequency signal in the system of *n*-coupled Chua's circuits where only the first circuit is alone driven by the biharmonic signal is described.

8.1 Single Chua's Circuit

The circuit diagram of the single Chua's circuit driven by a biharmonic force of the form $F_1(t) + F_2(t) = f \sin \omega t + g \sin \Omega t$ with $\Omega \gg \omega$ is depicted in Fig. 8.1a. This circuit without $F_1(t) + F_2(t)$ was invented in 1983 by Leon O. Chua, a Chinese-American Electrical Engineer, who was a visitor at Waseda University in Japan at that time. The ease of construction of the circuit has made it a ubiquitous real-world example of a chaotic system, leading some to declare it *a paradigm for chaos*.

The practical realization of the Chua's diode N_R is shown in Fig. 8.1b. N_R consists of two operational amplifiers and six linear resistors. The typical voltage-current characteristic of the Chua's diode shown in Fig. 8.1c consists of a five-segment piecewise linear form. We choose the values of the circuit parameters as $C_1 = 10 \, \text{nF}$, $C_2 = 100.5 \, \text{nF}$, $L = 18.75 \, \text{mH}$, $R = 1.98 \, \text{k}\Omega$, $R_1 = R_2 = 220 \, \Omega$, $R_3 = 2.2 \, \text{k}\Omega$, $R_4 = R_5 = 22 \, \text{k}\Omega$ and $R_6 = 3.3 \, \text{k}\Omega$. The values of the slopes in the voltage-current characteristic curve of the Chua's diode are $G_a = -0.757 \, \text{mA/V}$, $G_b = -0.409 \, \text{mA/V}$ and $G_c = 4.580 \, \text{mA/V}$, while the values of the breakpoints are $BP_1 = 1.37 \, \text{V}$ and $BP_2 = 9.54 \, \text{V}$.

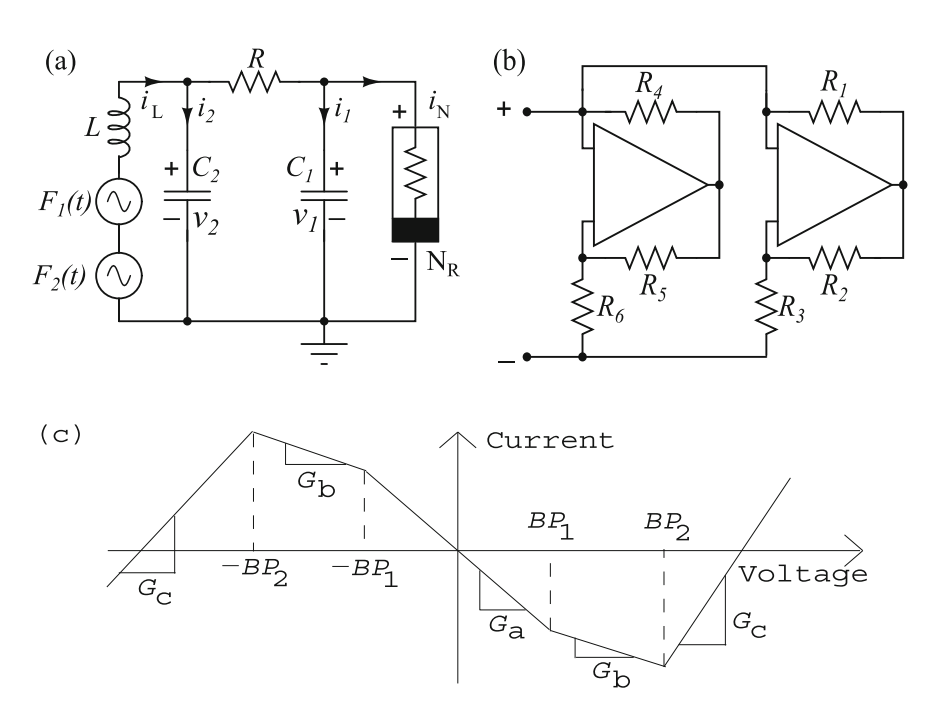


Fig. 8.1 (a) The Chua's circuit driven $F_1(t) = f \sin \omega t$ and $F_2(t) = g \sin \Omega t$. N_R represents the Chua's diode. (b) Schematic diagram of the Chua's diode. Here $R_1 = R_2 = 220 \Omega$, $R_3 = 2.2 k\Omega$, $R_4 = R_5 = 22 k\Omega$ and $R_6 = 3.3 k\Omega$. (c) The characteristic curve of the Chua's diode of (b)

In the experiment, we consider the case $\Omega\gg\omega$. Assume that in absence of the high-frequency input signal the amplitude A_ω of the output signal at the low-frequency ω is weak. Our interest is to enhance the amplitude of the output signal at the frequency ω by the high-frequency driving force. To measure A_ω the fast Fourier transform (FFT) of the output signal is obtained using the Agilent (MSO6014A) Mixed Signal Oscilloscope. A small fluctuation of A_ω is observed in the FFT displayed in the instrument. In view of this for a better accuracy an average value of A_ω over 25 measurements is obtained. The value of A_ω measured in the FFT is in dBV. It is then converted into the units of V. Then $Q=A_\omega$ (in V)/f termed as the response amplitude of the circuit at the frequency ω is computed.

We fix $f=0.3\,\mathrm{V}$, $\omega=50\,\mathrm{Hz}$ and $\Omega=500\,\mathrm{Hz}$. Figure 8.2 displays the power spectrum of the voltage v_1 of the circuit for a few fixed values of the amplitude g of the high-frequency input signal. The amplitude A_ω at $\omega=50\,\mathrm{Hz}$ increases and then decreases which is a typical signature of resonance. To characterize the resonance, we compute Q at the frequencies ω and Ω of the voltages v_1 and v_2 and the current i_L for a range of values of the control parameter g. Figure 8.3a shows the variation of Q of v_1 at ω and Ω with g. As g increases from a small value Q at ω increases slowly, varies sharply over an interval and reaches a maximum value at a critical value of g denoted as g_{VR} .

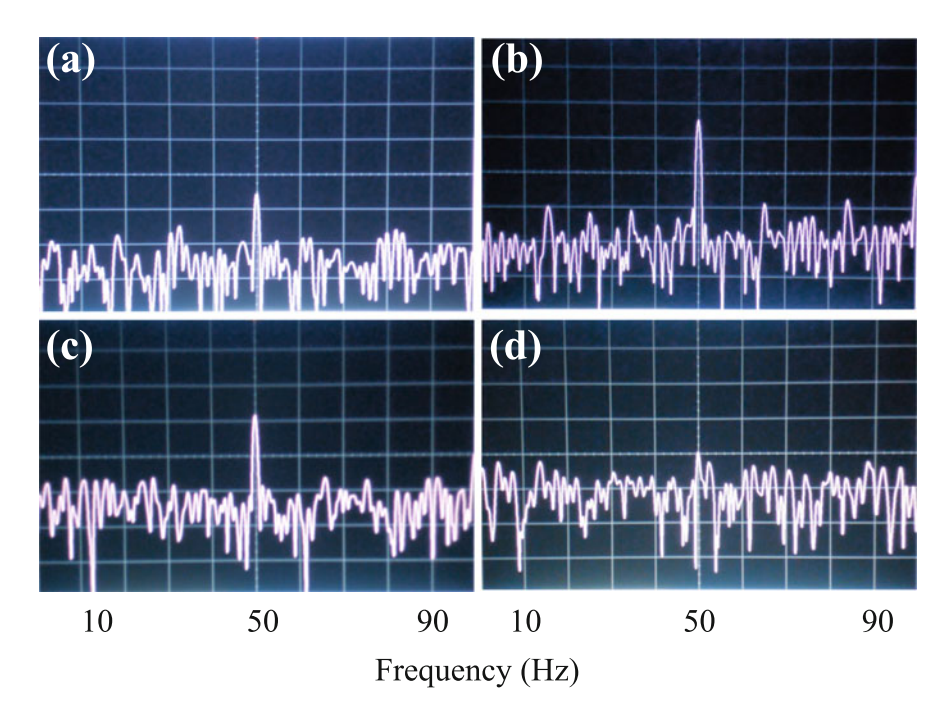


Fig. 8.2 The power spectrum of v_1 for four values of g. (a) $g=1\,\mathrm{V}$, (b) $g=1.3\,\mathrm{V}$, (c) $g=1.55\,\mathrm{V}$ and (d) $g=2\,\mathrm{V}$. The values of other parameters are $C_1=10\,\mathrm{nF}$, $C_2=100\,\mathrm{nF}$, $L=18\,\mathrm{mH}$, $R=1.98\,\mathrm{k}\Omega$, $A=0.3\,\mathrm{V}$, $\omega=50\,\mathrm{Hz}$, $\Omega=500\,\mathrm{Hz}$

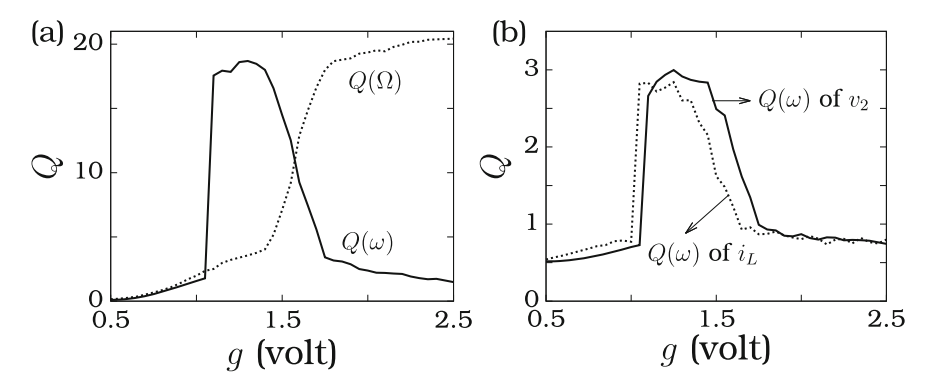


Fig. 8.3 (a) Q at ω (continuous curve) and Ω (dotted curve) associated with v_1 versus g. (b) Q at ω associated with v_2 (continuous curve) and i_1 (dotted curve) versus g

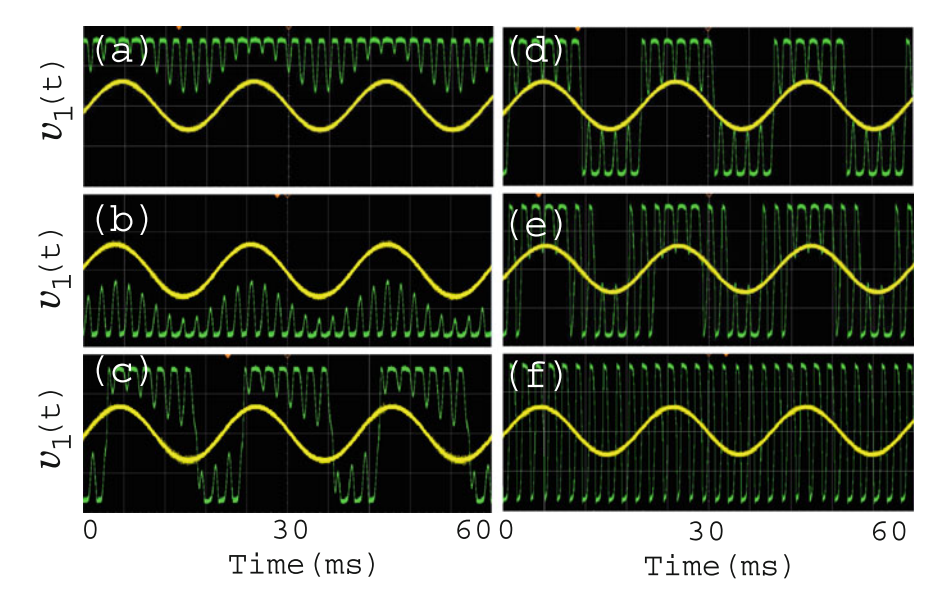


Fig. 8.4 Plots of $v_1(t)$ and the low-frequency input signal versus t for few values of g. (a) and (b) g = 1 V, (c) g = 1.15 V, (d) g = 1.3 V, (e) g = 1.55 V and (f) g = 2 V. In all the subplots the range of $v_1(t)$ is [-10 V, 10 V]. The input signal is 10 times enlarged for clarity

The value of g_{VR} is found as 1.3 V. When g is increased further from g_{VR} the response amplitude decreases rapidly to a small value. This type of resonance behaviour is not observed with Q at Ω . Figure 8.3b shows the plot of Q of v_2 and i_L at ω as a function of g. $Q(\omega)$ of v_2 and also that of i_L display resonance. In the rest of the analysis on the single Chua's circuit focus is on Q of v_1 at ω .

Now, we illustrate the mechanism of vibrational resonance using a time series plot and a phase portrait. Figure 8.4 presents $v_1(t)$ versus t for six fixed values of g.

In absence of a biharmonic force the Chua's circuit for the chosen parametric values has two stable equilibrium points $X_+ = (v_1, v_2, i_L) = (5.515 \text{ V}, 0 \text{ V}, -2.784 \text{ mA})$ and $X_- = (-5.515 \text{ V}, 0 \text{ V}, 2.784 \text{ mA})$ and one unstable equilibrium point $X_0 = (0, 0, 0)$. For g = 0, f = 0.3 V and $\omega = 50 \text{ Hz}$ two period- $T = 1/\omega$ 0 orbits coexist—one orbit about X_+ and another about X_- , that is, on either side of $v_1 = 0$. When the system is driven further by the high-frequency force with $\Omega = 500 \text{ Hz}$, then for small values of g, the two periodic orbits coexist and $v_1(t)$ is modulated by the high-frequency force. This is shown in Fig. 8.4a, b for g = 1 V.

At a value of g, a crossing of $v_1 = 0$ takes place. Now, we denote τ^+ as the time spent by the trajectory in the region $v_1 > 0$ before switching to the region $v_1 < 0$. Similarly, one can define τ^- . τ^+ and τ^- are the residence times of the trajectory in the regions $v_1 > 0$ and $v_1 < 0$, respectively. Then, we calculate the mean residence times τ_{MR}^+ and τ_{MR}^- . For g values just above the onset of switching between $v_1 < 0$ and $v_1 > 0$, the residence times τ_{MR}^+ and τ_{MR}^- are unequal. An example is shown in Fig. 8.4c where $g = 1.15 \,\mathrm{V}$. τ_{MR}^+ and τ_{MR}^- vary with g. At the critical value $g = g_{\mathrm{VR}} = 1.15 \,\mathrm{V}$. 1.3 V, $\tau_{MR}^+ = \tau_{MR}^- = T/2$ (see Fig. 8.4e). There is a periodic switching between the regions $v_1 < 0$ and $v_1 > 0$ with period equal to half the time of the period of the lowfrequency input signal. The response amplitude Q is maximum at this value of g. This is the mechanism of the observed vibrational resonance. (Note that periodic switching between equilibrium states is not a precursor to the onset of vibrational resonance as pointed out in Chaps. 3 and 4). In the Chua's circuit system, Q is not maximum, that is resonance does not occur, at the value of g for which the onset of crossing occurs. When g is further increased from g_{VR} the synchronization between $v_1(t)$ and the input signal $f \sin \omega t$ is lost (see Fig. 8.4e). For sufficiently large values of g, a rapid switching between the regions $v_1 < 0$ and $v_1 > 0$ occurs and now the oscillation is centered around the equilibrium point X_0 . This is evident in Fig. 8.4f where g = 2 V.

Next, we experimentally analyse the influence of the parameters ω , f and Ω on resonance. Figure 8.5 presents the results. In Fig. 8.5a as Ω increases $g_{\rm VR}$ also increases but $Q_{\rm max}$ (the value of Q at resonance) decreases. The width of the bell shape part of the resonance profile increases when Ω increases. In Fig. 8.5b $g_{\rm VR}$ decreases while $Q_{\rm max}$ increases with an increase in f. The width of the bell shape part increases for increasing values of f. Figure 8.5c shows Q versus g for different set of values (ω, Ω) keeping the ratio Ω/ω as 10. Increase in ω and Ω leads to the effect observed in Fig. 8.5a. In Fig. 8.5d increase in ω increases the value of $\Omega_{\rm VR}$ but decreases the corresponding $Q_{\rm max}$.

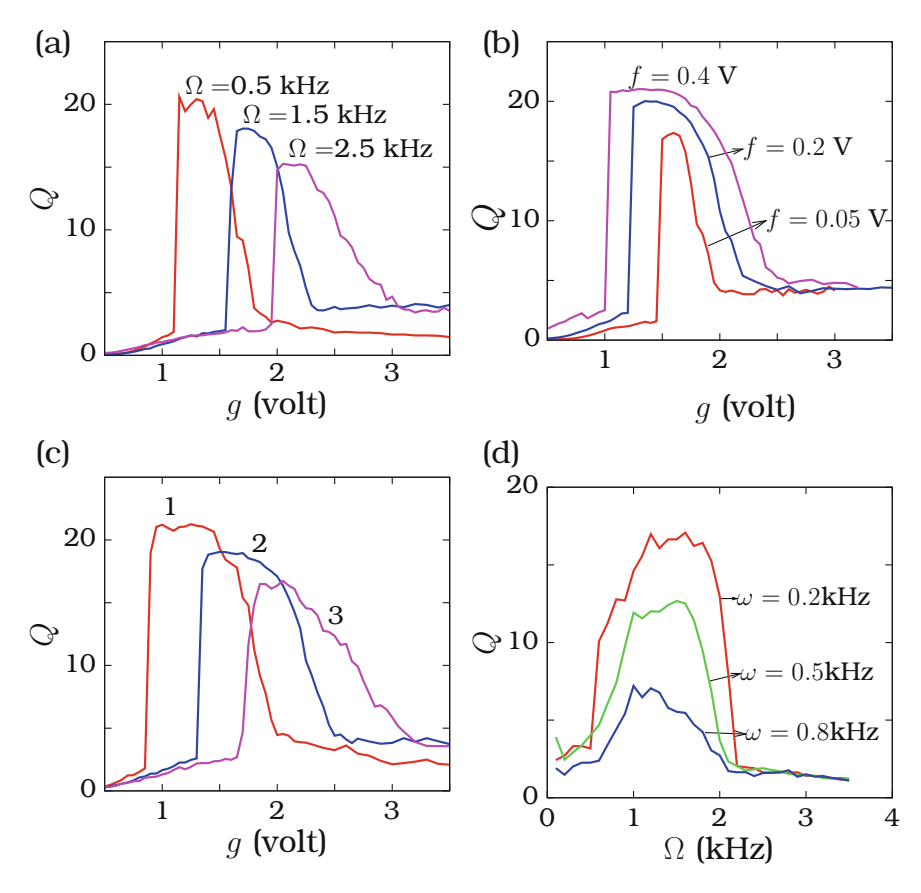


Fig. 8.5 The dependence of Q of v_1 versus g on (a) $\Omega=0.5, 1.5$ and 2.5 kHz with f=0.3 V and $\omega=50$ Hz, (b) f=0.05, 0.15 and 0.25 V with $\omega=50$ Hz and $\Omega=1000$ Hz and (c) different combinations of ω and Ω with $\Omega/\omega=10$ where for the curves 1, 2 and 3 the values of (ω,Ω) are (50 Hz, 500 Hz), (150 Hz, 1500 Hz) and (250 Hz, 2500 Hz) while f=0.5 V. (d) Variation of Q with Ω for three fixed values of ω with $\Omega=0.3$ V and $\Omega=0.5$ V.

8.2 Analog Simulation of the Overdamped Bistable System

Here we consider the system

$$\dot{x} - \omega_0^2 x + \beta x^3 = f \sin \omega t + g \sin \omega t.$$
 (8.1)

The electronic circuit for the analog simulation of Eq. (8.1) [1] is depicted in Fig. 8.6. It consists of three LM741 operation amplifiers, two AD633 analog multipliers, one capacitor and eight resistors. The circuit part with the operational amplifier OA1 and the resistors R_1 , R_2 and R_3 acts as an adder. This part of the circuit essentially adds the low- and high-frequency signals. The integrator part

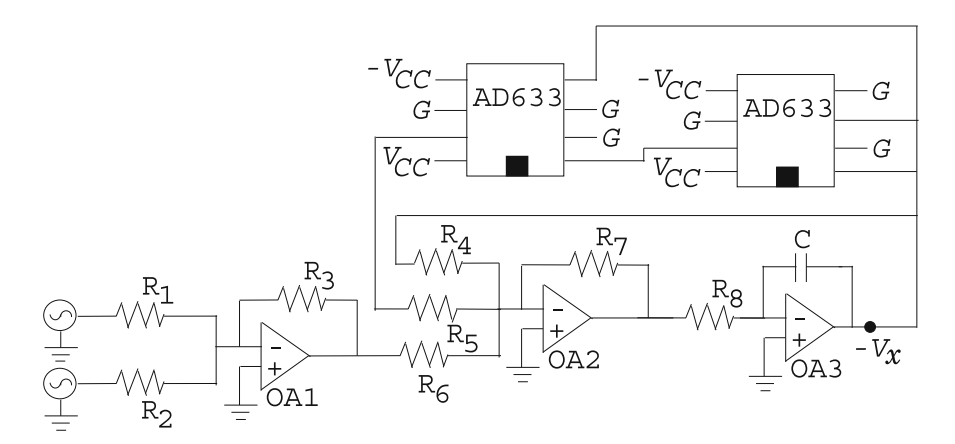


Fig. 8.6 Analog circuit simulation of Eq. (8.1)

consists of the adder with the components R_4 – R_7 and OA2 and two multipliers (AD633 with coefficient α). There is another integrator with the components R_8 , C and OA3.

The dynamical equation of the circuit is

$$R_8C\dot{V}_x = V_x \frac{R_7}{R_4} - \alpha^2 V_x^3 \frac{R_7}{R_5} + \frac{fR_3R_7}{R_1R_6} \sin \omega t + \frac{gR_3^2}{R_2R_6} \sin \Omega t , \qquad (8.2)$$

where $-V_x$ is the voltage at the output of the operational amplifier OA3. In the paper of Baltanas et al. [1] parameters were fixed as $R_1=6.7\,\mathrm{k}\Omega$, $R_2=R_3=2.2\,\mathrm{k}\Omega$, $R_4=15\,\mathrm{k}\Omega$, $R_5=150\,\Omega$, $R_6=22\,\mathrm{k}\Omega$, $R_7=56\,\mathrm{k}\Omega$, $R_8=10\,\mathrm{k}\Omega$ and $C=10\,\mu\mathrm{F}$. For these parametric values, the circuit gives rise a symmetric doublewell potential system with a separation between the minima equal to L=2 and the barrier height H=9.3. They were also used two 33120A Agilent wave form generators for the low- and high-frequency input periodic signals and captured the response V_x with a Tektronix digital oscilloscope. The response amplitude Q at the frequency ω was calculated from the time series of V_x . Further, Q was computed numerically by solving Eq. (8.1).

Figure 8.7 presents the experimental and numerical values of Q as a function of the amplitude g of the high-frequency force for few values of low-frequency amplitude f. This figure clearly shows the resonance behaviour. The experimental Q values are displaced to the right and slightly lower than the values of Q obtained in the numerical simulation. The differences in the values of Q are due to the fact that the components of the experimental circuit would have introduced a certain variability in the experimental values of the parameters of the bistable potential.

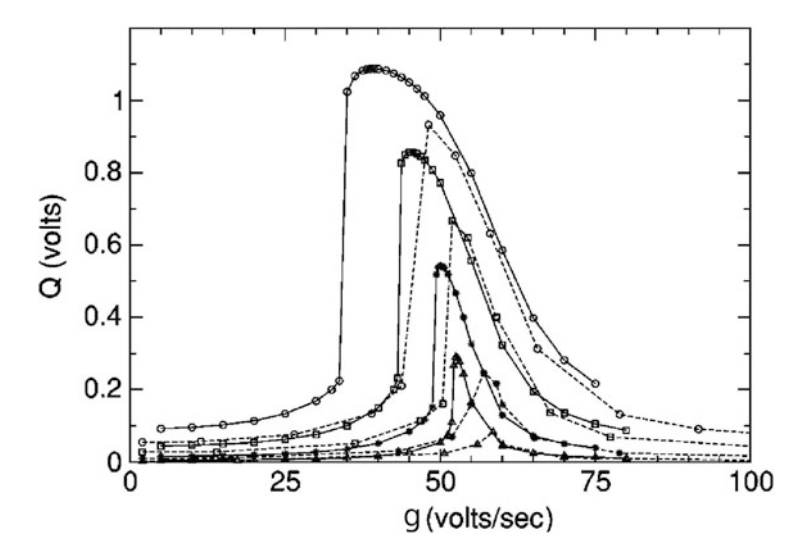


Fig. 8.7 Experimentally measured Q (continuous curves) and numerically computed Q (dashed curves) [1] of Eq. (8.1). The values of f for the top to bottom curves are 6.656, 3.328, 1.248 and 0.416

8.3 Vertical Cavity Surface Emitting Laser System

This section summarizes the experimental observation of vibrational resonance in a vertical cavity surface emitting laser reported in [3, 4].

In the experiment two periodic signals with different frequencies ω and Ω were applied to the injection current. The values of ω and Ω were kept at 500 and 100 kHz, respectively. The amplitudes of low-frequency and high-frequency forces are denoted as $A_{\rm LF}$ and $A_{\rm HF}$, respectively. The wave form used was a square-wave with an on-off time ratio 2. The injection current was chosen appropriately so that the laser operates in the polarization bistability regime. In this case switching between two states was induced by applying the deterministic modulation. The response of the laser system was detected using a fast photo detector and the data were stored by a digital oscilloscope which was interfaced with a computer.

To characterize vibrational resonance the statistical measure SNR and the gain factor G obtained from the Fourier transform of the time series were used. Twenty-five thousand sampling points corresponding to 50 periods of the low-frequency signal were used. For a better result average of the above quantities over a 10–50 time series were used. For the experimental time series SNR was defined as

$$SNR = 10 \log_{10} \left(\frac{I_{N}(f_{s}) + I_{S}(f_{s})}{I_{N}(f_{s})} \right) , \qquad (8.3)$$

where $I_S(f_s)$ is the power spectrum of the laser response at the frequency ω and $I_N(f_s)$ is the interpolated level of noise at ω . Then, the normalized SNR_n is computed through

$$SNR_{\rm n} = \frac{SNR}{SNR(A_{\rm HF} = 0)} \ . \tag{8.4}$$

Further, one can define the gain factor as

$$G = \frac{I_{S}(f_{s}) - I_{N}(f_{s})}{I_{0}(f_{s}) - I_{N0}(f_{s})},$$
(8.5)

where $I_0(f_s)$ and $I_{N0}(f_s)$ are the laser response and the interpolated level of noise of the system at the low-frequency ω in the absence of the high-frequency signal.

In the experiment, first the injection current was tuned so that the residence times in the two levels of the polarized laser emission were almost the same. This can be treated as corresponding to a nearly symmetric double-well quasipotential [8]. $A_{\rm LF}$ was then fixed at a value less than the critical value, corresponding to force switching between the two states at any semiperiod. Figure 8.8 presents [3] the evolution of the polarized laser emission for a few fixed values of $A_{\rm HF}$. In the presence of internal noise, the laser response displayed the vibrational resonance phenomenon when $A_{\rm HF}$ was varied. As $A_{\rm HF}$ was increased, rare switching between the two states were found (Figs. 8.8b and c).

This was due to the combined effect of low-frequency and high-frequency signals. At a critical value of $A_{\rm HF}$, a complete synchronization as shown in Fig. 8.8e between the input low-frequency signal and the laser response was obtained. There was almost a periodic switching between the two states. When $A_{\rm HF}$ was increased further erratic switching between the two states was observed (Fig. 8.8f).

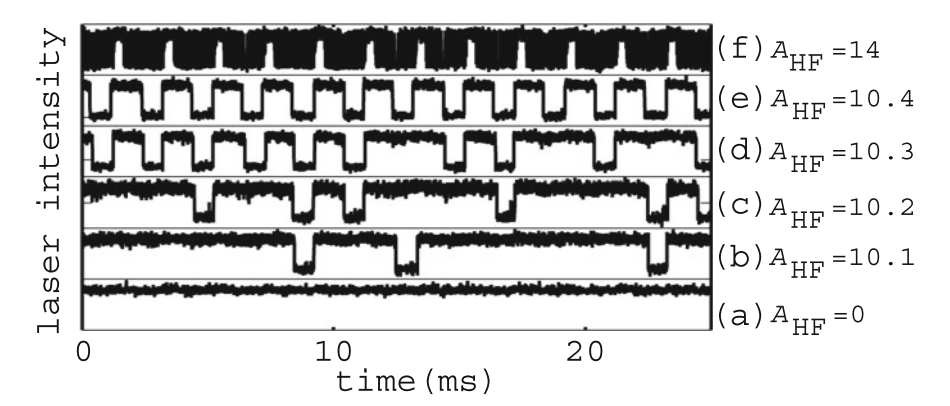


Fig. 8.8 Time series plots of the polarized laser intensity (in arbitrary units) for few values of $A_{\rm HF}$ [3]. The values of $A_{\rm HF}$ are in units of mV. (Figure 8.8 adapted with permission from Ref. [3]. Copyrighted by the American Physical Society.)

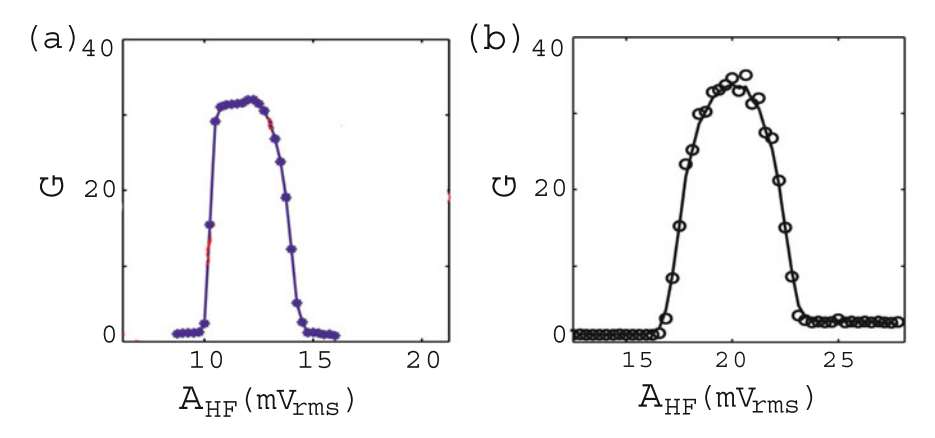


Fig. 8.9 Variation of the gain factor as a function of $A_{\rm HF}$ for (a) symmetric and (b) strongly asymmetric quasipotentials [3]. (Figure 8.9 adapted with permission from Ref. [3]. Copyrighted by the American Physical Society.)

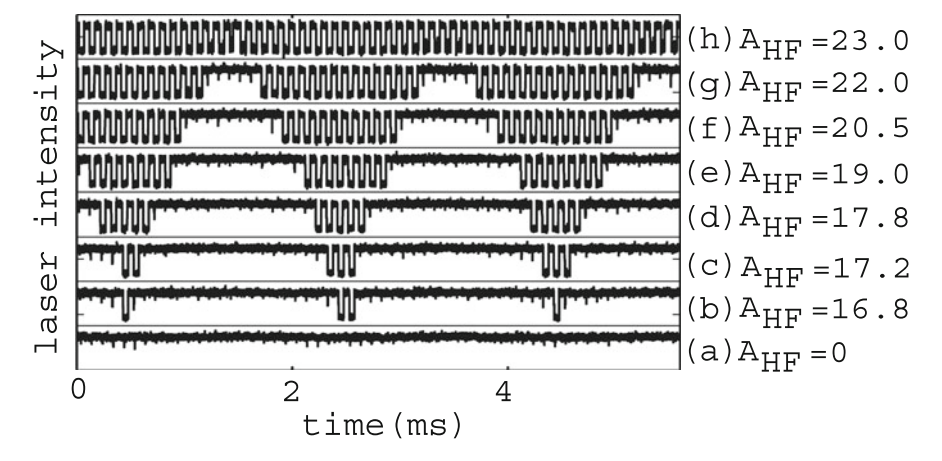


Fig. 8.10 Laser intensity (in arbitrary units) versus time for several values of $A_{\rm HF}$ [3]. The values of $A_{\rm HF}$ are in units of mV. (Figure 8.10 adapted with permission from Ref. [3]. Copyrighted by the American Physical Society.)

Figure 8.9a shows the plot of G versus $A_{\rm HF}$. As $A_{\rm HF}$ increased from a small value at about $10\,{\rm mV_{rms}}$ a sharp increase in G occurred. The gain factor G became a maximum at a value of $A_{\rm HF}$ in the interval $[10,15]\,{\rm mV_{rms}}$ and then decreased. It is a typical plot of a resonance curve and is the characteristic feature of vibrational resonance.

Next, we point out a different scenario noticed by Chizhevsky et al. for a strongly asymmetric quasipotential. Pump current was changed to introduce very different residence times for the two levels of the emitted polarization intensity. In Fig. 8.9b, the resonance curve is almost of a symmetrical bell-shaped form. Figure 8.10 depicts the variation of laser intensity with time for several values of $A_{\rm HF}$ where $\omega = 500\,{\rm Hz}$

and $\Omega=10\,\mathrm{kHz}$. In this figure one can clearly observe the occurrence of bursts and the influence of A_{HF} on the interval between consecutive sequence of bursts. In each pulse train, the number of high-frequency pulses increases with increase in the value of A_{HF} . The asymmetric case is very similar to the threshold-crossing systems reported in [9]. In an excitable system the spiking region is activated by applying an appropriate weak noise to a slowly changing modulating signal. In this case, the resonance is obtained comparing the rate of the spiking bursting events with the frequency of the slow input signal.

8.4 An Excitable Electronic Circuit

Figure 8.11 shows an excitable electronic circuit with Chua's diode as the nonlinear element [2]. The Chua's diode is implemented with an operational amplifier from the integrated circuit TL082. The circuit becomes excitable when the voltage controlling this operational amplifier is asymmetric [10]. The biharmonic signal with the frequencies 1 kHz and 50 kHz are produced from two function generators and introduced into the system through the 1 nF capacitor. The amplitude of the low-frequency signal is kept at 1.3 V. The response of the system is analysed by increasing the amplitude *g* of the high-frequency signal.

Figure 8.12 shows the experimental time series (the voltage drop at the 1 nF capacitor). For very small values of g, the total input signal is below the threshold and there are no spikes in the output. This is shown in Fig. 8.12a for $g=0.435\,\mathrm{V}$. Above a critical value of g, spikes start to appear. An example is presented in Fig. 8.12b for $g=0.465\,\mathrm{V}$. The number of spikes per half period of the low-frequency signal increases with further increase in the value of g. This is evident in Figs. 8.12c and d for g=0.66 and 0.985 V, respectively. The response amplitude Q

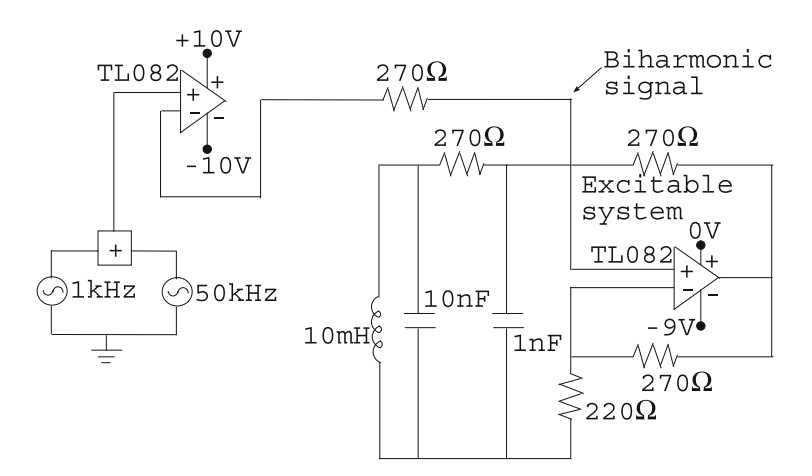


Fig. 8.11 An excitable electronic circuit driven by a biharmonic input signal

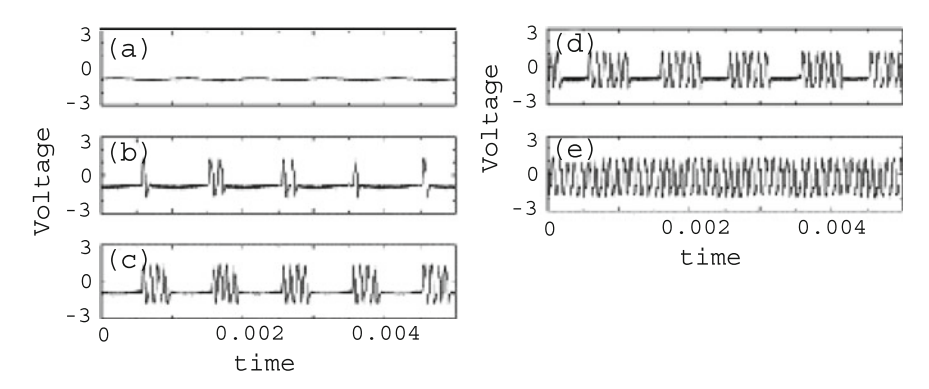


Fig. 8.12 Experimentally measured voltage drop at the 1 nF capacitor as a function of time for five fixed values of amplitude g of the high-frequency input signal [2]. The values of g for the subplots (a)–(e) are 0.435, 0.465, 0.66, 0.985 and 1.385 V, respectively. (Reprinted from E. Ullner, A. Zaikin, J. Garcia-Ojalvo, R. Bascones, J. Kurths, Phys. Lett. A **312**, 348 (2003). Copyright (2003), with permission from Elsevier.)

is found to be maximum at $g \approx 0.8$ V. For a sufficiently large value of g, the system fires immediately after reaching the equilibrium point, so that the output signal contains only the own frequency of the excitable system and the low-frequency component disappears as in the case for g = 1.385 V (Fig. 8.12e). This is a manifestation of vibrational resonance in an excitable system.

8.5 Unidirectionally Coupled Chua's Circuits

In [2] numerical evidence for amplified signal propagation in a chain of coupled excitable oscillators was reported. In this work a chain of 1000 oscillators was considered in which first 100 were driven by biharmonic signals and uncoupled. The rest of the oscillators were subjected to a high-frequency signal only and coupled unidirectionally. Yao and Zhan [11] have shown both theoretically and numerically, low-frequency signal transmission in unidirectionally coupled systems with first system alone subject to the biharmonic force. The present section provides an experimental evidence for this in a *n*-coupled bistable Chua's circuits.

Constructing a large size electronic circuit on a circuit board and investigating its performance have limitations due to the physical effects such as parasitic capacitance effects, internal noise and mismatch in the circuit components. The tolerance effects and circuit loading can also affect the behaviour of the circuit. Moreover, parametric identification during the initial stage of circuit design is difficult because for each parametric values one has to make a search of availability of the off-shelf components. In view of these reasons, circuit simulators based on SPICE, for example PSpice (Personal Simulation Program with Integrated Circuit Emphasis), have been widely used for investigating the dynamics of nonlinear

circuits [12–16]. Evaluation of circuit functions and performance through PSpice is more productive than on a breadboard. With PSpice one can quickly check a circuit idea and perform simulated test measurements and analyses which are difficult, inconvenient and unwise for the circuits built on a breadboard. Therefore, we choose PSpice circuit simulation of a system of n-coupled Chua's circuits with n=75 units instead of its real hardware construction. The simulation shows the evidence for improved transmission of low-frequency signal by the combined action of a high-frequency signal and a unidirectional coupling.

Figure 8.13 depicts the system of n-coupled Chua's circuits. The ith and (i+1)th circuits (the single Chua's circuit is shown in Fig. 8.1) are coupled unidirectionally by feeding the voltage across the capacitor C_1 of the ith circuit to the (i+1)th circuit through a buffer. The high input and low output impedances of the buffer ensure that the flow of the signal between ith and (i+1)th circuits is in forward direction, that is, from the ith circuit to the (i+1)th circuit only. The coupling resistor R_C characterizes the strength of the coupling.

The values of the circuit parameters are fixed as $C_1=10\,\mathrm{nF},\,C_2=100\,\mathrm{nF},\,L=18\,\mathrm{mH},\,R=2.15\,\mathrm{k}\Omega,\,\omega=100\,\mathrm{Hz},\,\Omega=1\,\mathrm{kHz}$ and $f=0.3\,\mathrm{V}$ and treat R_C and g as the control parameters. Figure 8.14a presents the variation of Q_i with i (the number of the Chua's circuit) for few values of g where $R_\mathrm{C}=1\,\mathrm{k}\Omega$. Q_i varies with i and approaches a limiting value. When $Q_2>Q_1(< Q_1)$ then Q_i increases (decreases) with i and reaches a saturation with $Q_{75}>Q_1(< Q_1)$. When $Q_{75}>Q_1$ then the signal propagation through the coupled circuits is termed as undamped. The measured values of Q_i for $g=1.2\,\mathrm{V}$ and for five different values of R_C are presented in Fig. 8.14b. Figure 8.15 displays Q_i versus g and i for two values of R_C . For $R_\mathrm{C}=2.165\,\mathrm{k}\Omega$, Q_i versus g (Fig. 8.15a) decays to zero as i increases (damped signal propagation). In Fig. 8.15b where $R_\mathrm{C}=1\,\mathrm{k}\Omega$ the signal propagation is undamped $Q_i>Q_1$, i>1 for a range of values of g. Only for certain set of values of R_C and g undamped signal propagation takes place.

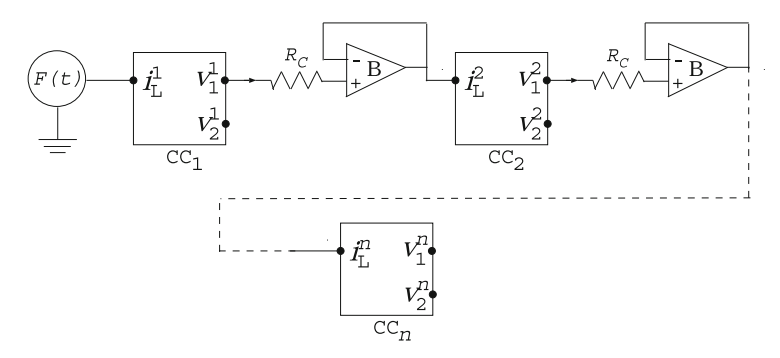


Fig. 8.13 The block diagram of a system of n unidirectionally coupled Chua's circuits. In the first circuit (CC₁), a biharmonic signal F(t) is connected in series with current $(i_{\rm L}^{\rm l})$ and the remaining circuits are driven by the voltage v_1 of the previous circuit. Here B is a buffer circuit and the *arrowhead* represents the direction of coupling

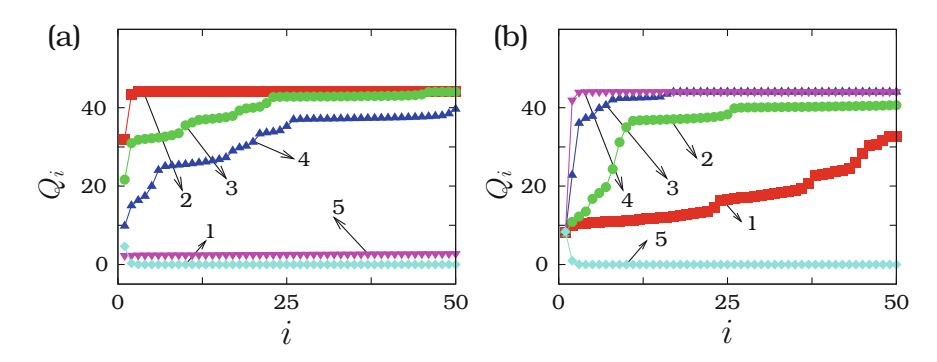


Fig. 8.14 (a) Q_i versus i (the number of the Chua's circuit) for few values of g with $R_C = 1 \text{ k}\Omega$. For the curves 1–5 the values of g are 0.6, 0.85, 1.1, 1.15 and 1.6 V, respectively. (b) Q_i versus i for five values of R_C with g = 1.2 V. The values of R_C for the curves 1–5 are 1, 1.2, 1.4, 1.8, and $2 \text{ k}\Omega$, respectively

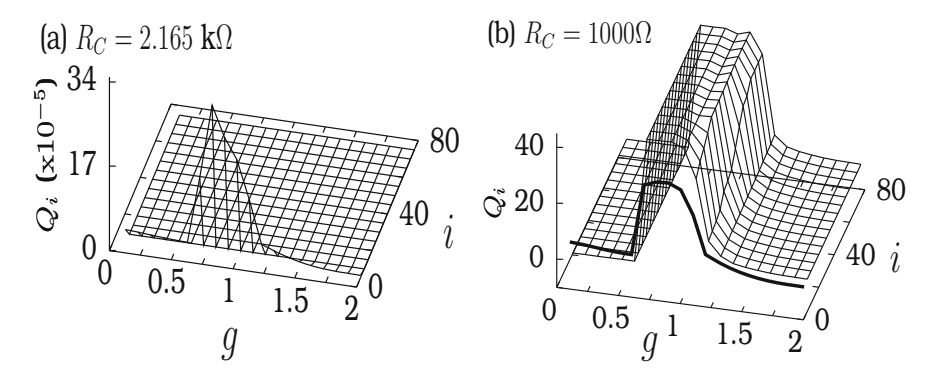


Fig. 8.15 Q_i as a function of i and g illustrating (**a**) damped propagation of signal (for $R_C = 2.165 \,\mathrm{k}\Omega$) and (**b**) undamped signal propagation (for $R_C = 1 \,\mathrm{k}\Omega$). The *thick curve* in (**b**) represents Q_1 . In (**a**) Q_1 is not shown because Q_i 's with i > 1 are much lower than Q_1

Figure 8.16 presents another interesting result. In this figure, v_1 of the ith circuit versus t is plotted for four values of i. v_1 is periodic with period $T=1/\omega$. The v_1 of the first circuit (i=1) is modulated by the high-frequency drive. Since $\Omega/\omega=10$, v_1 has ten peaks over one period. The high-frequency oscillation is weakened as the number of the circuit i increases as seen clearly in Fig. 8.16 for i=5 and i=15. For sufficiently large i, the amplitude modulation of v_1 disappears. The output signal appears as a rectangular pulse (Fig. 8.16d), of low-frequency ω . It is noteworthy to point out that in the coupled Chua's circuits, the biharmonic input signal is applied only to the first circuit. Essentially, the unidirectional coupling serves as a low-pass filter by weakening the propagation of the high-frequency component while enhancing the low-frequency component for a range of values g and R_C of the circuits.

References 239

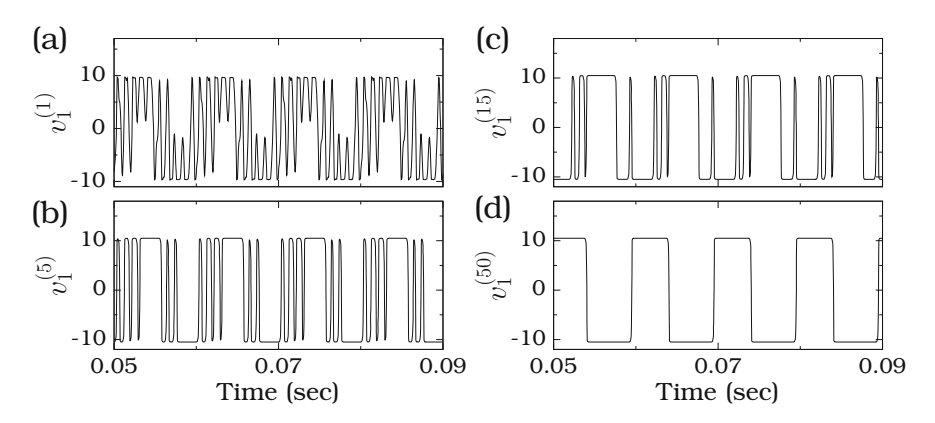


Fig. 8.16 Plot of v_1^i versus time at four different nodes denoted as i where $R = 2.15 \,\mathrm{k}\Omega$, $R_{\rm C} = 1 \,\mathrm{k}\Omega$ and $g = 1.1 \,\mathrm{V}$. Notice the suppression of high-frequency oscillations as i increases

8.6 Concluding Remarks

The present chapter reported vibrational resonance in certain experimental systems and weak signal amplification through the vibrational resonance. The PSpice simulation study of a system of n-coupled Chua's circuits revealed undamped signal propagation for a range of values of the amplitude g of the high-frequency input signal and the coupling parameter $R_{\rm C}$. Another interesting result is the experimental evidence for suppression of the high-frequency component in distant circuits while maintaining an enhanced signal propagation of low-frequency signal. That is, unidirectional coupling is found to act as a low-pass filter. The effect of noise on vibrational resonance has been studied [17] both experimentally and numerically in a FitzHugh–Nagumo system. Vibrational resonance is found to occur in the presence of noise. However, the noise is shown to decrease the response amplitude at resonance.

References

- J.P. Baltanas, L. Lopez, I.I. Blechman, P.S. Landa, A. Zaikin, J. Kurths, M.A.F. Sanjuan, Phys. Rev. E 67, 066119 (2003)
- 2. E. Ullner, A. Zaikin, J. Garcia-Ojalvo, R. Bascones, J. Kurths, Phys. Lett. A 312, 348 (2003)
- 3. V.N. Chizhevsky, E. Smeu, G. Giacomelli, Phys. Rev. Lett. 91, 220602 (2003)
- 4. V.N. Chizhevsky, G. Giacomelli, Phys. Rev. A 71, 011801(R) (2005)
- 5. G. Giacomelli, F. Marin, I. Rabbiosi, Phys. Rev. Lett. 82, 675 (1999)
- 6. S. Barbay, G. Giacomelli, F. Marin, Phys. Rev. E 61, 157 (2000)
- R. Jothimurugan, K. Thamilmaran, S. Rajasekar, M.A.F. Sanjuan, Int. J. Bifurcation Chaos 23, 1350189 (2013)
- 8. G. Giacomelli, F. Marin, Quantum Semiclassical Opt. 10, 469 (1998)
- 9. J.J. Collins, C.C. Chow, T.T. Imhoff, Phys. Rev. E 52, R3321 (1995)

- 10. R. Bascones, G. Garcia-Ojalvo, J.M. Sancho, Phys. Rev. E 65, 061108 (2002)
- 11. C. Yao, M. Zhan, Phys. Rev. E 81, 061129 (2010)
- I. Ozden, S. Venkataramani, M.A. Long, B.W. Connors, A.V. Nurmikko, Phys. Rev. Lett. 93, 158102 (2004)
- 13. Y.S. Heo, J.W. Jung, J.M. Kim, M.K. Jo, H.J. Song, J. Korean Phys. Soc. 60, 1140 (2012)
- 14. J.C. Zhou, H.J. Song, J. Korean Phys. Soc. **61**, 1303 (2012)
- 15. P.W. Tuinenga, SPICE-A Guide to Circuit Simulation and Analysis Using PSpice (Prentice Hall, New Jersey, 1995)
- 16. G.W. Roberts, A.S. Sedra, SPICE (Oxford University Press, New York, 1995)
- 17. M. Bordet, S. Morfu, Chaos Solitons Fractals 54, 82 (2013)

Chapter 9 Ghost Resonances

As shown in Sect. 2.2, when a bistable or an excitable system is driven by a periodic force of frequency, say, f and subjected to a weak noise it exhibits the phenomenon of stochastic resonance at an optimum noise level. Essentially, the signal-to-noise ratio (SNR) measured at the frequency f of the driving periodic force becomes maximum at a value of the noise intensity. At resonance, in the bistable system almost a periodic switching between the two coexisting states or potential wells occurs, with frequency 2f or period 1/(2f). That is, the mean residence time about a coexisting state or a potential well is 1/(2f). In excitable systems at resonance, the mean time duration (also called *waiting time*) between two consecutive bursts/pulses is 1/(2f) or the mean frequency of bursts is 2f. Note that in the noise-induced stochastic resonance phenomenon the system is driven by a single periodic force. The study of the response of a system to external signals comprising the number of periodic forces of different frequencies is of great important in understanding the response and functioning of many physical and biological systems. For example, signals such as musical tones and human speech received by sensory neurons often contain numerous discrete spectral lines.

Motivated by the above one can ask: What is the nature of noise-induced resonance in the case of an input signal with more than one periodic force? This problem has been investigated by the Argentinian physicist Dante R. Chialvo and his collaborators [1]. They considered an excitable system driven by the two periodic forces of the form

$$F(t) = A(\sin k f_0 2\pi t + \sin(k+1) f_0 2\pi t), \quad k = 2, 3, \dots$$
 (9.1)

kept in subthreshold limit and subjected to an external noise with intensity D. When the parameter D is varied, the system is found to give rise a sequence of pulses spaced at random intervals and at an optimum value of D the output pulses are spaced with an interval $\sim 1/f_0$ [1, 2]. That is, there exists a noise-induced stochastic resonance at a frequency f_0 that is missing in the input driving force. This fascinating

phenomenon of resonance wherein enhancement of response of the system at a frequency absent in the input is termed as *ghost resonance*. Note that at higher noise intensities, a resonance at the frequencies present in the input occurs. The ghost-resonance due to an external noise is the *ghost-stochastic resonance*. This ghost resonance phenomenon can be used to explain the missing fundamental illusion in which a third lower pitched tone is often heard when two tones occur together [2].

The occurrence of a ghost resonance induced by noise has been studied in several excitable systems [1–9]. In the ghost-stochastic resonance set up when a noise source is replaced by a high-frequency force the result is the *ghost-vibrational resonance* [10]. That is, a ghost resonance can be realized either by a noise or by a high-frequency force. This chapter is devoted for the analysis of ghost-stochastic and ghost-vibrational resonances in uncoupled systems and in unidirectionally coupled systems.

9.1 Ghost-Stochastic Resonance in a Single System

Consider a threshold system which is capable of emitting a rectangular pulse of short fixed duration whenever the input signal x(t) crosses the preassumed threshold value, say 1 [1]. In a neuronal system, this process of giving a spike depending upon the input signal is called *firing*. Assume that the input signal is

$$x(t) = F(t) + D\xi(t), \qquad (9.2a)$$

where

$$F(t) = \frac{A}{n} \sum_{i=1}^{n} \sin(2\pi f_i t), \quad f_i = (k-1+i)f_0, \quad k > 1.$$
 (9.2b)

In Eq. (9.2b) f_0 is a fundamental frequency that is missing in F(t). The signal F(t) has frequencies kf_0 , $(k+1)f_0, \dots, (k+n)f_0$. The noise term $\xi(t)$ in Eq. (9.2b) is a Gaussian white noise with mean zero and unit variance, where D is the strength of the noise.

9.1.1 System with Periodic Forces

First, consider x(t) with two periodic terms, that is, n = 2. We fix A = 0.9, $f_0 = 1$ and k = 2 so that x(t) has two frequencies $2f_0$ and $3f_0$. There are no firings in absence of noise. We add noise after every 0.01 time step. Then we vary the noise intensity D and analyse the response of the system. Our particular interest is on the distribution of time intervals between consecutive firings (also called *firing intervals*

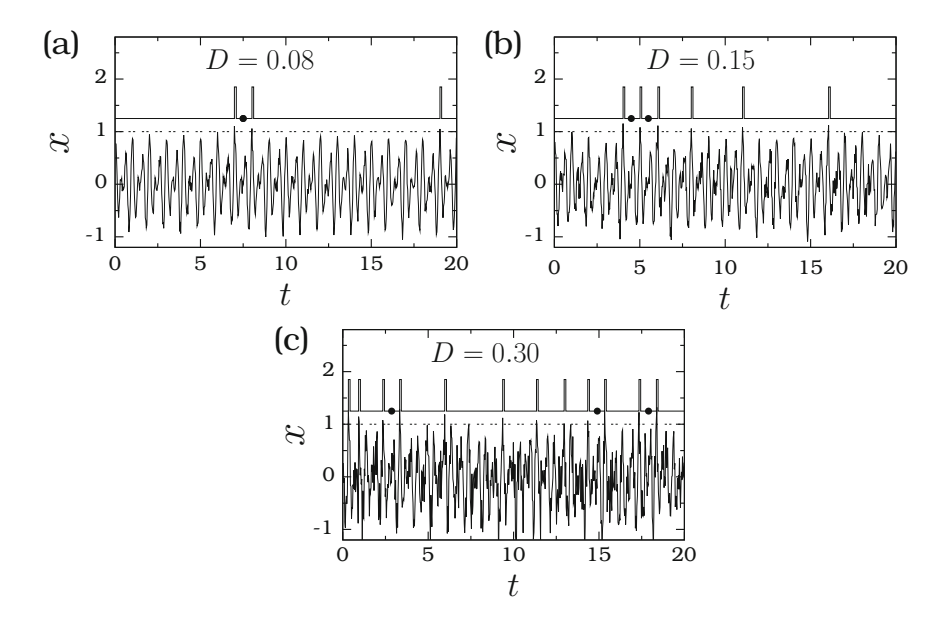


Fig. 9.1 x(t) (lower curve) given by Eq. (9.2) for (a) D = 0.08, (b) D = 0.15 and (c) D = 0.30. Here k = 2, n = 2, $f_0 = 1$ and A = 0.9. The dashed line indicates the threshold value 1. The upper trace is the output of the neuron model in the presence of x(t). Whenever x(t) crosses the threshold limit $x_{th} = 1$ the system issues a pulse. Solid circles mark the time duration $\approx 1/f_0$ between two consecutive pulses

or *waiting times* before give rise a pulse). Now we denote this time interval as τ and the corresponding (firing) frequency as $f = 1/\tau$.

Figure 9.1 shows the plot of x(t) for $t \in [0, 20]$ and for three values of D. As D increases the number of spikes per unit time interval increases. In Fig. 9.1 the solid circles represent the time intervals with the value $\approx 1/f_0 \approx 1$ between the two consecutive pulses. Though the periodic component of the input signal has no frequency f_0 , the response of the model considered here issues pulses with the firing frequency f_0 also.

Now we identify the various frequencies present in the output signal and their chances of occurrence. For a fixed value of D, we collect 10^5 values of firing frequencies. Using these data we compute the probability for the occurrence of each frequency in the interval [0,4] with step size 0.1. Counting the number of occurrences of firing frequency with a value f' allows $\pm 5\%$ of tolerance. Then, we divide the probability of each frequency by the total probability of all the frequencies considered. Figure 9.2 presents the probability distribution P(f) versus f for four values of D. For relatively low and sufficiently large noise intensities, firings of pulses takes place with various frequencies. This is the case in Figs. 9.2a and d. In

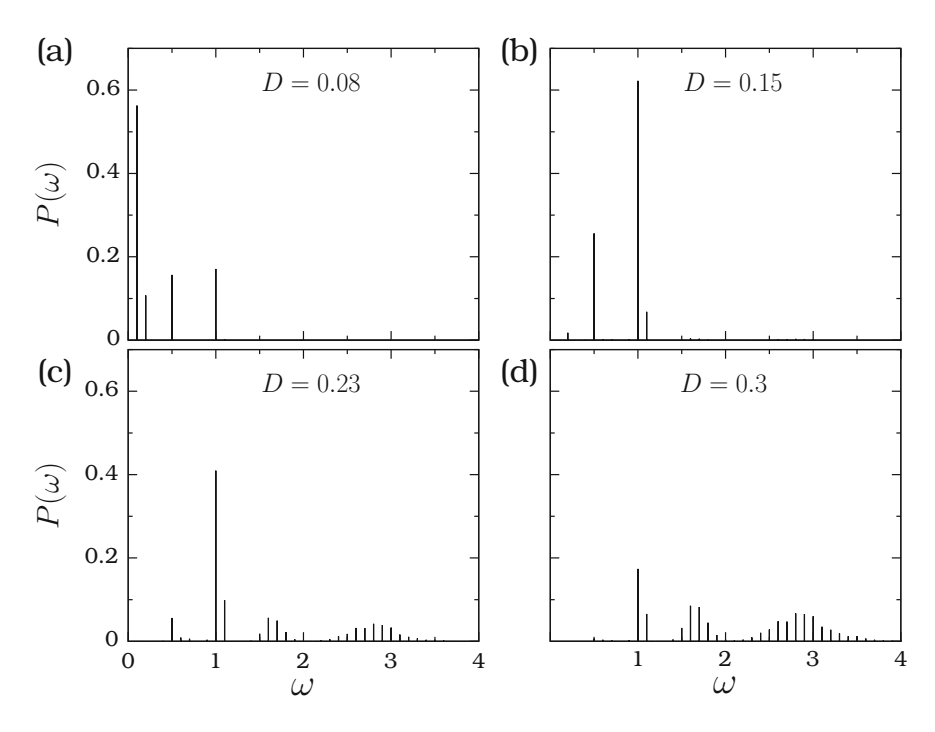
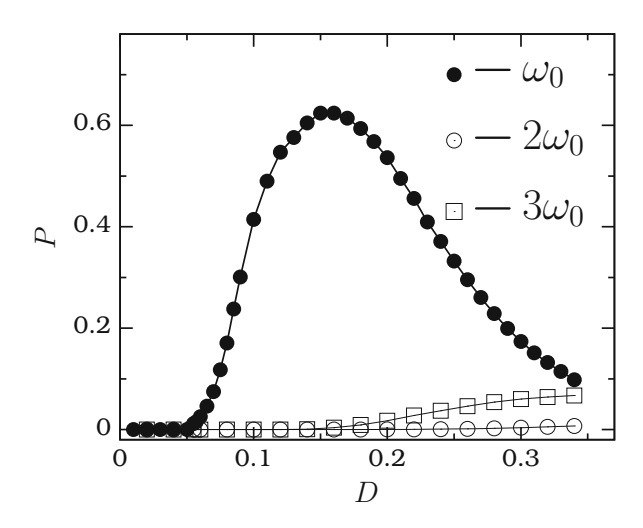


Fig. 9.2 Probability distribution (P(f)) of firing frequencies (f) for four values of noise intensity D. $P(f_0 = 1)$ is maximum for $D = D_{\text{max}} = 0.15$

Fig. 9.2b corresponding to D=0.15 the most frequent spike interval corresponds to $t=1/f_0=1$. When D is further increased, P(f) of $f=f_0$ decreases while those of other frequencies increases as shown in Figs. 9.2c, d for D=0.23 and 0.3, respectively. An interesting result for $D=D_{\max}=0.15$ is that not only $P(f_0)$ is not only nonzero, but is the maximum. For further details Fig. 9.3 shows P(f) versus the noise intensity for $f=f_0$, $2f_0$ and $3f_0$. For a range of values of $P(f_0)$ is much higher than that of the frequencies $2f_0$ and $3f_0$. As D increases from a small value $P(f_0)$ increases, reaches a maximum at $D=D_{\max}=0.15$ and then decreases. $P(2f_0)$ and $P(3f_0)$ are maximum at a higher value of D but their maximum values are much smaller than that of f_0 . P(f) exhibits resonance when the noise intensity D is varied. However, the resonance at the frequency f_0 is the strongest resonance even though this frequency is not present in the input. This resonance phenomenon occurring at a frequency that is absent in the input signal is termed as ghost resonance [1].

One can easily verify that for the cases of n > 2 and as well as for k > 2 the strongest resonance occur at the frequency f_0 .

Fig. 9.3 Variation of P(f) with D for $f = f_0$ (solid circles), $2f_0$ (open squares) and $3f_0$ (open circles)



9.1.2 System with Aperiodic Forces

The various frequencies present in F(t) given by Eq. (9.2b) are multiples of f_0 . Next, consider the more general case of a signal with different frequencies, for example, of the form [1]

$$F(t) = \frac{A}{n} \sum_{i=1}^{n} \sin(2\pi f_i t), \quad f_i = (k-1+i)f_0 + \Delta f, \quad k > 1.$$
 (9.3)

In the above F(t), the frequencies of each periodic component are not integer multiples of f_0 , however, the difference between f_{n+1} and f_n is Δf . The periodic terms are essentially shifted multiples of f_0 : $f_1 = kf_0 + \Delta f$, $f_2 = (k+1)f_0 + \Delta f$, \cdots , $f_n = (k-1+n)f_0 + \Delta f$. In this signal the fundamental frequency f_0 is also missing. The addition of Δf makes the frequencies incommensurate and the signal becomes anharmonic.

Assume that the neuron model detects the location of the highest peaks of the constructive interference of the signals $\sin(2\pi f_1 t)$ and $\sin(2\pi f_2 t)$. Then

$$\sin(2\pi f_1 t) + \sin(2\pi f_2 t) = 2\sin(\pi f^- t)\cos(\pi f^+ t), \qquad (9.4)$$

where $f^{\pm} = f_2 \pm f_1$. It represents a sinusoidal signal with a frequency $f^-/2$ and with amplitude modulated with the carrier frequency $f^+/2$. One can show that the two most dominant peaks are separated with the interval equal to the nearest integer n, of half-periods of the carrier lying within a half-period of the modulating signal [1]. When $f_1 = kf_0$ and $f_2 = (k+1)f_0$, then $n = f^+/f^- = 2k+1$ and the corresponding interval is $n/f^+ = 1/f_0$. For the case of a shifted anharmonic signal [1], with sufficiently small amount of shift, n remains constant while the

most probable interval is given by

$$\frac{n}{f^{+}} = \frac{2K+1}{(2k+1)f_0 + 2\Delta f} = \frac{1}{f_0 + \frac{\Delta f}{k+1/2}}.$$
 (9.5)

That is, one can expect resonances at a frequency

$$f_{\rm r} = f_0 + \frac{\Delta f}{k + 1/2} \tag{9.6}$$

when n = 2. For the general case of n = N

$$f_{\rm r} = f_0 + \frac{\Delta f}{k + (N - 1)/2} \tag{9.7}$$

Now, we are going to verify the above theoretical result through numerical simulation. First, we calculate f_r by varying $\Delta f \in [-0.5, 0.5]$. In calculating P(f), we vary f from 0 to 8 in steps of 0.001. Figures 9.4a, b presents the numerical results for n=2 and 3, respectively. The theoretical prediction given by Eq. (9.7) is in a very good agreement with the numerical simulation. Though the difference between f_{n+1} and f_n remains as f_0 , there is a shift in the resonance frequency. The point is that when a constant shift Δf is made to the frequencies of the input signal, the resonance does not occur at the missing frequency f_0 but at a shifted frequency. f_r follows a simple linear relation with f_r .

The theoretical expression for f_r given by Eq. (9.7) is found to be in remarkable agreement with the experimental results, as well [3–7, 9]. Chialvo [2] has shown a good agreement between the theory-based simulation data and the physiological data points of pitches measured from the prominent firing interval in the discharge patterns of cat auditory nerve fibers in response to complex tones [11] and the

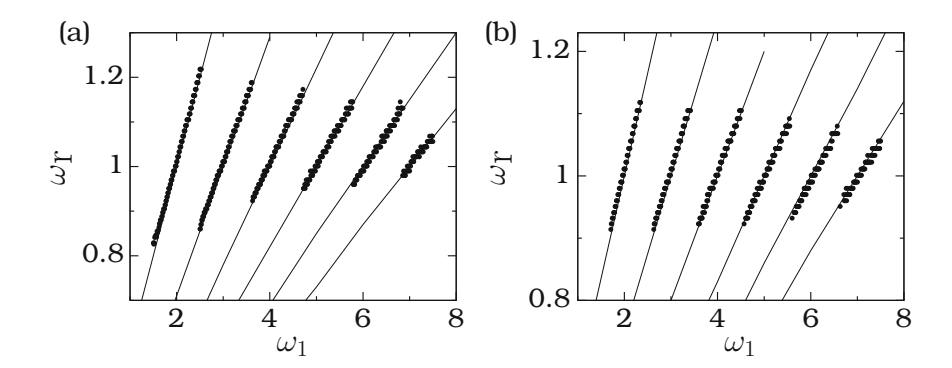


Fig. 9.4 Variation of the numerically computed resonance frequency f_r (marked by *solid circles*) with the frequency f_1 for (**a**) n = 1 and (**b**) n = 2. The *continuous lines* in both the subplots from *left to right* correspond to the theoretical f_r for k = 2 to 7

psychoacoustic experimental data of Schouten et al. [12]. In an experiment with binaural pitch perception, input harmonics are separately presented to human subjects but through different ears. In this case, a resonance with the missing fundamental frequency is also realized [13].

9.2 Ghost-Stochastic Resonance in a Network System

The numerical study of dynamics of n-coupled systems described by ordinary differential equations is time consuming. Therefore, to analyze ghost-stochastic resonance in n-coupled systems, we choose each unit in the coupled system as a Bellows map and also we choose the coupling as unidirectional.

In Eq. (7.28), we replace $f \cos \omega n$ by

$$F(n) = \sum_{i=1}^{n_{\rm f}} f_i \cos(\omega_i + \Delta\omega_0)n, \quad \omega_i = (k+i-1)\omega_0$$
 (9.8)

with $k \ge 2$ and $f_i = f$. For the single map [Eq. (7.28a) alone] and for $\omega_0 = 0.05$, k = 2, $n_{\rm f} = 2$, f = 0.4, $\Delta\omega_0 = 0$ and r = 2. Figure 9.5 shows the variation of the numerically computed $Q(\omega)$ for $\omega = \omega_0$, ω_1 and ω_2 as a function of the noise intensity D. A typical noise-induced resonance is realized with theses frequencies. $\omega_1 = 2\omega_0$ and $\omega_2 = 3\omega_0$ are present in the input signal. The resonance observed with these frequencies is the usual stochastic resonance. The resonance associated with the missing frequency ω_0 is ghost-stochastic resonance. The ghost-stochastic resonance occurs at D = 0.033. Note that the Bellows map is a bistable system.

Next, we consider the *n*-coupled Bellows maps, Eq. (7.28) with F(n) given by Eq. (9.8). Figure 9.6 reports Q_i versus i for the *n*-coupled Bellows maps for two

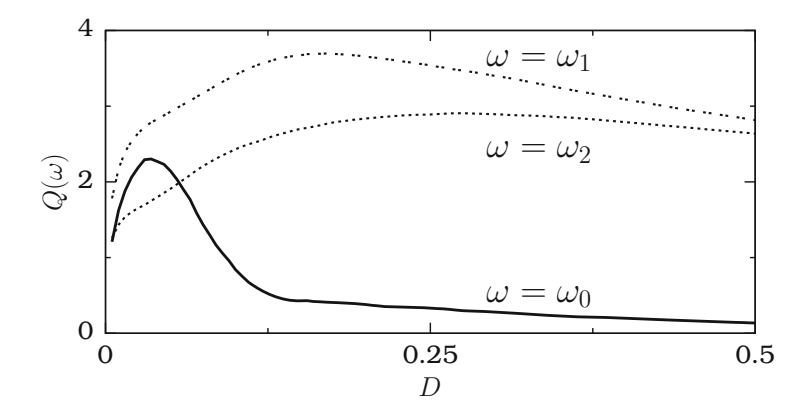


Fig. 9.5 $Q(\omega)$ at $\omega = \omega_0$, ω_1 and ω_2 versus the noise intensity D for a single Bellows map

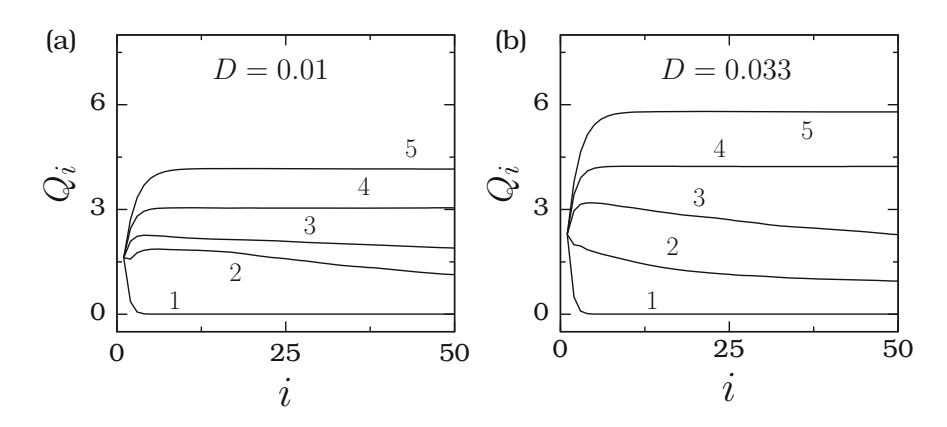


Fig. 9.6 Q_i versus i of the n-coupled Bellows maps. In (**a**) and (**b**) the values of δ for the curves 1-5 are 0.2, 0.28, 0.31, 0.5 and 0.7, respectively

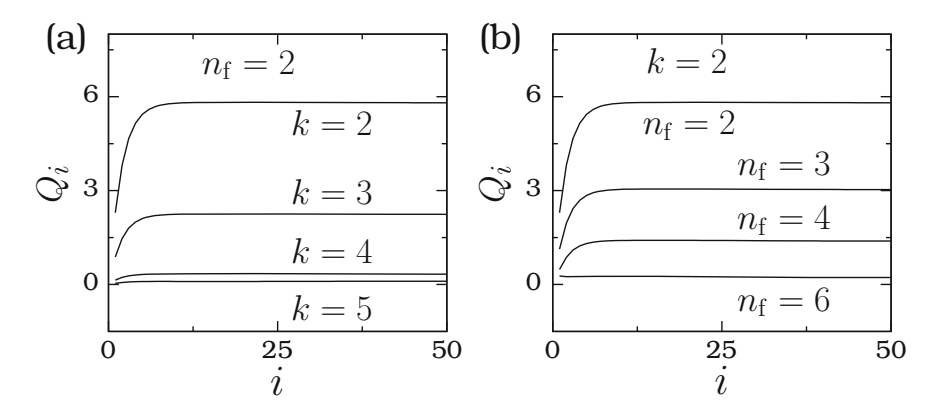


Fig. 9.7 Dependence of Q_i versus i for (a) first few values of k where $n_{\rm f}=2$ and (b) a few values of $n_{\rm f}$ where k=2 for the n-coupled Bellows maps. Here $\delta=0.7$ and D=0.033

values of D. For D=0.01 and 0.033 the Q_i decays to zero for $\delta < \delta_c$. Above δ_c the response amplitude increases with increase in i and then reaches a stationary value. Interestingly, the limiting value of Q_i , $Q_L(i \to \infty)$, for $\delta > \delta_c$ displays resonance-like behaviour. These are shown in Fig. 9.6a for five values of δ . Q_L increases rapidly with $\delta(\delta_c)$ for each fixed value of D (Fig. 9.6b). For $i \gg 1$, $x_n^{(i)}$ appears as a rectangular pulse-like solution.

Next, we report the effect of k and n_f . Figure 9.7a shows the variation of Q_i with i for k=2,3,4 and 5 where $n_f=2,D=0.033$ and $\delta=0.7$. Q_i for k=2 is the largest. For each unit Q_i is found to decrease with increase in k. For each fixed k, Q_i displays sigmoidal type variation with i. For each fixed k, Q_i for each i decreases with increase in n_f as shown in Fig. 9.7b. In Figs. 9.8a–c Q_L as a function of D is plotted for k=2,3 and 6 and for $\omega=\omega_0,\omega_1,\omega_2$ and ω_3 with $\omega_0=0.05,\delta=0.7$,

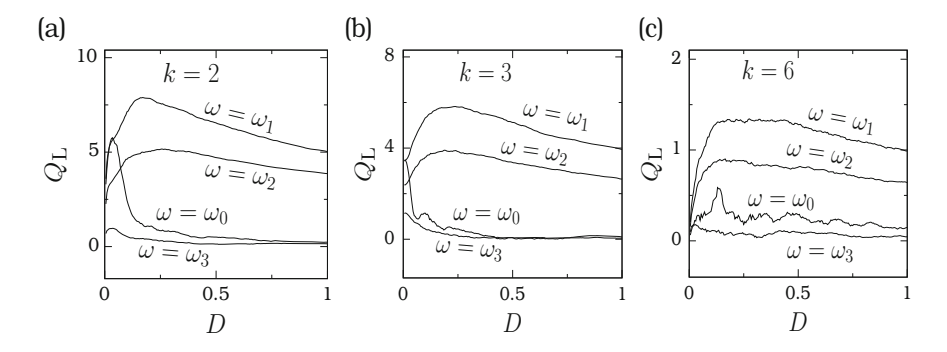


Fig. 9.8 Variation of Q_L with D for (a) k=2, (b) k=3 and (c) k=6 and for four values of ω for the n-coupled Bellows maps

 $n_{\rm f}=2$ and L=2000. For a range of D, the value of $Q(\omega_0)$ is not zero. However, Q at $\omega=\omega_1$ and ω_2 are $>Q(\omega_0)$ for a wide range of values of D.

9.3 Ghost-Vibrational Resonance in a Single System

This section is concerned with the ghost resonance induced by a high-frequency force rather than a noise. For this purpose, we consider the Duffing oscillator driven by n harmonic forces F(t) and a high-frequency periodic force $g \cos \Omega t$:

$$\ddot{x} + d\dot{x} + \alpha x + \beta x^3 = F(t) + g\cos\Omega t, \tag{9.9}$$

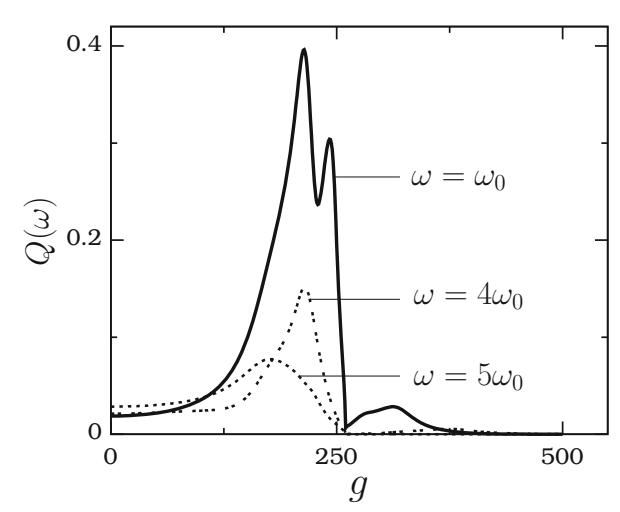
where

$$F(t) = \sum_{i=1}^{n_{\rm f}} f_i \cos(\omega_i + \Delta\omega_0)t, \quad \omega_i = (k+i-1)\omega_0. \tag{9.10}$$

We fix d=0.5, $\alpha=-2$, $\omega_0=0.5$, $\beta=1$, $\Omega=30\omega_0$, $f_i=0.1$ and treat g as the control parameter. In the presence of these two periodic low-frequency forces and with g=0 the solution of the system (9.9) contains periodic components with certain frequencies other than $2\omega_0$ and $3\omega_0$. However, Q at these frequencies is very weak.

Figure 9.9 presents $Q(\omega)$ versus g for $\omega = \omega_0$, $4\omega_0$ and $5\omega_0$ where $Q(\omega_0) \neq 0$ for g = 0 but ≈ 0 . As g increases $Q(\omega)$ at $\omega = \omega_0$, $4\omega_0$, $5\omega_0$ displays a resonance. The resonance of $Q(\omega_0)$ is much stronger than at the frequencies $4\omega_0$ and $5\omega_0$. Note that the fundamental frequency ω_0 is missing in F(t). The high-frequency induced resonance at the missing frequency of the input signal is termed as *ghost-vibrational resonance* [10]. There are two fundamental differences between the ghost resonance induced by noise and by the high-frequency force. In the noise driven case, when

Fig. 9.9 Variation of $Q(\omega)$ with g in the system (9.9) for $\omega = \omega_0$ (= 0.5), $4\omega_0$ and $5\omega_0$ missing in F(t) [Eq. (9.1)] with n=2, k=2, $\Delta\omega_0=0$ and $f_1=f_2=f=0.1$



the intensity D of the noise is varied, the *SNR* at ω_0 becomes maximum at one value of D. Further, the resonances at the frequencies present in the input signal are weak. In the high-frequency induced ghost resonance, the response amplitude can be maximum at more than one value of the parameter g (as shown in Fig. 9.9). In the system (9.9), the resonance at the frequencies present in the input signal are stronger than the resonance at ω_0 . The resonance at $2\omega_0$ and $3\omega_0$ is the well known vibrational resonance.

9.3.1 Theoretical Calculation of $Q(\omega_0)$

Now we proceed to obtain analytical expressions for $Q(\omega)$ at various values of ω . For the system (9.9) with n=2, we assume that its solution consists of a low-frequency component X and a high-frequency (Ω) component ψ . Substitution of $x=X+\psi$ in Eq. (9.9) gives (with $\tau=\Omega t$)

$$\ddot{X} + d\dot{X} + \alpha X + \beta X^3 + 3\beta X^2 \langle \psi \rangle + 3\beta X \langle \psi^2 \rangle = f_1 \cos \omega_1 t + f_2 \cos \omega_2 t,$$
(9.11)

$$\ddot{\psi} + d\dot{\psi} + \alpha\psi + \beta\psi^3 + 3\beta X^2 (\psi - \langle \psi \rangle) + 3\beta X (\psi^2 - \langle \psi^2 \rangle) = g \cos \Omega t.$$
(9.12)

As usual, we approximate Eq. (9.12) as $\ddot{\psi} = g \cos \Omega t$, which gives $\psi = -(g/\Omega^2) \cos \Omega t$. For this solution $\langle \psi \rangle = 0$, $\langle \psi^2 \rangle = g^2/(2\Omega^4)$ and $\langle \psi^3 \rangle = 0$.

Then, Eq. (9.11) becomes

$$\ddot{X} + d\dot{X} + CX + \beta X^{3} = f_{1} \cos \omega_{1} t + f_{2} \cos \omega_{2} t, \tag{9.13}$$

where $C = \alpha + 3\beta g^2/(2\Omega^4)$. Slow oscillations of (9.13) occur about its stable fixed points. Equation (9.13) with $f_1 = f_2 = 0$ admits three fixed points

$$X^* = 0, \pm \sqrt{-C/\beta} \text{ for } g < g_c = \left[-\frac{2\alpha\Omega^4}{3\beta} \right]^{1/2}$$
 (9.14)

and only one fixed point $X^* = 0$ for $g > g_c$. The change of variable $Y = X - X^*$ gives

$$\ddot{Y} + d\dot{Y} + \omega_r^2 Y + \beta Y^3 + 3\beta Y^2 X^* = f_1 \cos \omega_1 t + f_2 \cos \omega_2 t, \qquad (9.15a)$$

where

$$\omega_{\rm r}^2 = \alpha + \frac{3\beta g^2}{2\Omega^4} + 3\beta X^{*2}.$$
 (9.15b)

For a weak nonlinearity, an approximate solution of Eq. (9.15) can be constructed through an iterative process [14], wherein the sequence of approximations $Y_0(t)$, $Y_1(t)$, \cdots are obtained by solving

$$\ddot{Y}_0 + d\dot{Y}_0 + \omega_r^2 Y_0 = F(t), \tag{9.16}$$

$$\ddot{Y}_1 + d\dot{Y}_1 + \omega_r^2 Y_1 = F(t) - \beta Y_0^3 - 3\beta X^* Y_0^2$$
(9.17)

and so on. Now, we attempt to find out both Y_0 and Y_1 . The solution of Eq. (9.16) in the long time limit is

$$Y_0(t) = A_1 \cos(\omega_1 t + \phi_1) + A_2 \cos(\omega_2 t + \phi_2), \tag{9.18a}$$

where

$$A_{i} = \frac{f}{\sqrt{(\omega_{\rm r}^{2} - \omega_{i}^{2})^{2} + d^{2}\omega_{i}^{2}}}, \quad \phi_{i} = \tan^{-1}\left(-\frac{d\omega_{i}}{\omega_{\rm r}^{2} - \omega_{i}^{2}}\right), \quad i = 1, 2.$$
(9.18b)

Substitution of Y_0 in (9.17) gives Y_1 . Y_1 contains the frequencies ω_1 and ω_2 and certain other frequencies, namely, $l\omega_0$, where l=1,k-1,k,k+1,k+2,2k,2k+1, 2k+2,3k,3k+1,3k+2,3k+3 due to the terms Y_0^2 and Y_0^3 in Eq. (9.17). When k=2 the various frequencies present in Y_1 are $\omega=l\omega_0, l=1,2,\cdots,9$. The lowest and the highest frequencies in Y_1 are $\omega_2-\omega_1=\omega_0$ and $3\omega_2$, respectively.

Retaining only the terms containing ω_0 , ω_1 , ω_2 , $\omega_1 - \omega_0$ (which will become ω_0 if k = 2) in the right-side of Eq. (9.17) leads to [with $Y_1 = Y_1$ (ω_0 , ω_1 , ω_2 , $\omega_1 - \omega_0$)]

$$Y_{1} = \frac{a_{01}}{s_{0}} \cos (\omega_{0}t + \phi_{0} - \phi_{1} + \phi_{2})$$

$$+ \frac{a_{02}}{s_{01}} \cos ((\omega_{1} - \omega_{0})t + \phi_{0} + 2\phi_{1} - \phi_{2})$$

$$+ \frac{a_{1}}{s_{1}} \cos (\omega_{1}t + \phi_{1} + \phi_{2}) + \frac{f}{s_{1}} \cos (\omega_{1}t + \phi_{1})$$

$$+ \frac{a_{2}}{s_{2}} \cos (\omega_{2}t + 2\phi_{2}) + \frac{f}{s_{2}} \cos (\omega_{2}t + \phi_{2}), \qquad (9.19a)$$

where

$$\phi_i = \tan^{-1} \left(-\frac{d\omega_i}{\omega_i^2 - \omega_i^2} \right), \quad i = 0, 1, 2$$
 (9.19b)

$$\omega_i = (k+i-1)\omega_0 + \Delta\omega_0, \quad i = 1, 2$$
 (9.19c)

$$s_i = \sqrt{(\omega_{\rm r}^2 - \omega_i^2)^2 + d^2 \omega_i^2}, \quad i = 0, 1, 2$$
 (9.19d)

$$s_{01} = s_0 (\omega_0 \to \omega_1 - \omega_0), \ A_i = \frac{f}{s_i}, \ i = 1, 2$$
 (9.19e)

$$a_{01} = 3\beta X^* A_1 A_2, \ a_{02} = \frac{3}{4}\beta A_1^2 A_2,$$
 (9.19f)

$$a_1 = \frac{3}{4}\beta A_1 \left(A_1^2 + 2A_2^2 \right), \quad a_2 = \frac{3}{4}\beta A_2 \left(A_2^2 + 2A_1^2 \right).$$
 (9.19g)

 $\omega_1 - \omega_0 = \omega_0$ for k = 2 and $\Delta \omega_0 = 0$. For this case, the first two terms in the right-side of Eq. (9.19a) are periodic with frequency ω_0 , otherwise the first term alone is periodic with the frequency ω_0 .

In Eq. (9.19a) for $|f_1 = f_2 = f| \ll 1$ the third and the fifth terms in the right-side can be neglected because a_1 and a_2 are of the order of f^3 , while the fourth and sixth terms are of the order of f only and the minimum value of s_i is $d\omega_i$ which is not very small for d = 0.5 and $\omega_0 = 0.5$. Then the amplitude of the periodic components in the solution (9.19a) with the frequencies ω_0 , ω_1 and ω_2 are

$$A(\omega_1) = \frac{f}{s_1}, \quad A(\omega_2) = \frac{f}{s_2},$$

$$A(\omega_0, k = 2, \Delta\omega_0 = 0) = \frac{1}{s_0} \sqrt{a_{01}^2 + a_{02}^2 + 2a_{01}a_{02}\cos(2\phi_2 - 3\phi_1)},$$
(9.20b)

 $A(\omega_0, k \neq 2 \text{ or } \Delta\omega_0 \neq 0) = \frac{a_{01}}{\varsigma_0} = \frac{3\beta X^* f^2}{\varsigma_0 \varsigma_1 \varsigma_2}.$ (9.20c)

Then $Q(\omega_i) = A(\omega_i)/f$.

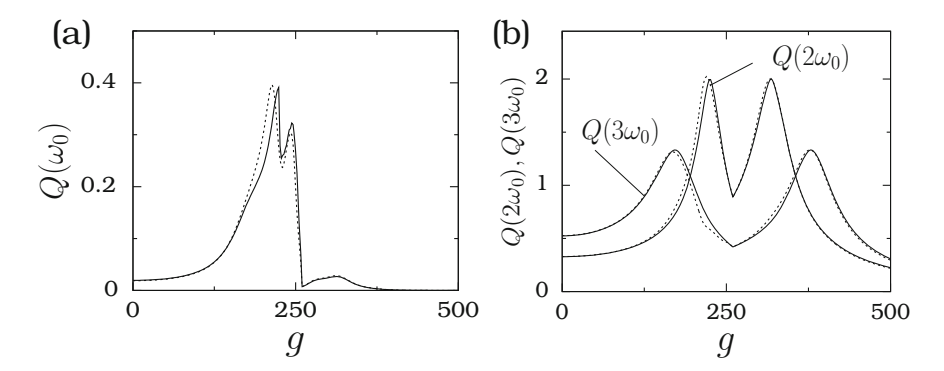


Fig. 9.10 Theoretical (continuous curve) and numerical (dashed curve) (a) $Q(\omega_0)$, (b) $Q(2\omega_0)$ and $Q(3\omega_0)$ versus g for the system (9.9) with $\omega_0=0.5$, n=2, k=2, $\Delta\omega_0=0$ and $f_1=f_2=f=0.1$

In Fig. 9.10, both theoretically and numerically calculated $Q(\omega_0)$, $Q(2\omega_0)$ and $Q(3\omega_0)$ as a function of the parameter g are plotted. Theoretical Q at $\omega = \omega_0$, $2\omega_0$ and $3\omega_0$ are in very good agreement with the numerically computed Q. Because $A(\omega_0)$ is a complicated function of g it is very difficult to find an analytical expression for g_{VR} at ω_0 .

9.4 Effect of k, n and $\Delta \omega_0$ on Resonance

The theoretical procedure employed in the previous section for the determination of an analytical expression for $Q(\omega_0)$ can be extended for n > 2. However, such an analysis involves tedious mathematics, so that we prefer to perform a numerical simulation. For this purpose, we choose $f_i = f$, $i = 1, 2, \dots, n$.

Figure 9.11a presents $Q(\omega_0)$ versus g for several values of k with n=2 and $\Delta\omega_0=0$. $Q(\omega_0)$ (as well as $Q(\omega_1)$ and $Q(\omega_2)$) decays to zero with k. For $k\neq 2$ the theoretical expression for $A(\omega_0)$ in $Q(\omega_0)=A(\omega_0)/f$ is given by Eq. (9.20c). For a fixed value of g as k increases, the quantities s_i , i=0,1,2 increase and A_1 and A_2 decrease. Since $A(\omega_0)$ is directly proportional to A_1,A_2 and $1/s_0$, its value decreases with increasing values of k. In Fig. 9.11a $Q(\omega_0)=0$ for $g>g_c(=259.81)$ when k>2. This is because for $g>g_c$ the fixed point about which a slow oscillation occurs is $X^*=0$ and hence $Q(\omega_0)$ becomes zero [refer Eq. (9.20c)]. That is, for k>2 the output signal will have a periodic component with the missing frequency ω_0 only if the center of oscillation of the output x(t) is $\neq 0$ which will happen for $g<g_c$. The value of $Q(\omega_0)$ at resonance, as shown in Fig. 9.11b, increases with the number of periodic forces, n, and attains a saturation. For k>2 resonance occurs for $n\geq 2$, but the value of $Q(\omega_0)$ at resonance decreases when n increases.

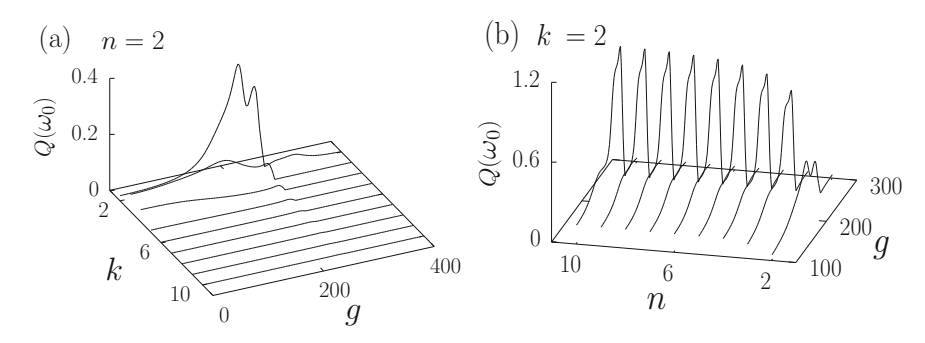


Fig. 9.11 Three-dimensional plot of $Q(\omega_0)$ versus g and (a) k for n=2 and (b) n for k=2 for the system (9.9) with $\omega_0=0.5$ and f=0.1

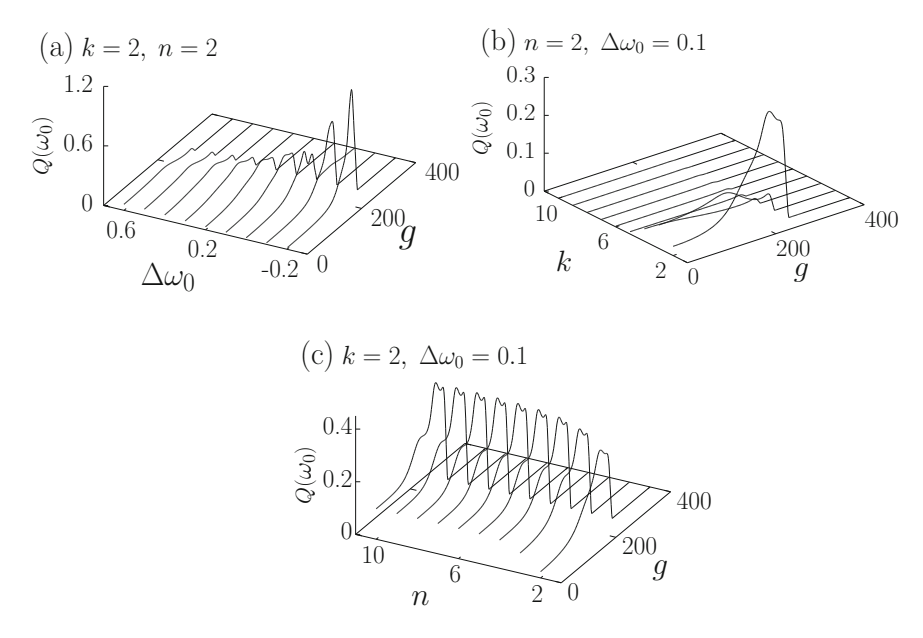


Fig. 9.12 $Q(\omega_0)$ versus g for various values of (a) $\Delta\omega_0$ for k=2, n=2, (b) k for n=2, $\Delta\omega_0=0.1$ and (c) n for k=2, $\Delta\omega_0=0.1$. In all the cases $\omega_0=0.5$ and f=0.1

Next, consider the system (9.9) with $\Delta\omega_0 \neq 0$. Figure 9.12a displays the effect of $\Delta\omega_0$ on the response amplitude profile for k=2, n=2 and $\omega_0=0.5$. For $\Delta\omega_0 \neq 0$ the amplitude $A(\omega_0)$ given by Eq. (9.20c) is inversely proportional to $s_0s_1s_2$. For a fixed value of g, the quantities s_i , i=0,1,2 increase with increase in $\Delta\omega_0$. As a result, $Q(\omega_0) = A(\omega_0)/f$ decreases with an increase in $\Delta\omega_0$. This is evident in Fig. 9.12a. A similar result is seen in Fig. 9.12b, where $Q(\omega_0)$ is plotted as a function of k and k for k for k for k fixed k for k

saturation. This result is similar to the one shown in Fig. 9.11b for $\Delta\omega_0=0$. In all the subplots in Fig. 9.12 $Q(\omega_0)=0$ for $g>g_c(=259.81)$ because $A(\omega_0)\propto X^*$ and $X^*=0$ for $g>g_c$.

9.5 Ghost-Vibrational Resonance in a Network System

This section analyses the features of signal propagation at the missing fundamental frequency in a regular network of one-way coupled N(=200) units. Here, we consider the cases of multi-frequency signal applied to (1) first unit only and (2) to all the units.

9.5.1 Description of the Network Model

The network has N identical Duffing oscillators. The first unit is uncoupled and is alone driven by both F(t) and $g \cos \Omega t$. The interaction is along one direction. We choose the coupling term to be linear. The equation of motion of the network is

$$\ddot{x}_1 + d\dot{x}_1 + \alpha x_1 + \beta x_1^3 = F(t) + g \cos \Omega t, \tag{9.21a}$$

$$\ddot{x}_i + d\dot{x}_i + \alpha x_i + \beta x_i^3 = \delta x_{i-1}, \quad i = 2, 3, \dots, N$$
 (9.21b)

and F(t) is given by Eq. (9.1). Fix d=0.5, $\alpha=-2$, $\beta=1$, $\omega_0=0.5$ and $\Omega=30\omega_0$.

9.5.2 Undamped Signal Propagation

In the input signal F(t) the fundamental frequency ω_0 is absent. Now, we calculate the response amplitude $Q_i(\omega_0)$ numerically. Figure 9.13a shows $Q_i(\omega_0)$ as a function of the unit i for a few fixed values of the coupling strength δ with the values of the parameters in F(t) as n=2, k=2, $\omega_0=0.5$, $\Delta\omega_0=0$, $f_1=f_2=\cdots=f_n=f=0.1$ and g=0. When g=0, $Q_1=0.01874$. For $\delta<\delta_c=1.78$, $Q_i< Q_1$ for $i\gg 1$. For $\delta\geq\delta_c$ as i increases the value of Q_i increases slowly then increases rapidly and reaches a saturation. $Q_{200}>Q_1$ and the network displays undamped signal propagation. For very large i, Q_i oscillates about a value with small amplitude. Neglecting this small oscillation, Q_i becomes almost a constant for sufficiently large values of i. Denote Q_L as the saturation value of Q_i . In Fig. 9.13a Q_L increases with increase in δ from δ_c . The undamped and enhanced propagation of signal with the frequency ω_0 missing in the input signal takes place even when g=0. The enhanced

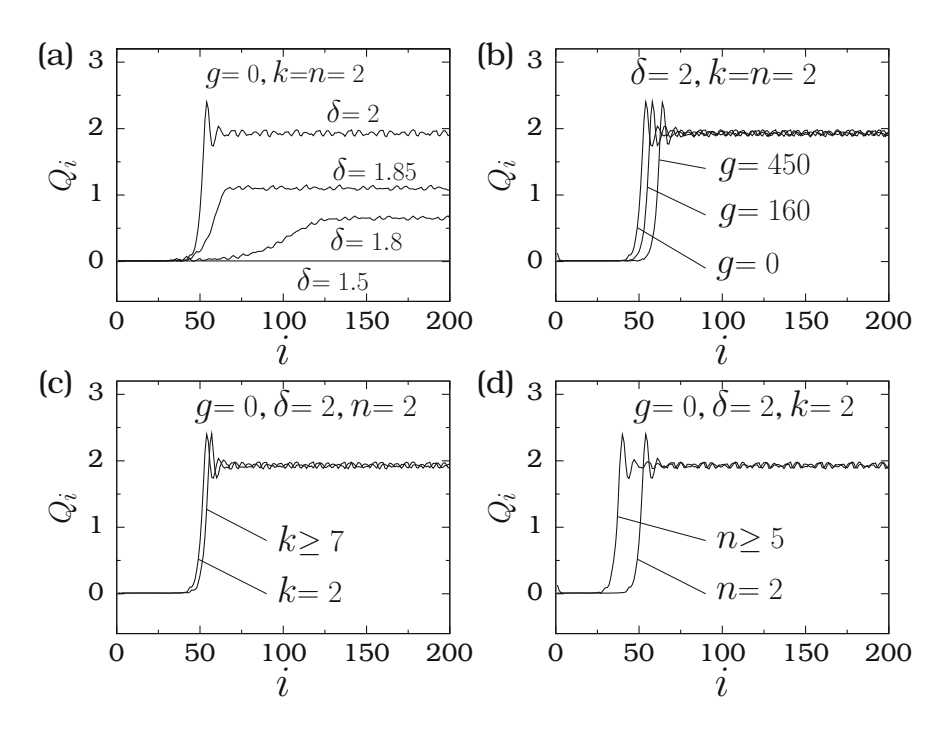


Fig. 9.13 Dependence of Q_i versus i curve on (a) δ for g=0, k=n=2, (b) g for $\delta=2$, k=n=2, (c) k for $\delta=2$, n=2 and n=0 and (d) the number of periodic forces in n=0 for n=0 and n=0 and

signal propagation is due to the unidirectional coupling. Note that the input signal F(t) is applied to the first oscillator only.

 Q_i versus i for three values of g with $\delta=2$ is shown in Fig. 9.13b. Q_L is independent of g. The values of g have a strong influence on Q_i only for a certain range of values of i denoting the oscillators number. In Fig. 9.13b roughly in the 40th to 70th oscillators Q_i varies with g. In this interval of i, Q_i rapidly increases with i. As g increases from 0 the Q_i profile oscillates and becomes stationary for sufficiently large values of g. Similar effects are found for various values of g and g and g are 0. In Fig. 9.13c the g versus g profile evolves to a stationary one with increase in the value of g are g profile remains the same for g and g and g and depends on g and g are observed. In Fig. 9.13d, an interesting result is that g is independent of g, g and g and depends on g. A numerical simulation is performed for g are observed. Furthermore, g is found to be independent of g.

9.5.3 A Network with All the Units Driven by External Forces

Next, we consider the network with all the units driven by the force F(t) and $g \cos \Omega t$ and the units are coupled unidirectionally. The equation of motion of the network is

$$\ddot{x}_1 + d\dot{x}_1 + \alpha x_1 + \beta x_1^3 = F(t) + g \cos \Omega t, \tag{9.22a}$$

$$\ddot{x}_i + d\dot{x}_i + \alpha x_i + \beta x_i^3 = \delta x_{i-1} + F(t) + g \cos \Omega t,$$
 (9.22b)

where $i = 2, 3, \dots, N$. Figure 9.14 shows Q_i versus g and i for two fixed values of δ . We observe ghost resonance in each unit. For $\delta = 0.3$ (Fig. 9.14a) the value of Q_i at resonance increases with the unit number i and then reaches a saturation with $Q_{N,\max} > Q_{1,\max}$. For $\delta = 0.5$ (Fig. 9.14b) we can clearly notice small oscillatory variation of Q_i with i for the values of g near resonance. The oscillatory variation of Q_i is found in the network system (9.21) also. Comparing Figs. 9.13 and 9.15, we observe that the enhancement of the response amplitude at resonance in the network (9.22) is relatively higher than that of the network (9.21).

For the network system (9.21), in Fig. 9.14a Q of the last unit is < 3 for $\delta < 2$. Furthermore, Q of the last unit is independent of the value of g. For the network system (9.22), in Fig. 9.14 Q of the last unit depends on the value of g. In the system (9.21) undamped signal propagation with $Q_N > Q_1$ occurs for $\delta > 1.78$ and even for g = 0. In contrast to this, in the system (9.22) $Q_N > Q_1$ takes place

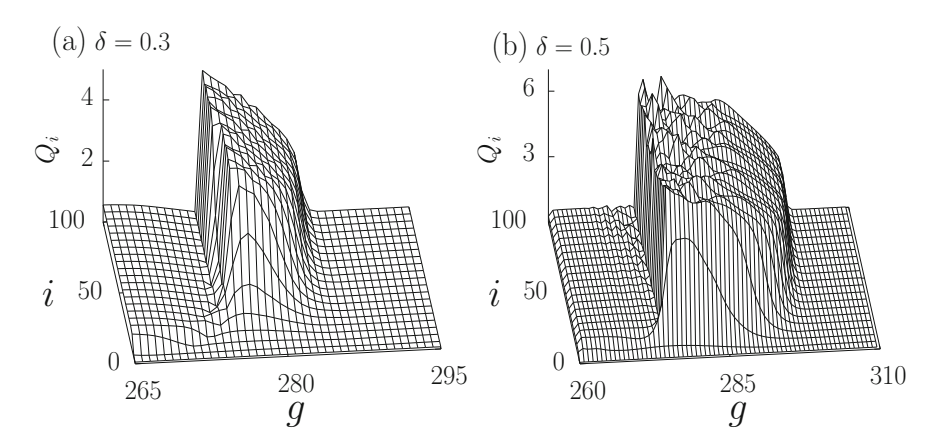


Fig. 9.14 Variation of Q_i with g and i for two values of δ of the network system (9.22) where $d=0.5, \alpha=-2, \beta=1, f=0.1, \omega_0=0.5, \Omega=30\omega_0, k=2, n=2$ and $\Delta\omega_0=0$

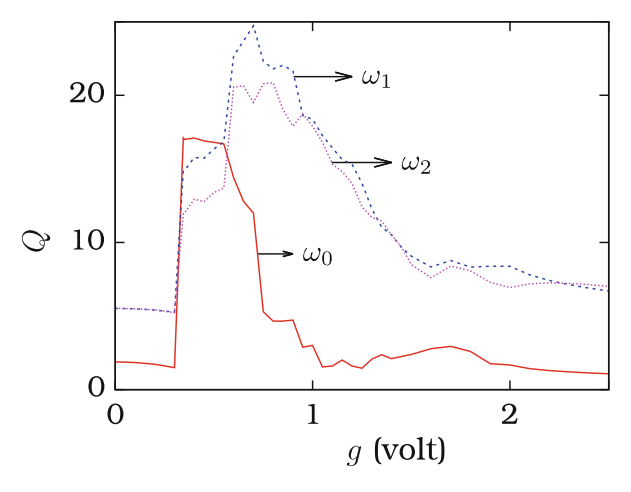
only for certain range of values of g, however, $\langle Q \rangle > Q_1$ even for a wide range of values of $\delta < 1.78$. As far as the signal amplification and propagation at a missing frequency ω_0 is concerned, driving all units in the unidirectionally coupled system considerably improves the response amplitude over a certain range of values of g and δ compared to the driving the first unit alone.

9.6 Ghost-Vibrational Resonance in Chua's Circuit

The ghost-vibrational resonance is observed experimentally in the Chua's circuit. The Chua's circuit shown in Fig. 8.1 is modified by including multi-frequency driving signal $F(t) = (1/n) \sum_{i=1}^n f_i \sin \omega_i t + g \sin \Omega t$ where $\omega_i = (k + (i-1))\omega_0$. The response of the circuit is analysed for the parametric choice $R = 2150 \,\Omega$, $C_1 = 10 \,\text{nF}$, $C_2 = 100 \,\text{nF}$, $L = 18 \,\text{mH}$, $f_i = 600 \,\text{mV}$ and $\Omega = 1500 \,\text{Hz}$. For n = 2, k = 2 and $\omega_0 = 25 \,\text{Hz}$ from the power spectrum of the signal v_1 the amplitudes of the signal at frequencies ω_0 , ω_1 and ω_2 are measured by varying the amplitude g of the high-frequency signal. Then Q is computed. Figure 9.15 shows the result. The $Q(\omega_0)$, $Q(\omega_1)$ and $Q(\omega_2)$ of the state variable v_1 exhibit a typical resonance.

 $Q(\omega_0)$ is measured for several fixed values of ω_0 as a function of g and the result is presented in Fig. 9.16. Ghost-vibrational resonance occurs for each fixed value of ω_0 . Figure 9.17a depicts $Q(\omega_0)$ versus g for $k=2,3,\cdots,10$ for n=2. For these values of k also resonance at ω_0 is observed. $Q(\omega_0)$ as a function of g and g for g and g for g is presented in Fig. 9.17b.

Fig. 9.15 Plot of $Q(\omega_i)$, i = 0, 1, 2 measured from the Chua's circuit as a function of g with $\omega_0 = 25$ Hz



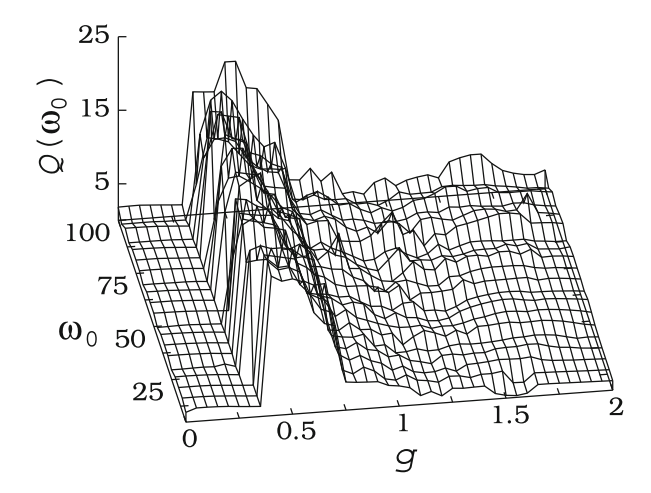


Fig. 9.16 Experimentally measured $Q(\omega_0)$ versus g and ω_0 for the Chua's circuit

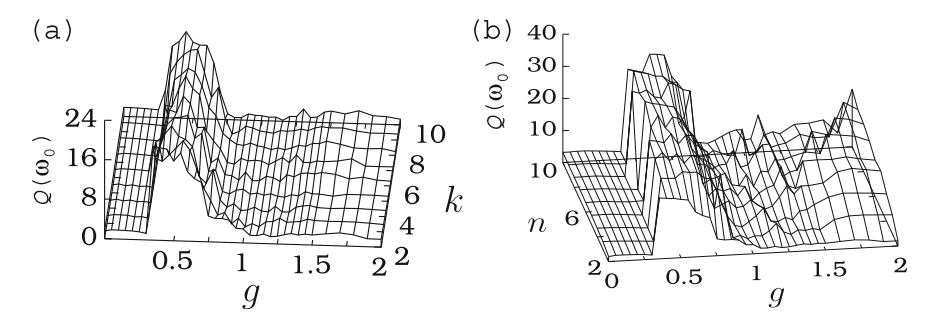


Fig. 9.17 The dependence of $Q(\omega_0)$ with g for (a) $k=2,3,\cdots,10$ with n=2 and (b) $n=2,3,\cdots,10$ with k=2 for the Chua's circuit. Here $\omega_0=25\,\mathrm{Hz}$

9.7 Concluding Remarks

The output of a linear system subjected to a periodic force with a single frequency ω contains only the frequency ω . In contrast to this, the output of a nonlinear system has the frequency ω and its integral multiples. If a linear system is driven by a multifrequency signal, the frequencies present in the output are the same as those in the input. Interestingly, the output of a nonlinear system driven by a multi-frequency force not only contains the harmonics of the input frequencies, but inter-modulation components of harmonics can also be generated.

This chapter has shown the enhancement of the response amplitude in the output of a nonlinear system by a noise or a high-frequency force at the missing fundamental frequency in the input multi-frequency signal. For the ghost-stochastic resonance to occur, we must consider a bistable or excitable system. High-frequency induced ghost resonance can occur even in a single-well nonlinear system. The

ghost-stochastic resonance in excitable systems is different from that of it in bistable systems. In excitable systems the ghost resonance at the missing frequency is dominant over a wide range of noise intensity. But in the bistable systems resonance at the missing frequency occurs but is not the dominant resonance.

In the excitable systems, when there is a shift in the input frequencies, then the resonance frequency is given by Eq. (9.3). The resonance frequency is not the missing frequency. It is a function of the number of periodic terms present in F(t), the parameter k, frequency shift and the fundamental frequency. In the bistable systems this is not the case. Resonance occurs at the fundamental frequency, however, only for small values of k.

References

- D.R. Chialvo, O. Calvo, D.L. Gonzalez, O. Piro, G.V. Savino, Phys. Rev. E 65, 050902(R) (2002)
- 2. D.R. Chialvo, Chaos 13, 1226 (2003)
- J.M. Buldu, D.R. Chialvo, C.R. Mirasso, M.C. Torrent, J. Garcia-Ojalvo, Europhys. Lett. 64, 178 (2003)
- 4. J.M. Buldu, C.M. Gonzalez, J. Trull, M.C. Torrent, J. Garcia-Ojalvo, Chaos 15, 013103 (2005)
- 5. G. Van der Sande, G. Verschaffelt, J. Danckaert, C.R. Mirrasso, Phys. Rev. E 72, 016113 (2005)
- A. Lopera, J.M. Buldu, M.C. Torrent, D.R. Chialvo, J. Garcia-Ojalvo, Phys. Rev. E 73, 021101 (2006)
- 7. O. Calvo, D.R. Chialvo, Int. J. Bifurcation Chaos 16, 731 (2006)
- P. Balen Zuela, J. Garcia-Ojalvo, E. Manjarrez, L. Martinez, C.R. Mirasso, Biosystems 89, 166 (2007)
- 9. I. Gomes, M.V.D. Vermelho, M.L. Lyra, Phys. Rev. E 85, 056201 (2012)
- S. Rajamani, S. Rajasekar, M.A.F. Sanjuan, Commun. Nonlinear Sci. Numer. Simul. 19, 4003 (2014)
- 11. P.A. Cariani, B. Delgutte, J. Neurophysiol. **76**, 1717 (1996)
- 12. J.F. Schouten, R.J. Ritsma, B.L. Cardozo, J. Acoust. Soc. Am. 34, 1418 (1962)
- 13. C. Pantev, T. Elbert, B. Ross, C. Eulitz, E. Terhardt, Hear. Res. 100, 164 (1996)
- D.W. Jordan, P. Smith, Nonlinear Ordinary Differential Equations (Oxford University Press, Oxford, 2007)

Chapter 10 Parametric Resonance

In a weakly nonlinear oscillator driven by an external periodic force, the response is generally amplified near the natural frequency of the system and the response at all other frequencies far away from the natural frequency is very weak. A different kind of resonance and response of an oscillator occurs when one or more of its parameters vary periodically in time. When the parameter of an oscillator varies with time, then the oscillator is called a *parametric oscillator* or a parametrically driven oscillator. An example is the pendulum whose support oscillates vertically with an angular frequency ω and a forcing amplitude F (Fig. 10.1). The equation of motion for the evolution of the pendulum angle θ with respect to the vertical is given by

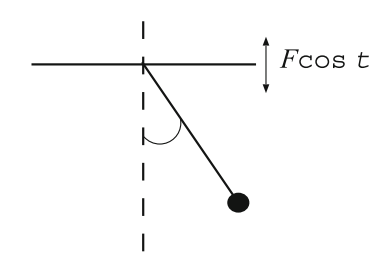
$$\ddot{\theta} + d\dot{\theta} + \omega_0^2 (1 + f \cos \omega t) \sin \theta = 0, \qquad (10.1)$$

where d>0, $\omega_0^2=g/l$, $f=F/\omega_0^2$. Here g, l and d are acceleration of gravity, length of the pendulum and the damping coefficient, respectively. The force $F\cos\omega t$ serves as an energy source. The natural frequency is not a constant now, but varies periodically. In such a case for a certain specific choice of the parameter f, the amplitude of the induced oscillation grows steadily. This phenomenon is termed as parametric resonance [1–8].

Usually, a parametric resonance is not considered in systems driven by an additive external periodic force, but it is considered for systems where one or more coefficients in the equation of motion vary periodically with time. Examples include periodic variation of stiffness, mass, density and environmental change. In a varactor parametric oscillator oscillations occur when the capacitance of the diode is varied periodically. Parametric instability can be realized when a tank with a liquid vibrates vertically. In this case standing waves on the free surface can be observed which is known as *Faraday instability*. The parametric resonance underlies the physics of swings [9] and of the Botafumeiro censer in the Cathedral of Santiago de Compostela in Spain [10]. Neutrino systems can display parametric resonance. In neutrino systems, a periodically varying condition is realizable when a beam of

262 10 Parametric Resonance

Fig. 10.1 A parametrically driven pendulum



oscillating neutrinos passes through a medium with a periodically varying density. The parametric resonance can then occur leading to enhanced oscillations. For example, atmospheric neutrinos traversing the earth passes through an alternatively varying density of layers and thus can show enhanced oscillations [11].

This chapter provides some examples of parametric resonance, the conditions for parametric instability in the linear and certain nonlinear systems, a quantum analogue and various applications of the parametric resonance.

10.1 Examples of Parametric Resonance

Some of the notable examples of parametric resonances [12] are listed below:

- 1. In 1831, Michael Faraday reported the occurrence of ripples at the surface of a liquid when a tank containing a liquid is periodically excited at twice the frequency of the ripples [13]. This is a classic example of parametric resonance, because of the fact that the vertical vibration of the tank is an intrinsic parameter of the system and it depends on time due to the periodic vibration.
- 2. In 1883 Lord Rayleigh observed that when the tuning fork attached to the end of a stretched string, vibrated with frequency f, then the response frequency of the vibrations of the string was f/2 [14].
- 3. In 1908 Andrew Stephenson realized the changing of an unstable equilibrium state of an inverted pendulum through a vertical periodic force at the pin [15].
- 4. A spectacular parametric oscillator, the Botafumeiro [10], has been presented to prayers, pilgrims and the public in the Cathedral of Santiago de Compostela (Galicia, Spain) since the Middle Ages. There, a heavy censer about 1.5 m tall is forced to oscillate with fast increasing amplitudes by a small number of people, up to the top of the Cathedral vault in only about 80 s-while the incense fumes spread over the attendant souls-and passing the equilibrium point at about 70 kmh⁻¹, half a meter above the floor.
- 5. In 1859, Franz Melde noticed the parametric resonance in a taut string [16, 17] by exciting a transverse oscillation of the string by forcing the tension of the string to oscillate with a tuning fork at twice the fundamental frequency of the string.

- 6. When the capacitance of a capacitor in an amplified circuit is modulated, for example by varying the separation between the plates with an external voltage source, then it can amplify an input weak signal voltage of a different frequency applied to the capacitor [18].
- 7. Parametric oscillation is the key phenomenon in optical parametric oscillators (OPOs) which are used in several advanced experiments in nonlinear optics and quantum optics. For example, an OPO is used in the generation of entangled Einstein–Podolsky–Rosen quantum states of two photons employed in quantum information. In an OPO, a noncentro-symmetric nonlinear crystal is placed in a cavity resonator. The crystal is excited to oscillate by a strong pump laser beam focused into the crystal [19]. A second-order nonlinear polarization is induced in the crystal. This leads to the mixing of the pump beam with two outgoing beams from the crystal. These two beams get amplified at the expense of the pump beam energy.
- 8. Suppose a string attached to a bob is passed through a small fixed smooth ring. The other end of the string is held by our hand and let the bob to oscillate. When the bob passes its equilibrium point, pull the thread by a small amount and further extend it to its initial length as the bob reaches the maximum deflection. The result is the fast growing amplitude of the parametric oscillations of the bob [5].
- 9. In the Watt governor with a sinusoidal variation in the engine speed the greatest chance of instability can occur when the excitation frequency in the engine becomes double of the natural frequency of a conical pendulum [20].
- 10. Parametric resonance has been realized in micro- and nano-electromechanical systems [21–23], MEMS/NEMS devices [24–26] and cutting process [27].

10.2 Parametric Instability in a Linear System

Linearisation of Eq. (10.1) gives

$$\ddot{\theta} + d\dot{\theta} + \omega_0^2 (1 + f \cos \omega t)\theta = 0.$$
 (10.2)

When d=0, Eq. (10.2) is the Mathieu equation. Equation (10.2) models many physical systems. In 1868 Emile Mathieu introduced this equation to model the vibrations of an elliptical membrane [28]. This equation is found to describe the dynamics of parametrically driven micro capacitive cantilever [29] and the motion of an ion trapped in a linear rf trap [30]. The Mathieu equation, though linear, is not solvable analytically in terms of standard functions.

264 10 Parametric Resonance

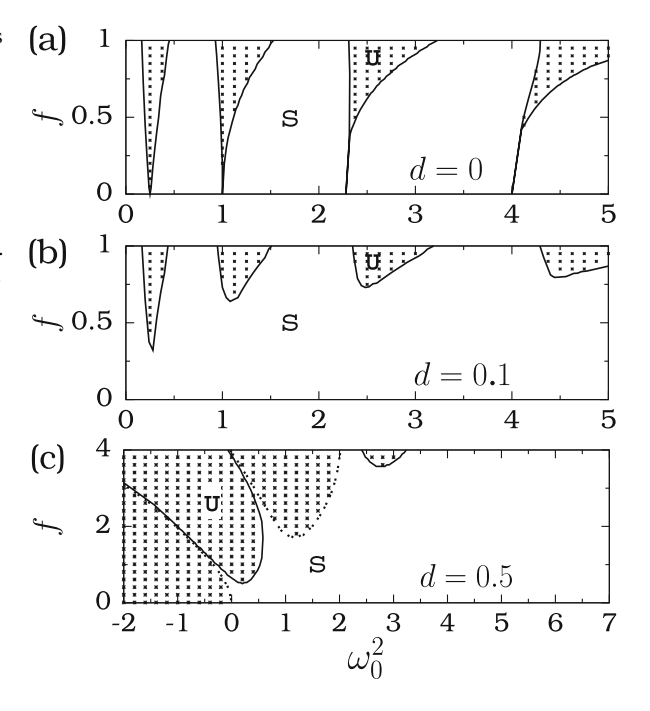
10.2.1 Illustration of Parametric Resonance

Parametric resonance is best explained through Eq. (10.2). Suppose it is desired to know the regions in the (ω_0^2, f) parameter space where the equilibrium point $(\theta, \dot{\theta}) = (0, 0)$ is stable, it is unstable and periodic solutions exist. Figure 10.2 show the numerical result for $\omega = 1$ and for three values of d. In the dotted regions the equilibrium point (0, 0) is unstable and the amplitude of oscillation grows with time. This phenomenon is called *parametric resonance* and it occurs when

$$\omega = \omega_n = 2\omega_0/n \,, \tag{10.3}$$

where n is a positive integer. In the blank regions all the solutions are bounded (quasiperiodic motion for d=0 and for d>0 the solutions in the long time limit approach an equilibrium point). The stable and unstable regions of the equilibrium point are separated by smooth boundaries. On the continuous curve periodic solutions exist. The shape of the resonant tongues change when the damping coefficient d is increased. The area of stable regions (blank regions) increases with increase in the value of d. Figure 10.3a shows the Poincaré map of the system for d=0, f=1/3 and $\omega_0^2=3$. The five orbits in this figure are obtained for five different initial conditions. All the orbits are quasiperiodic and bounded. In Fig. 10.3b for d=0.1, f=1/3 and $\omega_0^2=3$ the trajectory approaches

Fig. 10.2 Resonance tongues of the system (10.2) showing the regions of stable (*blank regions*, marked as 'S') and unstable (*dotted regions*, marked as 'U') solutions for (a) d = 0, (b) d = 0.1 and (c) d = 0.5. On the *curves* stable periodic solutions exist. In the *blank regions*, the fixed point (0,0) is stable while in the *dotted regions* the motion is unbounded. Here $\omega = 1$



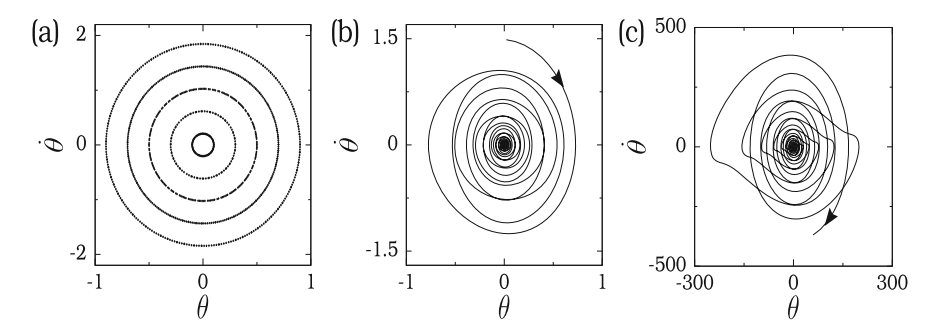


Fig. 10.3 (a) Poincaré map of the parametrically driven linear system (10.2) for d = 0, f = 1/3 and $\omega_0^2 = 3$. (b) An example of a trajectory approaching the equilibrium point (0,0) for d = 0.1, f = 1/3 and $\omega_0^2 = 3$. (c) An unbounded motion for d = 0.1, f = 1 and $\omega_0^2 = 3$

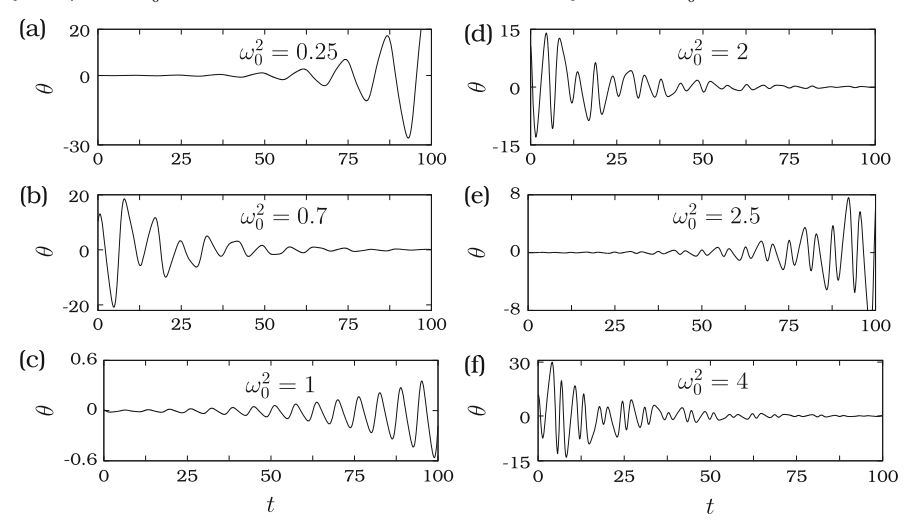


Fig. 10.4 Time series of the system (10.2) with $f=1, \omega=1$ and for (a) $\omega_0^2=0.25$, (b) $\omega_0^2=0.7$, (c) $\omega_0^2=1$, (d) $\omega_0^2=2$, (e) $\omega_0^2=2.5$ and (f) $\omega_0^2=4$

the equilibrium point (0,0) in the long time limit. Figure 10.3c shows an example for amplitude growth.

Consider Fig. 10.2 for f=1 with d=0.1. When ω_0^2 is varied from a small value, the stability of the equilibrium point (0,0) of the system undergoes the transition stable \rightarrow unstable \rightarrow unstable \rightarrow unstable \cdots . In Fig. 10.4 x(t) versus t is shown for several fixed values of ω_0^2 . This figure illustrate the above transition. Figure 10.5 shows both x versus t and x versus \dot{x} with f=0.1, $\omega=1$, d=0 and for two values of ω_0^2 —one in a blank region and another in a dotted region. For $\omega_0^2=1$ (lying in the dotted region of Fig. 10.2) a trajectory started near the equilibrium point oscillates with diverging amplitude as shown in Figs. 10.5a(i), a(ii). In Figs. 10.5b(i), b(ii) for $\omega_0^2=2$ (lying in the blank region of Fig. 10.2) the long time motion of the system is a bounded quasiperiodic orbit and the equilibrium point (0,0) is stable.

266 10 Parametric Resonance

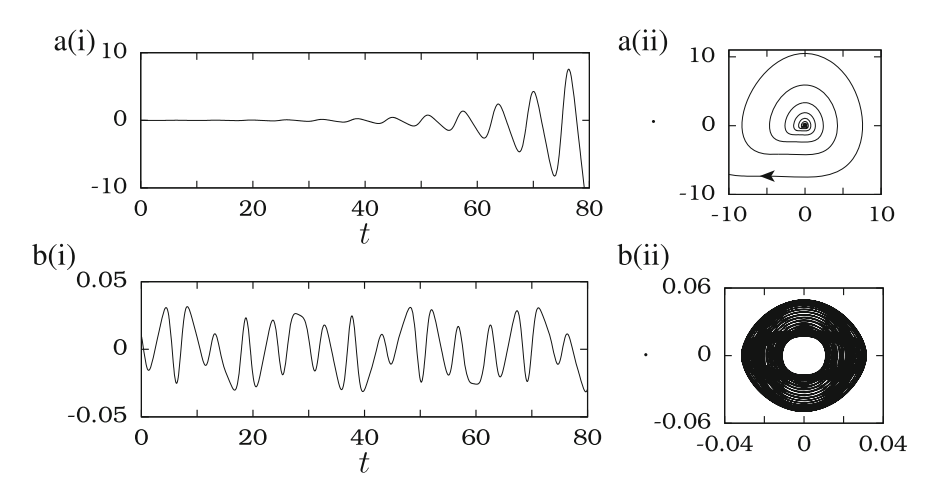


Fig. 10.5 Time series and phase portrait of the system (10.2) for two values of ω_0^2 and for f=0.1, $\omega=1$ and d=0. The values of ω_0^2 are 1 and 2 for the subplots (a) and (b), respectively

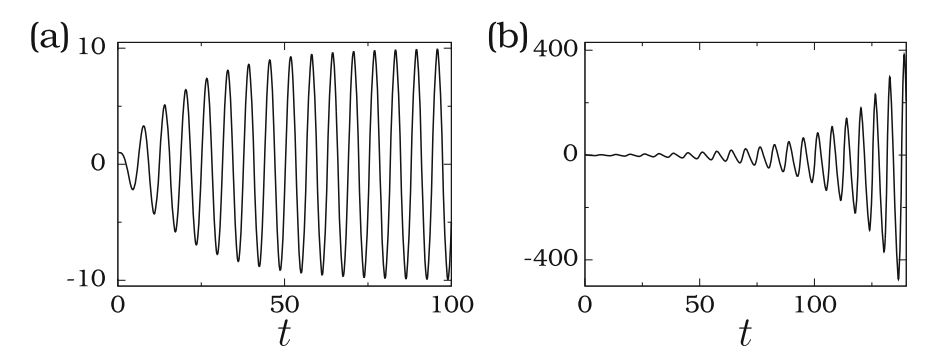


Fig. 10.6 $\theta(t)$ versus t for (a) the linear system (10.4) and (b) the system (10.2). The values of the parameters are d = 0.1, $\omega_0^2 = 1$, f = 1 and $\omega = 1$. Here x(0) = 1 and $\dot{x}(0) = 0$

The causes and characteristics of parametric resonance are significantly different from those of the resonances occurring when the oscillator responds to a periodic force. For example, the strongest parametric oscillations are excited when the cycle of modulation is repeated twice during one period of natural oscillations in the system, that is, when the frequency of parametric modulation is twice the natural frequency of the system. In this case maximum energy transfer to the system occurs. The oscillator phase-locks to the parameter variation and absorbs energy at a rate proportional to the energy already stored in it.

Now, bring out an important difference between parametric resonance and resonance due to an additive external periodic force. Figures 10.6a, b show $\theta(t)$ versus t for the linear system

$$\ddot{\theta} + d\dot{\theta} + \omega_0^2 \theta = f \cos \omega t \tag{10.4}$$

and the system (10.2). In Fig. 10.6a the externally forced resonance causes the state variable θ to grow slowly to a maximum value. In Fig. 10.6b the parametric resonance causes $\theta(t)$ to grow exponentially for the linear system.

10.2.2 Theoretical Treatment

Now we present a theoretical treatment for the analysis of the parametric resonance. First, we consider the system with d=0. Since the dominant parametric resonance occurs if ω is close to $2\omega_0$, one can write $\omega=2\omega_0+\epsilon$ where ϵ is a small resonance determining parameter. Assume the solution of (10.2) in the form

$$\theta = a(t)\cos\left(\omega_0 + \frac{\epsilon}{2}\right)t + b(t)\sin\left(\omega_0 + \frac{\epsilon}{2}\right)t. \tag{10.5}$$

Using (10.5) in (10.2) with $\omega = 2\omega_0 + \epsilon$, after simple algebra, it gives

$$a' = -\frac{1}{4}(f\omega_0 + 2\epsilon)b, \quad b' = -\frac{1}{4}(f\omega_0 - 2\epsilon)a.$$
 (10.6)

The above equation indicates that to get an oscillation of $\theta(t)$, the initial value of a(0) or b(0) must be nonzero, that is, $\theta(0)$ and $\dot{\theta}(0)$ must be nonzero. One can assume the solution of (10.6) as

$$a(t) = a_0 e^{\mu t}, \quad b(t) = b_0 e^{\mu t}.$$
 (10.7)

Then, Eq. (10.6) becomes

$$\begin{pmatrix} \mu & (f\omega_0 + 2\epsilon)/4 \\ (f\omega_0 - 2\epsilon)/4 & \mu \end{pmatrix} \begin{pmatrix} a_0 \\ b_0 \end{pmatrix} = 0.$$
 (10.8)

For a nontrivial solution, the condition is that the determinant of the coefficient matrix in the above equation must be zero. That is,

$$\mu^2 - \frac{1}{16} \left(f^2 \omega_0^2 - 4\epsilon^2 \right) = 0 \tag{10.9}$$

which gives

$$\mu = \pm \frac{1}{4} \sqrt{f^2 \omega_0^2 - 4\epsilon^2} \,. \tag{10.10}$$

In Eq. (10.7) the amplitude of oscillation grows with time if $\mu > 0$ leading to parametric instability. This happens for values in the range $-f\omega_0 < 2\epsilon < f\omega_0$.

268 10 Parametric Resonance

Outside this instability frequency window, one finds that

$$\mu = i\Omega, \quad \Omega = \frac{1}{4}\sqrt{|f^2\omega_0^2 - 4\epsilon^2|}$$
 (10.11)

and the solution has the terms

$$\sin\left[\left(\omega_0 + \frac{\epsilon}{2} - \Omega\right)t\right] \text{ and } \cos\left[\left(\omega_0 + \frac{\epsilon}{2} - \Omega\right)t\right].$$
 (10.12)

The frequency of oscillation is neither ω_0 nor $\omega/2$. In the limit $f \to 0$ the system (10.2) oscillates with its natural frequency ω_0 .

When $d \neq 0$ in Eq. (10.2)

$$a(t) = a_0 e^{(\mu - d)t}, \quad b(t) = b_0 e^{(\mu - d)t}.$$
 (10.13)

Then, the condition for the parametric instability is

$$\mu = \frac{1}{4} \sqrt{f^2 \omega_0^2 - 4\epsilon^2} - d > 0.$$
 (10.14)

The parametric resonance window is

$$\epsilon^2 < \frac{1}{4} f^2 \omega_0^2 - d^2 \ . \tag{10.15}$$

The numerical simulation supports the above theoretical prediction.

10.2.3 Analog Simulation

Let us show the occurrence of the parametric resonance in the Mathieu equation in an analog circuit simulation. Figure 10.7 depicts an analog circuit of (10.2). For this circuit the evolution equation for the variable V is

$$R^{2}C^{2}\frac{d^{2}V}{dt^{2}} + \frac{R^{2}C}{R1}\frac{dV}{dt} + \frac{R}{R2}(1 + F\sin\omega t)V = 0.$$
 (10.16)

With the change of variables t = RCt', $\omega = RC\omega'$, F = f, $V = \theta$ and dropping the prime in t' and ω' this equation reduces to Eq. (10.2) with d = R/R1 and $\omega_0^2 = R/R2$. Fix the parameters in the circuit as $R = 10 \,\mathrm{k}\Omega$, $C = 100 \,\mathrm{nF}$, $R1 = 100 \,\mathrm{k}\Omega$, $F = 1 \,\mathrm{V}$ and $\omega = 159 \,\mathrm{Hz}$. In this case d = 0.1. ω_0^2 can be varied by varying the resistance of the resistor R2. The experimental time series

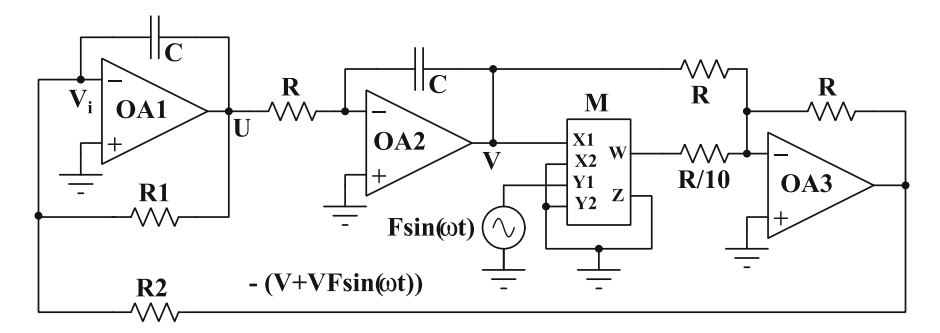


Fig. 10.7 An analog circuit of the damped Mathieu equation. In this circuit 'M' is a multiplier chip (AD633JN)

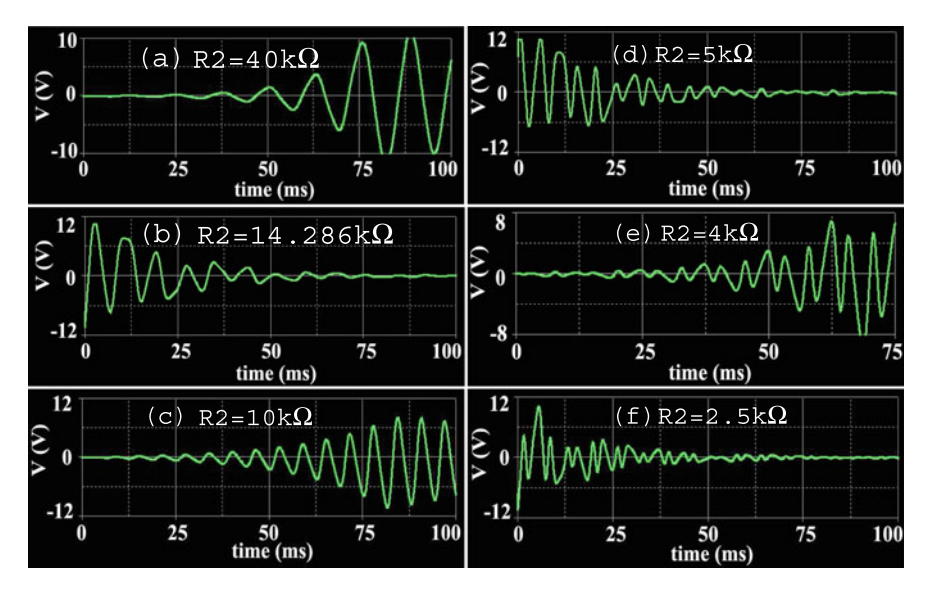


Fig. 10.8 Analog circuit simulation time series of the system (10.2) for several values of R2 in the circuit shown in Fig. 10.7

obtained for six different values of R2 corresponding to the values of ω_0^2 used in Figs. 10.4a–f are presented in Figs. 10.8a–f, respectively. The qualitative features of the time series shown in Figs. 10.4 and 10.8 are similar. The resonance behaviour of the system (10.2) for d=0 is also realized in the electronic circuit simulation. The circuit shown in Fig. 10.7 without the resistor R1 corresponds to Eq. (10.1) with d=0. The experimental simulation plots corresponding to the parametric choices used in Fig. 10.5 are shown in Fig. 10.9.

270 10 Parametric Resonance

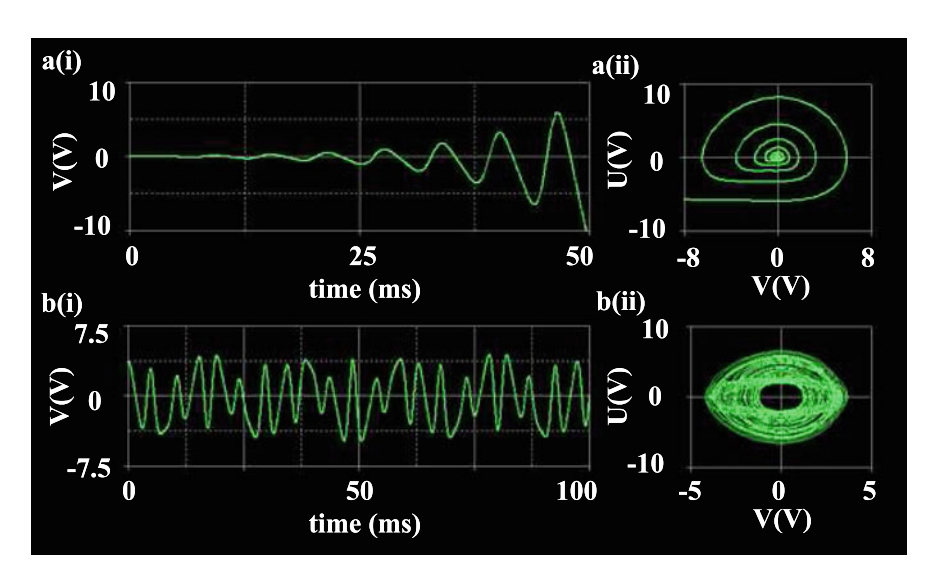


Fig. 10.9 Analog circuit simulation of time series and phase portrait of the system (10.2) for two values of R2 in the circuit shown in Fig. 10.7 without the resistor R1. The values of R2 for the subplots **a** and **b** are 10 and 5 kΩ, respectively

10.3 Parametrically Driven Pendulum

For a certain range of values of the parameters, the pendulum system (10.1) exhibits a parametric instability in which the amplitude of the oscillation increases with time. Figure 10.10a shows the resonance tongues for d=0. The area of the stable regions increases with increase in d as shown in Figs. 10.10b and c.

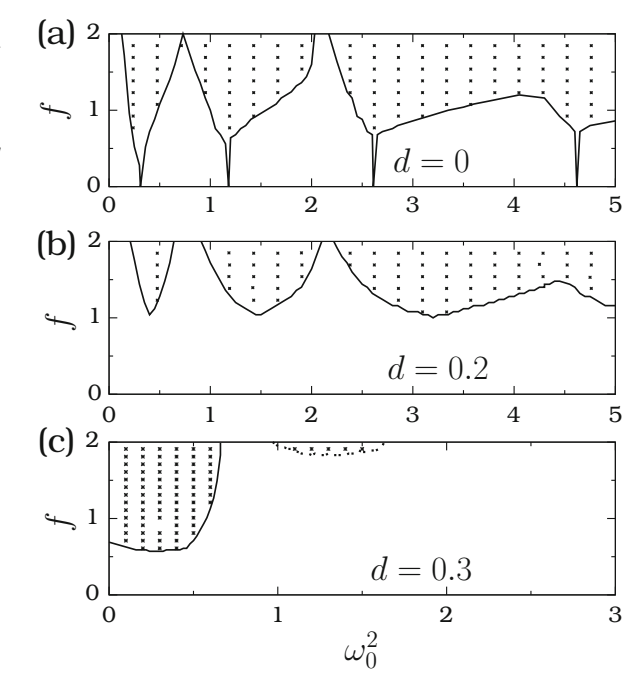
In the linear system (10.2) with d=0, when $f\to 0$ parametric resonance takes place for $\omega/\omega_0=2/n$ where n is an integer [1]. n=1, that is, $\omega=2\omega_0$ corresponds to the most unstable oscillation. Now, we analyse this case theoretically employing the multiple-time scales method [31]. For convenience, we rewrite Eq. (10.1) as

$$\ddot{\theta} + 2\lambda\dot{\theta} + \left[1 + 4\mu\sin\left(\frac{\omega}{\omega_0}\tau\right)\right]\sin\theta = 0, \qquad (10.17)$$

where $\tau = \omega_0 t$, $\lambda = d/(2\omega_0)$, $\mu = f/(4\omega_0^2)$ and define $\nu = \frac{1}{2} \left(\frac{4\omega_0^2}{\omega} - 1 \right)$ as the detuning parameter. For small oscillations the equation becomes

$$\ddot{\theta} + 2\lambda\dot{\theta} + \left[1 + 4\mu\sin\left(\frac{\omega}{\omega_0}\tau\right)\right]\left(\theta - \frac{1}{6}\theta^3\right) = 0.$$
 (10.18)

Fig. 10.10 Resonance tongues of the parametrically driven pendulum system (10.1) showing the regions of stable (blank regions) and unstable (dotted regions) solutions. On the curves, stable periodic solutions exist. In the blank regions, the fixed point (0,0) is stable while in the dotted regions the motion is unbounded. Here $\omega = 1$



The parametric excitation acts on both the linear and cubic terms. We write

$$\theta(\tau) = \sqrt{\epsilon} \,\theta_0(\tau, T) + \epsilon \,\theta_1(\tau, T) + \epsilon^{3/2} \,\theta_2(\tau, T) + \cdots, \tag{10.19}$$

where $T = \epsilon \tau$, substitute it in Eq. (10.18) and then collect terms containing the same powers of ϵ .

The zeroth-order equation is $\theta_0'' + \theta_0 = 0$, where the prime denotes differentiation with respect to τ . The solution of this equation is

$$\theta_0 = X(T) e^{i\tau} + C.C,$$
 (10.20)

where C.C denotes complex conjugate of the preceding term. From the terms containing $\sqrt{\epsilon}$ one gets $\theta_1'' + \theta_1 = 0$ whose solution is

$$\theta_1 = Y(T) e^{i\tau} + C.C.$$
 (10.21)

Next, the equation obtained from the terms containing ϵ is

$$\theta_2'' + \theta_2 = G\left[\theta_0, \lambda \theta_0', \mu \theta_0 \sin\left(\frac{\omega}{\omega_0}\tau\right)\right].$$
 (10.22)

G of the above equation should not contain terms proportional to $e^{i\tau}$ in order to avoid a secular growth of θ_2 . Using Eq. (10.20) and $\omega/\omega_0 = 2 - 4\nu$, this condition gives [31]

$$\frac{dX}{dT} = (-\lambda + i\nu)X + \mu \bar{X}e^{-4i\nu T} - \frac{i}{4}|X|^2 X, \qquad (10.23)$$

where \bar{X} is the complex conjugate of X. Writing $X = Ae^{-2i\nu T}$, the above equation becomes

$$\frac{dA}{dT} = (-\lambda + i\nu)A + \mu \bar{A} - \frac{i}{4}|A|^2 A.$$
 (10.24)

Consider both the linear and nonlinear stability of the equilibrium point $\theta = 0$. Dropping the nonlinear terms in Eq. (10.24) and defining $A = A_R + iA_I$ lead to the equations

$$A'_{R} = -\lambda A_{R} - \nu A_{I} + \mu A_{R} , \quad A'_{I} = -\lambda A_{I} + \nu A_{R} - \mu A_{I} .$$
 (10.25)

For the equilibrium point $(A_R, A_I) = (0, 0)$, the stability determining eigenvalues Λ_{\pm} are

$$\Lambda_{\pm} = -\lambda \pm \sqrt{\lambda^2 - (\lambda^2 + \nu^2 - \mu^2)}$$
 (10.26)

For the equilibrium point to be stable, the condition is $\lambda^2 + \nu^2 - \mu^2 > 0$, that is, $\mu < \mu_c$ where $\mu_c = \sqrt{\lambda^2 + \nu^2}$.

For $\mu > \mu_c$, write $A = Re^{i\phi}$. Substitution of this in Eq. (10.24) (with the nonlinear term) gives

$$R' = -\lambda R + \mu R \cos 2\phi, \quad \phi' = \nu - \frac{R^2}{4} - \mu \sin 2\phi.$$
 (10.27)

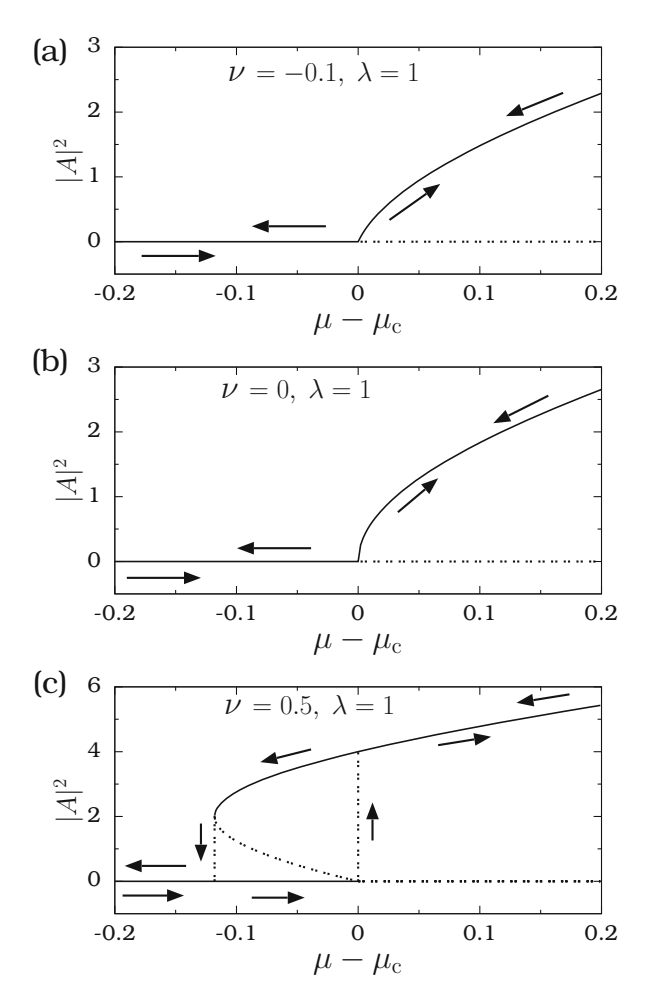
The steady state amplitude |A|=R is obtained by setting $R'=\phi'=0$. Then, solving the resultant equations gives

$$|A|_0^2 = R_0^2 = 0, \quad |A|_{\pm}^2 = 4(\nu \pm \sqrt{\mu^2 - \lambda^2}).$$
 (10.28)

The following are the key results:

- For $\nu<0$, $|A|^2=0$ is the only stable solution for $\mu<\mu_{\rm c}=\sqrt{\lambda^2+\nu^2}$. For $\mu>\mu_{\rm c}$, $|A|_+^2$ is stable while $|A|_0^2$ is unstable. Figure 10.11a shows $\mu-\mu_{\rm c}$ versus $|A|^2$ for $\nu=-0.1$ and $\lambda=1$.
- For $\nu=0$, $|A|_0^2$ is stable for $\mu<\mu_c=\lambda$. For $\mu>\mu_c$, $|A|_0^2$ is unstable, while $|A|_+^2$ is stable (Fig. 10.11b).
- When $\nu > 0$, $|A|_0^2$ is the only solution for $\mu < \lambda$ and is stable. For $\lambda < \mu < \mu_c$ there are three solutions for $|A|^2$ and are given by Eq. (10.28). The solutions

Fig. 10.11 Plot of $\mu - \mu_c$ versus $|A|^2$ for the pendulum system (10.17). The continuous curve and the dashed curve represent stable and unstable branches of solutions, respectively. The arrows indicate the evolution of $|A|^2$ when μ is increased and decreased



 $|A|_0^2$ and $|A|_+^2$ are stable, while $|A|_-^2$ is unstable. For $\mu > \mu_c$ there are only two solutions. $|A|_0^2$ is unstable and $|A|_+^2$ is stable. Figure 10.11c shows $\mu - \mu_c$ versus $|A|^2$ for $\lambda = 1$ and $\nu = 0.5$. When μ increases from a small value jump phenomenon occurs at $\mu = \mu_c$. When μ is decreased from a value greater than μ_c , a jump in the response amplitude occurs at $\mu = \lambda$.

For the system (10.2) driven by noise, a theoretical procedure based on Green's functions and averaging techniques has been developed for the calculation of *SNR* [32]. The occurrence of parametric resonance in Duffing oscillator was investigated in [33].

For more details on parametric resonance and instability of the pendulum system one may refer to the [5, 6, 34–37].

274 10 Parametric Resonance

10.3.1 Effective Parametric Resonance

In the linear system (10.2) and in the nonlinear system (10.1), as shown in Figs. 10.2 and 10.10, respectively, periodic orbits in the (ω_0^2, f) parameter space exist only for the parameter values represented by the continuous curve. It is possible to realize stable periodic oscillations induced by a parametric perturbation with high frequency for a wide range of parameters values. As an illustrative example, we can consider the parametrically driven Duffing oscillator system

$$\ddot{x} + d\dot{x} + \beta x^3 + fx \sin \omega t = 0 \tag{10.29}$$

with $\omega \gg d$. Assume the solution of (10.29) as

$$x(t) = z(t) + \frac{f}{\omega^2} z(t) \sin \omega t , \qquad (10.30)$$

where z(t) is a slow motion and the last term represents the small fast motion [38]. To determine z(t) substitute (10.30) in (10.29) and obtain

$$\ddot{z} + \dot{z} \left(d - \frac{2f}{\omega} \cos \omega t + \frac{df}{\omega^2} \sin \omega t \right) + \dot{z} \left(\frac{f}{\omega^2} \sin \omega t \right)$$

$$+ z \left(\frac{f^2}{2\omega^2} - \frac{f^2}{2\omega^2} \cos 2\omega t + \frac{df}{\omega} \cos \omega t \right)$$

$$+ z^3 \beta \left(1 + \frac{f}{\omega^2} \sin \omega t \right)^3 = 0.$$

$$(10.31)$$

For $\omega \gg 1$ and $f/\omega^2 \ll 1$ averaging over a period $T=2\pi/\omega$ gives

$$\ddot{z} + d\dot{z} + \frac{f^2}{2\omega^2}z + \beta z^3 = 0.$$
 (10.32)

When $f/\omega^2 < 1$ but not small, then Eq. (10.31) becomes

$$\ddot{z} + \dot{z}\left(d + \frac{2f}{\omega}\cos\omega t\right) + \frac{f^2}{2\omega^2}z + \beta z^3 = 0.$$
 (10.33)

The model Eq. (10.33) can be regarded as an oscillator with an induced natural frequency $\omega_1 = f/(\sqrt{2}\omega)$.

In Eq. (10.33) the term $(2f/\omega)\dot{z}\cos\omega t$ can be neglected when $f\ll\omega^2$. In this case the effective force is $(f^2/(2\omega^2))z$. The key result is that the system (10.29) with a high frequency driving force is equivalent to a parametrically driven system with the natural frequency ω_I . For large ω , ω_I increases with f. However, the amplitudes of the terms neglected in the above analysis grow. The combined effect is that as ω_I

approaches $\omega/2$, then the dissipative and forcing terms get balanced and the system can resonate by parametrically amplifying itself. This phenomenon is termed as *effective parametric resonance* [38] and it gives rise to attractive periodic solutions.

Carrying out a modal expansion for the system (10.33) by retaining the terms up to order f/ω , the stability curve for the equilibrium point $(x, \dot{x}) = (0, 0)$ is obtained as [38]

$$\left(\frac{f}{2\omega}\right)^2 - \left(\frac{d}{2}\right)^2 - \left(\frac{\omega}{2} - \frac{f}{\omega\sqrt{2}}\right)^2 = 0. \tag{10.34}$$

The equilibrium point (0,0) is stable for (note that f is assumed to be $\ll \omega^2$)

$$f < f_{\rm c} = \sqrt{2}\,\omega^2 - \omega\sqrt{\omega^2 - d^2}$$
 (10.35)

Figure 10.12a presents the plot of f_c versus ω for d=0.2 and $\beta=10$. For $f\geq f_c$ the equilibrium point is unstable and the trajectories starting near the origin end up on a stable limit cycle attractor. For $\omega=10$, the theoretical value of f_c is 41.44. In Fig. 10.12b, for f=40, the trajectory started with the initial condition x(0)=0.1 and $\dot{x}(0)=0$ exhibits a damped oscillation and is attracted to the equilibrium point. For f=41 (Fig. 10.12c) the trajectory after a transient evolution becomes a limit cycle orbit. In Fig. 10.12a the solid circles represent the numerically computed f_c for several fixed values of ω . The theoretical prediction is in good agreement with the numerical simulation.

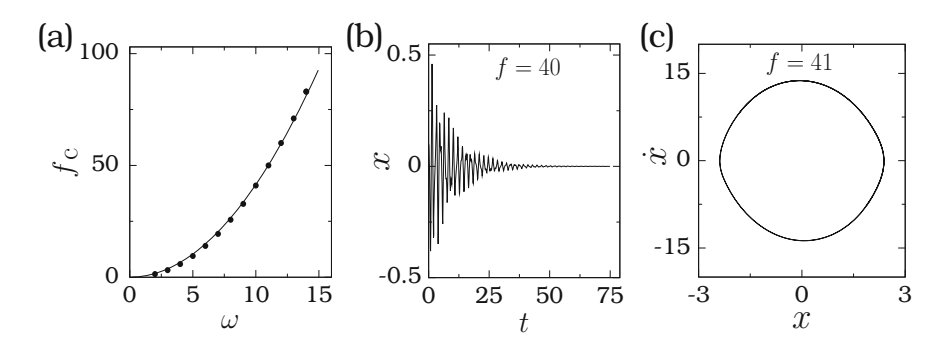


Fig. 10.12 (a) Plot of f_c as function of ω of the system (10.29) for d=0.2 and $\beta=10$. The *continuous curve* is the theoretically predicted value of f below which the equilibrium point (0,0) is stable. The *solid circles* are the numerically computed values of f_c . (b) x(t) versus t for f=40 and $\omega=1$. (c) Phase portrait of the system for f=41 and $\omega=1$

276 10 Parametric Resonance

10.4 The Quasiperiodic Mathieu Equation

Consider the equation

$$\ddot{x} + (\omega_0^2 + \epsilon \cos \omega t + \epsilon \mu \cos(\omega + \epsilon \Delta)t)x = 0.$$
 (10.36)

Parametric resonance in Eq. (10.36) was studied in [39, 40]. To identify the regions in the (ω_0^2, Δ) parameter space where stable bounded and unstable diverging solutions exist, the region $\omega_0^2 \in [-0.1, 0.4]$ and $\Delta \in [-10, 5]$ is divided into 300×500 grid points. For each grid point, Eq. (10.36) is integrated using the fourth-order Runge–Kutta method with step size $(2\pi/\omega_1)/500$ with the initial condition x(0) = 1 and $\dot{x}(0) = 0$. If |x(t)| < 20, for t < 100T where $T = 2\pi/\omega$, then the solution is assumed to be bounded solution otherwise unbounded. The set of values of (ω_0^2, Δ) for which bounded solutions exist are collected.

Figure 10.13a presents the stability charts for $\epsilon=0.1,~\mu=1$ and $\omega=1$ in (ω_0^2,Δ) parameter space. In the black regions the solutions are bounded. Figures 10.13b–d display the fine resolution of stability regions. The fine structures in the subplots clearly show the intricate pattern of stable and unstable regions in the parameter space. Figure 10.14a presents x versus \dot{x} for two values of ω_0^2 with $\Delta=3$. For $\omega_0^2=0.25$ (corresponding to the unstable region) the state variables x and \dot{x} diverge. In Fig. 10.14b where $\omega_0^2=0.3$ (chosen in the black region of Fig. 10.13a) the orbit is bounded. In [39] different methods for computing boundaries of regions of stable and unstable solutions (transition curves) are described.

It is possible to determine the analytical expressions for the transition curves, that is, boundaries between stable and unstable solutions in the (ω_0^2, Δ) parameter space through an approximation analysis [40].

Introduction of the two times scales $\xi = t$ and $\eta = \epsilon t$ transforms Eq. (10.36) into

$$x_{\xi\xi} + 2\epsilon x_{\xi\eta} + \epsilon^2 x_{\eta\eta} + \left[\omega_0^2 + \epsilon \cos \omega \xi + \epsilon \xi \cos(\omega \xi + \Delta \eta)\right] x = 0 ,$$
(10.37a)

where

$$x_{\xi\xi} = \frac{\partial^2 x}{\partial \xi^2}, \quad x_{\eta\eta} = \frac{\partial^2 x}{\partial \eta^2}, \quad x_{\xi\eta} = \frac{\partial^2 x}{\partial \xi \partial \eta}.$$
 (10.37b)

Substitution of the power series

$$x(\xi, \eta, \epsilon) = x_0(\xi, \eta) + \epsilon x_1(\xi, \eta) + \cdots, \qquad (10.38a)$$

$$\omega_0^2 = \frac{1}{4} + \epsilon \omega_1 + \dots \tag{10.38b}$$

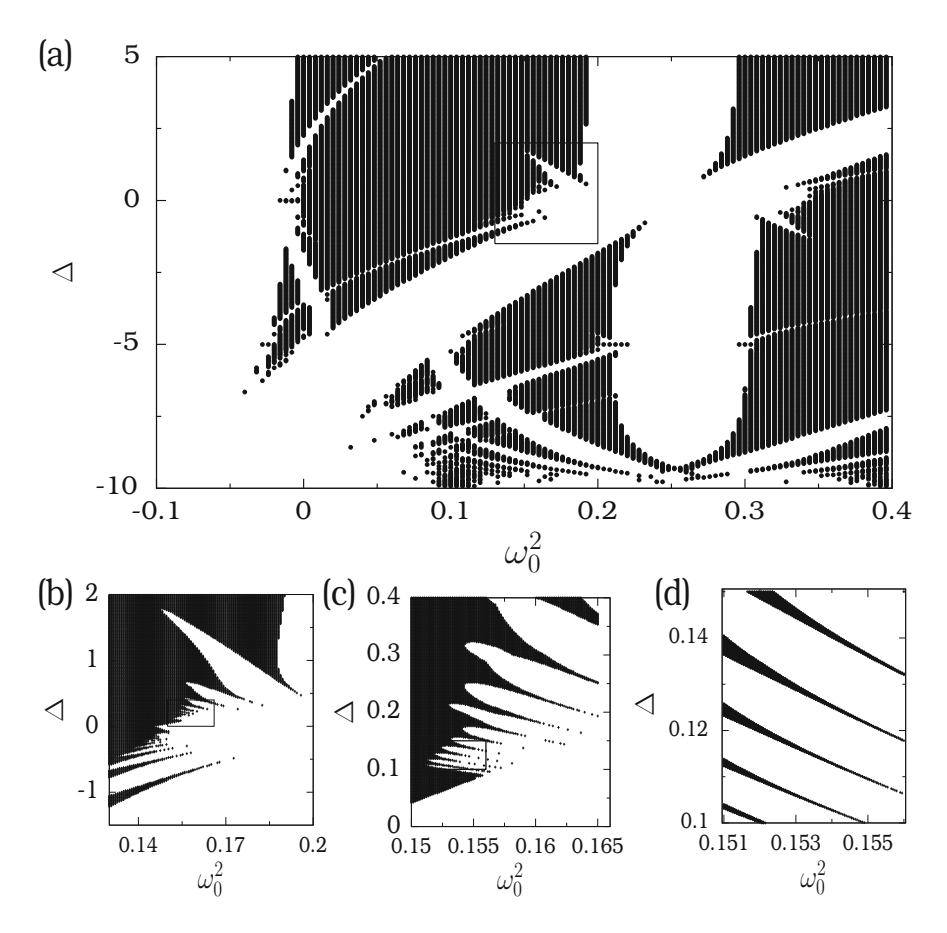


Fig. 10.13 Regions of stable solutions (*black region*) and unstable solutions (*white region*) for Eq. (10.36) with $\epsilon=0.1, \mu=1$ and $\omega=1$. (**b-d**) Magnification of a small rectangular region in the previous subplots

in Eq. (10.37) gives

$$x_{0\xi\xi} + \frac{1}{4}x_0 = 0 , (10.39a)$$

$$x_{1\xi\xi} + \frac{1}{4}x_1 = -2x_{0\xi\eta} - \omega_1 x_0 - x_0 \cos \xi - \mu x_0 \cos(\xi + \Delta \eta) . \quad (10.39b)$$

Solution of (10.39a) is

$$x_0 = R(\eta) \cos\left(\frac{\xi}{2} - \theta(\eta)\right) . \tag{10.40}$$

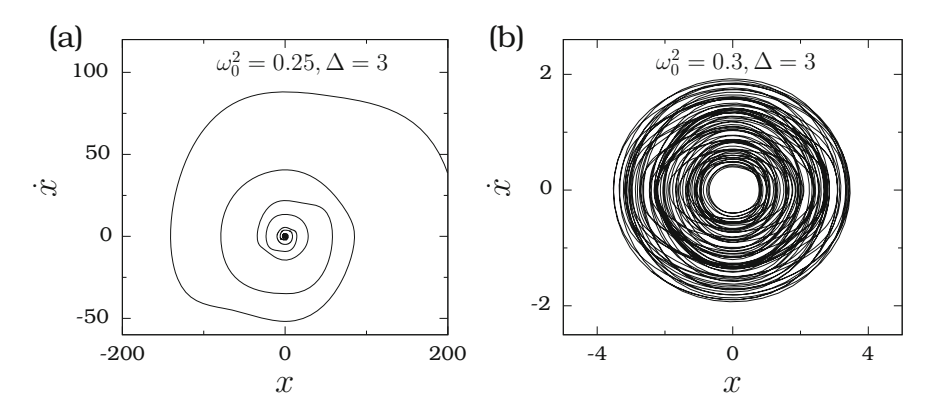


Fig. 10.14 Phase portrait of the system (10.36) for $\epsilon=0.1,\,\mu=1,\,\omega=1$ and $\Delta=3$ and (a) $\omega_0^2=0.25$ (in an unstable region) and (b) $\omega_0^2=0.3$ (in a stable region)

To determine R and θ , we substitute (10.40) in (10.39b). Then, we replace

$$\cos\left(\frac{\xi}{2} - \theta\right)\cos\xi$$
 by $\cos 2\theta\cos 3\left(\frac{\xi}{2} - \theta\right) - \sin 2\theta\sin 3\left(\frac{\xi}{2} - \theta\right)$ (10.41a)

and

$$\cos\left(\frac{\xi}{2} - \theta\right)\cos\left(\xi + \Delta\eta\right) \text{ by } \cos\left(2\theta + \Delta\eta\right)\cos 3\left(\frac{\xi}{2} - \theta\right)$$
$$-\sin\left(2\theta + \Delta\eta\right)\sin 3\left(\frac{\xi}{2} - \theta\right). \tag{10.41b}$$

After some algebra the removal of secular terms leads to the equations

$$\frac{\mathrm{d}R}{\mathrm{d}\eta} = -\frac{R}{2} \left[\sin 2\theta + \mu \sin(2\theta + \Delta\eta) \right] , \qquad (10.42a)$$

$$\frac{\mathrm{d}\theta}{\mathrm{d}\eta} = -\omega_1 - \frac{1}{2} \left[\cos 2\theta + \mu \cos(2\theta + \Delta \eta) \right] . \tag{10.42b}$$

The solution of (10.42a) is written as

$$R(\eta) = R(0)e^{-(1/2)\int (\sin 2\theta + \mu \sin(2\theta + \Delta \eta))d\eta}.$$
 (10.43)

It has been pointed out in [40] that $R(\eta)$ diverge if θ is periodic because the integral in Eq. (10.43), in general, does not vanish if $\theta(\eta)$ is periodic. When $\theta(\eta)$

(10.47b)

is nonperiodic, then the torus flow of θ will be ergodic so that the integral in (10.43) becomes zero implying boundedness of $R(\eta)$. This property can also be used to identify stable and unstable regions in the parameter space.

Next, the change of variables $A = R \cos \theta$, $B = R \sin \theta$ and $\tau = \Delta \eta$ lead to the equations

$$\Delta \dot{A} = \left(\omega_1 - \frac{1}{2}\right) B - \frac{\mu}{2} A \sin \tau - \frac{\mu}{2} B \cos \tau , \qquad (10.44a)$$

$$\Delta \dot{B} = -\left(\omega_1 + \frac{1}{2}\right)A + \frac{\mu}{2}B\sin\tau - \frac{\mu}{2}B\cos\tau , \qquad (10.44b)$$

where the over dot refers to differentiation with respect to τ .

Differentiating (10.44a) with respect to τ and then eliminating B and \dot{B} using (10.44), finally leads to the equation

$$\ddot{A} + f_1(\tau)\dot{A} + f_2(\tau)A = 0, \qquad (10.45a)$$

where

$$f_1(\tau) = O(\mu), \ f_2(\tau) = \frac{1}{\Delta^2} \left(\omega_1^2 - \frac{1}{4}\right) + O(\mu)$$
 (10.45b)

and f_1 and f_2 are 2π periodic in τ .

One can assume the solution of (10.45) as

$$A = \sum_{n=0}^{\infty} c_n \cos \frac{n\tau}{2} + d_n \sin \frac{n\tau}{2} . \tag{10.46}$$

The software MACSYMA [40] was used to compute c_n , d_n and the condition for nontrivial solutions. The expressions obtained for the first two transition curves are

$$\Delta = (4\omega_1^2 - 1)^{1/2} \pm \frac{\mu \left[2\omega_1 \left(4\omega_1^2 - 1 \right)^{1/2} + 4\omega_1^2 - 1 \right]}{2 \left(4\omega_1^2 - 1 \right)}$$

$$- \frac{\mu^2 \left[\left(8\omega_1^2 - 1 \right) \left(4\omega_1^2 - 1 \right)^{1/2} - 16\omega_1^3 + 4\omega_1 \right]}{16 \left(16\omega_1^4 - 8\omega_1^2 + 1 \right)} + \cdots, \qquad (10.47a)$$

$$\Delta = \frac{1}{2} \left(4\omega_1^2 - 1 \right) - \frac{\mu^2 \left[\left(4\omega_1 + 3 \right) \left(4\omega_1^2 - 1 \right)^{1/2} + 16\omega_1^2 - 5 \right]}{12 \left(4\omega_1^2 - 1 \right)^{3/2}} + \cdots,$$

respectively.

280 10 Parametric Resonance

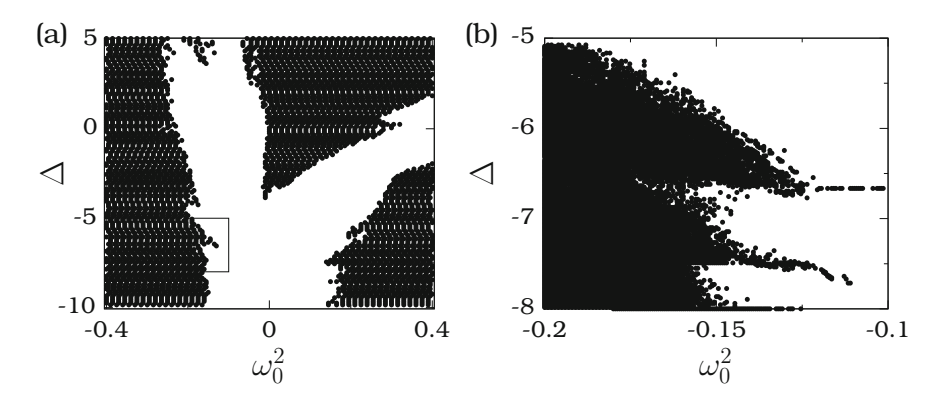


Fig. 10.15 Stability chart of the nonlinear system (10.48) for $\epsilon = 0.1$, $\mu = 2$ and $\omega = 1$

A complex stability chart occurs for nonlinear systems with quasiperiodic parametric perturbation. For example, we can consider the nonlinear oscillator

$$\ddot{x} + (\omega_0^2 + \epsilon \cos \omega t + \epsilon \mu \cos(\omega + \epsilon \Delta)t) (x - x^3/3) = 0.$$
 (10.48)

Figure 10.15 presents the stability chart in the ω_0^2 and Δ plane $\epsilon=0.1$, $\mu=2$ and $\omega=1$. Though Fig. 10.15 is less complex than Fig. 10.13 of the Mathieu equation, Fig. 10.15b clearly indicates the fine structure in the stability chart.

10.5 Quantum Parametric Resonance in a Two-Coupled Systems

In this section the focus is to show the occurrence of quantum parametric resonance in a two-coupled systems [41]. Though there is no classical analogous of quantum entanglement, the investigation of entanglement dynamics in a coupled system of driven harmonic oscillators by Bastidas et al. [41] indicates certain signatures of classical parametric resonance.

Consider a system of coupled harmonic oscillators with a time-dependent coupling coefficient. The Hamiltonian of this system is

$$\hat{H} = \frac{1}{2} \left(\hat{p}_{+}^{2} + \hat{p}_{-}^{2} \right) + \frac{1}{2} \omega^{2} \left(\hat{q}_{+}^{2} + \hat{q}_{-}^{2} \right) + \gamma(t) \hat{q}_{+} \hat{q}_{-} , \qquad (10.49)$$

where $\gamma(t) = g + \Delta g \cos \Omega t$. The Hamiltonian of the uncoupled system can be expressed in terms of the so-called *ladder operators* \hat{a} and \hat{a}^{\dagger} .

The annihilation operator of the uncoupled system with $\hat{H}=\hat{p}_+^2/2+(\omega^2(t)/2)\hat{x}_+^2$ is given by

$$\hat{a}_{+}(t) = -\dot{B}_{+}(t)\hat{q}_{+} + B_{+}(t)\hat{p}_{+}, \qquad (10.50)$$

where $B_{+}(t)$ is the solution of the classical equation of motion

$$\ddot{B}_{+} + \omega^{2}(t)B_{+} = 0 \tag{10.51}$$

with the Wronskian condition

$$\dot{B}_{+}B_{+}^{*} - B_{+}\dot{B}_{+}^{*} = i. {(10.52)}$$

 \hat{a} and \hat{a}^{\dagger} satisfy the condition

$$\frac{\mathrm{d}\hat{A}}{\mathrm{d}t} = \frac{\partial\hat{A}}{\partial t} + \mathrm{i}\left[\hat{H},\hat{A}\right] = 0 \;, \quad \hat{A} = \hat{a},\hat{a}^{\dagger} \;. \tag{10.53}$$

With $\hat{n}(t) = \hat{a}_{+}^{\dagger}(t)\hat{a}_{+}(t)$ one has

$$\hat{n}|n,t\rangle = n|n,t\rangle, \quad |n,t\rangle = \frac{(a_+^{\dagger})^n}{\sqrt{n!}}|0,t\rangle,$$
 (10.54)

where $|0,t\rangle$ denotes the ground state. Note that the dynamics of the system is completely determined through the solution of Eq. (10.51).

Using a unitary transformation \hat{U} the Hamiltonian $\hat{H}(t)$ of the coupled system can be mapped to the Hamiltonian $\hat{H}_{R}(t)$ of the two uncoupled systems. That is,

$$\hat{H}_{R}(t) = \hat{U}^{\dagger} \hat{H}(t) \hat{U}, \tag{10.55a}$$

$$\hat{H}_{R}(t) = \frac{1}{2} \left(p_{+}^{2} + \epsilon_{+}^{2} \hat{q}_{+}^{2} \right) + \frac{1}{2} \left(p_{-}^{2} + \epsilon_{-}^{2} \hat{q}_{-}^{2} \right), \tag{10.55b}$$

$$|\psi, t\rangle_{\mathbf{R}} = \hat{U}|\psi, t\rangle, \tag{10.55c}$$

$$\epsilon_{+}^{2} = \omega^{2} \pm 2\omega |\gamma(t)|. \tag{10.55d}$$

One can write the quantum state of the system with $\hat{H}_{R}(t)$ as

$$|\psi_{n_{-},n_{+}},t\rangle_{R} = \exp\{i\left[\theta_{n_{-}}(t) + \theta_{n+1}(t)\right]\} |n_{-},t\rangle_{R}|n_{+},t\rangle_{R}.$$
 (10.56)

In (10.56) $|n_{\pm},t\rangle_{\rm R}$ are the quantum states with energy $\epsilon_{\pm}(t)$ and

$$\theta_{n_{\pm}}(t) = \int_0^t \langle n_{\pm}, t | i \frac{\partial}{\partial t} - \hat{H}_{R} | n_{\pm}, t \rangle dt. \qquad (10.57)$$

282 10 Parametric Resonance

To determine the wave functions corresponding to $|n_{\mp}, t\rangle_{\mathbb{R}}$ start with

$$\hat{a}_{\mp}|0,0,t\rangle_{R} = 0, \quad \hat{a}_{\mp}(t) = -\dot{B}_{\mp}(t)\hat{q}_{\mp} + B_{\mp}(t)\hat{p}_{\mp},$$
 (10.58)

where \hat{a}_{\mp} corresponds to the oscillator mode with energy $\epsilon_{\mp}(t)$ and $B_{\mp}(t)$ satisfy the Mathieu equation [refer Eq. (10.51)]

$$\ddot{B}_{\mp}(t) + [\epsilon_{\mp}(t)]^2 B_{\mp}(t) = 0 \tag{10.59}$$

and B_{+} and B_{-} are subjected to the condition (10.52) which requires [41]

$$B_{\mp}(t_0) = \frac{\mathrm{i}}{\sqrt{2\epsilon_{\mp}(t_0)}}, \quad \dot{B}_{\mp}(t_0) = -\sqrt{\frac{\epsilon_{\mp}(t_0)}{2}}.$$
 (10.60)

Once B_{\mp} are determined, then the solution (wave function) of (10.58), that is, the solution of

$$\left(-\dot{B}_{\mp}q_{\mp} - iB_{\mp}\frac{\partial}{\partial q_{\mp}}\right)\Phi_{\mp,0}(q_{\mp},t) = 0 \tag{10.61}$$

is

$$\Phi_{\mp,0}(q_{\mp},t) = \left(\frac{1}{2\pi|B_{\mp}|^2}\right)^{1/4} \exp\left[i\frac{\dot{B}_{\mp}}{2B_{\mp}}q_{\mp}^2\right]. \tag{10.62}$$

The normalized ground state wave function is

$$\Phi_{R,0,0}(q_-,q_+,t) = \Phi_{-,0}(q_-,t)\,\Phi_{+,0}(q_+,t)\,. \tag{10.63}$$

Now, we turn our attention to Eq. (10.59). Substitution of explicit form of ϵ_{\mp} in Eq. (10.59) leads to the equation

$$\ddot{B}_{\mp} + \left[\left(\omega^2 \mp 2\omega g \right) \mp 2\omega \Delta g \cos \Omega t \right] B_{\mp} = 0.$$
 (10.64)

This equation is in the form of the Mathieu equation.

We solve Eq. (10.64) by writing

$$B_{\pm}(t) = B_{\pm R}(t) + iB_{\pm I}(t)$$
 (10.65)

with the initial conditions given by Eq. (10.60). Now, we identify the stable and unstable solutions of B_- . Figure 10.16 depicts the stability chart in (Ω, g) parameter space with $\omega = 1$ and $\Delta g = 0.1g$. In the white region the solution B_- is bounded in the long time limit. In the black region $B_-(t)$ diverges with time. For $\Omega = 1$, B_- is unstable for $g \in [0.357, 0.394]$ and stable in the remaining intervals of g. In

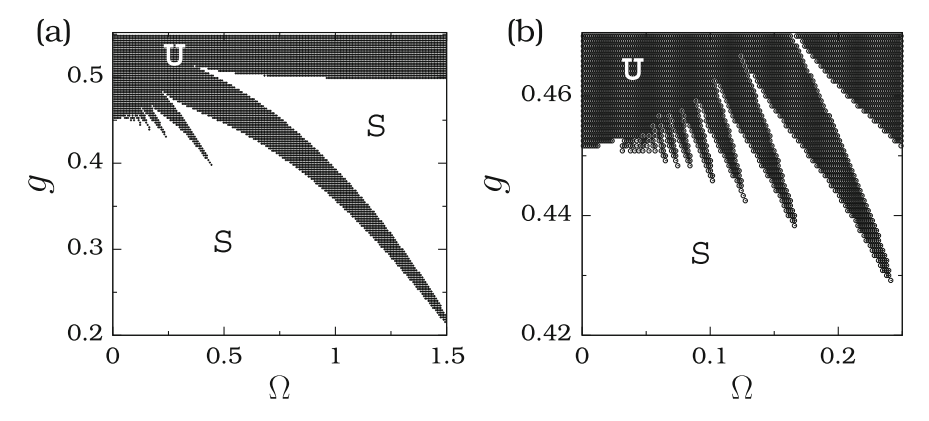


Fig. 10.16 (a) Showing stable (white region) and unstable (black region) behaviour of $B_{-}(t)$ in the (Ω, g) parameter space of Eq. (10.64) where $\omega = 1$ and $\Delta g = 0.1g$. (b) Magnification of part of a region of the subplot (a)

Figs. 10.17a, b for g=0.35 lying in the stable region both $B_+(t)$ and $B_-(t)$ are bounded and quasiperiodic. For g=0.36, Figs. 10.17c and d, $B_+(t)$ is bounded while $B_-(t)$ spirals outward about the origin and diverges with t. Both $B_\pm(t)$ are bounded for g=0.4 (Figs. 10.17e and f).

In [41] the relation between the entanglement behaviour and the dynamics of the Wigner function and the ground state wave packet were reported.

The Wigner function is considered as a representation of the density operator $\hat{\rho}$ for a pure or a mixed state of quantum mechanical system [42]. It is given by

$$W(q,p) = \frac{1}{2\pi} \int_{-\infty}^{\infty} e^{ips} \left\langle q - \frac{s}{2} |\hat{\rho}| q + \frac{s}{2} \right\rangle ds . \qquad (10.66)$$

For the reduced system (10.55) W is worked out as [42]

$$W_{R}(q, p, t) = \Lambda \sqrt{\frac{1}{\pi \left[2Re(\alpha) + \beta\right]}} \exp\left[\frac{4Im(\alpha)qp}{2Re(\alpha) + \beta}\right]$$

$$\times \exp\left[\frac{-q^{2}\left(4|\alpha|^{2} - \beta^{2}\right) + p^{2}}{2Re(\alpha) + \beta}\right], \qquad (10.67)$$

where

$$\Lambda = \left(\frac{\text{Re}(\xi^{-})\text{Re}(\xi^{+})}{\pi \text{Re}(\xi^{-})c^{2} + \text{Re}(\xi^{+})s^{2}}\right)^{1/2},$$
(10.68a)

$$\xi^{\mp} = -i\frac{\dot{B}_{\mp}(t)}{B_{\mp}(t)}, \quad c = s = \frac{1}{\sqrt{2}},$$
 (10.68b)

284 10 Parametric Resonance

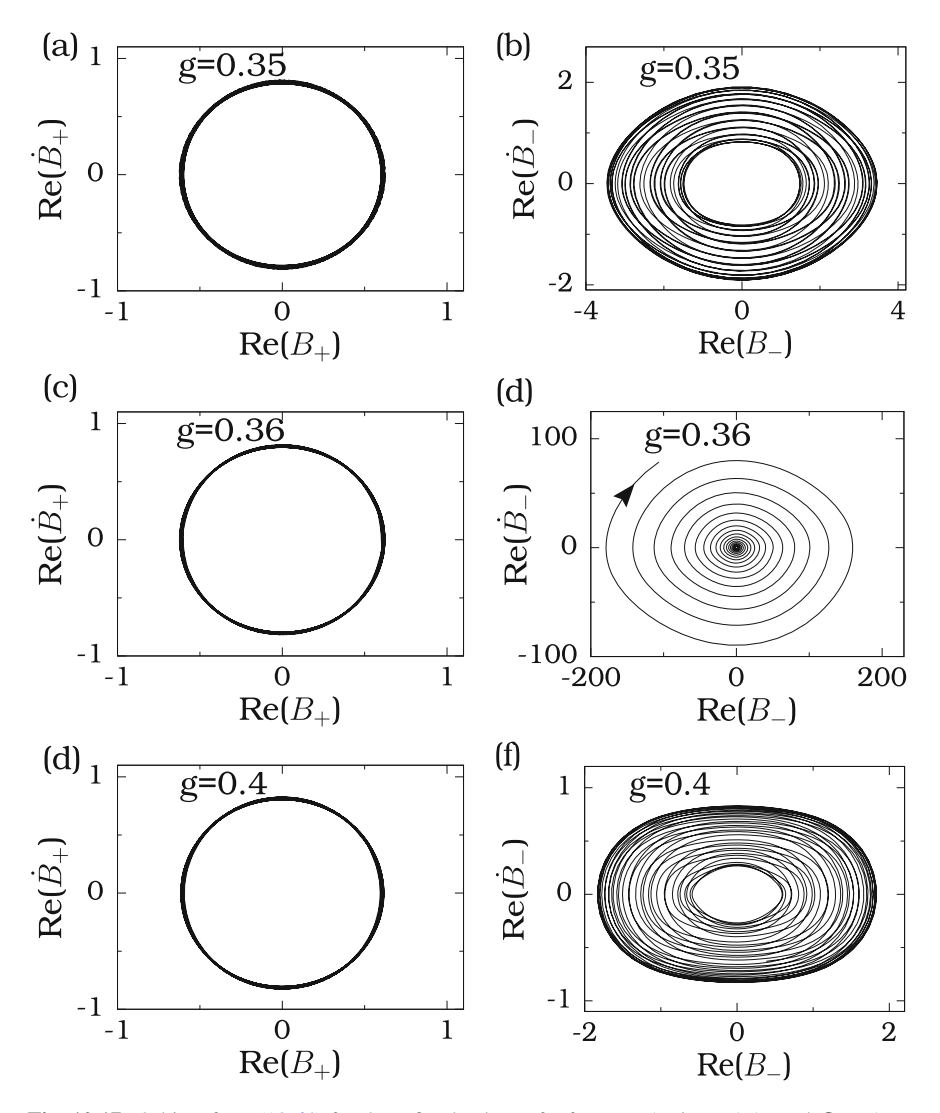


Fig. 10.17 Orbits of Eq. (10.64) for three fixed values of g for $\omega = 1$, $\Delta g = 0.1g$ and $\Omega = 1$

$$\alpha = \frac{(\xi^{-})^* s^2 + (\xi^{+})^* c^2}{2} - \frac{c^2 s^2 \left[(\xi^{-} - \xi^{+})^* \right]^2}{4 \left[\operatorname{Re}(\xi^{-}) c^2 + \operatorname{Re}(\xi^{+}) s^2 \right]}, \quad (10.68c)$$

$$\beta = \frac{c^2 s^2 (\xi^- - \xi^+)^* (\xi^- - \xi^+)}{2 \left[\text{Re}(\xi^-) c^2 + \text{Re}(\xi^+) s^2 \right]} \,. \tag{10.68d}$$

10.6 Applications 285

The plot of the Wigner function for various values of Ω and g indicate signatures of quantum parametric resonance [42]. In the stable regions of Fig. 10.16, the Wigner function is found to show stretching along a dynamical axis and localization with time. In the unstable regions, the Wigner function displays a stretching along a dynamical rotating axis and contraction in the perpendicular axis.

The quantum analogue of classical parametric resonance has been investigated in the harmonic oscillator subjected to an impulsive force [43]. The Hamiltonian of the perturbed system is

$$\hat{H} = \frac{1}{2m}\hat{p}^2 + \frac{1}{2}m\omega^2\hat{x}^2 + \frac{1}{2}\alpha(\hat{x}\hat{p} + \hat{p}\hat{x})\delta_T(t), \qquad (10.69)$$

where $\delta_T(t)$ is periodic with period T. The properties of the quantum system is found to reflect the stable and unstable dynamics of the corresponding classical system. The energy eigenvalues and eigenfunctions of quantum mechanical evolution operator or Floquet operator are analysed. The eigenfunctions of the classical system corresponding to the stable regions are found to be normalizable while singular in the classically unstable parameter regions.

10.6 Applications

Parametric resonance has promising applications in signal amplification [44], noise squeezing [45, 46], mechanical modulation [47], mass sensor [48, 49] and stability of floating bodies like boats, balloons and parachutes [50]. It finds applications in detecting very small change in mass and forces using micromechanical systems [51, 52], microsystems and nanosystems for quadrupole ion guides and ion traps [53], optomechanical cavities [54], magnetic resonance force microscopy [55] and trapping-mode force microscopy [56]. Parametric resonance has been explored to amplify a signal in cantilevers [57], resonators [58], magnetometers [59] and MEMS Gyroscopes [60–62]. Let us enumerate some other notable applications of parametric resonance.

- 1. Columns and beam columns with distributed mass and under pulsating axial forces may undergo finite lateral displacements. In this case the lateral stiffness is a function of the amplitude of the axial force. When the axial force is varied with time, then the stiffness parameter also vary correspondingly. A resonance-like behaviour can occurs with forcing. In this condition an infinitesimally small amplitude of a periodic axial force can destabilize the system [63].
- 2. Gyroscopes are often used in commercial applications for rotation measurements, for example in a Global Positioning System (GPS), automatic safety systems, vehicle control, interactive consumer electronic systems and navigation and guidance systems. Loss in sensitivity present in harmonic oscillations based micro-gyroscopes [64] can be overcome by an actuation scheme

employing parametric resonance. This has been studied both theoretically and experimentally in a micro-gyroscope [65].

- 3. A two-slab neutron interferometer set up is proposed for precision experimental tests for exotic gravitation interactions. The equation for neutron propagation in between the slabs is given by a modified Mathieu equation. The neutron transmission coefficient determined by solving this equation has predicted the possibility of enhanced neutron propagation under proper parametric resonance conditions [66].
- 4. Parametric resonance can be utilized in micromechanical systems including sensors in automobile air bag systems and actuators in printer cartridges. The parametric resonance can destabilize the system and lead to growth of amplitude of oscillation exponentially with time. This effect is useful to improve the performance of parametrically excited MEMS [67]. Knowledge about parametric resonance is useful in MEMS filter design [68].
- 5. In parametrically driven oscillators there is a sharp transition between a stable equilibrium state (zero response) and a large response. This transition is sensitive to the parameters including its mass. Consequently, a change in the mass can be sensed with a parametric oscillator by measuring the frequency shift. It has been pointed out that the mass detection by a parametrically driven MEMS oscillator can be enhanced two orders of magnitude higher than the harmonic resonator based mass sensor [69]. Further, frequency shifts can be exploited for recognition of chemical substances such as water, alkanes and alcohols [70].
- 6. In the NEMS resonators, useful for resonant sensing and precision measurement operating at high frequencies (> 30 MHz), the signal transduction is limited by the presence of even a very low noise in electronic readouts devices. In such cases parametric resonance can be utilized for amplifying the signal of a device before employing electronic amplification [71].
- 7. It has been demonstrated experimentally that the coupling between mechanical motion and single-electron charging in a nanomechanical transistor is useful in a parametric actuation scheme where the voltage applied between drain electrodes and the source is varied periodically. This novel scheme gives rise to mechanical vibrations through a parametric instability [72].
- 8. In a harmonic oscillator with modulated parabolic confinement, the bosonic rising and lowering operators diverge strongly in time when the modulation is approximately twice the natural frequency of the oscillator. That is, parametric resonance becomes a spectroscopic tool in many-body quantum systems, particularly, in cold atoms in optical lattices. It has been shown that spatially homogeneous time-periodic modulation of optical lattice's intensity gives rise to the amplification of charged and density waves in ultracold fermionic atoms [73].
- 9. Parametric resonance can be realized in point-contact spin-valve nanodevices. For example, in [74] a nano scale point contact was used experimentally to inject a high-density ac current into an IrMn/NiFe/Cu/NiFe spin valve capable of producing spin transfer torque (STT) on NiFe moments in the contact region.

10.6 Applications 287

A time-dependent modulation of the effective damping parameter was induced by a time-dependent STT. As a result, magnetic moments undergone parametric resonance. This phenomenon can be utilized for increasing speed and reducing the power of logic and memory devices.

- 10. Systems with trapped and cooled ions isolated from surrounding environments are useful for studying quantum simulations, quantum information processing and frequency standards. Trapped and cooled ions possess excess micromotion if the rf potential node does not coincide with the minimum of the effective static potential. Experimentally, such excess motion has been detected through parametric resonance by modulating the trapping voltage [30]. The micromotion can then be eliminated minimizing the resonance signal by applying a compensating voltage.
- 11. In certain systems the occurrence of parametric resonance has to be avoided. For example, *parametric roll resonance* is a disastrous resonance severely damaging ships [75–77].

10.6.1 Parametric Resonance Based Scanning Probe Microscopy

Now we present in detail an application of parametric resonance in a highly sensitive nanoscale imaging and force spectroscopy [56]. An important technique for nanoscale imaging and force spectroscopy is dynamic scanning probe microscopy (SPM). The sensitivity and the minimum force exerted on a sample with ambient conditions are limited by the low quality factor (Q factor) of the SPM microcantilever. Moreno and his coworkers [56] proposed the use of the parametric resonance to increase the sensitivity in dynamic SPM.

In the experiment with SPM the cantilever deflection from the photodiode was passed through a high-pass filter in order to isolate the ac component. It was amplified by a variable gain amplifier and then multiplied with a periodic driving signal. The frequency ω of the driving signal was chosen close to twice the natural frequency ω_0 of the microcantilever. The resulting output was then feedback to the dither piezo. In order to understand the occurrence of parametric resonance in the above experiment an approximate model equation for the cantilever dynamics in the above setup was constructed.

We denote the modal mass of the cantilever and tip as m, the modal stiffness or cantilever spring constant as k and the velocity proportional modal defining strength representing linear hydrodynamic losses as c. Define z(t) be the base motion of the dither piezo, x(t) the instantaneous displacement of the tip, both measured in an inertial frame of reference and d_0 the equilibrium gap between the tip and the fixed sample. Since the photodiode detects the bending of the cantilever as x(t) - z(t) the dither piezo motion is $z(t) = G[x(t) - z(t)] \cos \omega t$ where G is the total gain of the optical measurement system. G is essentially the strength of the parametric

288 10 Parametric Resonance

excitation. For $G \ll 1$

$$z(t) = \frac{Gx(t)\cos\omega t}{1 + G\cos\omega t} \sim Gx(t)\cos\omega t + O(G^2).$$
 (10.70)

Then the equations of motion for the tip can be written as

$$\ddot{x} + \omega_0^2 (1 - G\cos\omega t)x + \frac{\omega_0}{O}\dot{x} = \frac{1}{m} \left[F_c(x, \dot{x}) + F_f(x, \dot{x}) + F_t(x, \dot{x}, d_0) \right] , \quad (10.71)$$

where $\omega \sim 2\omega_0$ and F_c , F_f and F_t are the intrinsic geometric and inertial nonlinearities of the microcantilever, the dissipative nonlinear fluid forces and the tip-sample nonlinear forces, respectively. Here $\omega_0 = \sqrt{k/m}$ is the natural frequency of the microcantilever and $Q = m\omega_0/c$ is the natural quality factor of the resonance in the absence of the feedback circuit. Equation (10.71) becomes the damped Mathieu equation when $F_c = F_f = F_t = 0$.

Parametric resonance was implemented in SPM with the use of Nanotech Electronica SPM [56]. To observe parametric resonance, the excitation frequency was varied so that $\omega=2\omega_0$ and the feedback gain increased gradually until a significant cantilever response was observed at half of the driving frequency. In this way the threshold value of G was determined. Then G was kept constant and the excitation frequency was slowly increased across the principal parametric resonance and the response of the cantilever was recorded. The response curve of the cantilever was found to be extremely sharp and was almost zero outside a 50 Hz bandwidth.

10.7 Concluding Remarks

An interesting feature of parametrically excited oscillators is that a large response over a large bandwidth can be achieved even for the excitation frequency far away from the natural frequency. On the other hand, through a parametric perturbation an unstable equilibrium point can be made into stable. That is, an inverted pendulum can become stable for certain conditions on ω_0^2 and f. In such a case, any small deviation from the unstable vertical position would not be amplified without bound but the motion of the system will be bounded. Parametric amplification can be considered as an open-loop control strategy and can be implemented in MEMS sensors to monitor the behaviour of the device.

Parametric resonance has been investigated in the sine-Gordon equation [78], nonlinear Schrödinger equation [79], Bose-Einstein condensates [80], theoretical model of electrostatically interacting carbon nano tube arrays [81], tunable superconducting cavities [82], micro-ring gyroscope [83], microstructure operated by a parallel-plate electrode [84], very high-frequency NEMS resonators [85], micro-ring MEMS sensors [86], periodically tapered optical fibers [87], \mathcal{PT} -symmetric system [88]. The possibility and the features of parametric resonance dominated

References 289

production of gravitational waves during the inflationary period to the radiation dominated period of the universe was investigated [89].

Parametric resonance has been investigated experimentally in an array of electromechanical parametric resonators [90], AlN-Mo double damped NEMS resonators [91], piezoelectric NEM [92], coupled micromechanical oscillators [93], silicon microcantilevers [94], doubly clamped NEMS [95] and optically trapped aerosols [96]. Five resonance modes have been observed experimentally in a parametrically driven torsional oscillator. And they were found near the drive frequencies $2\omega/n$, where ω is the natural mechanical resonant frequency and n is an integer equal to 1 or larger [97].

References

- 1. L. Landau, E. Lifschitz, *Mechanics* (Pergamon, London, 1960)
- 2. R. Berthet, A. Petrosyan, B. Roman, Am. J. Phys. 70, 744 (2002)
- 3. F.L. Curzon, A.L.H. Loke, M.E. Lefrancois, K.E. Novik, Am. J. Phys. 63, 132 (1995)
- 4. D.R. Rowland, Am. J. Phys. 72, 758 (2004)
- 5. E.I. Butikov, Eur. J. Phys. 25, 535 (2004)
- 6. F. Verhulst, Perturbation analysis of parametric resonance, in *Encyclopedia of Complexity and Systems Science*, ed. by R.A. Meyers (Springer, New York, 2009), p. 6625
- 7. A.P. Seyranian, J. Appl. Math. Mech. **68**, 757 (2004)
- T.M. Morrison, Three problems in nonlinear dynamics with 2:1 parametric excitation. Ph.D. Thesis, Cornell University, 2006
- 9. S.M. Curry, Am. J. Phys. 44, 924 (1976)
- 10. J.R. Sanmartin, Am. J. Phys. **52**, 937 (1985)
- 11. E.Kh. Akhmedov, Nucl. Phys. B **538**, 25 (1999)
- 12. G. Donoso, C.L. Ladera, Eur. J. Phys. 33, 327 (2012)
- 13. M. Faraday, Phil. Trans. R. Soc. Lond. 121, 299 (1831)
- 14. L. Rayleigh, Philos. Mag. 15, 229 (1883)
- 15. A. Stephenson, Mem. Proc. Manchester Literary Philos. Soc. 52, 1907 (1908)
- 16. F. Melde, Ann. Phys. Chem. Ser. 2 109, 193 (1859)
- 17. L. Ruby, Am. J. Phys. 64, 39 (1996)
- 18. R.E. Collin, Foundations for Microwave Engineering (McGraw-Hill, New York, 1966)
- 19. R.L. Byer, *Quantum Electronics Volume I* (Academic, New York, 1975)
- 20. S. Bhattacharjee, K. Kumar, Eur. J. Phys. 35, 035006 (2014)
- K.I. Turner, S.A. Miller, P.G. Hartwell, N.C. Macdonald, S.H. Strogatz, S.G. Adams, Nature 396, 49 (1998)
- B. Ilie, S. Krylov, K. Aubin, R. Reichenbach, H.G. Craighead, Appl. Phys. Lett. 86, 193114 (2005)
- 23. M.F. Yu, G.J. Walker, R.S. Ruoff, M.J. Dyer, Phys. Rev. B 66, 073406 (2002)
- K. Aubin, M. Zalalutdinov, T. Alan, R.B. Reichenbach, R.H. Rand, A. Zehnder, J. Parpia, H.G. Craighead, J. Microelectron. Mech. Syst. 13, 1018 (2004)
- 25. W. Zhang, G. Meng, Sens. Actuators A 119, 291 (2005)
- J.F. Rhodes, S.W. Shaw, K.L. Turner, J. Moehlis, B.E. DeMartini, W. Zhang, J. Sound Vib. 296, 797 (2006)
- 27. G. Stepan, T. Insperger, R. Szalai, Int. J. Bifurcation Chaos 15, 2783 (2005)
- 28. E. Mathieu, J. Math. 13, 137 (1868)

 M. Napoli, R. Baskaran, K. Turner, B. Bamieh, Understanding mechanical domain parametric resonance in microcantilevers, in *Proceedings of the IEEE 16th Annual International Confer*ence on Micro Electro Mechanical Systems, Kyoto, Japan (2003), pp. 169–172

- 30. Y. Ibaraki, U. Tanaka, S. Urabe, Appl. Phys. B **105**, 219 (2011)
- 31. R. Berthet, A. Petrosyan, B. Roman, Am. J. Phys. 70, 744 (2002)
- 32. A.A. Batista, R.S.N. Moreira, Phys. Rev. E **84**, 061121 (2011)
- 33. K.R. Asfar, J. Sound Vib. 124, 529 (1988)
- 34. A.A. Batista, R.S.N. Moreira, Phys. Rev. E 84, 061121 (2011)
- 35. F.L. Curzon, A.L.H. Loke, M.E. Lefrancois, K.E. Novik, Am. J. Phys. 63, 132 (1995)
- 36. J. Porter, I. Tinao, A. Laveron-Simavilla, J. Rodriguez, Phys. Rev. E 88, 042913 (2013)
- 37. X. Xu, M. Wiercigroch, M.P. Cartmell, Chaos Solitons Fractals 23, 1537 (2005)
- 38. M.G. Clerc, C. Falcon, C. Fernandez-Oto, E. Tirapegui, Europhys. Lett. 98, 30006 (2012)
- 39. R.S. Zounes, R.H. Rand, SIAM J. Appl. Math. 58, 1094 (1998)
- 40. R. Rand, K. Guennoun, M. Belhaq, Nonlinear Dyn. 31, 364 (2003)
- 41. V.M. Bastidas, J.H. Reina, C. Emary, T. Brandes, Phys. Rev. A 81, 012316 (2010)
- 42. S. Rajasekar, R. Velusamy, *Quantum Mechanics II: Advanced Topics* (CRC Press, New York, 2014)
- 43. S. Weigert, J. Phys. A Math. Gen. 35, 4169 (2002)
- 44. M.J. Thompson, D.A. Horsley, Lorentz force MEMS magnetometer, in *Proceedings of the* 2010 Workshop on Solid State Sensors and Actuators, Hilton Head Island, South Carolina (June 2010), pp. 44–48
- 45. D. Rugar, P. Grutter, Phys. Rev. Lett. 67, 699 (1991)
- 46. G. Prakash, A. Raman, J. Rhoads, R. Reifenberger, Rev. Sci. Instrum. 83, 065109 (2012)
- 47. M. Koskenvuori, I. Tittonen, Sens. Actuators A Phys. 142, 346 (2008)
- 48. W. Xhang, K. Turner, Sens. Actuators A Phys. 122, 23 (2005)
- 49. Z. Yie, M.A. Zielke, C.B. Burgner, K.L. Turner, J. Micromech. Microeng. 21, 025027 (2011)
- 50. L. Ruby, Am. J. Phys. 64, 39 (1996)
- K.L. Turner, P.G. Hartwell, F.M. Bertsch, N.C. Macdonald, Parametric resonance in a microelectromechanical torsional oscillator, in ASME International Mechanical Engineering Congress and Exposition Proceedings of Microelectromechanical Systems (MEMS), Anaheim, CA (1998), pp. 335–340
- 52. K.L. Turner, W. Zhang, Design and analysis of a dynamic MEM chemical sensor, in *Proceedings of the 2001 American Control Conference, Arlington, VA* (2001), pp. 1214–1218
- 53. W. Paul, Rev. Mod. Phys. **62**, 531 (1990)
- 54. A. Dorsel, J.D. McCullen, P. Meystre, E. Vignes, H. Walther, Phys. Rev. Lett. 51, 1550 (1983)
- 55. W.M. Dougherty, K.J. Bruland, J.L. Garbini, J. Sidles, Meas. Sci. Technol. 7, 1733 (1996)
- M.M. Moreno, A. Raman, J. Gomez-Herrero, R. Reifenberger, Appl. Phys. Lett. 88, 193108 (2006)
- 57. M.V. Requa, K.I. Turner, Appl. Phys. Lett. 90, 173508 (2007)
- 58. R. Baskaran, K.I. Turner, J. Micromech. Microeng. 13, 701 (2003)
- M. Thompson, D. Horsley, Parametrically-amplified MEMS magnetometer, in *Proceedings of the 15th International Conference Solid State Sensors Actuators & Microsystems (Transducers, Denver, 2009)* (2009), p. 1194
- Z.X. Hu, B.J. Gallacher, J.S. Burdess, C.P. Fell, K. Townsnd, Sens. Actuators A 167, 249 (2011)
- 61. L.A. Oropeza-Ramos, Sens. Actuators A **152**, 1194 (2009)
- 62. M. Sharma, E.H. Sarraf, R. Baskaran, E. Cretu, Sens. Actuators A 177, 79 (2012)
- 63. M.R. Sharma, A.K. Singh, G.S. Benipal, Latin Am. J. Solids Struct. 11, 925 (2014)
- 64. N. Yazdi, F. Ayazi, K. Najafi, Proc. IEEE **86**, 1640 (1998)
- 65. L.A. Oropeza-Ramos, C.B. Burgner, K.L. Turner, Sens. Actuators A 152, 80 (2009)
- 66. V. Gudkov, H.M. Shimizu, G.L. Greene, Phys. Rev. C 83, 025501 (2011)
- 67. J. Rhoads, S.W. Shaw, K. Turner, R. Baskaran, J. Sound Vib. **296**, 797 (2006)
- 68. J. Rhoads, S.W. Shaw, K. Turner, R. Baskaran, J. Sound Acoust. 127, 423 (2005)
- 69. W. Zhang, R. Baskaran, K.L. Turner, Sens. Actuators A Phys. 102, 139 (2002)

References 291

 F.M. Batiston, J.P. Ramseyer, H.P. Lang, M.K. Baller, C. Gerber, J.K. Gimzewski, E. Meyer, H.J. Guntherodt, Sens. Actuators B Chem. 77, 122 (2001)

- 71. R.B. Karabalin, X.L. Feng, M.L. Roukes, Nano Lett. 9, 3116 (2009)
- 72. D. Midtvedt, Y. Tarakanov, J. Kinaret, Nano Lett. 11, 1439 (2011)
- 73. C.D. Graf, G. Weick, E. Mariani, Europhys. Lett. **89**, 40005 (2010)
- 74. C. Wang, H. Seinige, M. Tsoi, J. Phys. D. Appl. Phys. 46, 285001 (2013)
- 75. S.M. Carmel, J. Trans. Res. Board **1963**, 56 (2006)
- C. Holden, Modeling and control of parametric roll resonance. Ph.D. Thesis, Norwegian University of Science and Technology, Trondheim, 2011
- 77. B.J.H. van Laarhoven, Stability analysis of parametric roll resonance. Ph.D. Thesis, Eindhoven University of Technology, Eindhoven, 2009
- 78. N.R. Quintero, P.G. Kevrekidis, Physica D **170**, 31 (2002)
- 79. B. Baizakov, G. Gilatrelta, B. Malomed, M. Salerno, Phys. Rev. E 71, 036619 (2005)
- 80. W. Cairncross, A. Pelster, Eur. Phys. J. D 68, 106 (2014)
- 81. A. Isacsson, J.M. Kinaret, Phys. Rev. B 79, 165418 (2009)
- 82. W. Wustmann, V. Shumeiko, Phys. Rev. B 87, 184501 (2013)
- 83. B.J. Gallacher, J.S. Burdess, K.M. Harish, J. Micromech. Microeng. 16, 320 (2006)
- 84. S. Krylov, Y. Gerson, T. Nachmias, U. Keren, J. Micromech. Microeng. 20, 015041 (2010)
- 85. R.B. Karabalin, X.L. Feng, M.L. Roukes, Nano Lett. 9, 3116 (2009)
- K.M. Harish, B.J. Gallacher, J.S. Burdess, J.A. Neasham, J. Micromech. Microeng. 19, 015021 (2009)
- 87. A. Armaroli, F. Biancalana, Opt. Exp. 20, 25096 (2012)
- 88. J. D'Ambroise, B.A. Malomed, P.G. Kevrekidis, Chaos 24, 023136 (2014)
- 89. P.M. Sa, A.B. Henriques, Phys. Rev. D 77, 064002 (2008)
- 90. I. Mahboob, M. Mounaix, K. Nishiguchi, Sci. Rep. 4 (2014). doi:10.1038/srep04448
- 91. L.G. Villanueva, R.B. Karabalin, M.H. Matheny, E. Kenig, M.C. Cross, M.L. Roukes, Nano Lett. 11, 5054 (2011)
- 92. R.B. Karabalin, S.C. Masmanidis, M.L. Roukes, Appl. Phys. Lett. 97, 183101 (2010)
- 93. J. Zhu, C.Q. Ru, A. Mioduchoski, Eur. Phys. J. B 58, 411 (2007)
- 94. M.V. Requa, K.L. Turner, Appl. Phys. Lett. 88, 263508 (2006)
- 95. N. Kacem, S. Hentz, D. Pinto, B. Reig, V. Nguyen, Nanotechnology 20, 275501 (2009)
- R.D. Leonardo, G. Ruoccio, J. Leach, M.J. Padgett, A.J. Wright, J.M. Girkin, D.R. Burnham,
 D. MacGlolm, Phys. Rev. Lett. 99, 010601 (2007)
- 97. K. Turner, S. Miller, P. Hartwell, N. MacDonald, S. Strogatz, S. Adams, Nature 396, 149 (1998)

Chapter 11 Autoresonance

Autoresonance (also called self-sustained resonance) is a phenomenon that occurs when a resonant forced nonlinear system stays phase-locked with an adiabatically varying driving force whose frequency is a function of time [1, 2]. Essentially, the system automatically adjusts its amplitude continuously so that its instantaneous period of oscillation matches with the period of the driving force leading to the growth of its energy. That is, autoresonance is a method of exciting a nonlinear dynamical system to high energies by means of a weak driving force whose frequency is varying with time. Autoresonance was first realized in relativistic particle accelerators [3] and in the analysis of the cyclotron resonance stability [4].

In the autoresonance phenomenon the nonlinearity of the system is used to lock in resonance thereby giving significant amplification even when the parameters of the system vary. Consider the excitation of a resonant nonlinear system by means of variations of one or more parameters. Due to the variations of the parameters the resonant frequency of the system changes and the system is detuned from resonance. In order to maintain the system in resonance an appropriate feedback control or suitable monitoring of driving force has to be implemented. In a different approach, in autoresonance the system phase-locks with the external additive driving force and keeps phase-locking in the presence of variations of the parameters of the system. The point is that the phase-locking is completely a nonlinear process and it takes place due to the slow self-adjustment of amplitude of frequency of oscillation of the nonlinear system.

The phase-locking, an important feature of autoresonance, plays a significant role in coupled oscillators, Raman scattering, higher harmonics generation, nonlinear frequency conversion and wave guide arrays. It can be used to realize a suitable control of electron dynamics in quantum solid state devices. There is a class of autoresonance termed as *parametric autoresonance*, where one or more parameters and the frequency of the driving force are chirped [5–7]. That is, autoresonance can be induced by means of an external additive driving force or by a parametric

perturbation. In both cases, the frequency of the perturbation is time-dependent. Theory of autoresonance has been developed for single and coupled oscillators [8–12].

11.1 Illustration of Autoresonance

In the earlier chapters the frequency of an external deterministic force applied to a nonlinear system to realize different resonances is assumed to be time-independent. Often the force is chosen as $f \cos \omega t$ or $f \sin \omega t$. The phase of the force is ωt and is linear in time. As shown in Chap. 1 for $|f| \ll 1$ the amplitude of oscillation settles to a periodic state and there is no growth of it. When the phase of the force is chosen as a nonlinear function of time, for example, $\omega t \pm \alpha t^2$, then, on average, the growth of the oscillation amplitude leading autoresonance can be realized.

To illustrate the phenomenon of autoresonance, we consider a pendulum system described by the equation of motion

$$\ddot{\theta} + d\dot{\theta} + \omega_0^2 \sin \theta = f \cos(\omega_0 t - \alpha t^2 / 2). \tag{11.1}$$

In the above equation, $\omega_0/2\pi$ is the linear frequency of the pendulum while $\omega_0 - \alpha t$ is the time-dependent frequency of the driving force. α is the *frequency sweep rate* (also called *chirp rate*). Assume that the system is excited initially at $t=t_0=-1000$.

We solve Eq. (11.1) using the fourth-order Runge-Kutta method with step size $\Delta t = 0.001$ with $\theta(0) = \dot{\theta}(0) = 0$. Collect the values of time t and θ (amplitude of oscillation) corresponding to $\dot{\theta}(t) = 0$ with $\dot{\theta}(t - \Delta t) > 0$ and $\dot{\theta}(t + \Delta t) < 0$. Figure 11.1 presents the variation of amplitude of oscillation with time for three

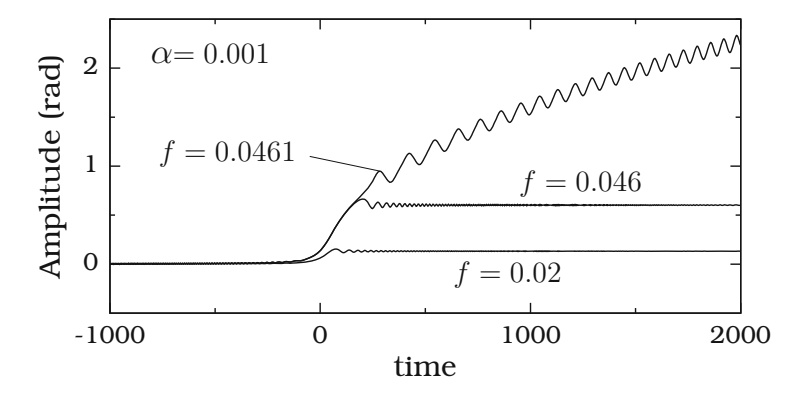


Fig. 11.1 Variation of the oscillation amplitude of the pendulum system for three values of the amplitude f of the driving force with $\omega_0=2\pi$, d=0 and $\alpha=0.001$. Onset of autoresonance occurs at f=0.0461

values of f with $\omega_0 = 2\pi$, d = 0 and $\alpha = 0.001$. For $f \le f_c = 0.046$, in the long time limit, the oscillation amplitude becomes a constant. This is shown in Fig. 11.1 for f = 0.02 and 0.046. The amplitude of oscillation, on average, grows with time for $f > f_c$ (see Fig. 11.1 for f = 0.0461). Though the difference between f = 0.0461 and f = 0.046 is very small, the system exhibits a distinct response. There is a sharp threshold near f = 0.046. The system is said to be captured into autoresonance for $f > f_c$, where the system automatically phase-locks with the drive and evolves in autoresonance at later times. That is, for $f > f_c$, the instantaneous driving frequency is locked to the instantaneous excitation frequency so that the condition for resonance is met. In this case, the oscillation amplitude grows without saturation until certain other effects kick in.

The observed autoresonance is a reversible process and the pendulum can be returned to its nearly initial equilibrium state by reversing the direction of variation of the frequency of the driving force. The slow oscillatory variation of the oscillation amplitude (shown in Fig. 11.1 for f=0.0461) is an indication of stability of the autoresonance state. It is to be noted that to realize the nonlinear stochastic and vibrational resonances fine tuning of a control parameter is required while it is not necessary for autoresonance. In Fig. 11.1 three distinct stages of evolution of the oscillation amplitude is clearly seen. For $t_0 < t < t_1 (\approx 0)$ the system is far from the resonance and the amplitude is almost a constant. The system is in a weakly nonlinear autoresonant evolution stage for $t_1 < t < t_2$, where the amplitude grows almost linearly. For $t > t_2$ the system is in a strongly nonlinear region and the autoresonance continues.

11.2 Threshold Analysis

Now we present a mathematical analysis of the threshold for autoresonance [2] with reference to the pendulum system (11.1).

In the linear region ($t_0 < t < t_1 (\approx 0)$), the system is effectively linear and described by a linear differential equation. The applied force excites a driven mode at the drive frequency and an undriven, homogeneous mode at the linear frequency. These modes have equal but opposite amplitudes. They are proportional to the drive and inversely proportional to $\Delta\omega(t) = \omega(t) - \omega_0 = -\alpha t$. Thereafter, the amplitude of the driven mode is approximately inversely proportional to $\Delta\omega(t)$. As a result the driven mode grows in proportion to 1/t as $t \to 0$. The homogeneous mode is not further excited by the sweeping frequency. The resultant motion of the system is the sum of the free-running homogeneous mode and the phase-locked driven mode.

In the weakly nonlinear region $(t_1 < t < t_2)$, it is reasonable to approximate $\sin \theta$ by $\theta - \theta^3/6$ and rewrite Eq. (11.1) as

$$\ddot{\theta} + d\dot{\theta} + \omega_0^2 \left(\theta - \frac{1}{6} \theta^3 \right) = f \operatorname{Re} \left(e^{i\psi} \right) , \qquad (11.2)$$

where $\psi = \omega_0 t - \alpha t^2/2$. Assume the solution of the form

$$\theta = a\cos\phi = \operatorname{Re}\left(a\,\mathrm{e}^{\mathrm{i}\phi}\right)\,. \tag{11.3}$$

Substitution of

$$\dot{\theta} = \operatorname{Re} \left(\dot{a} e^{i\phi} + i \dot{\phi} \, a \, e^{i\phi} \right), \quad \ddot{\theta} \approx \operatorname{Re} \left[\left(\ddot{a} + 2i \dot{a} \, \dot{\phi} + i a \ddot{\phi} - a \dot{\phi}^2 \right) e^{i\phi} \right], (11.4a)$$

$$\theta^3 = \text{Re}\left(\frac{3}{4}a^3 e^{i\phi}\right) \tag{11.4b}$$

in Eq. (11.2) gives

$$2i\dot{a}\dot{\phi} + ia\ddot{\phi} + ida\dot{\phi} - a\dot{\phi}^2 + \omega_0^2 a - \frac{1}{8}\omega_0^2 a^3 = fe^{i(\psi - \phi)}, \qquad (11.5)$$

where \ddot{a} is neglected since a is assumed to be small.

Defining $\Phi = \phi - \psi$ as the phase mismatch and equating real and imaginary parts separately to zero give

$$\dot{a}\dot{\phi} = -\frac{1}{2}a\ddot{\phi} - \frac{1}{2}da\dot{\phi} - \frac{1}{2}f\sin\Phi$$
, (11.6a)

$$\omega_0^2 - \dot{\phi}^2 = \frac{1}{8}\omega_0^2 a^2 + \frac{1}{a}f\cos\Phi . \tag{11.6b}$$

For a nearly resonance case the oscillation frequency of the pendulum is $\omega_{0S} = \dot{\phi} \approx \omega_0$ and $\ddot{\phi} \approx 0$. Then $\omega_0^2 - \dot{\phi}^2 \approx (\omega_0 + \dot{\phi})(\omega_0 - \dot{\phi}) = 2\omega_0(\omega_0 - \dot{\phi})$. Now, Eq. (11.6) become

$$\dot{a} = -\frac{1}{2}da - \frac{1}{2\omega_0}f\sin\Phi , \qquad (11.7a)$$

$$\dot{\Phi} = \omega_0 - \dot{\psi} - \frac{1}{16}\omega_0 a^2 - \frac{1}{2\omega_0 a} f \cos \Phi . \tag{11.7b}$$

Next, neglecting the dissipation (d=0), define $I=a^2/2$, $\Omega(I)=\omega_0-\omega_0a^2/16=\omega_0(1-I/8)$ and $F=f/(\sqrt{8}\,\omega_0)$. Then Eq. (11.7) become

$$\dot{I} = -2\sqrt{IF}\sin\Phi , \qquad (11.8a)$$

$$\dot{\Phi} = \Omega(I) - \omega_0 + \alpha t - \frac{F}{\sqrt{I}} \cos \Phi . \tag{11.8b}$$

Equation (11.8) differ from that describing the usual nonlinear resonance by the slow time variation of the driving frequency $\dot{\psi} = \omega_0 - \alpha t$.

In the absence of the external periodic force and damping $\dot{I} = 0$ and $\dot{\Phi} = \Omega(I)$. Then I = a constant and $\Phi = \Omega(I)t$. The action I remains the same while the phase mismatch Φ will increase. When the system is subjected to the external force the action will increase if the system is in phase with the driving force. If it is out of phase with the drive then the action will decrease. The rate of change of action depends on the action itself and is inversely proportional to \sqrt{I} .

At $t \approx 0$ (refer Fig. 11.1) the system enters from the linear region to the weakly nonlinear region. At this time the system is phase-locked and Φ starts out near π . In order to stay in autoresonance Φ must stay near π . Substitution of $d\Phi/dt = 0$ in Eq. (11.8b) gives

$$\alpha t - \frac{1}{8}\omega_0 I_0 + \frac{F}{\sqrt{I_0}} = 0 , \qquad (11.9)$$

where I_0 is the equilibrium action and assume that $I = I_0 - \Delta$ where Δ is small. Because I is a slow motion of time, one can use series expansion of I about I_0 in Eq. (11.8). This leads to

$$\dot{\Delta} = 2F\sqrt{I_0}\sin\Phi + \frac{\alpha}{\varsigma}\,,\tag{11.10a}$$

$$\dot{\Phi} = S\Delta \,, \tag{11.10b}$$

where $S = \omega_0 + F/(2I_0^{3/2})$.

The Hamiltonian of (11.10) is

$$H(\Phi, \Delta) = \frac{1}{2}S\Delta^2 + V_{\text{eff}}(\Phi), \quad V_{\text{eff}}(\Phi) = 2F\sqrt{I_0}\cos\Phi - \frac{\alpha}{S}\Phi.$$
 (11.11)

Equation (11.10) can be viewed as a particle of effective mass S moving in the effective potential $V_{\rm eff}$. Figure 11.2a depicts the form of the effective potential. It has a series of tilted potential wells. For the system to remain in a phase-locked state with Φ staying near π the particle must be trapped at the bottom of one of the wells of $V_{\rm eff}$. The system will stay in autoresonance as long as the phase mismatch Φ will be near zero and Eq. (11.9) will be satisfied. The effective potential wells will exist only if the tilt is less than the depth of the wells [2]:

$$\frac{\alpha}{S} < 2F\sqrt{I_0} \text{ or } S\sqrt{I_0} > \frac{\alpha}{2F}$$
 (11.12)

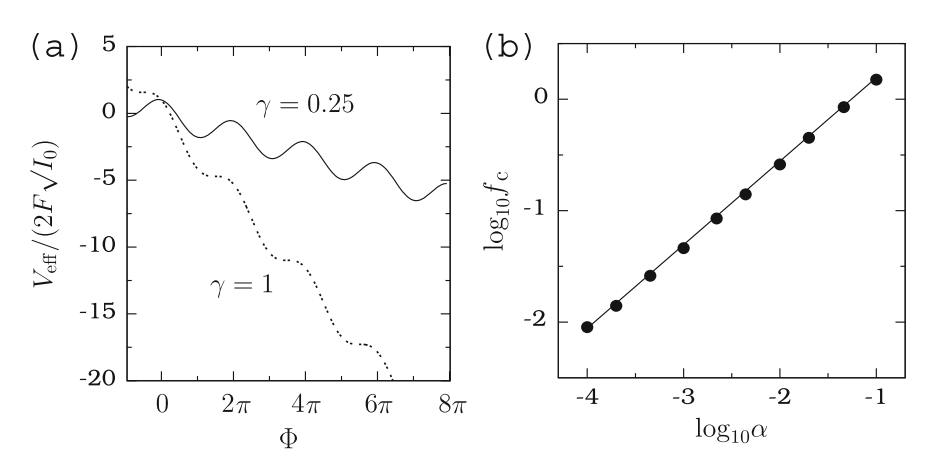


Fig. 11.2 (a) Plot of $V_{\rm eff}/(2F\sqrt{I_0})=\cos\Phi-\gamma\Phi$ for two values of the parameter $\gamma=\alpha/(2FS\sqrt{I_0})$. The critical $V_{\rm eff}$ defined by Eq. (11.12) happens for $\gamma=1$. (b) Numerically computed (solid circles) f_c , the value of f above which autoresonance occurs, versus the parameter α in $\log_{10}-\log_{10}$ scale. The continuous curve is the theoretically predicted relation (11.14) between f_c and α . Here $\omega_0=2\pi$ and d=0

The critical value of I_0 above which the wells will be retained effectively is obtained by differentiating $S\sqrt{I_0}$ with respect to I_0 after substituting the expression for S. The result is

$$I_{0,c} = \left(\frac{8F}{\omega_0}\right)^{2/3} . {(11.13)}$$

Substitution of $I_{0,c}$ for I_0 in Eq. (11.12) gives

$$F_{\rm c} = \sqrt{\frac{8}{\omega_0}} \left(\frac{\alpha}{3}\right)^{3/4} \text{ or } f_{\rm c} = 8\sqrt{\omega_0} \left(\frac{\alpha}{3}\right)^{3/4}$$
 (11.14)

Figure 11.2b shows numerically computed f_c versus α in $\log_{10} - \log_{10}$ scale with $\omega_0 = 2\pi$ and d = 0.

In Fig. 11.1 the variation of amplitude is shown for t < 2000. For each value of $f > f_c$ the autoresonance does not continue forever but it breaks down at a certain time. This is illustrated in Fig. 11.3 for f = 0.0461 and 0.065. The pendulum system considered above is undamped (d = 0). The autoresonance occurs for weak damping also. For example, Fig. 11.4 displays the variation of the oscillation amplitude with time for two fixed values of d and for two values of f. For d = 0.001 and 0.005 the numerical simulation predicts that $f_c = 0.0477$ and 0.0548, respectively. Furthermore f_c depends on d. It has been shown that the breaking time for autoresonance is $\sim d^{-1}$ [2].

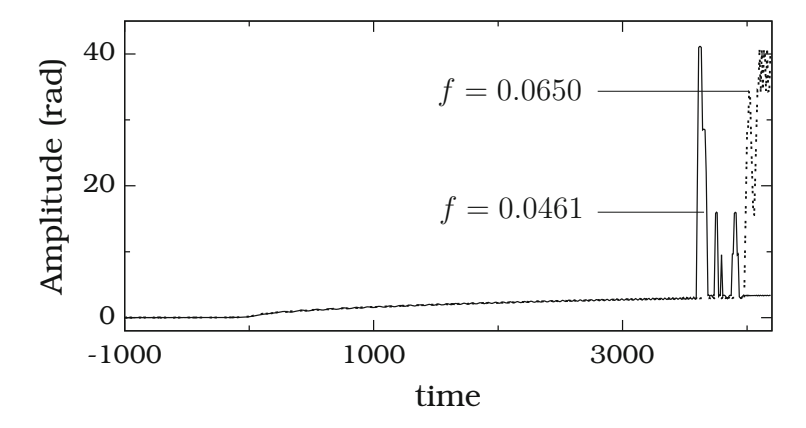


Fig. 11.3 Plot of the oscillation amplitude as a function of time illustrating a breaking of autoresonance at a large time. Here d=0, $\omega_0=2\pi$ and $\alpha=0.001$

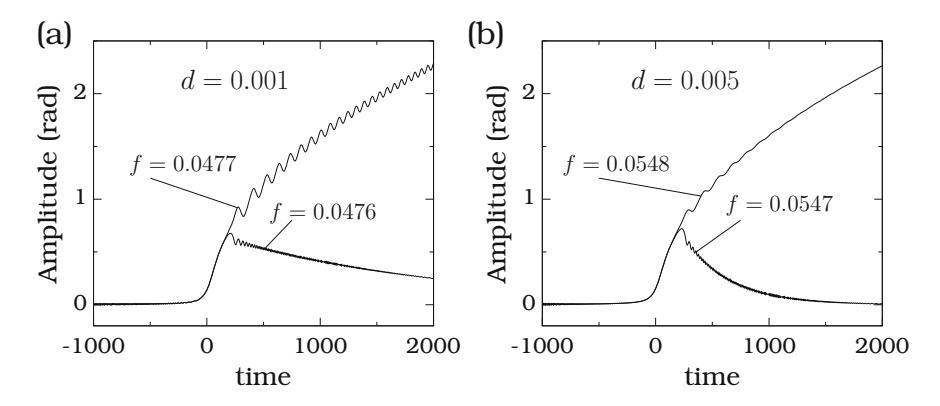


Fig. 11.4 Amplitude versus time in the presence of damping (**a**) d=0.001 and (**b**) d=0.005 for $\omega_0=2\pi$ and $\alpha=0.001$

11.3 Parametric Autoresonance in the Duffing Oscillator

Assaf and Meerson [13] pointed out the difference between autoresonance achievable by additive force and parametric force. Consider a child on a swing. When a mother pushes the swing, once in each swing, essentially the time-interval between the pushes increases as the amplitude of the swing grows. This is an external autoresonance. Differently, when the child swings himself, by moving up and down the position of his center-of-mass twice in each cycle, the period of these modulations increases as the amplitude of the swing increases. This is a parametric autoresonance.

Now we analyse the parametric autoresonance in the ubiquitous Duffing oscillator [6]. In the system (11.1), the frequency of the additive force is treated as time-dependent. Now, we consider the case without an additive force but with

the parametric perturbation in which the frequency of the perturbation is timedependent. We choose the system as the Duffing oscillator equation

$$\ddot{x} + d\dot{x} + \omega_0^2 x + fx \cos \theta(t) + \beta x^3 = 0, \qquad (11.15)$$

where $\theta(t) = 2\omega_0 t - \mu t^2$ with $\mu \ll 1$ being the chirp rate. The linear frequency chirp is, say, $v(t) = \dot{\theta} = 2\omega_0 - 2\mu t$.

11.3.1 Approximate Solution

Assume the solution of (11.15) as

$$x = a\cos\phi = \text{Re}\left(ae^{i\phi}\right). \tag{11.16}$$

The various terms in Eq. (11.15) are then given by

$$\dot{x} = \text{Re} \left(\dot{a} e^{i\phi} + i \dot{\phi} a e^{i\phi} \right) , \quad \ddot{x} = \text{Re} \left(2i \dot{a} \dot{\phi} e^{i\phi} - a \dot{\phi}^2 e^{i\phi} \right) , \quad (11.17a)$$

$$x^3 \approx \text{Re}\left(\frac{3}{4}a^3e^{i\phi}\right)$$
, (11.17b)

$$x\cos\theta = a\cos\phi\cos(2\omega_0 t - \mu t^2) = \frac{1}{2}a\text{Re}\left(e^{i\phi}e^{-2i(\phi - \theta/2)}\right)$$
, (11.17c)

where \ddot{a} is neglected due to its smallness. For nearly resonance case one can assume $\dot{\phi} \approx \omega_0$ and $\ddot{\phi} \approx 0$. Substitution of (11.17) in (11.15) and neglecting $d\dot{a}$ gives

$$2i\dot{a}\dot{\phi} - a\dot{\phi}^2 + ida\dot{\phi} + \omega_0^2 a + \frac{3}{4}\beta a^3 + \frac{1}{2}fae^{-2i(\phi - \theta/2)} = 0.$$
 (11.18)

Equating real and imaginary parts of Eq. (11.18) separately to zero and the substitution of

$$\omega_0^2 - \dot{\phi}^2 \approx (\omega_0 + \dot{\phi})(\omega_0 - \dot{\phi}) = 2\omega_0(\omega_0 - \dot{\phi}) , \quad \psi = \phi - \theta/2$$
 (11.19)

result in

$$\dot{a} = -\frac{1}{2} da + \frac{1}{4\omega_0} fa \sin 2\psi , \qquad (11.20a)$$

$$\dot{\psi} = \mu t + \frac{3}{8\omega_0} \beta a^2 + \frac{1}{4\omega_0} f \cos 2\psi$$
 (11.20b)

The chirping rate μ appears in the evolution equation of the phase and not explicitly in the equation for the amplitude a. Notice the difference between Eqs. (11.7a) and (11.20a).

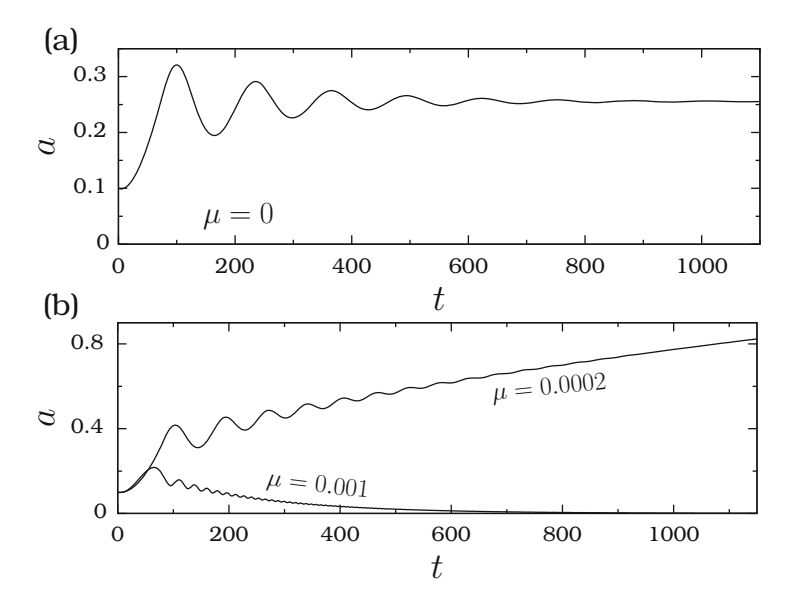


Fig. 11.5 a versus t for three values of μ of the parametrically driven Duffing oscillator Eq. (11.15). The values of the parameters are d=0.01, $\omega_0^2=1$, $\beta=-1$ and f=0.1

To excite the system the initial value of a should be nonzero. Figure 11.5 presents the variation of a with time for three values of μ for d=0.01, $\omega_0^2=1$, $\beta=-1$ and f=0.1. When $\mu=0$, the amplitude exhibits a damped oscillation, however, a(t) decays to a nonzero value. For $0<\mu<0.0007$ autoresonance occurs. An example is shown in Fig. 11.15b for $\mu=0.0002$. For $\mu>0.0007$ a(t) decays to zero (Fig. 11.5b).

11.3.2 Analytical Theory of Parametric Autoresonance

For simplicity, we start with the case d=0. With the change of variable $I=a^2/2$ and defining $\alpha=4\omega_0\mu t/f$ Eq. (11.20) becomes

$$\dot{I} = \frac{f}{2\omega_0} I \sin 2\psi , \qquad (11.21a)$$

$$\dot{\psi} = \frac{f}{4\omega_0} \left(\alpha + \cos 2\psi \right) + \frac{3\beta}{4\omega_0} I. \tag{11.21b}$$

The Hamiltonian function for the above system is

$$H(I, \psi, t) = \frac{f}{4\omega_0} I(\alpha(t) + \cos 2\psi) + \frac{3\beta}{8\omega_0} I^2.$$
 (11.22)

Now, we proceed to describe the slow trend in the amplitude and phase. When $\mu = 0$ and d = 0 the frequency ν is a constant and an equilibrium point of (11.21) is

$$I^* = -\frac{f}{3\beta} , \quad \psi^* = 0 .$$
 (11.23)

 (I^*, ψ^*) is an elliptic equilibrium point. For $\mu \neq 0$ this equilibrium point does not exist. But for $\mu \ll 1$ it is reasonable to define a quasi-equilibrium point $(I^*(t), \psi^*(t))$ and assume that it is a slowly varying function of time. This point actually represents the slow trend in autoresonance and is associated with an ideal phase-locking regime.

To determine the quasi-equilibrium point, substitute $I = I^*$, $\psi = \psi^*$ and $\dot{\psi}^* = 0$ in Eq. (11.21b) and obtain

$$f(\alpha + \cos 2\psi^*) + 3\beta I^* = 0. \tag{11.24}$$

For small ψ^* approximating $\cos 2\psi^* \approx 1$ gives $I^* = f(\alpha + 1)/(3\beta)$. To find ψ^* , differentiate (11.24) with respect to t and use Eq. (11.21) for \dot{I}^* and $\dot{\psi}^*$. The result is

$$2\alpha \sin 2\psi^* + \sin 4\psi^* = \frac{16\omega_0^2 \mu}{f^2} \,. \tag{11.25}$$

Writing $\sin 2\psi^* \approx 2\psi^*$, and $\sin 4\psi^* \approx 4\psi^*$ in the above equation gives ψ^* . Now,

$$I^* = -\frac{f(\alpha+1)}{3\beta} , \quad \psi^* = \frac{k}{\alpha+1} , \quad k = \frac{4\omega_0^2 \mu}{f^2} .$$
 (11.26)

Equation (11.26) is valid for $\mu \ll 1$ or $t \gg 1$. In Fig. 11.6 a(t), $\psi(t)$, I(t), $a^*(t)$, $\psi^*(t)$ and $I^*(t)$ versus t obtained with $a(0) = a^*(0) = \sqrt{2I^*(0)}$, $\psi(0) = \psi^*(0)$ and $I(0) = I^*(0)$ are presented. In this figure the dashed lines are $a^*(t)$, $\psi^*(t)$ and

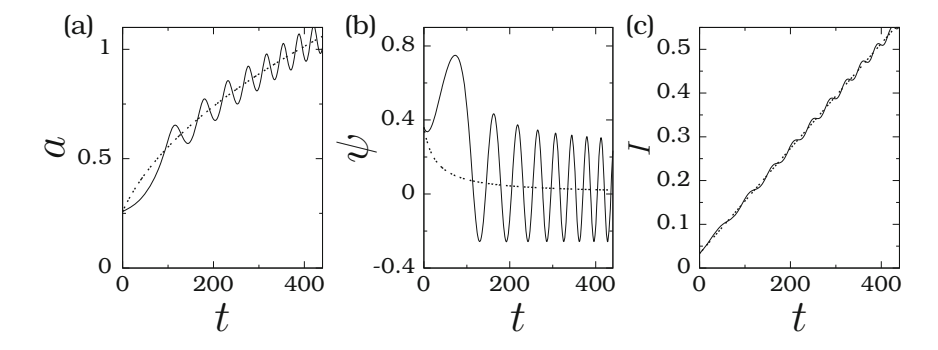


Fig. 11.6 a(t), $\psi(t)$ and I(t) versus t for the Duffing oscillator system. The values of the parameters are d=0, $\omega_0^2=1$, f=0.1, $\beta=-1$ and $\mu=0.0009$. The dashed curves in the subplots (a)–(c) are $a^*(t)$, $\psi^*(t)$ and $I^*(t)$, respectively

 $I^*(t)$. Oscillations occur around the quasi-equilibrium point and hence $I^*(t)$ and $\psi^*(t)$ are called *trends* [6] and are the essence of parametric autoresonance. The amplitude

$$a^*(t) = \sqrt{2I^*(t)} = \sqrt{\frac{2}{3\beta} (f + 4\omega_0 \mu t)}$$
 (11.27)

steadily grows with t and is a function of the chirp rate. On the other hand, for $t \gg 1$ the phase $\psi^*(t) \approx \omega_0/(ft)$ decreases with time and is independent of μ .

It is convenient to describe the phase ψ through a second-order equation. Differentiation of (11.21b) with respect to time and eliminating I give rise to the equation

$$\ddot{\psi} + \frac{f^2}{16\omega_0} \sin 4\psi + \frac{f\mu t}{2} \sin 2\psi - \mu = 0.$$
 (11.28)

It can rewritten as

$$\ddot{\psi} + \frac{\partial}{\partial \psi} V(\psi, t) = 0 , \quad V(\psi, t) = -\frac{f^2}{4\omega_0} \cos 4\psi - f\mu t \cos 2\psi - \mu\psi . \quad (11.29)$$

Interestingly, defining

$$v = \frac{3\beta}{4\omega_0}I + \frac{f}{4}\cos 2\psi + \mu t \tag{11.30}$$

[refer Eq. (11.20b)] allows us to introduce a new time-dependent Hamiltonian

$$H(\psi, v, t) = \frac{1}{2}v^2 + V(\psi, t)$$
 (11.31)

which describes a unit mass particle in a time-dependent potential with velocity v. This Hamiltonian description can be used for small values of μ .

11.3.3 Dynamics in the Neighbourhood of (I^*, ψ^*)

Define $\delta I = I - I^*$ and $\delta \psi = \psi - \psi^*$ as the deviations of I and ψ from I^* and ψ^* , respectively. Writing $H(I, \psi, t) = H(I^*, \psi^*, t) + H(\delta I, \delta \psi, t)$ and assuming δI and $\delta \psi$ are small, then substitution of $\delta I = I - I^*$ and $\delta \psi = \psi - \psi^*$ in (11.22) gives

$$H(\delta I, \delta \psi, t) = -\frac{fk}{\omega_0(\alpha + 1)} \delta I \delta \psi + \frac{3\beta}{8\omega_0} (\delta I)^2 + \frac{f^2}{6\omega_0 \beta} (\alpha + 1)(\delta \psi)^2.$$
 (11.32)

Then the Hamilton's equations are

$$\dot{\delta I} = -\frac{\partial H}{\partial \delta \psi} = \frac{fk}{\omega_0(\alpha + 1)} \, \delta I - \frac{f^2(\alpha + 1)}{3\omega_0 \beta} \, \delta \psi \,\,, \tag{11.33a}$$

$$\delta \dot{\psi} = -\frac{\partial H}{\partial \delta I} = -\frac{fk}{\omega_0(\alpha + 1)} \, \delta \psi + \frac{3\beta}{4\omega_0} \, \delta I \,. \tag{11.33b}$$

We proceed now to find the local maxima and period of δI and $\delta \psi$ [6]. Consider the adiabatic invariant [14]

$$J = \frac{1}{2\pi} \oint \delta I d(\delta \psi) \approx \text{constant} . \tag{11.34}$$

|J| represents the area of the ellipse defined by (11.32). Therefore,

$$J = \frac{2H}{f\sqrt{\alpha + 1}} \approx \text{constant} \,. \tag{11.35}$$

For $k \ll 1$ one can neglect the term with $\delta I \delta \psi$ in |J|. The result is

$$|J| = \frac{3|\beta|}{4\omega_0 f \sqrt{\alpha + 1}} (\delta I)^2 + \frac{f \sqrt{\alpha + 1}}{3\omega_0 |\beta|} (\delta \psi)^2.$$
(11.36)

Both terms in (11.36) are positive. As a consequence of it, when one term becomes a maximum then the other would vanish. Consequently, the maxima of δI and $\delta \psi$ denoted as δI_{max} and $\delta \psi_{\text{max}}$, respectively, are given by

$$\delta I_{\text{max}}(t) = \left(\frac{4\omega_0 f \sqrt{\alpha + 1}}{3|\beta|}\right)^{1/2} , \qquad (11.37a)$$

$$\delta\psi_{\text{max}}(t) = \left(\frac{3\omega_0|\beta|J}{f\sqrt{\alpha+1}}\right)^{1/2} . \tag{11.37b}$$

The period of oscillations of the action and phase given by $T = 2\pi (\partial J/\partial H)$ is

$$T = \frac{4\pi}{f\sqrt{\alpha + 1}}\tag{11.38}$$

which decreases with increase in t. It is possible to find the analytical solution of (11.33).

11.3.4 Analytical Solution of Equation (11.33)

From (11.33), the second-order linear equation for $\delta \psi$ is obtained as

$$\ddot{\delta\psi} + \omega^2(t)\delta\psi = 0 , \quad \omega^2(t) = \frac{f^2(\alpha + 1)}{4\omega_0^2} ,$$
 (11.39)

where the term containing μ^2 is neglected since $\mu \ll 1$. With the change of variable $\tau = \alpha = 4\omega_0 \mu t/f$ the above equation becomes

$$(\delta\psi)'' + \frac{(\tau+1)}{4k^2}\psi = 0.$$
 (11.40)

Its general solution can be written in terms of Airy functions [15]. A simple form of $\delta \psi(t)$ can then be obtained for a large argument of the Airy functions. In [6] using the WKB method the solution of (11.39) is found as

$$\delta\psi(t) = \frac{\sqrt{2kc}}{(\alpha+1)^{1/4}}\cos\left(q_0 + \frac{(\alpha+1)^{3/2} - 1}{3k}\right),\tag{11.41}$$

where c and q_0 are to be determined. Substitution of (11.41) in (11.33b) gives, in the second-order accuracy,

$$\delta I(t) = -\frac{2f\sqrt{2kc}(\alpha+1)^{1/4}}{3\beta}\sin\left(q_0 + \frac{(\alpha+1)^{3/2} - 1}{3k}\right). \tag{11.42}$$

To find c, consider the sum of the squares of Eqs. (11.41) and (11.42):

$$2kc = \sqrt{\alpha + 1} (\delta \psi)^2 + \frac{9\beta^2}{4f^2 \sqrt{\alpha + 1}} (\delta I)^2.$$
 (11.43)

Comparison of this equation with Eq. (11.36) gives

$$c = \frac{3\omega_0|\beta|J}{2fk} \,. \tag{11.44}$$

Then q_0 in Eq. (11.41) is determined by the initial condition. The phase ψ and the action I are given by $\psi = \delta \psi + \psi^*$ and $I = \delta I + I^*$. Theoretically predicted I(t), $\psi(t)$, $I_{\text{max}}(t)$ and $\psi_{\text{max}}(t)$ are found to be in very good agreement with the numerical simulation [6].

11.3.5 Dynamics for Arbitrary Initial Conditions

It is possible to determine the maximum (and minimum) deviations of I and ψ denoted as δI_{max} (δI_{min}) and $\delta \psi_{\text{max}}$ ($\delta \psi_{\text{min}}$), respectively.

From Eq. (11.32) let us write

$$I_{\pm} = -\frac{f}{3\beta} (\alpha + \cos 2\psi) \pm \left[\frac{f^2}{9\beta^2} (\alpha + \cos 2\psi)^2 + \frac{8\omega_0}{3\beta} H \right]^{1/2} . \tag{11.45}$$

When $I=I_{\max}$ or $I=I_{\min}$, because of $\dot{I}=0$ the phase $\psi=0$. Denote the $H(I,\psi=0)$ corresponding to $I=I_{\max}$ and I_{\min} as $H_{\rm up}$ and $H_{\rm d}$, respectively, one can write

$$I_{\text{max,min}} = -\frac{f(\alpha+1)}{3\beta} \pm \left[\frac{f^2(\alpha+1)}{9\beta^2} + \frac{8\omega_0}{3\beta} H_{\text{u,d}} \right]^{1/2} . \tag{11.46}$$

Using the fact that $\dot{\psi} = 0$ at $\psi = \psi_{\text{max}}$ and ψ_{min} in Eq. (11.21b) gives $I = -(f/3\beta)(\alpha + \cos 2\psi)$. This in turn in (11.22) yields

$$H_{\rm r,l} = -\frac{f^2}{24\omega_0\beta}(\alpha + \cos 2\psi_{\rm max,min})^2$$
, (11.47)

where r and l refer to right and left, respectively. The above equation gives

$$\psi_{\text{max,min}} = \pm \frac{1}{2} \cos^{-1} \left[\left(-\frac{24\omega_0 \beta}{f^2} H_{\text{r,l}} \right)^{1/2} - \alpha \right].$$
(11.48)

Knowing the value of $H_{\rm u}$, $H_{\rm d}$, $H_{\rm r}$ and $H_{\rm l}$ the values of $I_{\rm max}$, $I_{\rm min}$, $\psi_{\rm max}$ and $\psi_{\rm min}$ can be calculated. The theoretical predictions are found to be in good agreement with the numerical results [6].

11.3.6 Effect of Damping

From (11.20) after some simple algebra the quasi-equilibrium point is obtained as

$$a^* = \left(\frac{-2f}{3\beta}\right)^{1/2} \left[\alpha + \left(1 - \frac{4\omega_0^2 d^2}{f^2}\right)^{1/2}\right]^{1/2}, \qquad (11.49a)$$

$$\psi^* = \frac{1}{2}\sin^{-1}\left[\frac{2\omega_0 d}{f} + \frac{2k}{\alpha + (1 - 4\omega_0^2 d^2/f^2)^{1/2}}\right]$$
(11.49b)

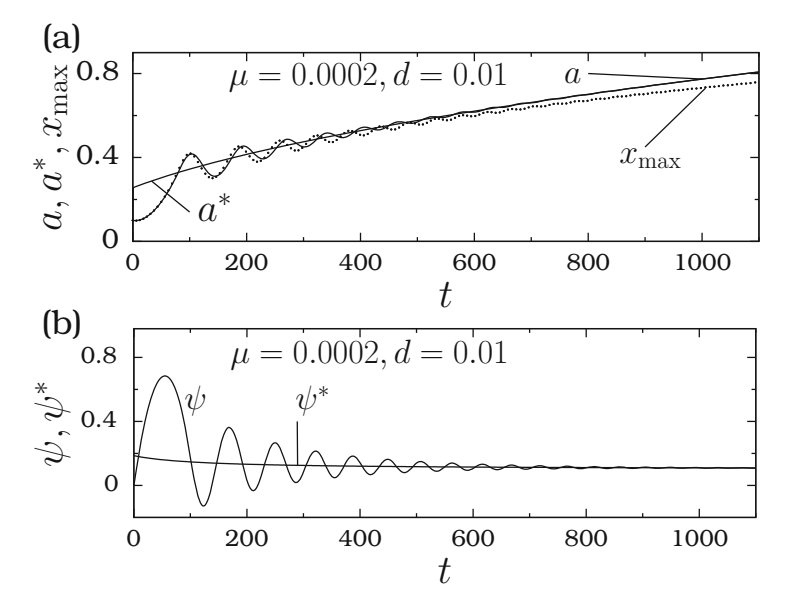


Fig. 11.7 (a) a(t), $a^*(t)$, $x_{\max}(t)$, and (b) $\psi(t)$ and $\psi^*(t)$ versus t for the Duffing oscillator for $\omega_0^2 = 1$, f = 0.1, d = 0.01, $\beta = -1$ and $\mu = 0.0002$

with $d < f/2\omega_0$. Figure 11.7 presents the variation of a(t), $a^*(t)$, $x_{\max}(t)$, $\psi(t)$ and $\psi^*(t)$ for $\omega_0^2 = 1$, f = 0.1, d = 0.01, $\beta = -1$ and $\mu = 0.0002$. As t increases from 0, $a(t) \to a^*(t)$. Further, a(t) obtained by solving (11.20) closely matches with the numerically computed x_{\max} solving the system (11.15) for small values.

11.4 Autoresonance and Limiting Phase Trajectories

In the previous two sections we have considered a nonlinear system subjected to (1) an additive driving force and (2) a parametric perturbation both with time-varying frequency. This section considers a nonlinear system with an additive external force with fixed frequency while assuming the coefficient of the linear term nonoscillating and monotonically increasing with time. Kovaleva and Manevitch [16] investigated the condition for the transitions from bounded oscillations to autoresonance.

Consider the following undamped and periodically driven Duffing oscillator equation with the coefficient of the linear term as time-varying [16]:

$$\ddot{x} + (1 - 2\epsilon \zeta(\tau_1))x + \epsilon \delta \alpha x^3 = 2\epsilon F \sin t , \qquad (11.50)$$

where $\zeta_1 = \epsilon t$, $\zeta(\tau_1) = s + b\zeta_1^n$, $s, \alpha > 0$ and $\epsilon > 0$ is a small parameter.

11.4.1 Approximate Solution

Solution (11.50) in the limit of $t \to \infty$ for $\epsilon \ll 1$ can be obtained by applying the method of multiple scale [17]. Introduce the complex conjugate change of variables

$$\Phi = y + ix, \quad \Phi^* = y - ix.$$
 (11.51)

Writing Eq. (11.50) as

$$\dot{x} = y \,, \tag{11.52a}$$

$$\dot{y} = -[1 - 2\epsilon \zeta(\tau_1)] x - \delta \epsilon \alpha x^3 + 2\epsilon F \sin t \qquad (11.52b)$$

and replacing x and y in terms of Φ and Φ^* result in

$$\dot{\Phi} = i\Phi - i\epsilon\zeta\Phi + i\epsilon\zeta\Phi^* - i\epsilon\alpha(\Phi - \Phi^*)^3 + 2\epsilon F \sin t. \tag{11.53}$$

The multiple-scale method begins by writing approximate solution in the series form as

$$\Phi(t,\epsilon) = \Phi_0(\tau_0, \tau_1) + \epsilon \Phi_1(\tau_0, \tau_1) . \tag{11.54}$$

With $d/dt = \partial/\partial \tau_0 + \epsilon \partial/\partial \tau_1$, $\tau_0 = t$ and $\tau_1 = \epsilon t$ where τ_0 and τ_1 are the fast and slow time-scales, respectively, Eq. (11.53) becomes

$$\frac{\partial \Phi_0}{\partial \tau_0} + \epsilon \frac{\partial \Phi_0}{\partial \tau_1} + \epsilon \frac{\partial \Phi_1}{\partial \tau_0} = i\Phi_0 + i\epsilon\Phi_1 - i\epsilon\zeta\Phi_0 + i\epsilon\zeta\Phi_0^*
-i\epsilon\alpha(\Phi_0 - \Phi_0^*)^3 - i\epsilon F \left[e^{i\tau_0} - e^{-i\tau_0}\right], \quad (11.55)$$

where terms containing ϵ^2 and higher powers of ϵ are neglected. The leading order approximation gives

$$\frac{\partial \Phi_0}{\partial \tau_0} = i\Phi_0 \ . \tag{11.56}$$

the solution of (11.56) is $\Phi_0(\tau_0, \tau_1) = \Phi_0(\tau_1) e^{i\tau_0}$ where $\Phi_0(\tau_1)$ is a slow function. Equation (11.56) with terms containing ϵ after substitution of $\Phi_0 = \Phi_0 e^{i\tau_0}$ is

$$\frac{\partial \Phi_{1}}{\partial \tau_{0}} + \frac{d\Phi_{0}}{d\tau_{1}} e^{i\tau_{0}} = i\Phi_{1} - i\zeta\Phi_{0}e^{i\tau_{0}} + i\zeta\Phi_{0}^{*}e^{-i\tau_{0}}
-i\alpha \left(\Phi_{0} - \Phi_{0}^{*}\right)^{3} - iF\left(e^{i\tau_{0}} - e^{-i\tau_{0}}\right) .$$
(11.57)

Secular growth of $\Phi_1(\tau_0, \tau_1)$ in τ_0 to be avoided which gives

$$\frac{d\Phi_0}{d\tau_1} = -i\zeta \Phi_0 + 3i\alpha \Phi_0^* \Phi_0^2 - iF. \qquad (11.58)$$

The parameter β in Eq. (11.58) can be eliminated by the change of variables

$$\tau = s\tau_1, \ \beta = \frac{b}{s^{n+1}}, \ \psi(\tau_1) = \left(\frac{3\alpha}{s}\right)^{1/2} \Phi_0(\tau_1), \ f = F\left(\frac{3\alpha}{s}\right)^{1/2}.$$
 (11.59)

Equation (11.58) then takes the form

$$\frac{\mathrm{d}\psi}{\mathrm{d}\tau} = -\mathrm{i}\left(1 + \beta\tau^n - |\psi|^2\right)\psi - \mathrm{i}f. \tag{11.60}$$

In terms of the polar representation $\psi = a e^{i\Delta}$ with a > 0 the above equation is rewritten as

$$(\dot{a} + ia\Delta)e^{i\Delta} = -i\left(1 + \beta\tau^n - a^2\right)ae^{i\Delta} - if, \qquad (11.61)$$

where an over dot refers to differentiation with respect to τ . Equating the real and imaginary parts of Eq. (11.61) separately to zero and after some simple algebra one arrives to

$$\dot{\Delta} = -1 - \beta \tau^n + a^2 - \frac{f}{a} \cos \Delta . \tag{11.62b}$$

In the leading-order approximation, the solution of Eq. (11.50) is

$$x(t) = \left(\frac{s}{3\alpha}\right)^{1/2} a(\tau_1) \sin(\Delta + \tau_0) . \tag{11.63}$$

The nature of x(t) is thus completely determined by the amplitude a and the phase Δ . The system (11.50) is not excited if $a(\tau_1) = 0$. Assume that a(0) = 0.

11.4.2 Limiting Phase Trajectories

When $\beta = 0$ (that is b = 0 in $\zeta(\tau_1)$) then dH/dt = 0 where

$$H = a\left(-\frac{1}{2}a + \frac{1}{4}a^3 - f\cos\Delta\right). \tag{11.64}$$

H is a constant of motion and is zero for $a(\tau_1) = 0$ or for

$$a^3 - 2a - 4f\cos\Delta = 0. {(11.65)}$$

For $\beta = 0$ the equilibrium points of (11.62) are defined through

$$\Delta^* = 0$$
, $a^{*3} - a^* - f = 0$, (11.66a)

$$\Delta^* = 0$$
, $a^{*3} - a^* + f = 0$, (11.66b)

where the range of Δ^* is considered as $\Delta^* \in [-2\pi, 2\pi]$.

For $\beta = 0$ and f = 0.25 the equilibrium points of (11.64) are

$$\left(\Delta_{\rm e}^*, a_{\rm e}^*\right) = (0, 1.10716), \ (\pm \pi, 0.26959),$$
 (11.67a)

$$(\Delta_s^*, a_s^*) = (\pm \pi, 0.83757)$$
 (11.67b)

The points $(\Delta_{\rm e}^*, a_{\rm e}^*)$ are elliptic type and $(\Delta_{\rm s}^*, a_{\rm s}^*)$ are saddles. Equation (11.64) indicates that for a(0)=0, if $\Delta(0)=\pm\pi/2$ then H(0)=0. Thus, $H(\tau)=0$ for orbits starting from a(0)=0, $\Delta(0)=\pm\pi/2$, $\pm3\pi/2$. For a(0)=0, $\Delta(0)=-\pi/2$ to $\pi/2$, $3\pi/2$ to 2π , $-3\pi/2$ to -2π the quantity H is < 0 while for other values of $\Delta(0)$ and a(0)=0 the quantity H>0.

Figure 11.8a depicts the phase trajectories of (11.62) for $\beta=0$ and f=0.25. This figure is obtained for a set of initial conditions. In this figure the stable elliptic equilibrium points and saddles are marked by solid circles and 'x', respectively. The dashed orbits are the heteroclinic orbits connecting two saddles. The thick orbits correspond to the initial conditions a(0)=0, $\Delta(0)=-\pi/2$ and $3\pi/2$ and $a(0)=\sqrt{2}$, $\Delta(0)=-\pi$. In Fig. 11.8b $a(\tau)$ versus τ is shown. The sign of H of some of the orbits in Fig. 11.8a is indicated. H is nonzero for the heteroclinic orbits. For f=0.25 the value of H for the heteroclinic orbits is -0.01833. The thick orbits are

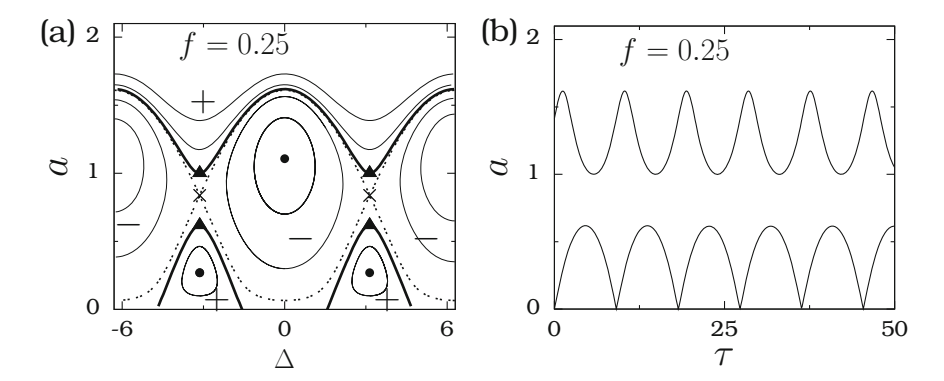


Fig. 11.8 (a) Phase space orbits of the system (11.64) for $\beta = 0$ and f = 0.25. For details see the text. (b) Two limiting phase trajectories for which H = 0

the boundaries between the orbits with H > 0 and H < 0. Such orbits are termed as the *limiting phase orbits* [17, 18] or the *limiting phase trajectories* (LPT). LPTs can be effectively used to describe the strong energy exchange between coupled systems or targeted energy transfer to a system from an energy source. It has been shown that autoresonance is due to the loss of stability of the limiting phase orbits of small oscillations [17, 18].

Equations (11.64) and (11.65) imply that for $\Delta(0) = -\pi/2$ there are either three real values of a(0) or only one real value of a(0) giving rise to LPT. For simplicity, consider the LPT with $\Delta(0) = -\pi/2$. In this case Eq. (11.65) becomes $a(a^2-2)=0$ giving a(0)=0, $\sqrt{2}$ (discard the choice $a(0)=-\sqrt{2}$ because it is < 0). Thus, there are two LPTs. Since the system (11.62) with $\beta=0$ is an autonomous system the part of LPT with $\Delta(0)=-\pi/2$ and $a(0)=\sqrt{2}$ right to $\Delta(0)=-\pi/2$ is obtained by integrating (11.62) in the forward time direction while the part lying left to $\Delta(0)=-\pi/2$ is computed by integrating (11.62) in the backward time direction (that is, replacing dt by -dt in Eq. (11.62) and then integrating it in the forward time direction). The two LPTs are shown in Fig. 11.8b. These two LPTs are functions of the parameter f. Denote the lower and upper LPTs as LPT₁ and LPT_u, respectively.

What will happen to the two orbits LPT₁ and LPT_u when f is varied from a small value? To find out this, consider the point $\Delta = -\pi$. In Fig. 11.8a at $\Delta = -\pi$, LPT_u becomes a minimum while LPT₁ becomes a maximum. Substitution of $\Delta = -\pi$ in Eq. (11.65) gives

$$a^* - 2a + 4f = 0. (11.68)$$

Its roots denoted as a' are the values of the maximum of LPT₁ and the minimum of LPT_u, respectively. Figure 11.9 presents the variation of equilibrium points of (11.66) and the roots of (11.68). The equilibrium points and only the roots that are > 0 are plotted in the figure. At a value of f the minimum and maximum of both

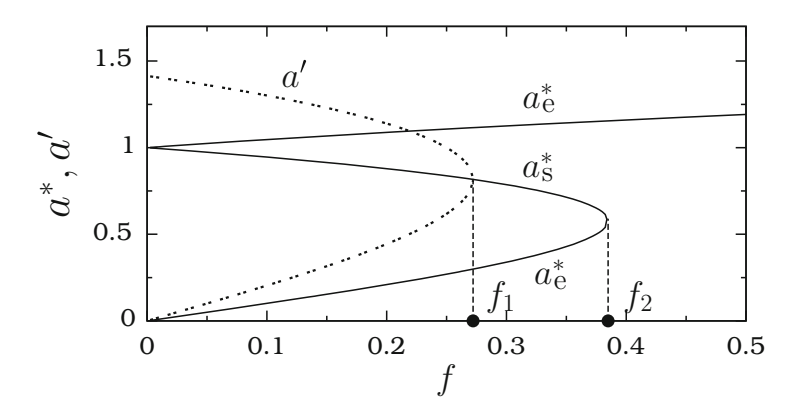


Fig. 11.9 a^* and a' as a function of the parameter f with $\beta = 0$. For details see the text

LPTs merge with the saddle point $(\Delta^*, a^*) = (-\pi, a_s^*)$. It is easy to determine the critical value of f at which above happens. This critical value f corresponds to a transition from three real roots to only one real root of (11.68). From (Appendix B), for the equation $y^3 + by + c = 0$ the condition for only one real root is $27c^2 + 4b^3 \le 0$. The critical value of f for Eq. (11.68) is $f_1 = \sqrt{2/27} \approx 0.27217$. For $f < f_1$ there are two LPTs and heteroclinic orbits lying between them. As f increases from a small value, the minimum of LPT_u and maximum of LPT₁ move towards the saddle point $(-\pi, a_s^*)$. At the threshold value $f = f_1$, the two LPTs merge with the heteroclinic orbits. The result is the amplitude of the orbit separating the orbits with H > 0 and H < 0 is large. This transition is essentially because of the loss of stability of the LPT of small oscillations. In Fig. 11.9 for values of f above a critical value (denote it as f_2) the system (11.62) with f = 0 has only one real equilibrium point which is of elliptic type. The value of f_2 is given by [obtained by setting the condition for only one real root of a in Eq. (11.66)]

$$f_2 = \frac{2}{\sqrt{27}} \approx 0.38490. \tag{11.69}$$

At this value of f the elliptic fixed points with $\Delta^* = \pm \pi$ coalesce with the two saddle points and disappear. The only equilibrium point is $(\Delta^*, a^*) = (0, a_c^*)$. Figure 11.10 illustrates the changes in the phase space trajectories in (Δ, a) phase space for three values of f. In all the subplots of Fig. 11.10 the thick orbits correspond to $(a(0), \Delta(0)) = (0, -\pi/2)$. $a(\tau)$ versus τ of the limiting phase orbit of the system is shown in Figs. 11.11a–c for f = 0.273, 0.37 and 0.39, respectively. In [16, 18] the system with $f < f_1, f_1 < f < f_2$ and $f > f_2$ are termed as quasilinear, moderately nonlinear and strongly nonlinear systems.

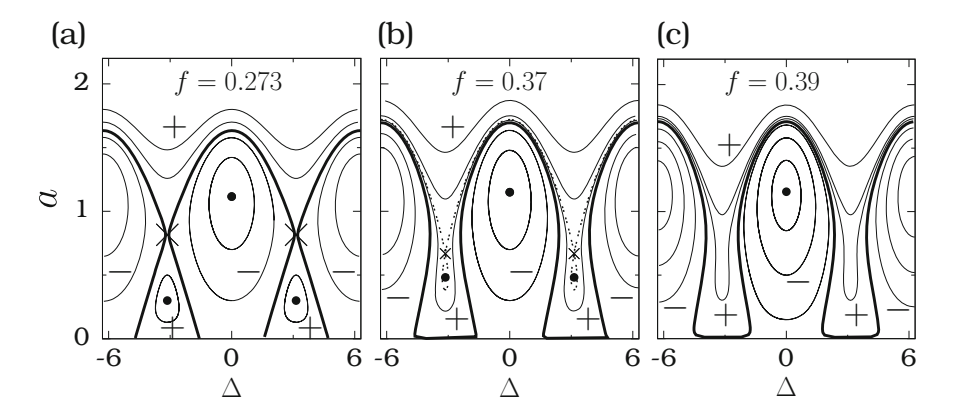


Fig. 11.10 Phase space trajectories of the system (11.62) for (a) f = 0.273, (b) f = 0.37 and (c) f = 0.39 with $\beta = 0$

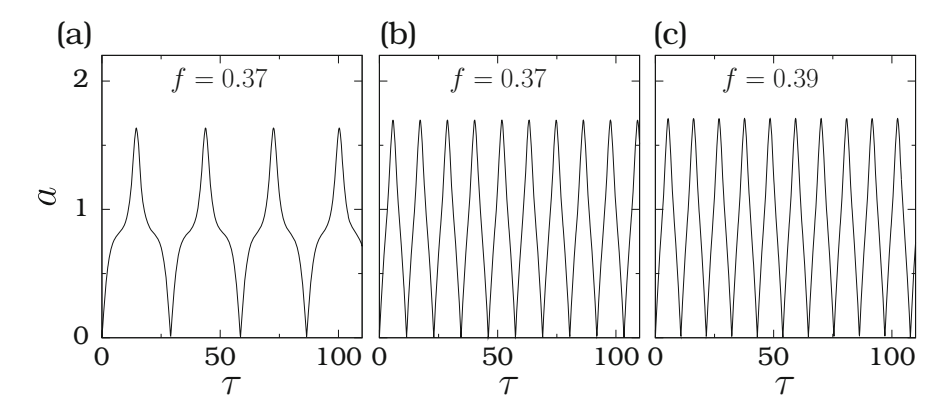


Fig. 11.11 $a(\tau)$ versus τ of the limiting phase orbit of the system (11.62) for the three values of f used in Fig. 11.10

11.4.3 Autoresonance

Now, we investigate the response of the system (11.62) with $\beta \neq 0$. Fix a(0) = 0 and $\Phi(0) = -\pi/2$ and restrict to n = 1 and n = 2. For $f < f_1$, in the numerical simulation $a(\tau)$ asymptotically approaches the upper (lower) branch of $a_{\rm e}^*$ for $\beta < 0$ ($\beta > 0$). In the long time limit $a(\tau)$ spirals about $a_{\rm e}^*$ and reach it in the limit $\tau \to \infty$. $a_{\rm e}^*$'s become a stable focus. That is, the system is shifted to the region of small and large oscillations for $\beta > 0$ and $\beta < 0$, respectively. Autoresonance does not occur.

For $f > f_1$, autoresonance takes place for a range of value of β . Figure 11.12 presents numerically computed $a(\tau)$ for two values of β for n = 1 and n = 2. When n = 1 and f = 0.3 growth of $a(\tau)$ occurs for $0 < \beta < 0.0231$. That is, autoresonance takes place. For $\beta > 0.0231$ there is no autoresonance and $a(\tau)$ approaches an equilibrium point. There are shown in Fig. 11.12a. For n=2 and f = 0.3 autoresonance is realized for $0 < \beta < 0.0058$ (Fig. 11.12b). For a short time interval the trajectory is found to be close to the LPT of quasilinear oscillations. However, in the autoresonance region the shape of $a(\tau)$ is similar to the LPT of the moderate nonlinear system ($\beta = 0$). That is, the growth of oscillation with an unbounded orbit from a bounded orbit in the system with slowly time-varying frequency ($\beta \neq 0$) is the same as that of the transition from a small to a large oscillation amplitude in the system with constant parameters $(\beta = 0)$. This essentially happens as a result of loss of stability of quasilinear oscillations. Interestingly, autoresonance occurs for certain range of values of β only for $f > f_1$. That is, $f > f_1$ where f_1 is the necessary condition for the occurrence of autoresonance.

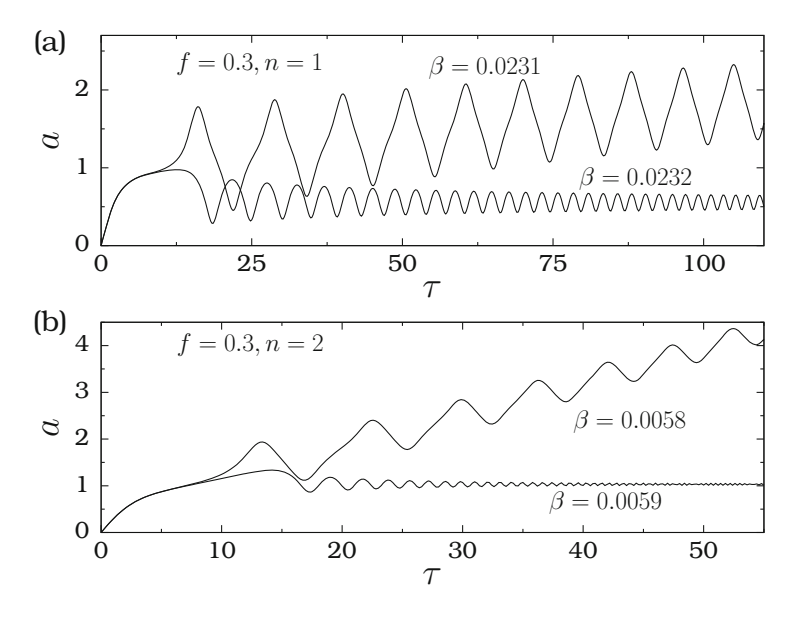


Fig. 11.12 $a(\tau)$ of the system (11.62) for two values of β with f = 0.3 and for two values of n

11.5 Autoresonance in Optical Guided Waves

The first observation of autoresonance in optics was reported in [19]. Consider a nonlinear two-coupled wave guides, in which one wave guide is spatially chirped by allowing its refractive index to increase monotonically in the direction of propagation of waves, and the medium exhibiting Kerr (cubic) nonlinearity. When refractive index profiles (linear + nonlinear) of the two wave guides are identical then a linear resonance occurs. The linear refractive index profile is

$$\Delta n_L(x,z) = \Delta n_1(x) + \Delta n_2(x)\alpha z \tag{11.70}$$

where $\Delta n_1(x)$ is a z-invariant symmetric couple profile while $\Delta n_2(x)$ represents the shape of the chirped wave guide and α is the linear spatial chirp rate and $-1/\alpha < z$. A pump wave is fed into the chirped wave guide and no input into the second wave guide.

The evolution of the envelope ψ is described by the nonlinear Schrödinger equation

$$-i\frac{\partial \psi}{\partial z} = \frac{\partial^2 \psi}{\partial z^2} + \left[\Delta n_{L}(x, z) + |\psi|^2\right] \psi . \qquad (11.71)$$

Assume the solution of (11.71) as

$$\psi = e^{i\beta_{0}z} \left[C_{R}(z) U_{R}(x) + C_{L}(z) U_{L}(x) \right] , \qquad (11.72)$$

where $U_{\rm L}$ and $U_{\rm R}$ are the eigenmodes of the left and right (chirped) wave guides, respectively, in the absence of nonlinearity and chirp. $C_{\rm L}$ and $C_{\rm R}$ are the amplitudes of $U_{\rm L}$ and $U_{\rm R}$, respectively, $\beta_0 = \int_{-\infty}^{\infty} U_{\rm R,L}^* H_0 U_{\rm R,L} dx$ and $H_0 = \partial^2/\partial x^2 + \Delta n_1(x)$ is the unperturbed Hamiltonian. Using the above form of ψ in Eq. (11.72) with $\kappa = \int_{-\infty}^{\infty} U_{\rm R}^* H_0 U_{\rm L} dx$, $\chi = 2 \int_{-\infty}^{\infty} |U_{\rm L}|^4 dx$ and $\Lambda_0 = \alpha \int_{-\infty}^{\infty} |U_{\rm R}|^2 \Delta n_2(x) dx$ leads to equations [19]

$$-i\dot{C}_{R} = \kappa C_{L} + \frac{\chi}{2}|C_{R}|^{2}C_{R} + \Lambda_{0}C_{R}z, \qquad (11.73a)$$

$$-i\dot{C}_{L} = \kappa C_{R} + \frac{\chi}{2}|C_{L}^{2}|C_{L},$$
 (11.73b)

where an overdot refers to differentiation with respect to z, In Eq. (11.73) R, χ and Λ_0 are the coupling coefficient, the effective nonlinearity and the effective chirp rate, respectively.

Assume that an initial wave packet ψ_i with the spatial form U_R is fed to the right wave guide. The equations for the population difference

$$R = (|C_{\rm L}|^2 - |C_{\rm R}|)/(|C_{\rm L}|^2 + |C_{\rm R}|^2)$$
(11.74)

and the phase mismatch $\phi = \theta_R - \theta_L$ where θ_R and θ_L are the phases of C_R and C_L , respectively, are obtained as

$$R' = -2\kappa\sqrt{1 - R^2}\sin\phi,\tag{11.75a}$$

$$\phi' = \Lambda_0 z - \frac{1}{2} \chi R |C_{R,i}|^2 + \frac{2\kappa R}{\sqrt{1 - R^2}} \cos \phi , \qquad (11.75b)$$

where $|C_{R,i}|$ is the amplitude of the wave fed into the right wave guide. If the refraction index does not cross the linear resonance then most of the power is concentrated in the right wave guide. In this case $|C_R| \gg |C_L|$ and $R \approx -1$. In Eq. (11.75b) when $\Lambda_{OZ} - \chi R |C_{R,i}|^2/2$ is zero then the linear resonance crossing takes place. After crossing the resonance the phase mismatch ϕ locks near zero and shows small autoresonant oscillations. As a result of this $|C_R|$ decreases to zero and $|C_L|$ increases almost to the value $|C_{R,i}|$ and R varies from -1 to 1. That is, a full power exchange results. The power flows unidirectionally from the right wave guide to the left wave guide thereby maintaining the refractive indices almost the same in spite of the chirp. The mechanism is that through nonlinearity the system self-adjusts to maintain resonance. In this way the wave guides are almost identical for long distance propagation. z and $|C_{R,i}|$ determines the limiting value of α . The transition to autoresonance takes place when $T=2.45\kappa\sqrt{\chi}|C_{R,i}|(\Lambda_0)^{-34}=1$. By

controlling $|C_{R,i}|$ this threshold can be achieved. No power propagates from right wave guide to the left wave guide for below the threshold. All the power tunnels above the threshold. When T < 1 the system crosses the linear resonance, but the nonlinear index variation rate in the left wave guide is too small to follow the variation in the right wave guide. So there is no phase lock and transfer of power is inefficient. On the other hand, for T > 1 power tunnels from one wave guide to another wave guide because in the left wave guide the variation of rate of the nonlinear index is enough to follow the variations in the right wave guide. The above theoretical predictions have been verified in an experiment with SBN:75 crystal. For details refer to [19].

11.6 Energy Conversion in a Four-Wave Mixing

The nature of wave propagation in a medium significantly depends on the type of nonlinearities present in it. For example, in a single wave propagation a lowest-order nonlinearity gives rise to a third-order self-modulation. When many different waves are made to propagation in a nonlinear medium, then apart from self-modulation other phenomena such as cross-modulation and wave mixing occur also due to resonant wave interactions (RWI). A RWI of two waves consists of a linear mixing term and the phase mismatch $\psi = \phi_1 \pm \phi_2$. A three-wave RWI involves mixing terms with product of two envelopes and $\psi = \phi_1 \pm \phi_2 \pm \phi_3$. If the three-wave resonance is not possible, then the four-wave mixing with $\psi = \phi_1 \pm \phi_2 \pm \phi_3 \pm \phi_4$ and product of three envelopes is important. In a plasma an incoming laser can decay via RWIs into another ion-acoustic or electrostatic plasma waves and electromagnetic waves [20]. RWIs are important in plasma [21], nonlinear optics [22], acoustics [23] and hydrodynamics [24].

In driven or interacting oscillatory or wave systems an autoresonance scheme can be utilized in order to

- maintain resonance even if the parameters of the system change in space and time slowly and
- transfer energy among the interacting waves efficiently.

Interestingly, autoresonant wave mixing suggests a new application of optical parametric amplification (OPA) [25–27]. Now, we proceed to illustrate the autoresonant four-wave mixing (FWM) process in an optical fiber [25].

Consider the following set of equations for slow wave envelopes A_l describing the interaction between four waves in a nondegenerate process in an optical fiber [28]:

$$\frac{dA_l}{dz} = i\gamma \left(|A_l|^2 A_l + 2 \sum_{j \neq l=1}^4 |A_j|^2 A_l + 2A_m A_n A_k^* e^{i\epsilon \psi} \right), \qquad (11.76)$$

where the phase mismatch $\psi = \int_0^z \Delta\beta(z')\mathrm{d}z'$ with $\Delta\beta(z) = -(\beta_1 + \beta_2) + (\beta_3 + \beta_4)$, β_l is the wavevector of the lth wave, γ is the nonlinear coefficient, l=1,2,3,4 and k,l,m and n are integers such that for l=1 or 2 (the two pump waves) the values of the other integers are k=3-l,m=3,n=4 and $\epsilon=1$. If l=3 or 4 (the signal and the idler) then k=7-l,m=1,n=2 and $\epsilon=-1$. In Eq. (11.76) $A_l(z)$ is the envelope of the electric field of the lth wave so that $E_l(z,t)=A_l(z)\mathrm{e}^{\mathrm{i}(\beta_lz-\omega_lt)}$. Defining $\zeta=\gamma P_0z$ with P_0 being the total power of the signal, $a_l=A_l/\sqrt{P_0}$ with $\sum_{l=1}^4 |a_l|^2=1$ and phase mismatch $S=\psi/(\gamma P_0)$ Eq. (11.76) becomes

$$\frac{da_l}{d\zeta} = i\left(2 - |a_l|^2\right)a_l + 2ia_m a_n a_k^* e^{i\epsilon S(\zeta)}, \quad l = 1, 2, 3, 4.$$
(11.77)

Next, we represent a_l 's and the phase mismatch Φ as

$$a_l = b_l e^{i2\zeta}, \quad l = 1, 2, 3, \quad a_4 = b_4 e^{-i(-2\zeta + S)},$$
 (11.78a)

$$b_l = B_l e^{i\phi_l}, \quad B_l = |b_l|, \quad \phi_l = \arg(b_l),$$
 (11.78b)

$$\Phi = -(\phi_1 + \phi_2) + (\phi_3 + \phi_4) . \tag{11.78c}$$

These transform Eq. (11.77) into

$$\frac{\mathrm{d}B_l}{\mathrm{d}t} = -2\epsilon B_k B_m B_n \sin \Phi, \quad l = 1, 2, 3, 4 \tag{11.79a}$$

$$\frac{\mathrm{d}\Phi}{\mathrm{d}\zeta} = R + Q\cos\Phi,\tag{11.79b}$$

where

$$R = B_1^2 + B_2^2 - B_3^2 - B_4^2 + \frac{\Delta\beta}{\nu P_0} , \qquad (11.80a)$$

$$Q = 2B_1 B_2 B_3 B_4 \left(-\frac{1}{B_1^2} - \frac{1}{B_2^2} + \frac{1}{B_3^2} + \frac{1}{B_4^2} \right) . \tag{11.80b}$$

Further, Eq. (11.79a) give the so-called Manley-Rowe relations

$$B_1^2 = B_{10}^2 + B_{40}^2 - B_4^2$$
, (11.81a)

$$B_2^2 = B_{20}^2 + B_{40}^2 - B_4^2 \,, \tag{11.81b}$$

$$B_3^2 = B_{30}^2 - B_{40}^2 + B_4^2 \,, \tag{11.81c}$$

where $B_{l0}(z=0)$ are the initial amplitude of *l*th wave.

Next, for simplicity we assume that $\Delta\beta$ is a linear function of position z and define α as the nonuniformity rate coefficient such that $\Delta\beta = \alpha(\gamma P_0)^2(z-z_0)$ where z_0 denotes the point at which $\Delta\beta = 0$. Further, we define a shifted normalized

coordinate

$$\xi = \frac{\Delta B_0^2}{\alpha} - \gamma P_0 z_0 + \zeta , \quad \Delta B_0^2 = B_{10}^2 + B_{20}^2 - B_{30}^2 - B_{40}^2 .$$
 (11.82)

Then, Eq. (11.79) take the form

$$\frac{\mathrm{d}\Phi}{\mathrm{d}\xi} = \alpha\xi - 4B_4^2 + Q\cos\Phi , \qquad (11.83b)$$

with $B_{1,2,3}$ are given by Eq. (11.81).

In the system (11.83), the spatial chirp rate α can be < 0 (or > 0) corresponding to the increasing or decreasing the radius of the fiber. Fix the initial time as $B_{10}^2 = B_{20}^2 = 0.49$, $B_{30}^2 = B_{40}^2 = 0.01$, $\Phi(-40) = 0$ and $B_4^2(-40) = 0.01$. Convert the phase mismatch ϕ into the range [-1, 1] for convenience. Figure 11.13 presents the numerically computed solutions of Eq. (11.83) for $\alpha = \pm 0.1$. For $\alpha = 0.1$ (Fig. 11.13a, b) the evolution of the system essentially consists of three main stages [25].

- $|\alpha|\zeta < -2$ is the *first initial stage*. In this stage Φ exhibits bounded oscillations around the average value of $\Phi \approx 0$. Its oscillations decrease as $|\alpha|\xi$ approach -2. Also, in Fig. 11.13 one does not observe a considerable transfer of energy from the pumps $(B_1 \text{ and } B_2)$ to the signal (B_3) and idler (B_4) .
- The second stage corresponds to $-2 < |\alpha|\xi < 4$ and is the autoresonant stage. This interval involves an efficient excitation of the signal and the idler with continuing phase-lock. On average, the square of the amplitudes of the four waves vary linearly with $|\alpha|\xi$. There are slow oscillating modulations. The amplification continues until almost complete pump depletion realized at $|\alpha|\xi \approx 4$.
- $|\alpha|\xi > 4$ is the *final stage*. In this stage, the signal and the idler attain saturation while the pumps decay.

Figures 11.13c, d depict the results for $\alpha=-0.1$. The qualitative dynamics for $\alpha=-0.1$ is almost similar to $\alpha=0.1$. The autoresonant second stage is how $-2<|\alpha|\xi<0$. In the initial phase-locking process the average value of $\Phi\approx\pi$. For higher values of α the autoresonant process is absent, an example for this is shown in Fig. 11.14 for $\alpha=1.5$.

The theoretical treatment presented in Sects. 11.3 and 11.4 for the deep understanding of the autoresonance in Duffing oscillators can be extended to the FWM system also. In [26] the autoresonant TWM process has been investigated. There are differences between autoresonant states in TWM and FWM. For details see [26].

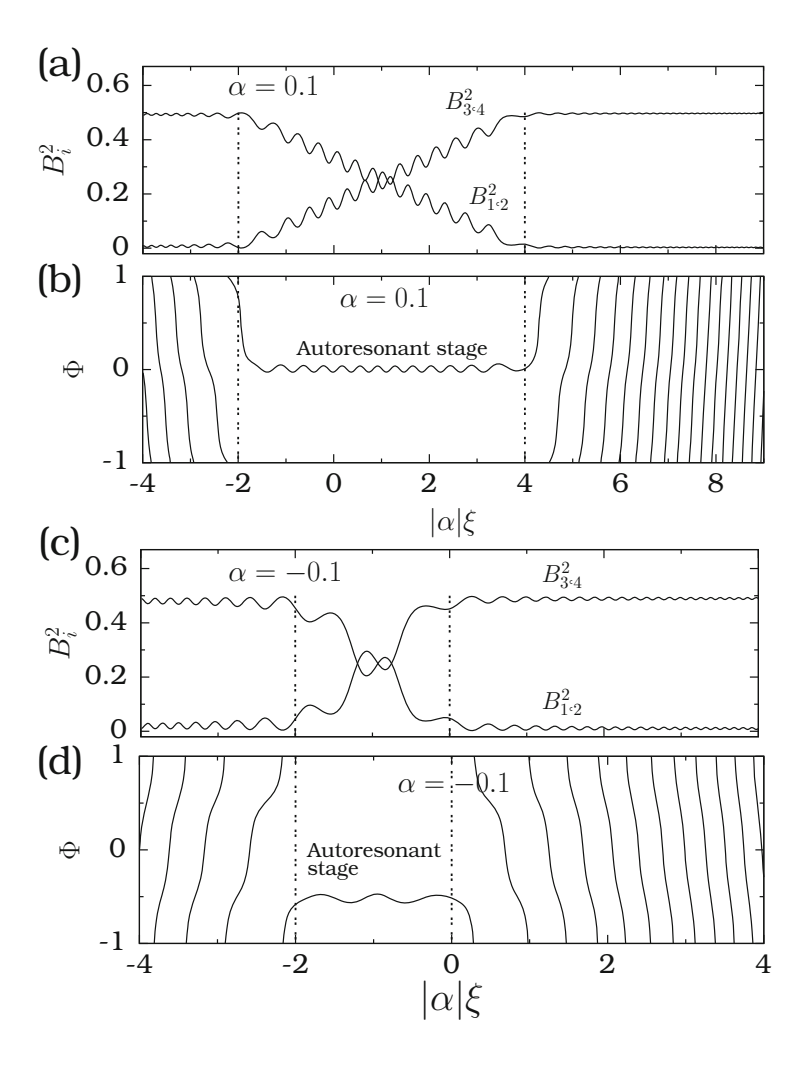


Fig. 11.13 Numerically computed wave envelopes B_l^2 and phase mismatch Φ for $\alpha=0.1$ and $\alpha=-0.1$

11.7 Autoresonance in a Nonlinear Wave System

An important nonlinear partial differential equation possessing a variety of localized solutions called solitons is the nonlinear Schrödinger equation (NLSE) $i\psi_t + \psi_{xx} + |\psi|^2\psi = 0$ This section explores the autoresonant excitation of a nonlinear wave of NLSE [29].

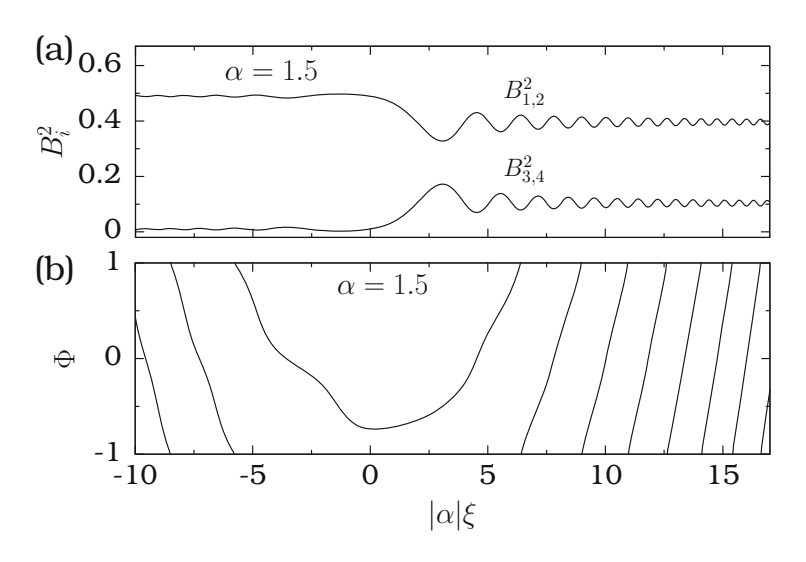


Fig. 11.14 Same as Fig. 11.13 but for $\alpha = 1.5$

Let us consider the driven NLSE

$$i\psi_t + \psi_{xx} + |\psi|^2 \psi = \epsilon e^{i(k_0 x - k_0^2 t + \phi(t))} = g(x, t)$$
, (11.84)

where g(x, t) is a plane wave with the wave vector k_0 and slowly varying frequency $k_0^2 - \Lambda(t)$ where $\Lambda(t) = \mathrm{d}\phi/\mathrm{d}t$. Assume the solution of (11.84) as

$$\psi(x,t) = a(x,t)e^{i(k_0x - k_0^2t + \theta(x,t))}$$
(11.85)

with $\text{Im}(a, \theta) = 0$. Defining $ae^{i\theta}$ as f, $v = 2k_0$ and then substituting (11.85) in (11.84) give

$$if_t + ivf_x + f_{xx} + |f|^2 f = \epsilon e^{i\phi(t)}$$
 (11.86)

Equating the real and imaginary parts of Eq. (11.86) separately to zero and defining $\Phi = \theta - \phi(t)$ lead to the equations

$$a_t + va_x + a\Phi_{xx} + 2a_x\Phi_x = -\epsilon\sin\Phi , \qquad (11.87a)$$

$$a(\Phi_t + v\Phi_x) - a_{xx} + a\Phi_x^2 + \Lambda a - a^3 = -\epsilon \cos \Phi . \qquad (11.87b)$$

For the solution with $\psi(x, t = t_0) = \psi_0$, where $|\psi_0| \ll 1$ and is independent of x, Eq. (11.87) becomes

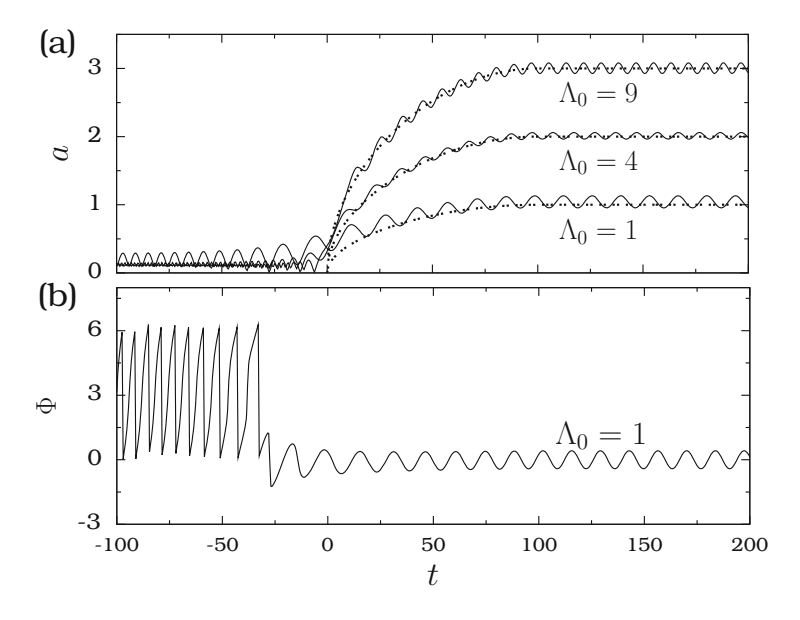


Fig. 11.15 (a) a(t) and (b) $\Phi(t)$ versus t for the NLSE for three values of Λ_0 and for $\epsilon = 0.1$, $T_0 = 100$, $a(-T_0) = 0.1$ and $\Phi(-T_0) = \pi$. Dashed lines represent $\sqrt{\Lambda(t)}$ for t > 0

$$a\Phi_t = a^3 - \Lambda(t)a - \epsilon\cos\Phi . \qquad (11.88b)$$

With $I = a^2$ the Hamiltonian of (11.88) is

$$H(I, \theta, t) = \frac{1}{2}I^2 + 2\epsilon\sqrt{I}\cos(\theta - \phi)$$
. (11.89)

That is, Eq. (11.88) can be thought of as a system with the Hamiltonian $H(I, \theta, t)$. Now, choose

$$\Lambda(t) = \begin{cases} \Lambda_0 \sin(\pi t/2T_0), & -T_0 \le t \le T_0 \\ \Lambda_0, & t > T_0. \end{cases}$$
 (11.90)

Figure 11.15 presents the variation of the amplitude a and the phase mismatch Φ (mod 2π) for $\epsilon=0.1$, $T_0=100$, $a(-T_0)=0.1$, $\phi(-T_0)=\pi$ and for three values of Λ_0 . Solution for t<0 corresponds to initial phase-locking stage. After phase-locking, a typical autoresonance dynamics occurs where the phase mismatch is close to zero. Further, for $t\gg 1$ the amplitude a(t) closely follows $\sqrt{\Lambda(t)}$, that is $a^2(t)\approx \Lambda(t)$ (driving frequency). Equilibrium points of (11.88) can be easily obtained. Equation (11.88a) gives $\Phi^*=0$. Then in the equation $a^3-a\Lambda(t)-\epsilon=0$ [refer Eq. (11.88b)] neglecting ϵ due to its smallness one gets $a^*\approx 0$ and $a^*\approx 0$

 $\sqrt{\Lambda(t)}$. That is, a(t) and $\Phi(t)$ vary around the nontrivial quasi-equilibrium point $a^* \approx \Lambda_0(t)$, $\Phi^* = 0$. $\Lambda(t) = \Lambda_0$ for $t > T_0$. When $\Lambda(t) \approx \Lambda_0$ the wave solution is given by

$$\psi \approx \sqrt{\Lambda_0} e^{i(k_0 x - k_0^2 t + \Lambda_0 t)} . \tag{11.91}$$

To study the stability of the autoresonant solution, we substitute $a=a^*+\delta a$, and $\Phi=\Phi^*+\delta \Phi$ in Eq. (11.88) and linearize it around (A^*,Φ^*) . Then writing δa , $\delta \Phi\approx \mathrm{e}^{\mathrm{i}\kappa x-\nu t}$ gives rise to the relation

$$(v - \kappa v)^2 = \left(\kappa^2 - \frac{\epsilon}{a^*}\right) \left(\kappa^2 - 2\Lambda_0 - 3\frac{\epsilon}{a^*}\right). \tag{11.92}$$

The above equation indicates an instability for $\epsilon/a^* < \kappa^2 < 2\Lambda_0 + 3\epsilon/a^*$. Note that when $\epsilon = 0$ the plane wave solution is always unstable for sufficiently small κ . But when $\epsilon \neq 0$, there is a stability window $\kappa^2 < \epsilon/a^*$ for the autoresonant solution. That is, the plane wave solution can be stabilized by an appropriate autoresonant driving.

For a detailed discussion on spatial autoresonance in NLSE and autoresonant excitation of waves in certain other soliton equations one may refer to the [29–33].

11.8 A Quantum Analogue of Autoresonance

A quantum analogue of autoresonance is the ladder climbing [34]. For the case of monochromatic radiation the transition dipole moment for the transition between initial and final state is small. Consequently, monochromatic light is inefficient to excite a molecule from an initial state to a final state. In such a case, a light pulse with time varying frequency is employed to make a system to go from an initial state to a final state through a series of intermediates states. This approach is termed as *ladder climbing*.

When the frequency of a wave can be made to vary with time in such a way to follow consecutive transitions is said to be *chirped*. Such chirped laser pulses are used to control molecular dissociation [35, 36] and to enhance the transfer to higher states [37, 38]. The autoresonance mechanism is proposed to explain many-photon ionization of Rydberge atoms [1].

This section briefly present the theoretical and numerical analysis of ladder climbing reported in [34].

Consider the classical system

$$m\ddot{x} + \omega_0^2 x + dx^3 = f \cos(\omega_0 t - \omega_0 \alpha t^2 / 2)$$
 (11.93)

Seeking solution in the from $x = a_0(t) + a(t) \cos \theta(t)$ gives

$$\dot{a} = -\frac{f}{2m\omega_0}\sin\Delta \,, (11.94a)$$

$$\dot{\Delta} = \omega_0 \beta a^2 - \alpha t - \frac{f}{2m\omega_0 a} \cos \Delta , \qquad (11.94b)$$

where

$$\Delta = \theta - \omega_0 t + \alpha t^2 / 2 , \quad \beta = -\frac{5d}{12m\omega_0^2} .$$
 (11.95)

Introduction of $\tau = \sqrt{\alpha} t$, $\mu = \sqrt{\omega_0 \beta} f/(2m\omega_0 \alpha^{1/4})$, $\psi = \sqrt{\omega_0 \beta} \alpha^{-1/4} a e^{i\Delta}$ yields

$$\psi' + (\tau - |\psi|^2) \psi + i\mu = 0.$$
 (11.96)

Numerical analysis predicts that for $\mu > \mu_c \approx 0.41$ [34] the amplitude grows continuously and phase locking persists (autoresonance). Using this value the threshold condition on f is given by

$$f_{\rm c} = 0.82m\alpha^{3/4}\sqrt{\omega_0/\beta} \ . \tag{11.97}$$

The energy eigenvalues of the system (11.93) for f = 0 are given by

$$E_n \approx \hbar \omega_0 \left(n + \frac{1}{2} \right) \left[1 - \beta' \left(n + \frac{1}{2} \right) \right], \quad \beta' = \frac{\beta \hbar}{m \omega_0},$$
 (11.98)

where $n = 0, 1, 2, \dots$. The spacing between adjacent energy levels is

$$\Delta E_n = E_{n+1} - E_n = \hbar \omega_0 [1 - 2\beta'(n+1)]. \tag{11.99}$$

As n increases ΔE_n decreases. The discrete energy levels can be viewed as a ladder. Consider the excitation of the system by an external field of driving frequency ω . Assume that initially the system is in the ground state $(E=E_0)$. To excite the system to the state E_1 , the frequency of the applied field has to be set to the value $(E_1-E_0)/\hbar$. When the probability of finding the system with E_1 is unity, then to excite it to the level E_2 the frequency has to be adjusted to $(E_2-E_1)/\hbar$. Because the energy levels are unequally spaced, in order to induce a transition from the nth state to the (n+1)th state, the driving frequency must be

$$\omega_{n,n+1} = \frac{\Delta E_n}{\hbar} = \omega_0 [1 - 2\beta'(n+1)]. \tag{11.100}$$

That is, at every transition the frequency is to be shifted by an amount $2\omega_0\beta$. Further, the frequency must be kept at a value over a certain interval of time allowing the

transition probability for n to (n + 1)th the state becomes unity. In contrast to this, in the classical autoresonance the driving frequency is continuously varied.

How does a quantum system proceed if the driving frequency varies continuously? To explain the response of the system define three time scales: T_R -Rabi time scale, T_S -the sweep rate scale and T_{NL} -the nonlinear transition time scale. They are defined as

$$T_{\rm R} = \frac{\sqrt{2m\hbar\omega_0}}{f}$$
, $T_{\rm S} = \frac{1}{\sqrt{\alpha}}$, $T_{\rm NL} = \frac{2\hbar\beta}{m\alpha}$. (11.101a)

For an efficient population transfer in a two-level system by a chirped pulse the requirement is

$$T_{\rm R} < \frac{T_{\rm S}}{\sqrt{2}}$$
, (11.102a)

To apply the classical theory several energy levels at all times must be coupled. This can be realized by means of the amplitude of the driving force. Therefore, the width of the resonance should include the resonance at $\omega_{m,m+1}$ in addition to $\omega_{n,n+1}$. Here n-m is the number of levels mixed by the applied force. The condition for the above is

$$\frac{T_{\rm S}^2}{T_{\rm R}T_{\rm NL}} > 1. {(11.102b)}$$

The decoupling between the adjacent resonances corresponds to

$$\frac{T_{\rm S}^2}{T_{\rm R}T_{\rm NL}} < 1. {(11.102c)}$$

The ladder climbing regions are defined by (11.102a) and (11.102c). In terms of the three time scales the classical threshold condition for autoresonance $f > f_c$ becomes

$$\frac{T_{\rm R}^2}{T_{\rm S}T_{\rm NL}} < 1.48 \ . \tag{11.102d}$$

Defining $P_1 = T_S/T_R$ and $P_2 = T_S/T_S$ the condition (11.102a) and (11.102c) for ladder climbing take the form

$$P_2 > P_1 > \sqrt{2} \tag{11.103}$$

while the conditions (11.102b) and (11.102d) for the classical autoresonance becomes $P_1 > P_2$ and $P_1 > \sqrt{0.67/P_2}$.

The results of a numerical simulation for the Morse oscillator with the potential

$$V(x) = \frac{\alpha}{\hbar\omega_0} (1 - e^{-ax})^2$$
 (11.104)

and the perturbed Hamiltonian

$$H' = \epsilon \sqrt{\hbar/(m\omega_0^3)} x \sin(t - \alpha t^2/2). \qquad (11.105)$$

appear in [34]. The unperturbed energy eigenvalues of the Morse oscillator are given by

$$E_n = D\beta'' \left(n + \frac{1}{2} \right) \left[2 - \beta'' \left(n + \frac{1}{2} \right) \right], \quad \beta'' = \left(\frac{\hbar^2 a^2}{2m\alpha} \right)^{1/2}.$$
 (11.106)

 E'_n s of the Morse oscillator given by (11.106) is similar to that of the system (11.93) given by (11.98). The time-dependent wave function is assumed as

$$\psi(t) = \sum_{n} C_n(t)\psi_n , \qquad (11.107)$$

where ψ_n are the eigenfunctions of the unperturbed system and C'_n s to be determined are generally complex valued. According to a time-dependent perturbation theory the evolution equations for C_n are [39, 40]

$$i\dot{C}_n = \sum_m H'_{n,m} C_m , \quad H'_{n,m} = \langle \psi_n | x | \psi_m \rangle .$$
 (11.108)

A coupled channel method can be used to solve (11.108) [40, 41]. In [34] numerical analysis is performed for $C_0^{(0)} = 1$ and $C_n^{(0)} = 0$ for n > 0. Figure 11.16 presents the result for $P_1 = 1.43$ and $P_2 = 16.3$. These values are above the threshold for ladder climbing. An autoresonance-like behaviour is clearly seen in this figure.

A ladder climbing quantum phenomenon was investigated [42] in the anharmonic oscillator system with the Hamiltonian

$$H = \frac{1}{2}p^2 + \frac{1}{2}(1 + f\cos\phi)x^2 + \frac{1}{4}\beta x^4 , \quad \phi = 2t + \alpha t^2/2 . \tag{11.109}$$

For this system the equations of C_m are given by (with $\hbar = 1$)

$$i\dot{C}_n = E_n C_n + \frac{f}{2} \sum_m C_m \langle \psi_m | x^2 | \psi_n \rangle \cos \phi , \qquad (11.110)$$

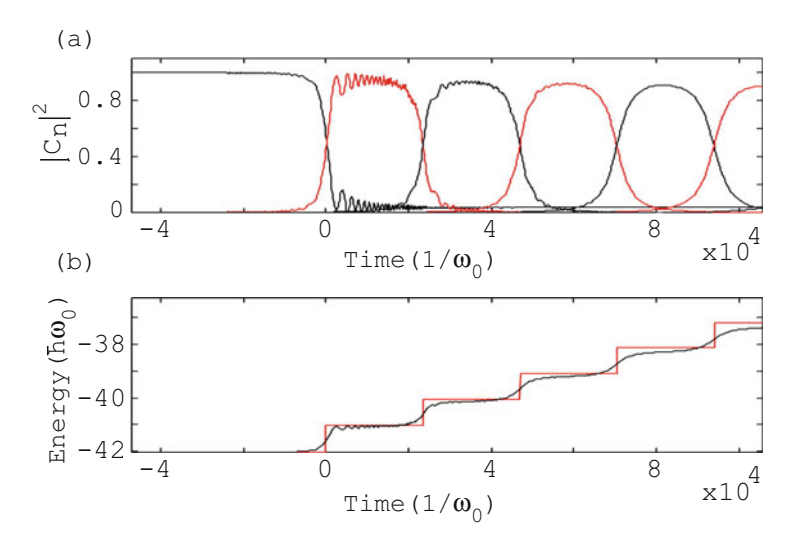


Fig. 11.16 (a) $|C_n(t)|^2$ versus time for $P_1 = 1.43$ and $P_2 = 16.3$ [34]. (b) Variation of energy of the Morse oscillator driven by a driving force with chirped frequency. (Figure 11.16 adapted with permission from Ref. [34]. Copyrighted by the American Physical Society.)

where for
$$\beta \ll 1$$
, $E_n \approx n + \frac{1}{2} + \frac{3\beta}{8} \left(n^2 + n + \frac{1}{2} \right)$, $n = 0, 1, 2, \cdots$. With $\langle \psi_m | x^2 | \psi_n \rangle \approx \frac{1}{2} \left[\sqrt{Q_n} \, \delta_{m,n-2} + (2n+1) \delta_{m,n} + \sqrt{Q_{n+1}} \, \delta_{m,n+2} \right]$ (11.111)

Eq. (11.110) becomes

$$i\dot{C}_n = E_n C_n + \frac{f}{4} \left[\sqrt{Q_{n-1}} C_{n-2} + (2n+1)C_n + \sqrt{Q_{n+1}} C_{n+2} \right] \cos \phi .$$
 (11.112)

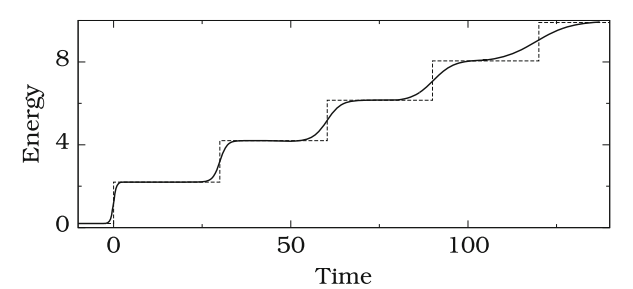
Equation (11.112) were solved numerically [42] with $C_n(t_0) = \delta_{n,0}$, $t_0 = -10/\sqrt{\alpha}$, $\alpha = 10^{-6}$, $\beta = 0.001$, f = 0.04 and including 40 energy levels for computation. Figure 11.17 depicts the result of the numerical simulation showing quantum autoresonance. For further details refer to the [42].

11.9 Applications

The autoresonance phenomenon enables numerous exciting and widespread applications in physics and engineering. Several applications of autoresonance has emerged in atomic and molecular physics [1–3, 34, 43–45], particle accelerators

11.9 Applications 327

Fig. 11.17 E_n versus time of the chirped parametrically driven quantum anharmonic oscillator [42]. (Figure 11.17 adapted with permission from Ref. [42]. Copyrighted by the American Physical Society.)



[46], nonlinear waves [30, 46–48], fluid dynamics [49–51], plasma physics [52, 53], superconducting Josephson junctions [54], optics [19] and planetary dynamics [55]. Autoresonance can be used to generate ratchet dynamics in Hamiltonian systems [56]. Let us summarize some of the promising applications of autoresonance.

- A precise control of magnetization switching dynamics is very essential for the
 retrieval and fast processing of data stored in magnetic data storage devices.
 Autoresonance mechanism can be used to control the magnetization reversal
 dynamics on a time scale of a few tens of nanoseconds. For example, a chirped
 microwave field hundred times smaller in amplitude than the static field is able
 to efficiently reverse the magnetization [57].
- 2. In nonlinear wave systems, particularly in soliton equations like the sine-Gordon equation, the Toda chain and the nonlinear Schrödinger equation, a realization of multi-phase waves is an intricate problem since it requires complicated initial conditions. It is possible to generate such waves and control them by exploiting the autoresonance oscillation from zero by employing plane wave-like disturbances possessing through resonances in the system [58].
- An autoresonant trap mass spectrometer has been developed. In this device detection of ions formed by electron ionization inside a cylindrical trap and mass selective ejection are achieved based on autoresonance based energy pumping process [59].
- 4. Autoresonance is applied for excitation of plasma wave [52], cnoidal wave formation in Korteweg-de Vries equation [30], nonlinear mode conversion [60], excitation of diocotron modes in non-neutral plasmas [53, 61, 62] and *m*-fold symmetric vortices formation in fluid dynamics [50, 63].
- 5. A computer model of ultrasonically assisted turning vibrating system with an autoresonant control has been proposed. In this system the autoresonance control is used to maintain the resonant oscillation automatically through a positive feedback, providing transformation (phase shift) and amplification of the control [64].
- 6. The autoresonance mechanism is used to inject antiprotons into a positron plasma leading to the formation of antihydrogen [65].
- 7. A Josephson chirped amplifier device has been proposed for a qubit readout applications [66].

8. In a nonparabolic quantum well (a small semiconductor device) the optical response depends on the strong peak present at the plasmon frequency. This resonance condition is lost when the electrons are in the anharmonic regions and hence the absorption becomes inefficient. As shown in [67], this problem can be overcome by the use of a chirped laser pulse. Simulations have shown efficient detrapping of electrons from a nonparabolic well by a sequence of few pulses.

- 9. The plasma beat-wave accelerator (PBWA) is used as an alternative to the shortpulse laser wave-field accelerator. In PBWA two lasers propagating in an underdense plasma are detuned from one another by means of a frequency shift in the neighbourhood of the electron plasma frequency ω_n . The beating between the lasers give rise to a modulated envelope. This can act on the plasma electrons and excite resonantly a large amplitude Langmuir wave desirable for particle acceleration. However, when the plasma wave increases, relativistic detuning effects prevent further growth. To over come this, chirped PBWA via adiabatic passage through resonance has been proposed. In this mechanism, before the onset of saturation of plasma oscillation amplitude, the frequency of the excited wave can be locked with the beat frequency of the drivers. As a result, the amplitude of the plasma wave grow automatically and moreover the frequency of the plasma wave adjust itself to the decreasing beat frequency. Interestingly, given the intensity of laser, it is easy to determine the maximum chirp rate tolerable to obtain large amplitude plasma waves [68]. Further, the scheme is much more robust to unavoidable uncertainties and changes in plasma and laser parameters.
- 10. In many processing machines such as cutting, drilling, sifting, etc. the workload depends on the treated materials. Because the behaviour of materials is complex and poorly predictable, the underlying processes in such machines which are essentially nonlinear are mathematically ill-defined. Autoresonance control is exploited to realize self-tuning and self-adaptation leading to resonant mode of functioning in the ill-defined cases. Industrial application of autoresonant control is described for high-power screening machines and ultrasonically assisted cutting machines [69].
- 11. By exciting the electron-positron clusters by a chirped laser pulse, it is possible to separate the electron ad positron populations [70].
- 12. Autoresonance has been analysed in a superconducting circuit. In this circuit system a nonlinear planar microwave cavity is coupled to a transmon qubit in a circuit quantum electrodynamics architecture. The autoresonant threshold is found to depend on the quantum state and may be utilized to achieve a high-fidelity and latching readout [71].

References 329

11.10 Concluding Remarks

An energy-based theory of autoresonance [11], a numerical method for determining optimal drive sweep rate for autoresonance applicable for Duffing type oscillators [72], theory of multi-dimensional autoresonance in three-wave interactions [27] have been developed. Autoresonance has been observed experimentally in Faraday waves [73], Diocotron mode in pure-electron plasmas [8] and an anharmonic oscillator [74, 75].

Autoresonance in the field of optics can play a significant role in phase locking and amplification in visible, soft X-rays and terahertz regions, optical switching in optically controlled unidirectional devices, self-synchronization of lasers and improving efficiency in light-matter interactions. The space-time generalization of autoresonance in nonlinear wave systems is investigated in a driven sine-Gordon equation by considering space-time variation of parameters [31, 32]. In this system the autoresonant interaction of waves is found to display three stages: initial excitation, autoresonant interaction and phase detrapping. Study of the space-time autoresonance is of interest in a variety of fields including plasma physics, acoustics and nonlinear optics.

References

- 1. B. Meerson, L. Friedland, Phys. Rev. A 41, 5233 (1990)
- 2. J. Fajans, L. Friedland, Am. J. Phys. 69, 1096 (2001)
- 3. M.S. Livingstone, High Energy Accelerators (Interscience, New York, 1954)
- 4. A.A. Kolomenski, A.N. Lebedev, Dokl. Akad. Nauk SSSR 145, 1259 (1962)
- 5. J. Fajans, E. Gilson, L. Friedland, Phys. Rev. E 62, 4131 (2000)
- 6. E. Khain, B. Meerson, Phys. Rev. E 64, 036619 (2001)
- 7. O.B. David, M. Assaf, J. Fineberg, B. Meerson, Phys. Rev. Lett. 96, 154503 (2006)
- 8. G. Cohen, B. Meerson, Phys. Rev. E 47, 967 (1993)
- 9. V. Rokni, L. Friedland, Phys. Rev. E 59, 5242 (1999)
- 10. E. Nakar, L. Friedland, Phys. Rev. E 60, 5479 (1999)
- 11. R. Chacon, Europhys. Lett. 70, 56 (2005)
- 12. R. Uzdin, L. Friedland, O. Gat, Phys. Rev. E 89, 012902 (2014)
- 13. M. Assaf, B. Meerson, Phys. Rev. E 72, 016310 (2005)
- H. Goldstein, C.P. Poole, J.L. Safko, Classical Mechanics, 3rd edn. (Addison-Wesley, Reading, 2001)
- M. Abramowitz, Hand Book of Mathematical Functions (National Bureau of Standards, Washington, DC, 1964)
- 16. A. Kovaleva, L.I. Manevitch, Phys. Rev. E 88, 024901 (2013)
- J. Kevorkian, J.D. Cole, Multiple Scale and Singular Perturbation Methods (Springer, New York, 1996)
- 18. L.I. Manevitch, A.S. Kovaleva, D.S. Shepelev, Physica D 240, 1 (2011)
- 19. A. Barak, Y. Lamhot, L. Friedland, M. Segev, Phys. Rev. Lett. 103, 123901 (2009)
- 20. W.I. Kruer, The Physics of Laser Plasma Interactions (Westview Press, Boulder, 2001)
- 21. C.R. Menyuk, A.T. Drobot, K. Papadopoulos, H. Karimabadi, Phys. Fluids 31, 3768 (1988)
- 22. A. Yariv, Quantum Electronics (Wiley, New York, 1989)
- 23. A.P. Mayer, Phys. Rep. 256, 237 (1995)

- 24. K. Trulsen, C.C. Mei, J. Fluid Mech. 290, 345 (1995)
- 25. O. Yaakobi, L. Friedland, Phys. Rev. A 82, 023820 (2010)
- O. Yaakobi, L. Caspani, M. Clerici, F. Vidal, R. Morandotti, Opt. Exp. 21, 1623 (2013)
- 27. O. Yaakobi, L. Friedland, Phys. Plasmas 15, 102104 (2008)
- E.M. Marhic, Fiber Optical Parametric Amplifiers, Oscillators and Related Devices (Cambridge University Press, Cambridge, 2008)
- 29. L. Friedland, Phys. Rev. E 58, 3865 (1998)
- 30. I. Aranson, B. Meerson, T. Tajima, Phys. Rev. A 45, 7500 (1992)
- 31. L. Friedland, Phys. Rev. E **55**, 1929 (1997)
- 32. L. Friedland, Phys. Rev. E 57, 3494 (1998)
- 33. L. Friedland, Phys. Plasmas 5, 645 (1998)
- 34. G. Marcus, L. Friedland, A. Zigler, Phys. Rev. A 69, 013407 (2004)
- 35. J.M. Yuan, W.K. Liu, Phys. Rev. A 57, 1992 (1998)
- T. Witte, T. Hornung, L. Windhom, D. Proch, R. de Vivie-Riedle, M. Motzkus, K.L. Kompa, J. Chem. Phys. 118, 2021 (2003)
- D.J. Maas, D.I. Duncan, R.B. Vrijen, W.J. Van der Zande, L.D. Noordam, Chem. Phys. Lett. 290, 75 (1998)
- 38. S. Chelkowski, A.D. Bandrauk, P.B. Corkum, Phys. Rev. Lett. 65, 2355 (1990)
- 39. L.I. Schiff, Quantum Mechanics (McGraw-Hill, New York, 1968)
- S. Rajasekar, R. Velusamy, Quantum Mechanics I: The Fundamentals (CRC Press, New York, 2014)
- 41. J. Wang, J.D. Champagne, Am. J. Phys. 76, 493 (2008)
- 42. I. Barth, L. Friedland, Phys. Rev. Lett. 113, 040403 (2014)
- 43. W.K. Liu, B.R. Wu, J.M. Yuan, Phys. Rev. Lett. 75, 1292 (1995)
- 44. G. Marcus, L. Friedland, A. Zigler, Phys. Rev. A 72, 033404 (2005)
- 45. H. Maeda, J. Nunkaew, T.F. Gallagher, Phys. Rev. A 75, 053417 (2007)
- 46. D. Bohm, L. Foldy, Phys. Rev. 70, 249 (1946)
- 47. L. Friedland, A.G. Shagalov, Phys. Rev. Lett. 90, 074101 (2003)
- 48. L. Friedland, A.G. Shagalov, Phys. Rev. E **71**, 036206 (2005)
- 49. L. Friedland, Phys. Rev. E 59, 4106 (1999)
- 50. L. Friedland, A.G. Shagalov, Phys. Rev. Lett. 85, 2941 (2000)
- 51. M.A. Borich, L. Friedland, Phys. Fluids 20, 086602 (2008)
- 52. M. Deutsch, J.E. Golub, B. Meerson, Phys. Fluids B 3, 1773 (1991)
- 53. J. Fajans, E. Gilson, L. Friedland, Phys. Rev. Lett. **82**, 4444 (1999)
- O. Naaman, J. Aumentado, L. Friedland, J.S. Wurtele, I. Siddiqi, Phys. Rev. Lett. 101, 117005 (2008)
- 55. R. Malhotra, Sci. Am. **281**, 56 (1999); L. Friedland, Astrophys. J. **547**, L75 (2001)
- 56. D.V. Makarov, E.V. Sosedko, M. Yu. Uleysky, Eur. Phys. J. B 73, 571 (2010)
- 57. G. Klughertz, P.A. Hervieux, G. Manfredi, J. Phys. D. Appl. Phys. 47, 345004 (2014)
- 58. A.G. Shagalov, L. Friedland, Physica D 238, 1561 (2009) and references therein
- 59. G.A. Brucker, G.J. Rathbone, Int. J. Mass Spectrom. 295, 133 (2010)
- 60. L. Friedland, Phys. Plasmas 2, 1393 (1995)
- 61. L. Friedland, J. Fajans, E. Gilson, Phys. Plasmas 7, 1712 (2000)
- 62. J. Fajans, E. Gilson, L. Friedland, Phys. Plasmas 8, 423 (2001)
- 63. L. Friedland, A.G. Shagalov, Phys. Fluids 14, 3074 (2002)
- S. Voronina, V. Babitsky, J. Sound Vib. 313, 395 (2008)
- 65. G.B. Andresen et al., (ALPHA collaboration), Phys. Rev. Lett. 106, 025002 (2011)
- O. Naaman, J. Aumentado, L. Friedland, J.S. Wurtele, I. Siddiqi, Phys. Rev. Lett. 101, 117005 (2008)
- 67. G. Manfredi, P.A. Hervievx, Appl. Phys. Lett. **91**, 061108 (2007)
- R.R. Lindberg, A.E. Charman, J.S. Wurtele, L. Friedland, B.A. Shadwick, Phys. Plasmas 13, 123103 (2006)
- 69. V.I. Babitsky, I.J. Sokolov, Nonlinear Dyn. 50, 447 (2007)
- 70. G. Manfredi, P.A. Hervieux, F. Haas, New. J. Phys. 14, 075012 (2012)

References 331

 K.W. Murch, E. Ginossar, S.J. Weber, R. Vijay, S.M. Grrin, I. Siddiqi, Phys. Rev. B 86, 220503 (2012)

- 72. C. Witkov, L.S. Liebovitch, J. Sound Vib. 329, 154 (2010)
- 73. O. Ben-David, M. Assaf, J. Fineberg, B. Meerson, Phys. Rev. Lett. 96, 154503 (2006)
- 74. J.N. Fox, J.J. Arlotto, Am. J. Phys. 36, 326 (1968)
- 75. H.J. Janssen, R. Serneels, L. Beerden, E.L.M. Flerackers, Am. J. Phys. **51**, 655 (1983)

Chapter 12 Coherence and Chaotic Resonances

Real systems are subjected to certain amount of unavoidable internal or external random perturbations, usually termed as noise. The presence of noise is not only unavoidable in electrical and electronic devices, but it can significantly affect their performance. As pointed out in the beginning of Chap. 2, a variety of phenomena can be induced by the presence of noise. An oscillating system in which noise is significant and is the source of its oscillatory dynamics, then it is generally called an *stochastic oscillator*. A mathematical model of such a system in the absence of noise and external periodic force does not exhibit any kind of oscillatory motion. A stochastic oscillator can be monostable, multistable or excitable. In certain cases the effect of noise in a stochastic oscillator is nontrivial. That is, the increase of noise intensity need not always increase the irregularity of the response. An appropriate weak noise can give rise to a maximum coherence similar to the stochastic resonance but in the absence of any external periodic force.

In the stochastic resonance the system is driven by both a weak periodic force and noise. It has been shown that resonance can occur in the absence of weak periodic force and the associated phenomenon is termed as *coherence resonance* also called *autonomous resonance* [1, 2]. That is, noise alone is able to induce or enhance temporal order in the dynamics of certain nonlinear systems, particularly, in excitable systems. Essentially, a coherence measure of stochastic oscillations attains an extremum at an optimal noise intensity, hence the word *resonance*. The coherence phenomenon was first introduced in 1993 by Gang, Ditzinger, Ning and Haken [1]. The presence of coherence resonance can be identified in terms of power spectrum showing a peak at a finite frequency [3, 4] and time correlation function showing a minimum at the resonance.

A nonlinear system subjected to perturbation which is chaotic in nature can display a resonance-like behaviour called *chaotic resonance*. It is to be noted that "chaotic resonance: a simulation" is the title of a paper published in Journal of Statistical Physics by three American physicists Ippen et al. [5]. It has been pointed

out that the role of noise in noise-induced dynamics can be played if the noise is replaced by a chaotic disturbance [6].

The present chapter is devoted to the study of coherence and chaotic resonances.

12.1 An Illustration of Coherence Resonance

The effect of noise in excitable systems is fascinating because in the absence of a noise term there is no response of the system, high noise leads to noisy response with large fluctuations while a moderate weak noise produces quite regular spikes. Many biological processes are modelled as excitable systems. In excitable systems, for example, in neural systems the temporal coherence of firing behaviour is an important dynamics for the time precision of processing of information. Because the temporal coherence can be greatly improved by the presence of noise, the study of features of coherence resonance in neural systems if of great interest. This section demonstrates the occurrence of coherence resonance in an excitable system. In Sect. 12.3 the features of coherence resonance in a modified Chua's circuit model equation with multiple equilibrium points is presented.

Consider the FitzHugh–Nagumo (FHN) model equations

$$\epsilon \dot{x} = x - \frac{1}{3}x^3 - y \,, \tag{12.1a}$$

$$\dot{y} = x + a + D\eta(t) . \tag{12.1b}$$

In Eq. (12.1) $\epsilon \ll 1$ is a small parameter. It allows to separate all motions as the fast (only x changes) and slow ($y = x - x^3/3$) ones. For |a| > 1 the system has only a stable equilibrium point. A limit cycle attractor occurs for |a| < 1. This limit cycle essentially consists of two parts of a slow orbit connected by fast jumps. For the values of |a| slightly higher than 1 the system is excitable wherein small deviations from the equilibrium point produce large pulses. In Eq. (12.1) $\eta(t)$ is Gaussian white noise with zero mean and unit variance.

We fix the values of the parameters as $\epsilon = 0.01$, a = 1.05 and vary the intensity D of the noise. Figure 12.1 displays the noise-induced excited dynamics for three values of D. The oscillatory motion is irregular for small and large values of D. For a moderate noise intensity relatively coherent oscillations occur. This is shown in Fig. 12.1b for D = 0.06.

The coherence resonance can be characterized by the normalized autocorrelation function given by

$$C(\tau) = \frac{\langle \bar{y}(t)\bar{y}(t+\tau)\rangle}{\langle \bar{v}^2\rangle} , \quad \bar{y} = y - \langle y\rangle . \tag{12.2}$$

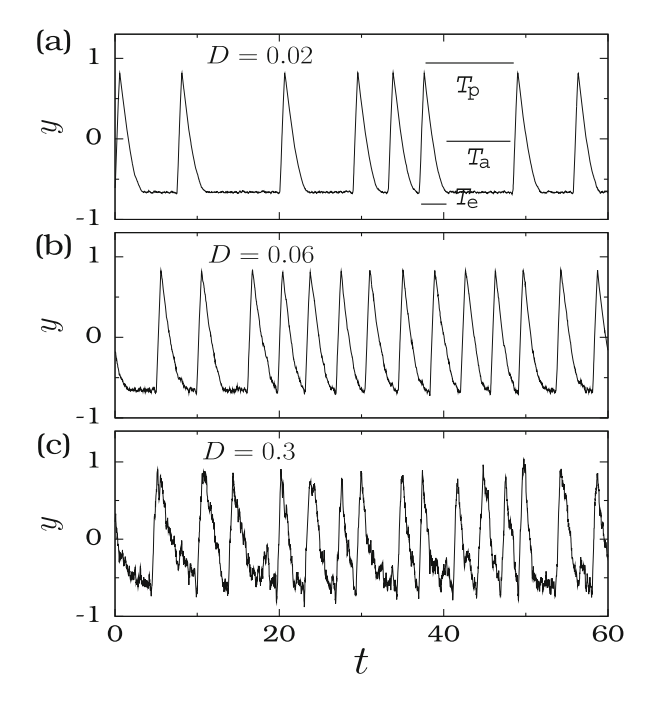


Fig. 12.1 y versus t of the FHN Eq. (12.1) for $a=1.05, \epsilon=0.01$ and for (a) D=0.02, (b) D=0.06 and (c) D=0.3

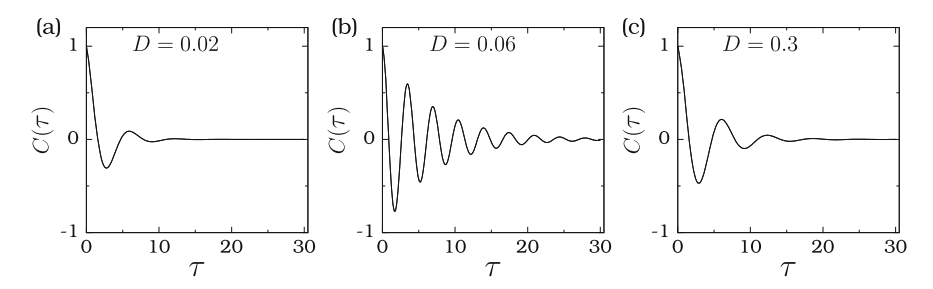


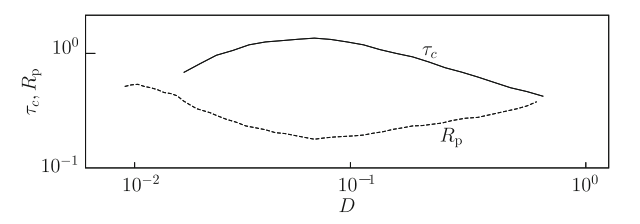
Fig. 12.2 $C(\tau)$ versus τ for the FitzHugh–Nagumo equations [2] with (a) D=0.02, (b) D=0.06 and (c) D=0.3

Then the correlation time τ_c is given by

$$\tau_{\rm c} = \int_0^\infty C^2(\tau) \, d\tau \ . \tag{12.3}$$

Figure 12.2 show the variation of autocorrelation function with τ for three values of D. For all the values of noise intensity $C(\tau)$ exhibits damped oscillation. However, the correlations are much more pronounced for D=0.06 at which coherence

Fig. 12.3 The dependence of the quantities τ_c and R_p on the noise intensity D for the FitzHugh–Nagumo equations [2]



resonance occurs. For a time series, the larger the value of τ_c the larger the temporal coherence.

In Fig. 12.1a T_p denotes the duration of a pulse. Pulses of different durations are clearly seen. The relative fluctuations of the time duration between adjacent pulses, denoted as, R_p is given by

$$R_{\rm p} = \frac{\sigma_{\rm p}}{\langle T_{\rm p} \rangle} = \frac{\sqrt{\langle (T_{\rm p} - \langle T_{\rm p} \rangle)^2 \rangle}}{\langle T_{\rm p} \rangle} \ . \tag{12.4}$$

This normalized variance of T_p is called the *coherence parameter* and can also be used to characterize coherence resonance. Figure 12.3 shows the variation of τ_c and R_p with the control parameter D. τ_c becomes maximum at D=0.06. On the other hand, R_p has a clear minimum at this value of D.

12.2 Mechanism of Coherence Resonance

A general mechanism of coherence resonance is the following [2, 4]. Consider an excitable system with a stable equilibrium point. By an appropriate perturbation, an excitable system can be made to cross a threshold value and return to the equilibrium point after executing a long excursion in phase space. That is, a pulse can be generated. The time duration of the pulse, generally, depends on the system and independent of the perturbation. The total time between pulses (T_p) (refer Fig. 12.1a) essentially consists of two times. One is the excursion time T_e and the other is the time required for the activation of the pulse denoted as T_a . The time T_a becomes a random variable if the firing of the pulse is due to the random fluctuations. For small noise, following Kramers, one can write $\langle T_a \rangle \sim e^{A/D^2}$ where A is a constant and D is the noise intensity. Further, the variance of T_a , $\sigma_a^2 \approx \langle T_a \rangle^2$ while $\sigma_e^2 \approx D^2 \langle T_e \rangle$. For small D, $\langle T_a \rangle \gg \langle T_e \rangle$ and approximate the time between pulses by the activation time $T_p \approx T_a$. For small noise $R_p \approx 1$.

For large noise T_a is very small and the system fires a pulse every time it returned from an excursion. As a result, T_p is dominated by T_e and in this case one can approximate R_p as $D/\sqrt{\langle T_e \rangle}$. If T_e is large and the threshold of excursion is small then for intermediate values of D one can have $R_p(D) < 1$. Therefore, for small D, $R_p(D) \rightarrow 1$. For large D, $R_p(D) \sim D/\sqrt{\langle T_e \rangle}$ while for intermediate values of D,

 $R_{\rm p}(D) < 1$. That is, as D increases from a small value the quantity $R_{\rm p}$ decreases from a value close to 1, reaches a minimum value at an optimal noise intensity and then increases again. This is the coherence resonance phenomenon.

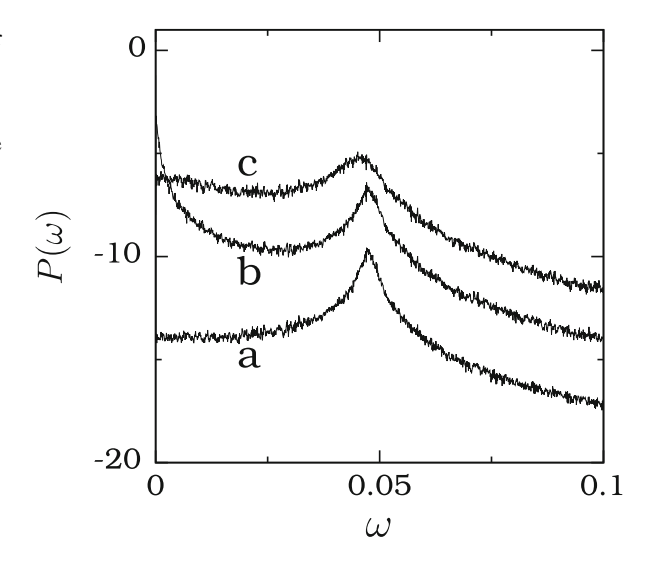
The system will display the highest degree of coherence at the value of noise intensity D at which $R_{\rm p}$ will become minimum. That is, the basic mechanism of coherence resonance is similar to the process of stochastic resonance. In both cases an external noise cooperates with a deterministic periodicity. When the periodicity is imposed externally then the occurrence of regular fluctuations is known as stochastic resonance. Conversely, if the regularity is internal to the dynamical system, the process is termed as *coherence resonance*.

12.3 Coherence Resonance in a Modified Chua's Circuit Model Equations

As an another example for the occurrence of coherence resonance consider the modified Chua's circuit Eq. (5.31) without the periodic driving force [7]. As noted in Chap. 5 the system (5.31), in the absence of the periodic force and noise, with $F_1(x)$ possesses N=2n equilibrium points while with $F_2(x)$ admits N=2n+1 equilibrium points. We fix the values of the parameters as $\alpha=6$, $\beta=14$, A=0.5, $\xi=0.25$ and analyse the response of the system by varying the noise intensity for various fixed values of N.

Prior to a detailed characterization of coherence resonance, we first show a signature of resonance in the power spectrum of the *x*-component of the system. Figure 12.4 presents the power spectrum for three values of noise intensity for

Fig. 12.4 Normalised power spectrum of *x*-component of the modified Chua's circuit equations for three values of noise intensity in the absence of external periodic force. The values of *D* for the spectra *a*, *b* and *c* are 0.01, 0.058 (optimum value) and 0.1, respectively



N=2. Even though there is no input periodic signal of definite frequency, the power spectrum shows the dominant peak at the particular frequency $\omega_0 \approx 0.045$. The presence of a dominant frequency in the trajectory of the system indicates the rotational motion about the equilibrium points. Additional peaks do not appear for a wide range of the noise intensity. The value of ω_0 is found to be the same for other values of N. In Fig. 12.4 notice that the width and the height of the peak increase with increase in D but they increase in different rates.

Figure 12.5 presents the dependence of the normalised autocorrelation function τ_c of the *x*-component of the state variable of the system versus noise intensity for various fixed values of *N*. The τ_c versus *D* profile resembles the *SNR* profile shown in Fig. 5.12 for stochastic resonance. For each fixed value of *N*, τ_c increases with increasing *D*, reaches a maximum at an optimum noise intensity and then decreases. In Fig. 12.6a the value of D_{MAX} at which τ_c becomes maximum increases with increasing *N*. In Fig. 12.6b the variation of maximum of τ_c with *N* is similar to the variation of SNR_{MAX} with *N* (refer Fig. 5.14b). $\tau_c(D_{\text{MAX}})$ is also found to be maximum for N = 6 (compare Fig. 12.6 with Fig. 5.14a).

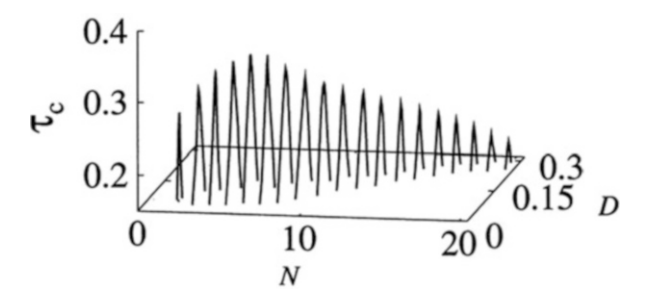


Fig. 12.5 Variation of correlation time with noise intensity for various fixed values of N of the modified Chua's circuit equations

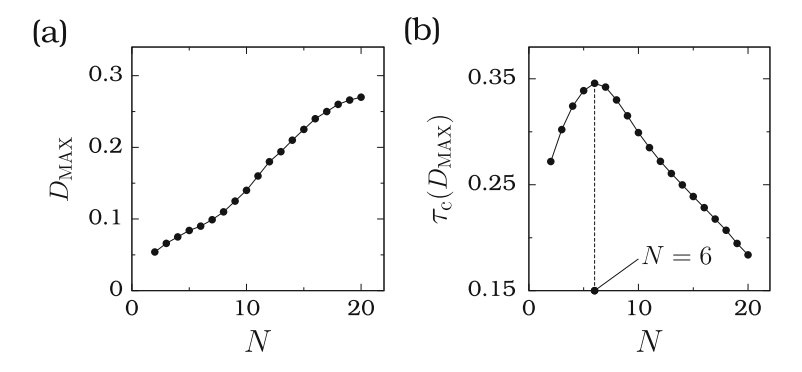


Fig. 12.6 Variation of (a) D_{MAX} , the value of D at which correlation time becomes maximum, and (b) τ_{c} , computed at $D = D_{\text{MAX}}$, with the number of equilibrium points N

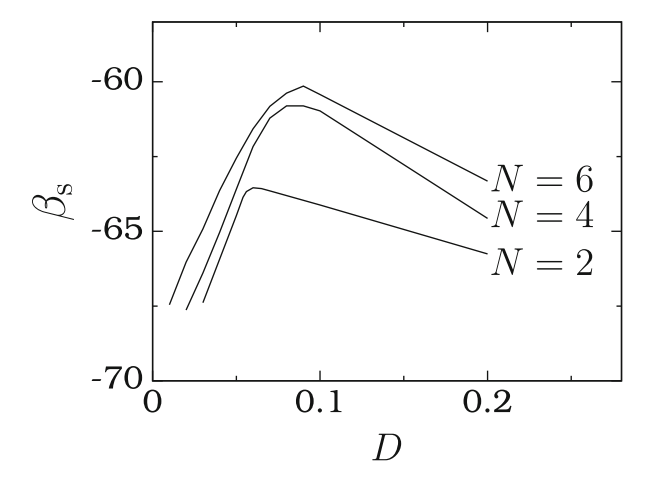


Fig. 12.7 Coherence resonance parameter β_s versus the noise intensity for three values of N for the modified Chua's circuit model equations

Another statistical measure of coherence resonance is the quantity β_s given by Gang et al. [1], Rappel and Strogatz [8], and Liu and Lai [9]

$$\beta_{\rm S} = 10 \log_{10}(H/W) \, \text{dB},$$
(12.5)

where H is the height of the peak in the power spectrum of the state variable, say, x at the dominant frequency ω_0 shown in Fig. 12.4. $W = \Delta w/\omega_0$ where Δw is the half-width of the power spectrum about ω_0 . β_s describes coherence in switching. H and W varies in different rates with D. The value of D at which β becomes maximum is considered as the optimum noise intensity D_{MAX} [1, 8, 9]. Figure 12.7 shows the dependence of β_s on D for three values of N. For N=2, 4 and 6 both β_s and τ_c are maximum at D=0.06, 0.08 and 0.09, respectively.

To gain more insight into the noise-induced coherence resonance dynamics, consider the mean residence times about the coexisting states. For very small noise intensity, the motion is mostly confined to an equilibrium point and very rare switching between the coexisting states occurs. In stochastic resonance the noise-induced switching is assisted by the periodic force. Consequently, resonance is realised when there is a synchronisation between switching motion and the input periodic signal. In the case of coherence resonance even though there is no input periodic signal, almost periodic switching between the coexisting states is found to occur at an optimum noise intensity. Figures 12.8a–c illustrate the nature of evolution of the x-component of the system at coherence resonance for N=2, 4 and 6, respectively. One can clearly see a staircase-like switching among the coexisting states.

Figure 12.9a shows the variation of the mean residence time $T_{\rm MR}$ at resonance $(D=D_{\rm MAX})$ with N. $T_{\rm MR}$ decreases with increasing in N. In Fig. 12.9b the quantity

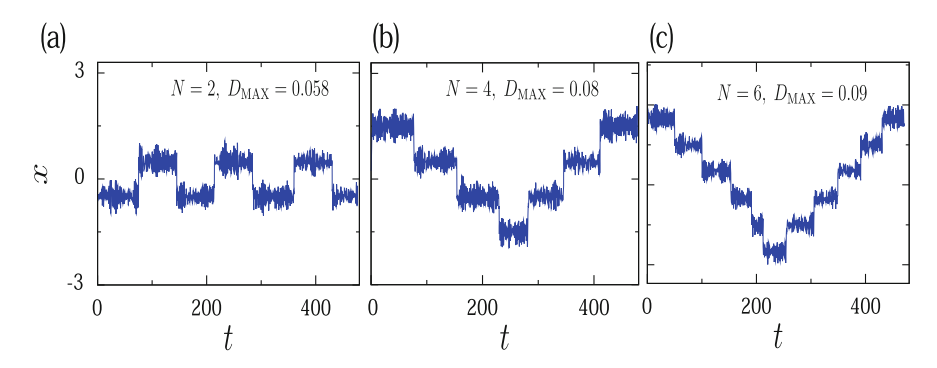


Fig. 12.8 The coherent switching dynamics at D_{MAX} for (a) N=2, (b) N=4 and (c) N=6

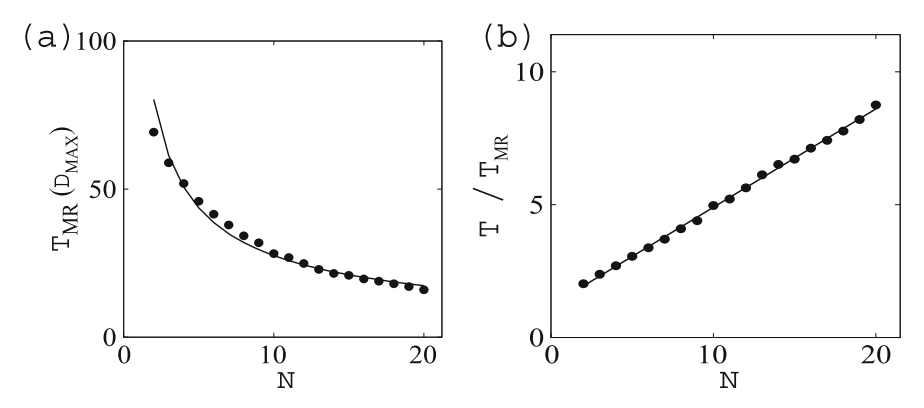


Fig. 12.9 (a) Plot of the mean residence time $T_{\rm MR}$ at $D=D_{\rm MAX}$ versus N of the modified Chua's circuit model equations driven by external noise in the absence of periodic input signal. (b) $T/T_{\rm MR}$ versus N where $T=2\pi/\omega_0$, $\omega_0=0.045$

 $T/T_{\rm MR}$ where $T=2\pi/\omega_0$ varies linearly with N. $T/T_{\rm MR}=aN+b$ where a=0.37 and b=1.2, while for stochastic resonance $T/T_{\rm MR}=2(N-1)$ with $T=2\pi/\omega$.

12.4 Theory of Coherence Resonance

Lindner and Schimansky-Greier [3] developed a theoretical treatment to obtain an expression for the output spectrum of a two-state noise driven system. This section provides a brief description of this theoretical analysis.

12.4.1 A Two-State Model

Let us consider the piecewise linear FitzHugh–Nagumo (FHN) model equation [10]

$$\tau \dot{v} = F(v) - u + c(t) , \qquad (12.6a)$$

$$\dot{u} = av - u + \sqrt{2Q}\,\xi(t)\,\,,\tag{12.6b}$$

where

$$F(v) = \begin{cases} -1 - v, & v \le -1/2 \\ v, & -1/2 < v < 1/2 \\ 1 - v, & v > 1/2 \end{cases}$$
 (12.6c)

v is the fast voltage and u is the slow recovery variable, a and b are parameters, $\xi(t)$ is Gaussian white noise and τ is $\ll 1$. A weak periodic signal $\tilde{f}(t) = \epsilon \cos \Omega t$ can be introduced by choosing $c(t) = \tilde{f}(t)$. The presence of $\xi(t)$ and $\tilde{f}(t)$ lead to stochastic resonance while $\epsilon = 0$ results in coherence resonance.

With the change of variable $\tilde{u} = u - c(t)$, Eq. (12.6) are rewritten as

$$\tau \dot{v} = F(v) - \tilde{u} \,, \tag{12.7a}$$

$$\dot{\tilde{u}} = av - \tilde{u} + b - c(t) - \dot{c}(t) + \sqrt{2Q}\,\xi(t)$$
 (12.7b)

Equations (12.7) become the linear equations

$$\dot{x} = -x + \sqrt{2D}\,\xi(t) \,, \tag{12.8a}$$

$$\dot{\mathbf{y}} = -\mathbf{y} + \sqrt{2D}\,\xi(t)\,\,,\tag{12.8b}$$

where

$$x = \tilde{u} - \frac{b - a}{1 + a} - \epsilon f(t) , \quad f(t) = A(\omega) e^{-i\omega t} + A^*(\omega) e^{i\omega t} , \qquad (12.9a)$$

$$y = -\tilde{u} + \frac{b+a}{1+a} + \epsilon f(t) , \qquad (12.9b)$$

$$\omega = \frac{\Omega}{1+a}, \quad D = \frac{Q}{1+a}, \quad A = -\frac{1/(1+a) + i\omega}{2(1-i\omega)}.$$
 (12.9c)

The equilibrium points of (12.6) in the absence of noise are the intersection points of u = F(v) + c and u = av + b. Denoting these points for C = 0 as x_-, y_-, x_+, y_+ , the points for $\epsilon \neq 0$ are written as [3]

$$x_{\mp} - \epsilon f(t) = \mp \frac{1}{2} - \frac{b-a}{1+a} - \epsilon f(t)$$
, (12.10a)

$$y_{\mp} + \epsilon f(t) = \mp \frac{1}{2} + \frac{b+a}{1+a} + \epsilon f(t)$$
 (12.10b)

For a=2/4 and b=0 the equilibrium points are $x_-=-0.1$, $y_-=-0.1$, $x_+=0.9$, $y_+=0.9$. When $\epsilon=0$ one can regard the motion of the system as a Brownian motion of particle jumping between two potential wells. It can be realized by means of absorption at x_- or y_- (called *sink points*) and by resetting to y_+ or x_+ (*source points*). Essentially, the system undergoes a circular flow $x_+ \to x_-$, jumping to $y_+ \to y_-$ and back to x_+ and thereby generates a two-state motion $\sigma(t)$. For the variable x, let us denote $\sigma=-1$ is the state left from source to sink if $x_->0$. Similarly, denote the right branch state as $\sigma=+1$.

For the Eq. (12.8) the Fokker-Planck equations are

$$\frac{\partial}{\partial t}P_x(x,t) = \frac{\partial}{\partial x}\left(x + D\frac{\partial}{\partial x}\right)P_x(x,t), \qquad (12.11a)$$

$$\frac{\partial}{\partial t} P_{y}(y, t) = \frac{\partial}{\partial y} \left(y + D \frac{\partial}{\partial y} \right) P_{y}(y, t) . \tag{12.11b}$$

The appropriate conditions for solving Eq. (12.6) are given at the points x_- , y_- , x_+ , y_+ . They are

$$P_x(x,t)|_{x_-} - \epsilon f(t) = 0$$
, $P_y(y,t)|_{y_-} + \epsilon f(t) = 0$, (12.12a)

$$[P_x(x,t)]_{x_+} - \epsilon f(t) = 0$$
, $[P_y(y,t)]_{y_+} + \epsilon f(t) = 0$. (12.12b)

In the above, the square brackets are used to represent the jump of a function, that is g(x): $[g]_x = g(x+0) - g(x-0)$.

The populations $p_x(t)$ and $p_y(t)$ of the two states are given by

$$p_x(t) = \int_{x = -\epsilon f(t)}^{\infty} P_x(x, t) dx$$
, (12.13a)

$$p_{y}(t) = \int_{y_{-}+\epsilon f(t)}^{\infty} P_{y}(y,t) \,\mathrm{d}y \qquad (12.13b)$$

with the normalization condition $p_x + p_y = 1$.

When $\epsilon = 0$, the Eq. (12.11) are ordinary differential equations. Normalization of their solutions leads to the stationary current [3]

$$J_0 = \frac{1}{\sqrt{\pi}} \left[\int_{x-/\sqrt{2D}}^{x+/\sqrt{2D}} e^{z^2} \operatorname{erfc}(z) \, dz + \int_{y-/\sqrt{2D}}^{y+/\sqrt{2D}} e^{z^2} \operatorname{erfc}(z) \, dz \right] . \quad (12.14)$$

The power spectrum $N(\omega)$ of the dynamics $\sigma(t)$ is given by the Fourier transforms of the waiting time distributions of $\sigma=-1$ and $\sigma=+1$. Denote these Fourier transforms as $W_x(\omega)$ and $W_y(\omega)$. $N(\omega)$ is given by Linder and Schimanwky-Geier [3]

$$N(\omega) = \int_{-\infty}^{\infty} \langle \sigma(t)\sigma(t+\tau)\rangle e^{i\omega\tau} d\tau$$

$$= \frac{8J_0}{\omega^2} \operatorname{Re}\left(\frac{[1-W_x(\omega)][1-W_y(\omega)]}{1-W_x(\omega)W_y(\omega)}\right), \qquad (12.15)$$

where

$$W_x(\omega) = \frac{\psi_{x_+}(\omega)}{\psi_{x_-}(\omega)} = \frac{e^{\left(x_+^2 - x_-^2\right)/4D}U(-i\omega - 1/2, x_+/\sqrt{D})}{U(-i\omega - 1/2, x_-/\sqrt{D})}, \quad (12.16a)$$

$$W_{y}(\omega) = \frac{\psi_{y_{+}}(\omega)}{\psi_{y_{-}}(\omega)} = \frac{e^{\left(y_{+}^{2} - y_{-}^{2}\right)/4D}U(-i\omega - 1/2, y_{+}/\sqrt{D})}{U(-i\omega - 1/2, y_{-}/\sqrt{D})}. \quad (12.16b)$$

In Eq. (12.16) ψ and U are the parabolic cylinder functions [11]. W_x and W_y are obtained by Laplace transformation of (12.11).

The circular function U(z, a), where a and z are real and complex variables, is given by

$$U(z,a) = \frac{e^{-z^2/4}}{\Gamma\left(a + \frac{1}{2}\right)} \int_0^\infty t^{a - \frac{1}{2}} e^{-\frac{1}{2}t^2 - zt} dt$$
 (12.17)

with

$$U(0,a) = \frac{\sqrt{\pi}}{2^{\frac{1}{2} + \frac{1}{4}\Gamma(\frac{3}{4} + \frac{1}{2}a)}}.$$
 (12.18)

A series expansion of U is given by

$$U(z,a) = U(0,a)u_1(z,a) + U(0,a)u_2(z,a),$$
(12.19)

where

$$u_{1}(z,a) = e^{-z^{2}/4} \left[1 + \left(a + \frac{1}{2} \right) \frac{z^{2}}{2!} + \left(a + \frac{1}{2} \right) \left(a + \frac{5}{2} \right) \frac{z^{4}}{4!} \cdots \right],$$

$$(12.20a)$$

$$u_{2}(z,a) = e^{-z^{2}/4} \left[z + \left(a + \frac{3}{2} \right) \frac{z^{3}}{3!} + \left(a + \frac{3}{2} \right) \left(a + \frac{7}{2} \right) \frac{z^{5}}{4!} \cdots \right].$$

$$(12.20b)$$

Substitutions of (12.16a) and (12.16b) in (12.15) give

$$N(\omega) = \frac{8J_0}{\omega^2} \operatorname{Re} \left[\frac{(\psi_{x-} - \psi_{x+})(\psi_{y-} - \psi_{y+})}{\psi_{x-} \psi_{y-} - \psi_{x+} \psi_{y+}} \right].$$
 (12.21)

For moderate values of the noise intensity D, the spectrum $N(\omega)$ of the bistable case of the system (12.6) with $x_+ > |x_-|$ and $y_+ > |y_-|$ displays a resonance-like spectrum as a function of ω implying coherence resonance. For more details one may refer to the Ref. [3].

12.5 Chaotic Resonance

For simplicity consider the bistable system [12]

$$x_{n+1} = S \tanh(x_n) + \epsilon \sin(2\pi n/T_0) + \alpha \xi_n, \tag{12.22}$$

where S, T_0 and α are parameters and ξ_n is random or chaotic. Figure 12.10 shows x versus $f(x) = S \tanh x$ for S = 2. In this figure the intersections of the diagonal line (dashed line) with f(x) (continuous line) mark the equilibrium points. When $\alpha = 0$, S = 2, $\epsilon = 0.5$ and $T_0 = 32$ the external periodic force is unable to induce jumping motion between the two equilibrium points.

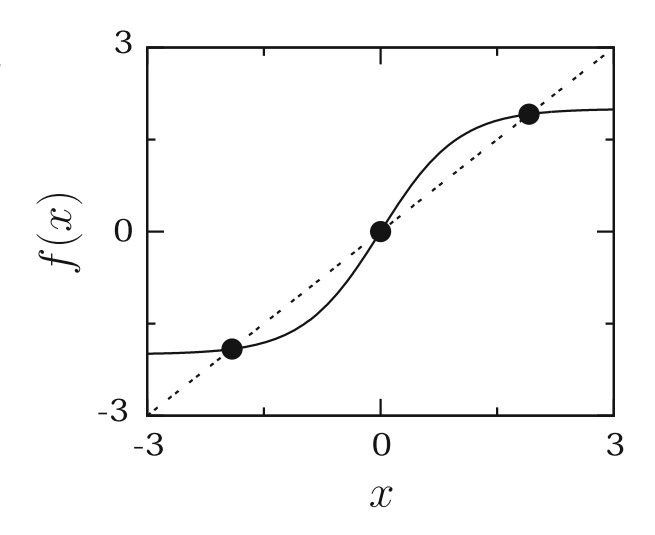
For resonance analysis, construct groups of chaotic and random perturbations having similar statistical properties so that their effects can be compared. Use the control parameter as the intensity of perturbation given by $D=2\sigma^2$ where σ is the standard deviation of the perturbation and

$$\sigma^2 = \alpha^2 \int_I (\xi - \langle \xi \rangle)^2 p(\xi) \, \mathrm{d}\xi, \tag{12.23}$$

where *I* is the interval to which ξ is restricted, $p(\xi)$ is either the probability density for the random perturbations and $\langle \xi \rangle$ is its mean value.

12.5 Chaotic Resonance 345

Fig. 12.10 Plot of x versus $f(x) = S \tanh(x)$ (continuous curve) with S = 2. The dashed line represents f(x) = x



12.5.1 Generating Similar Noise and Chaos

Consider random numbers uniformly distributed in the interval [-0.5, 0.5] and random numbers with Gaussian distribution. It is possible to generate these two types of random numbers using different methods. For example, the iterations of the tent map [13]

$$\xi_{n+1} = 1 - 2|x\xi_n| \tag{12.24}$$

become chaotic with $\xi_n \in [-0.5, 0.5]$ and $p(\xi) = 1$. For the Bernoulli shift map given by

$$\xi_{n+1} = \begin{cases} 2\xi_n + 0.5, & \xi_n \in [-0.5, 0] \\ 2\xi_n - 0.5, & \xi_n \in [0, 0.5] \end{cases}$$
 (12.25)

also $p(\xi) = 1$. That is, ξ_n of these two maps are uniformly distributed in the interval [-0.5, 0.5]. Employing the Park and Miller method [14] one can generate uniform random numbers in the interval [-0.5, 0.5]. The above methods give rise uniformly distributed random numbers in the interval [-0.5, 0.5]. Call these three perturbations as *tent perturbations*.

The iterated solution of the logistic map

$$\xi_{n+1} = 0.5 - 4\xi_n^2 \tag{12.26}$$

lies in the interval [-0.5, 0.5] and is chaotic, however, $p(\xi) \neq 1$. The solution of the modified logistic map

$$\xi_{n+1} = \begin{cases} 0.5 - 4\xi_n^2, & \xi_n \in [-0.5, 0] \\ 4\xi_n^2 - 0.5, & \xi_n \in [0, 0.5] \end{cases}$$
 (12.27)

is also chaotic with $p(\xi) \neq 1$. That is, ξ is not uniformly distributed in the interval [-0.5, 0.5]. For the logistic map and the modified logistic map the density of measure is

$$p(\xi) = \frac{1}{\pi\sqrt{(0.5 - \xi)(0.5 - \xi)}}.$$
 (12.28)

Interestingly, the trajectories of the tent map are related one-to-one with those of the logistic map through the relation [13]

$$C(x) = \frac{1}{2}\sin \pi x. {(12.29)}$$

Thus if one starts with a large number of η_i generated by the Park and Miller method or the tent map and obtain $\xi_n \equiv C(\eta_n)$, then the probability distribution of ξ is given by (12.28). The probability distribution of ξ obtained from the logistic map (12.26), modified logistic map (12.27) and through (12.29), all have the same $p(\xi)$ given by (12.28). We call these perturbations as *logistic chaos, modified logistic chaos* and *logistic noise*, respectively, or simply *logistic perturbations group* [6].

A third set of perturbations is the Gaussian perturbation. The Box-Muller formula [14, 15] for generating random numbers obeying Gaussian distribution is

$$\xi = \sigma \sqrt{-2 \ln \xi_1} \cos(2\pi \xi_2),$$
 (12.30)

where ξ_1 and ξ_2 are two random numbers uniformly distributed in the interval [0, 1] (for example, generated through Park and Miller method [14]). As pointed out above, the iterations of tent map become chaotic and distributed uniformly in the interval [-0.5, 0.5]. The iterations of the tent map (12.24) can be mapped into the interval [0, 1]. Instead of ξ_1 and ξ_2 in Eq. (12.30) as the numbers generated by the Park and Miller method one can choose them as the iterated values from the tent map. Call the random numbers generated in this way as chaotic Gaussian perturbations. Thus, there are two *Gaussian perturbations*. Figure 12.11 displays the probability distributions of the above mentioned three groups of perturbations.

12.5 Chaotic Resonance 347

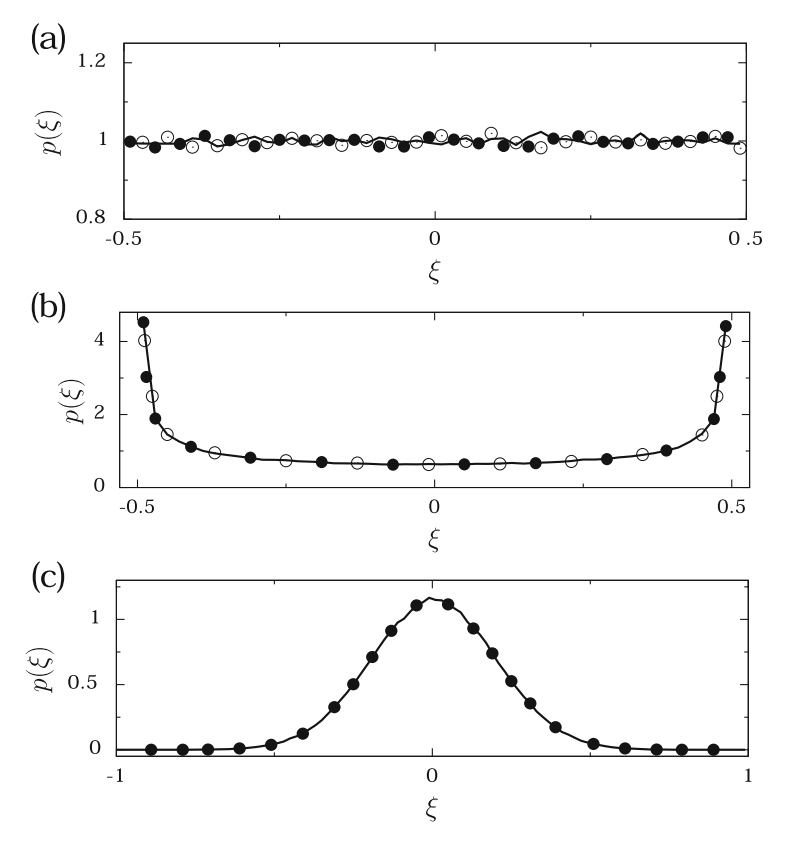


Fig. 12.11 (a) Probability density $p(\xi)$ of the solutions of the tent map (*continuous curve*), Bernoulli shift map (*solid circles*) and the random numbers generated by the Park and Miller method (*open circles*). (b) $p(\xi)$ of the chaotic solution of the modified logistic map (*continuous curve*), chaotic solution of the modified logistic map (*solid circles*) and the logistic noise (*open circles*). (c) $p(\xi)$ of the Gaussian noise (*continuous curve*) and the chaotic Gaussian perturbation (*solid circles*)

12.5.2 Effect of Chaotic Perturbations

Now, we analyse how these perturbations act in the system (12.22).

In the bistable system (12.22), the applied perturbations induce switching motion between stable states. The mean residence time of a trajectory about an equilibrium state varies with the parameter D. Consider the probability distribution of residence times. Denote t_j as the times at which jumps take place. The normalized distribution N(T) of $T(j) = t_j - t_{j-1}$ is called *residence time distribution function* (RTDF). This

distribution displays peaks centered at $T_k = (k - \frac{1}{2}) T_0$. Then define the areas under the various peaks as

$$P_k = \sum_{T_k - T_0/4}^{T_k + T_0/4} N(T). \tag{12.31}$$

 P_1 depends on D and treat it as a numerical quantifier of the coordination between switching and forcing. P_1 can exhibit resonance.

Figure 12.12 presents the variation of P_1 as a function of D for various perturbations. In Fig. 12.12a where the applied perturbations are tent perturbations, for each of the three perturbations P_1 increases, reaches a maximum and then decreases. That is, resonance occurs for both random and chaotic perturbations approximately at the same values of D, however, the shapes of the curves for each perturbation are quite different. The observed resonance is termed as *chaotic resonance* [6]. The value of P_1 at resonance for the Bernoulli map case is relatively higher than that of the uniformly distributed random numbers.

As shown in Figs. 12.12b and c resonance occurs for the logistic and Gaussian perturbations. Further, the resonance curves of logistic chaos is similar to that of logistic noise. In the cases of chaotic Gaussian perturbations and Gaussian white noise also the resonance curves are similar. Thus, one can conclude that the response of the system (12.22) to the random and chaotic perturbations are almost identical. The above examples points out that chaotic perturbations can give rise resonant responses very similar to those realized with noise.

It is noteworthy to mention that for the resonance induced by a chaotic perturbation new control possibilities exist [6]. Such possibilities are based on the adaptability of chaotic systems, the trajectories of which can lead to periodic dynamics by using small perturbations [16]. Thus, in the nonlinear dynamical systems exhibiting chaotic resonance one can take advantage of the ability to

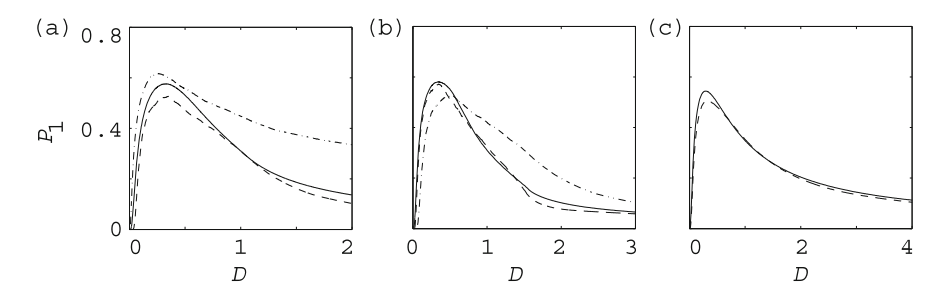


Fig. 12.12 Variation of P_1 with the perturbation intensity D for different perturbations [6]: (a) Chaotic solutions of the tent map (*dashed line*) and the Bernoulli shift map (*dash dotted line*) and random numbers uniformly distributed in the interval [-0.5, 0.5] (*solid line*); (b) Logistic chaos (*dashed line*), chaos from the modified logistic map (*dash dotted line*) and logistic noise (*solid line*). (c) Chaotic Gaussian perturbation (*solid line*) and Gaussian white noise (*dashed line*)

References 349

stabilize the source of the perturbation that gives rise the resonance in different periodic orbits.

12.6 Conclusion

Coherence resonance has been realized in different kinds of nonlinear systems. It is found in the dynamics of two phreatophyte species interacting with the water table [17] and in excitable prey-predator plankton system with infected prey [18], optical system [19], chemical systems [20, 21], atmospheric global circulation model [22, 23], carbon nano tube ion channel [24], Lorenz equations [25], logistic map [25], coupled systems [26–32], biomedical systems [33, 34], self-sustained bistable oscillator [35] and quantum dot semiconductor laser [36].

Maximization of differential entropy by coherence [37], optimal network configuration for maximal coherence [38], theoretical formula for computing normalized variance [39] have been proposed. Coherence resonance in the presence of timedelay [40–42], multiplicative noise [43], non-Gaussian noise [44], coloured noise [45] and near Hopf bifurcation [46] have been reported. Spatial coherence in a doubly piecewise linear potential [47], discrete neuronal media [33], in excitable biochemical media [34], small-world network [48–51] and feedforward network [52] were realized. Coherence resonance was experimentally realized in electronic circuits [4, 42, 46, 53] and in a vertical-cavity surface-emitting laser system [41].

Because much biological signalling is achieved through rhythmic dynamics of the systems [54, 55], the enhancing of coherence of biological systems is crucial in bioinformatics. For example, certain optimal characters of biological signalling systems, such as the number of molecules [56], the number of ion channels in clusters [55] and the volume of cells [57] are determined theoretically under the condition of optimal coherence. These theoretical results are often found to be in agreement with experimental observations. Therefore, a better understanding of biological characters of systems can be made by analysing how the enhancement of the coherence takes place.

References

- 1. H. Gang, T. Ditzinger, C.Z. Ning, H. Haken, Phys. Rev. Lett. 71, 807 (1993)
- 2. A.S. Pikovsky, J. Kurths, Phys. Rev. Lett. 78, 775 (1997)
- 3. B. Linder, L. Schimanwky-Geier, Phys. Rev. E **61**, 6103 (2000)
- 4. C. Palenzuela, R. Toral, C.R. Mirasso, O. Calvo, J.D. Gunton, Europhys. Lett. 56, 347 (2001)
- 5. E. Ippen, J. Lindner, W.L. Ditto, J. Stat. Phys. 70, 437 (1993)
- 6. S. Zambrano, J.M. Casado, M.A.F. Sanjuan, Phys. Lett. A 366, 428 (2007)
- 7. S. Arathi, S. Rajasekar, J. Kurths, Int. J. Bifurcation Chaos 23, 1350132 (2013)
- 8. W.J. Rappel, S.H. Strogatz, Phys. Rev. E 50, 3249 (1994)
- 9. Z. Liu, Y. Lai, Phys. Rev. Lett. **86**, 4737 (2001)

- 10. J.D. Murray, *Mathematical Biology* (Springer, Berlin, 1993)
- 11. M. Abramowitz, I.A. Stegun, Handbook of Mathematical Functions (Dover, New York, 1970)
- 12. P.M. Gade, R. Rai, H. Singh, Phys. Rev. E 56, 2518 (1997)
- K.T. Alligood, T.D. Sauer, J.A. Yorke, Chaos, an Introduction to Dynamical Systems (Springer, New York, 1996)
- W.H. Press, S.A. Teukolsky, W.T. Vetterling, B.P. Flannery, *Numerical Recipes in Fortran*, Indian edition (Foundation Books, New Delhi, 1993)
- 15. G.E.P. Box, M.E. Muller, Ann. Math. Stat. 29, 610 (1958)
- 16. E. Ott, C. Grebogi, J.A. Yorke, Phys. Rev. Lett. 64, 1196 (1990)
- 17. F. Borgogno, P. D'odorico, F. Laio, L. Ridolfi, J. Theor. Biol. 293, 65 (2012)
- 18. M. Sieber, H. Malchow, L. Schimanksy-Geier, Ecol. Complex. 4, 223 (2007)
- 19. G. Giacomelli, M. Giudici, S. Balle, J.R. Tredice, Phys. Rev. Lett. 84, 3298 (2000)
- 20. K. Mujakawa, H. Isikawa, Phys. Rev. E **66**, 046204 (2002)
- A. Kolbus, A. Lemarchand, A.L. Kawcyzynski, B. Nowakowski, Phys. Chem. 12, 13224 (2010)
- 22. V.P. Munuzuri, R. Deza, K. Fraedrich, T. Kunz, F. Lunkeit, Phys. Rev. E 71, 065602 (2005)
- 23. O. Carrillo, M.A. Santos, G. Garcia-Ojalvo, J.M. Sancho, Europhys. Lett. 65, 452 (2004)
- 24. C.Y. Lee, W. Choi, J.H. Han, M.S. Strano, Science 329, 1320 (2010)
- 25. M. Gosak, M. Perc, Phys. Rev. E 76, 037201 (2007)
- 26. C.S. Zhou, J. Kurths, B. Hu, Phys. Rev. Lett. 87, 098101 (2001)
- 27. C.S. Zhou, J. Kurths, Chaos 13, 401 (2003)
- 28. H.S. Wio, Phys. Rev. E 54, R3075 (1995)
- 29. S.K. Han, T.G. Yim, D.E. Postrov, O.V. Sosnovtseva, Phys. Rev. Lett. 83, 1771 (1999)
- 30. Z. Liu, Y.C. Lai, Phys. Rev. Lett. 86, 4737 (2001)
- 31. Y.C. Lai, Z. Liu, Phys. Rev. E 64, 066202 (2001)
- 32. M. Zhan, G.W. Wei, C.H. Lai, Y.C. Lai, Z. Liu, Phys. Rev. E 66, 036201 (2002)
- 33. M. Perc, Chaos Solitons Fractals 31, 64 (2007)
- 34. M. Gosak, M. Marhl, M. Perc, Biophys. Chem. 128, 210 (2007)
- A. Zakharova, T. Vadivasova, V. Anishchenko, A. Koseska, J. Kurths, Phys. Rev. E 81, 011106 (2010)
- 36. C. Otto, B. Lingnau, E. Scholl, K. Ludge, Opt. Exp. 22, 13288 (2014)
- 37. J. Rajhans, A.N. Sekar Iyengar (1 Dec 2013). arXiv:1312.02031v1 [nlin.CD]
- 38. M. Gosak, D. Korosak, M. Marhl, Phys. Rev. E 81, 056104 (2010)
- 39. S. Biswas, D. Das, P. Parmananda, A. Sain, Phys. Rev. E 80, 046220 (2009)
- 40. Y. Jim, H. Hu, Physica A **382**, 423 (2007)
- 41. M.A. Arteaga, M. Valencia, M. Sciamana, H. Thienpont, M. Lopez-Amo, K. Panajotov, Phys. Rev. Lett. 99, 023903 (2007)
- 42. R. Aust, P. Hovel, J. Hizanidis, E. Scholl, Eur. Phys J. Special Topics 187, 77 (2010)
- 43. T. Tang, Y. Jia, M. Yi, J. Ma, J. Li, Phys. Rev. E 77, 061905 (2008)
- 44. Y. Gong, Y. Xie, Y. Hao, J. Chem. Phys. **130**, 165106 (2009)
- 45. V. Beato, I.S. Nadal, I. Gerdes, H. Enge, Phil. Trans R. Soc. A 366, 381 (2008)
- A. Zakharova, A. Feoktistov, T. Vadivasova, E. School, Eur. Phys. J. Special Topics 222, 2481 (2013)
- 47. M. Perc, M. Marhl, Phys. Rev. E 73, 066205 (2006)
- 48. X. Lin, Y. Gong, L. Wang, Chaos 21, 043109 (2011)
- 49. X. Sun, M. Perc, Q. Lu, J. Kurths, Chaos 18, 023102 (2008)
- 50. M. Perc, Chaos Solitons Fractals 31, 280 (2007)
- 51. M. Perc, New J. Phys. 7, 252 (2005)
- 52. C. Men, J. Wang, Y.M. Qin, B. Deng, K.M. Tsang, W.L. Chan, Chaos 22, 013104 (2012)
- 53. O. Calvo, C.R. Mirasso, R. Toral, Elect. Lett. 37, 1062 (2001)
- 54. Y. Li, J. Rinzel, J. Theor. Biol. 166, 461 (1994)
- 55. J.W. Shuai, P. Jung, Phys. Rev. Lett. **88**, 068102 (2002)
- 56. Y. Morishita, T.J. Kobayashi, K. Aihara, Biophys. J. 91, 2072 (2006)
- 57. Z.H. Hou, J.Q. Zhang, H.W. Xin, Phys. Rev. E 74, 031901 (2006)

Chapter 13 Slow Passage Through Resonance and Resonance Tongues

In Chap. 11 the autoresonance phenomenon due to a slow variation of frequency of the driving force or the slow variation of a parameter of nonlinear systems is described. Two other interesting effects that can be realizable in the case of slowly varying a parameter are the *slow passage through resonance* and *resonance tongues*. For example, consider a linear or a nonlinear system driven by a periodic external force with a fixed frequency ω_f . Assume that the amplitude of oscillation is maximum at $\omega_f = \omega_{f,max}$ with a value A_{max} . Suppose ω is allowed to vary slowly with time and write $\omega_f(t) = \omega + \epsilon t$, $\epsilon \ll 1$. In a typical case when ω is fixed at a value smaller than $\omega_{f,max}$ then the amplitude of oscillation varies with time, reaches a maximum value at a certain time t' such that $\omega_f(t) = \omega + \epsilon t' < \omega_{f,max}$ and then decreases. The new resonance frequency $\omega_f(t)$ is lower than the frequency $\omega_{f,max}$. This is termed as *slow passage through resonance* and is a transient phenomenon. Such a passing through has been found to occur in systems exhibiting parametric resonance also.

The phenomenon of passing through resonance had been investigated almost a century ago by Duffing [1] and then by Stoker [2] and others [3, 4]. The study of effect of slow passage through resonance is important in the systems where one or more control parameters vary on a time scale that is slower than that of the dynamics. For example, in certain chemical reactions the concentrations of reactants vary slowly on the time scale of reactors. Generally, the response of a system with slowly varying a control parameter will be different from the dynamics of static system. The features of slow passage dynamics have been investigated in Mathieu equation with cubic and damping terms [5, 6], nonlinearly damped systems [7], chemical reaction system [8], a laser system with noise [9], Mathieu equation with two forcing [10, 11] and linear harmonic oscillator [12]. The problem of slowly passing through resonance has been analysed by slowly varying the length of a tank. The number of solitons is found to change with the slow change of the tank length [13]. In a catenary-vertical cable hoisting system [14] due to the slow passage through resonance natural frequencies and mode shapes change slowly due to a winding

cycle. Consequences of slow passage of a system through a Hopf bifurcation [15], multiple resonance tongues [11], multiple bifurcation points [16], near a limit point [17] and through a resonance in nonlinear Klein–Gordon equation perturbed by a small external force [18] have been reported.

In Chap. 10 parametrically driven linear and nonlinear systems are shown to possess resonance tongues in a parameter space. In such systems when the natural frequency is varied passage through one or more resonance tongues with grow in amplitude has been found to occur [10, 11]. In the present chapter focus is on slow passage through resonance and resonance tongues in certain dynamical systems.

13.1 Passage Through Resonance in Duffing Oscillator

Consider the Duffing oscillator equation

$$\ddot{x} + d\dot{x} + \omega_0^2 x + \beta x^3 = f \cos \omega_f t, \quad \omega_f(t) = \omega + \epsilon t.$$
 (13.1)

For d=0.1, $\omega_0=1$, $\beta=2$ and f=0.2 when ω_f is treated as a time-independent parameter ($\epsilon=0$) then the amplitude of the response oscillation of the system becomes a maximum at $\omega=1.73$ with the amplitude A=1.14. This is shown in Fig. 1.3. In this figure Q=A/f=5.75 at f=0.2. Then A is 1.14. It is possible to realize a maximum amplitude before ω reaches the resonance frequency value 1.73 by treating ω_f in Eq. (13.1) as a time-dependent parameter. Denote ω_r as the frequency of the driving force at which the response amplitude is maximum when $\epsilon=0$. $\omega_r(\epsilon)$ is the frequency $\omega_f(t')$ where t' is the time at which the amplitude of oscillation becomes a maximum. $\omega_f(t')$ depends on d and ω_0 .

Figure 13.1 shows the variation of x(t) as a function of $\omega_{\Gamma}(t)$ for a few fixed values of β and with $\omega=0.5$ and $\epsilon=10^{-5}$. For each fixed values of the parameters, initially x(t) exhibits a small amplitude oscillation. As $\omega_{\Gamma}(t)$ increases (as well as time) from the value $\omega=0.5$ the amplitude grows in a nonlinear manner and becomes maximum representing a large resonant response at a frequency far before the resonance frequency of the system corresponding to $\epsilon=0$. After resonance the amplitude decreases and in Fig. 13.1 we do not observe a large amplitude near the resonance frequency $\omega_{\Gamma}(\epsilon=0)$. In Fig. 13.1a, b corresponding to $\beta=0$ and 0.01 after resonance the amplitude of oscillation decreases smoothly. For these two values of β the frequency-response curve (plot of ω versus A or Q) displays a smooth variation. In Fig. 13.1c—e the frequency-response curve shows hysteresis similar to the one shown in Fig. 1.3. In order to distinguish the resonance frequency of the system $\epsilon=0$ and that with $\epsilon\neq0$ in [12] the resonance frequency for the case of $\epsilon\neq0$ is termed as β is termed as β in frequency and is denoted as ω_{Γ} .

Next, analyse the effect of the damping coefficient d and the parameter ϵ . Figure 13.2a–f illustrate the influence of d and ϵ , respectively, on the evolution of x for $\beta = 2$. Increase in the value of d not only preponed the resonance but also reduced the amplitude of trajectory at resonance. For sufficiently large values of d

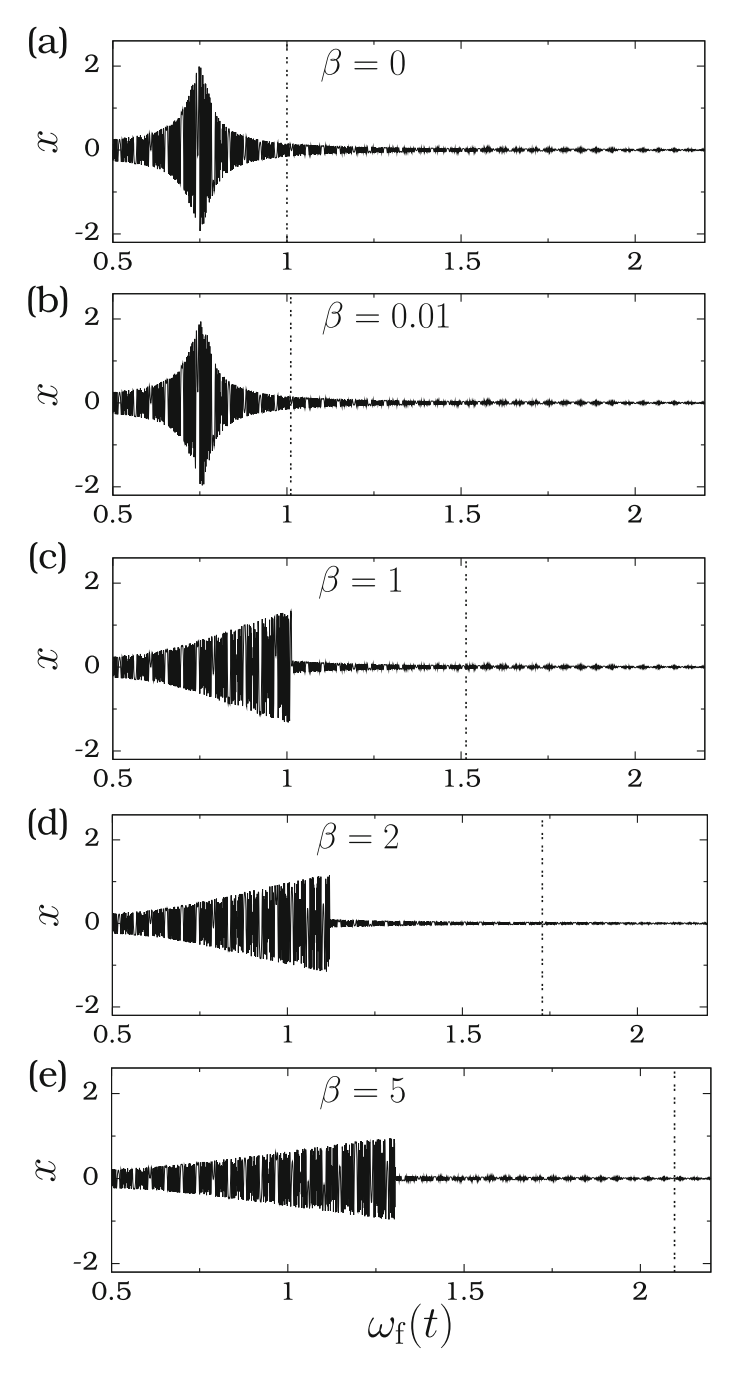


Fig. 13.1 x(t) versus $\omega_{\rm f}(t)$ for five fixed values of β of the system (13.1). The values of the other parameters are $d=0.1,\,\omega_0^2=1,f=0.2,\,\omega=0.5,\,\omega_{\rm f}(t)=\omega+\epsilon t$ and $\epsilon=10^{-5}$. The vertical dashed line indicates the resonance frequency of the system for $\epsilon=0$

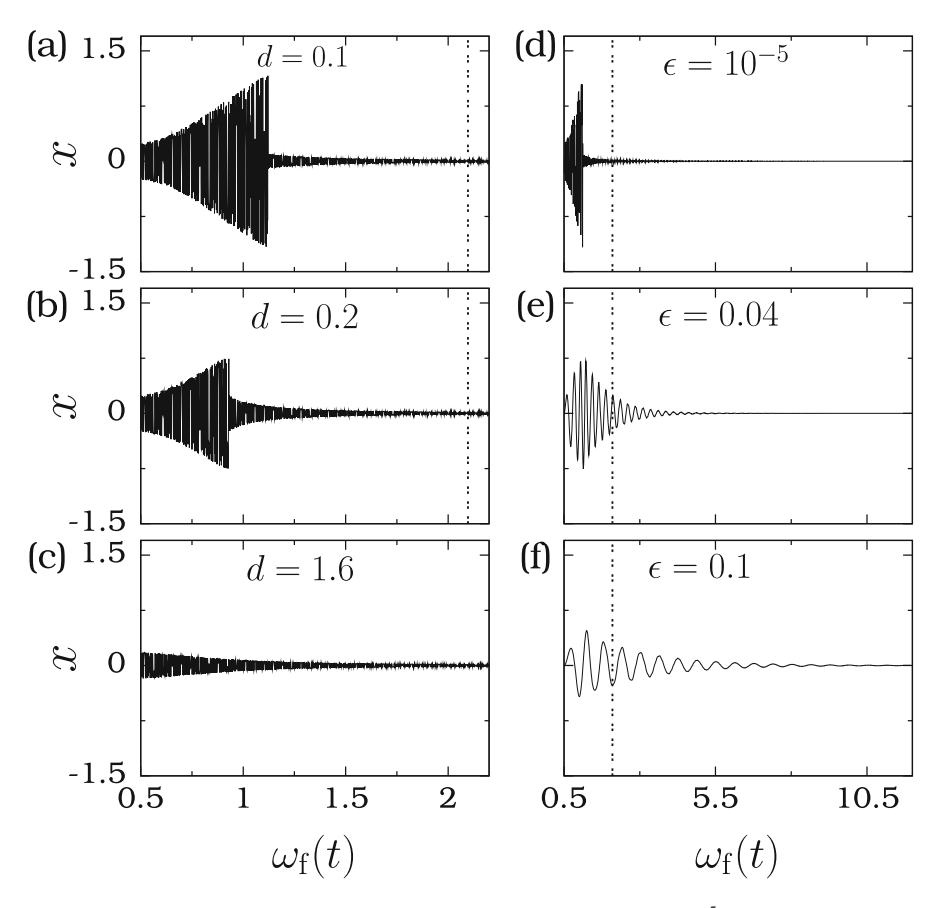


Fig. 13.2 (a)–(c) x(t) versus $\omega_f(t)$ for three values of d with $\epsilon = 10^{-5}$ and $\beta = 2$ for the system (13.1). (d)–(f) x(t) versus $\omega_f(t)$ for three values of ϵ with d = 0.1 and $\beta = 2$

there is no resonance as shown in Fig. 13.2c. The effect of increase in the value of ϵ is clearly seen in Fig. 13.2d–f. Not only the amplitude of the trajectory decreases but also the number of oscillation in an interval of $\omega_f(t)$ decreases with increases in the value of ϵ .

The values of $\omega_{\rm f}$ and the amplitude A at the jump frequency (resonance frequency) are computed through numerical simulation and the results are presented in Fig. 13.3. For sufficiently small values of ϵ both $\omega_{\rm j}$ and A are almost constant for each fixed value of the damping coefficient d. As pointed out in [12] the almost constancy of A is because of the constancy of $\omega_{\rm f}$ in the neighbourhood of the frequency $\omega_{\rm j}$ for a long time for x(t) to grow to a full resonant response amplitude. In Fig. 13.4 the variation of $\omega_{\rm j}$ and A with the parameter d in $\log_{10} - \log_{10}$ scale is shown for $\epsilon = 0.0001$ and $\beta = 2$. Power-law variation of $\omega_{\rm j}$ and A on d is found: $\omega_{\rm j} = 0.47551 d^{-0.38166}$ and $A = 0.32256 d^{-0.55132}$.

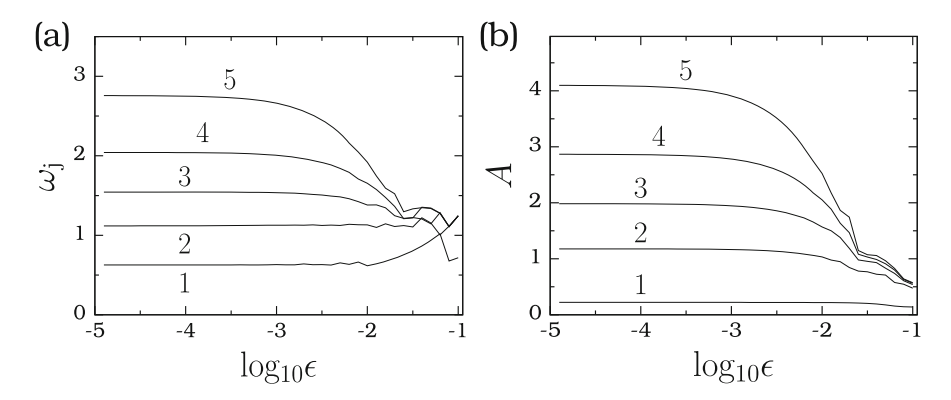


Fig. 13.3 Variation of (a) the jump frequency ω_j and (b) the amplitude A at the jump frequency with the parameter ϵ for the system (13.1). For the curves 1–5 the values of d are 1, 0.1, 0.4, 0.02 and 0.01, respectively. The values of the other parameters are $\omega_0 = 1$, $\beta = 2$ and f = 0.2

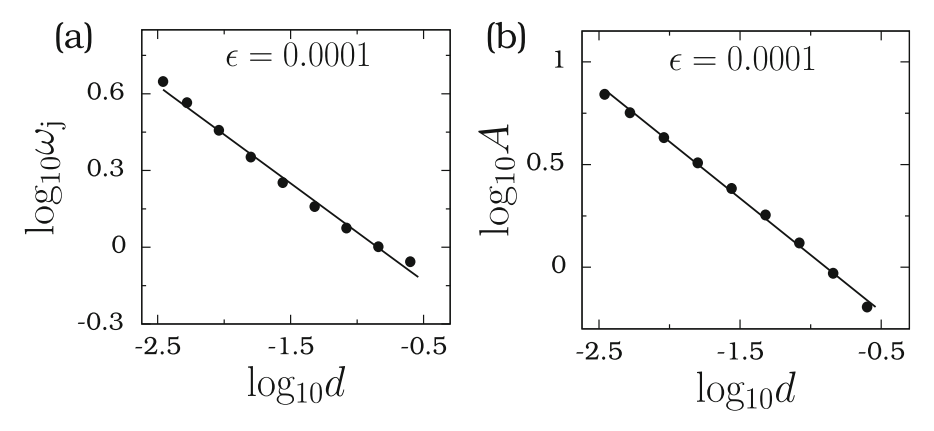


Fig. 13.4 Plot of (a) the jump frequency as a function of the parameter d and (b) the amplitude A at the jump frequency in $\log_{10} - \log_{10}$ scale for $\epsilon = 0.0001$ and $\beta = 2$. The *solid circles* are the numerical data and *continuous curve* is the best straight-line fit

For the undamped and linear system

$$\ddot{x} + x = \sin(\omega_f(t)t) , \quad \omega_f(t) = \omega_0 + \epsilon t$$
 (13.2)

an approximate solution obtained is [12]

$$x(t) \sim \begin{cases} 0, & \text{for } t \ll t_{j} \\ -\frac{\sqrt{\pi}}{2\sqrt{\epsilon}} & \cos\left[t - \frac{1}{\epsilon} \left(\frac{1 - \omega_{0}}{2}\right)^{2} + \frac{\pi}{4}\right], & \text{for } t \gg t_{j} \end{cases}$$
 (13.3)

where t_j is the time at which $\omega_f(t) = \omega_j$. The maximal amplitude A is found to be proportional to $\sqrt{\epsilon}$.

13.2 Mathieu Equation with Parametric Perturbation

In Eq. (10.2) the coefficient of θ term is assumed to be varying sinusoidally with a single frequency. What will happen if ω_0^2 varies monotonically but slowly with time? Suppose consider the system

$$\ddot{x} + \omega_0^2 x + \epsilon x \cos \omega t = 0 \tag{13.4}$$

and assume that ω_0^2 changes according to

$$\omega_0^2 = \epsilon^2 \mu t . \tag{13.5}$$

Such a slow variation of a parameter can happen during slow start-up or slow shut-down of physical and engineering systems. In (13.5) 0 is the starting value of ω_0^2 (at t=0) and $\epsilon^2\mu$ is the speed with which ω_0^2 changes.

13.2.1 Single Parametric Resonance

For $\epsilon \ll 1$ the first-order approximation of the transition curves bounding the 2:1 resonance tongue of Eq. (13.4) is given by Ng et al. [10]

$$\omega_0^2 = \frac{\omega^2}{4} \pm \frac{\epsilon}{2} + \mathcal{O}(\epsilon^2) . \tag{13.6}$$

The resonance window is $\omega_0^2 \in \left[\frac{\omega^2}{4} - \frac{\epsilon}{2}, \frac{\omega^2}{4} + \frac{\epsilon}{2}\right]$ and is depicted in Fig. 13.5. The '+' and '-' signs in Eq. (13.6) give rise the right and left transition curves in Fig. 13.5.

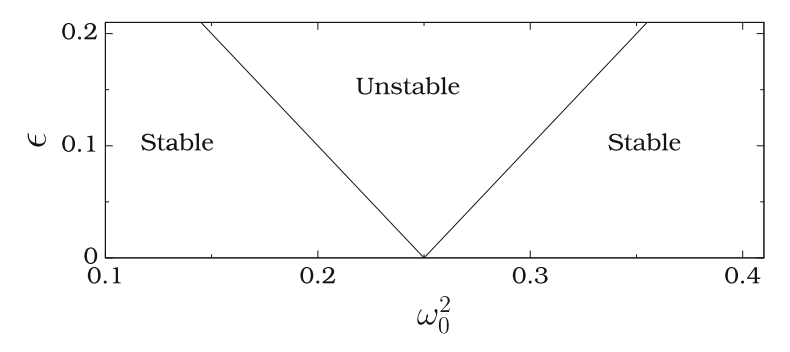


Fig. 13.5 The 2:1 resonance tongue of the system (13.4) in the first-order approximation. Here $\omega=1$

Replacing ω_0^2 by $\epsilon^2 \mu t$ in Eq. (13.6) gives

$$\epsilon^2 \mu t \approx \frac{\omega^2}{4} \pm \frac{\epsilon}{2} \,.$$
(13.7)

That is,

$$t_{\pm} \approx \frac{\omega^2}{4\epsilon^2 \mu} \pm \frac{1}{2\epsilon \mu} \,.$$
 (13.8)

The times t_{-} and t_{+} correspond to on the left and the right transition curves, respectively. Choose the initial conditions for the numerical simulation as

$$x(t_0) = \cos \gamma, \quad \dot{x}(t_0) = \sin \gamma, \quad 0 \le \gamma \le 2\pi. \tag{13.9}$$

Figure 13.6 shows the numerical solution x(t) for two values of γ for the parametric choice $\epsilon = 0.1$, $\mu = 0.1$ and $\omega = 1$. For this parametric values $t_- = 200$ while $t_+ = 300$. The vertical dashed lines in Fig. 13.6 represent t_{\pm} . In Fig. 13.6a corresponding the $\gamma = 0$ (x(0) = 1, $\dot{x}(0) = 0$) one can clearly observe amplification of response of the system during the time interval $t_- < t < t_+$, that is, when passing through the resonance tongue. However, x(t) becomes a maximum

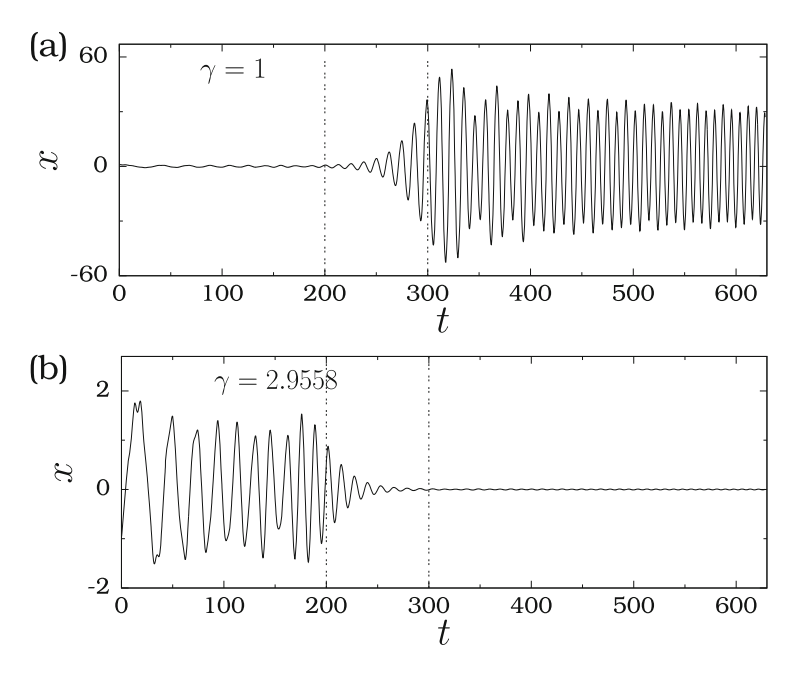


Fig. 13.6 Plot of x(t) versus t of the system (13.4) with $\epsilon = 0.1$, $\mu = 0.1$, $\omega = 1$ and for two initial conditions. The two *vertical dashed lines* denote t_{\pm} given by the Eq. (13.8)

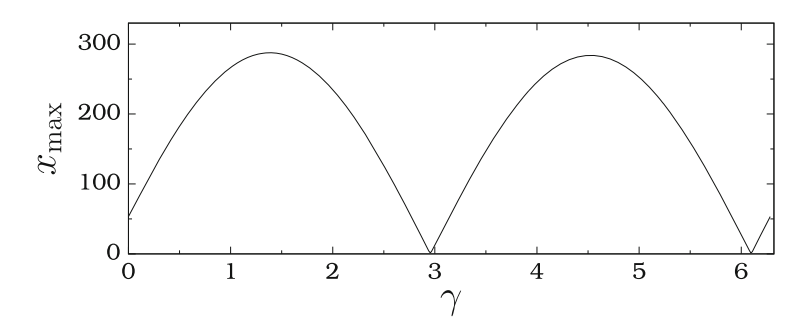


Fig. 13.7 Dependence of x_{max} on initial conditions characterized by the parameter γ [refer Eq. (13.9)]

at a time value beyond t_+ , that is, after the trajectory left the resonance tongue. Figure 13.6b depicts the result for $\gamma=2.9558$. In this case instead of amplification one observes de-amplification. The maximum amplitude in the resonance tongue interval is smaller than the maximum amplitude of the solution before entering the resonance tongue. The effect of initial conditions on the maximum response is nontrivial. The maximum value of x denoted as x_{max} is calculated for a set of initial conditions given by Eq. (13.9) by varying y. The result is depicted in Fig. 13.7. x_{max} is sensitive to the initial conditions.

13.2.2 Theoretical Treatment

It is possible to find an approximate analytical solution of (13.4) near 2:1 resonance tongue ($\omega_0^2 = 1/4$, $\omega = 1$) for $\epsilon \ll 1$ by applying the multiple scales method [10]. Writing $x(t) = x(\xi, \eta)$ with the slow time $\eta = \epsilon t$ and fast time $\xi = t$ the Eq. (13.4) takes the form

$$x_{\xi\xi} + 2\epsilon x_{\xi\eta} + \epsilon^2 x_{\eta\eta} + \left(\frac{1}{4} + \epsilon\mu\eta + \epsilon\cos\xi\right)x = 0.$$
 (13.10)

Introducing $x(\xi, \eta) = x_0(\xi, \eta) + \epsilon x_1(\xi, \eta) + \cdots$ and then collecting the terms containing ϵ^0 and ϵ^1 give

$$x_{0\xi\xi} + \frac{1}{4}x_0 = 0, (13.11a)$$

$$x_{1\xi\xi} + \frac{1}{4}x_1 = -2x_{0\xi\eta} - \mu\eta x_0 - x_0\cos\xi \ . \tag{13.11b}$$

The general solution of Eq. (13.11a) is given by

$$x_0(\xi, \eta) = A(\eta)\cos(\xi/2) + B(\eta)\sin(\xi/2).$$
 (13.12)

Substitution of Eq. (13.12) in Eq. (13.11b) leads to the equation

$$x_{1\xi\xi} + \frac{1}{4}x_1 = \left(A_{\eta} - \mu\eta B + \frac{B}{2}\right)\sin\frac{\xi}{2} - \left(B_{\eta} + \mu\eta A + \frac{A}{2}\right)\cos\frac{\xi}{2}$$
$$-\frac{A}{2}\cos\frac{3\xi}{2} - \frac{B}{2}\sin\frac{3\xi}{2}. \tag{13.13}$$

In Eq. (13.13) the first two terms in the right-side are the secular terms. Setting these two secular terms equal to zero results in

$$A_{\eta} = \left(\mu \eta - \frac{1}{2}\right) B, \tag{13.14a}$$

$$B_{\eta} = -\left(\mu\eta + \frac{1}{2}\right)A. \tag{13.14b}$$

Differentiating Eq. (13.14a) with respect to η once and then eliminating B and B_{η} using the Eq. (13.14) give

$$A_{\eta\eta} - \frac{\mu}{\mu\eta - \frac{1}{2}} A_{\eta} + \left(\mu^2 \eta^2 - \frac{1}{4}\right) A = 0.$$
 (13.15)

With the change of variable $\tau = \mu \eta$ Eq. (13.15) becomes

$$\mu^2 A_{\tau\tau} - \frac{\mu^2}{\tau - \frac{1}{2}} A_{\tau} + \left(\tau^2 - \frac{1}{4}\right) A = 0.$$
 (13.16)

Similarly, the equation for B is obtained as

$$\mu^2 B_{\tau\tau} - \frac{\mu^2}{\tau + \frac{1}{2}} B_{\tau} + \left(\tau^2 - \frac{1}{4}\right) B = 0.$$
 (13.17)

In order to compare the analytical solution with the numerical solution the initial conditions of both the solutions have to be identical. In order to identify A(0) and B(0) consider the first-order solution given by (13.12) as

$$x(t) \sim A(\epsilon t)\cos(t/2) + B(\epsilon t)\sin(t/2). \tag{13.18}$$

From Eq. (13.18) $\dot{x}(t)$ is written as

$$\dot{x}(t) \sim \left[\epsilon A'(\epsilon t) + \frac{1}{2} B(\epsilon t) \right] \cos(t/2) + \left[-\frac{1}{2} A(\epsilon t) + \epsilon B'(\epsilon t) \right] \sin(t/2).$$
 (13.19)

Then using Eq. (13.14) for A' and B' leads to

$$\dot{x}(t) \sim B \left[\epsilon \left(\mu \epsilon t - \frac{1}{2} \right) + \frac{1}{2} \right] \cos(t/2)$$

$$-A \left[\epsilon \left(\mu \epsilon t + \frac{1}{2} \right) + \frac{1}{2} \right] \sin(t/2). \tag{13.20}$$

At $t = t_0$ and for chosen $A(\eta_0 = \epsilon t_0)$ and $B(\eta_0 = \epsilon t_0)$ the corresponding $x(t_0)$ and $\dot{x}(t_0)$ can be determined from Eqs. (13.18) and (13.20).

13.2.3 Two Parametric Resonance

Now, consider the linear system driven by two parametric forces. The equation of motion of the system is

$$\ddot{x} + (\omega_0^2 + \epsilon \alpha_1 \cos \omega_1 t + \epsilon \alpha_2 \cos \omega_2 t) x = 0, \qquad (13.21)$$

where ω_0^2 is given by Eq. (13.5). Fix $\epsilon = 0.1$, $\mu = 0.1$, $\omega_1 = 1$, $\omega_2 = 2$, $\alpha_1 = 1$ and $\alpha_2 = 1$. The transition curves bounding the 2:1 resonance tongue of the above system is given by Eq. (13.6) with $\omega = \omega_1$ and ω_2 . Consequently, there are two resonance windows:

$$\omega_0^2 \in \left\lceil \frac{\omega_1^2}{4} - \frac{\epsilon \alpha_1}{2}, \frac{\omega_1^2}{4} + \frac{\epsilon \alpha_1}{2} \right\rceil, \quad \omega_0^2 \in \left\lceil \frac{\omega_2^2}{4} - \frac{\epsilon \alpha_2}{2}, \frac{\omega_2^2}{4} + \frac{\epsilon \alpha_2}{2} \right\rceil. \tag{13.22}$$

These windows are shown in Fig. 13.8.

The times (t_-, t_+) for the first and the second windows computed from Eq. (13.8) are (200, 300) and (950, 1050), respectively. Figure 13.9 presents x(t) for two initial conditions. For $\gamma=3$ amplification of amplitude of oscillation takes place in the two window regions corresponding to the time intervals (200, 300) and (950, 1050). For a slightly different initial condition specified by $\gamma=3.10644$ in Fig. 13.9b deamplification of amplitude of x is seen. The maximum amplitude of x is not only

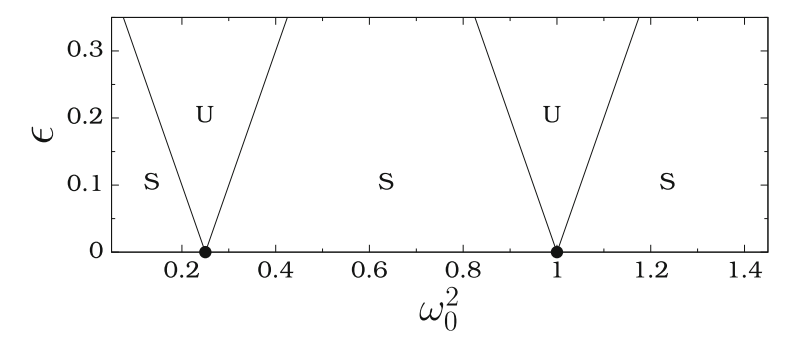


Fig. 13.8 Two resonance tongues of Eq. (13.21) for $\omega_1 = 1$, $\omega_2 = 2$, $\alpha_1 = 1$ and $\alpha_2 = 1$. 'S' and 'U' denote *stable* region and *unstable* region, respectively, of the solution. The first and the second *solid circles* represent the centers of the first and the second resonance tongues, respectively

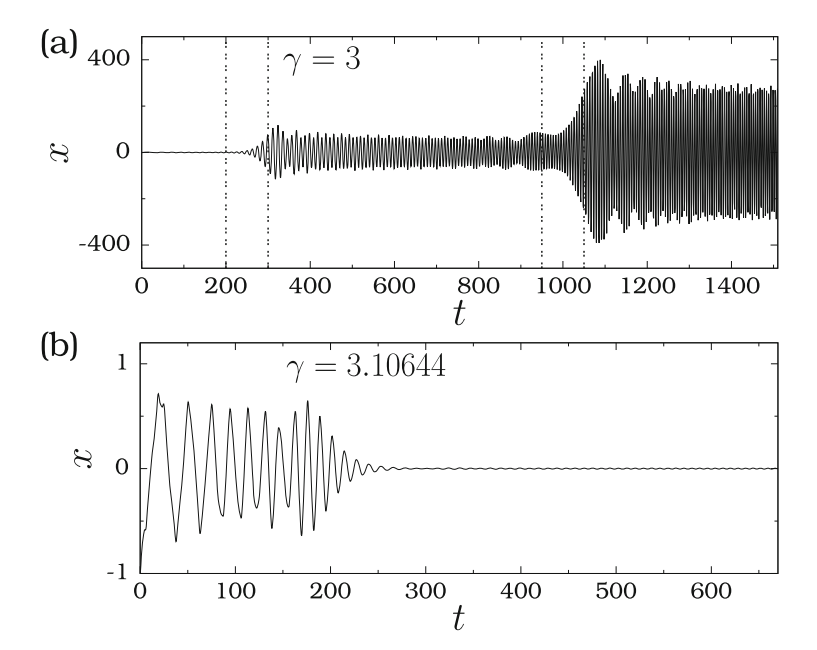


Fig. 13.9 Variation of x(t) with t of the system (13.21) with $\epsilon = 0.1$, $\mu = 0.1$, $\omega_1 = 1$, $\omega_2 = 2$, $\alpha_1 = 1$ and $\alpha_2 = 1$ and for two initial conditions

sensitive to the initial conditions but also sensitive to the amplitudes α_1 and α_2 of the parametric forces [11]. This is because the amplification factor depends on the width of the resonance tongue which can be varied by the values of the parameters ϵ , α_1 and α_2 .

In [11] a simplified model system for Eq. (13.21) is proposed to describe what is happening in the resonance tongues and in the remaining regime. Near each of the two resonance tongues, namely, when $\omega_0^2 \approx \omega_1^2/4$ and $\omega_2^2/4$, the respective forcing terms $\epsilon \alpha_i \cos \omega_i t$, i=1,2 are significant and the term $\omega_0^2 = \epsilon^2 \mu t$ can be neglected. Outside the resonance tongues (denoted by 'S' in Fig. 13.8) the term $\omega_0^2 = \epsilon^2 \mu t$ is significant and the forcing terms have a weak effect.

Noting that the boundaries of the resonance tongues are given by the Eq. (13.22) and the corresponding time intervals of the first and the second tongues for $\epsilon = 0.1$, $\mu = 0.1$, $\alpha_1 = 1$, $\alpha_2 = 1$ are (200, 300) and (950, 1050), the simplified model can be written as

$$\ddot{x} + \epsilon^2 \mu t x = 0, \quad 0 < t < 200 \tag{13.23a}$$

$$\ddot{x} + \left(\frac{\omega_1^2}{4} + \epsilon \alpha_1 \cos \omega_1 t\right) x = 0, \quad 200 < t < 300$$
 (13.23b)

$$\ddot{x} + \epsilon^2 \mu t x = 0, \quad 300 < t < 950 \tag{13.23c}$$

$$\ddot{x} + \left(\frac{\omega_2^2}{4} + \epsilon \alpha_2 \cos \omega_2 t\right) x = 0, \quad 950 < t < 1050$$
 (13.23d)

$$\ddot{x} + \epsilon^2 \mu t x = 0, \quad t > 1050$$
 (13.23e)

where $\omega_1^2/4$ and $\omega_2^2/4$ are the centers of the first and the second resonance tongues, respectively. In Fig. 13.10 the solution generated by numerically solving the simplified system (13.23) for the value of γ used in Fig. 13.9a is presented. The qualitative features of the solutions of Eqs. (13.23) and (13.21) are similar. An approximate analytical solution valid for each of the time interval given in Eq. (13.23) has been obtained in [11].

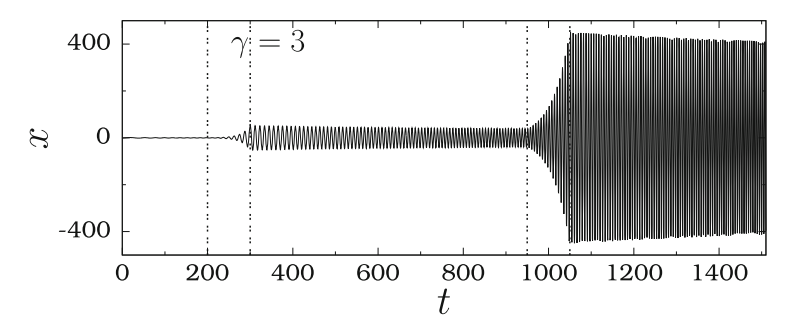


Fig. 13.10 Variation of x(t) with t of the system (13.23) with $\epsilon = 0.1$, $\mu = 0.1$, $\omega_1 = 1$, $\omega_2 = 2$, $\alpha_1 = 1$ and $\alpha_2 = 1$ and for $\gamma = 3$

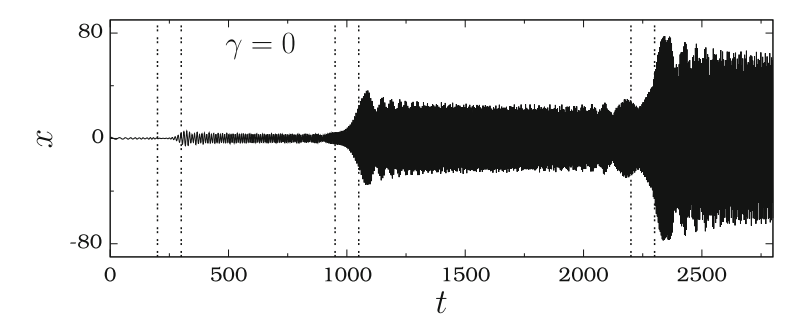


Fig. 13.11 Slow passage of x(t) with t of the system (13.24) with $\epsilon = 0.1$, $\mu = 0.1$, $\omega_1 = 1$, $\omega_2 = 2$, $\omega_3 = 3$, $\alpha_1 = 1$, $\alpha_2 = 1$ and $\alpha_3 = 1$ and for $\gamma = 0$

13.2.4 Three Resonance Tongues

Finally, in this section takeup the case of slow passage through three resonance tongues in the system

$$\ddot{x} + (\omega_0^2 + \epsilon \alpha_1 \cos \omega_1 t + \epsilon \alpha_2 \cos \omega_2 t + \epsilon \alpha_3 \cos \omega_3 t) x = 0, \qquad (13.24)$$

Consider the parametric choice $\epsilon = 0.1$, $\mu = 0.1$, $\alpha_1 = \alpha_2 = \alpha_3 = 1$, $\omega_1 = 1$, $\omega_2 = 2$ and $\omega_3 = 3$. Figure 13.11 shows the evolution of x for y = 0. Amplification of x(t) takes place in the three resonance tongues regime. That is, an additional resonance tongue also leads to an additional growth of x(t).

13.3 Nonlinear Systems with Parametric Perturbation

The slow passage dynamics reported in the previous section in a linear dynamical system can be observed in nonlinear systems also. The present section points out it in the perturbed pendulum system

$$\ddot{\theta} + (\omega_0^2 + \epsilon \alpha_1 \cos \omega_1 t + \epsilon \alpha_2 \cos \omega_2 t) \theta + 0.01 \sin \theta = 0$$
 (13.25)

and the parametrically driven Duffing oscillator

$$\ddot{x} + \left(\omega_0^2 + \epsilon \alpha_1 \cos \omega_1 t + \epsilon \alpha_2 \cos \omega_2 t\right) x + 0.01 x^3 = 0$$
 (13.26)

with $\omega_0^2 = \epsilon^2 \mu t$. Analytical determinations of resonance tongues and the values of t_- and t_+ at which a trajectory enters and leaves, respectively, of a resonance tongue are difficult. Therefore, very briefly, examples of the occurrence of growth of a state variable similar to the system (13.21) are presented in the following.

Figure 13.12a, b show the numerically computed maximum amplitude of oscillation of the system (13.25) for the cases of parametrically driven by one force and two forces, respectively. θ_{max} is periodic with period π in Fig. 13.12a and also in Fig. 13.12b. The maximum value of θ_{max} for the case of $\alpha_2 \neq 0$ is about ten times higher than that of $\alpha_2 = 0$. The variation of θ_{max} with γ is smooth. In Fig. 13.13a, b $\theta(t)$ versus t for $\alpha_2 = 0$ and $\alpha_2 = 1$, respectively, are shown for $\gamma = 0.2$. In both the figures rapid growth of amplitude of oscillation indicating passage through resonance tongues is seen.

The variations of x_{max} in the Duffing oscillator system (13.26) with γ for $\alpha_2 = 0$ and $\alpha_2 = 1$ are presented in Fig. 13.14. x_{max} varies irregularly and moreover displays a nonsmooth variation with γ . Here also the maximum value of x_{max} for $\alpha_2 = 1$ is higher than that of $\alpha_2 = 0$, however, the increase in x_{max} is not very high compared to the system (13.25). Figure 13.15 shows the evolution of x(t) for $\alpha_2 = 0$ and $\alpha_2 = 1$ for $\gamma = 0.2$.

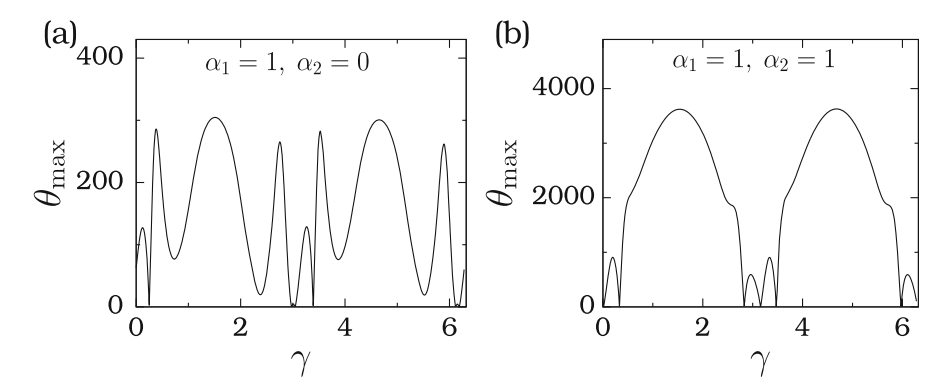


Fig. 13.12 θ_{max} as a function of initial conditions characterized by the parameter γ [refer Eq. (13.9)] for the system (13.25) with (**a**) $\alpha_2 = 0$ and (**b**) $\alpha_2 = 1$

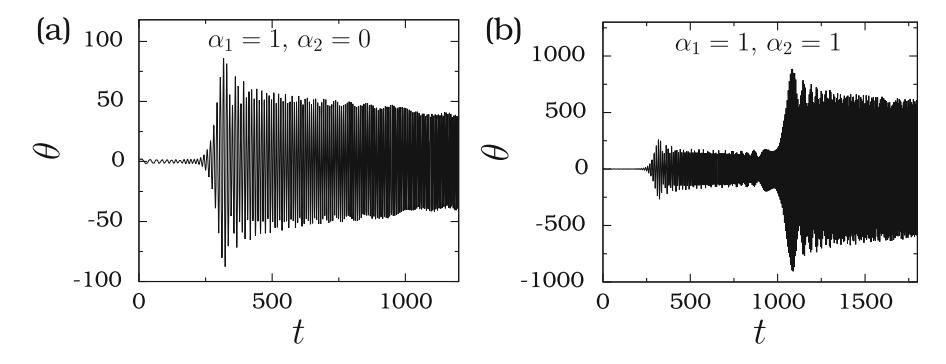


Fig. 13.13 $\theta(t)$ versus t of the system (13.25) with $\gamma = 0.2$, $\epsilon = 0.1$, $\mu = 0.1$, $\omega_1 = 1$, $\omega_2 = 2$, $\alpha_1 = 1$ and (a) $\alpha_2 = 0$ and (b) $\alpha_2 = 1$

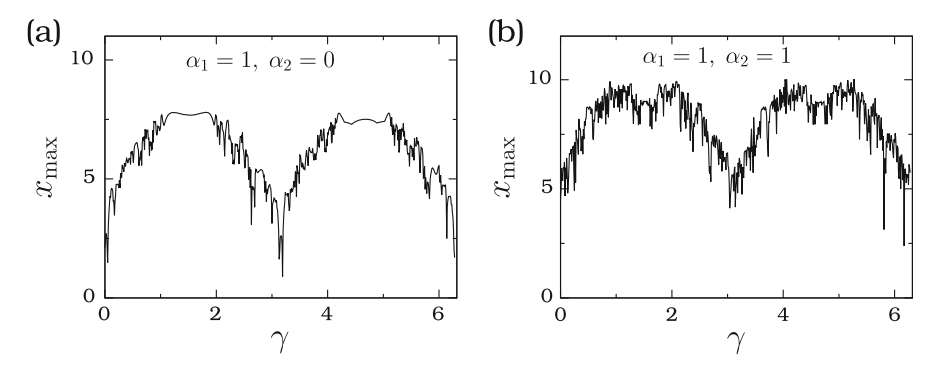


Fig. 13.14 x_{max} as a function of γ [refer Eq. (13.9)] for the system (13.26) with (a) $\alpha_2 = 0$ and (b) $\alpha_2 = 1$

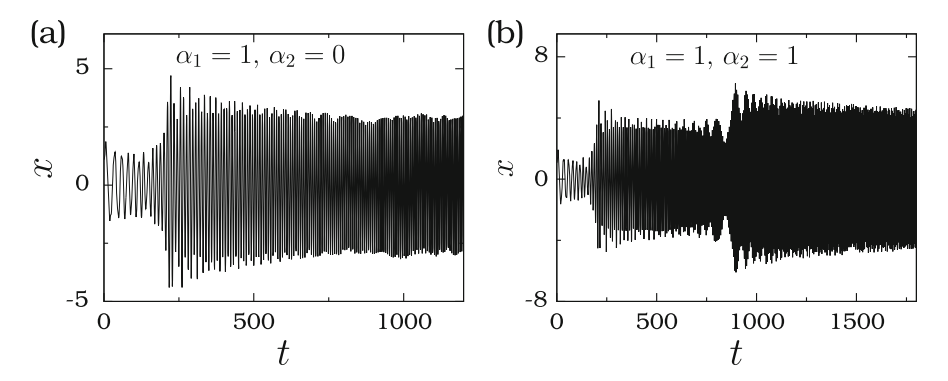


Fig. 13.15 x(t) versus t of the system (13.26) with $\gamma = 0.2$, $\epsilon = 0.1$, $\mu = 0.1$, $\omega_1 = 1$, $\omega_2 = 2$, $\alpha_1 = 1$ and (a) $\alpha_2 = 0$ and (b) $\alpha_2 = 1$

13.4 Concluding Remarks

A dynamical consequency of slow passage dynamical response is that unexpected large amplitude oscillations can be induced when an appropriate parameter of a system is varied slowly. When the frequency of the driving force is treated as linearly varying with time then resonance is preponed. In contrast to this in the case of a slow passage through a Hopf bifurcation, onset of oscillation is delayed, that is postponed [15]. In the case of a parametrically driven undamped systems growth of amplitude of oscillation is generally realized when a trajectory passess through the resonance tongues. For a certain set of initial conditions de-amplification occurs in the interval of first resonance tongue. The growth of amplitude of oscillation is found to be sensitive to the initial conditions.

So far in this book the various forms of the external force considered are time-dependent. The influence of a spatially periodic force in certain infinitedimensional systems has been reported. For example, its effect on pattern formation in Geierer–Meinhardt equation [19], Turing structures in a chemical reaction-diffusion [20], wave number locking and pattern formation in Swift–Huhenberg equation [21] and resonance in a bistable reaction-diffusion equation [22] were analysed. Further, responses of in infinite-dimensional systems with different types of forces such as spatially uniform time-periodic force [23–26], spatially periodic but time-independent [27–29] and travelling wave type [30–32] were investigated.

References

- 1. G. Duffing, Erzwungene Schwingungen bei veränderlicher Eigenfrequenz und ihre technische Bedeutung (Vieweg, Braunschweig, 1918)
- J.J. Stoker, Nonlinear Vibrations, Pure and Applied Mathematics, vol. II (Interscience, New York, 1950)
- 3. Y.A. Mitropolsky, *Problemes de la Theorie Asymptotique des Oscillations Nonstationairies* (Gauthier-Villas, Paris, 1966)
- 4. A.H. Nayfeh, D.T. Mook, Nonlinear Oscillations (Wiley-Interscience, New York, 1979)
- 5. A.H. Nayfeh, K.R. Asfar, J. Sound Vib. 124, 529 (1988)
- 6. H.L. Neal, A.H. Nayfeh, Int. J. Non-linear Mech. 25, 275 (1990)
- 7. A. Raman, A.K. Bajaj, P. Davies, J. Sound Vib. 192, 835 (1996)
- 8. P. Strizhak, M. Menzinger, J. Chem. Phys. 105, 10905 (1996)
- 9. J.C. Celet, D. Dangoisse, P. Glorieux, G. Lythe, T. Erneux, Phys. Rev. Lett. 81, 975 (1998)
- 10. L. Ng, R. Rand, M. O'Neil, J. Vib. Control. 9, 685 (2003)
- 11. J. Bridge, R. Rand, S.M. Sah, J. Vib. Control. 15, 1581 (2009)
- 12. Y. Park, Y. Do, J.M. Lopez, Phys. Rev. E 84, 056604 (2011)
- 13. E.A. Cox, J.P. Gleeson, M.P. Mortell, Z. Angew. Math. Phys. **56**, 645 (2005)
- 14. S. Kaczmarczyk, J. Sound Vib. 208, 243 (1997)
- 15. S.M. Baer, T. Erneux, J. Rinzel, SIAM J Appl. Math. 49, 55 (1989)
- 16. Y. Do, J.M. Lopez, Discret. Contin. Dyn. Syst. Ser. B 18, 95 (2013)
- 17. V. Booth, T.W. Carr, T. Erneux, SIAM J. Appl. Math. 57, 1406 (1997)
- 18. S. Glebov, O. Kiselev, V. Lazarev, SIAM J. Appl. Math. 65, 2158 (2005)
- 19. K.M. Page, P.K. Mainib, N.A.M. Monke, Phys. D **202**, 95 (2005)
- 20. M. Dolnik, I. Berenstein, A.M. Zhabotinsky, I.R. Epstein, Phys. Rev. Lett. 87, 238301 (2001)
- 21. R. Manor, A. Hagberg, E. Meron, New J. Phys. 11, 063016 (2009)
- 22. C. Yao, Z. He, J. Luo, J. Shual, Phys. Rev. E 91, 052901 (2015)
- 23. P. Coullet, J. Lega, B. Houchmanzadeh, J. Lajzerowicz, Phys. Rev. Lett. 65, 1352 (1990)
- 24. H. Riecke, J.D. Crawford, E. Knobloch, Phys. Rev. Lett. 61, 1942 (1998)
- A.L. Lin, M. Bertram, K. Martinez, H.L. Swinney, A. Ardelea, G.F. Carey, Phys. Rev. Lett. 84, 4240 (2000)
- 26. A.L. Lin, A. Hagberg, E. Meron, H.L. Swinney, Phys. Rev. E 69, 066217 (2004)
- 27. M. Dolnik, I. Berenstein, A.M. Zhabotinsky, I.R. Epstein, Phys. Rev. Lett. 87, 238301 (2001)
- R. Peter, M. Hilt, F. Ziebert, J. Bammert, C. Erlenkmper, N. Lorscheid, C. Weitenberg, A. Winter, M. Hammele, W. Zimmermann, Phys. Rev. E 71, 046212 (2005)
- G. Seiden, S. Weiss, J.H. McCoy, W. Pesch, E. Bodenschatz, Phys. Rev. Lett. 101, 214503 (2008)
- D.G. Mguez, E.M. Nicola, A.P. Munuzuri, J. Casademunt, F. Sagues, L. Kramer, Phys. Rev. Lett. 93, 048303 (2004)
- 31. S. Rudiger, E.M. Nicola, J. Casademunt, L. Kramer, Phys. Rep. 447, 73 (2007)
- 32. A. Beetz, C. Gollwitzer, R. Richter, I. Rehberg, J. Phys. Condens. Matter 20, 204109 (2008)

Chapter 14 Antiresonances

In a linear or nonlinear oscillator with a single degree of freedom subjected to an additive periodic driving force with a single frequency a typical frequency-response curve displays a single resonance peak as shown in the introductory chapter. In a linear and undamped system the response amplitude becomes a maximum when the frequency of the driving force matches with the natural frequency of the system. In other oscillators a single resonance peak occurs at a frequency different from their natural frequencies. In a N-coupled linear oscillators with first oscillator alone driven by an additive periodic force, for certain types of interaction (coupling) the frequency-response curve of each oscillator exhibits at most N peaks (maxima) depending upon the values of the parameters of the oscillators [1]. The peaks are the resonance (and the corresponding frequencies are the resonant frequencies). The valleys in the frequency-response curve are the antiresonance frequencies. There are N-1 antiresonance frequencies. In the absence of damping, for the driving frequency equal to the antiresonance frequencies the response amplitude vanishes. The multiple resonance and antiresonance phenomena occur in nonlinear systems also. Using resonance a dynamical system can be effected to give rise to the most effective signal output. On the other hand, an antiresonance is useful to make the system to deliver the lower signal output. These can be realized in systems subjected to different kinds of external perturbations. Antiresonances can occur in all types of coupled oscillator systems, including mechanical, acoustic, electromagnetic and quantum systems.

Now, one may ask: Can one observe the antiresonance in other resonance phenomena? That is, is it possible to induce parametric antiresonance, stochastic antiresonance, coherence antiresonance and vibrational antiresonance? Interestingly, they are found to occur in certain systems. However, so far very little knowledge on the source of antiresonance and its mechanism is known.

Why is the study of antiresonance important? Details of antiresonance is useful in the design of chemotherapeutic protocols [2], dynamic model updating [3–6] and desynchronizing undesired oscillations [7]. Driving a microelectronic motor

at antifrequencies has several practical advantages [8]. Antiresonance is employed to minimize unwanted vibrations of certain parts of a system in mechanical engineering and aerospace industries. In the vibration control of fixture controlling antiresonance frequencies are more important than resonant frequencies since the worst case can occur at antiresonance [9, 10]. Antiresonance is used in wave traps. These are used in series with antennas of radio receivers in order to disallow the flow of alternating current at the frequency of an interfering station. In electrical engineering the case of the impedance of an electrical circuit to become very high approaching infinity is referred as an antiresonance. In a vibratory structure system an addition of mass is found to shift the resonance frequencies without affecting the antiresonance frequencies [11]. It has been pointed out that shifts of resonance frequencies beyond antiresonance has been realized in quantum systems [12, 13]. Associated with the antiresonance is a transmission dip at the atomic frequency in a coupled atoms with intermediate coupling. In electronic transport systems such as coupled quantum dot systems an antiresonance corresponds to a zero point of electron transmission. In such systems an antiresonance leads to multiple negative differential conductance regions [14]. In a driven quantum nonlinear oscillator multiphoton transition is accompanied by an antiresonance [15] which can also be observable in Josephson junctions (JJS) and JJ-based systems.

The present chapter first analyse the occurrence of antiresonance in both nonlinear and linear system of N-oscillators with nearest neighbor interactions. Depending upon the parameters of the system at most N resonance and N-1 antiresonance can be observed. The role of damping and the coupling strength on resonance and antiresonance is brought out. Next, parametric antiresonance in a parametrically driven van der Pol oscillator is presented. Then the occurrence of stochastic and coherence antiresonances are illustrated with reference to certain systems.

14.1 Multiple Resonance and Antiresonance in Coupled Systems

In Sect. 7.2 the resonance dynamics in unidirectionally coupled Duffing oscillators with first oscillator alone driven by a periodic external force is analysed. In Fig. 7.4 when the frequency of the external force is varied only one resonance is found. In this section consider the *n*-coupled Duffing oscillators with nearest neighbour coupling. This coupling gives rise to more than one resonance and antiresonance.

The equation of motion of the *n*-coupled Duffing oscillators of our interest is

$$\ddot{x}_1 + d\dot{x}_1 + \omega_0^2 x_1 + \beta x_1^3 + \delta(x_1 - x_2) = f \cos \omega t, \quad (14.1a)$$

$$\ddot{x}_i + d\dot{x}_i + \omega_0^2 x_i + \beta x_i^3 + \delta(x_i - x_{i-1}) + \delta(x_i - x_{i+1}) = 0, \tag{14.1b}$$

$$\ddot{x}_n + d\dot{x}_n + \omega_0^2 x_n + \beta x_n^3 + \delta(x_n - x_{n-1}) = 0.$$
 (14.1c)

In this system first and last oscillators are not connected each other and δ is the strength of the coupling. Let us start with n = 2, that is two-coupled oscillators.

14.1.1 Theoretical Treatment for Two-Coupled Oscillators

Applying a perturbation approach a frequency-response equation can be obtained for the system (14.1). Seek a periodic solution of the system (14.1) with n = 2 as

$$x_i(t) = a_i(t)\cos\omega t + b_i(t)\sin\omega t, \quad i = 1, 2$$
 (14.2)

with a_i and b_i to be determined and are slowly varying functions of time. Substitute

$$\dot{x}_i(t) = \dot{a}_i \cos \omega t + \dot{b}_i \sin \omega t - a_i \omega \sin \omega t + b_i \omega \cos \omega t, \tag{14.3a}$$

$$\ddot{x}_i(t) = -2\dot{a}_i\omega\sin\omega t + 2\dot{b}_i\omega\cos\omega t - a_i\omega^2\cos\omega t - b_i\omega^2\sin\omega t, \quad (14.3b)$$

$$x_i^3 \approx \frac{3}{4} \left(a_i^2 + b_i^2 \right) \left(a_i \cos \omega t + b_i \sin \omega t \right), \tag{14.3c}$$

where in Eq. (14.3b) \ddot{a}_i and \ddot{b}_i are neglected due to their smallness, in Eq. (14.1) and then neglect $d\dot{a}_i$ and $d\dot{b}_i$ because they are assumed to be small. Next, setting the coefficients of $\sin \omega t$ and $\cos \omega t$ separately to zero gives

$$\dot{a}_1 = \frac{b_1}{2\omega} \left[\omega_0^2 - \omega^2 + \delta + \frac{3}{4}\beta \left(a_1^2 + b_1^2 \right) \right] - \frac{da_1}{2} - \frac{\delta b_2}{2\omega} , \qquad (14.4a)$$

$$\dot{b}_1 = -\frac{a_1}{2\omega} \left[\omega_0^2 - \omega^2 + \delta + \frac{3}{4}\beta \left(a_1^2 + b_1^2 \right) \right] - \frac{db_1}{2} + \frac{\delta a_2}{2\omega} + \frac{f}{2\omega} , \quad (14.4b)$$

$$\dot{a}_2 = \frac{b_2}{2\omega} \left[\omega_0^2 - \omega^2 + \delta + \frac{3}{4}\beta \left(a_2^2 + b_2^2 \right) \right] - \frac{da_2}{2} - \frac{\delta b_1}{2\omega} , \qquad (14.4c)$$

$$\dot{b}_2 = -\frac{a_2}{2\omega} \left[\omega_0^2 - \omega^2 + \delta + \frac{3}{4}\beta \left(a_2^2 + b_2^2 \right) \right] - \frac{db_2}{2} + \frac{\delta a_1}{2\omega} . \tag{14.4d}$$

The above equations under the transformation

$$a_i(t) = A_i(t)\cos\theta_i(t), \quad b_i(t) = A_i(t)\sin\theta_i(t)$$
 (14.5)

take the form (with $A_i^2 = a_i^2 + b_i^2$)

$$\dot{A}_{1} = -\frac{dA_{1}}{2} + \frac{\delta A_{2}}{2\omega} \sin(\theta_{1} - \theta_{2}) + \frac{f}{2\omega} \sin\theta_{1} ,$$

$$A_{1}\dot{\theta}_{1} = -\frac{A_{1}}{2\omega} \left[\omega_{0}^{2} - \omega^{2} + \delta + \frac{3}{4}\beta A_{1}^{2} \right]$$
(14.6a)

$$+\frac{\delta A_2}{2\omega}\cos\left(\theta_1 - \theta_2\right) + \frac{f}{2\omega}\cos\theta_1, \qquad (14.6b)$$

$$\dot{A}_2 = -\frac{dA_2}{2} - \frac{\delta A_1}{2\omega} \sin(\theta_1 - \theta_2) ,$$
 (14.6c)

$$A_2 \dot{\theta}_2 = -\frac{A_2}{2\omega} \left[\omega_0^2 - \omega^2 + \delta + \frac{3}{4} \beta A_2^2 \right] + \frac{\delta A_1}{2\omega} \cos(\theta_1 - \theta_2) . \quad (14.6d)$$

For a periodic solution, in the long time limit, $A_i(t) \to A_i^*$ and $\theta_i(t) \to \theta_i^*$. (A_i^*, θ_i^*) are the equilibrium points of (14.6). Setting $\dot{A}_i = 0$, $\dot{\theta}_i = 0$, dropping '*' in A_i^* and θ_i^* and then eliminating θ_i 's finally give rise to the set of equations

$$A_1^2 \left[u_1^2 + d^2 \omega^2 \right] + \left[2d^2 \omega^2 + \delta^2 \right] A_2^2 - 2u_1 u_2 A_2^2 = f^2 , \qquad (14.7a)$$

$$A_2^2 \left[u_2^2 + d^2 \omega^2 \right] - \delta^2 A_1^2 = 0$$
, (14.7b)

where

$$u_i^2 = \omega_0^2 - \omega^2 + \delta + \frac{3}{4}\beta A_i^2, \quad i = 1, 2.$$
 (14.7c)

It is easy to obtain the expressions for θ_1 and θ_2 .

14.1.2 Resonance and Antiresonance in a Linear System

For the linear, undamped and two-coupled oscillators $[n = 2, \beta = 0 \text{ and } d = 0 \text{ in Eq. (14.1)}]$ the amplitude A_1 and A_2 take the simple forms [1]

$$A_1 = \frac{f(\omega_0^2 - \omega^2 + \delta)}{(\omega_0^2 - \omega^2)(\omega_0^2 - \omega^2 + 2\delta)},$$
(14.8a)

$$A_2 = \frac{\delta A_1}{\omega_0^2 - \omega^2 + \delta} = \frac{\delta f}{(\omega_0^2 - \omega^2)(\omega_0^2 - \omega^2 + 2\delta)}.$$
 (14.8b)

For the linear and undamped system, from Eq. (14.8), both A_1 and A_2 are found to be maximum at $\omega = \omega_0$ and $\sqrt{\omega_0^2 + 2\delta}$. The amplitude A_1 becomes a minimum (antiresonance) when the term $(\omega_0^2 - \omega^2 + \delta)$ in (14.8a) is a minimum. This happens at $\omega = \sqrt{\omega_0^2 + \delta}$. Thus, the frequency at which antiresonance occurs in oscillator-1 is $\omega_{1,\text{ar}} = \sqrt{\omega_0^2 + \delta}$. At $\omega_{1,\text{ar}}$, $A_{1,\text{ar}} = 0$. This means the motion of the oscillator-1 at this frequency is ceased though the system is driven by a periodic force. From Eq. (14.8b), it is reasonable to expect A_2 to be minimum at a frequency ω at which A_1 is minimum. Substitution of $\omega^2 = \omega_{1,\text{ar}}^2 = \omega_0^2 + \delta$ in Eq. (14.8b) results in

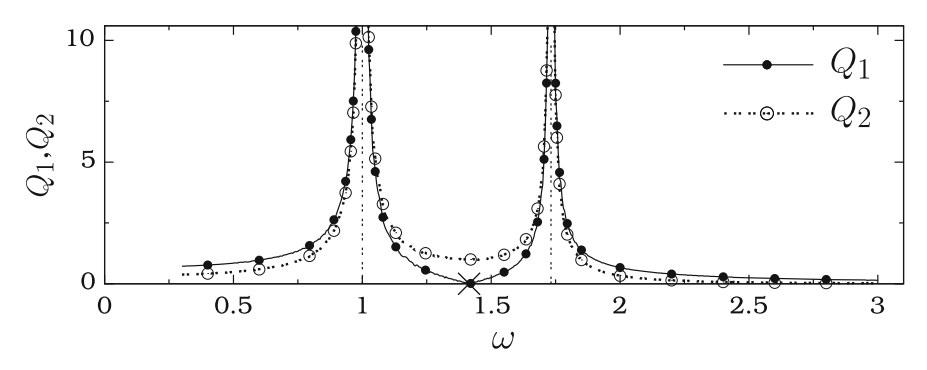


Fig. 14.1 Q_1 and Q_2 versus the frequency ω of the driving force for the two-coupled undamped linear oscillators where d=0, $\beta=0$, f=0.1, $\omega_0^2=1$ and $\delta=1$. The *continuous curves* are numerical result and *symbols* are theoretical prediction. The symbol *cross* on the ω -axis denotes the value of ω at which antiresonance occurs. The *vertical dashed lines* denote the two resonances

 $A_{2,\mathrm{ar}}=f/\delta \neq A_{1,\mathrm{ar}}$ and is nonzero. At the frequency $\omega_{1,\mathrm{ar}}$ the first oscillator is immobile after a transient evolution but the second oscillator is oscillating with period $2\pi/\omega_{1,\mathrm{ar}}$ with a minimum nonzero amplitude.

Figure 14.1 presents the frequency (ω)-response ($Q_{1,2}=A_{1,2}/f$) curves of the oscillators 1 and 2 for $\omega_0^2=1$, d=0, $\beta=0$, $\delta=1$ and f=0.1. For both the oscillators resonance occurs at $\omega=\omega_0=1$ and $\omega=\sqrt{\omega_0^2+2\delta}=\sqrt{3}$. Antiresonance takes place at $\omega=\omega_0^2+\delta=\sqrt{2}$. At the antiresonance $Q_1=0$ while $Q_2=A_2/f=1/\delta=1$.

For the damped $(d \neq 0)$ linear system

$$A_1 = \left(\frac{f^2 u_+}{u_+^2 + \delta^4 - 2\delta^2 u_-}\right)^{1/2} , \qquad (14.9a)$$

$$A_2 = \frac{\delta A_1}{\sqrt{u_+}}, \quad u_{\pm} = (\omega_0^2 - \omega^2 + \delta)^2 \pm d^2 \omega^2.$$
 (14.9b)

It is difficult to obtain explicit expressions for the two resonance frequencies and the corresponding amplitudes due to complexity of the expressions of A_1 and A_2 . However, the antiresonance frequency can be determined by seeking the value of ω at which the quantity u_+ becomes a minimum. This gives

$$\omega_{1,\text{ar}} = \sqrt{\omega_0^2 + \delta - \frac{d^2}{2}} \,. \tag{14.10}$$

Figure 14.2 depicts Q_1 and Q_2 variation for d=0.1, $\omega_0^2=1$, $\beta=0$, f=0.1 and $\delta=1$. The antiresonance frequency is 1.41244.

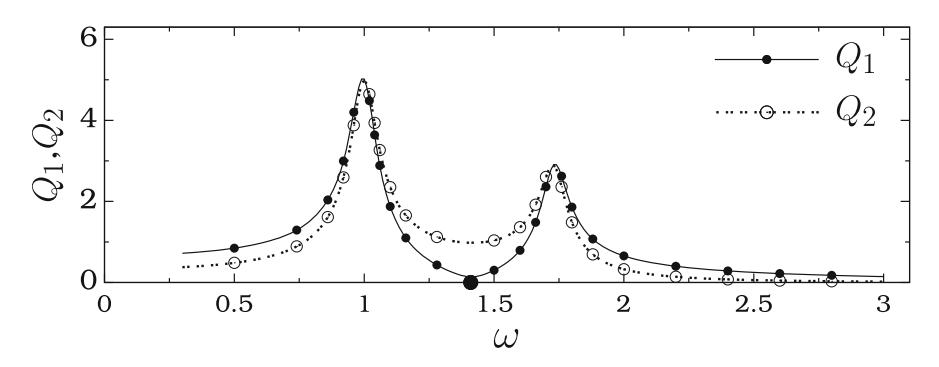


Fig. 14.2 Same as Fig. 14.1 but for the damped system with d = 0.1

14.1.3 Two-Coupled Duffing Oscillators

Now, consider the two-coupled Duffing oscillators. Decoupling of the amplitudes in Eq. (14.7) is very difficult. However, applying the Newton-Raphson method developed for coupled equations various possible values of A_1 and A_2 can be determined and then the frequency-response curve can be drawn. The Newton-Raphson iterative rule for a successive approximation of a root of the two-coupled equations of the form

$$f(x,y) = 0, \quad g(x,y) = 0$$
 (14.11)

is

$$x_{n+1} = x_n + \Delta x_n$$
, $y_{n+1} = y_n + \Delta y_n$, (14.12a)

where

$$\triangle x_n = (gf_y - fg_y)/\triangle$$
, $\triangle y_n = (fg_x - gf_x)/\triangle$, (14.12b)

$$\Delta = f_x g_y - g_x f_y . \tag{14.12c}$$

In the above $f_x = \partial f/\partial x$ and so on. Fix the values of the parameters as d=0.1, $\omega_0^2=1$, $\beta=1$ and $\delta=1$. Figure 14.3 presents both theoretical $Q_i=A_i/f$ and numerically computed Q_i , i=1,2 as a function of the driving frequency ω . Theoretical prediction very closely matches with the numerical results. Q_1 and Q_2 are maximum at $\omega=\omega_{\rm r}=(1.08,1.75)$ and (1.08,1.74), respectively. Antiresonance in Q_1 and Q_2 occurs at $\omega_{1,\rm ar}=1.43$ and $\omega_{2,\rm ar}=1.42$. However, $Q_{1,\rm ar}=0.1181$ while $Q_{2,\rm ar}=0.98041$. What are the significant effects of the linear coupling constant δ on resonance dynamics? Figure 14.4 displays the dependence of Q_1 and Q_2 versus ω on the parameter δ . Q_1 has single resonance for $0<\delta<0.1$ and two resonance peaks for for $\delta \geq 0.13$.

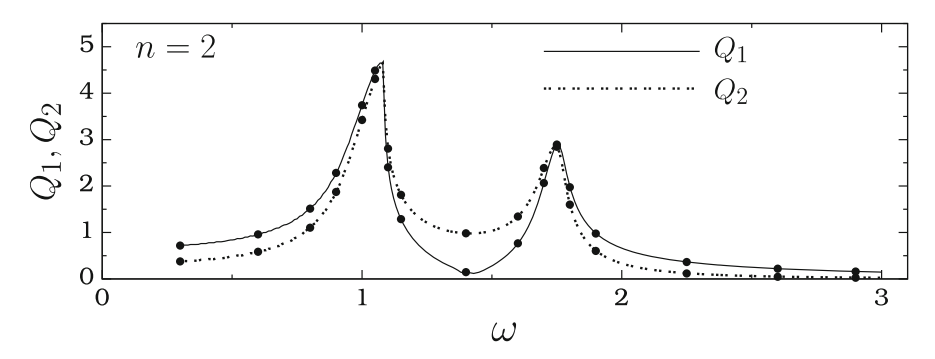


Fig. 14.3 Response amplitudes Q_1 (of oscillator-1) and Q_2 (of oscillator-2) versus the frequency ω of the driving force of the two-coupled Duffing oscillators, Eq. (14.1) with n=2. The *continuous* and *dotted curves* are theoretically predicted Q_1 and Q_2 , respectively. The *solid circles* are the numerical data. Here d=0.1, $\omega_0^2=1$, $\beta=1$, $\delta=1$ and f=0.1

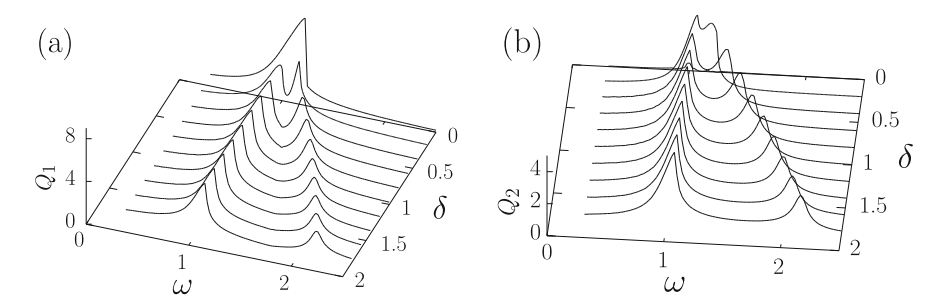


Fig. 14.4 Response amplitudes (a) Q_1 and (b) Q_2 as a function of the parameters δ and ω for the system (14.1) with n=2 and d=0.1, $\omega_0^2=1$, $\beta=1$ and f=0.1

Denote $\omega_{j,r}^{(i)}$ as the value of ω at which jth resonance occurs in the ith oscillator. $Q_{j,r}^{(i)}$ is the value of the response amplitude at $\omega_{j,r}^{(i)}$. For n=2 there is only one antiresonance. Therefore, denote $\omega_{1,ar}$ and $\omega_{2,ar}$ are the values of ω at which antiresonance occurs in the oscillators 1 and 2, respectively, and the corresponding values of Q as $Q_{1,ar}$ and $Q_{2,ar}$, respectively. These quantities are computed for a range of values of δ . Figure 14.5a displays the variation of $\omega_{1,r}^{(1)}$ (continuous curve), $\omega_{2,r}^{(1)}$ (dotted curve), $\omega_{1,r}^{(2)}$ (solid circles) and $\omega_{2,r}^{(2)}$ (open circles) with δ . The first resonance frequencies of both the oscillators are almost the same and independent of δ , however, $\omega_{2,r}^{(1)} \approx \omega_{2,r}^{(2)}$ for each fixed value of δ except for $\delta \ll 1$. In Fig. 14.5b $Q_{1,r}^{(i)}$, i=1,2 approach a same constant value where as $Q_{2,r}^{(i)}$, i=1,2 decreases with increase in the value of δ .

The dependence of antiresonance frequencies and the corresponding amplitudes of the oscillators are plotted in Fig. 14.6. In this figure the numerical results are represented by symbols and the appropriate curve fits are marked by continuous curves. $\omega_{1,ar}$ and $\omega_{2,ar}$ depend linearly on δ as $\omega_{1,ar} = 1.0759 + 0.325\delta$ and

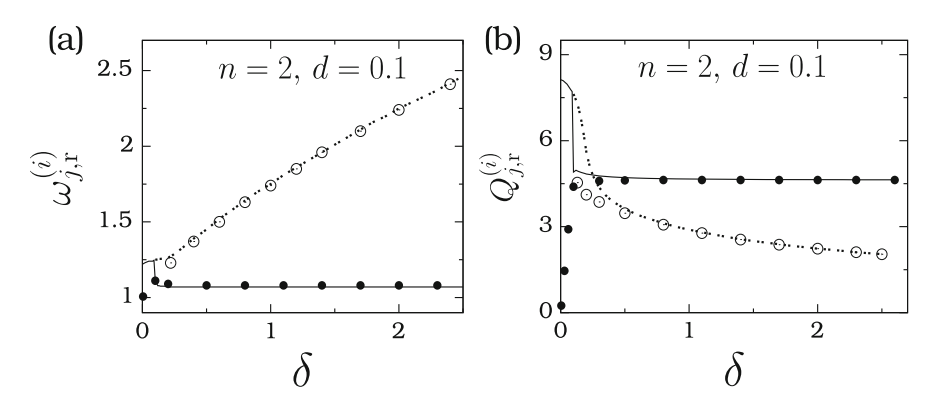


Fig. 14.5 Dependence of (a) resonance frequencies and (b) the response amplitudes at the resonance frequencies as a function of the coupling constant δ of the two-coupled Duffing oscillators. In both the subplots the *continuous* and *dotted lines* are associated with the first and second resonances, respectively, of the first oscillator. The *solid* and *open circles* correspond to the first and second resonances, respectively, of the second oscillator. Here d = 0.1, $\omega_0^2 = 1$, $\beta = 1$ and f = 0.1

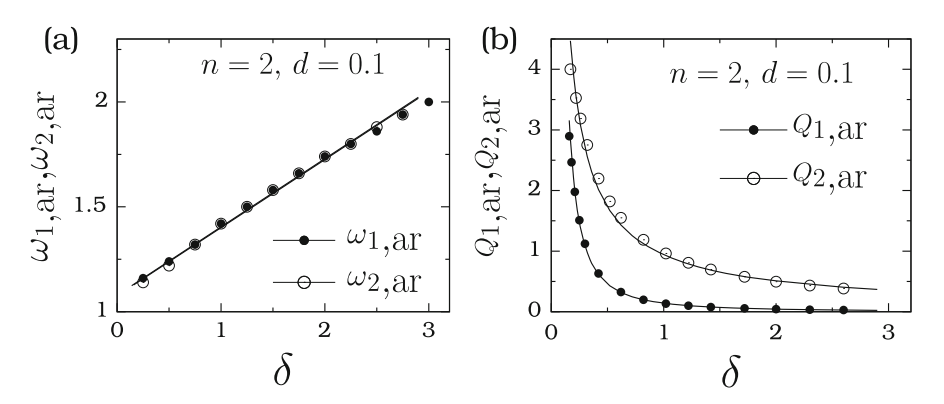


Fig. 14.6 Variation of (a) antiresonance frequencies $\omega_{1,ar}$ and $\omega_{2,ar}$ of the first and second oscillators, respectively, and (b) response amplitude at the antiresonance with the coupling strength δ of the two-coupled Duffing oscillators, Eq. (14.1) with n=2. The *symbols* are numerical data and *continuous curves* are the best fit

 $\omega_{2,\mathrm{ar}}=1.079+0.325\delta$. In the linear ($\beta=0$) as noted earlier $\omega_{1,\mathrm{ar}}=\sqrt{\omega_0^2+\delta}=1+0.5\delta$. $Q_{1,\mathrm{ar}}$ and $Q_{2,\mathrm{ar}}$ decreases rapidly following the power-law relations $0.14106\delta^{-1.696}$ (for $\delta>0.1$) and $0.939\delta^{-0.881}$ (for $\delta>0.13$). That is, increasing the value of δ increases the antiresonance frequency while reduces the response amplitude at the antiresonance. In Fig. 14.6a $\omega_{1,\mathrm{ar}}^{(1)}\approx\omega_{2,\mathrm{ar}}^{(2)}$ but $Q_{1,\mathrm{ar}}< Q_{2,\mathrm{ar}}$ for a wide range of values of δ . Increasing the value of damping coefficient decreases the response amplitudes and suppresses the second resonance in both the oscillators.

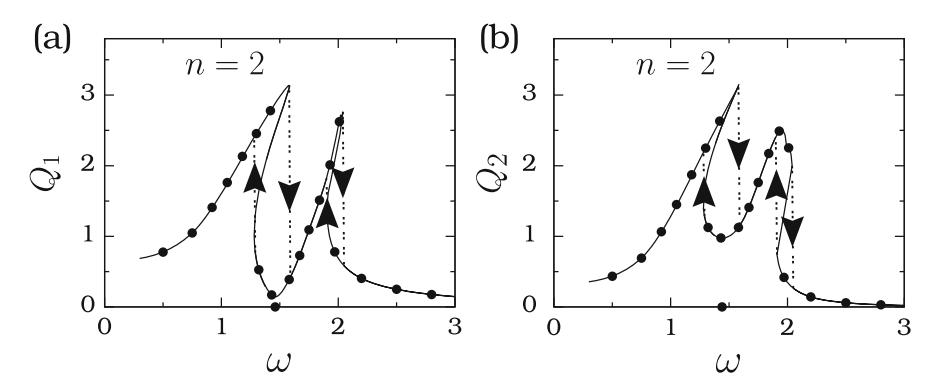


Fig. 14.7 Frequency-response curves (a) Q_1 versus ω and (b) Q_2 versus ω of the two-coupled Duffing oscillators (Eq. (14.1) with n=2). The *continuous curve* and the *solid circles* are the theoretically predicted and numerically computed values of Q_1 and Q_2 , respectively. The *solid circle* on the ω axis mark the values of ω at which antiresonance occurs. In both subplots the *downward* and *upward arrows* indicate the jump in the response amplitude when the frequency is varied in the forward and backward directions, respectively. The values of the parameters are d=0.1, $\omega_0^2=1$, $\beta=20$, $\delta=1$ and f=0.1

One of the features of the resonance in nonlinear oscillators is the appearance of hysteresis in the frequency response curve. This is also realized in the system (14.1) near two resonances for certain range of values of β . An example is presented in Fig. 14.7 for $\beta=20$ and $\delta=1$. In both the oscillators two stable periodic orbits with different amplitudes coexist for $\omega \in [1.28, 1.58]$ and [1.9, 2.04]. In these intervals the theoretical response curve has three branches. The upper and the lower branches are realized when the frequency is sweeped in the forward and backward directions, respectively. These are stable branches and observed in the numerical simulations also. For each ω in the intervals [1.28, 1.58] and [1.9, 2.04] two periodic orbits with different amplitudes coexist. They are observed for different set of initial conditions. The middle branch is not realized in the numerical simulation for a large set of initial conditions and is an unstable branch. When ω is increased from a small value, first resonance in both the oscillators occurs at $\omega=1.58$ but with $Q_1=3.14$ and $Q_2=3.11$. The second resonance in the oscillators 1 and 2 takes place at $\omega=2.04$ and 1.95, respectively, with $Q_1=2.76$ and $Q_2=2.52$.

14.1.4 Analog Simulation of Two-Coupled Duffing Oscillators

The occurrence of antiresonance can be realized in real experimental systems. The results presented in the previous section for the two-coupled Duffing oscillators are observed in the analog simulation of Eq. (14.1) with n = 2.

Figure 14.8 depicts the electronic circuit for solving the two-coupled Duffing equations. In this circuit OA1–OA6 are operational amplifiers and M1–M4 are

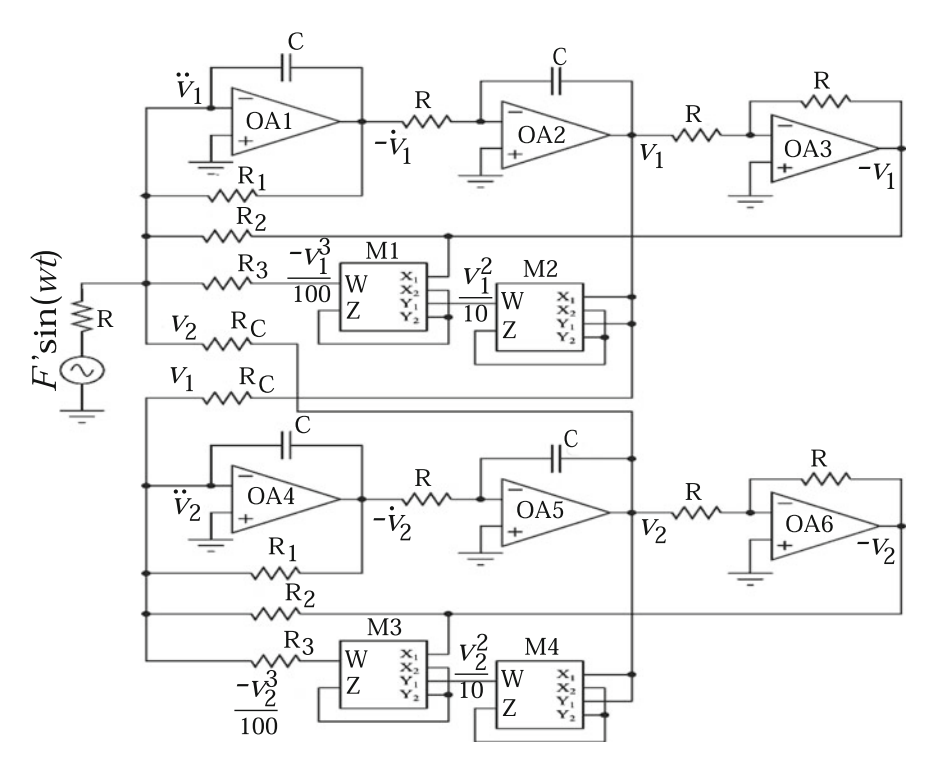


Fig. 14.8 Analog circuit design of the two-coupled Duffing oscillators. For details see the text

multipliers. The dynamic equations for the state variables v_1 and v_2 of the circuit are given by

$$RC^2\ddot{v}_1 + \frac{RC}{R_1}\dot{v}_1 + \frac{1}{R_2}v_1 + \frac{1}{100R_3}v_1^3 - \frac{1}{R_C}v_2 = \frac{F'}{R}\sin\omega t,$$
 (14.13a)

$$RC^2\ddot{v}_2 + \frac{RC}{R_1}\dot{v}_2 + \frac{1}{R_2}v_2 + \frac{1}{100R_3}v_2^3 - \frac{1}{R_C}v_1 = 0,$$
 (14.13b)

where an overdot refers to differentiation with respect to time t. In order to bring the above equations into dimensionless form introduce the following change of variables and parameters:

$$t = RCt', \quad \omega' = \omega/RC, \quad F' = f.$$
 (14.14)

The result is

$$\ddot{v}_1 + d\dot{v}_1 + (\omega_0^2 + \delta)v_1 + \beta v_1^3 - \delta v_2 = f\sin\omega t, \tag{14.15a}$$

$$\ddot{v}_2 + d\dot{v}_2 + (\omega_0^2 + \delta)v_2 + \beta v_2^3 - \delta v_1 = 0, \tag{14.15b}$$

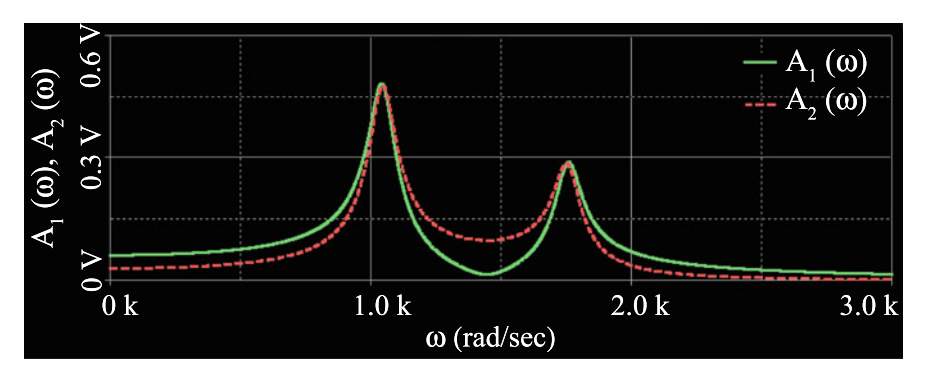


Fig. 14.9 Experimentally measured response amplitudes A_1 and A_2 of the oscillators 1 and 2 of the two-coupled Duffing oscillators as a function of the driving frequency ω

where prime in t' and ω' are dropped for convenience and

$$d = \frac{R}{R_1}, \quad \omega_0^2 + \delta = \frac{R}{R_2}, \quad \beta = \frac{R}{R_3}, \quad \delta = \frac{R}{R_C}.$$
 (14.15c)

Fix $R=10\,\mathrm{k}\Omega$ and $C=100\,\mathrm{nF}$. The choice $R_1=100\,\mathrm{k}\Omega$, $R_2=5\,\mathrm{k}\Omega$, $R_3=10\,\mathrm{k}\Omega$ and $R_C=10\,\mathrm{k}\Omega$ set d=0.1, $\omega_0^2=1$, $\beta=1$ and $\delta=1$. Fixing f=0.1 and varying ω in the circuit the amplitude $A_1(\omega)$ and $A_2(\omega)$ are measured. The result is presented in Fig. 14.9. The values of $A_1(\omega)$ and $A_2(\omega)$ predicted theoretically, computed numerically and measured in the analog simulation are almost the same.

14.1.5 Response of n-Coupled Oscillators

For the n(> 2)-coupled oscillators following the theoretical procedure employed for the n=2 case a set of n-coupled nonlinear equations for the amplitudes A_i can be obtained. Solving them numerically is very difficult. Therefore, analyse the case of n<2 by numerically integrating the Eq. (14.1) and computing the amplitudes A_i and the response amplitudes Q_i 's.

Choose the values of the parameters as d=0.05, $\omega_0^2=1$, $\beta=1$ and $\delta=1$. Figure 14.10a presents Q_1 versus ω for $n=2,3,\cdots$, 60. For first few values of n the frequency-response curve displays clearly n distinct resonance peaks and n-1 antiresonances (minimum values of response amplitude). The response amplitude at successive resonance in each oscillator, generally, decreases. For, say, n<10, the last resonance peak is visible. For sufficiently large n the resonance suppression and reduction in the response amplitude take place. In Fig. 14.10b ω_r and ω_{ar} of the first oscillator are plotted as a function of n. For n=2 and n=10 there are 2 and 10 resonances, respectively. These are clearly seen in this figure. A notable result is that as n increases from 2 the ω_r (as well as ω_{ar}) of first resonance (antiresonance)

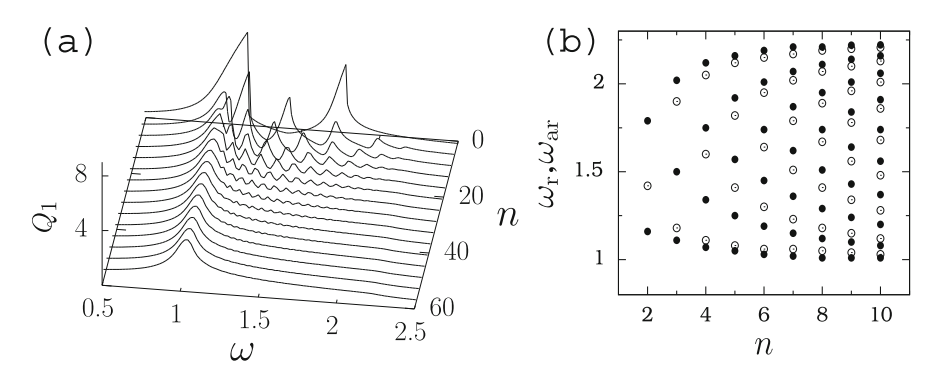


Fig. 14.10 (a) Frequency-response curve of the first oscillator as a function of n (number of oscillator) in the system (14.1) for some selective values of n in the interval [2, 60]. The values of the parameters are d = 0.05, $\omega_0^2 = 1$, $\beta = 20$, f = 0.1 and $\delta = 1$. (b) Variation of the resonance frequencies (ω_r) (solid circles) and antiresonance frequencies ω_{ar} (open circles) of the first oscillator as a function of the number of oscillators n

decreases and approaches a limiting value. This is clearly seen in Fig. 14.10b. For the parametric values chosen the limiting value of ω_r is 1.04 while the corresponding $Q_1 = 3.383$. The ω_r of last resonance increases with n and attains a saturation (2.23). The Q value at last resonance decreases with n (not shown). Denote ω' and ω'' are the limiting values of resonance frequencies of first and last resonance, respectively. Then as n increases the newer and newer ω_r and ω_{ar} should fall within the frequency interval $[\omega', \omega'']$ with decreasing response amplitude at successive resonances. The amplitude profile displays amplitude modulation. In Fig. 14.10a such modulations are visible for $n \in [20, 40]$. The modulations become weak for sufficiently large n as is the case of n = 60 in Fig. 14.10b where the frequency-response curve shows a single resonance peak. Similar behaviour occurs for the second and other oscillators in the system (14.1).

The dominant multiple resonances and antiresonances occur in a system of small number of oscillators coupled with coupling of the form $\delta(x_i - x_{i-1}) + \delta(x_i - x_{i+1})$. For the coupling of the form $\delta(\dot{x}_i - \dot{x}_{i-1}) + \delta(\dot{x}_i - \dot{x}_{i+1})$ multiple resonances and antiresonance are not found. They are observed in the case of coupling of the form $\delta(x_{i-1} + x_{i+1})$. When all the oscillators are driven by periodic forces then only a single resonance is observed for the above forms of coupling. The resonance behaviours noticed in the system (14.1) are not realized in unidirectionally coupled Duffing oscillators [16].

14.2 Parametric Antiresonance

When a linear or a nonlinear system is subjected to a periodic parametric perturbation in the absence of an additive periodic force, in certain ranges of parametric values in a parametric space an equilibrium point is stable. In some regions of parameters space an instability leading to growing of solutions occur. The system displays resonance tongues as illustrated in Chap. 10. It is possible to realize parametric antiresonance and suppression of parametric resonance by an appropriate parametric perturbation in a single system or through coupling of two or more systems. When destruction of an instability and stabilization of an equilibrium point occur at one or more discrete values of a control parameter then it is termed as *parametric resonance*. In certain systems instead of growing solutions a periodic solution can occur. An example of this type of behaviour is shown in Chap. 10. In such systems when a control parameter is varied a dip in the amplitude of response can take place and is called a *parametric antiresonance*. When destabilization of an instability (and stabilization of an equilibrium point) or destruction of large amplitude response is realized for a wide range of values of a control parameter then the phenomenon is referred as *suppression of parametric resonance*. In this section both parametric antiresonance and suppression of parametric resonance are illustrated.

14.2.1 Parametrically Driven van der Pol Oscillator

Antiresonance is found in a parametrically driven van der Pol oscillator [17]. The equation of motion this system is

$$\ddot{x} + \epsilon \left[1 + f \cos \omega t \right] (x^2 - 1) \dot{x} + \omega_0^2 x = 0 , \qquad (14.16)$$

where ω_0 is the natural frequency, ϵ is a small parameter and the coefficient of nonlinear damping is allowed to vary periodically.

To start with, construct a periodic solution of (14.16) in the form

$$x(t) = a(t)\cos\omega_0 t + b(t)\sin\omega_0 t. \qquad (14.17)$$

Assume that a(t) and b(t) are slowly varying functions of time so that \ddot{a} , \ddot{b} , $\epsilon \dot{a}$ and $\epsilon \dot{b}$ can be neglected with respect to \dot{a} and \dot{b} . The terms \ddot{x} , $\epsilon \dot{x}$ and $\epsilon x^2 \dot{x}$ are given by

$$\epsilon \dot{x} = \epsilon \omega_0 \left(-a \sin \omega_0 t + b \cos \omega_0 t \right) , \qquad (14.18a)$$

$$\epsilon x^2 \dot{x} = -\frac{1}{4} \epsilon \omega_0 a \left(a^2 + b^2 \right) \sin \omega_0 t + \frac{1}{4} \epsilon \omega_0 b \left(a^2 + b^2 \right) \cos \omega_0 t$$

$$-\frac{1}{4} \epsilon \omega_0 a \left(a^2 - 3b^2 \right) \sin 3\omega_0 t$$

$$-\frac{1}{4} \epsilon \omega_0 b \left(b^2 - 3a^2 \right) \cos 3\omega_0 t , \qquad (14.18b)$$

$$\ddot{x} = -\left(2\omega_0 \dot{a} + b\omega_0^2 \right) \sin \omega_0^2 t + \left(2\dot{b}\omega_0^2 - a\omega_0^2 \right) \cos \omega_0 t . \qquad (14.18c)$$

Substitution of Eq. (14.18) in (14.16), setting $\omega = 2\omega_0$ and equating the terms containing $\sin \omega_0 t$ and $\cos \omega_0 t$) separately to zero give the set of equations

$$\dot{a} = \frac{\epsilon a}{2} \left[\left(1 - \frac{f}{2} \right) - \frac{a^2}{4} - \frac{b^2}{4} \left(1 - 2f \right) \right], \tag{14.19a}$$

$$\dot{b} = \frac{\epsilon b}{2} \left[\left(1 + \frac{f}{2} \right) - \frac{b^2}{4} - \frac{a^2}{4} \left(1 + 2f \right) \right]. \tag{14.19b}$$

The stationary values of (a, b) are the equilibrium points of (14.19) obtainable by setting $\dot{a} = \dot{b} = 0$. The stationary values of (a, b), with at least one of a and b being > 0, and their stability determining eigenvalues are given below:

1.
$$(a_1, b_1) = (0, \sqrt{4+2f});$$
 $\lambda_{1,2} = \frac{1}{2} \epsilon f(f+1), -\frac{1}{2} \epsilon (f+2).$

2.
$$(a_2, b_2) = (\sqrt{4-2f}, 0);$$
 $\lambda_{1,2} = \frac{1}{2} \epsilon f(f-1), \frac{1}{2} \epsilon (f-2).$

3.
$$(a_3, b_3) = \left(\sqrt{1 + \frac{1}{f}}, \sqrt{1 - \frac{1}{f}}\right); \quad \lambda_{1,2} = \frac{1}{4} \epsilon \left[-1 \pm \sqrt{5 - 4f^2}\right].$$

For simplicity choose f>0. For a stable equilibrium point real part of all the eigenvalues must be <0. When $f\leq 1$ the equilibrium point (a_2,b_2) is the only stable and real equilibrium point. At f=1 the point (a_3,b_3) becomes real and it coincides with (a_2,b_2) . (a_3,b_3) is the only stable and real equilibrium point for f>1. To summarize, for $\omega=2\omega_0$ and for $f\leq 1$ the amplitude of oscillation of the system (14.16) is $A=\sqrt{a_2^2+b_2^2}=\sqrt{2(2-f)}$ while when f>1 it is $\sqrt{a_3^2+b_3^2}=\sqrt{2}$ and independent of f.

When $\omega = 4\omega_0$ the equations of motion for a and b are [17]

$$\dot{a} = \frac{\epsilon a}{16} \left[(f - 2) a^2 - (2 + 3f)b^2 + 8 \right], \tag{14.20a}$$

$$\dot{b} = \frac{\epsilon b}{16} \left[(f - 2) b^2 - (2 + 3f)a^2 + 8 \right]. \tag{14.20b}$$

The real and positive equilibrium values of (a, b) and their stability determining eigenvalues are the following:

1.
$$(a_1, b_1) = (0, \sqrt{8/(2-f)}); \quad \lambda_{1,2} = -2\epsilon, 2\epsilon f/(f-2).$$

2.
$$(a_2, b_2) = (\sqrt{8/(2-f)}, 0); \quad \lambda_{1,2} = -2\epsilon, 2\epsilon f/(f-2).$$

3.
$$(a_3, b_3) = (\sqrt{4/(2+f)}, \sqrt{4/(2+f)}); \quad \lambda_{1,2} = -\epsilon, (1+\epsilon)f.$$

 (a_3,b_3) is always unstable. Both (a_1,b_1) and (a_2,b_2) are real and stable for 0 < f < 2. For these two states $A = \sqrt{8/(2-f)}$. For f > 2 there is no real and stable

equilibrium point of (14.20). As f increases from 0, the amplitude A increases slowly and near the values 2 it diverges rapidly.

For the case of $\omega \neq 2\omega_0$ and $4\omega_0$ (including $\omega = \omega_0$ and $3\omega_0$)

$$\dot{a} = -\frac{\epsilon}{8} \left[a^3 + ab^2 - 4a \right],$$
 (14.21a)

$$\dot{b} = -\frac{\epsilon}{8} \left[b^3 + a^2 b - 4b \right].$$
 (14.21b)

It is easy to notice that the real and stable equilibrium values of (a, b) are $(\sqrt{2}, \sqrt{2})$. That is, A = 2 and is independent of f.

For fixed values of ϵ , f(<2) and ω_0 when ω is varied then the response amplitude becomes 2 except at $\omega=2\omega_0$ and $4\omega_0$. At $\omega=4\omega_0$ as pointed out above $A=\sqrt{8/(2-f)}>2$ while at $\omega=2\omega_0$ it is $\sqrt{2(2-f)}<2$. Because $A(\omega=4\omega_0)>A(\omega\neq 4\omega_0)$ there is a resonance at $A(\omega=4\omega_0)$. In contrast to this, $A(\omega=2\omega_0)<A(\omega\neq 2\omega_0)$ and there is an *antiresonance* at $\omega=2\omega_0$. The above theoretical predictions are confirmed in a numerical simulation.

In Fig. 14.11a numerically computed $A(\omega)$ is plotted as a function of ω for $\epsilon = 0.01$, $\omega_0 = 1$ and f = 0.5. Here $A(\omega) = (Q_{\rm C}^2(\omega) + Q_{\rm S}^2(\omega))^{1/2}$. $A \approx 2$ for all values

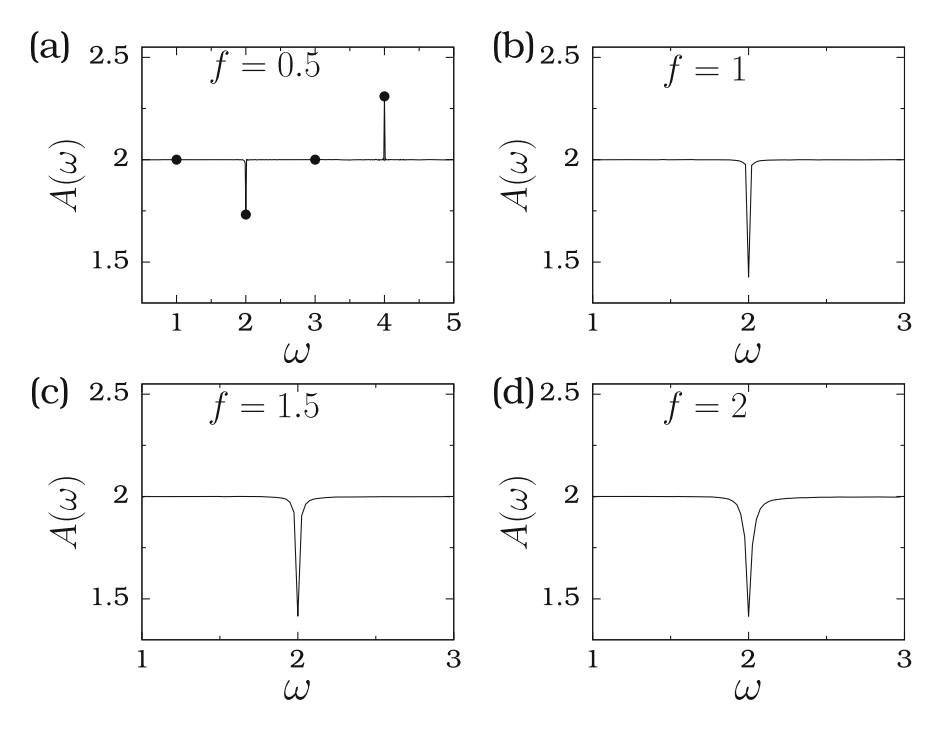


Fig. 14.11 Numerically computed amplitude $A(\omega)$ as a function of the frequency ω for the system (14.16) for four values of f. In the subplot (a) the solid circles are the theoretically predicted A. The values of the parameters are $\epsilon=0.01$ and $\omega_0^2=1$

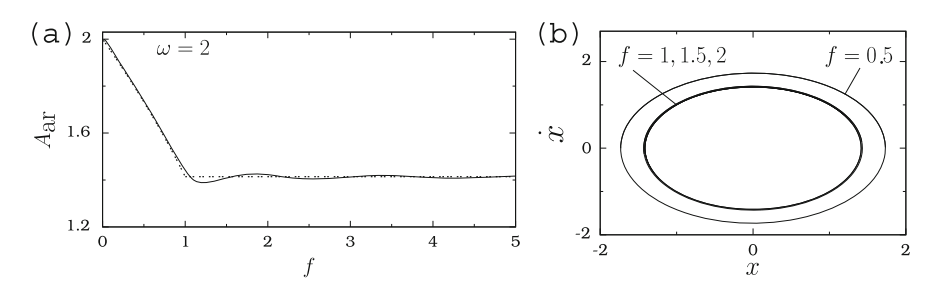


Fig. 14.12 (a) Numerically computed (*continuous curve*) and theoretically predicted (*dashed curve*) $A_{\rm ar}$ (the value of amplitude of oscillation with frequency ω at antiresonance) versus the parameter f at $\omega=2$ for the system (14.16). Here $\epsilon=0.01$ and $\omega_0^2=1$. (b) Phase portrait of the system (14.16) for four values of f with $\epsilon=0.01$, $\omega_0^2=1$ and $\omega=2\omega_0$

of $\omega \in [0.5, 5]$ except for $\omega = 2$ and 4. At $\omega = 4\omega_0 = 4$, numerically computed A = 2.30933 while the theoretically predicted A = 2.3094. At the antiresonance $(\omega = 2\omega_0)$ the numerically computed. $A = A_{\rm ar} = 1.73208$ and the theoretical $A_{\rm ar} = 1.73205$. If ω is irrational then the orbit can be quasiperiodic.

In Fig. 14.11b–d, numerically computed frequency-response amplitude curve in the interval $\omega \in [1,3]$ is plotted for three fixed values of f. A_{ar} varies with f. In Fig. 14.12a the variation of both theoretically and numerically computed A_{ar} as a function of f is presented. For f < 1, $A_{ar} = \sqrt{2(2-f)}$ and it decreases from 2 and becomes $\sqrt{2}$ at f = 1. For f > 1, theoretical A_{ar} is $\sqrt{2}$. Very near f = 1 the numerically calculated A_{ar} deviates slightly with the theoretical A_{ar} . For other values of f > 1 both the theoretical and numerical A_{ar} are the same. Figure 14.12b shows the phase portrait of the system for four values of f. The orbit remains the same for f > 1 implying that A_{ar} is independent of f for f > 1.

14.3 Suppression of Parametric Resonance

Let us show the possibility of suppression of instability (growing solution) and oscillatory motion in parametrically driven systems. These two are also referred as parametric antiresonance [18].

Consider s system of *n*-coupled oscillators with the coupling strength treated as a periodically varying:

$$\ddot{x}_i + \omega_{0i}^2 + \epsilon \sum_{j=1}^n \left(d_{ij} \dot{x}_j + f_{ij} x_j \cos \omega t + g_{ij} x_j \cos \eta t \right) = 0, \quad i = 1, 2, \dots, n.$$
(14.22)

When $g_{ij} = 0$ the resonance at $\omega = 2\omega_{01}$ is the parametric resonance of the first kind. In this case the trivial equilibrium point is unstable for [19]

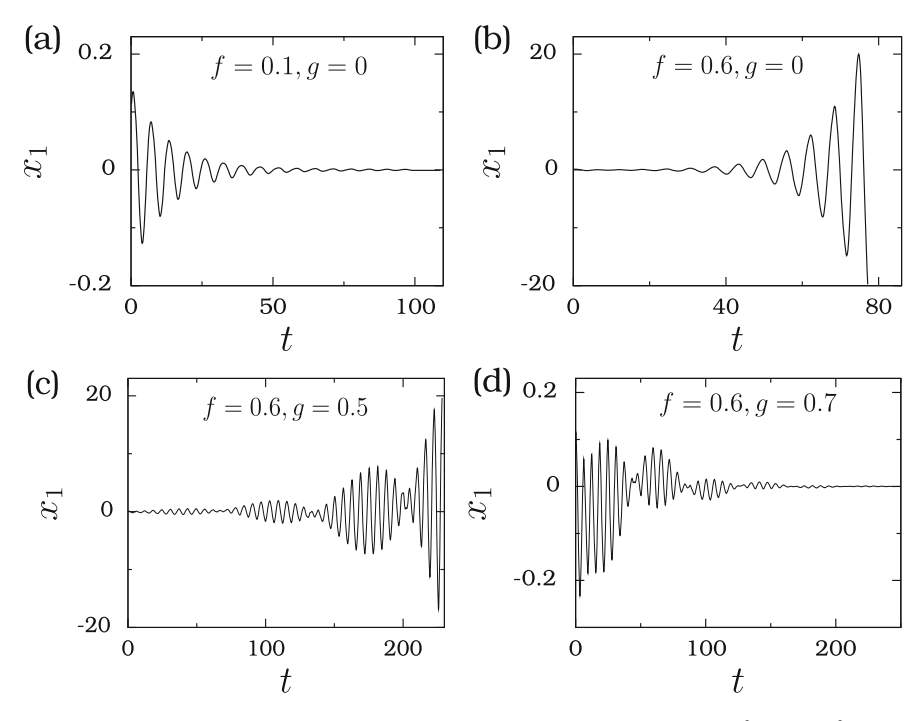


Fig. 14.13 $x_1(t)$ versus t of the system (14.22) with n=2, $d_{ij}=d=0.1$, $\omega_{01}^2=1$, $\omega_{02}^2=4$, $\omega=2\omega_{01}$, $\eta=|\omega_{02}-\omega_{01}|$ and for four sets of values of $f_{ij}=f$ and $g_{ij}=g$. In the subplots (a) and (d) $x_1(t)$ exhibits damped oscillation. In the subplots (b) and (c) the state variable $x_1(t)$ diverges with time

$$\left(\frac{f_{11}}{2\omega_{01}}\right)^2 - d_{11}^2 \ge 0. \tag{14.23}$$

Suppression of parametric instability can be realized by appropriately choosing the values of η and g_{ij} . For simplicity, consider the case of n=2, $d_{ij}=d$, $f_{ij}=f$, $g_{ij}=g$ and $\eta=|\omega_{02}-\omega_{01}|$. Fix d=0.1, $\omega_{01}^2=1$, $\omega_{02}^2=4$ and $\omega=2\omega_{01}$. When g=0 the origin is stable for f<0.2 and unstable for f>0.2. In Fig. 14.13a for g=0.0 and f=0.1, $x_1(t)$ exhibits damped oscillation. The solution grows with time for f=0.6 (Fig. 14.13b). Fix the value of f as 0.6 and vary g. In Fig. 14.13c for g=0.5 the instability persists. Decay of $x_1(t)$ is seen in Fig. 14.13d for g=0.7. The trivial equilibrium point is stable for $g>g_c=0.628$. Figure 14.14 depicts the variation of g_c with f. For g values above g_c suppression of parametric instability occurs.

In certain parametrically driven systems parametric resonance leading to oscillatory motion instead of a growing solution can occur. Suppression of such an oscillatory solution by an additional parametric perturbation with a different frequency of perturbation is possible. To illustrate this consider the system

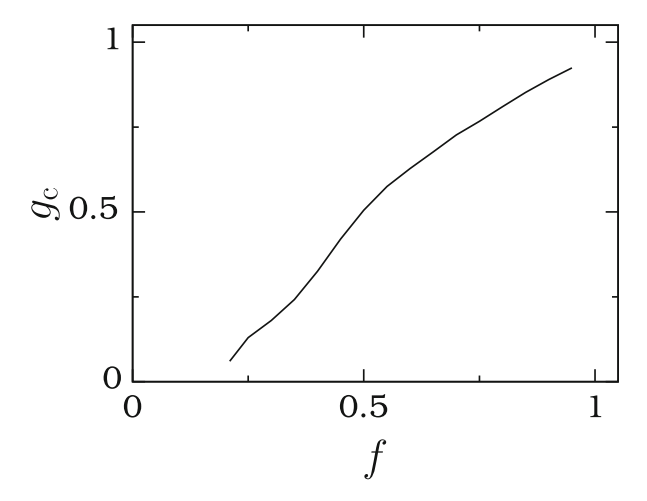


Fig. 14.14 Dependence of g_c , the value of g above which the trivial equilibrium point is stable, on f for the system (14.22) with n = 2

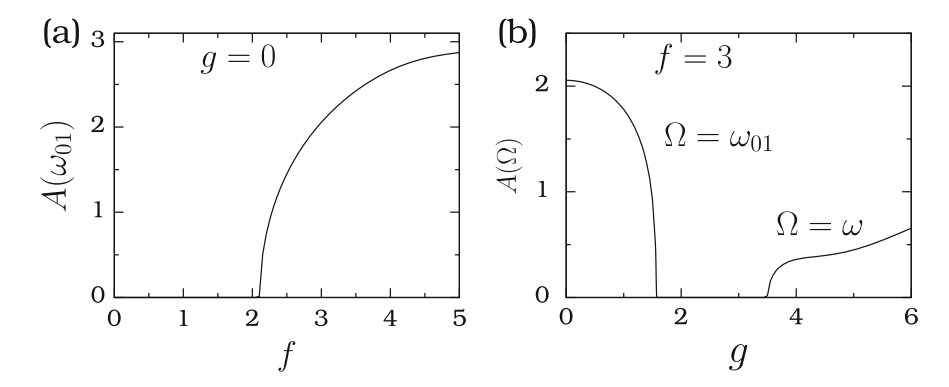


Fig. 14.15 (a) $A(\omega_{01})$ of the component x_1 versus the control parameter f for the system (14.24) with g=0. (b) $A(\omega_{01})$ and $A(\omega)$ versus g for f=3 of the state variable x_1 . The other values of the parameters are $\omega_{01}^2=1$, d=1, $\omega_{02}^2=4$, $\omega=2\omega_{01}$ and $\eta=|\omega_{02}-\omega_{01}|$

$$\ddot{x}_1 + d\dot{x}_1 + \omega_{01}^2 x_1 + f \cos \omega t \sin x_1 + g \cos \Omega t \sin x_2 = 0, \qquad (14.24a)$$

$$\ddot{x}_2 + d\dot{x}_2 + \omega_{02}^2 x_2 + f \cos \omega t \sin x_2 + g \cos \eta t \sin x_1 = 0.$$
 (14.24b)

Figure 14.15a shows the dependence of response amplitude of the state variable x_1 of the above system on f for g=0, $\omega_{01}^2=1$, $\omega_{02}^2=4$, $\omega=2\omega_0$ and d=1. For $f\leq 2.05$ the origin is the stable equilibrium point while it is unstable for f>2.05 and a periodic oscillatory motion is developed. The period of the oscillatory motion is $T=2\pi/\omega_{01}$, that is the frequency component present in the solution is ω_{01} . Now, fix f=3, $\eta=|\omega_{02}-\omega_{01}|$ and switch on the coupling term where the coupling strength is time-dependent. In Fig. 14.15b the amplitude of oscillatory

motion $(A(\omega_{01}))$ decreases with increases in g and for 1.41 < g < 3.5 the unstable equilibrium point $x_1^* = 0$ is stabilized. Then the additional parametric perturbation destabilizes the equilibrium point for g > 3.5 and induces an oscillatory solution with period $T = 2\pi/\omega$ (and not $2\pi/\omega_{01}$).

Parametric antiresonance can be used for suppressing or reducing self-excited oscillation [20–22]. In micromechanical systems vibration damping is low because they usually operate in vacuum. When it is desired to amplify the damping properties of such systems one can make use of parametric antiresonance [23]. Experimental study of parametric antiresonance in an axially forced beam has been studied [24]. In self-excited and auto-parametric unstable systems the antiresonance induced by a parametric excitation leads to stabilization of the systems [18, 25].

14.4 Stochastic Antiresonance

Stochastic antiresonance has been found to occur in a theoretical model equation proposed for the transmission of a periodic signal mixed with a noise through a static nonlinearity [26], squid axons model equation (Hodgkin-Huxley model equation) [27], the time evolution of interacting qubits of quantum systems [28] and certain piece-wise linear systems [29].

In conventional stochastic resonance as shown in Chaps. 2 and 7 the SNR and the response amplitude Q become maximum at a value of noise intensity. In certain nonlinear systems SNR and Q acquire a minimum value rather than the maximum when the noise intensity D is varied from a small value. This is referred as stochastic antiresonance. What types of systems can show stochastic antiresonance? In a linear system the force acting on it is directly proportional to the displacement. If the force on a system varies much slower than the linear one then the system is termed as soft [29] otherwise hard. Certain monostable systems are hard if the applied noise perturbation is weak and turn into soft for sufficiently large noise. It has been pointed out that [29] in such systems stochastic antiresonance can occur. That is, the characteristic measure SNR (or Q) should decrease at first with increase in the noise intensity and then increase.

Consider the overdamped Langevin equation

$$\dot{x} + \frac{\mathrm{d}V}{\mathrm{d}x} = f\cos\omega t + \eta(t),\tag{14.25a}$$

where

$$V(x) = \begin{cases} \alpha_1 |x|, & |x| < a \\ \alpha_2 (|x| - a) + \alpha_1 a, & |x| > a \end{cases}$$
 (14.25b)

is a piece-wise linear potential with only one local minimum and $\eta(t)$ is a Gaussian white noise with intensity D. The potential is shown in Fig. 14.16a. It is assumed that

386 14 Antiresonances

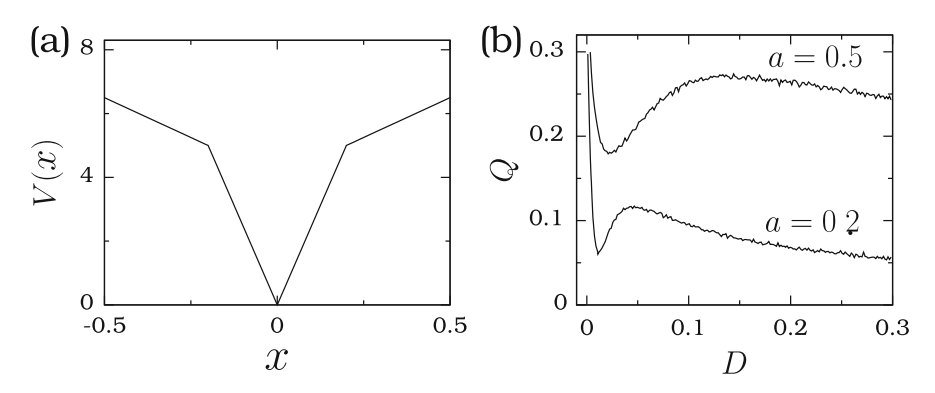


Fig. 14.16 (a) The shape of the potential V(x) given by Eq. (14.25b) with $\alpha_1 = 25$, $\alpha_2 = 5$, and a = 0.2. (b) Numerically computed Q versus D of the system (14.25) for two values of a

 $\alpha_1 > \alpha_2$. In Agudov and Krichigin (2008, Stochastic resonance in an overdamped monostable system, unpublished) an analytical expression for SNR is obtained. As the form of the expression of SNR is complicated one and for the illustrative purpose use the quantity O to characterize the response of the system to a weak periodic input signal and noise. Fix the parameters of the system (14.25) as f = 0.3, $\omega =$ 0.1, $\alpha_1 = 25$ and $\alpha_2 = 5$. Calculate Q as a function of the noise intensity for a = 0.2 and 0.5. Figure 14.16b presents the result. For both a = 0.2 and 0.5 first Q decreases sharply with D, reaches a minimum value at $D = D_{ar}$ and then increases. For $D > D_{ar}$ the response amplitude Q has a resonance peak at a value of $D = D_{r}$ or increases very slowly depending upon the values of the parameters of the system. For a = 0.2, $D_{ar} = 0.011$ and $D_r = 0.0465$ while for a = 0.5, $D_{ar} = 0.021$ and $D_{\rm r} = 0.144$. In Fig. 14.16b first stochastic antiresonance occurs and then stochastic resonance occurs. For small and large D the quantity Q is a decreasing function of D. Nonmonotonic variation of Q occurs for intermediate values of D. Because the system is monostable the effects of antiresonance and resonance are not seen in the time series explicitly.

Stochastic antiresonance has been observed in overdamped systems with the potentials [29]

$$V(x) = \begin{cases} 0, & |x| < a \\ \alpha(|x| - a) + h, & |x| > a, \end{cases}$$
 (14.26)

$$V(x) = \begin{cases} 0, & |x| < a_1 \\ h, & a_1 < |x| < a_2 \\ \infty, & |x| > a_2, \end{cases}$$
 (14.27)

$$V(x) = \frac{x^4}{1 + |x|^3} \,. \tag{14.28}$$

Double stochastic resonance (consequently, a local minimum between resonances) has been realized in double-well potential systems for large frequency of the driving force [30]. For example, in the overdamped system with $V(x) = -x^2/2 + x^4/4$ two resonance peaks are observed when noise intensity is varied for the frequency $\omega = 2$ and 3. The second resonance peak is associated with the conventional interwell motion. The first peak is due to the intrawell mechanism in single-well. That is, first resonance occurring for low noise intensity, for which barrier crossing is occasional, is concerned with the motion almost confined to one well alone. Between two resonance peaks a local minimum occurs.

14.5 Coherence Antiresonance

Consider the dynamical system

$$\dot{x} = (1 - x^2 - y^2)x + (x^2 - y^2 - b)y - \epsilon x^n(t - \tau) + \eta_1(t), \quad (14.29a)$$

$$\dot{y} = (1 - x^2 - y^2) y - (x^2 - y^2 - b) x - \epsilon y^n (t - \tau) + \eta_2(t) , \quad (14.29b)$$

where η_1 and η_2 are the two independent Gaussian white noise with zero mean and noise intensity D. The effect of the parameters η and τ has been reported in [31]. To identify the occurrence of resonance compute the FFT of the state variable x(t). From the power spectrum identify the peak frequency. For a better result compute the FFT for N different realization of $\eta_1(t)$ and $\eta_2(t)$ and obtain an average power spectrum. From the power spectrum identify the dominant peak and the corresponding frequency. Define the quantity [32]

$$\beta_{\rm s} = H \frac{\omega_0}{\Delta \omega} \tag{14.30}$$

where H is the height of the peak in the power spectrum, ω_0 is the frequency of the peak and $\Delta\omega$ is the half-width of the power spectrum about the frequency ω_0 . For the case of the output of a system free from noise containing the frequency ω_0 , H will be finite, $\Delta\omega\to 0$ and β will become large. For a noisy output containing the frequency ω_0 , $\Delta\omega$ will be nonzero and the value of β_s will be reduced. β thus represent the degree of coherence.

Figure 14.17a [31] depicts the variation of β with the time-delay τ for n=3, b=1.2, $\epsilon=1$ and for D=0.05 and 0.005. For both the cases β becomes a minimum at a value of τ . The value of τ at which β becomes a minimum depends on the noise intensity D. The minimum value of β at a value of $\tau=\tau_{\rm ac}$ indicates the maximization of incoherence of the response of the system. That is, the system shows coherence antiresonance at a value of τ . At an another value of τ the quantity β attains a maximum value implying the occurrence of coherence resonance. Coherence antiresonance is realized for a range of fixed values of b.

388 14 Antiresonances

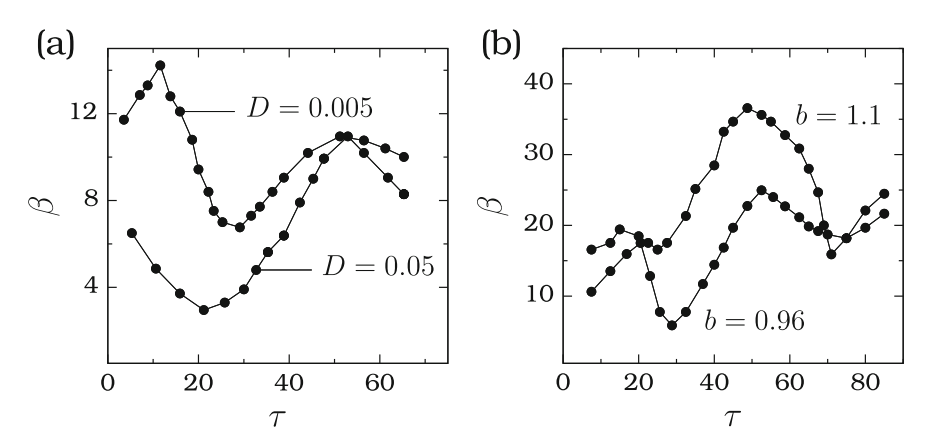


Fig. 14.17 β versus τ for the system (14.29) [31] with n = 3, $\epsilon = 1$, and for (a) two fixed values of D with b = 1.2 and for (b) two fixed values of b with b = 0.008. (With kind permission from Springer Science+Business Media, Ref. [31].)

In Fig. 14.17b β versus τ is shown for D=0.008 and b=0.95 and 1.1. Here again antiresonance occurs when τ is varied. In Fig. 14.17b antiresonance occurs at two values of τ . This figure depicts the effect of the parameter b on coherence resonance and coherence antiresonance. The coherence resonance is more remarkable for large values of b. In contrary to this, the value of β is reduced by decreasing the value of b. That is, antiresonance is more remarkable for smaller values of the control parameter b.

Coherence antiresonance due to time-delayed feedbacks has been found in a model of circadian rhythmicity in Drosophila [33] and in the FitzHugh-Nagumo neuron model subjected to both multiplicative and additive noise [34]. Time-delay can give rise antiresonance with single additive periodic force, vibrational antiresonance and stochastic antiresonance. For example, in Fig. 6.4 for fixed values of ω and γ (strength of the time-delayed feedback term) the amplitude of the response exhibits periodic variation with the time-delayed parameter α . The minima of A represent antiresonance. Similarly, in Fig. 6.7 for a range of fixed values of g the response amplitude attains a minimum value of certain values of α denoting vibrational antiresonance.

14.6 Concluding Remarks

This chapter explored the occurrence of antiresonance in systems subjected to (1) an additive periodic force, (2) a parametric perturbation, (3) free from noise and (4) in the presence of noise. The possibilities of antiresonance of different kinds in time-delayed systems and excitable systems have to be explored.

References 389

In this book the basic aspects and the salient features of certain nonlinear resonances including the antiresonance counterparts of them are presented with specific emphasize on vibrational resonance. So far, in the nonlinear dynamics literature a great interest on resonance has been focused on single systems. In recent years considerable attention is set on coupled systems. Very little is known on resonance on coupled systems. The role of different kinds of interaction between the oscillators on different types of resonance has to be investigated. Further, the progress made so far on the resonance dynamics in infinite degrees of freedom systems is little though there are numerous physically and biologically interesting such systems.

A topic associated with the resonance behaviour is the energy transfer between the oscillators. Complete energy transfer is often realized when the oscillators are resonant. Approaches have to be developed to achieve resonance and maximum energy transfer for a wide range of parametric choices. This is very important because energy transfer governs many natural processes.

References

- 1. S. Belbasi, M.E. Foulaadvand, Y.S. Joe, Am. J. Phys. 82, 32 (2014)
- 2. Z. Agur, J. Theor. Med. 1, 237 (1998)
- 3. W. D'Ambrogio, A. Fregolent, J. Sound Vib. 236, 227 (2000)
- 4. K. Jones, J. Turcotte, J. Sound Vib. 252, 717 (2002)
- 5. D. Hanson, T.P. Waters, D.J. Thompson, R.B. Randall, R.A.J. Ford, Mech. Syst. Signal Process. **21**, 74 (2007)
- 6. J.E. Mottershead, Mech. Syst. Signal Process. 12, 591 (1998)
- 7. B. Lysyansky, O.V. PopoVych, P.A. Tass, J. Neural Eng. 8, 036019 (2011)
- 8. K. Uchino, Smart Mater. Struct. 7, 273 (1998)
- 9. W.B. Jeong, W.S. Yoo, J.Y. Kim, KSME Int. J. 17, 1732 (2003)
- 10. N.C. Lien, G.C. Yao, J. Chin. Inst. Eng. 24, 45 (2001)
- 11. F. Wahl, G. Schmidt, L. Forrai, J. Sound Vib. 219, 379 (1999)
- C. Sames, H. Chibami, C. Hamsen, P.A. Altin, T. Wiek, G. Rempe, Phys. Rev. Lett. 112, 043601 (2014)
- 13. P. Rice, R. Breacha, Opt. Commun. 126, 230 (1996)
- 14. Y. Liu, Y. Zheng, W. Gong, T. Lu, Phys. Lett. A 360, 154 (2006)
- 15. M.I. Dykman, M.V. Fistul, Phys. Rev. B **71**, 10508 (2005)
- 16. S. Rajamani, S. Rajasekar, Phys. Scr. 88, 015010 (2013)
- 17. S. Chakraborty, A. Sarkar, Physica D **254**, 24 (2013)
- 18. L. Pesek, A. Tondl, Eng. Mech. 19, 333 (2012)
- 19. A. Tondl, T. Ruijgrok, F. Verhulst, R. Nabergoj, *Autoparametric Resonance in Mechanical Systems* (Cambridge University Press, Cambridge, 2000)
- 20. A. Tondl, L. Pust, Eng. Mech. 17, 135 (2010)
- 21. A. Tondl, Eng. Mech. 15, 297 (2008)
- M. Pelletier, B. Leang, Antiresonance and vibration suppression application in servo systems. Design News (2010). Document ID 229181
- 23. J. Welte, T.J. Kniffka, H. Ecker, Shock Vib. 20, 1113 (2013)
- 24. H. Ecker, I. Rottensteiner, Nonlinear Model Appl. 2, 149 (2011)
- 25. F. Dohnal, Acta. Mech. **196**, 15 (2008)
- 26. F.C. Blondeau, Phys. Lett. A 232, 41 (1997)

390 14 Antiresonances

- 27. L.S. Borkowski, Phys. Rev. E 82, 041909 (2010)
- 28. D.P.K. Ghikas, A.C. Tzemos, Int. J. Quantum Inf. 10, 1250023 (2012)
- 29. N.V. Agudov, A.V. Krichigin, Radiophys. Quantum Electron. 51, 812 (2008)
- 30. M. Evstigneev, P. Reimann, V. Pankov, R.H. Prince, Europhys. Lett. 65, 7 (2004)
- 31. P. Zhu, D.C. Mei, Eur. Phys. J. B 87, 109 (2014)
- 32. X. Sum, M. Perc, Q. Lu, J. Kurths, Chaos 18, 023102 (2008)
- 33. L. Ji, X. Wei, Q. Jin, M. Yu, Noise induced anticoherence resonance in a delayed circadian rhythm system, in *Proceedings of the International Workshop on Chaos-Fractals Theories and Applications* (IEEE Computer Society, 2009), p. 103
- 34. Y. Gao, J. Wang, Phy. Rev. E 86, 051914 (2012)

Appendix A Classification of Equilibrium Points of Two-Dimensional Systems

An *equilibrium point* (fixed point) is a steady state, that is a rest state, of a system. When a system is found at an equilibrium point at some time t_0 then it will remain in it for $t > t_0$. Consider a system described by the equation of motion

$$\dot{X} = F(X) , \qquad (A.1)$$

where $X = (x_1, x_2, \dots, x_n)^T$ and $(F_1, F_2, \dots, F_n)^T$. Since the state variables of a dynamical system do not change in time at an equilibrium state X^* , one can determine all the equilibrium points from

$$\dot{X}^* = 0 = F(X^*) \ . \tag{A.2}$$

The roots of the Eq. (A.2) are the equilibrium points. A system can have one or more or even no equilibrium point. When the neighbouring trajectories of an equilibrium point X^* approach it asymptotically in the limit $t \to \infty$ then it is said to be *stable*. X^* is *unstable* when the neighbouring trajectories move away from it as $t \to \infty$.

In order to identify the stable/unstable nature of X^* substitute

$$X = X^* + \delta X , \quad ||\delta X|| \ll 1 \tag{A.3}$$

where $\delta X = (\xi_1, \, \xi_2, \cdots, \, \xi_n)^{\mathrm{T}}$ in (A.1) and obtain the linearized equation

$$\delta \dot{X} = \frac{\partial F}{\partial X} \bigg|_{X = X^*} \delta X = A \, \delta X \,, \tag{A.4}$$

where A is called the Jacobian matrix with the elements

$$A_{ij} = \frac{\partial F_i}{\partial x_i} \bigg|_{X = X^*} . \tag{A.5}$$

© Springer International Publishing Switzerland 2016 S. Rajasekar, M.A.F. Sanjuan, *Nonlinear Resonances*, Springer Series in Synergetics, DOI 10.1007/978-3-319-24886-8 The solution of (A.4) can be written as

$$\delta X(t) = \delta X(0) e^{At}. \tag{A.6}$$

If A is diagonalized then

$$A\,\hat{e}_i = \lambda_i \hat{e}_i \,, \quad i = 1, 2, \cdots, n \tag{A.7}$$

where λ_i 's and \hat{e}_i 's are the eigenvalues and eigenvectors, respectively. If the eigenvectors are linearly independent then

$$\delta X(0) = \sum_{i=1}^{n} C_i \,\hat{e}_i \,. \tag{A.8}$$

Substitution of (A.7) and (A.8) in (A.6) and the use of

$$e^{At} = I + tA + \frac{t^2 A^2}{2!} + \cdots$$
 (A.9)

lead to the equation

$$\delta X(t) = \sum_{i=1}^{n} C_i e^{\lambda_i t} \hat{e}_i.$$
 (A.10)

For the stability of the equilibrium point the requirement is $\delta X(t) \to 0$ as $t \to \infty$. From Eq. (A.10) it is easy to note that $\delta X(t) \to 0$ as $t \to \infty$ only if the real parts of all the λ_i 's are less than zero for all i.

For a one-dimensional system $\dot{x} = F(x)$ when an equilibrium points is stable (unstable) then the trajectories started in the neighbourhood of it approach (move away from) it along a straight-line path. Other types of paths are not possible (why?).

For two-dimensional systems of the form $\dot{x} = F(x, y)$. $\dot{y} = g(x, y)$ the classification of equilibrium points [1] is summarized below:

1. Stable Star/Node

When the eigenvalues are real and $\lambda_1 = \lambda_2 < 0$ then the trajectories starting in the neighbourhood of an equilibrium point in phase space approach it along straight-line paths in the limit $t \to \infty$ and the equilibrium point is said to be *stable star*. For $\lambda_1 \neq \lambda_2$ and both < 0 the equilibrium point is a *node* and the trajectories in the neighbourhood of it are attracted exponentially.

2. Unstable Star/Node

In the case of $\lambda_1 = \lambda_2 > 0$ with both being real the trajectories move away from the equilibrium point along straight-line paths. The equilibrium point is then an *unstable star*. The equilibrium point is an *unstable node* if $\lambda_1 \neq \lambda_2 > 0$ for which the trajectories move away from the equilibrium point exponentially.

Reference 393

3. Stable/Unstable Focus

For complex conjugate eigenvalues with negative (positive) real parts the trajectories starting in the neighbourhood of an equilibrium point approach (move away) it along spiral paths. Such an equilibrium point is said to be *stable* (*unstable*) focus.

4. Elliptic/Center

If the eigenvalues are pure imaginary then the trajectories in the neighbourhood of an equilibrium point neither approach it nor deviate from it but form closed orbits about it. The equilibrium point is then called a *center* or an *elliptic point*.

5. Saddle

When one of the eigenvalues is real and positive while the other is real and negative then, generally, the trajectories move away from the equilibrium point along hyperbolic curves. However, only for certain initial conditions the trajectories approach the equilibrium point. This type of equilibrium point is called a *saddle* and is unstable.

6. Degenerate Cases

- 1. For $\lambda_1 = \lambda_2 = 0$ with $A = \begin{pmatrix} 0 & 0 \\ 0 & 0 \end{pmatrix}$ the equilibrium point is degenerate. That is, every point in phase space is an equilibrium point.
- 2. When $\lambda_1 = \lambda_2 = 0$ and $A = \begin{pmatrix} 0 & 1 \\ 0 & 0 \end{pmatrix}$ then all points on the *x*-axis are equilibrium points and the trajectories are parallel to the *x*-axis.
- 3. If $\lambda_1 = 1$ and $\lambda_2 = 0$ then all the points on the y-axis are unstable equilibrium points. The trajectories approach the equilibrium points along paths parallel to the x-axis.

For more details on the classification of equilibrium points two- and three-dimensional systems one may refer to the [1].

Reference

1. M. Lakshmanan, S. Rajasekar, Nonlinear Dynamics: Integrability, Chaos and Patterns (Springer, Berlin, 2003)

Appendix B **Roots of a Cubic Equation**

This appendix presents all the roots of the cubic equation (a polynomial of degree 3) of the form

$$y^3 + ay^2 + by + c = 0. (B.1)$$

In the year 1545 the Italian mathematician Girolamo Cardano (1501–1576) wrote his Ars Magna (Great Art) where the method known today as Cardano method was used to solve the roots of the cubic equation. Here, we present the trigonometric (and hyperbolic) method due to François Viete.

First eliminate y^2 in Eq. (B.1). The substitution

$$y = x - \frac{a}{3} \tag{B.2}$$

in Eq. (B.1) gives the equation

$$x^3 - qx - r = 0$$
, (B.3a)

where

$$q = \frac{1}{3}a^2 - b$$
, $r = -\frac{2}{27}a^3 + \frac{1}{3}ab - c$. (B.3b)

It is convenient to specify the roots of Eq. (B.3) separately for the following five cases [1].

- (i) $27r^2 \le 4q^3$, $q \ne 0$ (ii) $27r^2 > 4q^3$, $q \ne 0$
- (iii) $q = 0, r \neq 0$
- (iv) q = 0, r = 0
- (v) $q \neq 0, r = 0$

Case (i): $27r^2 \le 4q^3$, $q \ne 0$

There are three real roots and are given by

$$x_1 = 2\sqrt{q/3} \cos(\phi/3)$$
, (B.4a)

$$x_2 = -2\sqrt{q/3} \cos((\pi - \phi)/3)$$
, (B.4b)

$$x_3 = -2\sqrt{q/3} \cos((\pi + \phi)/3)$$
, (B.4c)

where

$$\phi = \cos^{-1} \left[(3/q)^{3/2} r/2 \right]$$
 (B.4d)

Case (ii): $27r^2 > 4q^3$, $q \neq 0$

Equation (B.3) has one real root and two complex roots. The expressions for the roots depend on the combinations of the signs of q and r. There are four subcases.

(a)
$$q, r > 0$$

The real root is given by

$$x_1 = 2\sqrt{q/3}\cosh(\phi/3), \quad \phi = \cosh^{-1}\left[(3/q)^{3/2}r/2\right].$$
 (B.5)

To obtain the complex conjugate roots divide Eq. (B.3) by $(x - x_1)$ and arrive at the quadratic equation

$$x^{2} + x_{1}x + (x_{1}^{2} - q) = 0. (B.6)$$

Then the two complex roots are

$$x_{2,3} = \frac{1}{2} \left[-x_1 \pm \sqrt{x_1^2 - 4(x_1^2 - q)} \right].$$
 (B.7)

(b) q < 0, r > 0

The real root is given by

$$x_1 = 2(-q/3)^{1/2} \sinh(\phi/3), \quad \phi = \sinh^{-1} \left[(-3/q)^{3/2} r/2 \right].$$
 (B.8)

Then the two complex roots are obtained from Eq. (B.7).

(c)
$$q < 0, r < 0$$

The change of variable $x \to -x$ in Eq. (B.3) yields the equation $x^3 - qx - (-r) = 0$. This is simply the case (ii)b. After obtaining the roots change their signs.

Reference 397

(*d*)
$$q > 0$$
, $r < 0$

The substitution $x \to -x$ in Eq. (B.3) gives an equation with q > 0, r > 0 and is the case (ii)a.

Case (iii): $q = 0, r \neq 0$

Equation (B.3) possesses one real root and a pair of complex root. The real root is given by

$$x_1 = \operatorname{sgn}(r)(|r|)^{1/3}$$
, (B.9)

where sgn(r) is sign of r. The complex roots are given by Eq. (B.7) with q = 0.

Case (iv): q = 0, r = 0

In this case Eq. (B.3) becomes $x^3 = 0$ and obviously its root is x = 0 with multiplicity 3.

Case (v): $q \neq 0, r = 0$

When r=0 and $q \neq 0$ Eq. (B.3) becomes $x(x^2-q)=0$. For q>0 the equation has three real roots and are $x_1=0$, $x_{2,3}=\pm \sqrt{q}$. For q<0, its roots are $x_1=0$ and $x_{2,3}=\pm i\sqrt{-q}$.

Finally, for all the cases the roots of Eq. (B.1) are obtained from the Eq. (B.2).

Example

Let us determine the roots of $y^3 - y^2 - 4y + 4 = 0$.

First eliminate y^2 in the given equation and write it in the standard form, Eq. (B.3). For the given equation a = -1, b = -4 and c = 4. Therefore, the change of variable y = x + 1/3 converts the given equation into

$$x^3 - qx - r = 0$$
, $q = 13/3$, $r = -70/27$. (B.10)

Since $27r^2 (= 181.48 \cdots) < 4q^3 (= 325.48 \cdots)$ Eq. (B.10) has three real roots. From Eq. (B.4d) ϕ is calculated as 2.414 radians. Then the roots computed from Eq. (B.4) are

$$x_1 = 1.66666 \cdots$$
, $x_2 = -2.33333 \cdots$, $x_3 = 0.66666 \cdots$. (B.11)

Finally, the roots of the given equation are $y_1 = 2$, $y_2 = -2$ and $y_3 = 1$.

Reference

1. L.A. Pipes, L.R. Harvill, *Applied Mathematics for Engineers and Physicists*, 3rd edn. (McGraw-Hill, Singapore, 1984)

Appendix C Analog Circuit Simulation of Ordinary Differential Equations

The analogue circuit simulation is a landing place to investigate the dynamics of dynamical systems described by linear and nonlinear ordinary differential equations. The operational amplifier (op-amp) based circuits such as inverter, scale changer, summer, integrator, summing integrator form the basic building blocks of analog circuit simulations [1, 2]. For implementing certain piecewise linear functions and certain nonlinear functions such as trigonometric functions some special circuits can be designed.

The governing evolution equation of a system can either be directly implemented as an analog circuit or it can be rescaled before constructing the circuit. The purpose of rescaling of an ordinary differential equation (ode) is to set the values of the variables in the evolution equations in a convenient operational range of the opamp. That is, the input and the output signals in the circuit should be higher than the internal noise level of the circuit and should be lower than the saturation voltage of the op-amp, otherwise clipping will affect the actual dynamics of the variable.

This appendix briefly outlines the construction of analog circuits of odes.

C.1 Building Blocks of an Analog Circuit

The op-amps in combination with resistors and capacitors can perform several fundamental mathematical operations such as scale changing, addition, subtraction, averaging, multiplication and division. Op-amps based inverting amplifier, inverting summing amplifier, subtractor, integrator and inverting summing integrator are utilized in the analog circuit designs. A single op-amp 8-pin mini dual in-line package (DIP) is shown in Fig. C.1. The pin configuration details are given in Table C.1. μ A741, TL071, TL081, LM741, and LM711 are some of the popular single op-amp ICs. TL082 is a commonly used two op-amp IC.

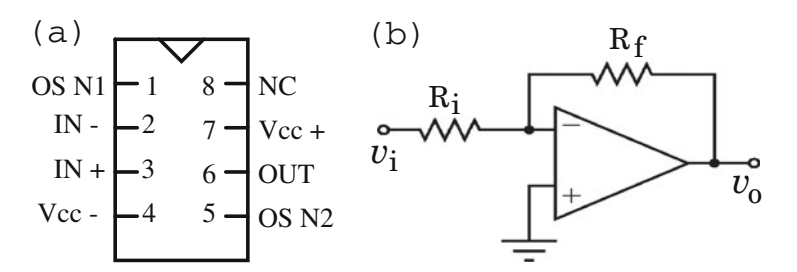


Fig. C.1 (a) Pin diagram of a single op-amp 8-pin mini DIP. (b) A schematic of an inverting amplifier

Table C.1 Pin configuration information of a single op-amp 8-pin mini DIP

| Pin No. | Configuration |
|---------|------------------------|
| 1 | Offset-null pin—1 |
| 2 | Inverting input |
| 3 | Non-inverting input |
| 4 | Power supply—negative |
| 5 | Offset-null pin—2 |
| 6 | Output |
| 7 | Power supply—positive |
| 8 | No internal connection |

C.1.1 Inverting Amplifier

Denote v_i and v_o as the input and output voltages of an op-amp. An inverting amplifier changes the sign of the input signal. The output of an inverting amplifier shown in Fig. C.1b is

$$v_{\rm o} = -\left(\frac{R_{\rm f}}{R_{\rm i}}\right)v_i\,,\tag{C.1}$$

where R_i and R_f are the input and feedback resistances, respectively. For a constant v_i , the choice $R_f = R_i$ gives $v_o = -v_i$, For a time varying input signal, for example, a sinusoidal function, the output signal will be 180° out of phase. The output signal can be amplified or attenuated by the factor R_f/R_i with respect to the input signal.

C.1.2 An Inverting Summing Amplifier

Multiple signals can be added using op-amp. Each signal can be connected to the input of the op-amp through a resistor. Such a circuit is called a *summing*

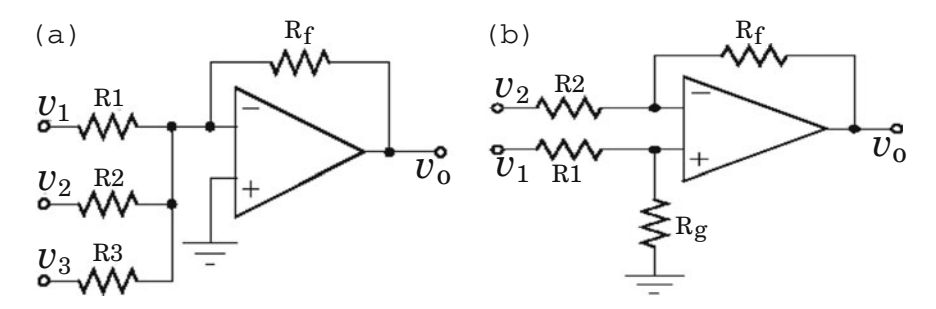


Fig. C.2 Schematic of (a) an inverting summing amplifier and (b) a subtractor

amplifier. An inverting summing amplifier with three inputs v_1 , v_2 and v_3 is shown in Fig. C.2a. The output voltage v_0 of the inverting summer is given by

$$v_{\rm o} = -\left(\frac{R_{\rm f}}{R1}v_1 + \frac{R_{\rm f}}{R2}v_2 + \frac{R_{\rm f}}{R3}v_3\right).$$
 (C.2)

The output is the inverted and sum of the input signals. For $R1 = R2 = R3 = R_f$ the output v_0 is

$$v_0 = -(v_1 + v_2 + v_3)$$
 (C.3)

C.1.3 A Subtractor

A circuit diagram for obtaining the difference signal $v_1 - v_2$ is depicted in Fig. C.2b and is called a *voltage subtractor*. In this circuit the output voltage v_0 is given by

$$v_{\rm o} = -\frac{R_{\rm f}}{R2} v_2 + \frac{R_{\rm g}}{R1 + R_{\rm g}} \left(1 + \frac{R_{\rm f}}{R2} \right) v_1 .$$
 (C.4)

If $R1 = R2 = R_f = R_g = R$ then

$$v_0 = v_1 - v_2$$
 (C.5)

Note that if v_1 is set to 0 then the circuit in Fig. C.2b becomes an inverting amplifier.

C.1.4 An Integrator

If the resistive feedback in an inverting amplifier is replaced with a capacitor then the resultant circuit is called an *integrator*. In an analog circuit design of an ode,

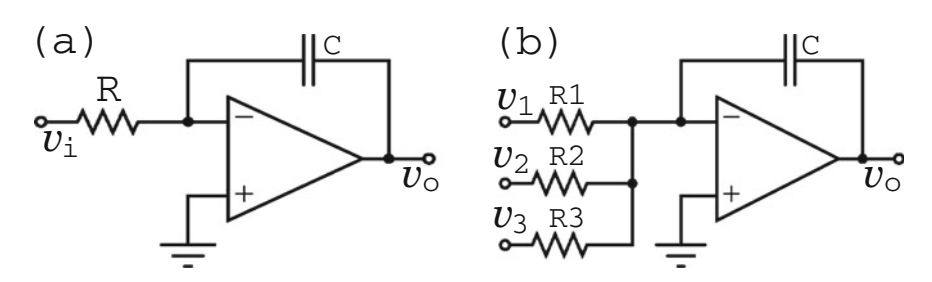


Fig. C.3 Schematic of (a) an inverting integrator circuit and (b) a summing inverting integrator circuit

integrators are preferred over differentiators because an integrator is more stable and relatively less sensitive to noise. The schematic of an integrator is given in Fig. C.3a. The output voltage of this circuit is integration of its input voltage with respect to time:

$$v_{\rm o} = -\frac{1}{RC} \int v_{\rm i} \, \mathrm{d}t \tag{C.6}$$

The minus sign in the Eq. C.6 is due to the inverting amplifier configuration of the op-amp. For multiple input voltages, for example, three input voltages the integrator circuit is given in Fig. C.3b and the output voltage is

$$v_{\rm o} = -\frac{1}{C} \int \left(\frac{v_1}{R1} + \frac{v_2}{R2} + \frac{v_3}{R3} \right) dt$$
 (C.7)

C.1.5 Multiplier

Dedicated standalone IC chips are available for performing multiplication operation. Figure C.4a shows the pin diagram of a multiplier chip. Its simplified internal structure is given in Fig. C.4b. It generally consists of two differential amplifiers in the input stage and a buffer isolation in the output stage.

In Fig. C.4 X1 and X2 are X-multiplicand of noninverting and inverting inputs, respectively, Y1 and Y2 are Y-multiplicand of noninverting and inverting inputs, respectively, of the differential amplifiers and Z is the summing input. The product output W of a typical multiplier is,

$$W = \frac{(X1 - X2)(Y1 - Y2)}{10} + Z. \tag{C.8}$$

The dividing factor 10 is used to avoid the overflow of product output. AD633, AD532 and AD534 are some of the standard multiplier chips.

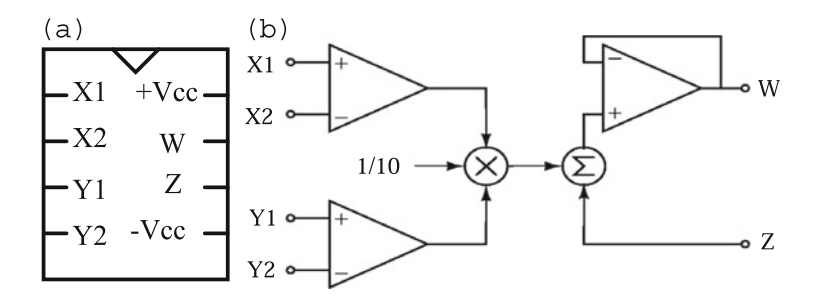


Fig. C.4 (a) 8-pin mini DIP of a multiplier chip. (b) Simplified internal structure of a multiplier chip

C.2 Analog Circuit for Duffing Oscillator Equation

In order to construct an analog circuit for the Duffing oscillator Eq. (1.1), first write it in the form

$$\dot{x} = y \,, \tag{C.9a}$$

$$\dot{y} = -dy - \omega_0^2 x - \beta x^3 + f \sin \omega t, \tag{C.9b}$$

where without loss of generality the force $\cos \omega t$ is replaced by $\sin \omega t$ since such a change will not affect the qualitative behaviour of the system and it is convention to denote the external sinusoidal force in an electronic circuit as $\sin \omega t$. As mentioned earlier in this appendix use of integration is preferred over differentiator. Therefore, integrate Eq. (C.9) and obtain

$$x = \int y dt \,, \tag{C.10a}$$

$$y = \int \left(-dy - \omega_0^2 x - \beta x^3 + f \sin \omega t\right) dt.$$
 (C.10b)

For the analog circuit use the variables V and U instead of x and y, $\omega = \omega'$ and rewrite the above equation as

$$V = \int U \mathrm{d}t \,, \tag{C.11a}$$

$$U = \int \left(-dU - \omega_0^2 V - \beta V^3 + f \sin \omega' t\right) dt.$$
 (C.11b)

The analog circuit for the Eq. (C.11) is depicted in Fig. C.5.

Now, from the outputs of the OA1 and OA2 one can construct the equation of the circuit and verify that it indeed the Duffing oscillator equation and represent the parameters of the equation in terms of the circuit elements. The outputs of OA1 and OA2 denoted as U and V, respectively, are given by

$$U = -\frac{1}{C} \int \left(\frac{U}{R1} - \frac{V}{R2} - \frac{V^3}{100R3} + \frac{f}{R} \sin \omega' t \right) dt, \qquad (C.12a)$$

$$V = -\frac{1}{C} \int \frac{U}{R} \, \mathrm{d}t \,. \tag{C.12b}$$

Differentiation of Eq. (C.12) with respect to t gives

$$\frac{dU}{dt} = -\frac{1}{C} \left(\frac{U}{R1} - \frac{V}{R2} - \frac{V^3}{100R3} + \frac{f}{R} \sin \omega' t \right) , \qquad (C.13a)$$

$$\frac{\mathrm{d}V}{\mathrm{d}t} = -\frac{1}{RC}U. \tag{C.13b}$$

Differentiation of Eq. (C.13b) with respect t and using Eq. (C.13a) yield

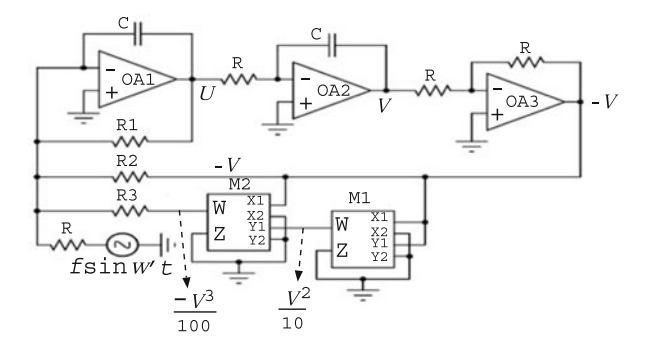
$$RC^{2}\frac{d^{2}V}{dt^{2}} + \frac{RC}{R1}\frac{dV}{dt} + \frac{1}{R2}V + \frac{1}{100R3}V^{3} = \frac{f}{R}\sin\omega't.$$
 (C.14)

The above equation describing the dynamics of the circuit shown in Fig. C.5 is in the form of Duffing oscillator equation. In order to bring it into a dimensionless form introduce the change of variables t = RCt', $\omega' = RC\omega$, V = x and then drop the ' in t'. The result is the Duffing oscillator equation

$$\ddot{x} + d\dot{x} + \omega_0^2 x + \beta x^3 = f \sin \omega t , \qquad (C.15)$$

where d=R/R1, $\omega_0^2=R/R2$ and $\beta=R/R3$. In the circuit fix C=100 nf and R=10 k Ω . For R1=100 k Ω , R2=10 k Ω , and R3=5 k Ω the corresponding values of the parameters in Eq. (C.15) are d=0.1, $\omega_0^2=1$ and $\beta=2$.

Fig. C.5 An analog circuit for the Duffing oscillator Eq. (1.1)



References 405

References

 D. Roy Choudhury, S.B. Jain, *Linear Integrated Circuits* (New Age International, New Delhi, 2012)

2. D.G. Luchinsky, P.V.E. McClintock, M.I. Dykman, Rep. Proc. Phys. 61, 889 (1998)

Index

| Analog circuit of | Chua's |
|--|--|
| Duffing oscillator, 404 | circuit, 226, 237 |
| Mathieu equation, 269 | ghost-vibrational resonance, 258, 259 |
| an overdamped bistable system, 231 | vibrational resonance, 228 |
| two-coupled Duffing oscillators, 376 | diode, 226, 235 |
| van der Pol oscillator, 22 | Coherence |
| Antiresonance, 367 | antiresonance, 387 |
| coherence, 387 | parameter, 336 |
| in a damped linear oscillator, 372 | resonance, 333, 337 |
| parametric, 379 | |
| stochastic, 385, 386 | |
| in a two-coupled Duffing oscillators, 373, 377 | Duffing oscillator, 41, 84, 120 asymmetry, 100 |
| in an undamped linear oscillator, 371 | autoresonance, 301, 302, 307, 314 |
| in van der Pol oscillator, 381 | ghost-vibrational resonance, 250, 253, |
| Autocorrelation, 334 | 254 |
| Autonomous resonance, 333 | jump phenomenon, 8 |
| Autoresonance, 293–295, 299 | parametric resonance, 273, 274, 280 |
| in Duffing oscillator, 301 | potential, 84, 85, 120 |
| in a four-wave mixing, 319 | vibrational resonance, 88, 123 |
| in a nonlinear Schrödinger equation, 321 parametric, 293 | violational resonance, 66, 125 |
| in a quantum anharmonic oscillator, 327 | Edges, 203 |
| quantum analogue, 322 | Equilibrium point, 391 |
| in quantum Morse oscillator, 326 | stable, 391 |
| • | unstable, 391 |
| | Excitable |
| Bellows map, 218 | electronic circuit, 235 |
| ghost-stochastic resonance, 247 | system, 119 |
| stochastic resonance, 218 | stochastic resonance, 134 |
| Bernoulli shift map, 345 | vibrational resonance, 132 |
| Chaotic resonance, 333, 348 | Faraday instability, 261 |
| Chirp rate, 294 | Firing, 242 |

© Springer International Publishing Switzerland 2016 S. Rajasekar, M.A.F. Sanjuan, *Nonlinear Resonances*, Springer Series in Synergetics, DOI 10.1007/978-3-319-24886-8 408 Index

| FitzHugh–Nagumo equation, 131, 334 | resonance, 15 |
|--|--|
| stochastic resonance, 134 | vibrational resonance, 109 |
| vibrational resonance, 132 | Mulitple time-delay, 161 |
| Fokker–Planck equation, 61 | |
| Frequency-locking, 21 | |
| Frequency-response equation | n-coupled |
| for Duffing oscillator, 6 | Bellows maps, 217 |
| for a jerk system, 18 | Duffing oscillators, 206, 211, 368 |
| for a linear system, 6 | Network, 203 |
| for <i>n</i> -coupled Duffing oscillators, 208 | one-way coupled, 205 |
| for Morse oscillator, 15 | Nodes, 203 |
| for a overdamped Duffing oscillator, 11 | , |
| for a pendulum system, 13 | |
| for a time-delayed Duffing oscillator, 165 | Overdamped system, 49, 61, 64, 66, 105, 127, |
| for a time delayed Builing oscillator, 100 | 145, 152, 161, 170, 177, 230, 385 |
| | 143, 132, 101, 170, 177, 230, 303 |
| Gamma distributed time-delay, 185 | |
| Ghost resonance, 242, 244 | Parametric |
| stochastic, 242, 245 | antiresonance, 379 |
| vibrational, 242, 249, 250, 253, 257–259 | oscillator, 261 |
| violational, 242, 249, 230, 233, 231–239 | resonance, 261, 264, 379 |
| | |
| Hustansia 150 | analog circuit simulation, 268 |
| Hysteresis, 150 | effective, 275 |
| | in a Duffing equation, 273, 274, 280 |
| T | in Mathieu equation, 264, 276 |
| Integrative time-delay, 161 | in a pendulum system, 271 |
| Integrative time-delayed feedback, 188 | quantum analogue, 285 |
| Interspike interval, 134 | in a quantum system, 283 |
| Isochronous oscillators, 35 | roll, 287 |
| | suppression, 379 |
| | Pendulum system, 12, 140, 145, 294 |
| Jacobian matrix, 391 | autoresonance, 294, 299 |
| Jerk equation, 16 | frequency-response equation, 13 |
| Jump | parametric resonance, 271 |
| frequency, 352 | stochastic resonance, 152 |
| phenomenon, 8 | vibrational resonance, 142, 145 |
| | Phase-locking, 21 |
| | Piezoelectric oscillator, 72 |
| Kramers time, 53 | |
| | |
| | Quantum |
| Ladder climbing, 322 | analogue of autoresonance, 326, 327 |
| Limiting phase orbits, 311, 313 | forced resonance, 32, 111 |
| Logistic map, 345 | parametric resonance, 285 |
| | vibrational resonance, 112, 113 |
| | Quintic oscillator, 90 |
| Mathieu equation, 263, 276, 282, 356 | - |
| Mean residence time, 41 | |
| Modified Chua's circuit equation, 146, 155 | Random delay, 162 |
| coherence resonance, 338 | Repressilator model, 205 |
| stochastic resonance, 156 | Residence time, 41 |
| vibrational resonance, 148 | Resonance |
| Morse oscillator, 14, 106 | auto, 293 |
| frequency-response equation, 15 | autonomous, 333 |
| 1 - J F | autonomous, ooo |

Index 409

| chaotic, 333, 348 | in a modified Chua's circuit equation, |
|---|---|
| coherence, 333, 337 | 156 |
| definition, 1 | in a monostable system, 63 |
| disaster, 34 | in <i>n</i> -coupled Bellows maps, 219, 220 |
| in Duffing oscillator, 8, 10, 11 | in a pendulum system, 152 |
| effective parametric, 275 | in a quantum system, 69 |
| ghost, 242, 249 | Subthreshold, 131 |
| stochastic, 242, 247 | Synchronization, 77 |
| vibrational, 242 | |
| in a jerk system, 18 | |
| in a linear system, 7, 18, 169 | Tent map, 345 |
| in Morse oscillator, 15 | Time-delay |
| in a <i>n</i> -coupled Duffing oscillators, 210 | constant, 161 |
| in NEM resonators, 26, 27 | gamma distributed, 185 |
| parametric, 379 | integrative, 161, 188 |
| in a pendulum system, 13 | multiple, 161 |
| quantum, 32 | random, 162 |
| slow passage, 351 | state-dependent, 162, 191, 194 |
| stochastic, 39 | time-dependent, 161 |
| in a time-delayed Duffing oscillator, 166, | Transient, 90 |
| tongues, 264, 271, 277, 283 | |
| in van der Pol oscillator, 21 | Unidirectional coupling, 204 |
| vibrational, 88 | 1 0 |
| Resonant frequency, 1, 87, 122, 367 | |
| Resonators, 2 | Van der Pol oscillator, 19, 379 |
| | frequency-locking, 21 |
| | resonance, 21 |
| Signal-to-noise ratio, 40, 232 | Vertices, 203 |
| for a linear system, 64, 68 | Vibrational resonance, 88 |
| for a modified Chua's circuit equation, | in a Chua's circuit, 228 |
| 156 | in Duffing oscillator, 88, 103, 106, 123 |
| for a monostable system, 62 | in an excitable system, 132 |
| for a overdamped bistable system, 54 | ghost, 249, 250, 253, 257–259 |
| for a quantum dot, 71 | in a laser system, 234 |
| for a quantum double-well system, 70 | in a <i>n</i> -coupled Duffing oscillators, 216 |
| Stochastic | in a modified Chua's circuit equation, 148 |
| antiresonance, 385, 386 | in Morse oscillator, 109 |
| encoding, 72 | in an overdamped system, 232 |
| oscillator, 333 | in a pendulum system, 142, 145 |
| resonance, 39 | in a quintic oscillator, 94, 130 |
| aperiodic, 78 | in a time-delayed Duffing oscillator, 174, |
| in a Bellows map, 218 | 179, 180, 183, 187, 190, 192–194 |
| in Duffing oscillator, 41 | 177, 100, 100, 107, 170, 172 174 |
| ghost, 245, 249 | |
| in a linear system, 69 | Waiting time, 134, 241, 243 |
| • • | |